

POLISH SOCIETY OF THEORETICAL AND APPLIED MECHANICS

**JOURNAL OF THEORETICAL
AND APPLIED MECHANICS**

No. 2 • Vol 54

Quarterly

WARSAW, APRIL 2016

JOURNAL OF THEORETICAL AND APPLIED MECHANICS

(until 1997 Mechanika Teoretyczna i Stosowana, ISSN 0079-3701)

Beginning with Vol 45, No. 1, 2007, *Journal of Theoretical and Applied Mechanics* (JTAM) has been selected for coverage in Thomson Reuters products and custom information services. Now it is indexed and abstracted in the following:

- **Science Citation Index Expanded** (also known as SciSearch®)
- **Journal Citation Reports/Science Edition**

Advisory Board

MICHAŁ KLEIBER (Poland) – Chairman

JORGE A.C. AMBROSÍO (Portugal) * ANGEL BALTOV (Bulgaria) * ROMESH C. BATRA (USA) *
ALAIN COMBESCURE (France) * JÜRI ENGELBRECHT (Estonia) * WITOLD GUTKOWSKI (Poland) *
JÓZEF KUBIK (Poland) * GERARD A. MAUGIN (France) * ZENON MRÓZ (Poland) *
RYSZARD PARKITNY (Poland) * EUGENIUSZ ŚWITOŃSKI (Poland) * HISAAKI TOBUSHI (Japan) *
DIETER WEICHERT (Germany) * JOSE E. WESFREID (France) * JÓZEF WOJNAROWSKI (Poland) *
JOSEPH ZARKA (France) * VLADIMIR ZEMAN (Czech Republic)

Editorial Board

WŁODZIMIERZ KURNIK – Editor-in-Chief,

KRZYSZTOF DEMS, KURT FRISCHMUTH (Germany), PIOTR KOWALCZYK, ZBIGNIEW KOWALEWSKI,
TOMASZ KRZYŻYŃSKI, TOMASZ ŁODYGOWSKI, EWA MAJCHRZAK, WIESŁAW NAGÓRKO,
JANUSZ NARKIEWICZ, BŁAŻEJ SKOCZEŃ, ANDRZEJ STYCZEK, ANDRZEJ TYLIKOWSKI,
UTZ VON WAGNER (Germany), JERZY WARMIŃSKI, ELŻBIETA WILANOWSKA – Secretary

Language Editor – PIOTR PRZYBYŁOWICZ

Technical Editor – EWA KOISAR



Articles in JTAM are published under Creative Commons Attribution – Non-commercial 3.0. Unported License <http://creativecommons.org/licenses/by-nc/3.0/legalcode>. By submitting an article for publication, the authors consent to the grant of the said license.

* * * * *

Editorial Office

Building of Civil Engineering Warsaw University of Technology
Al. Armii Ludowej 16, room 650
00-637 Warszawa, Poland
phone (+48 22) 825 7180, (+48) 664 099 345, e-mail: biuro@ptmts.org.pl

www.ptmts.org.pl/jtam.html

* * * * *

Publication supported by Ministry of Science and Higher Education of Poland

VIBRATION ANALYSIS OF A HALF-CAR MODEL WITH SEMI-ACTIVE DAMPING

URSZULA FERDEK, JAN ŁUCZKO

Cracow University of Technology, Faculty of Mechanical Engineering, Krakow, Poland

e-mail: uferdek@mech.pk.edu.pl; jluczko@mech.pk.edu.pl

In this paper, analysis of a half-car model with linear and nonlinear semi-active dampers is performed. Using Matlab-Simulink software, a response of the system to a harmonic excitation of variable frequency and to an impulse excitation is found. The effect of both the distribution of spring-supported mass and the asymmetry of the support on the frequency characteristics of velocities and displacements at the mounting points of the dampers are analyzed. Additionally, characteristics of forces generated by the semi-active dampers and the response of the system when crossing an obstacle are determined.

Keywords: semi-active damper, vibration damping, car suspension, hysteresis

Notations

a_0	–	excitation amplitude
c_b	–	sum of damping parameters of suspension
$c_{1f}, c_{2f}, c_{1r}, c_{2r}$	–	damping parameters of front and rear semi-active damper
c_{wf}, c_{wr}	–	damping coefficients of front and rear wheel
I_b	–	moment of inertia of body
k_{bf}, k_{br}, k_b	–	stiffness of front and rear spring, sum of stiffness
k_{wf}, k_{wr}	–	stiffness parameters of front and rear wheel
l_f, l_r	–	distance of axles from center of body mass
l	–	distance between both axles
m_b, m_{wf}, m_{wr}	–	mass of body (spring-supported mass), front and rear wheel (non-spring-supported mass)
$p^{min}, p^{max}, p^{mean}$	–	minimum, maximum and the mean value of the parameter p
t_0	–	delay time of kinematic excitation acting on rear wheel
u_f, u_r	–	control force of front and rear semi-active dampers
V_0	–	driving speed
v_{bf}, v_{br}	–	dimensionless velocity of front and rear body points
w_f, w_r	–	kinematic excitation applied to front and rear wheel
$x_{bf}, x_{br}, x_{wf}, x_{wr}$	–	dimensionless displacements of body points, front and rear wheel
y_b	–	displacement of center of body mass
$y_{bf}, y_{br}, y_{wf}, y_{wr}$	–	displacements of body points and front and rear wheel
α, α_0	–	dimensionless and dimensional scaling factors of Bouc-Wen force
β, γ, A, n	–	control shape parameters of hysteresis loops
δ	–	dimensionless amplitude of parameters $c_{1f}, c_{2f}, c_{1r}, c_{2r}$ α_{0f}, α_{0r}
κ_c	–	ratio of stiffness of front spring to sum of stiffnesses
η	–	dimensionless excitation frequency
λ	–	mass distribution index of body

ϕ_b	–	angle of rotation of body
ω, ω_0	–	excitation and reference frequency

1. Introduction

The primary cause of vibrations affecting the driver of a car are kinematic disturbances resulting from road surface irregularities. Elimination of these vibrations is essential in order to improve both the comfort and the safety of the passenger. When the vehicle is driving across a road with large irregularities (obstacles), its wheels might get separated from the surface of the road, which in turn decreases the efficiency of force transmission of the drive, braking and steering systems of the car. An improved driving dynamics and better road traction on curves and bumps can be achieved by using the so-called “hard suspension”. However, the cost is the reduction of comfort of the passenger. The criteria for assessing the quality of shock absorbers should therefore include both the minimization of car body vibration and appropriate wheel-road adhesion (Łuczko and Ferdek, 2012).

In order to perform dynamical analysis, either a quarter-car (Gopala Rao and Narayanan, 2009; Huang and Chen, 2006) or a half-car (Ihsan *et al.*, 2009; Sapiński and Rosół, 2008) model can be used. The quarter-car model that consists of a non spring-supported mass (a wheel with partial of suspension) and a spring-supported mass (1/4 car body) is a two-degrees of freedom model and is usually used for testing of the performance of control algorithms. The half-car four-degrees of freedom model consist of two non-spring supported masses and a spring-supported one (1/2 car body). It additionally includes rotation angle of the body and allows analysis of the response to the excitation applied to both wheels of the vehicle.

Dampers used in the suspension system can be either passive, semi-active or active. Dynamical properties of the dampers are usually defined by models with hysteresis characteristics, such as Bingham (Prabakar *et al.*, 2009), Bouc-Wen (Dominguez *et al.*, 2008; Yao *et al.*, 2002) or Spencer model (Spencer *et al.*, 1996).

Requirements set for the comfort and safety of driving can be fulfilled by using semi-active suspension systems, introduced by Crosby and Karnopp (1973). In comparison to passive ones, the semi-active systems allow the damping force to be adjusted depending on driving conditions. Additionally, they require less power than similar active systems.

Several methods of control have been used, some of which can be found in the paper by Ahmadian (2001). Liu *et al.* (2005) as well as Wu and Griffin (1997), when analyzing on-off control, assume that the damping force should be high if the product of relative and absolute velocity is more than zero. Fischer and Isermann (2004) analyzed the relation between parameters of the car suspension system and the driving comfort as well as the safety indexes. They defined the comfort index as the effective acceleration value while the safety index as the effective ratio of the dynamic and static response. In the study by Sapiński and Martynowicz (2005), the results were presented for the theoretical and experimental half-car model, in which the car suspension was controlled by two separate magneto-rheological dampers (MR damper).

Some interesting options for control of a semi-active car suspension were presented by Ahmadian (2001). The most common model to be analyzed was the quarter-car one. In the steady-state case, the response to the harmonic excitation was analyzed, while in the transient one (Ahmadian and Vahdati, 2006), the response to the unit step. To ensure a compromise between the requirements for both comfort and safety, hybrid control with a MR damper is used (Goncalves and Ahmadian, 2003) and a combination of sky-hook and ground-hook control. The damping control algorithm was changed by a step function (on-off control) in order to simulate the behaviour of the damper between the constant reference point and a spring-supported (sky-hook – comfort) or non spring-supported mass (ground-hook – safety).

In the paper by Łuczko and Ferdek (2012), the effectiveness of damping of vibration of a quarter-car model by both semi-active and passive dampers was compared. Several different algorithms were proposed for semi-active dampers. The effect of these algorithms on the factors corresponding to driving safety and comfort were analyzed.

In this paper, analysis of a half-car model of a car by semi-active suspension is performed. The influence of parameters of the model on the efficiency of spring-supported mass damping is considered.

2. Half-car suspension model

Figure 1 shows the analyzed half-car model of an automobile. Vibration of the system around the static equilibrium position can be written using the following differential equations

$$\begin{aligned}
 m_{wf}\ddot{y}_{wf} &= -c_{wf}(\dot{y}_{wf} - \dot{w}_f) - k_{wf}(y_{wf} - w_f) + k_{bf}(y_{bf} - y_{wf}) - u_f \\
 m_{wr}\ddot{y}_{wr} &= -c_{wr}(\dot{y}_{wr} - \dot{w}_r) - k_{wr}(y_{wr} - w_r) + k_{br}(y_{br} - y_{wr}) - u_r \\
 m_b\ddot{y}_b &= -k_{bf}(y_{bf} - y_{wf}) - k_{br}(y_{br} - y_{wr}) + u_f + u_r \\
 I_b\ddot{\phi}_b &= l_f k_{bf}(y_{bf} - y_{wf}) - l_r k_{br}(y_{br} - y_{wr}) - l_f u_f + l_r u_r
 \end{aligned} \tag{2.1}$$

where y_{wf} and y_{wr} , are displacements of the front and rear suspension systems (i.e. the non-spring-supported mass m_{wf} and m_{wr}), y_{bf} and y_{br} are displacements of the points connecting the car body (spring-supported mass m_b of inertia I_b) with the suspension systems.

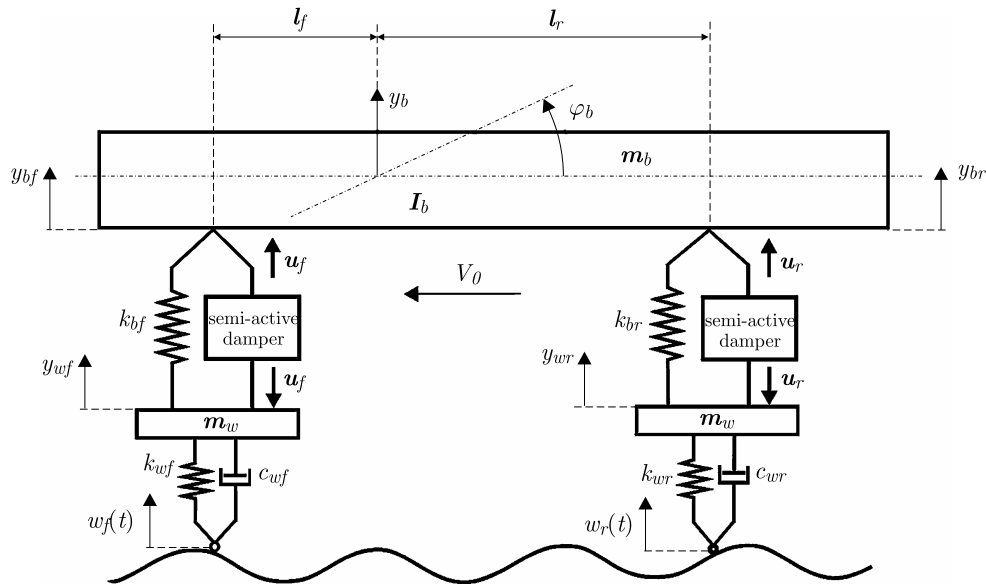


Fig. 1. Half-car model

Additionally, two parameters are introduced which are respectively: position y_b of the mass center and rotation angle ϕ_b of the car body. They can be found using the following equations (on the assumption of small displacements)

$$y_b = \frac{l_r y_{bf} + l_f y_{br}}{l} \quad \phi_b = \frac{y_{br} - y_{bf}}{l} \tag{2.2}$$

The function $w_f(t)$ and $w_r(t) = w_f(t - t_0)$ define the applied kinematic excitation, which corresponds to the profile of the road. The delay time t_0 is related to driving velocity V_0 and distance $l = l_f + l_r$ between both vehicle axles. The parameters: k_{wf} , k_{wr} and c_{wf} , c_{wr} define stiffness

and damping parameters of the front and rear wheel, while k_{bf} , k_{br} are stiffnesses of the front and rear spring respectively. The definition of forces u_f and u_r which are generated by semi-active dampers and applied to the non-spring-supported and spring-supported masses, are defined in Section 2 of this paper.

Equations (2.1) can be written in a matrix form. In order to do so, the third and the fourth equation of the system must be transformed (2.1), including additional relations (2.2). By choosing the displacements y_{wf} , y_{wr} , y_{bf} and y_{br} for coordinates of the vector \mathbf{y} , vibration of the system can be, after introduction of mass \mathbf{M} , damping \mathbf{C} and stiffness matrix \mathbf{K} , presented in form of the second-order matrix equation

$$\mathbf{M}\ddot{\mathbf{y}} + \mathbf{C}\dot{\mathbf{y}} + \mathbf{K}\mathbf{y} = \tilde{\mathbf{B}}\mathbf{u} + \tilde{\mathbf{F}}\mathbf{w}(t) \quad (2.3)$$

where $\mathbf{y} = [y_{wf}, y_{wr}, y_{bf}, y_{br}]^T$, $\mathbf{u} = [u_f, u_r]^T$ and $\mathbf{w} = [w_f, w_r]^T$. The stiffness matrix is as shown below

$$\mathbf{K} = \begin{bmatrix} k_{wf} + k_{bf} & 0 & -k_{bf} & 0 \\ 0 & k_{wr} + k_{br} & 0 & -k_{br} \\ -k_{bf} & 0 & k_{bf} & 0 \\ 0 & -k_{br} & 0 & k_{br} \end{bmatrix} \quad (2.4)$$

The damping matrix, after inclusion of passive dampers present in the vibroisolation systems, has the identical structure as the stiffness matrix. As damping properties of the wheels are usually omitted ($c_{wf} = c_{wr} = 0$) and the effect of passive dampers is already included in the forces u_f and u_r , the matrix \mathbf{C} is empty. The mass matrix can be presented in the form:

$$\mathbf{M} = \begin{bmatrix} \mathbf{M}_w & \mathbf{0} \\ \mathbf{0} & \mathbf{M}_b \end{bmatrix} \quad (2.5)$$

where

$$\mathbf{M}_w = \begin{bmatrix} m_{wf} & 0 \\ 0 & m_{wr} \end{bmatrix} \quad \mathbf{M}_b = \begin{bmatrix} \frac{m_b l_r^2 + I_b}{l^2} & \frac{m_b l_f l_r - I_b}{l^2} \\ \frac{m_b l_f l_r - I_b}{l^2} & \frac{m_b l_f^2 + I_b}{l^2} \end{bmatrix} \quad (2.6)$$

From Eqs (2.5) and (2.6), it can be seen that when the condition $m_b l_f l_r - I_b = 0$ is fulfilled, the matrix \mathbf{M} becomes diagonal, and with the matrix \mathbf{K} given in (2.4), decoupling of vertical vibration of the rear and front part of the vehicle, is possible. If the so-called ‘‘mass distribution index’’ $\lambda = I_b / m_b l_f l_r$ is close to 1, the excitation applied to one axle does not cause vibration of the other one. The matrices $\tilde{\mathbf{B}}$ and $\tilde{\mathbf{F}}$ can be written as follows

$$\tilde{\mathbf{B}} = \begin{bmatrix} -1 & 0 \\ 0 & -1 \\ 1 & 0 \\ 0 & 1 \end{bmatrix} \quad \tilde{\mathbf{F}} = \begin{bmatrix} k_{wf} & 0 \\ 0 & k_{wr} \\ 0 & 0 \\ 0 & 0 \end{bmatrix} \quad (2.7)$$

In order to transform matrix equation of motion (2.3) in the first-order form suitable for performing the numerical simulations, a modified state vector that includes velocities, is introduced

$$\mathbf{x} = \begin{bmatrix} \mathbf{x}_1 \\ \mathbf{x}_2 \end{bmatrix} = \begin{bmatrix} \mathbf{y} \\ \dot{\mathbf{y}} \end{bmatrix} \quad (2.8)$$

Motion of the system can be now written using the equation

$$\dot{\mathbf{x}} = \mathbf{A}\mathbf{x} + \mathbf{B}\mathbf{u} + \mathbf{F}\mathbf{w}(t) \quad (2.9)$$

The relation between the matrix A and the matrices present in equation (2.3) is

$$\mathbf{A} = \begin{bmatrix} \mathbf{0}^{(4 \times 4)} & \mathbf{I}^{(4 \times 4)} \\ -\mathbf{M}^{-1}\mathbf{K} & -\mathbf{M}^{-1}\mathbf{C} \end{bmatrix} \quad (2.10)$$

where $\mathbf{0}^{(4 \times 4)}$ and $\mathbf{I}^{(4 \times 4)}$ are, respectively, an empty and singular matrix of 4×4 size. The same holds for the matrices

$$\mathbf{B} = \begin{bmatrix} \mathbf{0}^{(4 \times 2)} \\ \mathbf{M}^{-1}\tilde{\mathbf{B}} \end{bmatrix} \quad \mathbf{F} = \begin{bmatrix} \mathbf{0}^{(4 \times 2)} \\ \mathbf{M}^{-1}\tilde{\mathbf{F}} \end{bmatrix} \quad (2.11)$$

where the matrix $\mathbf{0}^{(4 \times 2)}$ is an empty matrix of 4×2 size. Matrix equation (2.9) is well-suited for analysis of active systems in which the control vector \mathbf{u} is treated as the sought optimal control vector.

3. Semi-active dampers

The analysis presented below is limited to testing the effect of several selected half-car model parameters and two semi-active dampers on dynamical characteristics of the system. The forces generated by a simplified model of the semi-active damper (denoted as SA1) after introduction of the functions

$$u^{Lin}(\dot{y}_1, \dot{y}_2) = \begin{cases} c^{max}(\dot{y}_1 - \dot{y}_2) & \dot{y}_2(\dot{y}_1 - \dot{y}_2) \leq 0 \\ c^{min}(\dot{y}_1 - \dot{y}_2) & \dot{y}_2(\dot{y}_1 - \dot{y}_2) > 0 \end{cases} \quad (3.1)$$

can be calculated from the equations

$$\begin{aligned} u_f &= u^{Lin}(\dot{y}_{wf}, \dot{y}_{bf}) \\ u_r &= u^{Lin}(\dot{y}_{wr}, \dot{y}_{br}) \end{aligned} \quad (3.2)$$

In SA1 damper model, the forces are proportional to the relative velocity, with higher energy dissipation if the momentary power is less than zero (which means that energy is retrieved from the spring-supported mass). For $c^{max} = c^{min}$, equations (3.1) and (3.2) define the passive damper (PS).

The other type of a semi-active damper (SA2) is defined (Spencer *et al.*, 1996) using the Spencer model (Fig. 2). The mathematical description of the generated force is more complicated in this case. Based on the study by Ferdek and Łuczko (2011), a concise force definition can be presented

$$\begin{aligned} u_f &= u^{Spencer}(y_{wf}, \dot{y}_{wf}, \dot{y}_{bf}) \\ u_r &= u^{Spencer}(y_{wr}, \dot{y}_{wr}, \dot{y}_{br}) \end{aligned} \quad (3.3)$$

where

$$u^{Spencer}(y_1, \dot{y}_1, \dot{y}_2) = c_2(\dot{z}_1 - \dot{y}_2) \quad (3.4)$$

Additional parameters z_1 and z_2 can be obtained from the set of equations

$$\begin{aligned} k_1(y_1 - z_1) + c_1(\dot{y}_1 - \dot{z}_1) - \alpha_0 z_2 &= c_2(\dot{z}_1 - \dot{y}_2) \\ \dot{z}_2 &= A\dot{z}_0 \{1 - [\gamma + \beta \text{sgn}(z_2 \dot{z}_0)]|z_2|^n\} \end{aligned} \quad (3.5)$$

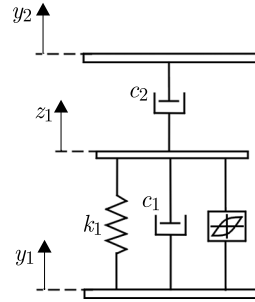


Fig. 2. Model of the semi-active Spencer damper

in which $z_0 = z_1 - y_1$ and $\beta + \gamma = 1$ ($0 < \beta < 1, 0 < \gamma < 1$). Equation (3.5)₁ can be interpreted as the equilibrium condition of forces acting on a massless middle element in the Spencer model (Fig. 2). The dimensionless variable z_2 , which is the solution of differential equation (3.5)₂ proposed in a similar form by Bouc-Wen (Spencer *et al.*, 1996), determined the appearance of a hysteresis. Its shape depends on the parameters A , γ , β and n . The parameters β and γ have impact on the characteristic only when A is small. In such a case, an increase in β causes the width of the hysteresis to be slightly decreased. Most often, when forming the characteristic, the value $n = 2$ is chosen, in rare cases $n = 1$ is taken. The parameter A is the one that strongly influences the shape of the hysteresis. With an increase in the parameter A , the lower and upper limits of the Bouc-Wen model characteristic are symmetrical. In the numerical calculations, emphasis is put on the analysis of coefficients α_0 , c_1 and c_2 and their impact on the solution. The parameters of $A = 50 \text{ m}^{-1}$, $\gamma = \beta = 0.5$ and $n = 2$ have been taken from the literature.

The slope of the force characteristic in the high velocity range depends on the value of a substitute damping coefficient $c_z = c_1 c_2 / (c_1 + c_2)$ with a relation close to linear. For lower velocities, the slope and inflection point of the characteristic are related to the parameter α_0 .

In the semi-active damper (e.g. magneto-rheological one), it is assumed that the parameters α_0 , c_1 and c_2 of the Spencer model are linearly dependent on the control voltage. By taking a control algorithm analogical to (3.1), it can be assumed that $c_k = p(\dot{y}_1, \dot{y}_2, c_k^{max}, c_k^{min})$, $k = 1, 2$ and $\alpha_0 = p(\dot{y}_1, \dot{y}_2, \alpha_0^{max}, \alpha_0^{min})$, with p defined using the formula

$$p(\dot{y}_1, \dot{y}_2, p^{max}, p^{min}) = \begin{cases} p^{max} & \dot{y}_2(\dot{y}_1 - \dot{y}_2) \leq 0 \\ p^{min} & \dot{y}_2(\dot{y}_1 - \dot{y}_2) > 0 \end{cases} \quad (3.6)$$

4. Results of numerical calculations

In the numerical calculations, the emphasis is placed on analyzing the effect of a few selected parameters of the system, with other parameters assumed as follows: $l_f = 0.94 \text{ m}$, $l_r = 1.66 \text{ m}$, $m_b = 510 \text{ kg}$, $m_{wf} = m_{wr} = 28 \text{ kg}$, $I_b = \lambda m_b l_f l_r$ (variable λ), $k_{wf} = k_{wr} = 180000 \text{ N/m}$, $k_b = 40000 \text{ N/m}$, $k_1 = 0.01 k_b$, $c_{wf} = c_{wr} = 0$, $A = 50 \text{ m}^{-1}$ and $\beta = \gamma = 0.5$. When analyzing the effect of stiffness of the front and rear suspension system, it is assumed that $k_{bf} = \kappa_k k_b$, $k_{br} = (1 - \kappa_k) k_b$, ($0 < \kappa_k < 1$), k_b – is the sum of stiffness parameters. Similarly, when considering the effect of energy dissipation, the parameters of PS damper are: $c_{bf} = \kappa_c c_b$, $c_{br} = (1 - \kappa_c) c_b$, ($0 < \kappa_c < 1$). The value of $c_b = 2260 \text{ Ns/m}$ has been chosen such that the dimensionless damping factor, given by equation

$$\zeta = \frac{c_b}{2m_b \omega_0} = \frac{c_{bf} + c_{br}}{2m_b \omega_0} \quad (4.1)$$

is $\zeta \approx 0.25$ – the recommended value for vehicle shock absorbers. The dimensionless angular velocity ω_0 (close to the two highest vibration modes of the system) present in Eq. (4.1) is defined as follows

$$\omega_0 = \sqrt{\frac{k_b}{m_b}} = \sqrt{\frac{k_{bf} + k_{br}}{m_b}} \quad (4.2)$$

When choosing the parameters of semi-active dampers, the same assumption is made regarding the parameters of front and rear dampers as well as the energy dissipation level. For SA1 damper, it is assumed that the mean value of damping coefficients are: $c_f^{mean} = \kappa_c c_b$, $c_r^{mean} = (1 - \kappa_c) c_b$, while the extreme values can be calculated from

$$p^{max} = (1 + \delta)p^{mean} \quad p^{min} = (1 - \delta)p^{mean} \quad (4.3)$$

where $p = c_f$ or $p = c_r$ and $0 < \delta < 1$.

SA2 damper has a higher number of significant parameters. Formulas (4.3) need to be used for the extreme parameters α_0 , c_1 and c_2 of the front and rear damper, while the mean values c_{1f}^{mean} , c_{2f}^{mean} , c_{1r}^{mean} and c_{2r}^{mean} must be chosen such that the coefficient ζ has the desired value. From literature (Prabakar *et al.*, 2009; Spencer *et al.*, 1996), it can be seen that c_{1f}^{mean} , c_{1r}^{mean} values are an order lower from c_{2f}^{mean} , c_{2r}^{mean} ones. These are chosen as follows: $c_{1f} = 1.1\kappa_c c_b$, $c_{2f} = 11\kappa_c c_b$, $c_{1r} = 1.1(1 - \kappa_c) c_b$ and $c_{2r} = 11(1 - \kappa_c) c_b$. For the chosen values, the relation $c_{zf} + c_{zr} = c_b$, where $c_z = c_1 c_2 / (c_1 + c_2)$ is true and coefficient (4.1) is equal to $\zeta = 0.25$.

The values of varying parameters are presented with analysis of the results of numerical simulations. When presenting the results, the dimensionless parameters are introduced relating the displacements with the excitation amplitude a_0 , velocities with the value $\omega_0 a_0$, while accelerations with $\omega_0^2 a_0$, and forces with $k_b a_0$.

One of less known parameters of the system is the delay time t_0 between the functions describing motion of the front and rear wheel of the vehicle. In order to estimate it, it is assumed that the angular frequency of the kinematic excitation ω is related for the given road profile linearly with the velocity V_0 , or using the formula: $\omega = \mu V_0$. For motion with constant velocity V_0 , the relation $t_0 = l/V_0$, where l is the distance between both axles, is also true. By additionally assuming that the lowest vibration mode of the approximate frequency ω_0 is related to a known velocity V_r , the value of the parameter $\mu = \omega_0/V_r$ and the delay time $t_0 = \omega_0 l/V_r \omega$ can be calculated, e.g. for given: $V_r = 20$ km/h, $l = 2.6$ m and $\omega_0 = 8.856$ rd/s a value of $t_0 \approx 4.15/\omega$ is found.

The frequency characteristics are ideal for the purpose of global evaluation of dynamical properties of the system. In the simulations, the kinematic excitation is usually defined by the harmonic function of a modulated angular frequency: (e.g. ‘‘Chirp Signal’’ in Simulink). If the simulation time is high enough, an approximate frequency characteristic can be acquired by graphing the maximal responses of the system.

In order to illustrate the effect of car body mass distribution, characteristics of maximal dimensionless velocities $v_{bf} = \dot{x}_3/\omega_0 a_0$ and $v_{br} = \dot{x}_4/\omega_0 a_0$ (in the points connecting the body and the suspension) with relation to the dimensionless angular frequency of the excitation $\eta = \omega/\omega_0$ are shown in Fig. 3. The analysis is limited to vibration comparison of systems with identical shock absorbers ($\kappa_k = \kappa_c = 0.5$). The parameter defining the semi-active damper has been chosen as $\delta = 0.5$. The only modified value is the mass distribution ratio λ . The corresponding inertia of the spring-supported mass is $I_b = \lambda m_b l_f l_r \approx 795.8\lambda$. The actual value of λ should be close to one. Several exemplary values of this coefficient, calculated from the data presented in the literature, are equal: $\lambda = 1.01$ (Feng *et al.*, 2003), $\lambda = 1.09$ (Sam *et al.*, 2008), $\lambda = 1.16$ (Lozia *et al.*, 2008), $\lambda = 0.823$ (Prabakar *et al.*, 2009). However, in some cases this value is different, e.g. (Shamsi and Choupani, 2008) $\lambda = 0.544$, which is far from one.

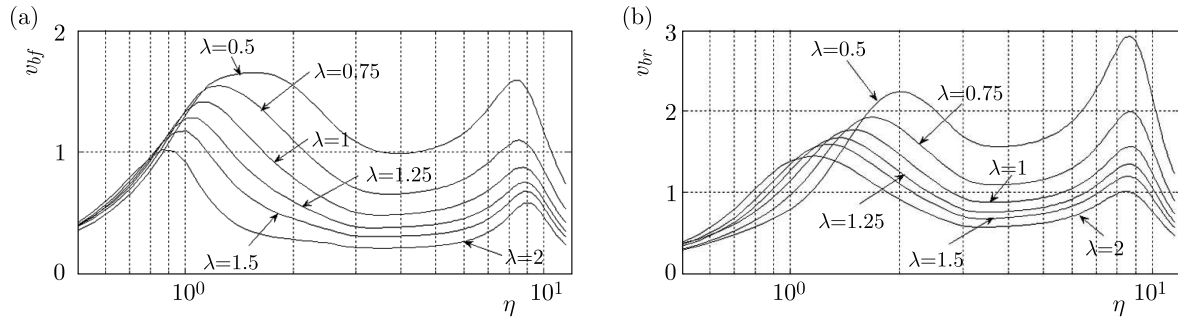


Fig. 3. Effect of spring-supported mass distribution on the frequency characteristics: (a) velocity v_{bf} , (b) velocity v_{br}

From the results presented in Fig. 3, it can be seen that the lower the coefficient λ becomes, the larger are the maximal velocities, especially within the resonance regimes. Although this model has four degrees of freedom, only two resonance regions can be seen on the presented frequency characteristics. This is caused by close proximity of the paired natural frequencies of the system. For example, when $\lambda = 0.5$, the natural frequency values of the linearized system related to ω_0 are equal to: 0.88 (dominant displacement of the front part of the vehicle), 1.44 (rear part), 8.97 and 9.16 (wheel vibration), while for $\lambda = 2$ these values are respectively: 0.67, 0.97, 9.14 and 9.21.

A consequence of such a distribution of frequencies is dislocation of the lowest frequency region towards the lower frequency with an increase in λ and its slightly different disposition in the velocity characteristics v_{bf} and v_{br} . The location of the “second” region is less vulnerable to a change in the parameter λ and is similar to Fig. 3a and Fig. 3b.

Although the obtained results are only for SA1 damping system, the conclusions are more general, and essentially similar results are obtained for PS and SA2 systems.

In the case of SA2 system described by the Spencer model, the effectiveness of the damper, depends on chosen values of c_{1f}^{mean} , c_{2f}^{mean} , c_{1r}^{mean} , c_{2r}^{mean} and δ , but mostly on the parameter α . Fig. 4 shows the dimensionless displacement characteristics $x_{wf} = x_1/a_0$ (non-spring-supported mass) and $x_{bf} = x_3/a_0$ (spring-supported mass) for several values of the parameter $\alpha = \alpha_0^{mean}/\alpha_0^{mean} k_b a_0$. At $\kappa_c = 0.5$ (symmetrical support), the relations are: $c_{1f} = c_{1r} = 0.55c_b$, $c_{2f} = c_{2r} = 5.5c_b$ and the mean value of the coefficient ζ is close to 0.25. By analyzing Fig. 4b, one can see that the characteristic closest to the optimal is the curve obtained for $\alpha = 0.5$. Too high values of α cause the forces to be much higher for low velocities, and also shift the inflation point location, which is undesirable especially in the range of high-frequency excitation. From the graphs shown in Fig. 4a, it can be concluded that within the range of high oscillation, which includes the third and fourth natural frequencies, the amplitudes of non-spring-supported

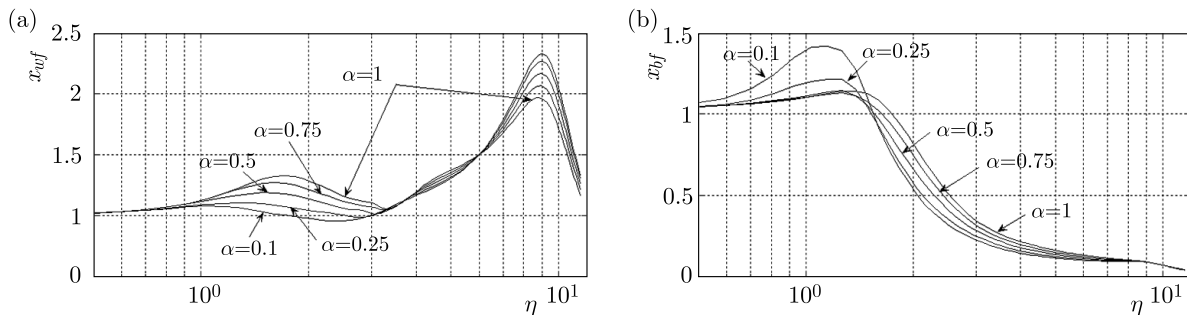


Fig. 4. Effect of the parameter α on the frequency characteristics of SA2 system: (a) displacement x_{wf} , (b) displacement x_{bf}

masses (wheels) are significant. Additionally, within this range, the dynamic response values are also large, and so the indexes related to the driving safety and comfort are lower, which means that these semi-active dampers are not efficient.

In order to compare SA1 and SA2 dampers, the dimensionless force characteristics $U_f = u_f/k_b a_0$ generated by both types of semi-active dampers are shown in Fig. 5. Only the front part of the car suspension is presented. As before, it is assumed that $\kappa_k = \kappa_c = 0.5$, (symmetrical model) with $\lambda = 1$, $\alpha = 0.5$, $\zeta = 0.25$ and $\delta = 0.5$.

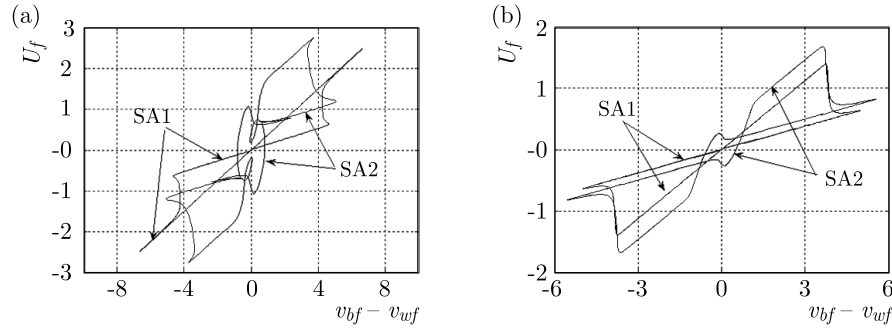


Fig. 5. Damper SA1 and SA2 characteristics: (a) $\omega = 1$, (b) $\omega = 4$

The characteristic of SA1 damper is relatively simple. Two of its branches are straight lines of slopes equal to the given c_f^{min} and c_f^{max} values, while the lines linking the other two, should be, in theory, vertical. The reason for this deviation is due to the approximation used for the continuous switching step function (based on arctan). Such an approach is recommended for discontinuous functions due to its accuracy and the time of numerical computation required, and also in some cases for avoidance of undesirable effects caused by too frequent switching, e.g. chattering.

The characteristic of SA2 damper in the range of high velocities is similar to the one described above. The differences are visible within the range of low velocities. The average slope of the characteristic is higher and depends primarily on the parameter α . The higher complexity of the graph is also due to the other parameters of the half-car model. Less complex characteristics can be obtained by analyzing a simpler model, such as a quarter-car model (Łuczko and Ferdek, 2012).

Figure 6 shows the frequency response of dimensionless displacements $x_{bf} = x_3/a_0$ and $x_{br} = x_4/a_0$ for passive PS and both semi-active SA1 and SA2 systems.

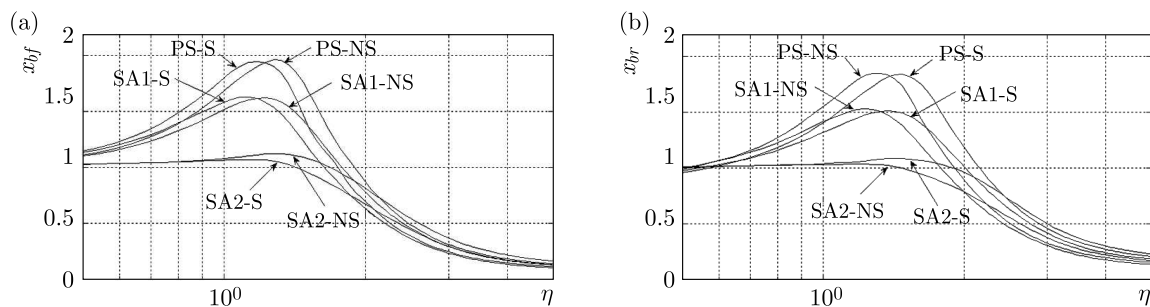


Fig. 6. Effect of the parameters κ_k and κ_c on frequency characteristics PS, SA1 and SA2: (a) displacement x_{bf} , (b) displacement x_{br}

The case of symmetrical mounting $\kappa_k = \kappa_c = 0.5$ (S systems, Fig. 6) and the asymmetrical one defined by parameters: $\kappa_k = \kappa_c = l_r/l_f \approx 0.638$ (NS systems) is considered. For selected values of the parameter κ_k , the static deflections of the spring-supported mass under its own mass are identical in both locations of the connection with the suspension systems, while the

center of stiffness overlaps the center of mass. The values $\lambda = 1$, $\alpha = 0.5$, $\zeta = 0.25$ and $\delta = 0.5$ have been assumed, while the other parameters of the Spencer model have been obtained using appropriate equations with known parameters κ_k and κ_c . When showing the results, only the region with the lowest natural mode (actually two lowest modes) are shown – the ones in which the car body vibration is dominant.

As the parameters for models PS, SA1 and SA2 are chosen in such a way that the natural frequencies are the same for the identical parameter κ_k , the dislocation of the resonance region is avoided. Such a dislocation is only visible between the curves obtained for $\kappa_k = 0.5$ (S systems) and $\kappa_k = 0.638$ (NS systems). The value of the parameter κ_k influences mostly the two lowest natural frequencies. The complex natural frequencies (related to ω_0) are equal: $\eta_1 = -0.16 \pm 0.83i$, $\eta_2 = -0.29 \pm 1.10i$ for S systems and: $\eta_1 = -0.195 \pm 0.927i$, $\eta_2 = -0.217 \pm 0.945i$ for NS ones.

The location of the resonance regions, as shown in Figs. 6a and 6b is directly related to the distribution of the natural frequencies of S and NS systems. As the low values correspond to the natural modes in which the displacement are dominant (and even more x_{br}), the resonance frequency of S systems is lower than that in NS ones for characteristics of the displacement x_{bf} (Fig. 6a). The opposite effect is observed for the displacement x_{br} (Fig. 6b).

The vibration reduction level is indeed related to the parameter κ_k (at least within the analyzed regimes). Using a more stiff front mounting, the comfort of the driver is only slightly decreased but seems to be important when considering safety of the driver (this is not a subject of analysis in this study). The systems with SA1 dampers reduce vibration by around 20% when compared with passive ones, while the semi-active SA2 dampers are proved to be even more effective, reducing the values of the displacement x_{bf} and x_{br} twice in the fundamental resonance.

Figure 7 shows the response of PS, SA1 and SA2 dampers (dimensionless displacements x_{bf} and x_{br} , velocities v_{bf} and accelerations a_{bf} in function of the dimensionless time $\tau = \omega_0 t$) to an impulse excitation defined by equation (Shekhar *et al.*, 1999; Łuczko, 2011)

$$w_f(t) = \frac{e}{4} a_0 \sum_{k=1}^3 \omega_k (t - t_k)^2 \exp[-\omega_k (t - t_k)] H(t - t_k) \quad (4.4)$$

where $H()$ is the unit step function. Function (4.4) is supposed to simulate the vehicle crossing the same obstacle at three different velocities $V_0 = \theta V_r$ (where $\theta = 1/2, 1, 4$), which in equations (4.4) are represented by angular frequencies $\omega_1 = 0.5\omega_0$, $\omega_2 = \omega_0$ and $\omega_3 = 4\omega_0$. The values of t_k

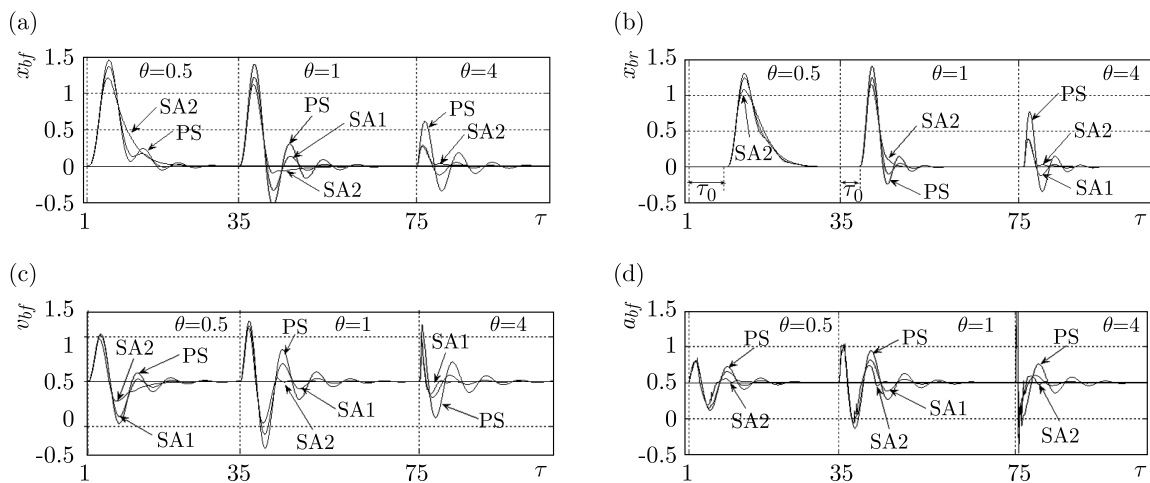


Fig. 7. Response of the system to an impulse excitation: (a) x_{bf} , (b) x_{br} , (c) v_{bf} , (d) a_{bf}

are chosen in such a way that the vibration caused by the previous impulse would vanish before the next one is applied.

When crossing the obstacle at a low speed ($\theta = 0.5$ and $\theta = 1$), the maximum displacements (Fig. 7a and Fig. 7b) are to a small extent related with the type of a damper, although the lowest ones are obtained for SA2 damper. The type of the used damper has a greater effect on the character of damping of vibration caused by an impulse excitation. For PS and SA1 systems, reduction of oscillatory vibration can be observed. In the case of SA2 systems, the damping is much faster and similar in shape to an exponential function. For high values of velocity, when crossing the obstacle ($\theta = 4$), the displacements are definitely lower. This is however at the cost of large acceleration values (Fig. 7d), for which the maximum values are practically independent of the type of the used vibroisolation system. With an increase in driving velocity, the time delay t_0 is decreased while the displacements of both front and back parts of the body are similar.

5. Summary

Based on the analysis of selected results of numerical calculations, several conclusions can be drawn:

- The algorithms for control of a semi-active on-off damper in which the switching is related to the actual power, enable improvement the driving comfort, especially within the low-frequency excitation range.
- From the tested dampers, definitely the best one is SA2 damper with a nonlinear characteristic. If the parameters for the damper are optimal, the vibration amplitude can be reduced twice as much within the range of fundamental resonance.
- Semi-active SA2 system is also effective when subjected to an impulse excitation which simulates obstacles (bumps) in the road.
- An improper mass distribution (low values of λ) might be an additional cause for an increased vibration level of the spring-supported mass.
- The introduction of an additional spring and damping elements to the front and back car suspension in which the center of stiffness overlaps the center of mass, does not cause a decrease in the indexes describing the driving comfort. It might be, however, beneficial when considering the safety.
- Semi-active systems are less efficient than passive ones when the driving velocity (excitation frequency) is high.

References

1. AHMADIAN M., 2001, Active control of vehicle vibrations, *Encyclopedia of Vibration*, Academic Press, London, 37-48
2. AHMADIAN M., VAHDATI N., 2006, Transient dynamics of semiactive suspensions with hybrid control, *Journal of Intelligent Material Systems and Structures*, **17**, 2, 145-153
3. CROSBY M.J., KARNOPP D.C., 1973, The active damper – a new concept for shock and vibration control, *Shock and Vibration Bulletin*, **43**, 119-133
4. DOMINGUEZ A., SEDAGHATI R., STIHARU I., 2008, Modeling and application of MR dampers in semi-adaptive structures, *Computers and Structures*, **86**, 407-415
5. FENG J.Z., LI J., YU F., 2003, GA-based PID and fuzzy logic control for active vehicle suspension system, *International Journal of Automotive Technology*, **4**, 4, 181-191

6. FERDEK U., ŁUCZKO J., 2011, Analysis of the quarter-car model suspension of a vehicle with a hydraulic damper (in Polish), *Symulacja w Badaniach i Rozwoju*, **2**, 2, 67-74
7. FISCHER D., ISERMANN R., 2004, Mechatronic semi-active and active vehicle suspensions, *Control Engineering Practice*, **12**, 1353-1367
8. GONCALVES F.D., AHMADIAN M., 2003, A hybrid control policy for semi-active vehicle suspensions, *Shock and Vibration*, **10**, 1, 59-69
9. GOPALA RAO L.V.V., NARAYANAN S., 2009, Sky-hook control of nonlinear quarter car model traversing rough road matching performance of LQR control, *Journal of Sound and Vibration*, **323**, 515-529
10. HUANG S-J, CHEN H-Y., 2006, Adaptive sliding controller with self-tuning fuzzy compensation for vehicle suspension control, *Mechatronics*, **16**, 607-622
11. IHSAN S., AHMADIAN M., FARIS W., BLANCHARD E.D., 2009, Ride performance analysis of half-car model for semi-active system using RMS as performance criteria, *Shock and Vibration*, **16**, 6, 593-605
12. LIU Y., WATERS T.P., BRENNAN M.J., 2005, A comparison of semi-active damping control strategies for vibration isolation of harmonic disturbances, *Journal of Sound and Vibration*, **280**, 21-39
13. LOZIA Z., SIMIŃSKI P., ZDANOWICZ P., 2008, The effect of the position of the center of mass on behaviour of the LTV vehicle in curvilinear motion (in Polish), *Czasopismo Techniczne*, 6-M, 65-83
14. ŁUCZKO J., 2011, Comparison of dynamical responses of semi-active dampers described by the Bouc-Wen and Spencer models (in Polish), *Czasopismo Techniczne*, **2**, 1-M, 127-136
15. ŁUCZKO J., FERDEK U., 2012, Comparison of different control strategies in a semi-active vehicle suspension system (in Polish), *Czasopismo Techniczne*, **11**, 6-M, 81-92
16. PRABAKAR R.S., SUJATHA C., NARAYANAN S., 2009, Optimal semi-active preview control response of a half car vehicle model with magnetorheological damper, *Journal of Sound and Vibration*, **326**, 400-420
17. SAM Y.M., SUAIB N.M., OSMAN J.H.S., 2008, Hydraulically actuated active suspension system with proportional integral sliding mode control, *WSEAS Transactions on Systems and Control*, **9**, 3, 859-868
18. SAPIŃSKI B., MARTYNOWICZ P., 2005, Vibration control in a pitch-plane suspension model with MR shock absorbers, *Journal of Theoretical and Applied Mechanics*, **43**, 3, 655-674
19. SAPIŃSKI B., ROSÓŁ M., 2008, Autonomous control system for a 3DOF pitch-plane suspension model with MR shock absorbers, *Computers and Structures*, **86**, 379-385
20. SHAMSI A., CHOUPANI N., 2008, Continuous and discontinuous shock absorber, Control through skyhook strategy in semi-active suspension system (4DOF Model), *International Journal of Mechanical, Industrial and Aerospace Engineering*, 254-258
21. SHEKHAR N.C., HATWAL H., MALLIK A.K., 1999, Performance of non-linear isolators and absorbers to shock excitations, *Journal of Sound and Vibration*, **227**, 2, 293-307
22. SPENCER JR B.F., DYKE S.J., SAIN M.K., CARLSON J.D., 1996, Phenomenological model for magnetorheological dampers, *ASCE Journal of Engineering Mechanics*, **123**, 3, 230-238
23. WU X., GRIFFIN M.J., 1997, A semi-active control policy to reduce the occurrence and severity of end-stop impacts in a suspension seat with an electrorheological fluid damper, *Journal of Sound and Vibration*, **203**, 5, 781-793
24. YAO G.Z., YAP F.F., CHEN G., LI W.H., YEO S.H., 2002, MR damper and its application for semi-active control of vehicle suspension system, *Mechatronics*, **12**, 963-973

EVALUATION OF AN ENERGY HARVESTING MR DAMPER-BASED VIBRATION REDUCTION SYSTEM

BOGDAN SAPIŃSKI

AGH University of Science and Technology, Department of Process Control, Cracow, Poland

e-mail: deep@agh.edu.pl

MACIEJ ROSÓŁ

AGH University of Science and Technology, Department of Automatics and Biomedical Engineering, Cracow, Poland

e-mail: mr@agh.edu.pl

MARCIN WĘGRZYŃSKI

AGH University of Science and Technology, Department of Process Control, Cracow, Poland

e-mail: mweg@agh.edu.pl

The paper deals with an MR damper-based vibration reduction system with energy harvesting capability. The main part of the system creates an MR damper and a power generator based on an electromagnetic transduction mechanism, which are integrated into a stand-alone device (so called energy harvesting MR damper). The main objective of the work is to evaluate performance of the proposed vibration reduction system employed in a single DOF mechanical structure. The material outlines the design structure and characteristics of the energy harvesting MR damper, presents the vibration reduction system based on this damper and explores experimental testing of the system implemented in a single DOF mechanical structure. To demonstrate that the devised system is feasible, performance figures maps completed by experimental data are shown.

Keywords: MR damper, energy harvesting, vibration reduction system, control

1. Introduction

Developments of MR damper systems in the last decade have concentrated on energy harvesting capability. Extensive research efforts have been made to develop MR dampers with self-powering and self-sensing capability and to investigate their performance in automobile, railway vehicles and civil engineering applications. Recent years have witnessed a growing number of scientific articles and technical reports on the subject. For example, Cho *et al.* (2004) investigated an MR damper-electromagnetic generator system whose performance is comparable to that of a conventional MR damper-based system. Besides, Cho *et al.* (2005) showed that the developed system could be well feasible in civil engineering applications. Hong *et al.* (2007) proposed an MR damper-electromagnetic generator system and verified its effectiveness in a seismic protection application. Choi *et al.* (2007) devised such system to generate electricity and ran the experimental testing. Choi and Werely (2009) investigated the feasibility and efficiency of a self-powered MR damper using a spring-mass electromagnetic induction device. Lam *et al.* (2010) developed and investigated performance of an MR damper with dual-sensing capability to facilitate closed-loop vibration control. Wang *et al.* (2010) proposed an MR damper-based vibration control system with energy regeneration and showed through of numerical simulations that the system could be feasible when used on an elevated highway bridge. It is worthwhile to mention that some MR damper-electromagnetic generator systems share the self-sensing capability, i.e. it is possible to obtain information about relative velocity across the MR damper based on voltage

delivered by the generator (Jung *et al.*, 2009, 2010; Wang *et al.*, 2010, 2013). Moreover, Chen and Liao (2012) investigated an MR damper with the power generation feature, integrating energy harvesting, dynamic sensing and MR damping technologies in a single device. Those authors also investigated an MR damper prototype that had the self-powered and self-sensing capabilities. Zhu *et al.* (2012) designed self-powered and sensor-based MR damper systems for use in large-scale civil structures. Li *et al.* (2013b) put forward an innovative concept of a mechanical motion rectifier converting bidirectional into unidirectional motion. Attention was also given to regenerative vehicle MR shock absorbers enabling energy recovery from suspension vibrations (Li *et al.*, 2013a). Finally, Snamina and Sapiński (2011) studied the energy balance in a MR damper-based vibration reduction system with the self-powering capability.

This study recalls two former papers by the author, see Sapiński (2011, 2014). The first work demonstrated that the developed MR damper-based vibration control system with energy harvesting capability (comprising a commercially available linear MR damper and an electromagnetic power generator prototype) was able to power-supply the MR damper whilst the generator served as a “velocity-sign” sensor. The other study, whose purpose was to integrate the MR damper and the power generator into a single device (also referred to as an energy harvesting linear MR damper) showed that the device was able to recover energy from vibration and that it displayed self-powering and self-sensing capabilities.

The primary objective of this paper is to evaluate the developed energy harvesting MR damper-based vibration reduction system implemented in a single DOF mechanical structure and to demonstrate its feasibility. This paper is organised as follows. Section 2 summarises the design structure and characteristics of the energy harvesting MR damper. Section 3 briefly describes the vibration reduction system based on an energy-harvesting MR damper whilst Section 4 deals with its implementation in a single DOF mechanical system. Section 5 summarises the experimental testing of the proposed system under conditions when the MR damper is not energised, while it was energised from an external power source and when it is energised using harvested energy. Final conclusions are given in Section 5.

2. Energy harvesting MR damper

The system comprising an MR damper and a power generator integrated into a single device is shown in Fig. 1. The power generator is connected to the MR damper via piston rod (1) and placed inside housing (2). Three systems of permanent magnets (3) in the generator are fixed on the rod separated by ferromagnetic spacers. In each system, the magnets are arranged in

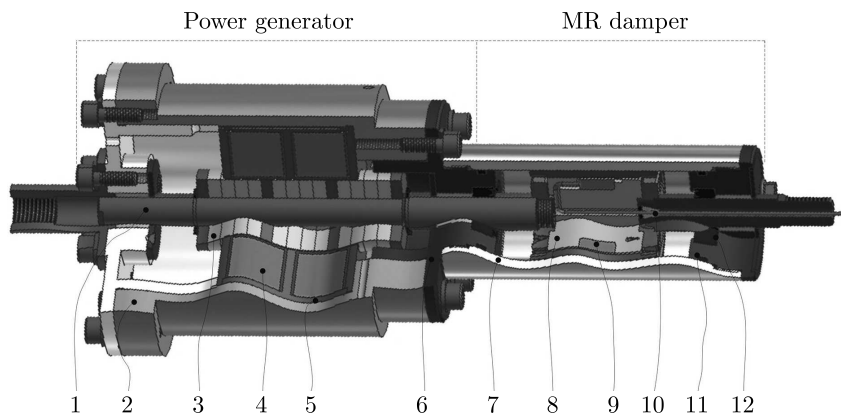


Fig. 1. Energy harvesting MR damper: 1 – shaft, 2 – generator housing, 3 – magnets, 4 – coil housing, 5 – generator coil, 6 – switch cover, 7 – cylinder, 8 – piston, 9 – control coil, 10 – wire, 11 – cover, 12 – seal

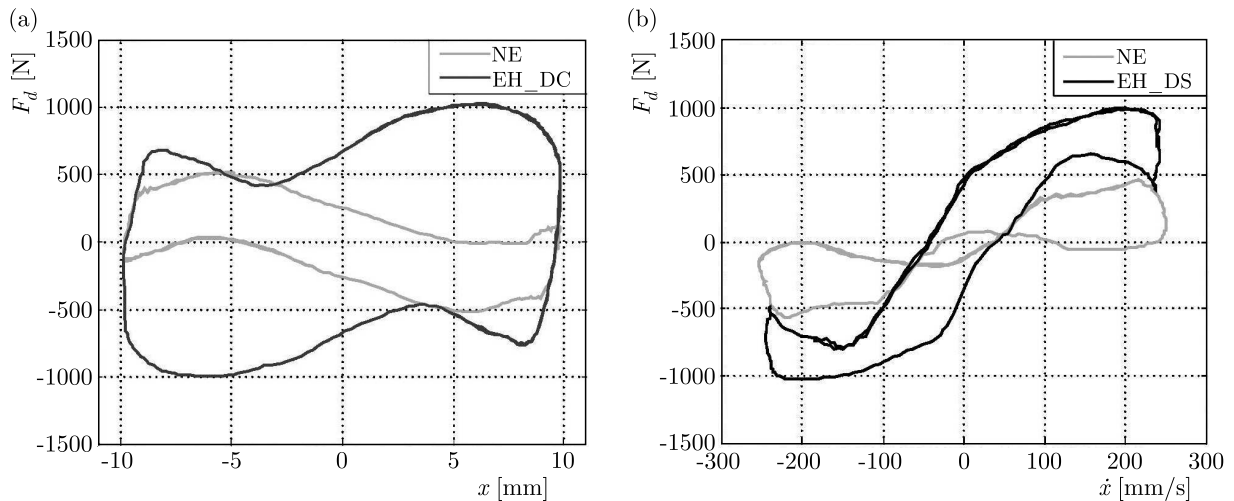


Fig. 2. Force vs.: (a) piston displacement, (b) piston velocity

accordance with their axial polarity whilst the systems of magnets have opposite polarisation with respect to each other. The rod with the magnet systems moves inside generator coil (4) placed inside ferromagnetic casing (5). The generator is separated from the damper by cover (6) to which cylinder (7) is fixed. Inside the cylinder, piston (8) is placed. On its both ends there are two rod sections attached: the solid section – from the generator end, the section with an opening – on the opposite end. Inside the piston there is control coil (9), and power supply cable (10) is led through the opening in the rod. The cylinder is closed with cover (11) and filled with MR fluid. Covers (6) and (11) are provided with pilot sleeves and sealing rings (12). The damper force vs piston displacement /piston velocity plots obtained for the applied kinematic input (sine excitation with amplitude $A = 10$ mm and frequency $f = 4$ Hz) are shown in Figs. 2a and 2b. The plots graphed with the continuous line represent the case when the generator coil is not connected to the damper coil – the damper is not energised (NE case), and those graphed with broken lines represent the case when the damper is energised using the harvested energy and the damper coil is directly connected to the MR damper coil (EH_DS case). Obviously, a larger force will be registered in EH_DS. case than in NE case.

3. Vibration reduction system

The structural design of the vibration reduction system is shown in Fig. 3. It comprises a spring (with stiffness coefficient 126.4 N/mm) and the energy harvesting MR damper connected in

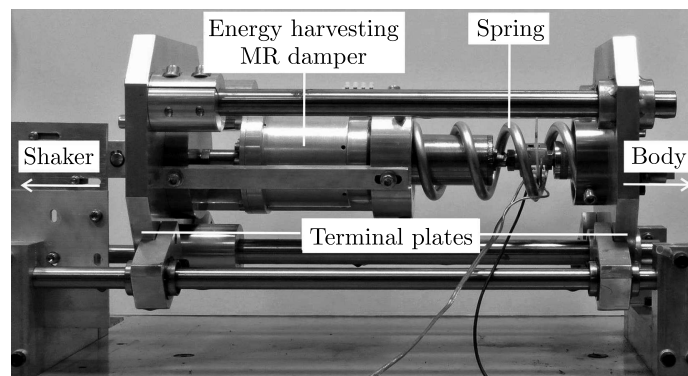


Fig. 3. Structure of the vibration reduction system

parallel. The damper and the spring are fixed between two terminal plates and connected on one end to a shaker and on the other end – to a mobile body mass comprising three horizontally arranged plates (with mass 153 kg). Trolleys moving along linear guides enable its movement along the horizontal axis. The energy harvesting MR damper is mounted in the vibration reduction system, on the shaker end, with a fixing grip and from the body mass end, via threaded connection in the rod.

4. Evaluation tests

4.1. Test facility

The test facility shown schematically in Fig. 4 incorporates a shaker, an energy harvesting MR damper, a spring and a body, two displacement sensors (Sensor 1, Sensor 2), force sensor (Sensor 3) and the measurement – control system comprising a PC computer with the AD/DA card supported by Windows and using the MATLAB/Simulink software. Recorded parameters include the shaker core displacement (excitation signal) – z , body displacement – x , damper force F_d , voltage in the damper coil /electromotive force (emf) produced in the generator coil – u/e , current i in the damper coil and voltage controlling the transistor switch (not shown) – u_c . The measured quantities are converted into voltage signals in the range $(-10, +10)$ V and sampled with a frequency of 1 kHz.

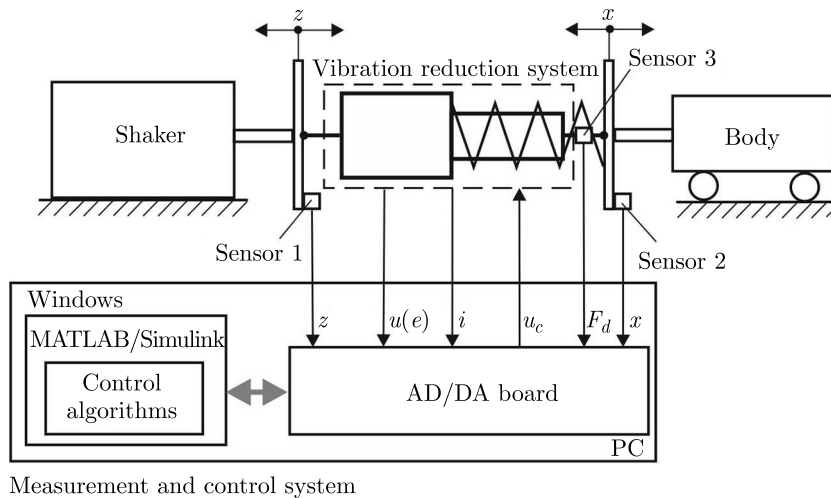


Fig. 4. Schematic diagram of the test facility

4.2. Results

The system is investigated under conditions when the MR damper is not energised (NE case) and when it is energised from the power generator (EH case). In the EH case, the damper is powered either directly with voltage produced by the generator (EH_DS case) or by using the control system with an on-off algorithm (EH_OO case) or a sky-hook algorithm (EH_SK case). Tests are performed under the applied sine excitations z with amplitude $A = 4.5$ mm and frequency f in the range $(1, 10)$ Hz. In further Sections, we show time patterns of registered quantities obtained for $f = 4$ Hz, which corresponds to the near-resonance frequency of the investigated system implemented in a single DOF mechanical structure.

NE case

Figure 5 shows time histories of emf generated in the generator coil and of the damper force. In this case, the damper force has the following components: force due to drag experienced during the fluid flow in the piston slit, friction force in the sealing elements and the cogging force in the generator. The maximal value of emf is found to be 10 V, and the maximal damper force becomes $F_d = 520$ N. In earlier work, it was demonstrated that emf was linearly related to piston velocity (Sapiński, 2014).

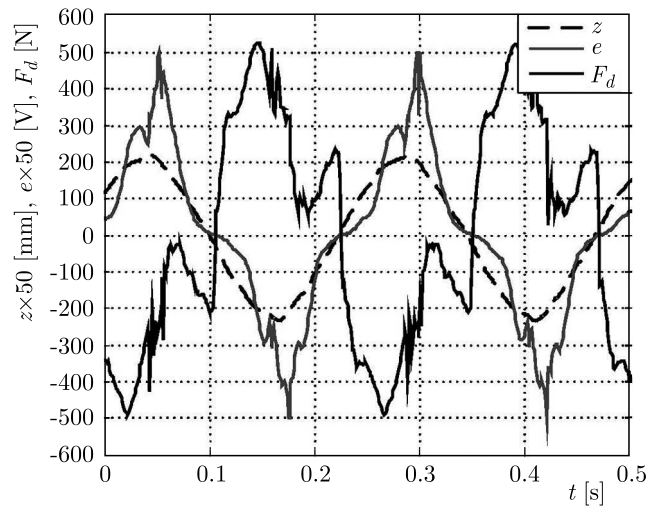


Fig. 5. Emf and force vs time

EH case

The equivalent electric circuit of the damper in the EH case is shown in Fig. 6. There is a Graetz bridge between the generator coil and the damper coil. R_g and L_g stand for the resistance and induction of the generator coil and R_d and L_d – resistance and induction of the damper coil. Plots of voltage vs. time and current vs. time in this circuit and the generated damper force are given in Fig. 7.

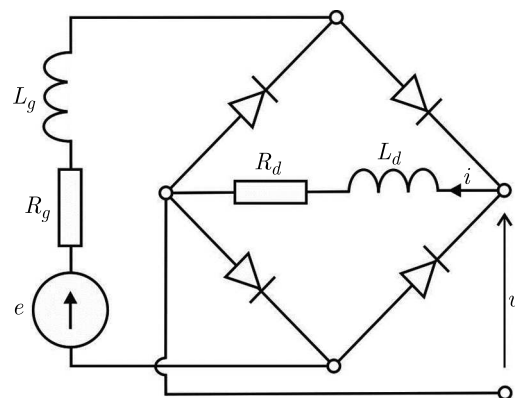


Fig. 6. Equivalent electric circuit of the energy harvesting MR damper with a Graetz bridge

The maximum voltage and current level in the damper coil is 2 V and 0.2 A. The plot of force reveals the presence of a force component related to the current in the damper force (unlike NE case). It appears that the maximal force value is reduced from 520 to 450 N, which is caused by the presence of the cogging force in the generator, arising in the permanent magnet-ferromagnetic

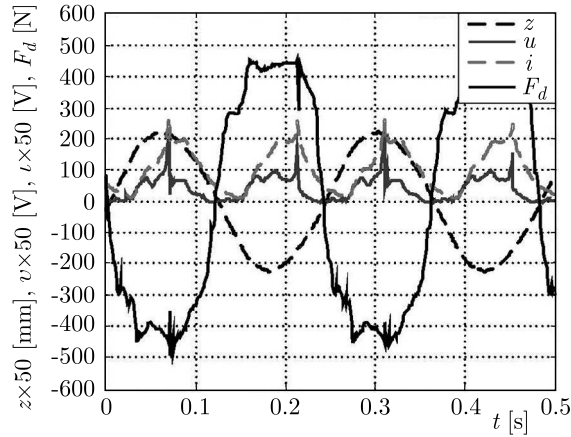


Fig. 7. Voltage, current and force vs. time

element systems (Sapinski, 2014), and the amplitude of piston displacement becomes 10 mm in the NE case and 2.5 mm in the EH_DS case. Plots of the force F_{MR} generated by the MR damper (Fig. 1) vs time for those two cases are compared in Fig. 8. It appears that the maximum force value tends to increase with the an increase in the coil current and becomes 325 N in the NE case and 520 N in the EH_DS case.

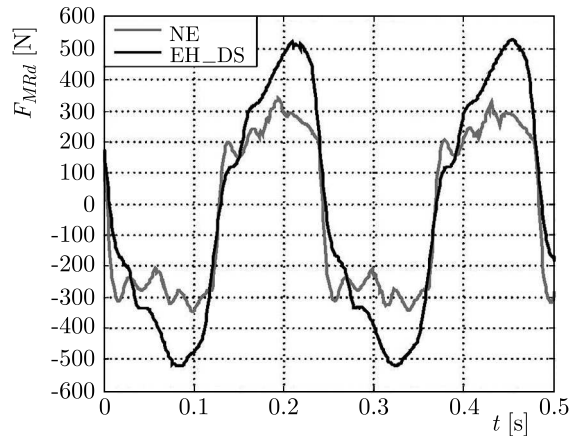


Fig. 8. MR damper force vs. time

Control of the current level in the damper coil is effected using the on-off and sky-hook control algorithms (Braun, 2002), utilising the information about velocity of the body \dot{x} and its relative velocity $(\dot{x} - \dot{z})$ based on the measured displacements x and z . The controllers performance is largely dependent on the quality of signals \dot{x} and \dot{z} . Because MR dampers are capable only of dissipating energy, on-off and sky-hook algorithms had to be modified such that the current level in the coil should be minimal in those time instants when energy should be supplied to the system. Figures 9a and 9b show a schematic diagram of the system for controlling coil current using the EH_OO and EH_SK algorithms. The current level in the damper coil depends on whether the damper coil is connected to the generator coil or disconnected, which is effected using a transistor switch K. The transistor switch K remains on as long as the voltage across its controls u_c should be 0 V. When voltage becomes 3.3 V, the transistor switch is off. A diode D_0 is provided to release the energy accumulated in the damper coil (when the transistor switch K is off).

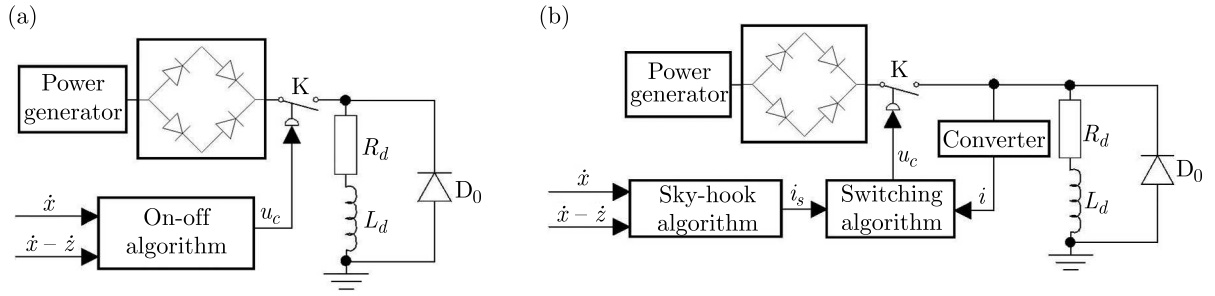


Fig. 9. Schematic diagram of the control system: (a) EH_OO case, (b) EH_SK case

The damper force generated in accordance with the on-off algorithm is expressed by (4.1)₁. To ensure the required force value, the current level in the damper coil should be governed by formula (4.1)₂

$$F_d = \begin{cases} F_{max} & \dot{x}(\dot{x} - \dot{z}) \geq 0 \\ 0 & \dot{x}(\dot{x} - \dot{z}) < 0 \end{cases} \quad i = \begin{cases} i_{max} & \dot{x}(\dot{x} - \dot{z}) \geq 0 \\ 0 & \dot{x}(\dot{x} - \dot{z}) < 0 \end{cases} \quad (4.1)$$

The operating principle of the vibration reduction system in the EH_OO case is illustrated by the plots of key parameters in function of time, shown in Figs. 10 and 11. When the energy in the system is to be dissipated ($\dot{x}(\dot{x} - \dot{z}) \geq 0$), the damper should deliver the maximum force, $F_d = F_{max}$. In order to achieve this, the transistor switch should be closed, producing the current flow $i = i_{max}$ in the damper coil. When energy is to be supplied ($\dot{x}(\dot{x} - \dot{z}) < 0$), the transistor switch K should be open ($i = 0$, $F_d = 0$).

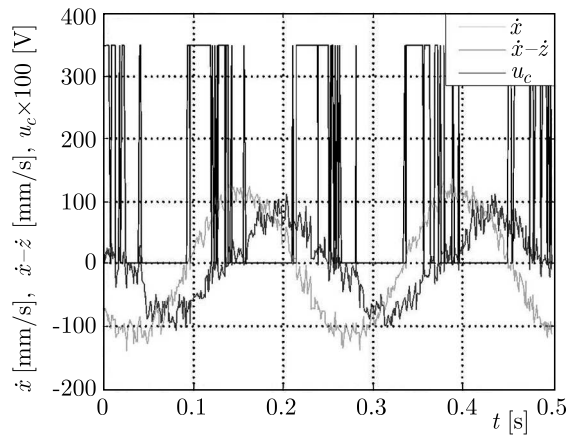


Fig. 10. Absolute velocity, relative velocity and control vs. time

However, the force $F_d \neq 0$, because of the contribution of the damper force components independent of the current level.

Frequent switching of the transistor switch K at instants when the signals and \dot{x} and $(\dot{x} - \dot{z})$ become zero is caused by signal disturbances. This effect has only slight influence on the current level in the damper coil, which can be also observed in the EH_SK case.

The damper force generated in accordance with the sky-hook algorithm is expressed by (4.2)₁. To ensure the required force value, the current level in the damper coil should be given by formula (4.2)₂

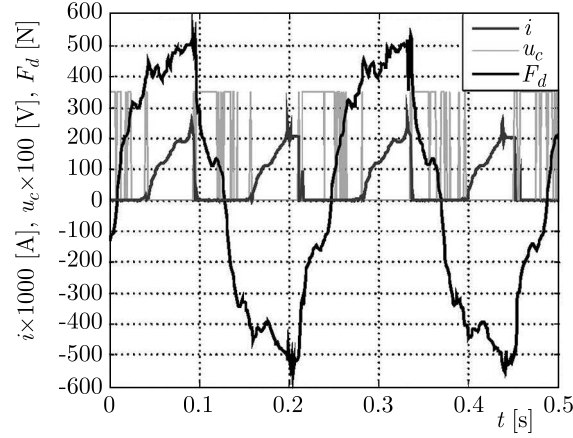


Fig. 11. Current level, control and force vs. time

$$F_d = \begin{cases} -c\dot{x} & \dot{x}(\dot{x} - \dot{z}) \geq 0 \\ 0 & \dot{x}(\dot{x} - \dot{z}) < 0 \end{cases} \quad i_s = \begin{cases} b|\dot{x}| & \dot{x}(\dot{x} - \dot{z}) \geq 0 \\ 0 & \dot{x}(\dot{x} - \dot{z}) < 0 \end{cases} \quad (4.2)$$

where c is the damping coefficient, b – proportionality factor.

The value of the proportionality factor $b = 0.0015$ A·s/mm has been chosen experimentally. The operating principle of the vibration reduction system in the EH_OO case is demonstrated by the plots of key parameters in function of time, shown in Figs. 12–14. The transistor switch K is switched by comparing the current level i (measured with a current-voltage converter and standard resistance) and the predicted value i_s , derived from the algorithm. The transistor switch K is closed ($u_c = 0$) when $i_s \geq i$.

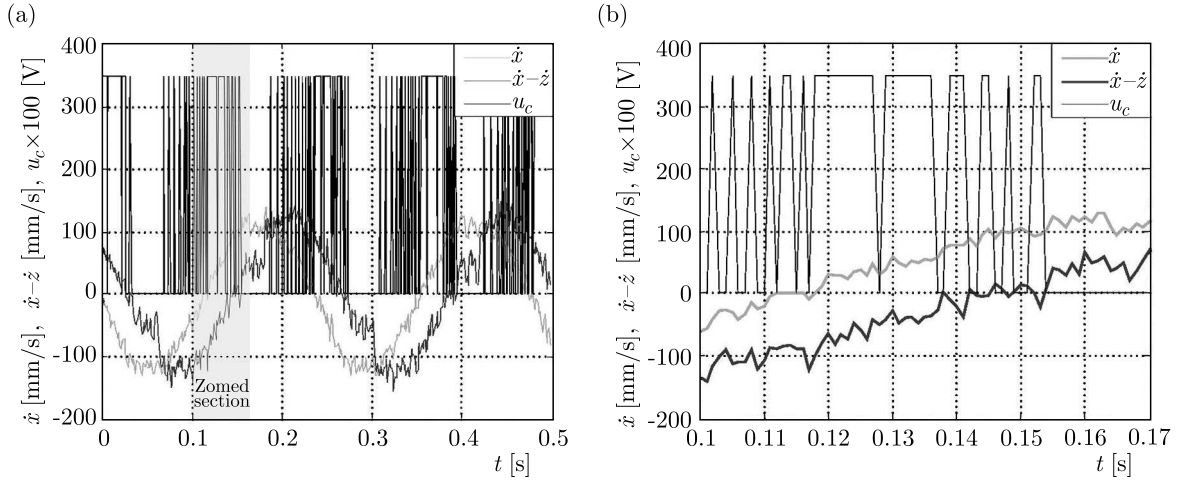


Fig. 12. Absolute velocity, relative velocity and control vs: (a) time, (b) time (zoomed section)

Frequent switching of the transistor switch K is caused not only by velocity signal disturbances (Fig. 12) as in the EH_OO case, but also by the current level exceeding i_s (Fig. 13). At the instant the damper coil is disconnected from the generator coil, the energy accumulated in the damper coil is discharged by the diode D_0 in a very short time, leading to rapid reduction of the current level i . The sampling frequency directly affects the current level stability with respect to the present value. An increase in the current during the subsequent switching of the transistor switch is associated with the damper coil inertia and the instantaneous voltage produced by the generator. Plots of the force F_d and current i in the EH_SK case in function of time are shown in Fig. 14.

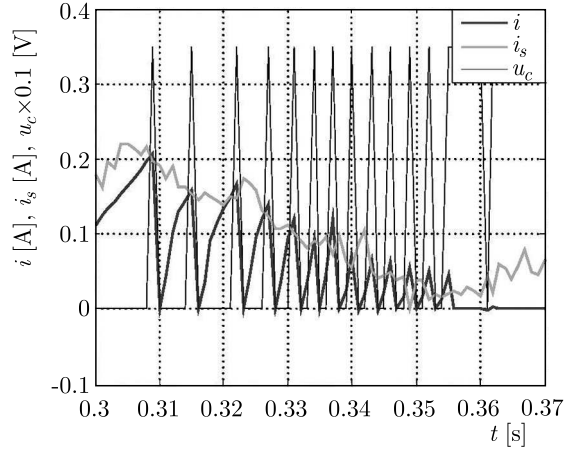


Fig. 13. Current and control vs. time

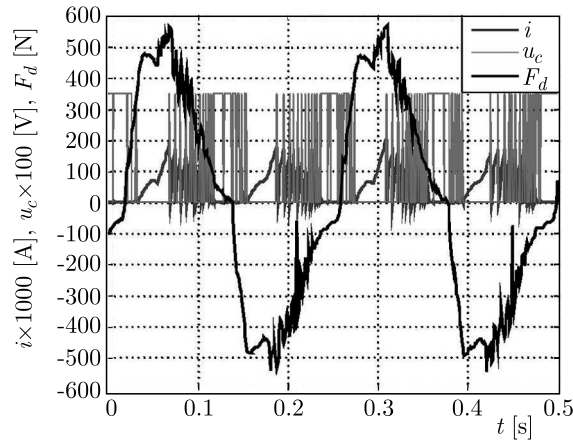


Fig. 14. Current level, control and force vs. time

The dependence of rms value of the damper force on frequency in each investigated case is given in Fig. 15, showing an increase in the rms value of the force F_d with an increase in the current level i . The efficiency of the investigated vibration reduction system is evaluated basing on the transmissibility coefficient (T_{xz}) expressed by the formula

$$T_{xz} = \frac{\sqrt{\frac{1}{T} \int_t^{t+T} x(t)^2 dt}}{\sqrt{\frac{1}{T} \int_t^{t+T} z(t)^2 dt}} \quad (4.3)$$

where T is the period of the signal.

The values of $T_{xz}(f)$ obtained in all analysed cases and in the predetermined frequency range are compared in Fig. 16. It appears that the system performance is the best in the EH_SK configuration. In this case, the value of T_{xz} for near-resonance frequencies approaches 1.17, for other frequencies it is near to that obtained in the NE case. Even though T_{xz} values for near-resonance frequencies are slightly lower in the EH_LOO and EH_DS case (1.11 and 1.12), one has to bear in mind that at higher frequencies, T_{xz} tends to increase, which results in deterioration of the system performance.

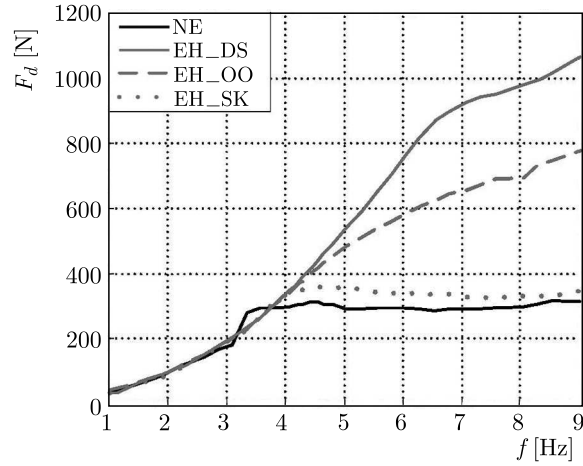
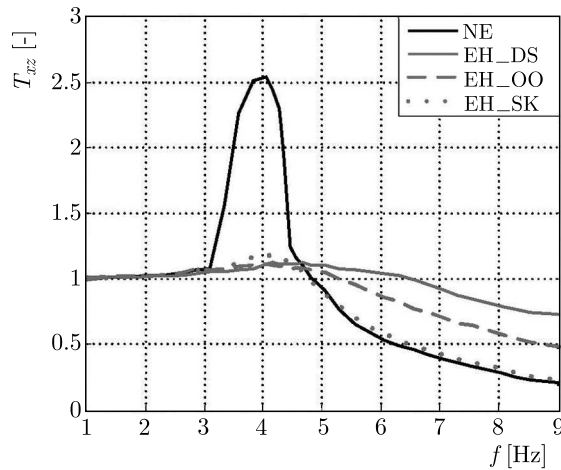
Fig. 15. *rms* force vs. frequency

Fig. 16. Transmissibility vs. frequency

5. Conclusions

This study summarises experimental investigations of a MR damper based vibration reduction system with energy harvesting capability employed in a single DOF mechanical structure. The main purpose is to evaluate the performance of the engineered vibration reduction system and to demonstrate its feasibility.

The system is investigated in four modes of its operation: when the damper is not energised (NE case), when the damper is energised and directly power-supplied with voltage produced by the generator (EH_DS case), when the control system with an on-off algorithm is used (EH_OO case) and when the sky-hook control algorithm is applied (EH_SK case). The experimental results lead us to the following conclusions:

- the vibration reduction system supplied with harvested energy features a decidedly lower transmissibility coefficient T_{xz} at near-resonance frequencies;
- despite a slight increase of T_{xz} in the frequency range (3, 4.5) Hz, the vibration reduction system performs best in the EH_SK case;
- the system performance in the EH_OO and EH_SK case is largely affected by the quality of signals \dot{x} and $(\dot{x} - \dot{z})$, obtained after processing of the measured displacement signals x and z ;

The research has been now undertaken to find out how to manage the harvested energy such that it could be effectively utilised to power-supply the components of the vibration reduction system (MR damper, sensors, control system).

Acknowledgement

This work has been supported by AGH University of Science and Technology under research program No. 11.11.130.958.

References

1. BRAUN S., EWINS D., RAO S.S., 2002, Encyclopedia of vibration, *Academic Press*, **1** (Active Control of Vehicle Vibration: Ahmadian M.), 37-45
2. CHEN C., LIAO W.H., 2012, A self-sensing magnetorheological damper with power generation, *Smart Materials and Structures*, **21**, 02501
3. CHO S.W., JUNG H.J., LEE I.W., 2005, Smart passive system based on a magnetorheological dampers, *Smart Materials and Structures*, **1**, 707-714
4. CHO S.W., PARK K.S., KIM CH.H., LEE I.W., 2004, Smart passive system based on MR damper, *1st International Conference "From Scientific Computing to Computational Engineering"*
5. CHOI K.M., JUNG H.J., LEE I.W., CHO S.W., 2007, Feasibility study of an MR damper-based smart passive control system employing an electromagnetic induction device, *Smart materials and Structures*, **16**, 2323-9
6. CHOI Y.T., WERELY N.M., 2009, Self-powered magnetorheological dampers, *Journal of Vibration Acoustics*, **131**, 44-50
7. HONG J.H., CHOI K.M., LEE J.H., OH J.W., LEE I.W., 2007, Experimental study on smart passive system based on MR damper, *Proceedings of the 18th KKCNN Symposium on Civil Engineering*, Taiwan
8. JUNG H.J., JANG D.D., CHO S.W., KOO J.H., 2009, Experimental verification of sensing capability of an electromagnetic induction system for an MR fluid damper based control system, *11th Conference on Electrorheological Fluids and Magnetorheological Suspensions, Journal of Physics: Conference Series*, **149**
9. JUNG H.J., JANG D.D., KOO J.H., CHO S.W., 2010, Experimental evaluation of a self-sensing capability of an electromagnetic induction system designed for MR dampers, *Journal of Intelligent Material Systems and Structures*, **21**, 837-836
10. LAM K.H., CHEN Z.H., NI Y.Q., CHAN H.L.W., 2010, A magnetorheological damper capable of force and displacement sensing, *Sensors and Actuators A: Physical*, **158**, 1, 51-59
11. LI Z., ZHUO L., KUANG J., LUHRS G., 2013a, Energy-harvesting shock absorber with a mechanical motion rectifier, *Smart Materials and Structures*, **22**, 028008
12. LI Z., ZHUO L., LUHRS G., LIN L., QIN Y., 2013b, Electromagnetic energy-harvesting shock absorbers: design, Modeling and Road Tests, *IEEE Transactions on Vehicular Technology*, **62**, 3, 1065-1074
13. SAPIŃSKI B., 2011, Experimental study of a self-powered and sensing MR damper-based vibration control system, *Smart Materials and Structures*, **20**, 105007
14. SAPIŃSKI B., 2014, Energy harvesting MR linear damper: prototyping and testing, *Smart Materials and Structures*, **23**, 035021
15. SNAMINA J., SAPIŃSKI B., 2011, Energy balance in self-powered MR damper-based vibration reduction system, *Bulletin of the Polish Academy of Sciences Technical Sciences*, **59**, 1, 75-80

16. WANG D.H., BAI X.X., 2013, A magnetorheological damper with an integrated self-powered displacement sensor, *Smart Materials and Structures*, **22**, 075001
17. WANG D.H., BAI X.X., LIAO W.H., 2010, An integrated relative displacement self-sensing magnetorheological damper: prototyping and testing, *Smart Materials and Structures*, **19**, 105008
18. ZHU S.Y., SHEN W.A., XU Y.L., LEE W.C., 2012, Linear electromagnetic devices for vibration damping and energy harvesting: Modeling and testing, *Engineering Structures*, **34**, 198-212

Manuscript received June 16, 2015; accepted for print July 28, 2015

A CONCENTRIC HYDRODYNAMIC JOURNAL BEARING WITH THE BOUNDARY SLIPPAGE

YONGBIN ZHANG

College of Mechanical Engineering, Changzhou University, Changzhou, Jiangsu Province, China
e-mail: engmech1@sina.com

The paper proposes a concentric hydrodynamic journal bearing constructed by the boundary slippage, which is opposed by conventional lubrication theory. Analysis for the carried load and friction coefficient of this bearing is presented. The optimum condition for the maximum load-carrying capacity of this bearing is examined. It is shown that the whole circumference of the bearing should be taken as the lubricated area, while on most of the stationary surface of the bearing there should be a hydrophobic coating covered so that the boundary slippage would occur on this surface. In this condition, the load-carrying capacity of the bearing is the highest but its friction coefficient is the lowest.

Keywords: hydrodynamics, boundary slippage, load, friction, bearing

1. Introduction

Conventional lubrication theory says that no hydrodynamic lubrication effect can be generated between two sliding parallel smooth plane surfaces (Pinkus, 1961). It also denies a concentric hydrodynamic journal bearing, where the lubricating film thickness is circumferentially constant. However, in practice, a concentric hydrodynamic journal bearing is very useful because of its high supporting precision, high lubricating film thickness, low viscous friction and low energy consumption.

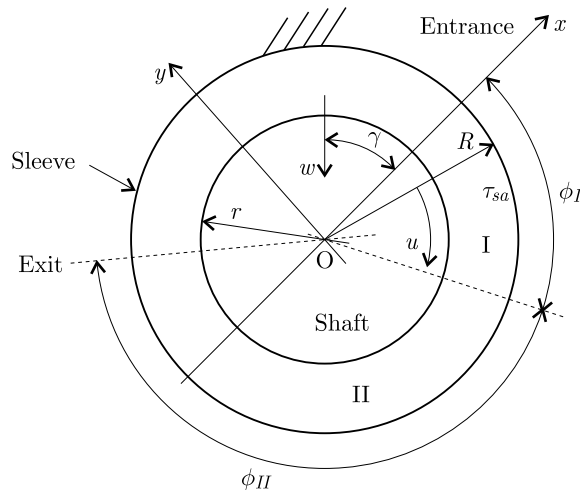
The boundary slippage has been found to be capable of improving the performance of a hydrodynamic lubrication (Salant and Fortier, 2004; Zhang, 2008, 2010, 2013, 2014, 2015b; Li *et al.*, 2014). It was found that hydrodynamic lubrication can be generated between two sliding parallel smooth plane surfaces because of the boundary slippage (Zhang, 2008). While, in conventional bearing configurations, the artificial introduction of the boundary slippage can increase the load-carrying capacity of the bearing but reduce its friction coefficient Zhang (2010, 2013, 2014, 2015b). In Zhang (2015b), the performance of a hydrodynamic journal bearing with an eccentricity was found to be able to be significantly improved by the boundary slippage. However, in that paper, a concentric hydrodynamic journal bearing was not addressed.

This paper proposes a concentric hydrodynamic journal bearing which is formed dependent on the boundary slippage. Analysis of this bearing is presented. It has been found that a significant load-carrying capacity can be generated depending on the design method applied. The optimum condition for the maximum load-carrying capacity of the bearing is also analyzed. In this optimum condition, the bearing also works with the lowest friction coefficient. The study shows a potential application value of such a bearing in practice.

2. The bearing configuration

Figure 1 shows the configuration of the studied bearing. The bearing is formed by a rotating shaft (with circumferential speed u) and a stationary sleeve. The two elements are concentric

and the lubricating film thickness in the bearing is constant and equal to the bearing clearance $c(= R-r)$. The clearance of the bearing is filled with a fluid. The lubricated area of the bearing is divided into two subzones, i.e. "I" and "II" subzones which are, respectively, the inlet and outlet zones of the bearing. On the stationary (sleeve) surface in "I" subzone there is a hydrophobic coating covered to yield a low fluid film-contact surface interfacial shear strength (τ_{sa}) at this surface so that the boundary slippage would occur at this coated surface. The envelope angles of "I" and "II" subzones are respectively ϕ_I and ϕ_{II} . On the other surfaces of the bearing, the fluid film-contact surface interfacial shear strength is relatively high so that the boundary slippage is absent on these surfaces. The radii of the shaft and sleeve are r and R , respectively. The carried load per unit contact width and attitude angle of the bearing are respectively w and γ . The coordinate system used in the analysis is also shown in Fig. 1.



The bearing is filled with a fluid between the shaft and the sleeve. The fluid film slips at the sleeve surface in subzone "I" because of low fluid-sleeve interfacial shear strength τ_{sa} . It does not slip at the other bearing surfaces because of relatively high interfacial shear strength there

Fig. 1. Configuration of the proposed bearing

3. Analysis

The analysis carried out by Zhang (2015b) is also applicable to the present bearing. The analysis is based on the following assumptions:

- The lubricant film thickness is high enough so that the lubricant is continuum across the film thickness;
- The lubricant film is Newtonian within the film;
- The lubricant is isoviscous and incompressible;
- Contact surface deformations are negligible;
- The side leakage in the bearing is negligible and the lubricant is in laminar flow;
- The operating condition is isothermal.

Accordingly to Zhang (2015b), the following dimensionless parameters are defined:

$$W = \frac{wc^2}{u\eta r^2} \quad P = \frac{pc^2}{u\eta r} \quad Q_v = \frac{q_v}{uc} \quad \bar{F}_x = \frac{F_x c^2}{u\eta r^2} \quad \bar{F}_y = \frac{F_y c^2}{u\eta r^2}$$

$$\bar{F}_{f,h} = \frac{F_{f,h}c^2}{u\eta r^2} \quad \bar{F}_{f,s} = \frac{F_{f,s}c^2}{u\eta r^2} \quad \bar{\tau} = \frac{\tau c^2}{u\eta r} \quad k_\tau = \frac{\tau_{sa}c}{u\eta} \quad DU = \frac{\Delta u}{u}$$

Here, η is fluid viscosity, p is film pressure, q_v is volume flow rate in the bearing per unit contact width, F_x and F_y are respectively components of the carried load in the x and y coordinate directions, $F_{f,h}$ and $F_{f,s}$ are respectively friction forces per unit contact width acting on the sleeve and shaft surfaces, τ is shear stress, and Δu is fluid film interfacial slipping velocity.

The pressure boundary conditions in the bearing are:

$$P|_{\phi=0} = 0 \quad P|_{\phi=\phi_I+\phi_{II}} = 0 \quad (3.1)$$

When the eccentricity ratio ε is zero, a lot of the analytical results obtained by Zhang (2015b) are applicable to the present bearing. The following Sections demonstrate those results.

3.1. “I” subzone

The dimensionless Reynolds equation in “I” subzone is:

$$\frac{dP_{slip}}{d\phi} = 3 - 3Q_{v,slip} - \frac{3k_\tau}{2} \quad (3.2)$$

Using the boundary condition in Eq. (3.1), integrating Eq. (3.2) gives dimensionless pressure in “I” subzone:

$$P_{slip} = \left(3 - 3Q_{v,slip} - \frac{3k_\tau}{2}\right)\phi \quad \text{for } 0 \leq \phi \leq \phi_I \quad (3.3)$$

The dimensionless pressure on the boundary between “I” and “II” subzones is:

$$P_{slip,max} = \left(3 - 3Q_{v,slip} - \frac{3k_\tau}{2}\right)\phi_I \quad (3.4)$$

3.2. “II” subzone

The dimensionless Reynolds equation in “II” subzone is:

$$\frac{dP_{slip}}{d\phi} = 6 - 12Q_{v,slip} \quad (3.5)$$

Using the boundary condition in Eq. (3.1), integrating Eq. (3.5) gives dimensionless pressure in “II” subzone:

$$P_{slip} = (6 - 12Q_{v,slip})(\phi - \phi_I - \phi_{II}) \quad \text{for } \phi_I \leq \phi \leq \phi_I + \phi_{II} \quad (3.6)$$

According to Eq. (3.6), the dimensionless pressure on the boundary between “I” and “II” subzones is:

$$P_{slip,max} = (12Q_{v,slip} - 6)\phi_{II} \quad (3.7)$$

Equations (3.3) and (3.6) show that the pressure is respectively linearly distributed in “I” and “II” subzones in the present bearing. Figure 2 schematically shows the pressure distribution in the present bearing.

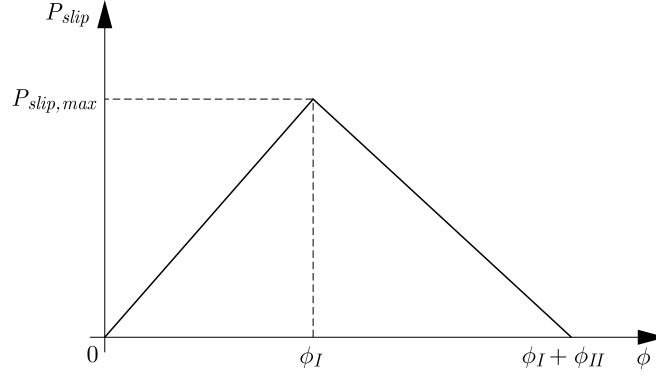


Fig. 2. Illustration of the pressure distribution in the proposed bearing

3.3. Volume flow rate and condition for the bearing

Define $\psi_\phi = \phi_{II}/\phi_I$, solving coupled equations (3.4) and (3.7) gives:

$$Q_{v,slip} = \frac{1 + 2\psi_\phi - \frac{1}{2}k_\tau}{1 + 4\psi_\phi} \quad (3.8)$$

and

$$P_{slip,max} = \bar{P}_{slip,max}(\phi_I + \phi_{II}) \quad (3.9)$$

where $\bar{P}_{slip,max} = 6\psi_\phi(1 - k_\tau)/[(1 + \psi_\phi)(1 + 4\psi_\phi)]$.

From $Q_{v,slip} > 0$, it is obtained that $k_\tau < 2 + 4\psi_\phi$. From $P_{slip,max} > 0$, it is obtained that $k_\tau < 1$. Therefore, $k_\tau < 1$ is the condition for the present bearing.

It is noted from Eq. (3.9) that for given values of k_τ and $\phi_I + \phi_{II}$, when $\psi_\phi = 1/2$, $P_{slip,max}$ reaches the maximum, and its maximum value is $2(1 - k_\tau)(\phi_I + \phi_{II})/3$.

3.4. Carried load and attitude angle of the bearing

The dimensionless hydrodynamic force component in the x axis direction acting on the shaft per unit contact width is:

$$\bar{F}_{x,slip} = - \int_0^{\phi_I + \phi_{II}} P_{slip} \cos \phi \, d\phi = \bar{P}_{slip,max} f_1(\psi_\phi, \phi_{tot}) \quad (3.10)$$

where $\phi_{tot} = \phi_I + \phi_{II}$ and (also Zhang (2015a))

$$f_1(\psi_\phi, \phi_{tot}) = \left(1 + \frac{1}{\psi_\phi}\right) \left[\frac{\psi_\phi \phi_{tot}}{1 + \psi_\phi} \sin\left(\frac{\phi_{tot}}{1 + \psi_\phi}\right) + \cos \phi_{tot} - \cos\left(\frac{\phi_{tot}}{1 + \psi_\phi}\right) \right] \\ - (1 + \psi_\phi) \left[\frac{\phi_{tot} \sin\left(\frac{\phi_{tot}}{1 + \psi_\phi}\right)}{1 + \psi_\phi} + \cos\left(\frac{\phi_{tot}}{1 + \psi_\phi}\right) - 1 \right] \quad (3.11)$$

The dimensionless hydrodynamic force component in the y axis direction acting on the shaft per unit contact width is:

$$\bar{F}_{y,slip} = \int_0^{\phi_I + \phi_{II}} P_{slip} \sin \phi \, d\phi = \bar{P}_{slip,max} f_2(\psi_\phi, \phi_{tot}) \quad (3.12)$$

where (also Zhang (2015a))

$$f_2(\psi_\phi, \phi_{tot}) = \left(1 + \frac{1}{\psi_\phi}\right) \left[\frac{\psi_\phi \phi_{tot}}{1 + \psi_\phi} \cos\left(\frac{\phi_{tot}}{1 + \psi_\phi}\right) - \sin \phi_{tot} + \phi_{tot} \cos \phi_{tot} + \sin\left(\frac{\phi_{tot}}{1 + \psi_\phi}\right) \right] \\ + (1 + \psi_\phi) \left[\sin\left(\frac{\phi_{tot}}{1 + \psi_\phi}\right) - \frac{\phi_{tot}}{1 + \psi_\phi} \cos\left(\frac{\phi_{tot}}{1 + \psi_\phi}\right) \right] \quad (3.13)$$

The dimensionless load per unit contact width carried by the bearing is:

$$W_{slip} = \sqrt{\bar{F}_{x,slip}^2 + \bar{F}_{y,slip}^2} = \bar{P}_{slip,max} f_w(\psi_\phi, \phi_{tot}) \quad (3.14)$$

where $f_w(\psi_\phi, \phi_{tot}) = \sqrt{f_1^2(\psi_\phi, \phi_{tot}) + f_2^2(\psi_\phi, \phi_{tot})}$ (Zhang, 2015a).

Figure 3 plots the values of f_w against ϕ_{tot} for the given values of ψ_ϕ . It is shown that for a given ψ_ϕ , the value of f_w reaches the maximum when $\phi_{tot} = 2\pi$. This means that for the maximum load-carrying capacity of the bearing, ϕ_{tot} should be taken as 2π .

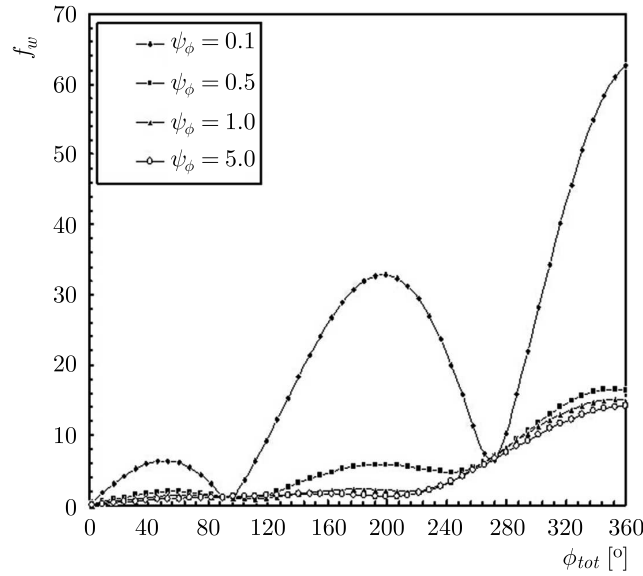


Fig. 3. Plots of f_w against ϕ_{tot} for given ψ_ϕ values (Zhang, 2015a)

When $\phi_{tot} = 2\pi$, the dimensionless load is:

$$W_{slip} = (1 - k_\tau)G(\psi_\phi) \quad (3.15)$$

where $G(\psi_\phi) = 6\psi_\phi f_w(\psi_\phi, 2\pi) / [(1 + \psi_\phi)(1 + 4\psi_\phi)]$.

The attitude angle of the bearing is:

$$\gamma = \arctan \left[\frac{f_2(\psi_\phi, \phi_{tot})}{f_1(\psi_\phi, \phi_{tot})} \right] \quad (3.16)$$

3.5. Friction coefficient and interfacial slipping velocity

The dimensionless shear stress on the shaft surface is:

$$\bar{\tau}_{s,slip} = \begin{cases} \frac{c}{r} \left(3 - \frac{k_\tau}{2} - 3Q_{v,slip}\right) & \text{for } 0 \leq \phi \leq \phi_I \\ \frac{c}{r} (4 - 6Q_{v,slip}) & \text{for } \phi_I < \phi \leq \phi_I + \phi_{II} \end{cases} \quad (3.17)$$

The dimensionless shear stress on the sleeve surface is:

$$\bar{\tau}_{h,slip} = \begin{cases} k_{\tau} \frac{c}{r} & \text{for } 0 \leq \phi \leq \phi_I \\ \frac{c}{r} (6Q_{v,slip} - 2) & \text{for } \phi_I < \phi \leq \phi_I + \phi_{II} \end{cases} \quad (3.18)$$

The dimensionless friction force on the shaft surface per unit contact width is:

$$\begin{aligned} \bar{F}_{f,s,slip} &= \int_0^{\phi_I + \phi_{II}} \bar{\tau}_{s,slip} d\phi = \int_0^{\phi_I} \bar{\tau}_{s,slip} d\phi + \int_{\phi_I}^{\phi_I + \phi_{II}} \bar{\tau}_{s,slip} d\phi \\ &= \frac{c}{r} \left(3 - \frac{k_{\tau}}{2} - 3Q_{v,slip} \right) \phi_I + \frac{c}{r} (4 - 6Q_{v,slip}) \phi_{II} \end{aligned} \quad (3.19)$$

The dimensionless friction force on the sleeve surface per unit contact width is:

$$\begin{aligned} \bar{F}_{f,h,slip} &= \int_0^{\phi_I + \phi_{II}} \bar{\tau}_{h,slip} d\phi = \int_0^{\phi_I} \bar{\tau}_{h,slip} d\phi + \int_{\phi_I}^{\phi_I + \phi_{II}} \bar{\tau}_{h,slip} d\phi \\ &= k_{\tau} \phi_I \frac{c}{r} + \frac{c}{r} (6Q_{v,slip} - 2) \phi_{II} \end{aligned} \quad (3.20)$$

The friction coefficients on the sleeve and shaft surfaces are respectively:

$$f_{h,slip} = \frac{\bar{F}_{f,h,slip}}{W_{slip}} \quad f_{s,slip} = \frac{\bar{F}_{f,s,slip}}{W_{slip}} \quad (3.21)$$

The dimensionless slipping velocity of the fluid film at the sleeve surface is:

$$DU = \begin{cases} \frac{3Q_{v,slip}}{2} - \frac{1}{2} - \frac{k_{\tau}}{4} & \text{for } 0 \leq \phi \leq \phi_I \\ 0 & \text{for } \phi_I < \phi \leq \phi_I + \phi_{II} \end{cases} \quad (3.22)$$

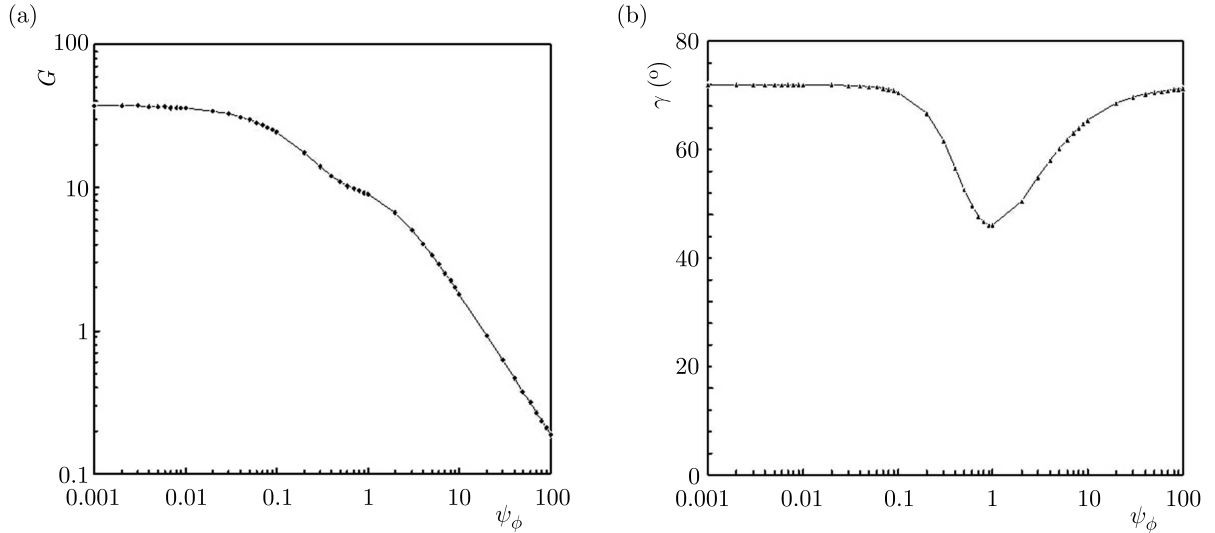
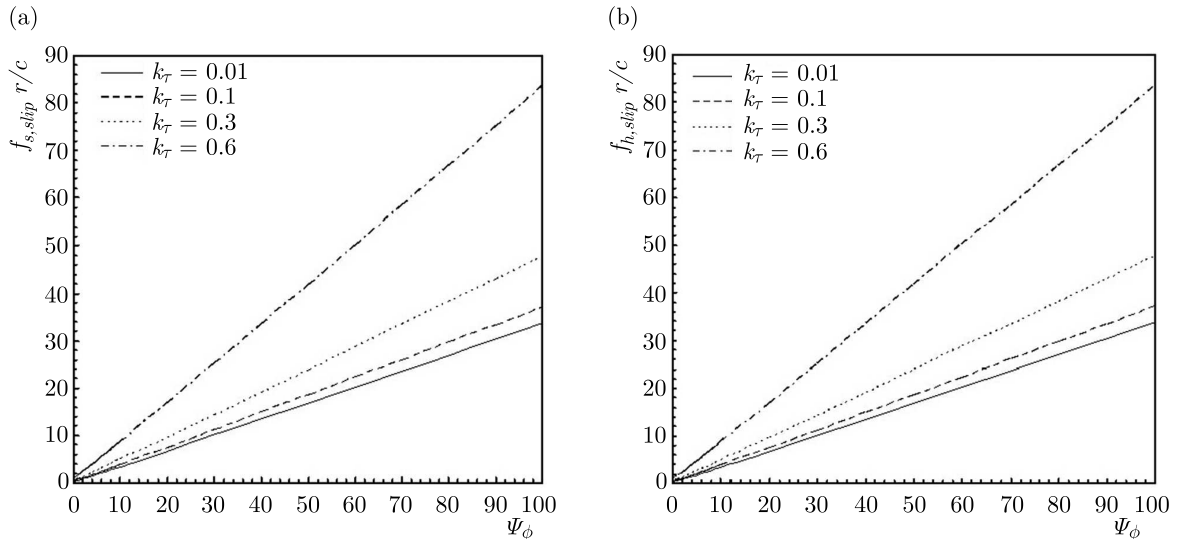
where DU should be positive for $0 \leq \phi \leq \phi_I$.

4. Results and discussion

Figure 4a plots the values of G against ψ_{ϕ} when $\phi_{tot} = 2\pi$. It is shown that G significantly increases with the reduction of ψ_{ϕ} when $\psi_{\phi} \geq 0.1$. While, for $\psi_{\phi} < 0.01$, G is weakly influenced by ψ_{ϕ} . According to Eq. (3.15), it means that for a given k_{τ} the load-carrying capacity of the bearing increases with the reduction of ψ_{ϕ} , especially when $\psi_{\phi} \geq 0.1$, while too low values of ψ_{ϕ} have no benefits in increasing the load-carrying capacity. As the optimum value of ψ_{ϕ} for the maximum value of $P_{slip,max}$ is 0.5, in the engineering design, the value of ψ_{ϕ} may be recommended to be chosen between 0.1 and 0.5.

Figure 4b plots values of γ against ψ_{ϕ} when $\phi_{tot} = 2\pi$. The minimum value of γ is about 57° , and it occurs when ψ_{ϕ} is around 1.0. For $\psi_{\phi} < 0.1$ or $\psi_{\phi} > 20$, γ approaches 90° .

Figures 5a and 5b plot respectively values of $f_{s,slip}r/c$ and $f_{h,slip}r/c$ against ψ_{ϕ} for different k_{τ} when $\phi_{tot} = 2\pi$. It is shown that for given values of k_{τ} and c/r , the friction coefficients $f_{s,slip}$ and $f_{h,slip}$ both are linearly reduced with the reduction of ψ_{ϕ} . This indicates that a relatively low value of ψ_{ϕ} has also benefit of giving a low friction coefficient to the bearing. The reduction of k_{τ} is shown to significantly reduce the friction coefficient, especially when ψ_{ϕ} is high.

Fig. 4. Plots of (a) G , (b) γ against ψ_ϕ when $\phi_{tot} = 2\pi$ Fig. 5. Plots of $f_{s,slip}r/c$ and $f_{h,slip}r/c$ against ψ_ϕ for different k_τ when $\phi_{tot} = 2\pi$

5. Conclusions

This paper proposes a concentric hydrodynamic journal bearing which is formed dependent on the boundary slippage. The configuration of the bearing is presented. The lubricated area of the bearing is divided into two subzones, which may respectively be the inlet and outlet zones. In the inlet zone, on the stationary surface a hydrophobic coating is covered to yield a low fluid film-contact surface interfacial shear strength so that the boundary slippage could occur on this surface. On the other bearing surfaces, the boundary slippage is absent because of relatively high interfacial shear strengths on these surfaces.

Analysis for the load-carrying capacity and friction coefficient of the bearing is presented. Typical calculations have been carried out. It has been found that the optimum value of the ratio of the circumferential length of the outlet zone to that of the inlet zone, i.e. the optimum value of ψ_ϕ is 0.5 for the maximum hydrodynamic pressure building-up. However for this value ψ_ϕ , the load-carrying capacity of the bearing is still not the maximum. The whole circumference of the bearing should be taken as the lubricated area for achieving a high load-carrying capacity.

In this condition, the carried load of the bearing is found to be increased with the reduction of ψ_ϕ , especially when $\psi_\phi \geq 0.1$. Nevertheless, for $\psi_\phi \leq 0.01$, the load-carrying capacity of the bearing is weakly influenced by variation of ψ_ϕ . It is recommended that in engineering design the value of ψ_ϕ should be chosen between 0.1 and 0.5. A low value of ψ_ϕ also has the benefit of giving a low friction coefficient to the bearing.

References

1. PINKUS O., STERNLICHT B., 1961, *Theory of hydrodynamic lubrication*, McGraw-Hill, New York
2. SALANT R.F., FORTIER A.E., 2004, Numerical analysis of a slider bearing with a heterogeneous slip/no-slip surface, *Tribology Transactions*, **47**, 328-334
3. ZHANG Y.B., 2008, Boundary slippage for generating hydrodynamic load-carrying capacity, *Applied Mathematics and Mechanics*, **29**, 1155-1164
4. ZHANG Y.B., 2010, Boundary slippage for improving the load and friction performance of a step bearing, *Transactions of the Canadian Society for Mechanical Engineering*, **34**, 373-387
5. ZHANG Y.B., 2013, A tilted pad thrust slider bearing improved by boundary slippage, *Meccanica*, **48**, 769-781
6. ZHANG Y.B., 2014, Hydrodynamic lubrication in line contacts improved by the boundary slippage, *Meccanica*, **49**, 503-519
7. ZHANG Y.B., 2015a, A concentric micro/nano journal bearing constructed by physical adsorption, *Journal of the Balkan Tribological Association*, **21**, 937-951
8. ZHANG Y.B., 2015b, An improved hydrodynamic journal bearing with the boundary slippage, *Meccanica*, **50**, 25-38
9. LI G., ZHANG Y.B., JIANG X.D., 2014, A study on the performance of a hydrodynamic step bearing by controlling its boundary slippage in the outlet zone, *Journal of Changzhou University, Natural Sciences Edition*, **26**, 33

Manuscript received April 24, 2015; accepted for print July 29, 2015

OPTIMIZED RE-ENTRY INPUT SHAPERS

PETR BENEŠ, MICHAEL VALÁŠEK

*Czech Technical University in Prague, Faculty of Mechanical Engineering Dept. of Mechanics,
Biomechanics and Mechatronics, Prague, Czech Republic
e-mail: petr.benes@fs.cvut.cz; michael.valasek@fs.cvut.cz*

The paper deals with the design of optimized input shapers for non-vibrational control of flexible mechatronic systems. The described method is based on a combination of advantages from two approaches – precomputed control curves and on-line shapers. The strategy has two steps. Primarily, an optimized precomputed curve is found as a solution to the point-to-point control problem with respect to any requested optimization goals. Then it is transformed into an on-line shaper with the re-entry property. The resulting shaper transforms any arbitrary input signal to a non-vibrational one. In contrast to other techniques, the shaper length is not determined from the system natural frequency. The shaper can be easily modified with respect to position, velocity, acceleration or jerk control. The theoretical results are verified by experiments using a laboratory crane.

Keywords: input shaper, command shaper, residual vibrations, re-entry

1. Introduction

The fast and precise positioning of mechatronic structures is a challenging problem when flexibility has to be taken into account and residual vibrations appear. There are basically two main control approaches – feedback and feedforward control. Application of shaped input signals belongs to the latter group. It is based on the input signal that is modified to achieve zero residual vibrations. This principle has been effectively used in many applications such as the robot manipulator (Chang *et al.*, 2005), telescopic handler (Park *et al.*, 2004), antisway crane (Valášek, 1995) etc.

The first form of command/input shaping was the posicast control (Smith, 1957). The step signal was broken into two smaller steps, one delayed in time with respect to the system natural frequency. Superposition of the responses to these steps led to elimination of vibrations. The method is very sensitive to modeling errors. Nevertheless, it was evolved using more step changes (Sugiyama and Uchino, 1986) or precisely timed sine waves (Aspinwall, 1980). Other approaches were based on an analysis using the Laplace transform (domain) synthesis (Bhat and Miu, 1990; Singh and Vadali, 1993) or using the theory of time-delayed systems (Vyhlídal *et al.*, 2012).

Today, we can divide existing shaping techniques into two groups – precomputed curves and on-line shapers (Singhose and Seering, 1997). The former ones solve the point-to-point control problem when both initial and final states of the system are known in advance, but they cannot be used in case the input is changing. Usually, they are based on a combination of precomputed signals with a zero contribution to the system natural frequency and are used, e.g. for design of cam profiles (Wiederrich and Roth, 1974) or in time optimal control (Lau and Pao, 2003). Some of them are based on the differential flatness property of a nonlinear system and enable generation of a trajectory following the control (Post *et al.*, 2011). Shapers, on the other hand,

act like filters of any arbitrary input signal and modify it not to excite vibration, Fig. 1. The price for that is a delay in the settling time and/or an increase in the required power (Beneš,

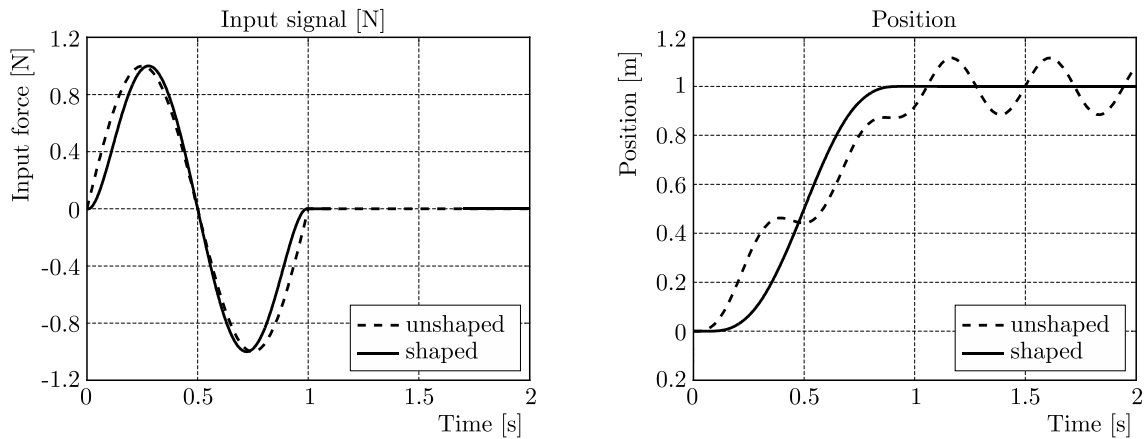


Fig. 1. Comparison of the system response to the shaped and unshaped control input

2012). Shapers are capable of processing a new input signal even if the previous task has not yet been finished. We call this behaviour re-entry property. Probably the most popular method in this group is the patented “Input Shaping” (Singhose, 1997; Singer and Seering, 1990; Singhose and Seering, 1991) based on the convolution of the input signal with a series of precisely timed and scaled pulses.

The advantages and disadvantages of both existing groups are obvious. Precomputed curves can be highly optimised but they do not have the re-entry property and, therefore, cannot be used for on-line systems, e.g. a manually operated crane. Shapers are capable of dealing with on-line control but usually they cannot be optimised to a greater extent because their time length is determined as a multiple of the system natural period and the shape is usually limited to pulses, steps and ramps.

Another problem is that the above mentioned approaches are designed and mostly applied to linear systems. Their extension towards nonlinear systems is a great challenge. The crane is in fact a non-linear system. Many on-line shapers assume that the influence of non-linearity is small and they are successful (Post *et al.*, 2011). The second approach is that non-linear dynamics is decomposed into quasi-linear subsystems. The example is a rotary crane (derrick) decomposed into an equivalent portal crane tangential to the trajectory where separate on-line shapers are used (Zavřel *et al.*, 2004; Piazzzi *et al.*, 2002). The third approach is usage of differential flatness that constructs the full relationship between the input and all outputs (Post *et al.*, 2011; Schindele *et al.*, 2009; Zimmert and Sawodny, 2010; Osmic *et al.*, 2014; Heyden and Woernle, 2006). The fourth approach is the use of a non-linear quadratic regulator (NQR) for stable solution of the trajectory (Kittnar *et al.*, 2004). The fifth approach is control using harmonic functions that constructs the missing control input for flexible modes (Neusser *et al.*, 2013). The third to fifth approaches heavily depend on the knowledge of the system model and complete state measurement. If this is not fulfilled, the control quality is deteriorated. The first and second approaches based on shapers show robustness to model uncertainties and are still worth further developing.

Therefore, this paper describes a new approach to the shaper design which combines the advantages of both groups of precomputed curves and on-line re-entry shapers. The completely new result is an optimized on-line shaper with adjustable time length which makes it possible to minimize the required power of the used drives for the chosen reasonable positioning time.

2. Theoretical background

The state space representation of a system with the system matrix \mathbf{A} , input matrix \mathbf{B} , state vector \mathbf{y} and input vector \mathbf{u} is written as

$$\dot{\mathbf{y}} = \mathbf{A}\mathbf{y}(t) + \mathbf{B}\mathbf{u}(t) \quad (2.1)$$

The solution to the point-to-point (PTP) control problem for (2.1) with the start time at t_1 , the finish time t_2 and known initial and final states $\mathbf{y}(t_1)$, $\mathbf{y}(t_2)$, respectively, can be derived in the form (Lewis, 1992)

$$\mathbf{y}(t_2) = e^{\mathbf{A}(t_2-t_1)}\mathbf{y}(t_1) + \int_{t_1}^{t_2} e^{\mathbf{A}(t_2-\tau)}\mathbf{B}\mathbf{u}(\tau) d\tau \quad (2.2)$$

which can be transformed to

$$e^{-\mathbf{A}t_2}\mathbf{y}(t_2) - e^{-\mathbf{A}t_1}\mathbf{y}(t_1) = \int_{t_1}^{t_2} e^{-\mathbf{A}\tau}\mathbf{B}\mathbf{u}(\tau) d\tau \quad (2.3)$$

The expression on the right side of (2.4) can be rewritten as a sum of contributions from particular inputs

$$e^{-\mathbf{A}t_2}\mathbf{y}(t_2) - e^{-\mathbf{A}t_1}\mathbf{y}(t_1) = \sum_{l=1}^n \int_{t_1}^{t_2} e^{-\mathbf{A}\tau} u_l(\tau) d\tau \mathbf{b}_l \quad (2.4)$$

where n is the total number of inputs, u_l is the l -th input, \mathbf{b}_l is the corresponding column of the \mathbf{B} matrix.

Assuming the controllability of system (2.1), there is a unique transform to the Jordan canonical form

$$\dot{\mathbf{z}}(t) = \mathbf{J}\mathbf{z}(t) + \mathbf{D}\mathbf{u}(t) \quad \mathbf{J} = \mathbf{P}^{-1}\mathbf{A}\mathbf{P} \quad \mathbf{z} = \mathbf{P}^{-1}\mathbf{y} \quad \mathbf{D} = \mathbf{P}^{-1}\mathbf{B} \quad (2.5)$$

where \mathbf{J} is a block diagonal matrix made of Jordan blocks, \mathbf{P} is a regular transform matrix. Then the solution to (2.3) can be expressed as

$$e^{-\mathbf{J}t_2}\mathbf{z}(t_2) - e^{-\mathbf{J}t_1}\mathbf{z}(t_1) = \int_{t_1}^{t_2} e^{-\mathbf{J}\tau}\mathbf{D}\mathbf{u}(\tau) d\tau \quad (2.6)$$

with

$$e^{\mathbf{J}t} = \text{diag}\{e^{\mathbf{J}_i t}\} \quad e^{\mathbf{J}_i t} = e^{p_i t} \begin{bmatrix} 1 & 0 & \dots & 0 & 0 \\ t & 1 & \dots & 0 & 0 \\ \vdots & \vdots & \ddots & \vdots & \vdots \\ \frac{t^{r_i-1}}{(r_i-1)!} & \frac{t^{r_i-2}}{(r_i-2)!} & \dots & 1 & 0 \\ \frac{t^{r_i}}{r_i!} & \frac{t^{r_i-1}}{(r_i-1)!} & \dots & t & 1 \end{bmatrix} \quad (2.7)$$

where p_i is the pole of the Jordan block \mathbf{J}_i with the order $r_i + 1$. Analogously to (2.4), the right side of (2.6) can be rewritten as a sum of particular inputs u_l

$$e^{-\mathbf{J}t_2}\mathbf{z}(t_2) - e^{-\mathbf{J}t_1}\mathbf{z}(t_1) = \sum_{l=1}^n \int_{t_1}^{t_2} e^{-\mathbf{J}\tau} u_l(\tau) d\tau \mathbf{d}_l \quad (2.8)$$

where \mathbf{d}_l is the l -th column of \mathbf{D} matrix corresponding to the input u_l .

Note that the convolution integral on the right side resembles the finite time Laplace transform as defined by Miu (1993)

$$U(s) = \int_{t_1}^{t_2} e^{-s\tau} u(\tau) d\tau \quad (2.9)$$

therefore, the solution to the PTP control problem can be written as

$$\sum_{l=1}^n U_l(s)|_{s=\mathbf{J}} \mathbf{d}_l = e^{-\mathbf{J}t_2} \mathbf{z}(t_2) - e^{-\mathbf{J}t_1} \mathbf{z}(t_1) \quad (2.10)$$

or more generally for the system not in the Jordan form

$$\sum_{l=1}^n U_l(s)|_{s=\mathbf{A}} \mathbf{b}_l = e^{-\mathbf{A}t_2} \mathbf{y}(t_2) - e^{-\mathbf{A}t_1} \mathbf{y}(t_1) \quad (2.11)$$

where $U_l(s)$ is the finite time Laplace transform of the l -th input. The solution $u_l(t)$ in the time domain is the inverse finite time Laplace transform of $U_l(s)$.

Note that general equation (2.11) enables calculation of the control input for any arbitrary boundary states $\mathbf{y}(t_1)$, $\mathbf{y}(t_2)$. The rest-to-rest positioning without vibrations in the final position is just one special application. Another application could be, e.g. smooth acceleration to a desired velocity or even vibration elimination from a known non-zero initial state. Moreover, conditions (2.11) are algebraic and, therefore, there is no need to solve differential equations. Finally, note that there is no limitation in terms of the time length. It is not necessarily defined by a multiple of the system natural frequency or by other constraints.

Now this approach will be applied to a simple model consisting of two masses m_1 , m_2 connected by a spring k and a viscous damper c as shown in Fig. 2.

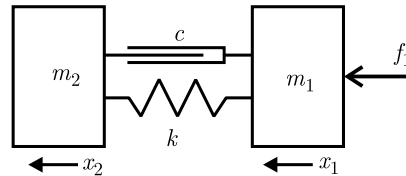


Fig. 2. Two-mass model

This system is described by the matrix equation

$$\mathbf{M}\ddot{\mathbf{x}}(t) + \mathbf{C}\dot{\mathbf{x}} + \mathbf{K}\mathbf{x}(t) = \mathbf{f}(x) \quad (2.12)$$

where \mathbf{x} is a vector of coordinates, \mathbf{M} , \mathbf{C} , \mathbf{K} are mass, damping and stiffness matrices, and \mathbf{f} is a vector of input forces (see Fig. 2) defined as

$$\mathbf{x} = \begin{bmatrix} x_1 \\ x_2 \end{bmatrix} \quad \mathbf{M} = \begin{bmatrix} m_1 & 0 \\ 0 & m_2 \end{bmatrix} \quad \mathbf{C} = \begin{bmatrix} c & -c \\ -c & c \end{bmatrix} \quad (2.13)$$

$$\mathbf{K} = \begin{bmatrix} k & -k \\ -k & k \end{bmatrix} \quad \mathbf{f} = \begin{bmatrix} f_1 \\ 0 \end{bmatrix} \dots$$

Non-vibrational conditions in the final position X_f of the PTP task are

$$\mathbf{x}(t_2) = \begin{bmatrix} X_f \\ X_f \end{bmatrix} \quad \dot{\mathbf{x}}(t_2) = \begin{bmatrix} 0 \\ 0 \end{bmatrix} \quad (2.14)$$

Differential equation of the second order (2.12) can be rewritten as a set of first order equations transformed to the Jordan canonical form and rewritten as

$$\underbrace{\begin{bmatrix} \dot{y}_1 \\ \dot{y}_2 \\ \dot{y}_3 \\ \dot{y}_4 \end{bmatrix}}_{\dot{\mathbf{y}}_1} = \underbrace{\begin{bmatrix} 0 & 1 & 0 & 0 \\ 0 & 0 & 0 & 0 \\ 0 & 0 & p & 0 \\ 0 & 0 & 0 & p^* \end{bmatrix}}_{\mathbf{A}} \underbrace{\begin{bmatrix} y_1 \\ y_2 \\ y_3 \\ y_4 \end{bmatrix}}_{\mathbf{y}} + \underbrace{\begin{bmatrix} 0 \\ 1 \\ 1 \\ 1 \end{bmatrix}}_{\mathbf{B}} u \quad (2.15)$$

where $u = f_1(m_1 + m_2)/(m_1 m_2)$ and p, p^* are complex conjugated poles of flexible modes

$$\begin{aligned} p &= -\xi\omega + j\sqrt{1 - \xi^2}\omega & p^* &= -\xi\omega - j\sqrt{1 - \xi^2}\omega \\ \omega &= \sqrt{\frac{k(m_1 + m_2)}{m_1 m_2}} & \xi &= \frac{c(m_1 + m_2)}{2\omega m_1 m_2} \end{aligned} \quad (2.16)$$

Actually, the use of the Jordan form is not necessary, but here it is used for a better understanding of the whole calculation process and also for the proof of the formula of Bhat and Miu (1991).

Boundary conditions (2.14) are transformed to

$$\mathbf{y}(t_2) = [X_f, 0, 0, 0]^T \quad (2.17)$$

The general solution to the PTP control problem is defined by equation (2.11). Assuming that $t_1 = 0, t_2 = T$ and zero initial conditions $\mathbf{y}(t_1) = \mathbf{0}$, the right side of (2.11) is

$$\begin{aligned} e^{-\mathbf{A}t_2}\mathbf{y}(t_2) - e^{-\mathbf{A}t_1}\mathbf{y}(t_1) &= e^{-\mathbf{A}T}\mathbf{y}(T) - e^{-\mathbf{A}0}\mathbf{y}(0) = e^{(-\mathbf{A}T)} \begin{bmatrix} X_f \\ 0 \\ 0 \\ 0 \end{bmatrix} - e^{(-\mathbf{A}0)} \begin{bmatrix} 0 \\ 0 \\ 0 \\ 0 \end{bmatrix} \\ &= \begin{bmatrix} 1 & -T & 0 & 0 \\ 0 & 1 & 0 & 0 \\ 0 & 0 & e^{-pT} & 0 \\ 0 & 0 & 0 & e^{-p^*T} \end{bmatrix} \begin{bmatrix} X_f \\ 0 \\ 0 \\ 0 \end{bmatrix} = \begin{bmatrix} X_f \\ 0 \\ 0 \\ 0 \end{bmatrix} \end{aligned} \quad (2.18)$$

The expression on the left side in (2.11) can be calculated as follows. Let us assume that the finite time Laplace transform $U(s)$ can be written as a Taylor series

$$U(s) = U_0 + U_1 s + U_2 s^2 + \dots \quad (2.19)$$

then

$$\begin{aligned} U(s)|_{s=\mathbf{A}} &= U_0 \begin{bmatrix} 1 & 0 & 0 & 0 \\ 0 & 1 & 0 & 0 \\ 0 & 0 & 1 & 0 \\ 0 & 0 & 0 & 1 \end{bmatrix} + U_1 \begin{bmatrix} 0 & 1 & 0 & 0 \\ 0 & 0 & 0 & 0 \\ 0 & 0 & p & 0 \\ 0 & 0 & 0 & p^* \end{bmatrix} + U_2 \begin{bmatrix} 0 & 0 & 0 & 0 \\ 0 & 0 & 0 & 0 \\ 0 & 0 & p^2 & 0 \\ 0 & 0 & 0 & p^{*2} \end{bmatrix} + \dots \\ U(s)|_{s=\mathbf{A}} &= \begin{bmatrix} U_0 & U_1 & 0 & 0 \\ 0 & U_0 & 0 & 0 \\ 0 & 0 & U_0 + U_1 p + U_2 p^2 + \dots & 0 \\ 0 & 0 & 0 & U_0 + U_1 p^* + U_2 p^{*2} + \dots \end{bmatrix} \end{aligned} \quad (2.20)$$

According to (2.11) $U(s)$ is multiplied by the input vector \mathbf{b}_1 (note that there is only one input)

$$\begin{aligned}
 U(s)|_{s=\mathbf{A}[0; 1; 1; 1]}^T &= \begin{bmatrix} U_0 & U_1 & & 0 & & 0 \\ 0 & U_0 & & 0 & & 0 \\ 0 & 0 & U_0 + U_1p + U_2p^2 + \dots & & 0 & \\ 0 & 0 & & 0 & U_0 + U_1p^* + U_2p^{*2} + \dots & \\ & & & & & \end{bmatrix} \begin{bmatrix} 0 \\ 1 \\ 1 \\ 1 \\ 1 \end{bmatrix} \\
 &= \begin{bmatrix} U_1 \\ U_0 \\ U_0 + U_1p + U_2p^2 + \dots \\ U_0 + U_1p^* + U_2p^{*2} + \dots \end{bmatrix} = \begin{bmatrix} \left. \frac{dU(s)}{ds} \right|_{s=0} \\ U(0) \\ U(p) \\ U(p^*) \end{bmatrix} \quad (2.21)
 \end{aligned}$$

Using (2.18) and (2.21), the conditions for non-vibrational control input (2.11) can be formulated in a component form as

$$\left. \frac{dU(s)}{ds} \right|_{s=0} = X_f \quad U(s)|_{s=0} = 0 \quad U(s)|_{s=p} = 0 \quad U(s)|_{s=p^*} = 0 \quad (2.22)$$

The simple analytical formulation of necessary conditions for non-vibrational control (2.22) used by Bhat and Miu (1991) is the result of description of the system in a canonical form. Other state space representations usually need a numerical solution of (2.11). According to the authors' best knowledge, the step-by-step derivation of these conditions presented here has not been published before.

Note that unlike other methods (Smith, 1957; Aspinwall, 1980; Sugiyama and Uchino, 1986) using this formulation, the time length of the input signal T is not strictly defined as a multiple of the system natural period and can be set arbitrarily. However, the solution $u(t)$ from (2.22) must be precomputed before the PTP operation and during the operation cannot be modified as it is often required (see Section 6).

3. Control input synthesis

There is an infinite number of functions $u(t)$ which satisfy equations (2.22). An algebraic method for the synthesis of the control input called the Laplace transform (domain) synthesis technique (Miu, 1993) assumes the control input as a linear combination of independent basis functions $\phi_i(t)$ multiplied by weighting coefficients λ_i

$$u(t) = \sum_{i=1}^{2q+2} \lambda_i \phi_i(t) \quad (3.1)$$

where q is a number of flexible modes pairs. Then, according to (2.22)

$$\begin{aligned}
 \left[\left. \frac{dU(s)}{ds} \right|_{s=0}, U(s)|_{s=0}, U(s)|_{s=p}, U(s)|_{s=p^*} \right]^T &= \mathbf{S}\boldsymbol{\lambda} = \underbrace{[X_f, 0, \dots, 0]^T}_{\mathbf{y}(T)} \\
 \mathbf{S} &= \begin{bmatrix} \frac{d\Phi_1(0)}{ds} & \dots & \frac{d\Phi_{2q+2}(0)}{ds} \\ \Phi_1(0) & \dots & \Phi_{2q+2}(0) \\ \Phi_1(p_1) & \dots & \Phi_{2q+2}(p_1) \\ \vdots & \ddots & \vdots \\ \Phi_1(p_q^*) & \dots & \Phi_{2q+2}(p_q^*) \end{bmatrix} \quad (3.2)
 \end{aligned}$$

where $\boldsymbol{\lambda} = [\lambda_1, \lambda_2, \dots, \lambda_{2q+2}]^T$ and $\Phi_i(s)$ are finite time Laplace transforms of the basis functions ϕ_i .

Using (3.2)₁, the weighting coefficients $\boldsymbol{\lambda}$ can be obtained as

$$\boldsymbol{\lambda} = \mathbf{S}^{-1}[X_f, 0, \dots, 0]^T \quad (3.3)$$

But such formulation does not take into account specific properties of the chosen basis functions $\phi_i(t)$. Some choices lead to non-invertible matrix \mathbf{S} , in some cases the solution does not exist (Beneš, 2012).

The solution to (3.2)₁ exists if the rank h of matrix \mathbf{S} is equal to the rank of the augmented matrix $[\mathbf{S}|\mathbf{y}(t_2)]$

$$h = h(\mathbf{S}) = h(\mathbf{S}|\mathbf{y}(t_2)) \quad (3.4)$$

Note that $h(\mathbf{S})$ is not necessarily equal to $2q + 2$ from (3.1) because the rows of \mathbf{S} could be linear dependent.

Therefore, instead of (3.1) the control input should be reformulated to the form

$$u(t) = \sum_{i=1}^j \lambda_i \phi_i(t) \quad j \geq h \quad (3.5)$$

In the case $j = h$, there is one and only one combination of weighting coefficients λ_i , in the case $j > h$ the infinite number of solutions exists. For $j < h$, the solution to (2.22) does not exist and j must be increased.

Equation (3.2)₁ ensures that no vibration appears in PTP positioning. To meet other criteria, more constrains could be added to this synthesis technique. These constrains can be formulated both in s-domain and time domain. The common one is e.g. the time-domain continuity constraint (Miu, 1993), but this could be fulfilled using a proper set of basis functions, see (4.2). Additional constraints can be used, e.g. for specifying states between the initial and final time (trajectory tracking) or to increase robustness of the control to modelling errors. The increasing of the robustness is based on placing multiple zeros in the system poles or on placing new zeros near to the system poles. This strategy is similar to the idea of ZVD or EI shapers in Singhose (1997), but as the time length can be still set arbitrarily this does not mean prolongation of the input signal. Instead of an increase of the necessary time, we can increase the power used for positioning. Or, probably more often, we can find the right balance between the signal length and the required power regardless of the system natural frequency.

4. Optimization using free weighting coefficients

The situation $j > h$ in (3.5) means that the first h coefficients can be expressed using non-vibrational conditions (2.22) as a function of the rest of them, $\lambda_i = f_i(\lambda_{h+1}, \dots, \lambda_j)$, $i = 1, \dots, h$. Then the free coefficients $\lambda_{h+1}, \dots, \lambda_j$ could be used to meet additional conditions or as optimization parameters. This will be demonstrated using the simple model in Fig. 2. The optimization goal is minimization of the required maximum power of the drive. Therefore, the cost function for minimization is defined as

$$f_c = \max |u(t)| \quad t \in \langle 0, t_2 \rangle \quad (4.1)$$

Consider the control input as a linear combination of sine waves in the form

$$u(t) = \sum_{i=1}^{2q+2} \lambda_i \phi_i(t) = \sum_{i=1}^4 \lambda_i \sin(\omega_s i t) \quad (4.2)$$

$$U(s) = \sum_{i=1}^{2q+2} \lambda_i \Phi_i(s) = \sum_{i=1}^4 \lambda_i \frac{e^{-st_2} (-s \sin(\omega_s t_2) - \omega \cos(\omega_s t_2)) + \omega_s}{s^2 + \omega_s^2}$$

with $\omega_s = 2\pi/t_2$, which ensures the time domain continuity requirement automatically. The supposed system parameters are $m_1 = m_2 = 1$ kg, $k = 100$ kg·s⁻², $c = 0$ kg·s⁻¹. The desired rigid body displacement is $X_f = 1$ m and $t_2 = 1$ s. Then the matrix \mathbf{S} is

$$\mathbf{S} = \begin{bmatrix} 0.1592 & 0.0796 & 0.0531 & 0.0398 \\ 0 & 0 & 0 & 0 \\ -0.0393 - 0.0391i & -0.3001 - 0.2986i & 0.1220 + 0.1214i & 0.0585 + 0.0582i \\ -0.0393 + 0.0391i & -0.3001 + 0.2986i & 0.1220 - 0.1214i & 0.0585 - 0.0582i \end{bmatrix} \quad (4.3)$$

and it has rank $h(\mathbf{S}) = 2$. Since $j = 4$, we have two free parameters for optimization. Using (3.2)₁, we obtain

$$\lambda_1 = 6.7239 - 0.5742\lambda_3 - 0.3719\lambda_4 \quad \lambda_2 = -0.8815 + 0.4818\lambda_3 + 0.2437\lambda_4 \quad (4.4)$$

The basic non-optimal solution is that with $\lambda_3 = \lambda_4 = 0$

$$\boldsymbol{\lambda}_{bas} = [6.7239, -0.8815, 0, 0]^T \quad (4.5)$$

Simple optimization of the parameters λ_i according to cost function (4.1) by e.g. *fminsearch* in the Matlab environment results in

$$\boldsymbol{\lambda}_{opt} = [5.6154, 0.0273, 1.7280, 0.3127]^T \quad (4.6)$$

The plots for a standard basic solution (4.5) and optimized solution (4.6) are compared in Fig. 3. The required power is reduced by about 25%.

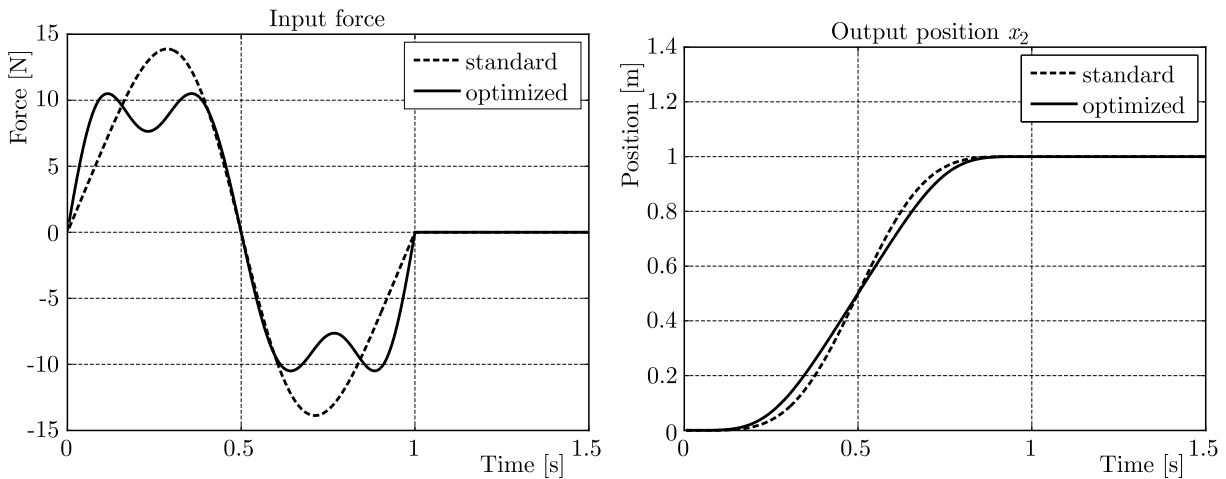


Fig. 3. System response to the basic and optimized shape of the input force

There could be more than one optimization goal. Figure 4 shows a Pareto set when both the required power and its derivative are minimized. The minimized derivative of the required power is important for reduction of costs of power electronics. The depicted points represent various combinations of λ_3 and λ_4 . Other optimization criteria can be formulated, e.g. to increase the robustness to model errors, etc.

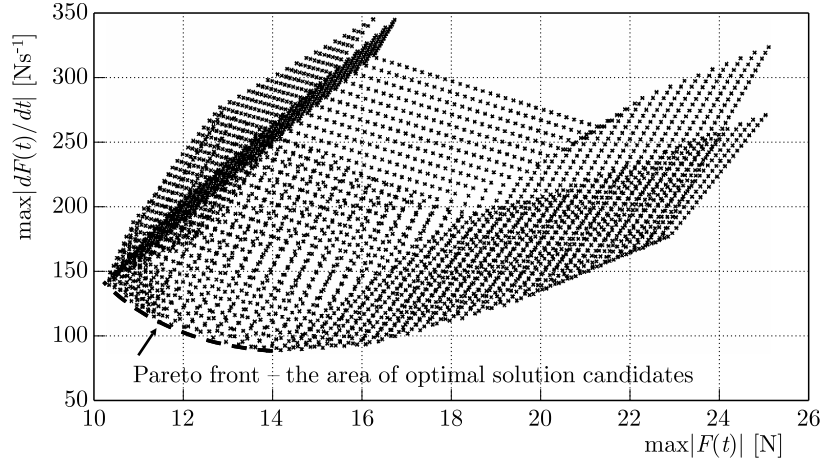


Fig. 4. Pareto set

5. Optimization using parametric basis functions

Besides searching for an optimal combination of weighting coefficients, different parametric basis functions can be used. In such a case, the optimization is focused on these parameters. A control function generated as a combination of damped sinusoids is used as an example

$$u(t) = \lambda_1 e^{a_1 t} \sin\left(\frac{2\pi}{T}t\right) + \lambda_2 e^{a_2 t} \sin\left(\frac{4\pi}{T}t\right) + \lambda_3 e^{a_3 t} \sin\left(\frac{6\pi}{T}t\right) + \lambda_4 e^{a_4 t} \sin\left(\frac{8\pi}{T}t\right) \quad (5.1)$$

where the coefficients $a_i < 0$ are the optimization parameters. The goal of the optimization is minimization of the required power.

The optimization leads to the following coefficients

$$\mathbf{a} = [-0.0164, -37.9986, -0.0001, -42.3485]^T \quad (5.2)$$

with the corresponding

$$\boldsymbol{\lambda}_{opt} = [5.9175, -101.8635, 1.1877, 75.6287]^T \quad (5.3)$$

The results are compared in Fig. 5 with basic non-optimal solution (4.5) which corresponds to the setting $a_{1,2,3,4} = 0$. The required power is reduced by about 28%, which is even slightly better than that in Fig. 3.

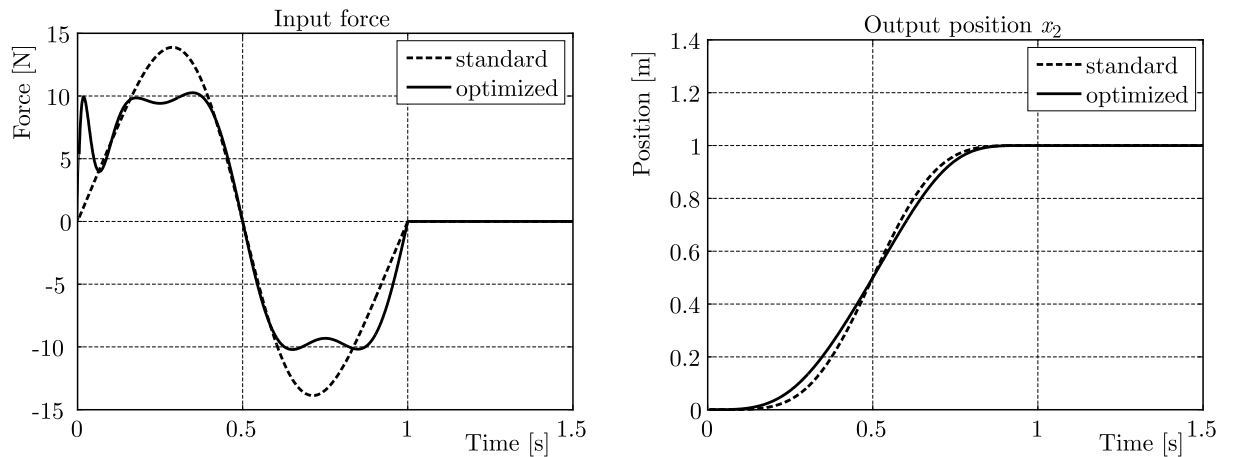


Fig. 5. System response to the parametrically optimized shape of the input force

6. Re-entry online shaper from a precomputed curve

An approach described in previous Sections produces control inputs in the form of precomputed curves. But these are not applicable when the system must be controlled on-line and the final state is not known in advance. This could be for example a crane manually controlled by a human operator. In such a case, we need a shaper which transforms any arbitrary input signal to a non-vibrational one (Beneš *et al.*, 2008). These shapers are usually based on the patented “Input Shaping” (Singhose, 1997; Singer and Seering, 1990; Singhose and Seering, 1991) series of pulses with time length fixed to the system natural frequency or even its multiples. Now a more general technique will be described, which transforms an optimized control curve with an arbitrarily set time length into a dynamic shaper.

The new approach (Beneš, 2012; Beneš *et al.*, 2008) for such cases is as follows. The general conditions for a control signal which does not excite vibrations are formulated in Section 2. Now the signal which fulfils these conditions should be a product of the convolution of any arbitrary input signal with the shaper. If the input signal is a unit pulse then the product of convolution should be of the same shape as the corresponding precomputed curve, as shown in Fig. 6. In other words, the shaper is a dynamic representation of a non-vibrational control curve. If the control curve transforms the system from a zero initial state to a unit final state then we obtain a shaper with the unit gain. The signal modified by this shaper transforms the system to the same final state as the unshaped one but with zero residual vibrations. The procedure to synthesize such a shaper is to find a differential equation and a corresponding dynamic block the solution to which is the non-vibrational control curve from Section 2. This is a so called re-entry shaper, and it can be re-entered during operation.

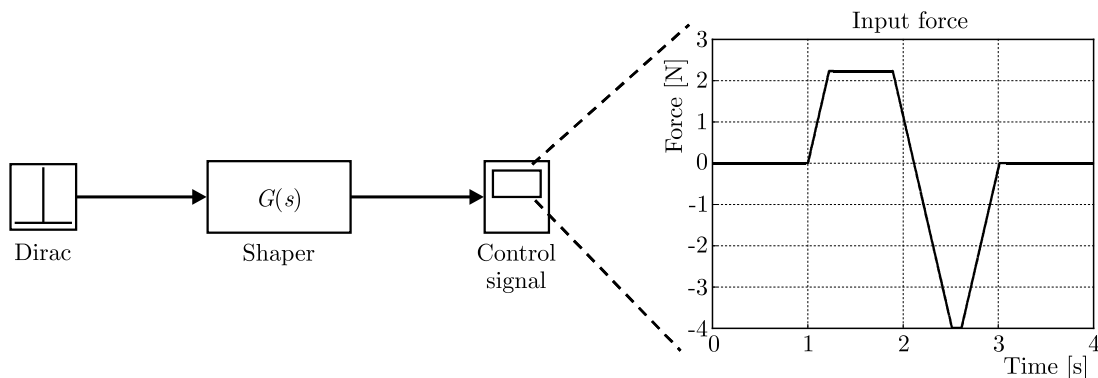


Fig. 6. Shaper convolution with the Dirac pulse

It is difficult to find a dynamic block corresponding to a certain general curve. Consequently, it is a great benefit that our control signal is a linear combination of the basis functions. The dynamic representation of the basis function is actually its finite time Laplace transform. For example, the ramp shaper used in Fig. 6 is described as a transfer function

$$U(s) = \frac{q}{s^2}(1 - e^{-st_1} - e^{-st_2} + e^{-st_3} + e^{-st_4} - e^{-st_5}) \quad (6.1)$$

where q is the ramp angle, t_i are the switching times. The shape of the control curve is shown in Fig. 7.

As the positive and negative parts of the ramp must be of the same length, the t_5 is defined as

$$t_5 = t_4 + t_3 - t_2 - t_1 \quad (6.2)$$

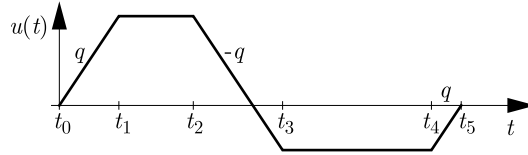


Fig. 7. Shape of the ramp control curve

Function (6.1) can be rewritten in a more compact form as

$$U(s) = \frac{q}{s^2} \sum_{i=0}^5 N_i e^{-st_i} \tag{6.3}$$

with

$$\mathbf{N} = [1, -1, -1, 1, 1, -1] \quad t_0 = 0 \tag{6.4}$$

For the two-mass model in Fig. 2 with the parameters $m_1 = m_2 = 1 \text{ kg}$, $k = 100 \text{ kg}\cdot\text{s}^{-2}$, $c = 1 \text{ kg}\cdot\text{s}^{-1}$ the non-vibrational conditions are (2.22). Applying these conditions to (6.3), we obtain the following set of conditions

$$\begin{aligned} \sum_{i=0}^5 N_i t_i &= 0 & \sum_{i=0}^5 N_i t_i^2 &= 0 & \sum_{i=0}^5 N_i t_i^3 &= -\frac{6X_f}{q} \\ \sum_{i=0}^5 N_i e^{\xi\omega t_i} \cos(\sqrt{1-\xi^2}\omega t_i) &= 0 & \sum_{i=0}^5 N_i e^{\xi\omega t_i} \sin(\sqrt{1-\xi^2}\omega t_i) &= 0 \end{aligned} \tag{6.5}$$

Two of them, (6.5)₁ and (6.5)₂, result from $U(s)|_{s=0} = 0$. According to the definition of t_5 in equation (6.2), constraint (6.5)₁ is fulfilled automatically and, therefore, we have a set of four equations (6.5)₁-(6.5)₅ with four unknowns t_1, \dots, t_4 . For $q = 5 \text{ m}\cdot\text{s}^{-3}$, the solution is a vector of the switching times

$$\mathbf{t} = [0, 0.2228, 0.8922, 1.5136, 1.6136, 2.0123] \tag{6.6}$$

Note that due to transformation between the input $u(t)$ and the control force $f_1(t)$, $u = f_1(m_1 + m_2)/m_1 m_2$, the defined value of q is a ramp with the slope $q_F = 10 \text{ N}\cdot\text{s}^{-1}$.

Equation (6.3) can be used for the direct design of a re-entry shaper (Fig. 8). Transfer function (6.3) is actually the description of the differential equation which reproduces the precomputed curve. In this case, it is the ramp shown in Fig. 7.

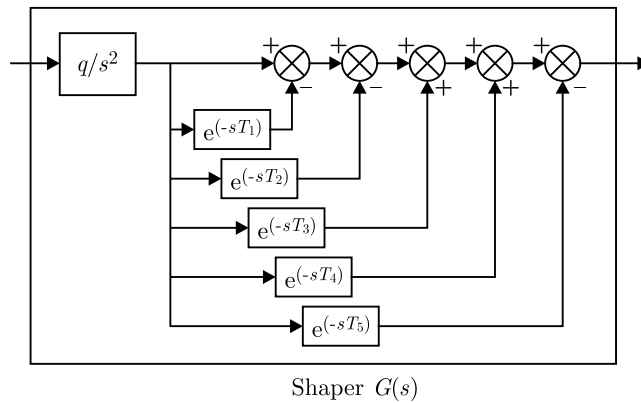


Fig. 8. Re-entry shaper $G(s)$, here $T_i = t_i$

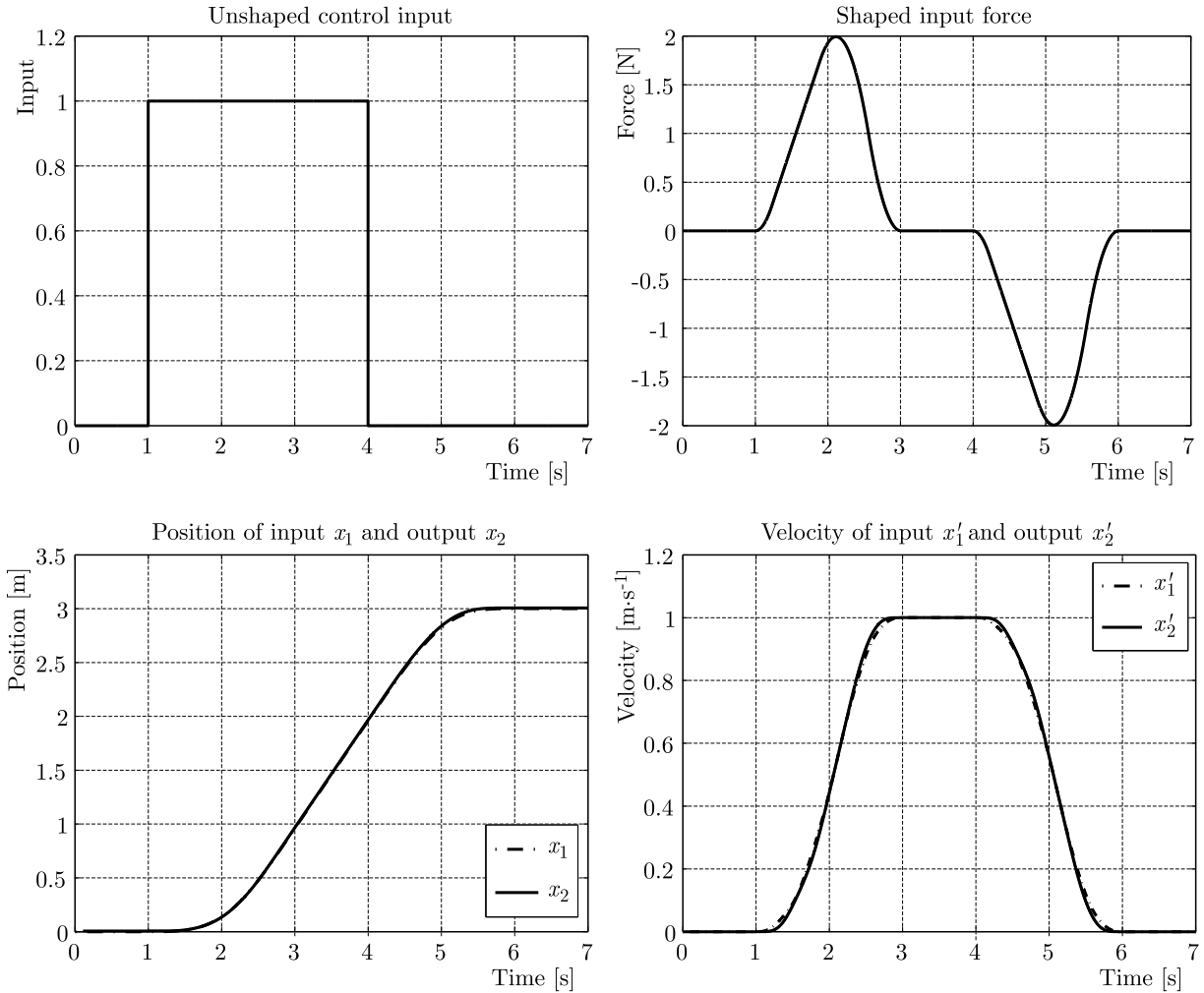


Fig. 9. Re-entry shaper – velocity control

The shaper created in this way represents velocity control, see Fig. 9. But it can be easily transformed to control position, acceleration or jerk. The only modification which has to be done is the change of the power of s in (6.1). If the denominator before the bracket is s^3 then it acts like acceleration control. If it is changed to s^4 then we have jerk control. Finally, if it is only s^1 then it acts like direct position control.

Note that we can use all methods described in the previous Sections, especially optimizations, to design the best precomputed curve with respect to requested criteria. For example, the ramp control function with limited both the slope and maximum value could be prepared to avoid actuator saturation (Beneš, 2012). Then, using the finite time Laplace transform we can change it to the form of the re-entry shaper.

This possibility to synthesize re-entry shapers of prescribed time lengths or optimized to chosen goals is the main contribution of this paper. It eliminates the drawbacks of both previous approaches (Bhat and Miu, 1990; Singhose, 1997).

7. Experiment – antisway crane

An antisway crane is one of the typical benchmarks for tests of non-vibration control strategies. The laboratory model shown in Fig. 10 is controlled by simple buttons with 2 states (on/off). But the rectangular input that goes from the buttons excites vibrations of the load. The goal

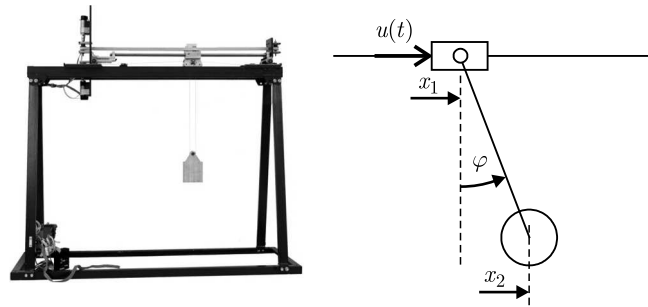


Fig. 10. Crane – a laboratory model and its diagram

is to design an on-line shaper which modifies the signal from the buttons to a non-vibrational one.

According to the approach described in previous Sections primarily the optimized control curve is calculated and then it is transformed using the finite time Laplace transform to an on-line shaper. The shape of the control curve in parametrical form (5.1) is used. The optimization is focused on settling time minimization with respect to the crane model parameters.

During the tests, the model was manually controlled by a human operator who performed a set of various manoeuvres with varied cable length as well. The results of one of them are shown in Fig. 11 (unshaped) and in Fig. 12 (shaped). The swinging in the final position was almost completely eliminated when the shaper was used.

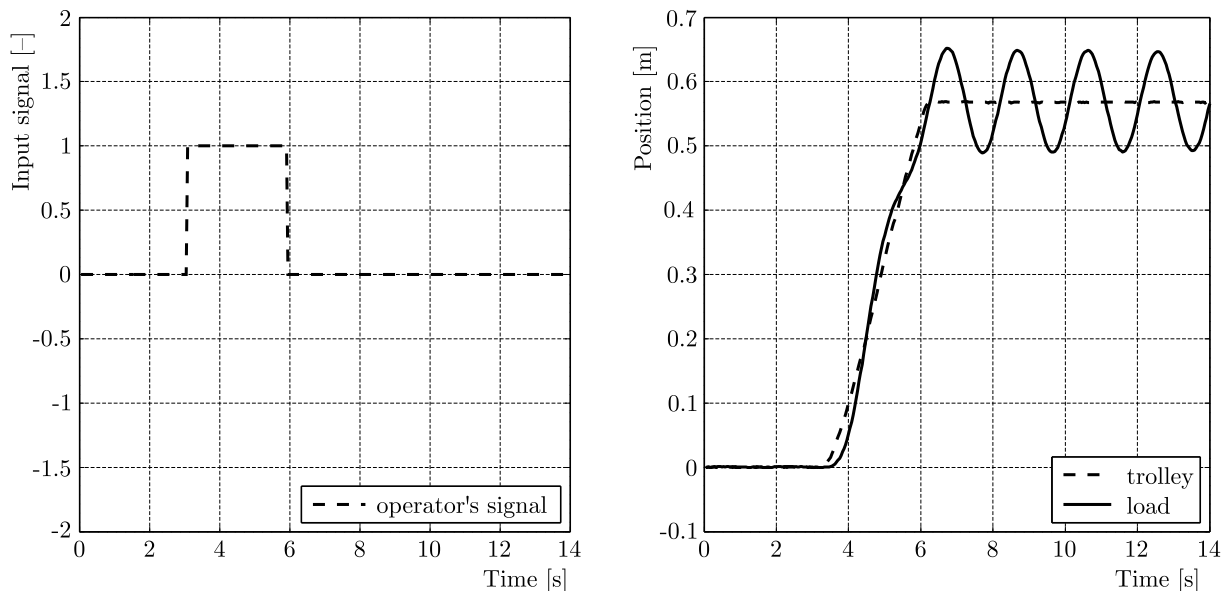


Fig. 11. Experiment – the system response without the shaper

Another test was focused on the re-entry property of the shaper. The operator randomly switched between the right and left direction of the trolley without waiting for the end of the previous manoeuvre. The results for unshaped control are given in Fig. 13a and for control with the shaper in Fig. 13b. Again, the swinging in the final position was eliminated by the shaper.

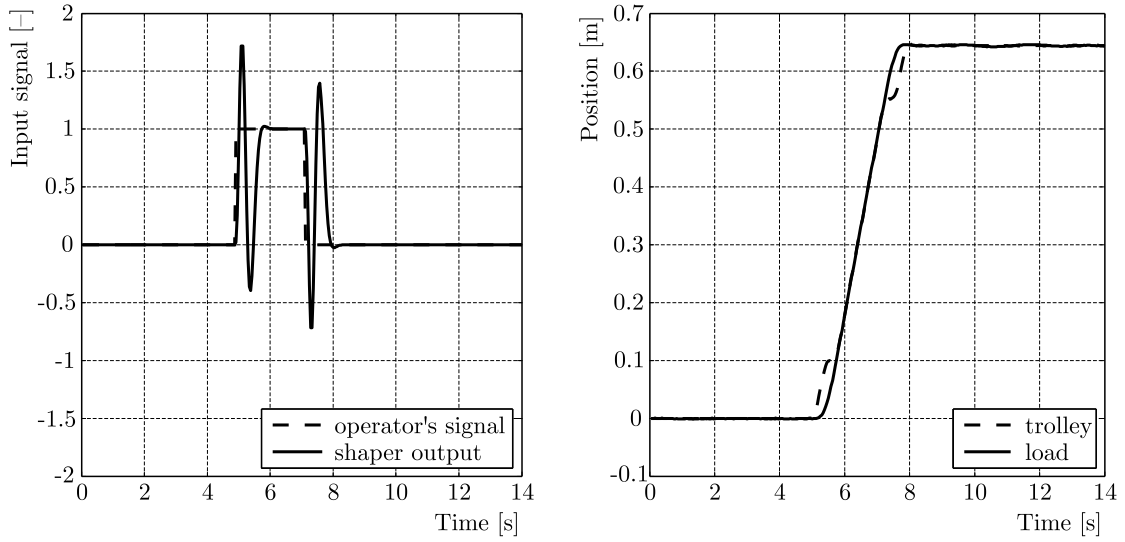


Fig. 12. Experiment the system response with the shaper

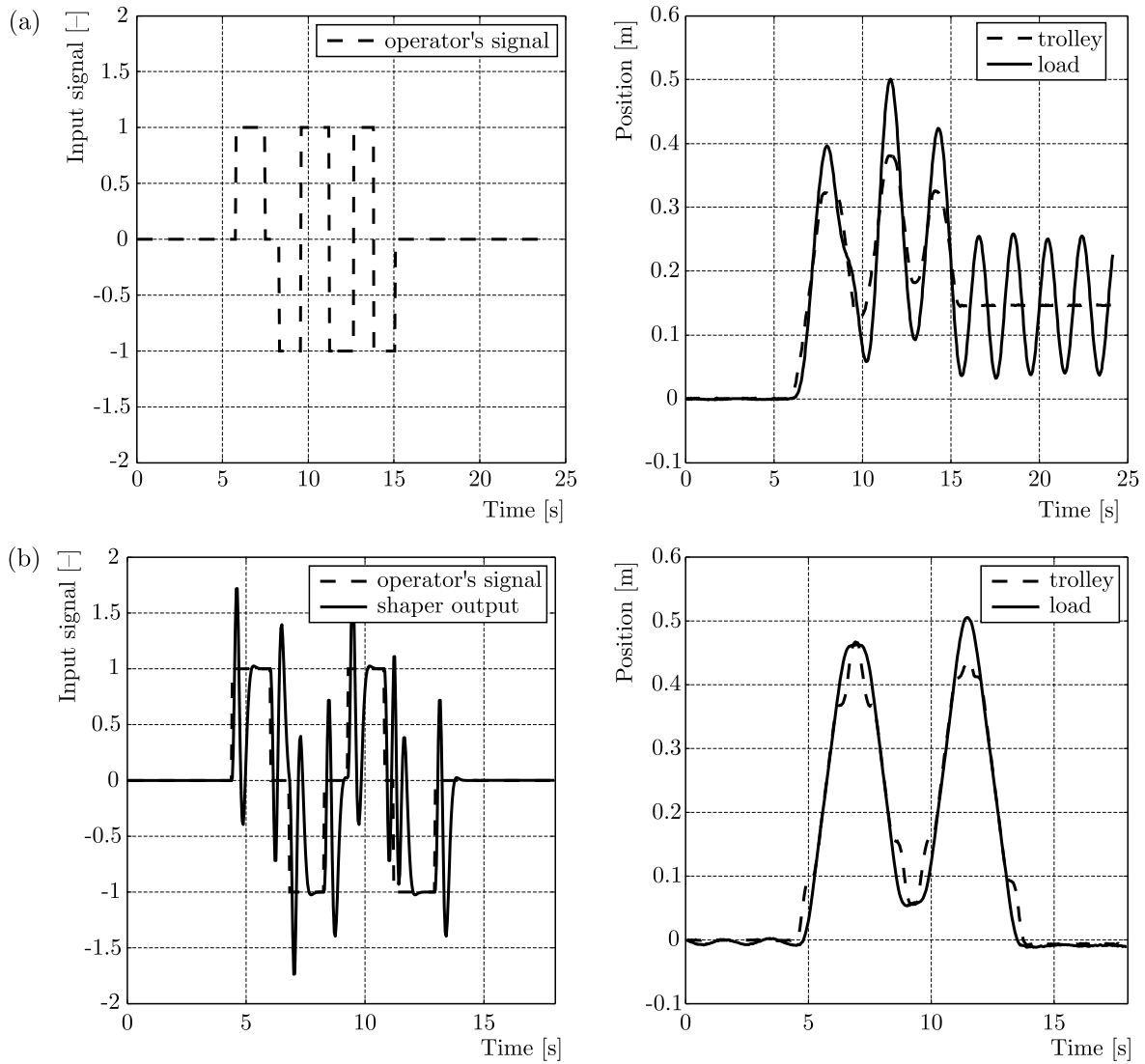


Fig. 13. Experiment a re-entry test (a) without the shaper, (b) with the shaper

8. Conclusions

The presented approach to the design of input shapers combines the advantages of optimized precomputed control curves with the ability of on-line control and the re-entry property. It is capable of dealing with any optimization criteria or additional conditions. The length of produced shapers can be set arbitrarily only with respect to the limits of available power.

The synthesis of control input is based on the modified Laplace domain synthesis technique which takes into account the specific properties of chosen basis functions and their influence on the solution. Additional constraints and optimization criteria are dealt with using free weighting coefficients and/or parametric basis functions. The result of this part of the synthesis is an optimized precomputed curve. Using the finite time Laplace transform, this profile is transformed to the form of an on-line shaper. The shaper inherits the optimized properties of the precomputed curve and, in contrast to common shaping techniques, its length is not strictly determined as a multiple of the system natural frequency and can be set arbitrarily. It is important that the new result reduces the required power of the drive for the chosen positioning time. In its basic form, the resulting shapers represent velocity control, but they can be also easily modified to position, acceleration or jerk control. The theoretical results have been verified by simulations and experiments.

Moreover, a detailed derivation of the necessary conditions for non-vibrational control (2.22) by Bhat and Miu (1991) has been achieved. According to the best knowledge of the authors, it is published for the first time.

Acknowledgement

The research has been supported by the Czech Science Foundation, Project No. GAP101/11/2110 Advanced input shaping control for precise positioning of mechanisms.

References

1. ASPINWALL D.M., 1980, Acceleration profiles for minimizing residual response, *Journal of Dynamic Systems, Measurement and Control*, **102**, 3-6
2. BENEŠ P., 2012, *Input Shaping Control with Generalised Conditions*, Ph.D. Thesis (in Czech), Praha, ČVUT v Praze
3. BENEŠ P., VALÁŠEK M., 2008, Input shaping control with reentry commands on prescribed duration, *Applied and Computational Mechanics*, **2**, 2, 227-234
4. BHAT S.P., MIU D.K., 1990, Precise point-to-point positioning control of flexible structures. *Journal of Dynamics Systems, Measurements and Control*, **4**, 667-674
5. BHAT S.P., MIU D.K., 1991, Solutions to point-to-point control problems using laplace transform technique, *Journal of Dynamics Systems, Measurement and Control*, **113**, 425-431
6. CHANG P.H., PARK H.S., 2005, Time-varying input shaping technique applied to vibration reduction of an industrial robot, *Control Engineering Practise*, **13**
7. HEYDEN T., WOERNLE C., 2006, Dynamics and flatness-based control of kinematically undetermined cable suspension manipulator, *Multibody System Dynamics*, **16**, 155-177
8. KITTNAR Z., VALÁŠEK M., 2004, Nonlinear control of crane manipulator, *Proceedings of International Congress on Mechatronics*, Prague: CTU, Faculty of Mechanical Engineering, 109-115
9. LAU M.A., PAO L.Y., 2003, Input shaping and time-optimal control of flexible structures, *Automatica*, **39**, 893-900
10. LEWIS F.L., 1992, *Applied Optimal Control and Estimation*, New Jersey, Prentice-Hall, Inc., ISBN 0-13-040361-X

11. MIU D.K., 1993, *Mechatronics, Electromechanics and Contromechanics*, New York, Springer-Verlag
12. NEUSSER Z., VALÁŠEK M., 2013, Control of the underactuated mechanical systems by harmonics, *Proceedings of the ECCOMAS Thematic Conference on Multibody Dynamics 2013*, Zagreb, University of Zagreb, 329-339
13. OSMIC S., BERNER M.O., SCHWUNG A., JOST M., MONNIGMANN M., 2014, Flatness-based feedforward control for fast operating point transitions of compressor systems, *Proceedings of 2014 IEEE Conference on Control Applications (CCA)*, 1753-1758
14. PARK J.Y., CHANG P.H., 2004, Vibration control of a telescopic handler using time delay control and commandless input shaping technique, *Control Engineering Practise*, **12**
15. PIAZZI A., VISIOLI A., 2002, Optimal dynamic-inversion-based control of an overhead crane, *IEEE Proceedings Control Theory Applications*, **149**, 405-411
16. POST B.K., MARIUZZA A., BOOK W.J., SINGHOSE W., 2011, Flatness-based control of flexible motion systems, *Proceedings of the ASME Dynamic Systems and Controls Conference*, 843-850
17. SCHINDELE D., MENN I., ASCHEMANN H., 2009, Nonlinear optimal control of an overhead travelling crane, *Proceedings of 18th IEEE Conference on Control Applications (CCA)*, 1045-1050
18. SINGER N., SEERING W., 1990, Preshaping command inputs to reduce system vibration, *Journal of Dynamics Systems, Measurements and Control*, **112**, 76-82
19. SINGH T., VADALI S.R., 1993, Robust time-delay control, *ASME Journal of Dynamic Systems, Measurement and Control*, **115**, 303-306
20. SINGHOSE W.E., 1997, *Command Generation for Flexible Systems*, s.l.: Massachusetts Institute of Technology
21. SINGHOSE W.E., SEERING W., 1991, Generating vibration reducing inputs with vector diagrams, *Proceedings of 8th IFTOMM World Congress*, 315-318
22. SMITH O.J.M., 1957, Posicast control of damped oscillatory systems, *Poceedings of the IRE*
23. SUGIYAMA S., UCHINO K., 1986, Pulse driving method of piezoelectric motors, *IEEE Journal*, 637-640
24. VALÁŠEK M., 1995, Input shaping control of mechatronical systems, *Proceedings of 9th World Congress IFTOMM*, 3049-3052
25. Vyhlídal T., Kučera V., Hromčík M., 2012, Input shapers with uniformly distributed delays, *Preprints of 10th IFAC Workshop on Time Delay Systems* (accepted)
26. WIEDERRICH J.L., ROTH B., 1974, Design of low vibration cam profiles, *Conference on Cams and Cam Mechanisms*, Liverpool
27. ZAVŘEL J., VALÁŠEK M., 2004, Anti-sway rotational crane (derrick), *Proceedings of International Congress on Mechatronics*, Prague, CTU, Faculty of Mechanical Engineering, 101-108
28. ZIMMERT N., SAWODNY O., 2010, Active damping control for bending oscillations of a forklift mast using flatness based techniques, *Proceedings of 2010 American Control Conference*, 1538-1543

Manuscript received April 2, 2015; accepted for print August 3, 2015

ANALYSIS OF FATIGUE CRACKS OF CYLINDER HEADS IN DIESEL ENGINES

HOJJAT ASHOURI, BABAK BEHESHTI

Department of Agricultural Machinery, Science and Research Branch, Islamic Azad University, Tehran, Iran
e-mail: ashori@samav-ac.ir; Beheshti-b@srbiau.ac.ir

MOHAMMAD REZA EBRAHIMZADEH

College of Agriculture, Yadegar-e-Imam Khomeini (Rah), Shahr-e-rey Branch, Islamic Azad University, Tehran, Iran
e-mail: mrebrahimzadeh@iausr.ac.ir

Loading conditions and complex geometry have led cylinder heads to become the most challenging parts of diesel engines. One of the most important durability problems in diesel engines is due to cracks in the valves bridge area. The purpose of this study is thermo-mechanical analysis of cylinder heads of diesel engines using a two-layer viscoplasticity model. The results of the thermo-mechanical analysis indicate that the maximum temperature and stress occur in the valves bridge. The results of the finite element analysis correspond with the experimental tests carried out by researchers, and illustrate cracks in cylinder heads in this region. The results of the thermo-mechanical analysis show that when the engine is running, the stress in the region is compressive, caused by thermal loading and combustion pressure. When the engine is shut off, the compressive stress turns into tensile stress because of assembly loads. The valves bridge is under cyclic tensile and compressive stress state and thus is subject to low cycle fatigue. After several cycles fatigue cracks will appear in this region. The lifetime of this part can be determined through finite element analysis instead of experimental tests. The viscous strain is greater than the plastic strain which is not negligible.

Keywords: thermo-mechanical fatigue, finite element analysis, cylinder head and valve bridge cracks

1. Introduction

Cylinder heads are important parts of internal combustion engines which are subject to high thermo-mechanical stresses for because the sake of their working environment (Azadi *et al.*, 2012a; Gocmez and Pishinger, 2011; Li *et al.*, 2013 ; Metzger *et al.*, 2014; Su *et al.*, 2002; Thalmair *et al.*, 2006; Trampert *et al.*, 2008; Zahedi and Azadi, 2012; Xuyang *et al.*, 2013). Therefore, selection of materials is of paramount importance since they must have sufficient mechanical strength at high temperatures to be able to withstand cyclic stresses caused by heat and pressure (Gocmez and Pishinger, 2011; Zahedi and Azadi, 2012; Takahashi and Sasaki, 2010).

High output capacity, low fuel consumption, low emission and reduction costs of maintenance are among the restrictions making the design of cylinder heads a complicated task (Mirsalim *et al.*, 2009; Li *et al.*, 2013). Thus, detailed analysis and design are essential. Escalation in environmental concerns and fuel costs underlines the need for research on more efficient engines with less energy dissipation and emission (Azadi *et al.*, 2012b; Mirsalim *et al.*, 2009). One way to decrease the fuel costs is to reduce weight of vehicles. Hence, lighter alloys must be used in the pursuit of this goal (Azadi *et al.*, 2012a; Zahedi and Azadi, 2012). Recently, the use of aluminum alloys has increased for economic reasons and for the improvement of engine power by

weight reduction. Aluminum-silicon is a casting alloy which has extensive use in the automotive industry, especially in cylinder heads of diesel engines. These materials have been replaced by a variety of cast iron which were previously used in the manufacture of cylinder heads (Azadi *et al.*, 2012a). Thermal deformation is the greatest challenge faced by aluminum cylinder heads (Takahashi *et al.*, 2002).

Cylinder heads are exposed to thermal and mechanical loads. The temperature difference, which is a result of turning the engine on and off, begets thermo-mechanical fatigue (TMF) loads on the cylinder heads (Azadi *et al.*, 2012a; Li *et al.*, 2013; Mirsalim *et al.*, 2009; Farrahi *et al.*, 2014; Thomas *et al.*, 2002; Thomas *et al.*, 2004) and, consequently, reduces their lifetime, especially in thinner regions (Remy and Petit, 2001). The crucial regions include the valves bridge and areas near spark plugs and injectors (Gocmez and Pishinger, 2011; Shojaefard *et al.*, 2006; Ziehler *et al.*, 2005). Cylinder heads endure out-of-phase TMF. Namely, the maximum stress occurs at the minimum temperature and the minimum stress occurs at the maximum temperature. When the engine shuts off and the temperature is low, the tensile stresses arising from the assembly loads will be applied to the cylinder heads. As the engine starts and temperature increases, the compressive stresses produced by thermal loading (σ_{th}) and combustion pressure (σ_p) will be applied to them (Azadi *et al.*, 2012b; Li *et al.*, 2013). This type of loading is displayed in Fig. 1. As the figure reveals, the changes in stress caused by thermal load are very high. The fluctuating stresses come out of the engine which is heated and cooled (Mirsalim *et al.*, 2009; Challen and Baranescu, 1999; Chamani *et al.*, 2009).

Plastic deformation is observed in structures like cylinder heads which bear high temperature fluctuations and assembly loads. Classical models are used to obtain steady responses of these structures. This approach is very expensive. Because many loading cycles are required to obtain a steady response. Cyclic analysis is used in order to avoid the cost of transient analysis (Zahedi and Azadi, 2012).

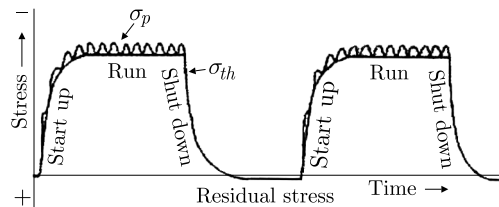


Fig. 1. The cyclic loading of a cylinder head (Challen and Baranescu, 1999)

Numerous papers have been presented on the analysis of stress and fatigue in cylinder heads. Koch *et al.* (1999) measured experimentally strain of cylinder heads and compared it with simulated results using a nonlinear isotropic/kinematic hardening model. A slight difference between the experimental and simulated strain was observed from 55°C to 120°C. The simulated strain, by increasing temperature from 110°C to 210°C was estimated larger than the experimental strain due to plastic deformation of the cylinder heads.

Takahashi *et al.* (2002) examined creep in aluminum cylinder heads. There was concordance between experimental and calculated strain. Creep strain increased as stress grew. Creep strain at 250°C significantly was higher than creep strain at 100°C and 175°C.

TMF of cylinder heads was studied by Thomas *et al.* (2002, 2004) using the energy model and elasto-viscoplastic law. Their research proved a good agreement between experimental and simulated results of the fatigue life of the cylinder heads and the location of crack initiation.

Thermo-mechanical analysis of cylinder heads and cylinders of AFV diesel engines was conducted by Venkateswaran *et al.* (2011). Their research demonstrates that the cylinder heads and engine blocks can tolerate more stress caused by pressure and thermal loads increase, and the next generation of engines does not need further alteration.

Su *et al.* (2002) predicted fatigue life of cylinder heads by finite element simulation via the model of damage total (Sehitoglu damage model) and compared with experimental results. Their research revealed that the difference between experimental and simulated results was less than 30%.

Zieher *et al.* (2005) simulated the complete process of lifetime. They used an energy model to predict the fatigue life of cast iron cylinder heads. Their research shows that the simulated results of the number of cycles of crack initiation and the location of crack initiation are in accord once with experimental results. The minimum lifetime was observed in the valves bridge.

The analysis of high/low cycle fatigue of cylinder heads was performed by Ghasemi (2012) using the thermo-mechanical analysis. His study verified that the cracks observed in the experimental test of low-cycle of cylinder heads acknowledged the simulated results of low-cycle fatigue. The simulated results of low-cycle fatigue of cylinder heads after modification of cooling systems indicate that high levels of damage parameters are do not observed.

Shoja'efard *et al.* (2006) experimentally measured stress in cylinder heads and compared it with simulated results. Their research confirmed the concordance between the experimental and simulated results at low temperature. The simulated stress at temperatures exceeding 200°C was estimated to be greater than the experimental stress due to inelastic material deformation.

Prediction of the fatigue life of cylinder heads of two-stroke linear engines was done by Rahman *et al.* (2008) using finite element analysis (FEA) and the stress-life approach. Their research refuted the possibility of failure in all spots. Compressive mean stress increases the fatigue life and tensile mean stress lessens the fatigue life.

Gomez and Pischinger (2011) investigated sophisticated interaction effects of thermal and mechanical loads, geometry of cylinder heads and TMF behavior of the cylinder heads material. They optimized the valves bridge based on the ratio of mechanical to thermal strain. Their research indicates that the vertical temperature gradients are mainly determined by the thickness of the valves bridge which plays a role in the distribution of temperature. Geometric dimensions of the valves bridge and thermal conductivity were the most outstanding parameters in the thermo-mechanical analysis of the cylinder heads.

Thalmair *et al.* (2006) established the TMF/computer aided engineering (CAE) process for fatigue assessment of cylinder heads. Their research proved an acceptable agreement between experimental and simulated results of the fatigue life of the cylinder heads. They predicted the locations of fatigue cracks in the cylinder heads accurately.

Mirslim *et al.* (2009) calculated low cycle fatigue life by finite element simulation of cylinder heads based on various criteria of the strain state. Their experiments show that by cutting the valves bridge, one can increase the fatigue life of cylinder heads.

Trampert *et al.* (2008) studied the effects of thermo-mechanical loads on cylinder heads. Their research indicated concordance between experimental and simulated results of the fatigue life of the cylinder heads. Crucial locations in the analysis of fatigue were the same locations of crack initiation in the experimental conditions. There was conformity between the number of cycles of calculated failure and the experimental results of macroscopic observation of cracks.

Zahedi and Azadi (2012) compared the stress and low-cycle fatigue life of aluminum and magnesium cylinder heads of diesel engines. Their research showed that the strain in magnesium cylinder heads was greater in comparison with the aluminum ones, while the magnesium cylinder heads had less stress. The fatigue life of the both cylinder heads was almost identical.

Azadi *et al.* (2012a) analyzed cracked cylinder heads of gasoline engines. Examining materials and doing finite element analysis of the cracked cylinder heads stress, they determined the cause of cracks and provided some solutions. Their research revealed that the main reason for cracks initiation in cylinder heads was high stress and plastic strain caused by assembly loads of the cylinder heads bolts.

TMF analysis of gray cast iron cylinder heads was conducted by Li *et al.* (2013). An acceptable agreement between experimental and simulated results of TMF life was proved. Improving and optimizing the structure of cylinder heads doubled their fatigue life.

Xuyang *et al.* (2013) predicted TMF life of diesel engines cylinder heads. Their research revealed that the discrepancy between experimental and simulated results was 3%. The energy criterion accurately predicted fatigue life in the valves bridge compared with thermal shock tests.

Metzger *et al.* (2014) predicted the lifetime of cast iron cylinder heads under thermo-mechanical loads and high-cycle fatigue. According to their study, the experimental and simulated results of temperature matched. The mechanical analysis correctly anticipated the position and direction of cracks in the valves bridge. Comparing with experimental results, the anticipation of fatigue life was rather conservative.

Aluminum cylinder heads must be adequately robust to tolerate gas pressure, assembly loads and high temperature resulting from ignition to avoid cracking the valves bridge (Takahashi *et al.*, 2010). Thermo-mechanical loading cylinder heads can only be controlled through modern cooling systems or protective coatings such as thermal barrier coating (TBC) reducing heat stress and thereby reducing the temperature gradient (Bialas, 2008).

Azadi and colleagues studied the impact of TBC on cylinder heads. The results of their research demonstrated the TBC reduced the temperature gradient and, consequently, the thermal stress. Hence fatigue life of cylinder heads was augmented (Azadi *et al.*, 2013; Moridi *et al.*, 2011a, 2011b; Moridi *et al.*, 2014).

According to the introduction, due to lack of information on the behavior of hardening, softening and viscosity of materials, the analysis of cylinder heads is mostly based on simple models of material behavior like elastic-plastic, and the effects of viscosity and creep of cylinder heads are less taken into consideration. Aluminum alloy has creep behavior at about 300°C and viscosity should also be taken into account (Su *et al.*, 2002; Thomas *et al.*, 2002, 2004; Koch *et al.*, 1999). The main objective of this study is to simulate thermo-mechanical behavior of cylinder heads based on the two-layer viscoplasticity model. In some analyses, it is assumed that temperature changes have no effect on the stress-strain curves, and the thermo-mechanical analysis of cylinder heads is non-coupled. Since changes in temperature influence the stress-strain curves, the thermo-mechanical analysis of cylinder heads in this study is coupled.

2. The material and its behavioral model

In this study, the cast alloy of aluminum-silicon-magnesium has been used to simulate the thermo-mechanical behavior. The alloy is known as A356.0 or AlSi7Mg0.3 which is applied in diesel engines cylinder heads (Farrahi *et al.*, 2014; Moridi *et al.*, 2011a, 2011b, 2014). The chemical composition of A356.0 is 7.06 wt. % Si, 0.37 wt. % Mg, 0.15 wt. % Fe, 0.01 wt. % Cu, 0.02 wt. % Mn, 0.13 wt. % Ti, and Al remainder (Farrahi *et al.*, 2014).

The two-layer viscoplasticity model divides the elastic and viscosity effects into two elastic-viscous and elastic-plastic networks. As displayed in Fig. 2, this model was presented by Kichenin *et al.* (1996). This model makes the cyclic stress-strain behavior of the material predictable with reasonable accuracy (Deshpande *et al.*, 2010).

This model consists of a network of elastic-plastic elements parallel to a network of elastic-viscous ones. Plastic deformation and creep can be seen in structures such as cylinder heads which are under assembly loads and temperature fluctuations. The two-layer viscoplasticity model is the best to examine the response of materials such as aluminum which remarkably dependent behavior on temperature and is plastic at high temperatures (Metzger *et al.*, 2014; Farrahi *et al.*, 2014; Zahedi and Azadi, 2012; Deshpande *et al.*, 2010; Thalmair *et al.*, 2006).

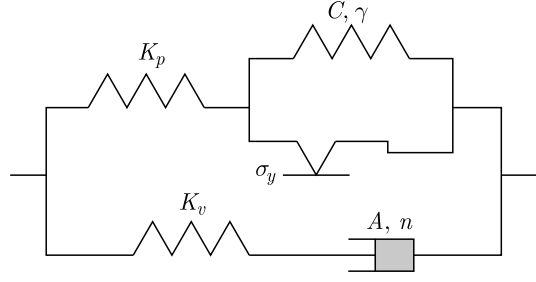


Fig. 2. The two-layer viscoplasticity model (Deshpande *et al.*, 2010)

This model is in good agreement with the results of experimental and thermo-mechanical tests on A356.0 alloy (Farrahi *et al.*, 2014).

The material behavior of different aluminum-silicon casting alloys was described by the nonlinear kinematic/isotropic hardening model in Abaqus software (Koch *et al.*, 1999).

In the plastic network, a nonlinear kinematic/isotropic hardening model is applied which predicts the behavior such as hardening, softening, creep and mean stress relaxation, and it is a suitable model for the plastic behavior of materials (Farrahi *et al.*, 2014; Deshpande *et al.*, 2010).

Kinematic hardening has both linear and nonlinear isotropic/kinematic models. The first model can be used with the Mises or Hill yield surface while the second one can only be used with the Mises yield surface, and it is the most accurate and comprehensive model to examine some issues with cyclic loading including cylinder heads of engines. The kinematic hardening model assumes that the the yield surface, proportional to the value of α , moves as the back stress in yield zone but it does not deform (Lemaitre and Chaboche, 1990). Abaqus software uses the Ziegler linear model (Lemaitre and Chaboche, 1990). To simulate this model, the following equation is given:

$$\dot{\sigma} = C \frac{1}{\sigma^0} (\sigma_{ij} - \alpha_{ij}) \dot{\epsilon}^{PL} + \frac{1}{C} \dot{C} \alpha_{ij} \quad (2.1)$$

where C is the kinematic hardening modulus, \dot{C} is the exchange rate of C in temperature and $\dot{\epsilon}^{PL}$ is the rate of equivalent plastic strain. In this model, σ^0 (size of the yield surface) remains constant. In other words, σ^0 is always equal to σ_0 (that is the yield stress in zero plastic strain) and remains constant. The nonlinear isotropic/kinematic hardening model includes motion of the yield surface proportional to the value of α in the stress zone, and also the changes in size of the yield surface are proportional to the plastic strain (Lemaitre and Chaboche, 1990). This model has been extracted from the Chaboche experience (Chaboche, 1986, 2008). In order to introduce this model a nonlinear term is added to equation (2.1) to indicate size of the yield surface (Lemaitre and Chaboche, 1990).

Abaqus software uses the nonlinear isotropic/kinematic hardening model given by the following equation:

$$\dot{\alpha} = C \frac{1}{\sigma^0} (\sigma_{ij} - \alpha_{ij}) \dot{\epsilon}^{PL} - \gamma_{ij} \dot{\epsilon}^{PL} + \frac{1}{C} \dot{C} \alpha_{ij} \quad (2.2)$$

where C and γ are material constants. In order to introduce this model in to Abaqus software the isotropic and the kinematics parts are required to be defined separately (Farrahi *et al.*, 2014). In order to define the isotropic part, equation (2.3) is used in which b and Q_∞ are material constants (Deshpande *et al.*, 2010).

$$\sigma^0 = \sigma_0 + Q_\infty (1 - \exp(b \dot{\epsilon}^{PL})) \quad (2.3)$$

The overall back stress is computed from relation (2.4) (Lemaitre and Chaboche, 1990):

$$\alpha = \sum_{K=1}^N \alpha_K \quad (2.4)$$

In equation (2.4), if we consider N equal to 3, the hardening variable is divided into three parts, which increases the accuracy of the model (Farrahi *et al.*, 2014).

The Norton-Hoff law is used for the viscous network in order to consider the effect of strain rate the equation of which is the following (Angeloni, 2011):

$$\dot{\epsilon}_V = A(\sigma_V)^n \quad (2.5)$$

where the $\dot{\epsilon}_V$ is viscous strain rate, A and n are material constants and σ_V is the viscous stress.

According to equation (2.6), the rate of the elastic modules in the two viscous and plastic networks is express by f , where k_v and k_p are elastic moduli in the elastic-viscous and elastic-plastic networks, respectively (Deshpande *et al.*, 2010)

$$f = \frac{k_v}{k_v + k_p} \quad (2.6)$$

3. The finite element model and material properties

Traditionally, optimization of engine components such as cylinder is was based on building a series of physical prototypes, and performing a series of different experiments and tests. Unfortunately, this method is time consuming, and building a prototype at the early stages of the design is arduous. Many samples must be constructed and tested in order to achieve the precise design. This process is costly. These problems are resolved using finite element analysis to evaluate the effectiveness of various designs. This technique is accepted for the design and development of geometrically complex components such as cylinder heads in a shorter period and with the least cost. Cylinder heads are complex and challenging components of engines, for which the finite element analysis plays a critical role in optimization (Shojaefard *et al.*, 2006). TMF analysis of each component needs the cyclic stress-strain distribution. Hot components of diesel engines have complex geometry and loading, and the application of analytical methods for detection of stress-strain distribution in them is impossible. Many researchers have used the finite element method to obtain stress-strain distributions in of geometrically complex components (Sun and Shang, 2010). Nowadays, simulation techniques are substituted to validation tests so as to decrease the cost and time of production (Trampert *et al.*, 2008).

The cylinder heads examined in this study are shown in Fig. 3.

The cylinder heads have three valve ports, each with an embedded valve seat, two valve guides and four bolt holes used to secure the cylinder head to the engine block. The cylinder heads are made of aluminum alloy (A356.0). The two valve guides are made of steel, with Young's modulus of 106 GPa and Poisson's ratio of 0.35. The valve guides fit tightly in the two cylinder heads and their behavior is presumed elastic. The three valve seats are made of steel with Young's modulus of 200 GPa and Poisson's ratio of 0.3. The valve seats are press-fit into the cylinder head valve ports. This is accomplished by defining radial constraint equations (ABAQUS User's Manual, 2010).

The model consists of 65580 nodes and approximately 80000 degrees of freedom. The loading of the cylinder heads loading is applied in two phases involving thermal analysis and mechanical analysis.

The values of f , n , A and Q_∞ are extracted from the experimental results of A356.0 by Farrahi *et al.* (2014) and they are entered into the Abaqus software.

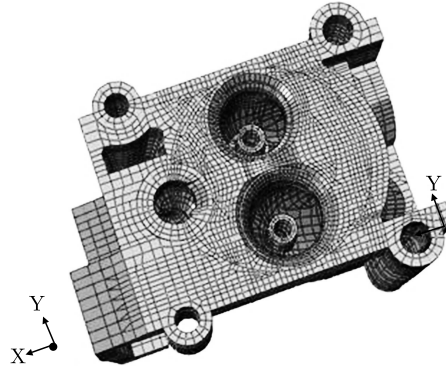


Fig. 3. A meshed cylinder head (ABAQUS/CAE User's Manual, 2010)

There are several methods to insert the values of C and γ into Abaqus software. One of them is entering the yield stress at plastic strain using the midlife cycle (Farrahi *et al.*, 2014). The yield stress at plastic strain was extracted from the data by Farrahi *et al.* (2014) by means of the results of conducted experiments on A356.0 and entered into the Abaqus software.

4. Results and discussion

4.1. Thermal analysis

Thermal stresses in the cylinder heads are the dominant stresses leading to low cycle fatigue. Low cycle fatigue is caused by repeated start-up and shut-down cycle of the engine (Mirsalim *et al.*, 2009; Thomas *et al.*, 2002, 2004; Ghasemi, 2012).

The main part of the cylinder heads stresses results from thermal loading and the rest is caused by the combustion pressure and mechanical constraints (Fig. 1) see Mirsalim *et al.* (2009) and Shojaefard *et al.* (2006). Therefore, thermal loading is the most important loading in the thermo-mechanical analysis. Knowing the precise distribution of temperature, one may increase the accuracy of thermal analysis (Mirsalim *et al.*, 2009). Accurate prediction of temperature of the engine is very crucial and increases the precision of the FEA results (Ghasemi, 2012). As the accuracy of thermal analysis increases, the accuracy of mechanical analysis and fatigue life estimation rises (Thomas *et al.*, 2002, 2004). The combustion pressure causes high cycle fatigue in the cylinder heads (Azadi *et al.*, 2012a; Metzger *et al.*, 2014). Many researchers believe that the combustion pressure has a secondary effect in the TMF (Takahashi *et al.*, 2002; Thomas *et al.*, 2002, 2004). In finite element simulation the valves bridge, where the greatest thermal concentration exists, is subjected to thermal loading ranging from a minimum of 35°C to the maximum of 300°C (Zahedi and Azadi, 2012). The temperature distribution when the cylinder heads are heated to its peak value is shown in Fig. 4. Thermal loading has a considerable effect on the fatigue life, and the temperature field identifies the critical regions (Trampert *et al.*, 2008). Crack initiation is due to changes in the temperature field (Thalmair *et al.*, 2006).

Plastic deformation and creep are observed under such conditions. The two-layer viscoplastic model is ideally suited to examination of the response of materials in these conditions (Metzger *et al.*, 2014; Farrahi *et al.*, 2014; Zahedi and Azadi, 2012; Deshpande *et al.*, 2010). The cyclic thermal loads are obtained by performing independent thermal analysis. In this analysis, three thermal cycles are applied to obtain a steady-state thermal cycle. Each thermal cycle involves two steps: heating the cylinder heads to the maximum operating temperature and cooling it down to the minimum operating temperature using *CFLUX and *FILM options. The nodal temperatures for the last two steps (one thermal cycle) are assumed to be a steady-state solution

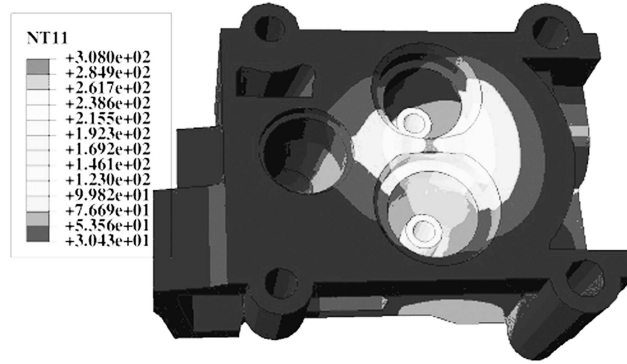


Fig. 4. Temperature distribution in the cylinder head

and the results are stored for use in the subsequent thermo-mechanical analysis (Zahedi and Azadi, 2012). The maximum temperature occurred in the valves bridge.

The temperature in this region (node 50417) is shown in Fig. 5 as a function of time for a steady-state cycle, representing the cycle of turning the engine on and off. The lower is temperature of the flame and the gradient temperature of the parts of cylinder heads, the less is the thermal stress. Thus, low cycle fatigue life, which is mainly affected by thermal fatigue, will increase (Chamani *et al.*, 2009).

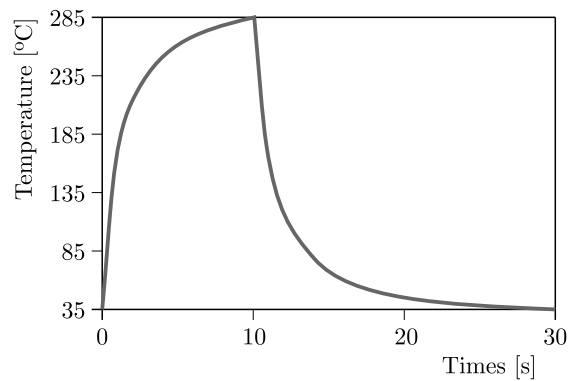


Fig. 5. The temperature at node 50147 versus time

4.2. Mechanical analysis

Mechanical analysis has been carried out in two stages. In the first stage, the three valve seats are press-fit into the corresponding cylinder heads valve ports. A static analysis procedure is used for this purpose. The maximum principal stress distribution is depicted in Fig. 6 proving that the stress in the valves bridge is tensile.

Figure 7 demonstrates the vectors of the maximum principal stress at this stage in the valves bridge. As can be seen, the maximum principal stress in the valves bridge is tensile.

The cyclic thermal loads are applied in the second step of the analysis. It is assumed that the cylinder heads are securely fixed to the engine blocks through the four bolt holes, so the nodes along the base of four bolt holes are secured in all directions during the entire simulation (Zahedi and Azadi, 2012). Von Mises stress distribution at the end of the second stage is shown in Fig. 8. The maximum stress and the maximum temperature occurred in the valves bridge. As shown in Fig. 9, some regions of the cylinder heads entered into yield zone. As mentioned by Azadi *et al.* (2012a), Metzger *et al.* (2014), Takahashi *et al.* (2002), Shojaefard *et al.* (2006), these regions are where the fatigue cracks initiate. These regions are also located in the valves bridge.

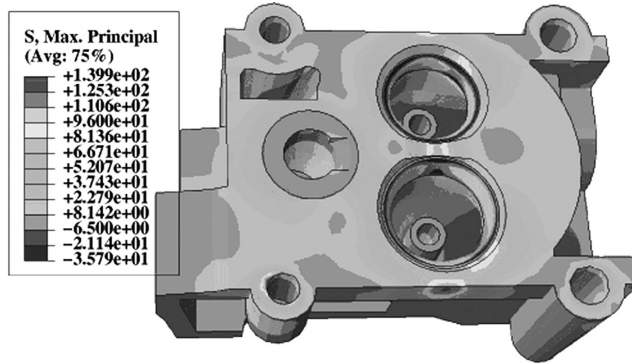


Fig. 6. The maximum principal stress distribution in the first stage of mechanical loading

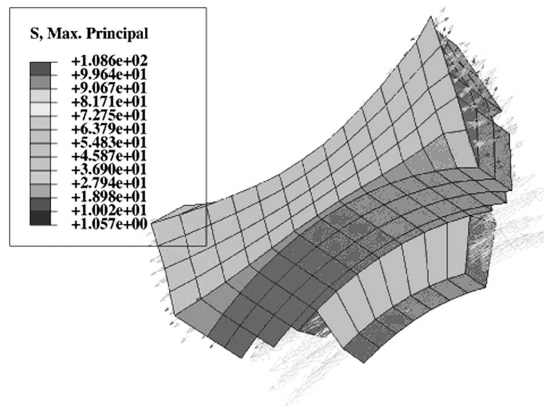


Fig. 7. The maximum principal stress vectors in the valve bridges due to assembly loads

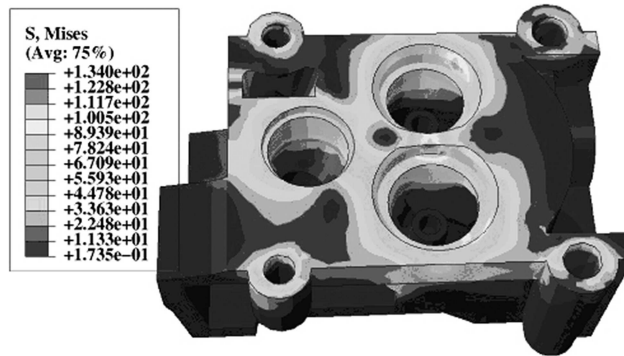


Fig. 8. Von Mises stress distribution at the end of the second stage of mechanical loading

Based on the works by Gocmez and Pishinger (2011) and Ghasemi (2012), the result of loading in the yield surface and ultimate strength is the initiation and propagation of fatigue cracks in less than 10.000 cycles. The equivalent plastic strain distribution is depicted in Fig. 10.

As stated by Li *et al.* (2013), Koch *et al.* (1999), the initiation of fatigue cracks in the cylinder heads occurs where the stress is tensile because of the assembly loads, and the plastic strain is due to thermo-mechanical loads. This region is also located in the valves bridge.

Based on the work by Metzger *et al.* (2014), the first fatigue cracks can be seen at the hottest spot of the cylinder heads (Fig. 4). The review of Fig. 4, 6-10 reveals that the results of finite element analysis corresponds with the experimental tests. Cracked cylinder heads in the experimental tests are shown in Fig. 11a and 11b. The location of cracks is in the valves bridge. This region endures the maximum stress due to smaller thickness of the material and

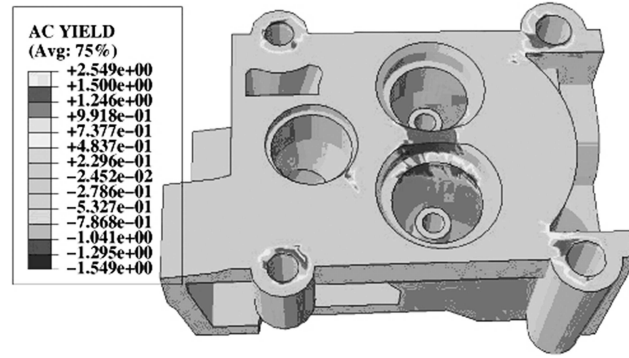


Fig. 9. Regions of the cylinder head entered into the yield zone

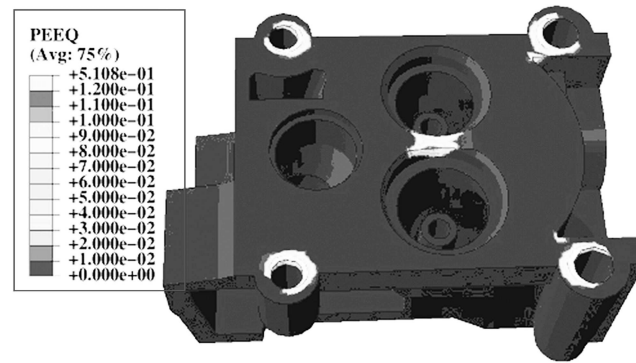


Fig. 10. The equivalent plastic strain distribution



Fig. 11. The cracked diesel engine cylinder head: (a) Takahashi *et al.* (2010), (b) Li *et al.* (2013)

high temperature caused by lack of proper cooling. Ergo, the cylinder heads will crack. Stress functions are inverse to the thickness of the material. Namely, the thinnest locations withstand the highest stress. If the valves bridge becomes wider, it will be cooled better and, consequently, the temperature gradient and thermal stress will reduce. Thus, the fatigue life of cylinder heads increases (Gocmez and Pishinger, 2011).

The finite element model predicts a large compressive stress field in the valves bridge as shown in Fig. 8. Thermal expansion of hot spots in the cylinder heads are constrained by cool regions which have less thermal expansion. As a result, compressive stress is created in the valves bridge which corresponds to the results by Shojaefard *et al.* (2006). Figure 12 displays a diagram of normal stresses (S11), plastic stress (PS11) and viscous stress (VS11) in the X direction for point 1 of element 50152. These elements are in the valves bridge.

The cracking mechanism takes place when the engine is running and warm, reaching the highest temperature. The engine experiences the maximum temperature in the tenth second of operation (Fig. 5). The stresses are compressive because of the thermal loading and combustion pressure at that moment (Fig. 12). Figure 13 demonstrates the vectors of the maximum principal

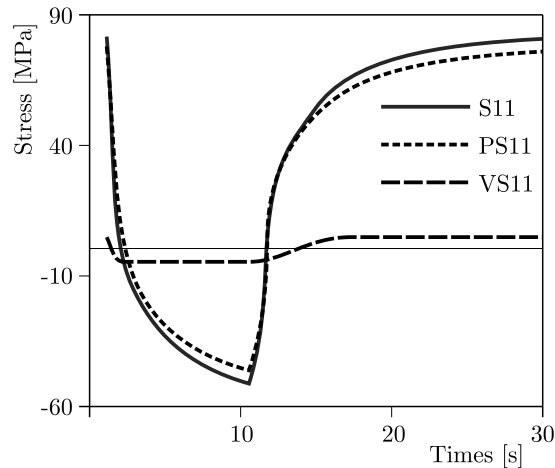


Fig. 12. Normal, plastic and viscous stresses in the X direction for point 1 of element 50152 versus time

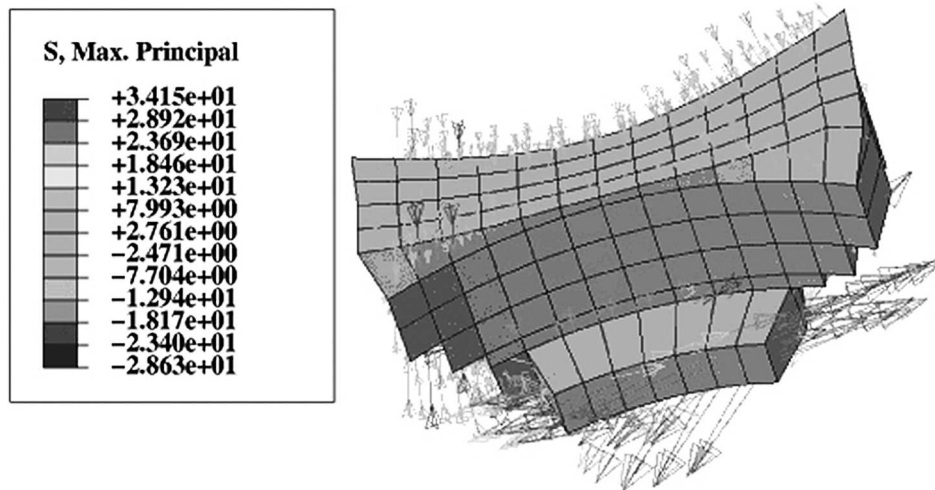


Fig. 13. The maximum principal stress vectors in the valve bridge when the engine is running (in the tenth second)

stress in the valves bridge when the engine is running. As can be seen the maximum principal stress in the valves bridge is compressive. The thermal loading and mechanical constraints generate a compressive stress field, which may lead drive to a compressive yield surface (Fig. 9). As the engine shuts off and its temperature gradually decreases to the room temperature, the stress is tensile due to assembly loads (Fig. 12). Figure 14 shows the vectors of the maximum principal stress in the valves bridge when the engine is shut off. As can be noticed the maximum principal stress in the valves bridge is tensile.

The yielding regions of the cylinder heads cannot return to the primary condition. Hence, tensile stress is created in this area and elastic regions. The stress field for the yield surfaces is compressive at high temperature and turns into tensile stress at low temperature. This corresponds to the results by Li *et al.* (2013), Takahashi *et al.* (2002), Koch *et al.* (1999). The valves bridge is under cyclic tensile and compressive stresses which correspond to the results by Xuyang *et al.* (2013). According to Takahashi *et al.* (2002), changes in the cyclic compressive and tensile stresses cause cracks in cylinder heads. As noted by Koch *et al.* (1999), after a few cycles the aluminum alloy ages and drastically loses its strength. The aged material is unable to resist high tensile stresses, then cracks in the cylinder heads appear. As seen in Fig. 12, the describes viscous stress is low and the normal and plastic stresses are almost identical. Diagrams of the equivalent plastic viscous strains for point 1 of element 50152 are displayed in Fig. 15.

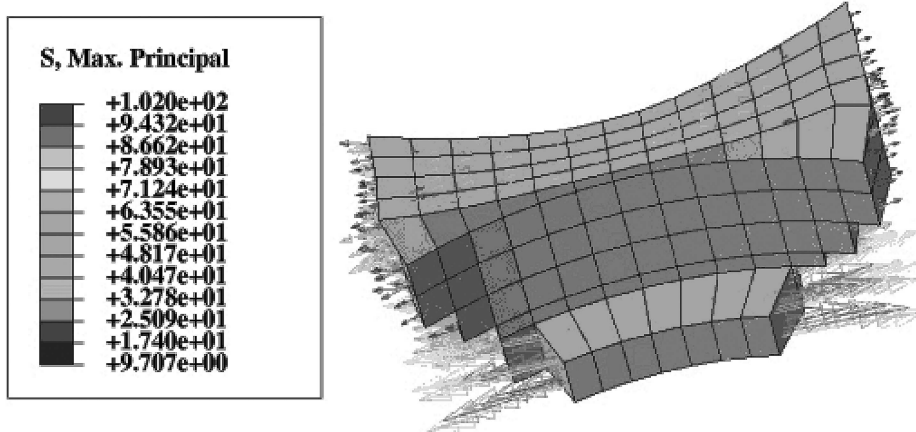


Fig. 14. The maximum principal stress vectors in the valve bridge when the engine shut off (in the thirtieth second)

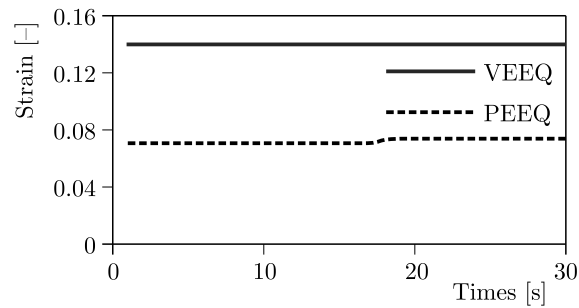


Fig. 15. The equivalent plastic and viscous strain for point 1 of element 50152 versus time

As can be observed, the viscous strain is greater than the plastic strain, and its amount is not negligible. Thus, viscous properties must be considered in the thermo-mechanical analysis of cylinder heads.

5. Conclusion

In this paper coupled thermo-mechanical analysis of cylinder heads in diesel engines is studied. A two-layer viscoplasticity model is used for this purpose. This model makes the cyclic stress-strain behavior of the material predictable. Finite element analysis provides an accurate and reliable prediction of temperature and fatigue for design of the cylinder heads. The obtained FEA results show that the stresses inside the combustion chamber exceed the elastic limit. The thermo-mechanical analysis indicates that the maximum temperature and stress occur in the valves bridge. The results of the finite element analysis correspond with the experimental tests carried out by researchers, and illustrate cracks of the cylinder heads in this region. The finite element analysis proves that the stresses in the valves bridge are compressive when the engine is running and become tensile when the engine is shut off. The valves bridge is subjected to cyclic tensile and compressive stress, in which the plastic strain appears. Low-cycle fatigue always occurs in this region and fatigue cracks appear after a few cycles. Changes in the cyclic compressive and tensile stresses cause cracks in the cylinder heads. In order to prevent them from cracking, it is recommended to modify the cooling system of engines as well as thickness and geometry of the material in crucial parts. Since thinner regions endure high stress, cylinder heads crack in these regions. TBC might also be used in the regions which not only boost the engine performance, but also increase the fatigue life of cylinder heads. Since they reduce thermal

stress, the fatigue life grows. Materials of high thermal conductivity can be used in these regions. Materials of high thermal conductivity decrease the maximum temperature in this region, leading to an increase in the fatigue life of the cylinder heads. Cutting the valves bridge approaches the region to word cooling jackets of cylinder heads. Consequently, the temperature in the region decreases and the fatigue life increases. Thermo-mechanical analysis can determine the optimum cutting to achieve the desired lifetime. It is worth noticing that the amount of the material which is cut is small. However, the increase in volume that is created in the combustion chamber can be compensated by cutting the liner to avoid changes in the engine compression ratio. The viscous strain is greater than the plastic strain, and it is of significant value. Thus, viscous properties must be considered in the thermo-mechanical analysis of cylinder heads. Temperature is effective on stress-strain curves, and the thermo-mechanical analysis of cylinder heads must be coupled.

References

1. ABAQUS/CAE(v6.10-1), 2010, *User's Manual*
2. ANGELONI M., 2011, *Fatigue Life Evaluation of A356 Aluminum Alloy Used for Engine Cylinder Head*, Ph.D. Thesis, University of Sao Palo, Brazil
3. AZADI M., BALO M., FARRAHI G.H., MIRSALEM S.M., 2013, A review of thermal barrier effects on diesel engine performance and components lifetime, *International Journal of Automotive Engineering*, **3**, 305-317
4. AZADI M., MAFI A., ROOZBAN M., MOGHADDAM F., 2012a, Failure analysis of a cracked gasoline engine cylinder head, *Journal of Failure Analysis and Prevention*, **12**, 286-294
5. AZADI M., WINTER G., FARRAHI G.H., EICHLSEDER W., 2012b, Design of cylinder head and block in international combustion engines based on fatigue strength of materials, *8th International Conference on Internal Combustion Engines and Oil*, Tehran
6. BIALAS M., 2008, Finite element analysis of stress distribution in thermal barrier coating, *Journal of Surface and Coating*, **202**, 6002-6010
7. CHABOCHE J.L., 1986, Time-independent constitutive theories for cyclic plasticity, *International Journal of Plasticity*, **2**, 2, 149-188
8. CHABOCHE J.L., 2008, A review of some plasticity and viscoplasticity constitutive theories, *International Journal of Plasticity*, **24**, 1642-1693
9. CHALLEN B., BARANESCU R., 1999, *Diesel Engine Reference Book*, Butterworth-Heinemann
10. CHAMANI H.R., SATTARIFAR I., MOHAMMADI AGHDAM M., 2009, Study of effect combustion gases and cooling thermal boundary conditions on temperature distribution of a heavy diesel engine cylinder head, *Journal of Engine Research*, **17**, 71-81
11. DESHPANDE A., LEEN S.B., HYDE T.H., 2010, Experimental and numerical characterization of the cyclic thermo-mechanical behavior of a high temperature forming tool alloy, *ASME Journal of Manufacturing Science and Engineering*, **132**, 1-12
12. FARRAHI G.H., GHODRATI M., AZADI M., REZVANI RAD M., 2014, Stress-strain time-dependent behavior of A356.0 aluminum alloy subject to cyclic thermal and mechanical loading, *Mechanics of Time-Dependent Materials*, **18**, 475-491
13. GHASEMI A., 2012, Cylinder head high/low cycle fatigue CAE analysis, *SAE International Paper*, No. 2012-01-1999
14. GOCMEZ T., PISHINGER S., 2011, A contribution to the understanding of thermo-mechanical fatigue sensitivities in combustion engine cylinder heads, *Journal of Automobile Engineering*, **225**, 461-477

15. KICHENIN J., DANG VAN K., BOYTARD K., 1996, Finite-element simulation of a new two-dissipative mechanisms model for bulk medium-density polyethylene, *Journal of Material Science*, **32**, 1653-1661
16. KOCH F., MASSAN F., DEUSTER U., LOEPRECHT M., MARCKWARD H., 1999, Low cycle fatigue of aluminum cylinder heads – calculation and measurement of strain under fired operation, *SAE International Paper*, No. 1999-01-0645
17. LEMAITRE J., CHABOCHE J., 1990, *Mechanics of Solid Materials*, Cambridge University Press, Cambridge
18. LI J., WANG P., CUI X., LI K., YI R., 2013, Gray cast iron cylinder head thermal mechanical fatigue analysis, *Proceedings of the FISITA 2012 World Automotive Congress Lecture Notes in Electrical Engineering*, **189**, 243-257
19. METZGER M., LEIDENFROST M., WERNER E., RIEDEL H., SEIFERT T., 2014, Lifetime prediction of EN-GJV 450 cast iron cylinder heads under combined thermo-mechanical and high fatigue loading, *SAE International Paper*, No. 2014-01-9047
20. MIRSALEM S.M., CHAMANI H.R., REZALOO Y., KESHAVARZ M., JAFARABADI M., 2009, Analysis of cracked cylinder head of diesel engine due to fatigue and improvement of its design, *6th International Conference on Internal Combustion Engines*, Tehran
21. MORIDI A., AZADI M., FARRAHI G.H., 2011a, Coating thickness and roughness effect on stress distribution of A356.0 under thermo-mechanical loading, *Journal of Procedia Engineering*, **10**, 1372-1378
22. MORIDI A., AZADI M., FARRAHI G.H., 2011b, Numerical simulation of thermal barrier coating system under thermo-mechanical loading, *Word Congress on Engineering*, London
23. MORIDI A., AZADI M., FARRAHI G.H., 2014, Thermo-mechanical stress analysis of thermal barrier coating system considering thickness and roughness effects, *Journal of Surface and Coating*, **243**, 91-99
24. RAHMAN M.M., ARFFIN A.K., ABDULLAH S., NOOR M.M., BAKER R.A., MALEQUE M.A., 2008, Fatigue life prediction of cylinder head for two stroke linear engine using stress-life approach, *Journal of Applied Science*, **8**, 3316-3327
25. REMY L., PETIT J., 2001, *Temperature-Fatigue Interaction*, Elsevier
26. SHOJA'EFARD M.H., GHAFFARPOUR M.R., NOURPOUR A.R., ALIZADENIA S., 2006, Thermo-mechanical analysis of an engine cylinder head, *Journal of Automotive Engineering*, **220**, 627-636
27. SU X., ZUBECK M., LASECKI J., ENGLER-PINTO JR C.C., TANG C., SEHITOGU H., ALLISON J., 2002, Thermal fatigue analysis of cast aluminum cylinder heads, *SAE International Paper*, No. 2002-01-0657
28. SUN G.Q., SHANG D.G., 2010, Prediction of fatigue lifetime under multiaxial cyclic loading using finite element analysis, *Journal of Material and Design*, **31**, 126-133
29. TAKAHASHI T.I., NAGAYOSHI T., KUMANO M., SASAKI K., 2002, Thermal plastic-elastic creep analysis of engine cylinder head, *SAE International Paper*, No. 2002-01-585
30. TAKAHASHI T.I., SASAKI K., 2010, Low cycle fatigue of aluminum alloy cylinder head in consideration of changing metrology microstructure, *Journal of Procedia Engineering*, **2**, 767-776
31. THALMAIR S., THIELE J., FISHERSWORRING-BUNK A., EHART R., GUILLOU M., 2006, Cylinder heads for high power gasoline engines thermo-mechanical fatigue life prediction, *SAE International Paper* No. 2006-01-0655
32. THOMAS J.J., VERGNER L., BIGNONNET A., BORRET S.M., 2002, Thermo-mechanical design in the automotive industry, *SAE International Paper*, No. 2002-01-0659
33. THOMAS J.J., VERGNER L., BIGNONNET A., CHARKALUK E., 2004, Thermo-mechanical design in the automotive industry, *Journal of Fatigue and Fracture of Engineering Material and Structure*, **27**, 887-895

34. TRAMPERT S., GOCMEZ T., PISHINGER S., 2008, Thermo-mechanical fatigue life prediction of cylinder head in combustion engines, *Journal of Engineering for Gas Turbines and Power*, **130**, 1-10
35. VENKATESWARAN N., VINOBAKRISHNAN R., BALAMURUGAN V., 2011, Thermo-mechanical analysis of the cylinder block with the liner of AFV diesel engine, *SAE International Paper*, No. 2011-28-0118
36. XUYANG G., CHENG Y., ZHANG Z., 2013, Thermo-mechanical fatigue life prediction of heavy duty diesel engine cylinder head, *ASME International Mechanical Engineering Congress and Exposition*, California
37. ZAHEDI F., AZADI M., 2012, Low cycle fatigue life analysis of magnesium alloy diesel engine cylinder head, *20th Annual International Conference on Mechanical Engineering*, Shiraz
38. ZIEHLER F., LANGMAYR F., JELATANCEV A., WIESER K., 2005, Thermal mechanical fatigue simulation of cast iron cylinder heads, *SAE International Paper*, No. 2005-01-0796

Manuscript received April 12, 2015; accepted for print August 4, 2015

FATIGUE LIFE ESTIMATION FOR SELECTED MATERIALS IN MULTIAXIAL STRESS STATES WITH MEAN STRESS

KRZYSZTOF KLUGER, TADEUSZ ŁAGODA

Opole University of Technology, Opole, Poland

e-mail: k.kluger@po.opole.pl; t.lagoda@po.opole.pl

This paper proposes a model for estimating fatigue life under multiaxial stress states, based on critical plane concepts, taking into account the effect of mean shear stress. The fatigue life test results calculated on the basis of the proposed model are compared to the experimental ones related to 2017A-T4 and 6082-T6 aluminium alloy, S355J0 alloy steel under constant-amplitude bending, torsion and proportional combinations of bending and torsion; Ti-6Al-4V alloy under tension-compression, torsion and combination tension-compression – torsion. For the results obtained, statistical analysis is performed by comparing the calculation results proposed by Findley and Dang Van criteria with the experimental data.

Keywords: multiaxial fatigue, mean stress, stress model

Nomenclature

A_σ, A_τ	– regression constant of the fatigue curve for bending/tension-compression and for torsion, respectively
$k_\sigma, k_{\tau 1}, k_{\tau 2}$	– normal, shear and compound (shear and normal) mean stress reduction coefficient
m_σ, m_τ	– slope coefficient of the fatigue curve for bending/tension-compression and for torsion
N_{cal}, N_{exp}	– calculation and experimental fatigue life
α	– critical plane orientation angle
σ, τ	– applied normal and shear stress
σ'_f	– fatigue strength coefficient
$\sigma_{a,f}, \tau_{a,f}$	– fatigue limit for bending/tension-compression and for torsion

Subscripts

a – amplitude, eq – equivalent, m – mean, η – normal to critical plane, η, a – amplitude in normal critical plane, η, m – mean value in normal critical plane, η_s – shear plane, η_s, a – amplitude in shear critical plane, η_s, m – mean value in shear critical plane.

1. Introduction

As design and structural requirements have grown, the industry demands from researchers faster and more accurate methods for estimation of fatigue life in multiaxial load condition so as to face the challenges related to computer-aided design due to complex geometry and load history. It is necessary to reduce the multiaxial condition to an equivalent uniaxial stress state. Such reduction is made possible by so-called fatigue criteria (Carpinteri *et al.*, 2011, 2013; Kluger and Łagoda, 2013; Macha, 1898; Karolczuk and Macha, 2008; Papuga, 2011; Kenmeugne *et al.*,

2012). Although there are several approaches to life estimation of metallic materials reported in the literature (Findley, 1959; Matake, 1977; Fatemi and Socie, 1998; McDiarmid, 1994), those associated with the concept of critical plane have gained widespread usage. The main difference between them relies upon the fatigue damage measure which is considered to determinate the critical plane. Fatigue life depends on a combination of stresses acting in that plane. Depending on the stress condition, environment, component geometry and stress amplitude, the fatigue process is dominated by cracking in either the maximum shear or normal stress plane. However, in such criteria, only the effect of the mean normal stress is assumed, and the effect of shear stress is not or insufficiently taken into account.

In the recent years, alternative approaches to classical models based on the critical plane have been proposed. Morel (2000) presented a critical plane model associated with the accumulated plastic strain at the grain level (in the mesoscopic scale). Papadopoulos and Panoskaltzis (1996), Papadopoulos *et al.* (1997) and Papadopoulos (2001) proposed a fatigue criterion where fatigue strength is determined by a linear combination of the maximum hydrostatic stress $\sigma_{H,max}$ and amplitude of generalised shear stress $\langle T_a \rangle$ defined in the critical plane. In the Dang Van criterion (Dang Van, 1983; Kluger and Łagoda, 2004), the mesoscopic scale of stress observation is applied. However, the above criteria do not take into account mean shear stress either. Additional approaches were proposed by Carpinteri *et al.* (2014), Araujo *et al.* (2014).

The non-zero mean value of stress is often a result of the effect of deadweight of the working element or the entire structure, and is also a result of initial tension of load-bearing elements (such as V-belts in transmissions). The mean stress includes also residual stress resulting from material connections. In the literature on high-cycle fatigue, the effect of the mean shear stress is not examined (Findley, 1959; Matake, 1977; McDiarmid, 1994). Classic Sines approach (Sines, 1959) is often quoted to support that opinion. Sines (1959) concluded that application of the mean torsion stress does not affect fatigue strength of metals subjected to cyclic torsion. Such an assumption was based on the data collected by Smith (1939, 1942), who gathered independent test results on the fatigue limit in torsion of various metals, including steels, aluminium alloys and bronze. In the papers (Krgo *et al.*, 2000; Kallmyer *et al.*, 2001) on experimental tests related to the Ti-6Al-4V titanium alloy, it was proven that the mean torsion stress leads to a reduced fatigue life in comparison to symmetric loads. During the experimental tests of 2017(A)-T4 aluminium alloy (Kluger and Łagoda, 2013, 2014; Kluger, 2015) the effect of mean torsion stress on fatigue life was discovered. It must be noted that not all materials exhibit sensitivity to the mean torsion stress (e.g. 30NCD16 steel) (Niesłony *et al.*, 2014).

This paper aims at presenting a stress-based model for estimation of fatigue life at compound stress state taking into account the mean stress (for bending and torsion). Usefulness of the model was verified by comparing calculation fatigue life and experimental test results of 2017A-T4 and 6082-T6 aluminium alloys (Kluger and Łagoda, 2014; Niesłony *et al.*, 2014), S355J0 alloy steel (Pawliczek, 2000) and Ti-6Al-4V titanium alloy (Krgo *et al.*, 2000; Kallmyer *et al.*, 2001) for which sensitivity to mean torsion stress was discovered. The proposed model is very satisfactory in terms of calculation time. Another beneficial feature is that the material parameters used can be easily determined based on a set of experimental data of fatigue tests related to pure bending and torsion and static tests.

2. Fatigue tests

Experimental tests have been performed on 2017A-T4 (Kluger and Łagoda, 2013, 2014; Kluger, 2015) and 6082-T6 aluminium alloys (Niesłony *et al.*, 2014; Kluger, 2015), S355J0 alloy steel (Pawliczek, 2000) and Ti-6Al-4V titanium alloy (Krgo *et al.*, 2000; Kallmyer *et al.*, 2001). The strength and fatigue properties of tested materials are listed in Table 1.

Table 1. Strength and fatigue properties of the tested materials

Material (EN)	E [GPa]	σ_{UTS} [MPa]	$R_{p0.2}$ [MPa]	σ'_f [MPa]	σ_{af} [MPa]	τ_{af} [MPa]	A_σ	m_σ	A_τ	m_τ
2017(A)-T4	72	545	395	987	142 ¹⁾	78 ¹⁾	21.8	6.9	20.3	7.1
6082-T6	72	385	365	651	126 ¹⁾	74 ¹⁾	23.8	8.0	21.4	7.7
S355J0	213	611	357	880	271	175	23.8	7.1	32.8	11.7
Ti-6Al-4V	116	850	704	2479	450 ²⁾	260 ²⁾	19.6	5.5	15.3	4.1

¹⁾ for $N_f = 10^7$ cycles; ²⁾ for $N_f = 10^6$ cycles

For aluminium alloys 2017(A)-T4, 6082-T6 and S355J0 steel, the results of tests under pure bending, torsion and two combinations of proportional constant-amplitude bending and torsion are analysed, whereas for Ti-6Al-4V titanium alloy under tension-compression, torsion and combination tension-compression – torsion. The tests for 2017(A)-T4, 6082-T6 aluminium alloys and S355J0 steel have been performed with a fatigue testing machine enabling control of bending and torque moment. The tests for Ti-6Al-4V titanium have been performed with a fatigue testing machine enabling control of strain. Stress amplitudes and their mean values are calculated as nominal stresses (without plastic strains).

3. Comparison of the multiaxial fatigue models

3.1. Findley, Dang Van models

Findley (1959) proposed to calculate the equivalent shear stress amplitude $\tau_{eq,a}$ taking into account the maximum value of normal stress $\sigma_{n,max}$ on the plane with maximum value of the equivalent shear stress $\tau_{eq,a}$. The proposed equation is as follows

$$\tau_{eq,a} = \tau_{ns,a} + k\sigma_{n,max} \quad (3.1)$$

where k is the material constant including the influence of the normal stress. Findley assumed that the principal stress directions under proportional loadings do not change. The parameter k is determined on the basis of the fatigue limits for the alternating torsion τ_{af} and bending σ_{af} from the following equation

$$\frac{\sigma_{af,b}}{\tau_{af}} = \frac{2}{1 + \frac{k}{\sqrt{1+k^2}}} \quad (3.2)$$

In the Dang Van criterion (Dang Van, 1983), the mesoscopic scale of stress observation is applied. In this criterion it is assumed that the material fatigue does not occur when all grains reach a stable elastic shakedown state. It means that after the initial loading period the material is subjected to isotropic hardening, and the further relation between stress and strain is expected in the elastic range. The Dang Van criterion defines the condition of crack initiation and it does not allow oneto calculate the fatigue life. The condition of exceeding the stable elastic strain state is dependent on the mesoscopic shear and hydrostatic stresses. However, it is very common to use this criterion on the macroscopic level and in a such case the condition for crack initiation is as follows

$$\tau_{ns}(t) + k\sigma_h(t) \leq b \quad (3.3)$$

where σ_h is hydrostatic stress; k , b are constants determined from uniaxial fatigue tests:

$$k = 3\frac{\tau_{af}}{\sigma_{af,b}} - \frac{3}{2} \quad b = \tau_{af} \quad (3.4)$$

It is assumed that the critical plane is a plane with the maximum value of shear stress.

3.2. New proposed model

The new fatigue life estimation model is based on the criterion by Macha (1989). The equivalent stress is a linear combination of normal and shear stresses and takes up the form

$$\sigma_{a,eq} = B(\tau_{\eta s,a} + \tau_{\eta s,m}) + K(\sigma_{\eta,a} + \sigma_{\eta,m}) \quad (3.5)$$

where

$$\begin{aligned} \sigma_{\eta,a} &= \sigma_a \cos \alpha^2 + \tau_a \sin 2\alpha & \sigma_{\eta,m} &= k_\sigma \sigma_m \cos \alpha^2 + k_{\tau 1} k_{\tau 2} \tau_m \sin 2\alpha \\ \tau_{\eta s,a} &= -\frac{1}{2} \sigma_a \sin 2\alpha + \tau_a \cos 2\alpha & \tau_{\eta s,m} &= -\frac{1}{2} k_\sigma \sigma_m \sin 2\alpha + k_{\tau 1} k_{\tau 2} \tau_m \cos 2\alpha \end{aligned} \quad (3.6)$$

and

$$\begin{aligned} k_\sigma &= \sqrt{\frac{\sigma_{max}}{\sigma'_f}} & \sigma_{max} &= \sigma_a + \sigma_m \\ k_{\tau 1} &= \frac{\tau_a}{\sqrt{3}\tau_m + \tau_a} & k_{\tau 2} &= 1 + \frac{\sqrt{2}\sigma_m}{\sigma_m + \tau_m} \end{aligned} \quad (3.7)$$

The share of individual components of stress in the fatigue process depends on B and K coefficients. By analysing the stress condition for pure torsion and pure bending at constant-amplitude load conditions, a relationship is formulated which describes important factors for the combination of individual components. The coefficients can be presented as follows (Kluger, 2015; Łagoda and Ogonowski, 2005)

$$B = \frac{\sigma_a(N_f)}{\tau_a(N_f)} \quad K = 2 - \frac{\sigma_a(N_f)}{\tau_a(N_f)} \quad (3.8)$$

In general, the values of B and K coefficients are dependent on the amplitude of normal stress σ_a and the amplitude of shear stress τ_a for a specified number of loading cycles. The values $\sigma_a(N_f)$ and $\tau_a(N_f)$ are calculated from S-N fatigue curves for simple load states, respectively: tension (bending), shear (torsion). If there are no clear divergences between S-N curves (σ_a-N_f , τ_a-N_f), in order to simplify the calculations, it may be assumed $K(N_f) = \text{const}$ and $B(N_f) = \text{const}$, e.g. for 10^5 or 10^6 cycles or mainly for the fatigue limit level. However, attention must be paid to make sure that the curves are parallel over the entire high-cycle range. For aluminium alloys, a change of curve inclination coefficients is quite frequent and the effect of such a phenomenon on calculation results must be analysed (Karolczuk and Kluger, 2014).

The plane with maximum shear stress $\tau_{\eta s}$ is assumed as the critical plane for the materials being examined. Analysis criterion (3.5) for zero and non-zero mean stress carried out in (Kluger and Łagoda, 2013; Kluger, 2015; Łagoda and Ogonowski, 2005) has shown that for elastic-plastic materials, the shear plane has to be taken into account, whereas the normal plane for brittle materials.

The normal mean stress reduction coefficient k_σ reported in Eq. (3.7)₁ depends on the applied amplitude of normal stress σ_a , its mean value σ_m and the material constant σ'_f . Along with an increase in the mean stress, the values of k_σ grow proportionally.

The value of the shear mean stress reduction coefficient $k_{\tau 1}$ (see Eq. (3.7)₃) depends on both the applied amplitude of shear stress τ_a and its mean value τ_m . The coefficient value is highest at lower values of the mean shear stress. With such a notation of the $k_{\tau 1}$ coefficient, the effect of higher mean stress values, if they occur, is not amplified.

The compound (shear and normal) mean stress reduction coefficient $k_{\tau 2}$ reported in Eq. (3.7)₄ depends on both the applied in the specimen mean value of normal and shear stresses. If the mean stress from bending not occurs, the coefficient takes the value 1, i.e. it remains neutral

and does not affect the equivalent stress (Eq. (3.5)). In the case of low values of the mean shear stress, the coefficient increases.

The coefficients k_σ , $k_{\tau 1}$ and $k_{\tau 2}$ are relationships developed on the basis of observations related to fatigue tests on 2017A-T4, 6082-T6, S355J0 and Ti-6Al-4V.

The number of loading cycles to failure is calculated from the following relationship

$$N_f = 10^{A_\sigma - m_\sigma \log \sigma_{eq,a}} \quad (3.9)$$

derived from the high-cycle fatigue curve S-N (Basquin) equation

$$\log N_f = A_\sigma - m_\sigma \log \sigma_a \quad (3.10)$$

assuming $\sigma_a = \sigma_{eq,a}$.

4. Models verification

A statistical analysis is performed to assess the proposed model. The analysis involves the determination of the mean scatter E_m described through the following relationship (Karolczuk and Macha, 2008)

$$E_m = \frac{1}{n} \sum_{i=1}^n E^{(i)} \quad (4.1)$$

where

$$E^{(i)} = \log \frac{N_{cal}^{(i)}}{N_{exp}^{(i)}} \quad (4.2)$$

and the scatter coefficient is given by

$$E_{std} = \sqrt{\frac{1}{n} \sum_{i=1}^n (E^{(i)} - E_m)^2} \quad (4.3)$$

where n denotes the number of specimens.

The entire scatter band is expressed with the relationship

$$E_{eq} = 10^{\sqrt{E_m^2 + E_{std}^2}} \quad (4.4)$$

Figures 1-12 show comparisons of the calculation fatigue life using the proposed model with the Findley and Dang Van criteria against the experimental data for uniaxial and multiaxial loadings with zero and non-zero mean stresses. The values of both mean scatter and total scatter band are also reported. For material fatigue, the minimum confidence level 95% (Sutherland and Veers, 2000) is generally adopted, i.e. 95% of the results fall within the range of the scatter band with the coefficient equal to E_{eq} . Ideal consistency of the results is marked with the continuous line, and the dashed lines represent the result scatter in the band with 2 and 3 coefficient (see Figs. 1-12).

Figures 1-3 show the comparison between the calculated and experimental fatigue life for 2017A-T4 aluminium alloy. For loadings with the zero mean stress, all of analyzed models give satisfactory results of the calculated fatigue life (close to 3). In the case of loadings with a non-zero mean stress, the calculations based on the proposed model give the smallest scatter ($E_{eq} = 2.99$). Other models of calculations give a very larges cattering of the results. Findley and Dang Van models overestimate fatigue life calculation.

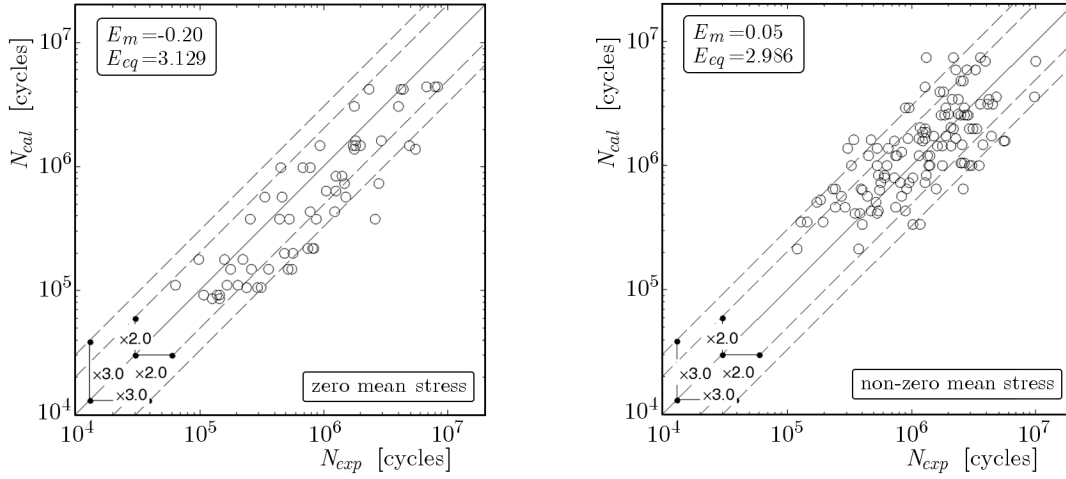


Fig. 1. Comparison of the calculated and experimental fatigue lives for aluminum alloy 2017A-T4 using the proposed model

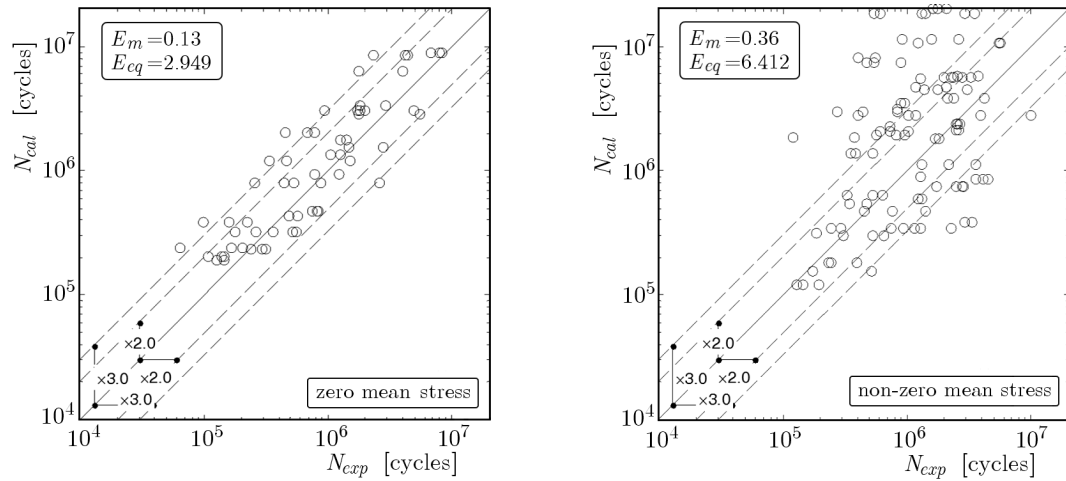


Fig. 2. Comparison of the calculated and experimental fatigue lives for aluminum alloy 2017A-T4 using Findley criterion

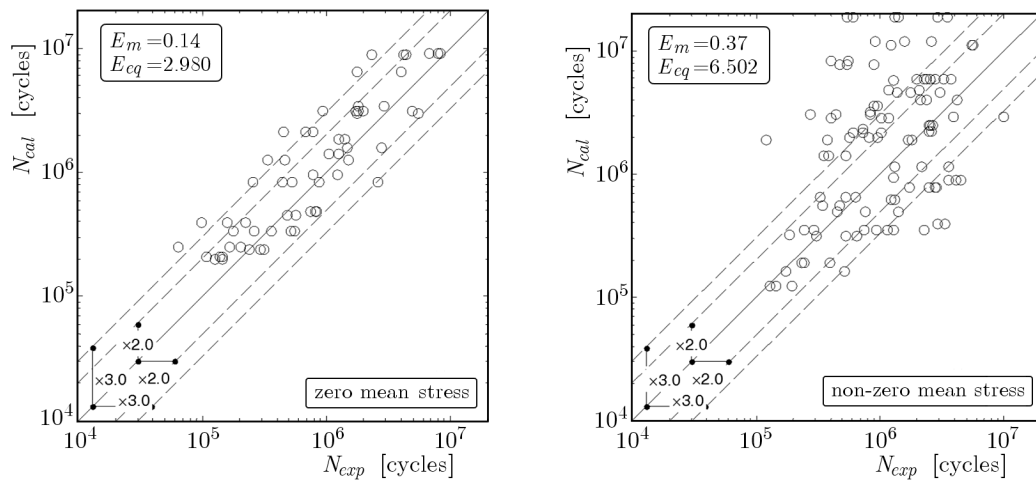


Fig. 3. Comparison of the calculated and experimental fatigue lives for aluminum alloy 2017A-T4 using Dang Van criterion

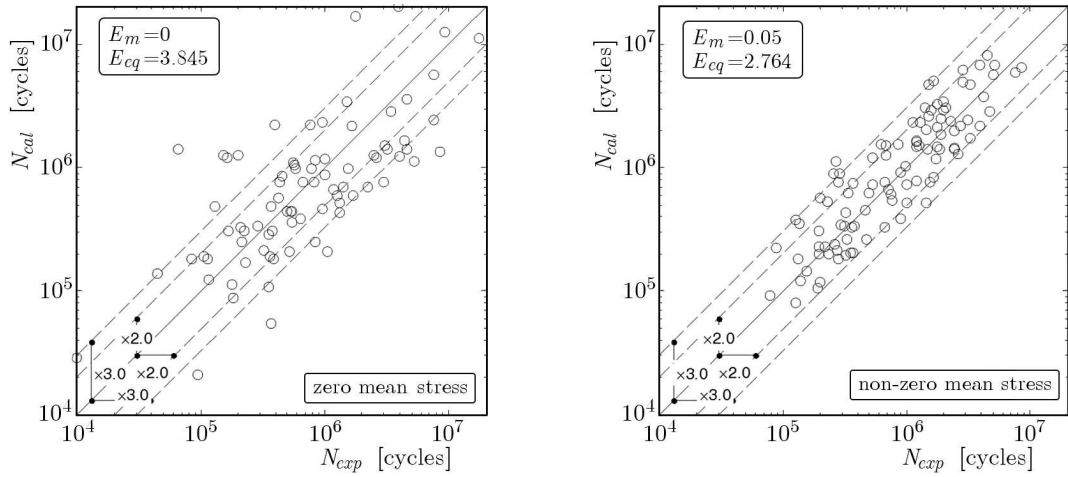


Fig. 4. Comparison of the calculated and experimental fatigue lives for aluminum alloy 6082-T6 using the proposed model

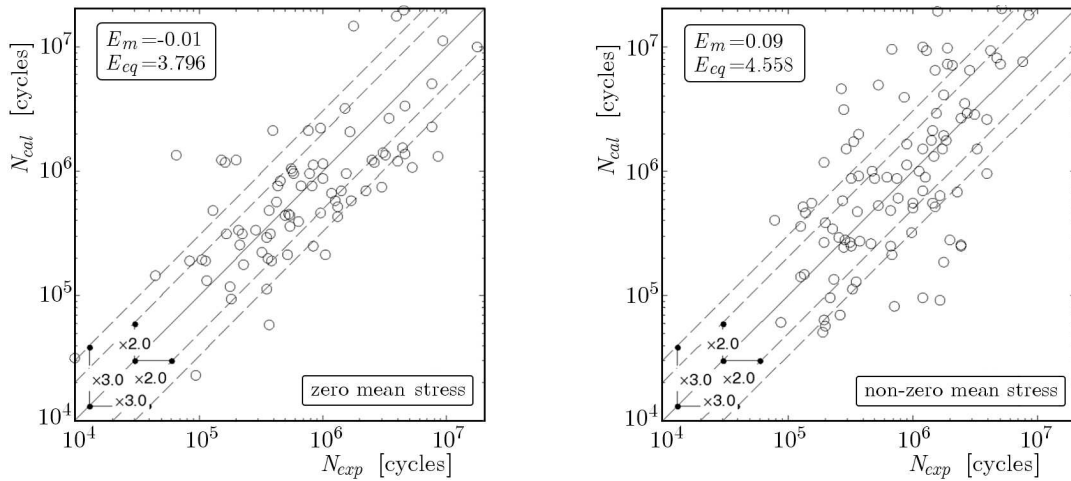


Fig. 5. Comparison of the calculated and experimental fatigue lives for aluminum alloy 6082-T6 using Findley criterion

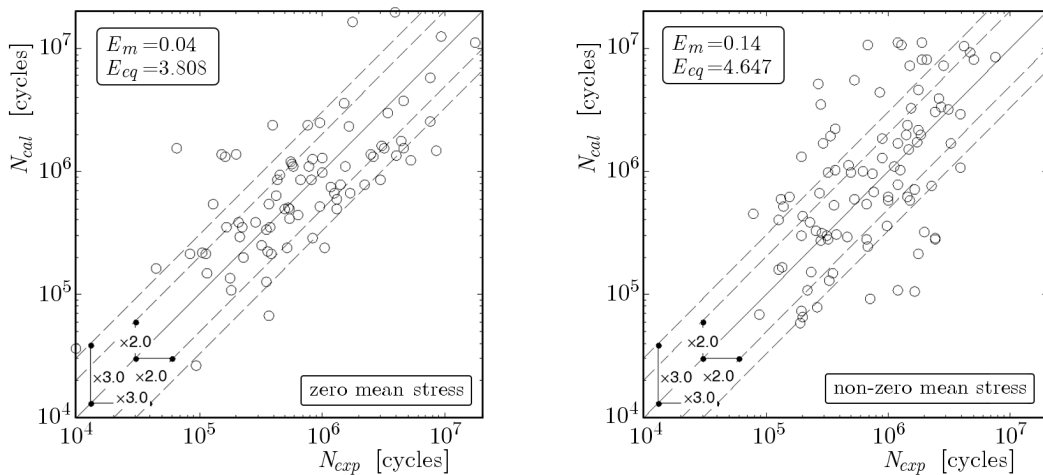


Fig. 6. Comparison of the calculated and experimental fatigue lives for aluminum alloy 6082-T6 using Dang Van criterion

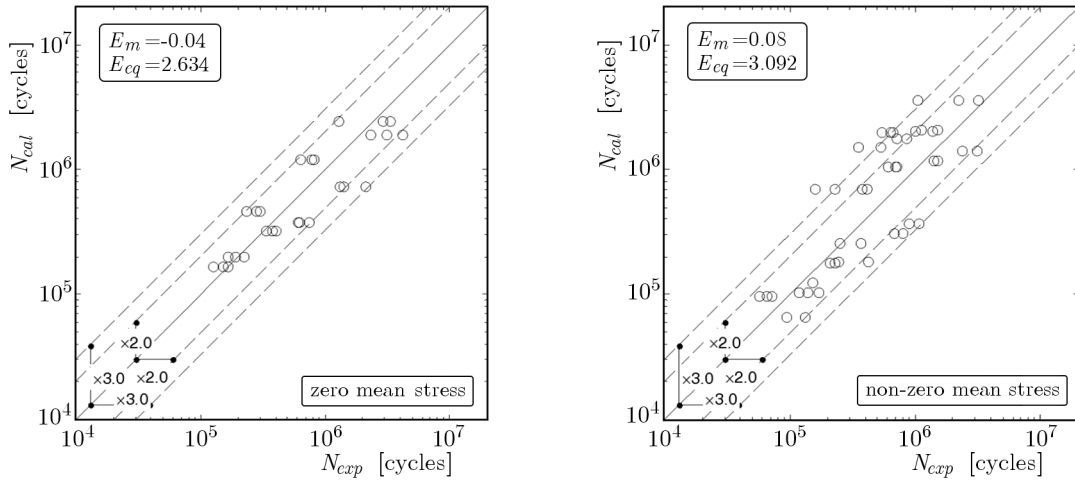


Fig. 7. Comparison of the calculated and experimental fatigue lives for steel alloy S355J0 using the proposed model

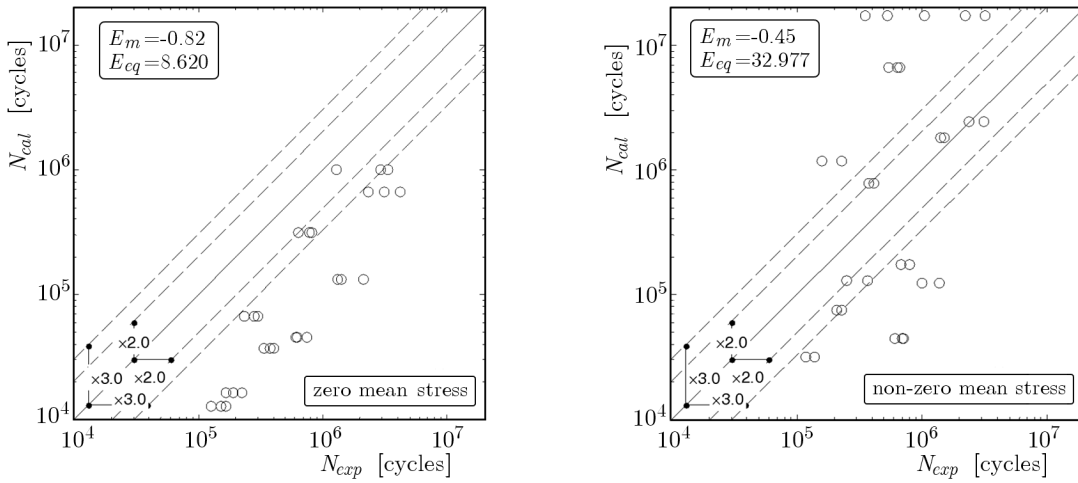


Fig. 8. Comparison of the calculated and experimental fatigue lives for steel alloy S355J0 using Findley criterion

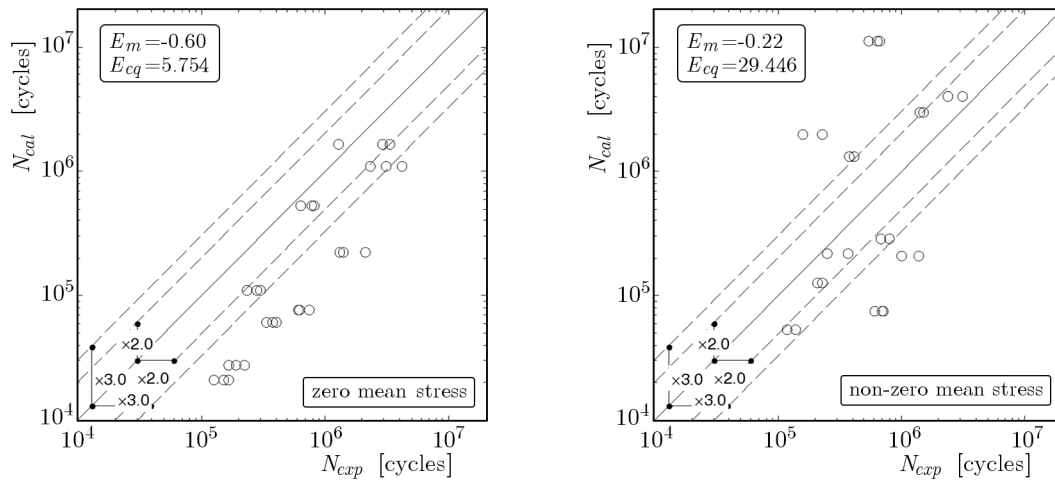


Fig. 9. Comparison of the calculated and experimental fatigue lives for steel alloy S355J0 using Dang Van criterion

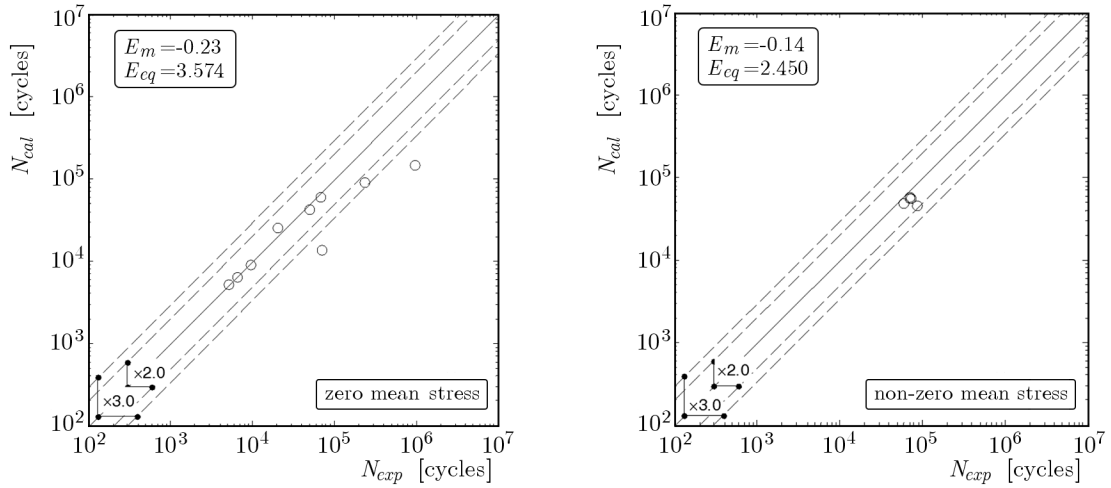


Fig. 10. Comparison of the calculated and experimental fatigue lives for titanium alloy Ti-6Al-4V using the proposed model

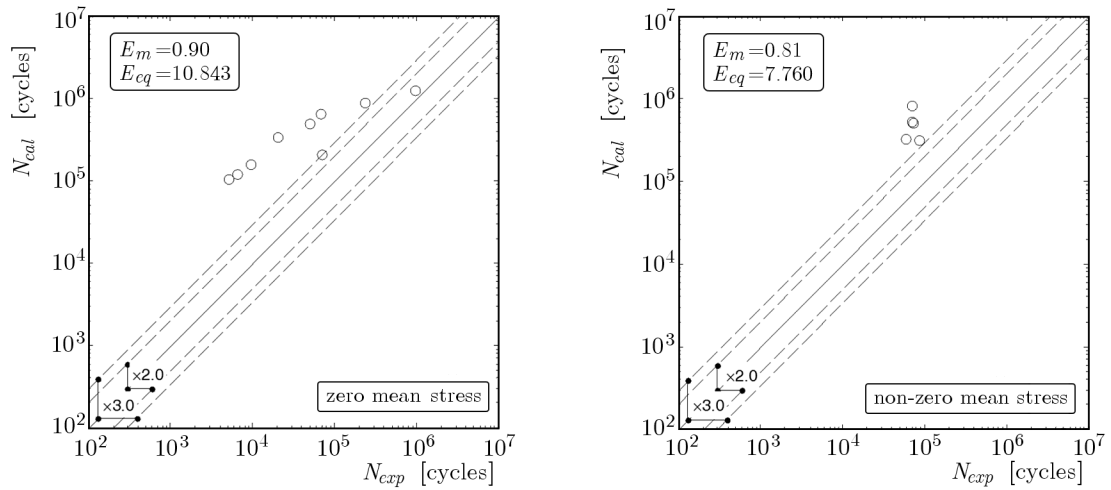


Fig. 11. Comparison of the calculated and experimental fatigue lives for titanium alloy Ti-6Al-4V (Findley criterion)

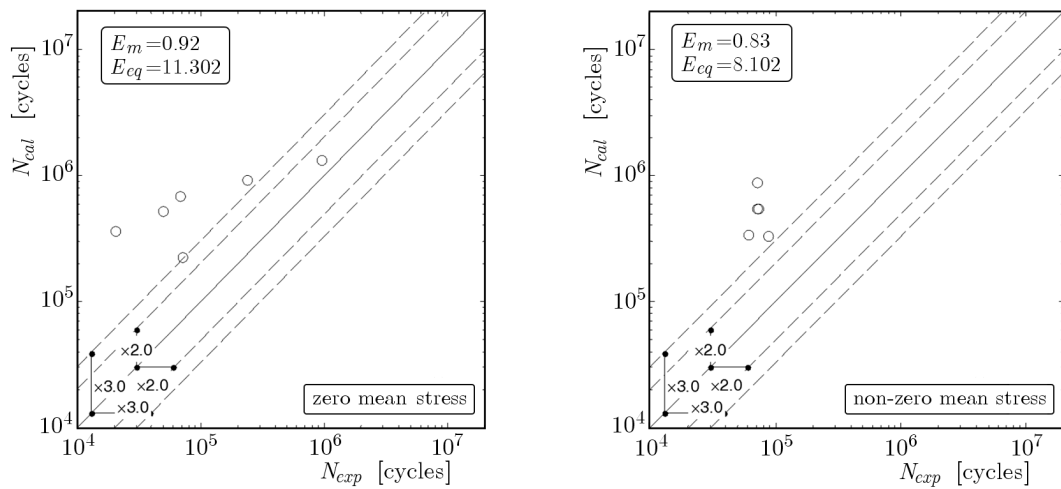


Fig. 12. Comparison of the calculated and experimental fatigue lives for titanium alloy Ti-6Al-4V (Dang Van criterion)

For 6082-T6 aluminium alloy, for which the results of the comparison are shown in Figs. 4-6, the smallest scattering for the zero mean loading are obtained using Findley's model ($E_{eq} = 3.71$), but the other models gives similar results. The large scatter of the data is a result of the very large scatter in the experimental results. The proposed model applied for fatigue life calculation with a non-zero mean stress provides satisfactory results of the calculated fatigue life for which the scatter band is less than 3. Other models of calculations give a very large scattering of the results.

The comparison between the calculated and experimental fatigue life with the zero mean stress for two other analyzed materials S355J0 (see Figs. 7-9) and Ti-6Al-4V (see Figs. 10-12) show that the Findley and Dang Van models overestimate fatigue life calculation. Similar results are obtained for non-zero mean stresses. Only the proposed model applied for fatigue life calculation with the zero mean stress provides satisfactory results of the calculated fatigue life for zero and non-zero mean stresses.

The model presented is suitable for estimation of fatigue life of materials dependent on the mean torsion stress (2017A-T4, 6082-T6, S355J0, Ti-6Al-4V) as is proven by a statistical analysis. The share of the mean bending and torsion stress in the model is limited by the reduction coefficients k_{σ} , k_{τ_1} and k_{τ_2} . The coefficients applied allow one to estimate fatigue life also for the combination of bending and torsion. For non-proportional loads with zero mean stresses, criterion (3.5) gives good results of the estimated fatigue life (Walat *et al.*, 2012). Due to the lack of other studies and limited number of experimental data, the suitability of the model to estimate the fatigue life of non-proportional loads with a non-zero mean value cannot be definitively determined. Only for one of the materials (steel 30NCD16), experimental studies for non-proportional loads of a non-zero mean value of stress (Froustey and Lasserre, 1989) were carried out. Unfortunately, this material is not sensitive to the mean shear stress.

The model proposed is very satisfactory in terms of calculation time. Another beneficial feature of the model is that the material parameters used can easily be determined based on a set of experimental data of fatigue tests related to pure bending and torsion and static tests. The coefficients k_{τ_1} and k_{τ_2} depend on the load state only.

The results of experimental tests outside the scatter band with the coefficient equal to 3 can be due to the fact that the material for tests is of commercial quality, without homogenisation and normalisation after mechanical treatment.

5. Conclusions

- As a result of verifications of the presented model, satisfactory results of comparisons between the calculation and experimental data have been obtained for 2017A-T4 and 6082-T6 aluminium alloys, S355J0 steel alloy and Ti-6Al-4V titanium alloy for all types of load analyzed.
- Mean torsion stresses affect fatigue life of the materials analysed, and have to be taken into account in the calculation process.
- The value of the shear mean stress reduction coefficient k_{τ_1} depends on both the amplitude of shear stress and its mean value. The coefficient is highest at lower values of the mean shear stress.
- The compound (shear and normal) mean stress reduction coefficient k_{τ_2} depends on values of both mean normal and shear stresses. If the mean stress from bending does not occur, the coefficient takes the value 1, i.e. it does not affect the equivalent stresses. In the case of low values of mean shear stress, the coefficient increases.

- The material susceptibility to the mean stress coefficient k_σ depends on the amplitude of the normal stress k_σ and the fatigue life coefficient σ'_f . Along with an increase in the mean stress, the values grow proportionally.
- The reason for large scatter of the results for the other analyzed models could be the disregarding of the effect of the mean shear stress.

References

1. ARAUJO J.A., CARPINTERI A., RONCHEI C., 2014, An alternative definition of the shear stress amplitude based on the Maximum Rectangular Hull method and application to the C-S (Carpinteri-Spagnoli) criterion, *Fatigue and Fracture of Engineering Materials and Structures*, **37**, 7, 764-771
2. CARPINTERI A., SPAGNOLI A., VANTADORI S., 2011, Multiaxial assessment using a simplified critical plane-based criterion, *International Journal of Fatigue*, **33**, 969-976
3. CARPINTERI A., SPAGNOLI A., VANTADORI S., 2014, Reformulation in the frequency domain of a critical plane-based multiaxial fatigue criterion, *International Journal of Fatigue*, **67**, 55-61
4. CARPINTERI A., SPAGNOLI A., VANTADORI S., BAGNI C., 2013, Structural integrity assessment of metallic components under multiaxial fatigue: the C-S criterion and its evolution, *Fatigue and Fracture of Engineering Materials and Structures*, **36**, 870-883
5. DANG VAN K., 1983, Macro-micro approach in high-cycle multiaxial fatigue, *American Society for Testing and Materials*, **STP 1191**, 120-130
6. FATEMI A., SOCIE D.F., 1998, A critical plane approach to multiaxial fatigue damage including out-of-phase loading, *Fatigue and Fracture of Engineering Materials and Structures*, **11**, 3, 149-165
7. FINDLEY W.N., 1959, A theory for the effect of mean stress on fatigue of metals under combined torsion and axial load or bending, *Journal of Engineering for Industry*, 301-306
8. FROUSTEY C., LASSERRE S., 1989, Multiaxial fatigue endurance of 30NCD16 steel, *International Journal of Fatigue*, **11**, 3, 169-175
9. KALLMEYER A.R., KRGO A., KURATH P., 2001, Multiaxial fatigue life prediction methods for notched bars of Ti-6Al-4V, *Proceedings of the 6th National Turbine Engine High Cycle Fatigue Conference*, Jacksonville
10. KAROLCZUK A., KLUGER K., 2014, Analysis of the coefficient of normal stress effect in chosen multiaxial fatigue criteria, *Theoretical and Applied Fracture Mechanics*, **73**, 39-47, doi: 10.1016/j.tafmec.2014.07.015
11. KAROLCZUK A., MACHA E., 2008, Selection of the critical plane orientation in two-parameter multiaxial fatigue failure criterion under combined bending and torsion, *Engineering Fracture Mechanics*, **75**, 389-403
12. KENMEUGNE B., SOH FOTSING B.D., ANAGO G.F., FOGUE M., ROBERT J.-L., KENNE J.-P., 2012, On the evolution and comparison of multiaxial fatigue criteria, *International Journal of Engineering and Technology*, **4**, 1, 37-46
13. KLUGER K., 2015, Fatigue life estimation for 2017A-T4 and 6082-T6 aluminium alloys subjected to bending-torsion with mean stress, *International Journal of Fatigue*, **80**, 22-29, doi: 10.1016/j.ijfatigue.2015.05.005
14. KLUGER K., ŁAGODA T., 2004, Application of the Dang-Van criterion for life determination under uniaxial random tension-compression with different mean values, *Fatigue and Fracture of Engineering Materials and Structures*, **27**, 505-512
15. KLUGER K., ŁAGODA T., 2013, Fatigue life of metallic material estimated according to selected models and load conditions, *Journal of Theoretical and Applied Mechanics*, **51**, 3, 581-592
16. KLUGER K., ŁAGODA T., 2014, New energy model for fatigue life determination under multiaxial loading with different mean values, *International Journal of Fatigue*, **66**, 229-245

17. KRGO A., KALLMEYER A.R., KURATH P., 2000, Evaluation of HCF multiaxial fatigue life prediction methodologies for Ti-6Al-4V, *Proceedings of the 5th National Turbine Engine High Cycle Fatigue Conference*, Arizona
18. ŁAGODA T., OGONOWSKI P., 2005, Criteria of multiaxial random fatigue based on stress, strain and energy parameters of damage in the critical plane, *Mat.-wiss. u. Werkstofftech*, **36**, 9, 429-437
19. MACHA E., 1989, Generalization of fatigue fracture criteria for multiaxial sinusoidal loadings in the range of random loadings, [In:] *Biaxial and Multiaxial Fatigue*, EGF 3, M.W. Brown and K.J. Miller (Edit.), Mechanical Engineering Publications, London, 425-436
20. MATAKE T., 1977, An explanation on fatigue limit under combined stress, *Bulletin of the JSME*, **20**, 257-263
21. MCDIARMID D.L., 1994, A shear-stress based critical-plane criterion of multiaxial fatigue failure for design and life estimation, *Fatigue and Fracture of Engineering Materials and Structures*, **17**, 12, 1475-1484
22. MOREL F., 2000, A critical plane approach for life estimation of high cycle fatigue under multiaxial variable amplitude loading, *International Journal of Fatigue*, **22**, 2, 101-119
23. NIEŚLONY A., ŁAGODA T., WALAT K., ET AL., 2014, Multiaxial fatigue behaviour of AA6068 and AA2017A aluminium alloys under in-phase bending with torsion loading condition, *Mat.-wiss. u. Werkstofftech*, **45**, 10, 947-952
24. PAPADOPOULOS I.V., 2001, Long life fatigue under multiaxial loading, *International Journal of Fatigue*, **23**, 831-849
25. PAPADOPOULOS I.V., DAVOLI P., GORLA C., FILIPPINI M., BERNASCONI A., 1997, A comparative study of multiaxial high-cycle fatigue criteria for metals, *International Journal of Fatigue*, **19**, 3, 219-235
26. PAPADOPOULOS I.V., PANOSKALTSIS V.P., 1996, Invariant formulation of a gradient dependent multiaxial high-cycle fatigue criterion, *Engineering Fracture Mechanics*, **55**, 4, 513-528
27. PAPUGA J., 2011, A survey on evaluating the fatigue limit under multiaxial loading, *International Journal of Fatigue*, **33**, 153-165
28. PAWLICZEK R., 2000, *Fatigue Fracture Plane Orientation Under Combined Bending and Torsion for 18G2A Steel*, Opole University of Technology, Faculty of Mechanical Engineering, Opole, Poland
29. SINES G., 1959, Behaviour of metals under complex static and alternating stresses, [In:] *Metal Fatigue*, Sines G., Waisman J.L. (Edit.), New York, McGraw-Hill, 5-14
30. SMITH J.O., 1939, The effect of range of stress on the torsional fatigue strength of steels, *Bulletin Series No. 316, Engineering Experiment Station*, University of Illinois
31. SMITH J.O., 1942, The effect of range of stress on the torsional fatigue strength of metals, *Bulletin Series No. 334, Engineering Experiment Station*, University of Illinois
32. SUTHERLAND H.J., VEERS P.S., 2000, The development of confidence limits for fatigue strength data, *Wind Energy, ASME/AIAA*
33. WALAT K., KUREK M., OGONOWSKI P., ŁAGODA T., 2012, The multiaxial random fatigue criteria based on strain and energy damage parameters on the critical plane for the low-cycle range, *International Journal of Fatigue*, **37**, 100-111

MULTIOBJECTIVE AND MULTISCALE OPTIMIZATION OF COMPOSITE MATERIALS BY MEANS OF EVOLUTIONARY COMPUTATIONS

WITOLD BELUCH, ADAM DŁUGOSZ

Silesian University of Technology, Institute of Computational Mechanics and Engineering, Gliwice, Poland
e-mail: witold.beluch@polsl.pl; adam.dlugosz@polsl.pl

The paper deals with the multiobjective and multiscale optimization of heterogeneous structures by means of computational intelligence methods. The aim of the paper is to find optimal properties of composite structures in a macro scale modifying their microstructure. At least two contradictory optimization criteria are considered simultaneously. A numerical homogenization concept with a representative volume element is applied to obtain equivalent macro-scale elastic constants. An in-house multiobjective evolutionary algorithm MOOPTIM is applied to solve the considered optimization tasks. The finite element method is used to solve the boundary-value problem in both scales. A numerical example is attached.

Keywords: composite, numerical homogenization, multiobjective optimization, evolutionary algorithm

1. Introduction

Composites are structural materials which are increasingly used and constantly gain in popularity due to their properties. In particular, the favourable strength/weight ratio causes them to displace traditional structural materials such as metals and their alloys in many areas of technology. Their properties depend on such parameters as the properties of constituent materials, volume fraction of the constituents as well as shape and location of the reinforcement. Proper manipulation of such parameters allows obtaining the desired behaviour of composite structures.

In order to obtain the best (for given criteria) properties, optimization methods have to be applied. Since the application of conventional, typically gradient-based, optimization methods for composites may encounter difficulties due to multimodality and discontinuity of the objective function, it is reasonable to use global optimization methods, like bio-inspired optimization algorithms, e.g. evolutionary algorithms, artificial immune systems or particle swarm optimizers (Michalewicz and Fogel, 2004; De Castro and Timmis, 2002; Kennedy and Eberhart, 2001).

In real optimization problems, it is very often necessary to consider more than one criterion at the same time. If the criteria are contradictory, the optimization task belongs to multiobjective ones. The dedicated implementations of bio-inspired global optimization methods can be applied to solve multiobjective optimization tasks. A survey of the state of the art of the multiobjective evolutionary algorithms can be found in Zhoua *et al.* (2011).

Proper determination of the effect of micro-structure of heterogeneous materials on their behaviour at the macro level allows the optimal design of heterogeneous materials. Multiscale optimization allows designing materials in one scale level to obtain the desired properties of the material on different scale(s). Different homogenization methods are typically applied to perform calculations in more than one scale in a reasonable time (Kouznetsova, 2002; Buryachenko, 2007; Zohdi and Wriggers, 2005).

There are numerous approaches to the multiscale modelling. Analytical or semi-analytical methods are typically used to determine the equivalent material constants for inclusions or voids of regular shape, e.g. circular, elliptical or spherical (Eshelby, 1957; Bensoussan *et al.*, 1978).

The applied in the present paper attitude is based on numerical homogenization methods belonging to so-called upscaling methods. Simulation in this group of homogenization methods is carried out hierarchically in different scales utilizing the representative volume element attitude. The computational intelligence methods have been successfully applied by the authors to multi-objective optimization problems of composite structures at the macro scale only, see e.g. Beluch *et al.* (2008). The application of computational intelligence methods for the single-objective multiscale identification of material constants in heterogeneous materials was presented by Beluch and Burczyński (2014).

2. Multiscale modelling

Many structural materials like composites, porous materials or polycrystalline materials are non-homogeneous on a certain observation level. In order to model such materials more precisely, considerations in a macro scale only may be insufficient. Taking into account different scales allows modelling different geometric and material properties of the structures. A macro-scale model may contain various types of external loads (mechanical, thermal, electrical, etc.). Meso and micro scales make it possible to consider such elements as discontinuities or imperfections, like cracks, voids, inclusions or surface roughness (Nemat-Nasser and Hori, 1993; Vernerey and Kabiri, 2014). A nano-scale level includes e.g. crystal lattice defects while an atom-scale level allows incorporating molecular mechanics effects (Burczyński *et al.*, 2007). The number of considered scales depends on the required accuracy of the model (Ilic and Hackl, 2009).

The proper determination of the influence of the micro-structure of heterogeneous materials on their behaviour at the macro level allows optimal designing of them. An appropriate selection of the component materials, geometry and volume ratio of constituents allows creating materials with desired properties, including those which cannot be obtained with the application of homogeneous materials only (Takano and Zako, 2000).

The direct application of more than one scale in numerical calculations by means of numerical methods such as the finite element method (FEM) (Zienkiewicz and Taylor, 2000) or boundary element method (BEM) (Brebbia and Dominiguez, 1989) leads to systems with such large numbers of degrees of freedom that they are very hard or even impossible to be solved. In order to overcome this problem, different homogenization techniques are employed. In the present paper, numerical homogenization techniques are applied to find the parameters of the equivalent material for composite structures. The behaviour of heterogeneous media is described by differential equations with discontinuous coefficients like elastic constants in linear-elastic problems. The aim of the numerical homogenization is to determine continuous, effective coefficients of differential equations which are applied to a higher scale. A typical attitude in the numerical homogenization consists in the determination of constitutive relation between averaged field variables, like stresses and strains (Ptaszny and Fedeliński, 2011).

2.1. Numerical homogenization of heterogeneous materials

Numerical homogenization techniques belong to upscaling methods which perform hierarchical simulation in particular scales and make use of the representative volume element (RVE) concept (Hill, 1963). They allow obtaining macroscopically homogeneous, equivalent materials which behave in the macro scale as microscopically heterogeneous ones.

RVEs are used for globally or locally periodical structures. RVE represents the structure of the whole medium or its part, so it has to include all information required for a thorough description of the structure and properties of the medium (Hashin, 1964).

Numerical homogenization can be performed under certain conditions:

- a) The principle of the scales separation requires that RVE size l_{RVE} must be significantly greater than the microstructure characteristic dimensions l_{micro} and considerably smaller than the characteristic dimensions l_{macro} in the macro scale (Zohdi and Wriggers, 2005)

$$l_{micro} \ll l_{RVE} \ll l_{macro} \quad (2.1)$$

It is commonly assumed that the RVE is the smallest possible volume representing the entire medium or its part. RVE should meet two conflicting criteria: be large enough to be representative of the entire structure and as small and uncomplicated (geometrically and materially) as possible in order to carry out its precise numerical analysis (Madi *et al.*, 2006). In the case of fully regular structures (commonly used for fiber-reinforced composites), RVE may contain only one centrally placed core. Such an RVE is called a unit cell.

- b) Averaging is performed according to the relation

$$\langle \cdot \rangle = \frac{1}{|V|} \int_V (\cdot) dV \quad (2.2)$$

where $\langle \cdot \rangle$ is the averaged value of the field under consideration, V – RVE volume.

- c) The condition specifying the equality of the average energy density in the micro scale and the macroscopic energy density at the point of macrostructure corresponding to the RVE (Hill condition) has the form (Kröner, 1972)

$$\langle \sigma_{ij} \varepsilon_{ij} \rangle = \langle \sigma_{ij} \rangle \langle \varepsilon_{ij} \rangle \quad (2.3)$$

where: σ_{ij} and ε_{ij} are stress and strain tensors in the micro scale.

- d) Appropriate boundary conditions, e.g. periodic boundary conditions (Kouznetsova, 2002): periodic displacements and anti-periodic tractions on opposite faces of the RVE, as shown in Fig. 1, are

$$\begin{aligned} u_i^+ &= u_i^- & \forall r \in \partial V : & n_i^+ = -n_i^- \\ t_i^+ &= -t_i^- & \forall r \in \partial V : & n_i^+ = -n_i^- \end{aligned} \quad (2.4)$$

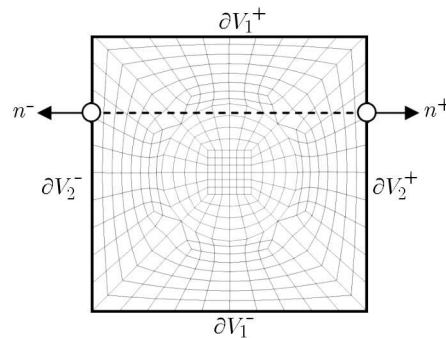


Fig. 1. RVE boundaries for periodic boundary conditions

In addition to the boundary conditions, strain boundary conditions from the higher scale are imposed on every RVE (localization). If FEM is applied to solve the boundary-value problem in both scales, the RVE is assigned to each integration point in the micro scale (Kuczma, 2014).

Averaged stresses, calculated according to Eq. (2.2), are obtained as a result of numerical computations in the micro scale (homogenization). Averaged stresses are transferred to the

higher scale in order to calculate homogenized material parameter values at the macro scale taking into account the constitutive equation for the homogenized material. Assuming that the considered composites can be treated as orthotropic materials in the plane strain state, the constitutive equation in the Voight notation has the form (Gibson, 2012)

$$\begin{bmatrix} \langle \sigma_{11} \rangle \\ \langle \sigma_{22} \rangle \\ \langle \sigma_{12} \rangle \end{bmatrix} = \begin{bmatrix} Q_{11} & Q_{12} & 0 \\ \cdot & Q_{22} & 0 \\ \cdot & \cdot & Q_{33} \end{bmatrix} \begin{bmatrix} \langle \varepsilon_{11} \rangle \\ \langle \varepsilon_{22} \rangle \\ \langle \varepsilon_{12} \rangle \end{bmatrix} = \frac{E}{(1+\nu)(1-2\nu)} \begin{bmatrix} 1-\nu & \nu & 0 \\ \cdot & 1-\nu & 0 \\ \cdot & \cdot & 0.5-\nu \end{bmatrix} \begin{bmatrix} \langle \varepsilon_{11} \rangle \\ \langle \varepsilon_{22} \rangle \\ \langle \varepsilon_{12} \rangle \end{bmatrix} \quad (2.5)$$

where Q_{ij} are the elements of the resultant elastic constants tensor \mathbf{Q} , $i, j = 1, 2, 3$.

In the considered case, determination of the \mathbf{Q} matrix elements requires performing of 3 independent analyses in the micro scale for each RVE. If the material is linear and fully periodic, only one RVE has to be analysed for the whole structure.

Having determined the components of the \mathbf{Q} matrix, the elastic constants of the equivalent material are calculated according to Eq. (2.5).

3. Formulation of the optimization problem

In many engineering optimization problems, more than one optimization criterion have to be taken into account simultaneously. Moreover, the considered criteria are often contradictory, which leads to multiobjective optimization (MOO) tasks. MOO results in a set of trade-off solutions instead of only one optimal solution in single-objective optimization tasks.

The aim of the two-scale multiobjective optimization of composite structures is to find some of its properties in the micro scale (represented by the RVE) which optimize the behaviour of the structure in the macro scale. To solve the boundary value problem in the macro and micro scales, the commercial FEM software MSC Marc and MSC Nastran has been applied. In order to combine MOOPTIM with FEM software, appropriate programming interfaces have been developed. The block diagram of the multiobjective and multiscale evolutionary optimization is presented in Fig. 2.

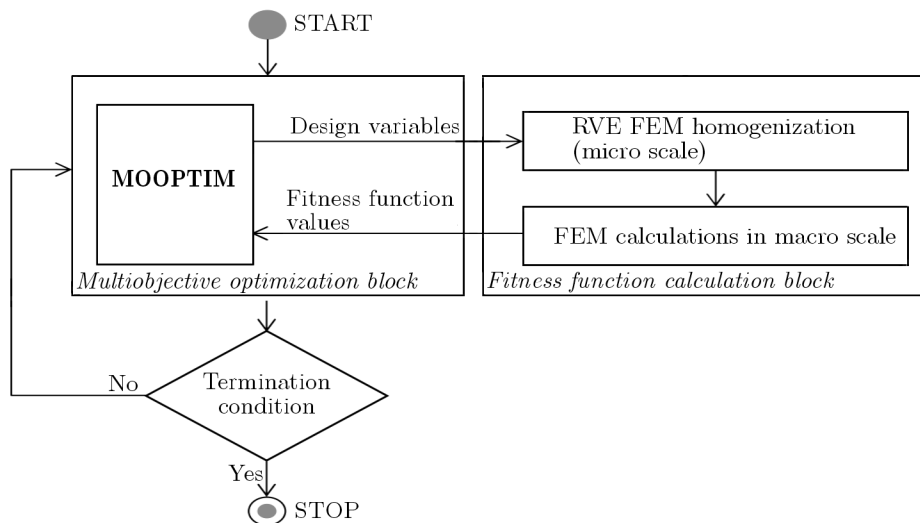


Fig. 2. A block diagram of the multiobjective and multiscale evolutionary optimization

3.1. Definition of the multiobjective optimization task

A MOO problem can be treated as a search for a vector $\mathbf{x} \in \mathbf{D}$, where \mathbf{D} is a set of admissible solutions being a subset of design space \mathcal{X} (Deb, 2001)

$$\mathbf{x} = [x_1, x_2, \dots, x_n]^T \quad (3.1)$$

which minimizes the vector of k objective functions

$$f(\mathbf{x}) = [f_1(\mathbf{x}), f_2(\mathbf{x}), \dots, f_k(\mathbf{x})]^T \quad (3.2)$$

The vector \mathbf{x} has to satisfy m inequality constrains $g_i(\mathbf{x}) \geq 0$, $i = 1, 2, \dots, m$ and p equality constrains $h_i(\mathbf{x}) = 0$, $i = 1, 2, \dots, p$.

There exist many attitudes to the multi-objective optimization problems (Laumann *et al.*, 2004). *A priori* methods are based on the transformation of a multiobjective problem into a single-objective one (Collette and Siarry, 2003). The most popular methods from this group are: i) weighted sum method in which each criterion has its own weight value; and ii) ε -constraint method in which the optimization is performed for a chosen criterion while the remaining criteria are treated as constrains. The advantage of the *a priori* methods is that single-objective methods can be applied, but the drawback is that some very often unrealistic assumptions of the objectives have to be made before the optimization starts.

The second group state interactive methods, which demand an interaction with the decision-maker (DM) during the optimization to achieve additional information (Luque *et al.*, 2011). There exist many multi-criteria decision-making principles. For example, in Phelps and Koksalan (2003), a pair-wise comparison of solutions is used to include DM's preference. The guided multiobjective evolutionary algorithm (G-MOEA) uses a modified definition of dominance (see: Section 3.2) which has been modified based upon the DM's preference information (Branke and Deb, 2004).

Both aforementioned groups of methods result in one solution of the optimization process. In the *a posteriori* methods, a set of compromise (trade-off) solutions is determined in the first step of the optimization procedure. The DM is required to choose the most preferred solution in the second step.

3.2. Pareto concept in multiobjective optimization of composites

An attitude belonging to *a posteriori* methods is employed in the present paper. The multi-objective optimization is performed using the Pareto concept of non-dominated solutions (Ehrgott, 2005). If the minimization problem is considered, a solution \mathbf{x} is strongly dominated by the solution \mathbf{x}^* if

$$\forall i \in \{1, 2, \dots, k\} : \quad f_i(\mathbf{x}^*) < f_i(\mathbf{x}) \quad (3.3)$$

The solution \mathbf{x} is weakly dominated by the solution \mathbf{x}^* if

$$\begin{aligned} \forall i \in \{1, 2, \dots, k\} : \quad & f_i(\mathbf{x}^*) \leq f_i(\mathbf{x}) \quad \wedge \\ \exists j \in \{1, 2, \dots, k\} : \quad & f_j(\mathbf{x}^*) < f_j(\mathbf{x}) \end{aligned} \quad (3.4)$$

An example of domination areas for an arbitrary point (solution) A for a two-objective minimization problem is presented in Fig. 3. The set of non-dominated solutions is called the Pareto front.

In the present paper, a multi-objective optimization problem is solved by means of the proposed multiobjective evolutionary algorithm MOOPTIM, which belongs to bio-inspired global optimization methods (see: Section 4).

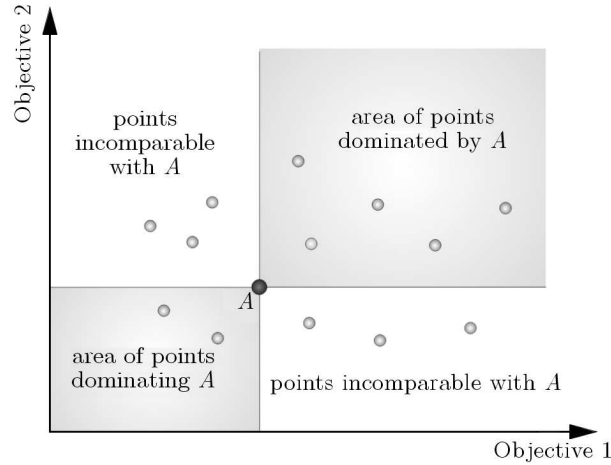


Fig. 3. An exemplary Pareto front and domination areas for point A

The real-value coding of the design variables is applied in MOOPTIM. The vector of the design variables (chromosome) has the form

$$\mathbf{x} = [l_{RVE}, E_m, E_f] \quad (3.5)$$

where l_{RVE} is the characteristic dimension of the RVE, E_m, E_f – Young's moduli for the matrix and fibre materials, respectively.

3.3. Optimization criteria

The following optimization criteria have been considered simultaneously:

1. The minimization of the (dimensionless) structure cost C

$$\arg \min\{C(\mathbf{x}); \mathbf{x} \in \mathbf{D}\} \quad C(\mathbf{x}) = \rho_f C_f V_f(\mathbf{x}) + \rho_m C_m V_m(\mathbf{x}) \quad (3.6)$$

where ρ_f, ρ_m are fibre and matrix densities, V_f, V_m – fibre and matrix volumes, C_f, C_m – fibre and matrix unit costs per kilogram.

2. The minimization of the complementary energy of the structure Π_σ being a measure of the averaged susceptibility of the structure (Burczyński, 1995)

$$\arg \min\{\Pi_\sigma(\mathbf{x}); \mathbf{x} \in \mathbf{D}\} \quad \Pi_\sigma(\mathbf{x}) = \int_{\Omega} W(\sigma) d\Omega - \int_{\Gamma_1} \mathbf{p}\mathbf{u}^0 d\Gamma_1 \quad (3.7)$$

where $W(\sigma)$ is the stress potential related to a volume unit, Ω – a domain occupied by the body, Γ_1 – part of the boundary on which the function $\mathbf{p}\mathbf{u}^0$ is defined, \mathbf{p}, \mathbf{u}^0 – tractions and displacements on Γ_1 .

4. Multiobjective evolutionary algorithm

An in-house multiobjective evolutionary algorithm MOOPTIM based on the Pareto concept is used for solving optimization tasks (Długosz, 2010). Some ideas in MOOPTIM are inspired by Deb's NSGAI algorithm (Deb *et al.*, 2002). Similarly as in NSGAI, the proposed algorithm uses a non-dominated sorting procedure to classify individuals in the population and a crowding coefficient to preserve diversity in the population. The main differences between MOOPTIM and

NSGA II are: i) application of a different number and different types of evolutionary operators and ii) selection mechanism.

Two types of mutation (uniform and Gaussian ones) and two crossover operators, in form of a simple crossover and an arithmetical one, are used. As previously tested, the Gaussian mutation operator has significant influence on the effectiveness of searching ability of the algorithm. This operator requires an extra parameter, called the mutation range, which can take values from 0 to 1. It is observed that higher values of the mutation range usually improve the convergence of the algorithm, especially for difficult optimization tasks (Długosz, 2013).

Instead of binary tournament selection in NSGA-II, in MOOPTIM, individuals are selected on the basis of a non-domination level as well as the crowding coefficient.

A pseudo code of the algorithm is presented in Fig. 4. In the initialization step, besides determining all settings of the algorithm, the populations Q_i and P_i of the same size are generated, and the fitness functions are evaluated for the population Q_i . In the main loop, after the evaluation of the fitness functions values for P_i , the populations Q_i and P_i are combined into a set R_i . Next, the selection procedure is performed on the set R_i . The individuals from the population R_i are selected to P_{i+1} on the basis of the non-domination level and the crowding coefficient. Individuals from P_{i+1} are copied to Q_{i+1} and then, evolutionary operators modify the individuals in the population P_{i+1} to obtain new possible solutions.

```

MOOPTIM algorithm
begin
   $i \leftarrow 0$ 
  randomly generate population  $Q_i$ 
  evaluate objective functions for  $Q_i$ 
  randomly generate population  $P_i$ 
  while (not termination condition) do
    begin
      evaluate objective functions for  $p_i$ 
      join populations  $Q_i$  and  $P_i$  ( $R_i = Q_i + P_i$ )
      use selection (choose  $P_{i+1}$  from  $R_i$ )
      copy  $P_{i+1}$  to  $Q_i$ 
      apply evolutionary operators for  $P_{i+1}$ 
    end
     $i \leftarrow i + 1$ 
  end
end

```

Fig. 4. The pseudo code of the MOOPTIM algorithm

MOOPTIM has been tested on several benchmarks typical for the multiobjective problems like: SCH, ZDT1, ZDT2, ZDT3, ZDT4, ZDT6, CONSTR, SRN, TNK (Deb, 1999; Zitzler and Thiele, 1999). The results obtained using MOOPTIM in most cases are better in comparison with the results obtained by means of NSGA-II. The advantage of using MOOPTIM (instead of NSGA-II) especially appears in the case of functions difficult to optimize, i.e. having strong multimodality, non-convex or a discontinuous Pareto front. Functionals defined for engineering problems, which are solved by using FEM, are usually strongly multimodal and, sometimes, design variables are discontinuous.

The ability of finding global solutions by the optimization algorithm for such problems is essential. The application of the proposed algorithm to solve different optimization tasks has shown its superiority on NSGAII in many cases (Długosz, 2010, 2013). Moreover, MOOPTIM has been successfully applied in the optimization of parameters for porous microstructures in two-scale thermoelastic problems (Długosz, 2014).

5. Numerical example

A box beam structure of dimensions $200 \times 80 \times 60$ mm made of a composite material is considered (Fig. 5). The thickness of each side is constant and equal to 2 mm. The structure is fixed on one end and loaded by a pair of nodal forces of value $P = 300$ N each. The structure is divided into 700 Quad4 finite elements having linear shape functions.

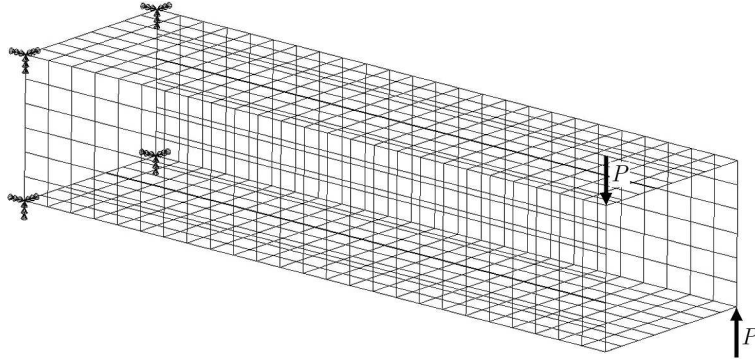


Fig. 5. A box beam – dimensions, mesh and boundary conditions

Global periodicity of the structure is assumed and, as a result, the structure can be fully represented by a RVE containing a single centrally positioned fibre (unit cell) of dimension equal to $15 \mu\text{m}$. The volume fraction of the fibre can vary within the range 4%-45%, which is achieved through different sizes of the RVE (RVE side length $l_{RVE} = 60\text{-}20 \mu\text{m}$), as presented in Fig. 6. Regardless of the fibre volume fraction, each RVE is divided into 820 Quad4 four-node finite elements.

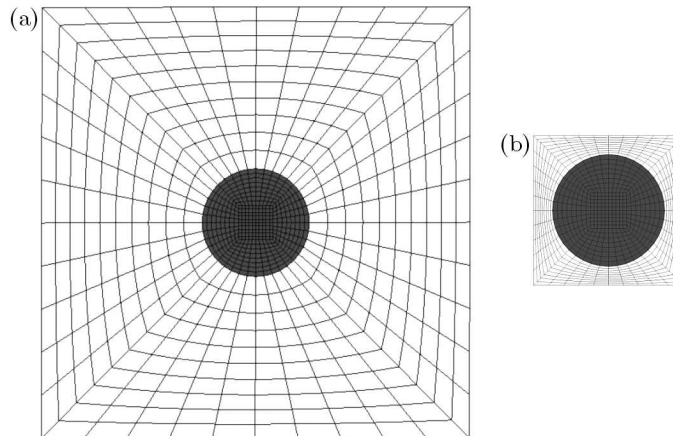


Fig. 6. Exemplary RVEs with mesh for fibre volume fractions: (a) 4% ($RVE_l = 60 \mu\text{m}$), (b) 45% ($RVE_l = 20 \mu\text{m}$)

The matrix of the composite is an epoxy resin, while different types of fibres may be applied as reinforcement. The fibres are characterized by some parameters, like Young's modulus, Poisson's ratio, density and unit price. The selected parameters of the matrix and fibres materials are collected in Table 1.

It is assumed that the fibre material cost is dependent on material Young's modulus. Two cases are considered:

- i) the fibre material cost is approximated by a polynomial function of Young's modulus, as presented in Fig. 7. This attitude assumes the possibility of designing the fibre material that has the desired properties;

Table 1. Parameters of the composite constituent materials

No.	Material	E [GPa]	ν [-]	Density [g/cm ³]	Unit price [€/kg]
1	E glass (fibre)	72	0.22	2.54	1.5
2	S-2 glass (fibre)	87	0.22	2.49	5
3	HS carbon (fibre)	230	0.2	1.8	25
4	IM carbon (fibre)	285	0.2	1.8	55
5	HM carbon (fibre)	400	0.2	1.8	175
6	Epoxy resin (matrix)	2.4	0.35	1.14	8

ii) the fibre material cost is taken from the database of material parameters (materials 1-5 from Table 1).

Each chromosome which is a design variable vector consists of two genes representing:

- i) size of the RVE and Young's modulus of the fibre (case i);
- ii) size of the RVE and the fibre material number (case ii).

Two variants of the case i) are taken into consideration, as presented in Fig. 7:

- i) only carbon fibres are considered (solid line);
- ii) carbon and glass fibres are taken into account (dashed line).

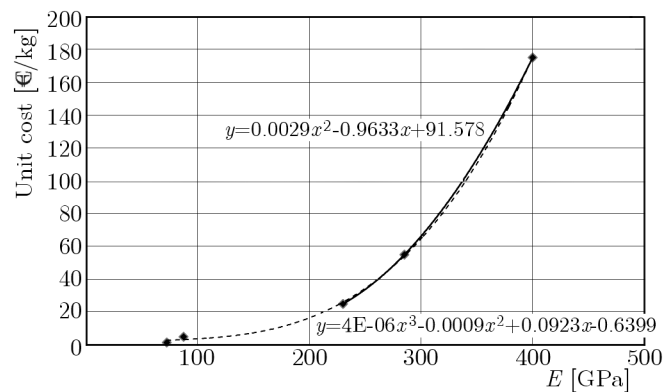


Fig. 7. Young's modulus of the fibre – unit cost diagrams for polynomial approximation

The results of the optimization in form of Pareto frontiers for cases i) and ii) are presented in Fig. 8.

As revealed from Fig. 8, the best optimization results have been obtained for a wider search space (glass and carbon fibres).

The design variables values, fibre volume fractions and fitness function values for exemplary points 1-4 for carbon and glass fibres with different approximations are collected in Table 2.

The following parameters of MOOPTIM are assumed:

- probability of the Gaussian mutation $p_{gm} = 0.7$;
- probability of the uniform mutation $p_{um} = 0.1$;
- probability of the simple crossover $p_{sc} = 0.1$;
- probability of the arithmetic crossover $p_{ac} = 0.1$;
- number of chromosomes $n_{ch} = 70$;
- number of generations $n_g = 70$.

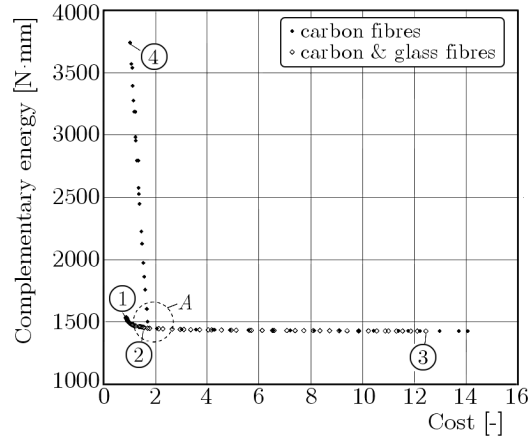


Fig. 8. Box beam – results of multiobjective optimization for case i)

Table 2. Multiobjective optimization results for the box beam

Point	Design variable		Fitness function	
	RVE length [μm]/fibre volume fraction [%]	E of the fibre [GPa]	Structure unit cost [-]	Complementary energy [Nm]
1	20/45	70	0.848	1541.43
2	20/45	204.6	1.754	1454.38
3	20/45	400	12.429	1431.94
4	58.0764/5.24	70	0.941	3736.95

The multiobjective optimization results for case ii) (the choice of the material from the database) compared to the results obtained for case i) (carbon and glass fibres, polynomial approximation, also shown in Fig. 8), are presented in Fig. 9.

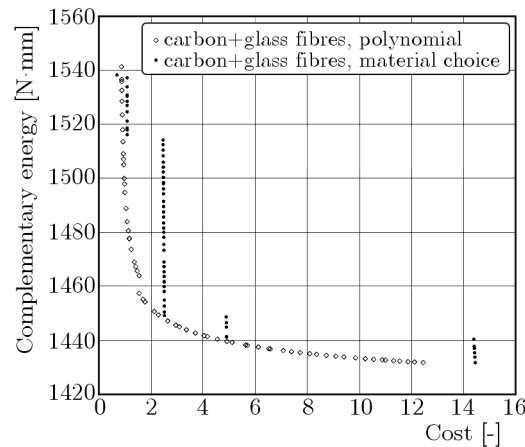


Fig. 9. Box beam – results of multiobjective optimization for cases i) and ii)

The information obtained from the results for the approximated cost values may be used to search for or for designing materials the cost of which is a function of selected parameters. The multiobjective optimization in the case where materials are chosen from the database of the available materials is more practical, but typically gives worse optimization results due to narrower search space.

6. Final conclusions

The multiscale and multiobjective optimization of heterogeneous structures has been performed. Periodic fibre-reinforced composite structures have been examined. The RVE concept has been employed to perform numerical homogenization. FEM calculations have been performed to solve boundary-value problems in both scales. Two contradictory optimization criteria have been considered to obtain the optimal behaviour of the macrostructure modifying the volume fraction of the fibre and the fibre material in the micro scale. An in-house multiobjective evolutionary algorithm MOOPTIM has been applied to solve the multiobjective optimization problems.

The proposed approach enables designing of composite microstructure based on the criteria defined in the macro scale. The paper presents an example with a unchangeable (circular) shape of the reinforcement. In that case, the optimization was to determine the reinforcement material and its volume fraction in the RVE.

The optimization results have been presented in form of Pareto frontiers of non-dominated solutions and in graphical form of optimal microstructures for selected non-dominated solutions. Graphical presentation of the non-dominated solutions also carries information about the nature of the conflict between the criteria. For instance, the frontier presented in Fig. 8 for variant i) (carbon fibres) has two distinct areas merging at an approximately straight angle, while the front for variant ii) (carbon and glass fibres) does not have clearly demarcated sub-areas. These places at the Pareto front, where a small change in the value of one of the objective function results in a large change in the value of other objective functions (area *A* in Fig. 8) require particular attention in the design process.

The application of the MOOPTIM algorithm to the considered multiobjective problems proves that the proposed algorithm is useful. The defining and using of the optimization criteria other than those presented in this paper do not pose problems in the proposed approach.

References

1. BELUCH W., BURCZYŃSKI T., 2014, Two-scale identification of composites' material constants by means of computational intelligence methods, *Archives of Civil and Mechanical Engineering*, **14**, 4, 636-646
2. BELUCH W., BURCZYŃSKI T., DŁUGOSZ A., 2008, Evolutionary multi-objective optimization of laminates, [In:] *Evolutionary Computation and Global Optimization*, J. Arabas (Edit.), Warsaw University of Technology Publishing House, Scientific Papers, Electronics 165, 43-50
3. BENSOUSSAN A., LIONIS J.L., PAPANICOLAOU G., 1978, *Asymptotic Analysis for Periodic Structures*, North-Holland, Amsterdam
4. BRANKE J., DEB K., 2004, Integrating user preferences into evolutionary multi-objective optimization, [In:] *Knowledge Incorporation in Evolutionary Computation*, Y. Jin (Edit.), Springer, 461-477
5. BREBBIA C.A., DOMINIGUEZ J., 1989, *Boundary Elements an Introductory Course*, Computational Mechanics Publications, Southampton Boston
6. BURYACHENKO V., 2007, *Micromechanics of Heterogeneous Materials*, Springer, New York
7. BURCZYŃSKI T., 1995, *Boundary Element Method in Mechanics* (in Polish), WNT, Warsaw
8. BURCZYŃSKI T., MROZEK A., KUŚ W., 2007, A computational continuum-discrete model of materials, *Bulletin of the Polish Academy of Sciences – Technical Sciences*, **55**, 1, 85-89
9. COLLETTE Y., SIARRY P., 2003, *Multiobjective Optimization: Principles and Case Studies*, Springer

10. DE CASTRO L.N., TIMMIS J., 2002, *Artificial Immune Systems: a New Computational Intelligence Approach*, Springer
11. DEB K., 1999, Multi-objective genetic algorithms: problem difficulties and construction of test problems, *Evolutionary Computation*, **7**, 3, 205-230
12. DEB K., 2001, *Multi-Objective Optimization Using Evolutionary Algorithms*, Wiley
13. DEB K., PRATAP A., AGARWAL S., MEYARIVAN T., 2002, A fast and elitist multi-objective genetic algorithm: NSGA-II, *IEEE Transactions on Evolutionary Computation*, **6**, 2, 181-197
14. DŁUGOSZ A., 2010, Multiobjective evolutionary optimization of MEMS structure, *Computer Assisted Mechanics and Engineering Sciences*, **17**, 1, 41-50
15. DŁUGOSZ A., 2013, *Multicriteria Optimization in Coupled Field Problems* (in Polish), Monography (497), Silesian University of Technology Publishing House
16. DŁUGOSZ A., 2014, Optimization in multiscale thermoelastic problems, *Computer Methods in Materials Science*, **14**, 1, 86-93
17. EHRGOTT M., 2005, *Multicriteria Optimization*, Springer
18. ESHELBY J.D., 1957, The determination of the field of an ellipsoidal inclusion and related problems, *Proceedings of the Royal Society of London*, **241**, 376-396
19. GIBSON R. F., 2012, *Principles of Composite Material Mechanics*, CRC Press
20. HASHIN Z., 1964, Theory of mechanical behavior of heterogeneous media, *Applied Mechanics Reviews*, **17**, 1-9
21. HILL R., 1963, Elastic properties of reinforced solids: Some theoretical principles, *Journal of the Mechanics and Physics of Solids*, **11**, 357-372
22. ILIC S., HACKL K., 2009, Application of the multiscale FEM to the modeling of nonlinear multi-phase materials, *Journal of Theoretical and Applied Mechanics*, **47**, 3, 537-551
23. KENNEDY J., EBERHART R., 2001, *Swarm Intelligence*, Morgan Kaufmann, San Francisco
24. KOUZNETSOVA V., 2002, Computational homogenization for the multi-scale analysis of multi-phase materials, Ph.D. thesis, Technische Universiteit Eindhoven
25. KRÖNER E., 1972, *Statistical Continuum Mechanics*, Springer, Berlin
26. KUCZMA M., 2014, Two-scale numerical homogenization of the constitutive parameters of reactive powder concrete, *International Journal for Multiscale Computational Engineering*, **2**, 5, 361-374
27. LAUMANN M., ZITZLER E., BLEULER S., 2004, A tutorial on evolutionary multiobjective optimization, Metaheuristics for multiobjective optimisation, [In:] *Lecture Notes in Economics and Mathematical Systems*, X. Gandibleux, M. Sevaux, K. Sorensen, V. T'kindt (Edit.), Springer, 3-37
28. LUQUE M., RUIZ F., MIETTINEN K., 2011, Global formulation for interactive multiobjective optimization, *OR Spectrum*, **33**, 1, 27-48
29. MADI K., FOREST S., JEULIN D., BOUSSUGE M., 2006, *Estimating RVE Sizes for 2D/3D Visco-plastic Composite Materials*, HAL – CCSD
30. MICHAŁEWICZ Z., FOGEL D., 2004, *How to Solve It: Modern Heuristics*, Springer Science & Business Media
31. NEMAT-NASSER S., HORI M., 1993, *Micromechanics: Overall Properties of Heterogeneous Materials*, Elsevier, Amsterdam
32. PHELPS J.S., KOKSALAN M., 2003, An interactive evolutionary metaheuristic for multiobjective combinatorial optimization., *Management Science*, **49**, 12, 1726-1738
33. PTASZNY J., FEDELIŃSKI P., 2011, Numerical homogenization by using the fast multipole boundary element method, *Archives of Civil and Mechanical Engineering*, **11**, 1, 181-193

34. TAKANO N., ZAKO M., 2000, Integrated design of graded microstructures of heterogeneous materials, *Archive of Applied Mechanics*, **70**, 8/9, 585-596
35. VERNEREY F.J., KABIRI M., 2014, Adaptive concurrent multiscale model for fracture and crack propagation in heterogeneous media, *Computer Methods in Applied Mechanics and Engineering*, **276**, 566-588
36. ZHOUA A., QU B., LI H., ZHAO S., SUGANTHAN P., ZHANG Q., 2011, Multiobjective evolutionary algorithms: a survey of the state of the art, *Swarm and Evolutionary Computation*, **1**, 32-49
37. ZIENKIEWICZ O.C., TAYLOR R.L., 2000, *The Finite Element Method*, vol. 1-3, Butterworth, Oxford
38. ZITZLER E., THIELE L., 1999, Multiobjective evolutionary algorithms: a comparative case study and the strength Pareto approach, *IEEE Transactions on Evolutionary Computation*, **3**, 4, 257-271
39. ZOHDI T.I., WRIGGERS P., 2005, An introduction to computational micromechanics, *Lecture Notes in Applied and Computational Mechanics*, Springer-Verlag

Manuscript received May 7, 2015; accepted for print August 6, 2015

A PRELIMINARY STUDY ON THE OPTIMAL CHOICE OF AN IMPLANT AND ITS ORIENTATION IN VENTRAL HERNIA REPAIR

IZABELA LUBOWIECKA, KATARZYNA SZEPIETOWSKA

Gdansk University of Technology, Faculty of Civil and Environmental Engineering, Gdańsk, Poland
e-mail: lubow@pg.gda.pl; katszepi@pg.gda.pl

CZESŁAW SZYMCZAK

Gdansk University of Technology, Faculty of Ocean Engineering and Ship Technology, Gdańsk, Poland
e-mail: szymcze@pg.gda.pl

AGNIESZKA TOMASZEWSKA

Gdansk University of Technology, Faculty of Civil and Environmental Engineering, Gdańsk, Poland
e-mail: atomas@pg.gda.pl

This paper addresses the problem of ventral hernia repair. The main goals are to find an optimal surgical mesh for hernia repair and to define its optimal orientation in the abdominal wall to minimise the maximum force at the tissue-implant juncture. The optimal mesh is chosen from a set of orthotropic meshes with different stiffness ratios for typical hernia placement in the abdominal area. The implant is subjected to an anisotropic displacement field, different for the selected hernia placements. The assumed displacement fields correspond to regular human activity. Proper implantation of the mesh may determine the success of hernia repair and/or the postoperative comfort of patients. The proposed solution is based on FEM simulations of different surgical meshes behaviour. In typical hernia placements, the optimal orientation of the stiffer direction of the implant is perpendicular to the spine. However, the presented results show some cases that an oblique direction may be the optimum one.

Keywords: biomechanics, surgical mesh, finite element modelling, optimisation

1. Introduction

Ventral hernia is a common medical problem researched by surgeons and engineers for many years, but question about the main factors influencing hernia repair efficiency still remains open (Muysoms *et al.*, 2013). This problem refers to primary hernias as well as to incisional ones. It is estimated that there is a 12% chance of incisional ventral hernia occurrence after abdominal surgery and a 3.2% chance after laparoscopic operation (Bensley *et al.*, 2013). Laparoscopic ventral hernia repair is believed to be superior to an open operation (Qadri *et al.*, 2010), however the best treating scheme is not specified for the time being, and such problems as recurrences or chronic pain happen (Sommer and Friis-Andersen, 2013). It is believed that the success of ventral hernia repair depends mainly on selection of an appropriate implant and its fixation (Muysoms *et al.*, 2013). In the authors' opinion, mathematical modelling and simulations can provide information about the best course of the treatment, and then, a combination of medical and mechanical knowledge may lead to an increase in hernia treatment efficiency.

This paper refers to laparoscopic repairs. The principle that the properties of surgical meshes should match the properties of the abdominal wall and that implants should be oriented in the human body in accordance with the mechanics of the abdominal wall has been reported in the literature since 2001 (Junge *et al.*, 2001). This issue was discussed e.g., by Kirilova *et al.* (2012), Hernández-Gascón *et al.* (2013), Anurov *et al.* (2012). All these studies are limited to just one

position of hernia orifice and two perpendicular orientations of implants. As the abdominal wall is subjected to various strains during human activity, both in magnitudes and in orientations in different locations (Szymczak *et al.*, 2012), it is reasonable to find the best orientation of the implant for different hernia locations in the abdominal wall. This problem was already addressed in (Lubowiecka *et al.*, 2014).

The main goal of this study is to investigate the influence of implants orientation on forces in fasteners. The value of this force determines the success of hernia repair since its increase can lead to the junction failure which is a common cause of the illness recurrence. The maximum force on a fastener affixing an implant should be smaller than the allowable tearing force for a selected tack (Tomaszewska *et al.*, 2013). The proposed solutions are derived from structural mechanics and optimisation methodology. In order to analyse the behaviour of the surgical mesh, a mathematical model of the tissue-implant system, which is created during laparoscopic hernia operation, is applied. The modelling of implant-tissue systems began with the cable model (Szymczak *et al.*, 2010). Next, two-dimensional finite element (FE) membrane models with various boundary conditions were defined (Lubowiecka *et al.*, 2010; Lubowiecka, 2015; Tomaszewska *et al.*, 2013). An FE model of the implant-hernia system was also proposed by Guérin and Turquier (2013) and Hernández-Gascón *et al.* (2013). Some mechanical properties of surgical meshes were recognized for their application in different material models including an orthotropic linear or bilinear elastic material model (Lubowiecka *et al.*, 2014) or a dense net material model (Lubowiecka, 2015), a hyperelastic constitutive model (Hernández-Gascón *et al.*, 2013) and a beam model reflecting the implant material structure (Hernández-Gascón *et al.*, 2012).

The novel approach presented in this paper is formulating and solving the optimisation problem, which results in the selection of the optimal orthotropic implant and its best orientation in the anisotropic abdominal wall. We consider five possible hernia placements, where implants are imposed to different fields of displacements caused by deformation of abdominal wall during daily activities. The optimisation criterion is minimising the maximum forces on tissue-implant junctures resulting from the patient's body movements.

2. Materials and methods

2.1. Formulation of the optimisation problem

The force acting on a single fastener of a given type of mesh implant depends on the implant mechanical properties, its orientation relative to the direction of the spine, and the layout of the fasteners. In this model, a circular layout of point fasteners is assumed. To find the optimal orientation for an implant, the minimisation of the force $F(i, \alpha, s)$ is defined as an objective function

$$\min_{i \in I} \max_{0 \leq \alpha \leq 2\pi, s \in S} F(i, \alpha, s) \quad (2.1)$$

where i denotes the number of fasteners indicating their position, I stands for the fastener set, α is the angle between the implant primary axis and the spine, and s indicates the implant number from the set of implants S considered.

A three-stage process of minimising objective function (2.1) is proposed herein. During the first stage, the maximum force $F_{max}(i, \alpha, s)$ in the fastener is sought for a chosen implant s and the implant angle of orientation as a solution of the sub-problem (according to Eq. (2.2)). The outcome of this step is the number i_0 that indicates the fastener at which F_{max} occurs

$$\max_{i \in I} F(i, \alpha, s) \quad (2.2)$$

In the second stage, the angle specifying the implant orientation in relation to the spine is sought. The problem is formulated as a minimisation of the maximum force obtained in the first stage with respect to the angle α

$$\min_{0 \leq \alpha \leq 2\pi} F_{max}(i_0, \alpha, s) \quad (2.3)$$

The minimisation procedure is conducted in a discrete manner; the implant orientation angle α changes by the assumed increment $\Delta\alpha$. Thus the orientation angle of the implant α_0 for which the minimal force in tack i_0 (selected in the first step), is identified.

In the last stage, steps one and two are repeated for each implant s from the considered set of implants S

$$\min_{s \in S} F_{max}(i_0, \alpha_0, s) \quad (2.4)$$

Finally, the implant s_0 , its orientation α_0 and the corresponding fastener number i_0 are determined to solve the objective function. This finalises the optimisation procedure.

2.2. Modelling and simulation of the implanted surgical mesh

Four popular synthetic implants used in ventral hernia repair are considered in this study, ProceedTM Surgical Mesh (Ethicon Endo-Surgery, Inc., USA), ParietexTM Composite (Covidien, USA), DynaMesh[®]-IPOM (FEG Textiltechnik mbH, Germany) and Gore[®] Dualmesh[®] Biomaterial (W.L. Gore & Associates, Inc., USA). They are knitted structures made of polypropylene and cellulose, polyester, polypropylene and polyvinylidene fluoride treads, respectively. The latter material is in form of a smooth membrane made of expanded polytetrafluoroethylene. A suggestion concerning proper orientation of the implant in the abdominal wall can be found only in specification of DynaMesh[®]. The manufacturer recommends a craniocaudal orientation of the mesh, but does not distinguish different hernia locations. The analysis refers to practical cases concerning the first few weeks following the operation, when the implant is not yet encapsulated by a fibrous capsule and when most hernia recurrences occur. The correct mesh orientation decreases the risk of possible postoperative fixation failure even when the mechanical properties of the implant are changed due to tissue overgrowth (Oettinger *et al.*, 2013).

Hernia with an orifice diameter of 5 cm is considered in this study. A standard clinical case is taken into account, in which the implant is affixed to the tissue with point fasteners in a circular order. The least favourable situation is applied with 4 cm spacing between fasteners. The circle of joints has a diameter of 13 cm, and then a radial distance of 4 cm between the hernia orifice edge and joints is preserved according to medical standards. There are 10 fasteners in such a layout.

The mesh is modelled with a polygonal membrane structure (Fig. 1a), supported in 10 points. The numerical model of the implant is defined within the Finite Element Method using the MSC.Marc[®] commercial system. Eight-node membrane elements QUAD(8) with 3 translational degrees of freedom at each node are used. The model is discretised by 960 finite elements with mesh refinement around the tissue-implant joints (Fig. 1b).

The model is subjected to kinematic extortions related to displacements of the abdominal wall when the patient moves. The range of extortions can be derived from a map of possible strains of the external layer of the abdominal wall, which was discussed by Szymczak *et al.* (2012). A summary of those results is presented in Fig. 2a. However, the strains on the internal surface of the abdominal wall are 2.6-fold smaller than on the external surface (Podwojewski *et al.*, 2013). Thus the reduction factor of 2.6 is applied to the results described by Szymczak *et al.* (2012). The values and directions of maximal strains of the abdominal wall are different in its various regions, so the implant is subjected to various extortions when placed in different parts

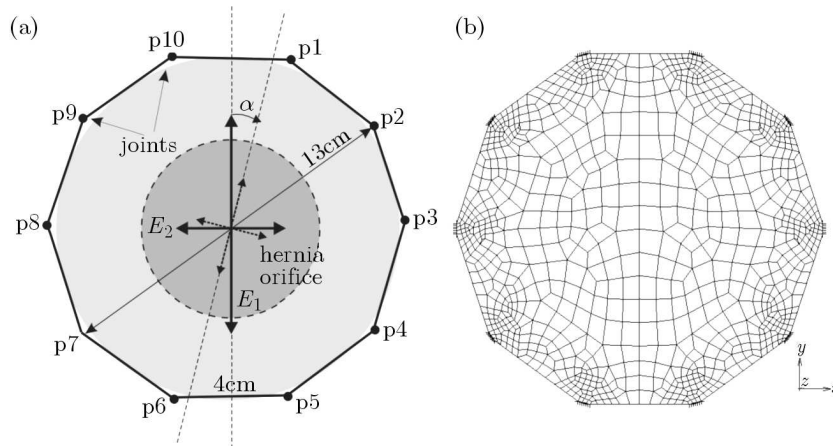


Fig. 1. (a) Scheme model of the implanted surgical mesh; b) Finite Element mesh

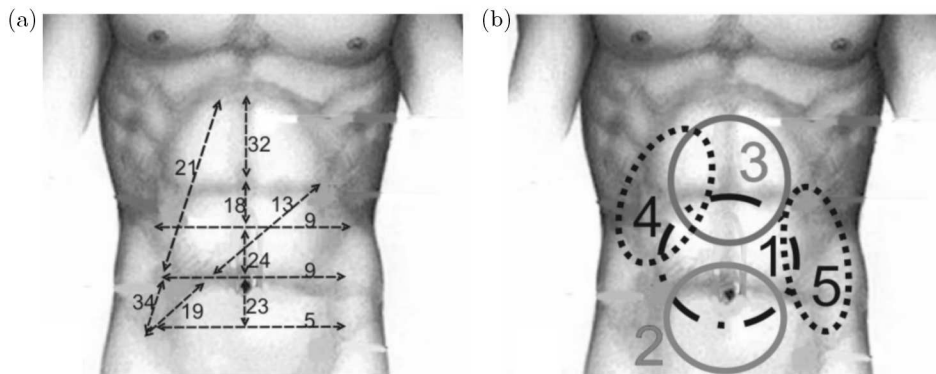


Fig. 2. (a) Directions and values (in %) of strains on the external abdominal surface in different sections, according to Szymczak *et al.* (2012); (b) considered hernia cases

Table 1. Reduced abdominal strains in the radial direction at the fastener imposed in the model supports [%]

[%]	p1	p2	p3	p4	p5	p6	p7	p8	p9	p10
Case 1	9	3	3	6	7	7	6	3	3	9
Case 2	9	3	2	6	7	7	6	2	3	9
Case 3	12	4	3	7	9	9	7	3	4	12
Case 4	9	6	3	5	13	13	5	3	0	0
Case 5	9	5	3	7	13	13	7	3	5	9

of the abdomen. Thus, five hernia locations are considered as marked in Fig. 2b. For each case, the extortions are estimated basing on the abdominal strains presented in Fig. 2a, scaled by a factor of 2.6 and they are applied to the supporting points of the model (p1 to p10, see Fig. 1a). The final values of the extortions applied to each supporting point are included in Table 1.

Mechanical properties of the meshes selected for the analysis differ significantly. Orthotropic or isotropic, linear or bilinear elastic constitutive models have been identified for them, basing on Biot stress and Biot strain experimentally measured in one-dimensional tensile tests. The experiments are presented in (Tomaszewska *et al.*, 2013). As one can notice, basing on the data summarised in Table 1, in each hernia case the meshes are subjected to strains smaller than 0.3. Thus, constitutive models of the meshes have been specified for the strain range 0-0.3. The least squares method applied in the Marquardt-Levenberg algorithm is used for parameters

identification. Finally, the obtained parameters of the constitutive models applied for each kind of the implant are presented in Table 2. It has been observed that Dualmesh[®] is a nearly isotropic material. The rest of the meshes considered here is distinctly orthotropic, but with different orthotropy ratios calculated as E_1/E_2 . E_1 and E_2 are the elastic moduli of the implants derived for two perpendicular directions wherein $E_1 > E_2$. The directions of orthotropy, indicated by E_1 and E_2 , for the considered meshes are marked in Fig. 3.

Table 2. Parameters of linear or bilinear elastic orthotropic material models of the implants for the strain range 0-0.3

Mesh	\mathcal{A}	Limit stress [N/mm]	E [N/mm]		E_1/E_2		ε_l [-]	Poisson's ratio ν_{21} [-]
			for $\varepsilon < \varepsilon_l$	for $\varepsilon > \varepsilon_l$	for $\varepsilon < \varepsilon_l$	for $\varepsilon > \varepsilon_l$		
Dualmesh	(2.1)	8.4	28		1.1		N/A	0.3
	(2.2)	6.1	26					
DynaMesh	(2.1)	4.5	6.4	14	18	39	0.15	0.3
	(2.2)	1.7	0.36				N/A	
Parietex	(2.1)	3.7	1.6	21	1.8	10	0.15	0.3
	(2.2)	2.0	0.87	2.1				
Proceed	(2.1)	4.2	40		5.3		N/A	0.3
	(2.2)	4.1	7.6					

\mathcal{A} – Direction of bigger (2.1) or smaller (2.2) stiffness of the mesh

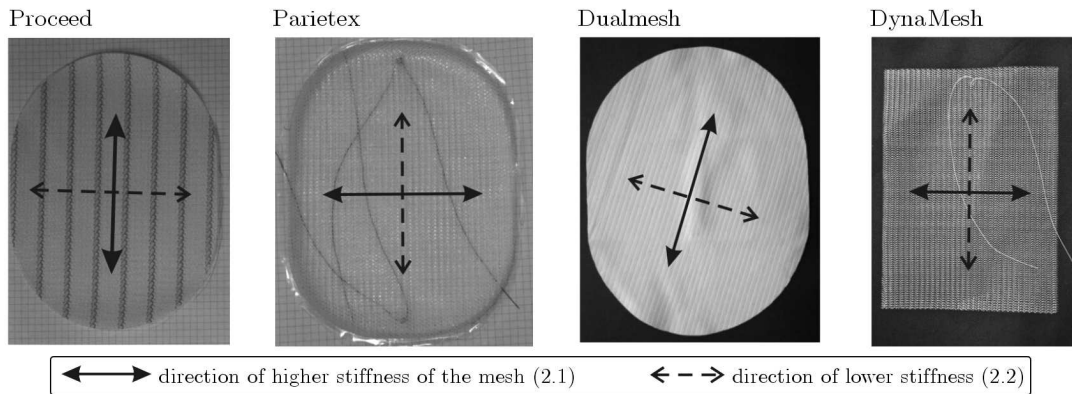


Fig. 3. Directions of the higher and lower stiffness of the considered meshes

The accuracy of the implant model with a proposed polygonal shape has been successfully verified against experiments on a physical model of the system subjected to impact loads resulting from postoperative cough (Lubowiecka, 2015). The h -convergence analysis has been performed within simulations.

According to the optimisation procedure described in Section 2.1, for each implant placed in each hernia case, the reaction forces in the supporting points are calculated (stage 1). Nonlinear static analysis in the range of large strains is performed. Twelve orientations of each implant in each simulated hernia location are considered ($\alpha = 0-180$ degrees with 15 degree intervals). The angle $\alpha = 0$ stands for the craniocaudal orientation of E_1 direction of the considered implant as marked in Fig. 1a.

The influence of the implant orientation on reaction forces is expressed by the value of the coefficient $D = (F_{max} - F_{min})/F_m \cdot 100\%$, where F_{max} is the maximum reaction obtained for the orientation α_{max} , F_{min} is the maximum reaction obtained for the orientation α_0 (stage 2 of the optimisation). The smallest maximum reaction occurs for the optimal orientation α_0 of the

implant and α_{max} is the orientation corresponding to the largest maximum reaction that occurs in the supporting points of the mesh. α_{max} is the least appropriate orientation. The larger the value of the D coefficient, the greater is the effect of the implant orientation on the reaction force. In the final step of the optimisation problem, the optimal solution described by the implant type along with its optimal orientation is found (implant type along with its optimal orientation).

3. Results

The calculated values of the angles α_0 and α_{max} along with D coefficients are presented in Table 3. For almost isotropic Dualmesh[®], D value does not exceed 5% in any area, but for other meshes it is visibly higher. The largest values of D are obtained for DynaMesh[®] (36%-55%) and for Proceed[™] (35%-53%). D value of Parietex[™] is in the range of 26%-34%.

Table 3. The best and the worst orientations of implants

Case	DynaMesh			Parietex			Proceed			Dualmesh		
	α_{max} [deg]	α_0 [deg]	D [%]									
1	15	75	36	15	90	28	30	90	36	15	75	4
2	15	75	42	15	90	26	30	90	35	15	75	5
3	15	75	47	30	90	29	15	90	47	15	90	4
4	165	75	55	90	60	34	0	75	53	165	75	3
5	15	90	48	15	90	33	15	90	50	15	90	4

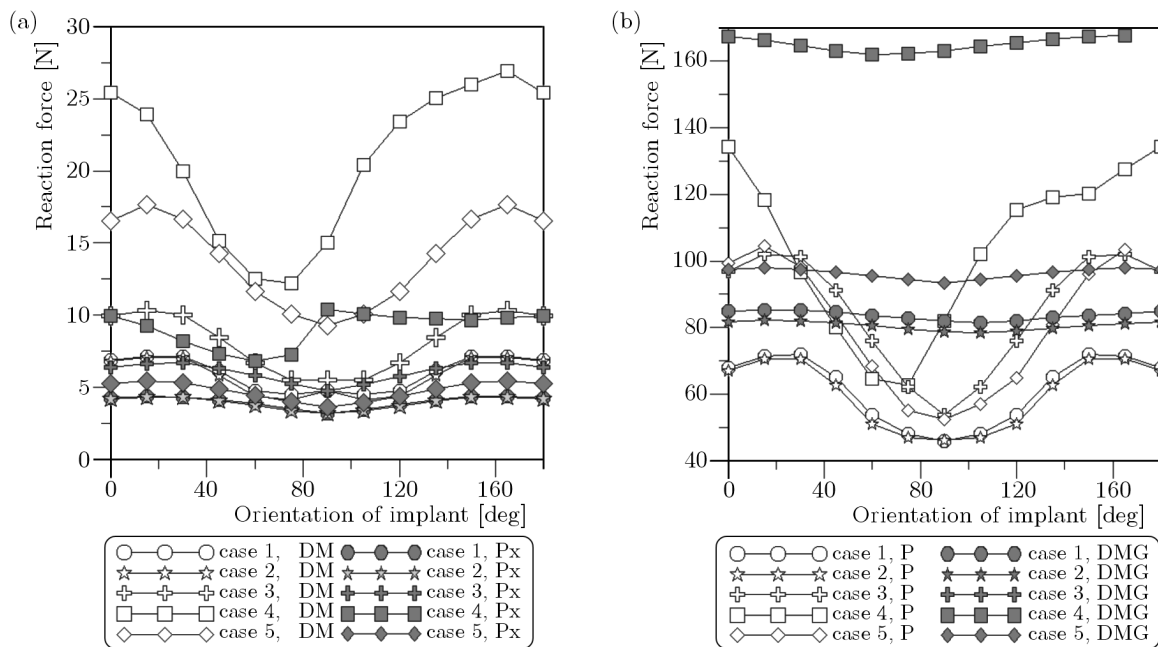


Fig. 4. Maximum reactions F_{max} in meshes depending on the orientation angle α for the following implants: DynaMesh (DM), Parietex (Px), Proceed (P) and Dualmesh (DMG)

The values of all maximum reaction forces obtained in this study are presented in Fig. 4. The distribution of all reactions in the worst and best orientation case is shown in Fig. 5. Finally, the identified optimal orientations of three considered anisotropic implants for each hernia location considered here are shown in Fig. 6. Dualmesh[®] is the only mesh investigated in this study that

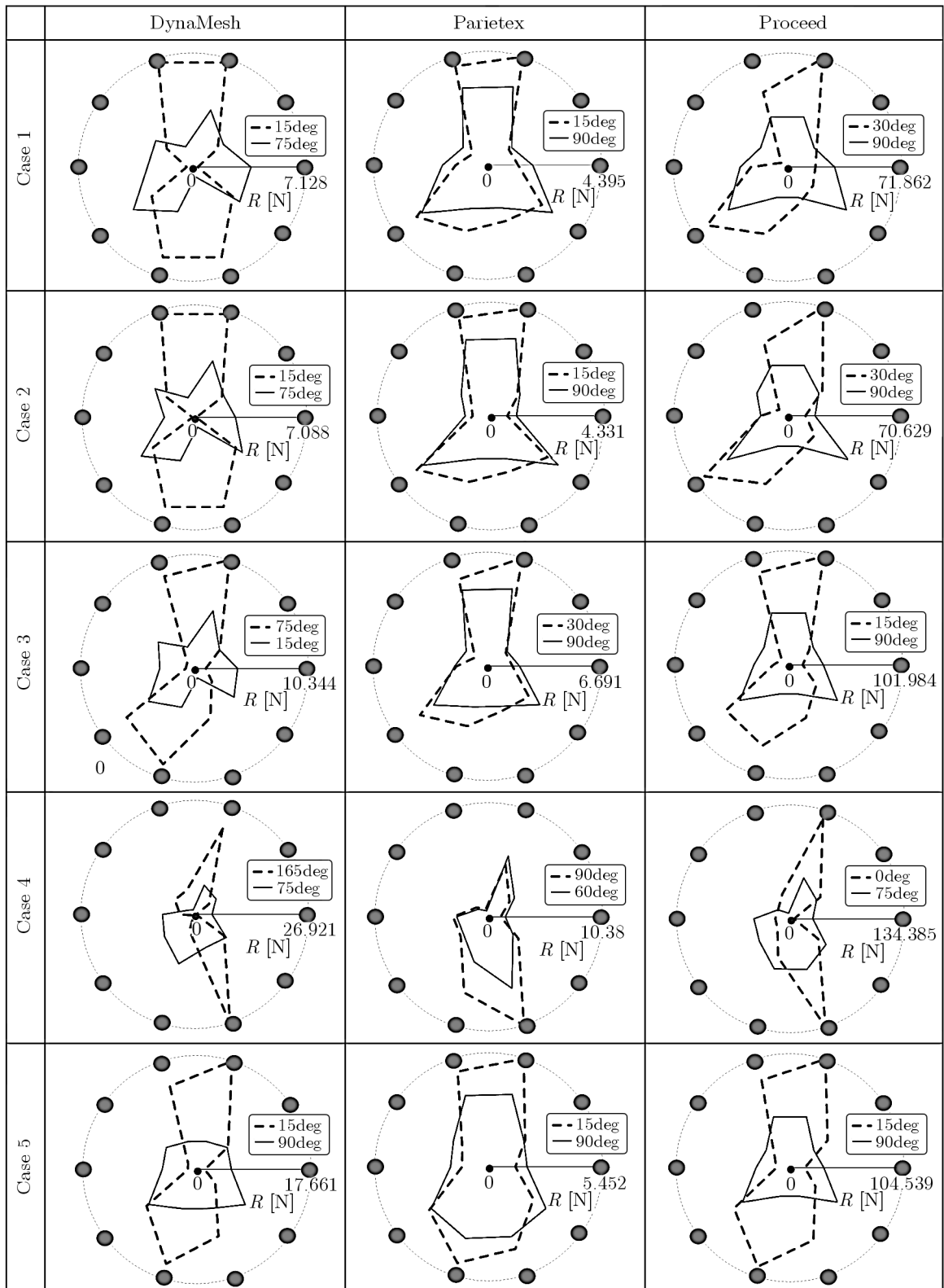


Fig. 5. Reactions F obtained in each support for all investigated orientations of the implant, the solid line is for the best orientation, the dashed line is for the worst orientation of the mesh

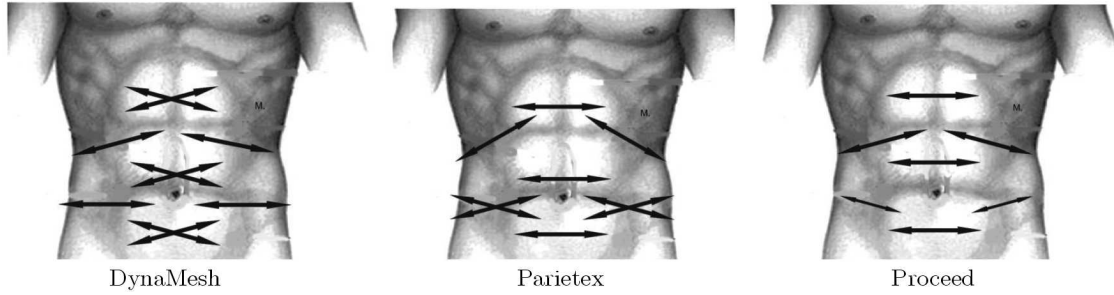


Fig. 6. Optimal orientation angles α_0 (orientation of the direction of E_1)

does not have distinct anisotropic properties. A single optimal orientation does not exist in such a case, any orientation is acceptable.

4. Discussion

Figures 4-6 describe the effects of the implant material orientation on the reaction forces that occur at the supporting points in the tissue-implant interface. These forces cannot exceed the capacity of the tissue-implant juncture, otherwise the junction damage and recurrence of the sickness occurs. The larger the range of junction forces between the most and least appropriate orientations of the implant, the greater is the influence of the implant orientation on the forces in the supporting tacks. This range is measured by D coefficient presented in Table 3. D values of Dualmesh[®] are relatively small (3%-5%), so any orientation of this mesh can be applied in practice. The largest D values are obtained for DynaMesh[®] (33%-55%) and for Proceed[™] (36%-53%), which means that surgeons should pay special attention to the proper orientations of those implants. Values of D for Parietex[™] are in the range of 28%-34%. Those results relate to the orthotropy ratio of each mesh (Table 2). The largest forces for each implant can be found in zone 4 (see Fig. 4). Also the influence of orientation (represented by D value) is the highest in that zone. The results presented in Fig. 4 prove that the lowest maximal reactions are observed for Parietex[™] in each hernia case.

Variability of reaction forces in all fixation points for certain mesh orientations is shown in Fig. 5. These results prove that in the optimal orientation, the reactions are relatively low and they are the most evenly distributed on the supporting points comparing to other orientations. It is visible that in the case of Parietex, which initially has a small orthotropy ratio, the change of orientation from the worst to the optimal one causes reduction of the reaction forces but does not change significantly the shape of the reaction distribution graph. Whereas for strongly orthotropic meshes, like DynaMesh[®] and Proceed[™] in their optimal orientations, the distribution of forces is more even. Such even force distribution justifies regularly spaced fixing joints. For an orientation different than the optimal, more joints (or stronger ones) should be used in places where larger reaction forces occur than in places with smaller reaction forces.

In the majority of cases considered in this study, the optimal orientation of the stiffer direction of an implant is the transverse direction (90 deg) of the abdominal wall (Table 3 and Fig. 6). This observation corresponds to the results obtained experimentally by Anurov *et al.* (2012) and numerically by Hernández-Gascón *et al.* (2013), who investigated only two orientations of a surgical mesh in the central area of the abdominal wall. However, also a frequent solution of our optimisation scheme is 75 deg especially for hernia located in zone 4. In this case when operating with Parietex[™], the optimal orientation of its stiffer direction is 60 deg.

The study emphasises the importance of the proper orientation of surgical mesh when imposed to kinematic extortions related to abdominal wall movements. Thus we do not include constrains on the implant deflection related to bulging in the optimisation procedure. Bulging

is related to intraabdominal pressure load and does not take place when the implant undergoes only kinematic extortions. However, in a more general procedure of finding an optimal implant, additional constraints upon the maximum displacements could be included to avoid excessive bulging of the implant.

5. Conclusions

This paper presents an investigation on the influence of orthotropic implant orientation on forces on tissue-implant junctures caused by deformation of the anisotropic abdominal wall. Moreover, it gives a study on the optimal choice of surgical orthotropic meshes and their orientation in ventral hernia repair. Surgeons may consider these results when choosing an implant and when determining its position in different areas of the abdominal wall, particularly when no manufacturer's recommendation exists. The most important findings are presented below.

- The implant ParietexTM best minimises reaction forces. Hence, according to our optimisation procedure, application of this mesh gives the optimal solution. However DynaMesh[®] has a better orthotropy ratio giving more even distribution of forces on all supporting points.
- For optimal orientations of implants in the abdominal wall, forces acting on different supporting points have the most similar values. Then, a regular distribution of supporting points is the most justified. When the implant orientation is far from the optimal one, then the reaction forces are very different in various fixation points, and there is no mechanical justification for the regular joint distribution around the hernia orifice, and some fixation regions should be strengthened.
- In zone 4, in the upper lateral part of the abdominal wall, the supporting points face the largest forces (see Fig. 4) and the implant orientation has the greatest influence on those forces.
- The orientation of orthotropic implants (DynaMesh[®], ParietexTM and ProceedTM) strongly influences the forces on the supporting points (up to 55%, 34% and 53%, respectively).
- Placing the implant in the optimal orientation, as shown in Fig. 6, greatly reduces the forces on the supporting points, which may determine the success of hernia repair or postoperative comfort of patients. Although significant influence of the orientation of an orthotropic implant in the anisotropic abdominal wall on hernia repair persistence seems to be expected from the mechanical point of view, this fact is still underestimated in surgical practice as confirmed by the newest medical conference reports and scientific papers, see e.g., Oettinger *et al.* (2013), Li *et al.* (2014).
- Our results show not only an optimal mesh placement but also results for other orientations (Fig. 4). On the basis of that, safer and less safe range of orientations can be established. Information about this range can be useful in clinical practice. Surgeons should pay attention to the orientation of the implant, which currently is not a common practice, and try to avoid orientations which may highly increase reactions in fasteners and, in consequence, increase the risk of exceeding the capacity of tack and cause hernia relapse.
- Displacement of the fasteners during regular activity influences the level of junction forces. As a result, the displacement of fasteners should be considered when analysing and designing the fixation of implants. These results may serve as a basis for the formulation of a relationship between the optimisation of mesh implantation and the recurrence rate of hernias as well as they can be applied in the process of individualisation of the treatment of abdominal hernias.

Acknowledgments

This study has been partially supported by the EU as a part of the Innovative Economy Operational Programme (contract No. UDAPOIG.01.03.01-22-086/08-00) and by the subsidy for the development of young scientists given by the Faculty of Civil and Environmental Engineering, Gdansk University of Technology. The computations have been done in TASK Computer Science Centre, Gdańsk, Poland.

References

1. ANUROV M.V., TITKOVA S.M., OETTINGER, A.P., 2012, Biomechanical compatibility of surgical mesh and fascia being reinforced: dependence of experimental hernia defect repair results on anisotropic surgical mesh positioning, *Hernia*, **16**, 2, 199-210
2. BENSLEY R.P., SCHERMERHORN M.L., HURKS R., SACHS T., BOYD C.A., O'MALLEY A.J., COTTERILL P., LANDON B.E., 2013, Risk of late-onset adhesions and incisional hernia repairs after surgery, *Journal of the American College of Surgeons*, **216**, 6, 1159-1167
3. GUÉRIN G., TURQUIER F., 2013, Impact of the defect size, the mesh overlap and the fixation depth on ventral hernia repairs: a combined experimental and numerical approach, *Hernia*, **17**, 5, 647-655
4. HERNÁNDEZ-GASCÓN B., ESPÉS N., PEÑA E., PASCUAL G., BELLÓN J.M., CALVO B., 2012, Computational framework to model and design surgical meshes for hernia repair, *Computer Methods in Biomechanics and Biomedical Engineering*, 1-15, doi:10.1080/10255842.2012.736967
5. HERNÁNDEZ-GASCÓN B., PEÑA E., GRASA J., PASCUAL G., BELLÓN J.M., CALVO B., 2013, Mechanical response of the herniated human abdomen to the placement of different prostheses, *Journal of Biomechanical Engineering*, **135**, 5, p. 051004
6. JUNGE K., KLINGE U., PRESCHER A., GIBONI P., NIEWIERA M., SCHUMPELICK V., 2001, Elasticity of the anterior abdominal wall and impact for reparation of incisional hernias using mesh implants, *Hernia*, **5**, 3, 113-118
7. KIRILOVA M., PASHKOULEVA D., KAVARDZHNIKOV V., 2012, A selection of hernia meshes on the basis of experimental results for abdominal layers, *Biotechnology and Biotechnological Equipment*, **26**, 5, 3292-3295
8. LI X., KRUGER J.A., JOR J.W.Y., WONG V., DIETZ H.P., NASH M.P., NIELSEN P.M.F., 2014, Characterizing the ex vivo mechanical properties of synthetic polypropylene surgical mesh, *Journal of the Mechanical Behavior of Biomedical Materials*, **37**, 48-55
9. LUBOWIECKA I., 2015, Mathematical modelling of implant in an operated hernia for estimation of the repair persistence, *Computer Methods in Biomechanics and Biomedical Engineering*, **18**, 4, 438-445
10. LUBOWIECKA I., SZEPIETOWSKA K., TOMASZEWSKA A., SZYMCZAK C., 2014, Mechanical compatibility of implants used in hernia repair with abdominal wall, [In:] *Shell Structures. Theory and Applications*, Vol. 3., W. Pietraszkiewicz, J. Górski (Eds.), Taylor & Francis Group, London, 351-354
11. LUBOWIECKA I., TOMASZEWSKA A., SZYMCZAK C., ŚMIETAŃSKI M., 2010, A FEM membrane model of human fascia-synthetic implant system in a case of a stiff ventral hernia orifice, [In:] *Shell Structures. Theory and Applications*, Vol. 2, W. Pietraszkiewicz, I. Kreja (Eds.), Taylor & Francis Group, London, 311-314
12. MUYSOMS F., VANDER MIJNSBRUGGE G., PLETINCKX P., BOLDO E., JACOBS I., MICHIELS M., CEULEMANS R., 2013, Randomized clinical trial of mesh fixation with “double crown” versus “sutures and tackers” in laparoscopic ventral hernia repair, *Hernia*, **17**, 5, 603-612
13. OETTINGER A.P., ANUROV M., TITKOVA S., POLIVODA M., SHAPOVALIANTS S., 2013, Comparison of biomechanical properties of light meshes with different structural characteristics, *Hernia*, **17** (supplement 2), S7

14. PODWOJEWSKI F., OTTÉNIO M., BEILLAS P., GUÉRIN G., TURQUIER F., MITTON D., 2013, Mechanical response of animal abdominal walls in vitro: evaluation of the influence of a hernia defect and a repair with a mesh implanted intraperitoneally, *Journal of Biomechanics*, **46**, 3, 561-566
15. QADRI S.J.F., KHAN M., WANI S.N., NAZIR S.S., RATHER A., 2010, Laparoscopic and open incisional hernia repair using polypropylene mesh – a comparative single centre study, *International Journal of Surgery*, **8**, 6, 479-483
16. SOMMER T., FRIIS-ANDERSEN H., 2013, DynaMesh(®) in the repair of laparoscopic ventral hernia: a prospective trial, *Hernia*, **17**, 5, 613-618
17. SZYMCZAK C., LUBOWIECKA I., TOMASZEWSKA A., SMIETAŃSKI M., 2010, Modeling of the fascia-mesh system and sensitivity analysis of a junction force after a laparoscopic ventral hernia repair, *Journal of Theoretical and Applied Mechanics*, **48**, 4, 933-950
18. SZYMCZAK C., LUBOWIECKA I., TOMASZEWSKA A., SMIETAŃSKI M., 2012, Investigation of abdomen surface deformation due to life excitation: Implications for implant selection and orientation in laparoscopic ventral hernia repair, *Clinical Biomechanics*, **27**, 2, 105-110

Manuscript received May 27, 2014; accepted for print August 10, 2015

ANALYTICAL DISCRETE STACKING SEQUENCE OPTIMIZATION OF RECTANGULAR COMPOSITE PLATES SUBJECTED TO BUCKLING AND FPF CONSTRAINTS

ALEKSANDER MUC, MAŁGORZATA CHWAŁ

Cracow University of Technology, Kraków, Poland

e-mail: olekmuc@mech.pk.edu.pl; mchwal@pk.edu.pl

A special type of new discrete design variables is introduced in order to find optimal stacking sequences for laminated structures. Using the proposed new design variables, we demonstrate how to find analytical (i.e. without any numerical optimization algorithm) optimal solutions for laminates made of plies having three different fibre orientations: 0° , $\pm 45^\circ$, 90° . It is proved that the definition of design variables enables us to distinguish two types of optimal solutions, i.e. unimodal and bimodal ones. The form of optimal stacking sequences affects the multiplicity (bimodal problems) or uniqueness (unimodal problems) of the solutions. The decoding procedure between membrane and flexural design variables is also proposed. The results demonstrate the effectiveness, simplicity and advantages of the use of design variables, especially in the sense of the accuracy, repeatability of results and convergence of the method.

Keywords: stacking sequence optimization, composite plates, buckling, first-ply-failure

1. Introduction

The superior mechanical properties of composite materials such as high stiffness, weight ratio and anisotropic properties that can be tailored through variation of fiber orientations and stacking sequence give the designer an added degree of flexibility. However, this additional tool should be used by engineers in a proper manner, i.e. it requires an application of optimization methods. For many design problems using the 2D approach (beams, plates, shells), most notably for those where stiffness requires domination, there are multiple designs with similar performance. These designs may have very different stacking sequences but very similar or almost identical values of stiffnesses \mathbf{A} and \mathbf{D} . In such cases, it is important to produce all or most of the design alternatives.

The effectiveness of optimal design, especially for composite structures, is strongly dependent on the proper choice of two elements: i) definition of design variables, ii) application of an appropriate optimization algorithm.

The simplest definition of design variables depends on direct application of real continuous variables (i.e. fibre orientations θ_l and thicknesses t_l in the l -th ply, $l = 1, 2, \dots, N$). Now, such an approach is commonly used in finite element codes, such as e.g. ANSYS, ABAQUS etc. This method is not very convenient for many engineering or analytical applications and is replaced by the introduction of so-called lamination parameters (Miki, 1986; Fukunaga and Vanderplaats, 1991). The lamination parameters are usually determined for thin walled composite structures (i.e. beams, plates or shells) with the use of the Love-Kirchhoff kinematical hypothesis. For an arbitrary laminate, the structural stiffness is characterized by 12 independent parameters instead of $2 \times N - 1$ variables for the previous real continuous variables (θ_i and t_i). In fact, analytical

studies deal mainly with the use of four of them, i.e. $\xi_{[1]}^{\{A\}}$, $\xi_{[2]}^{\{A\}}$, $\xi_{[1]}^{\{D\}}$, $\xi_{[2]}^{\{D\}}$ corresponding to laminates in which the stiffnesses B_{ij} , A_{16} , A_{26} , D_{16} and D_{26} are assumed to be equal to zero.

The past few decades have seen an increased interest in general-purpose “black-box” optimization algorithms that exploit limited knowledge concerning the optimization problem on which they are run. In particular, the two most popular black-box optimization strategies, evolutionary algorithms and simulated annealing, mimic processes in natural selection and statistical mechanics, respectively. Commonly, they are based on the standard use of the lamination parameters. In this case it is impossible to find a unique laminate configuration, and, in addition, the correctness and accuracy of solutions can be verified by the comparison with other numerical result only.

According to the definitions and classifications of IEEE NNC (1996) the four types of algorithms constitute evolutionary computation methods (Genetic Algorithms – GA, Evolutionary Programming – EP, Evolution Strategies – ES and Genetic Programming – GP) but in general they are based on the Darwinian concept of evolution. In fact, now hybrids of the four methodologies are becoming most popular. The distinguishing feature of traditional Darwinistic evolution is selection, the survival of the fittest members of each generation. For composite materials it is much better to look beyond that view in the sense of the above algorithms and to explore a new view of evolution that includes natural selection plus self-organization – see Kauffmann (1993). It is worth to emphasize that Grosset *et al.* (2006) formulated almost the same conclusions and stated that it was necessary to abandon partially the Darwinistic theory of evolution and finally introduced to the analysis of composites the concept of estimation of distribution algorithms. They used a statistical framework to formalize the search mechanisms.

However, it has become important to understand the relationship between how well an algorithm performs and the optimization problem on which it is run. In this paper, we present an analysis that contributes toward such an understanding by addressing questions like the following: how we can best match design variables and algorithms to the problems, i.e., how best we can relax the black-box nature of lamination parameters and the algorithms and have them exploit some knowledge concerning the optimization problem?

In the present paper, we intend to solve the problem of optimal design of bi-axially compressed rectangular multilayered composite plates having discrete fibre orientations in each individual ply and subjected to buckling and FPF constraints. Contrary to the identical problems discussed in the literature, we look deeper into the physical problem considered herein. We demonstrate that the appropriate definition of design variables allow us to obtain unique, exact and accurate solutions. Using the proposed new design variables we show how to find analytical (i.e. without any numerical optimization algorithm) optimal solutions for laminates made of plies having three different fibre orientations: 0° , $\pm 45^\circ$, 90° . For a higher number of different discrete fibre orientations, we propose the application of an effective numerical algorithm based on the evolution strategy, see Muc and Muc-Wierzgoń (2012). We explain also the discussed in the literature problem of multiplicity of optimal solutions. We prove that the multiplicity is an artificial result since it is caused by wrong coding of laminate configurations and wrong interpretation of optimal solutions.

The numerical results, presented in the paper, are obtained for a graphite/epoxy resin material having the following mechanical properties: $E_1 = 127.59$ GPa, $E_2 = 13.03$ GPa, $G_{12} = 6.41$ GPa, $\nu_{12} = 0.3$, and the thickness of an individual ply in the laminate is equal to 1.27 mm. The ultimate allowable strains are following: $\varepsilon_{1allowable}^{local} = 0.008$, $\varepsilon_{2allowable}^{local} = 0.029$, $\gamma_{12allowable}^{local} = 0.015$. A safety factor equal to 1.5 is used to calculate the strain allowables.

2. Fundamental relations for 2D multilayered composite structures

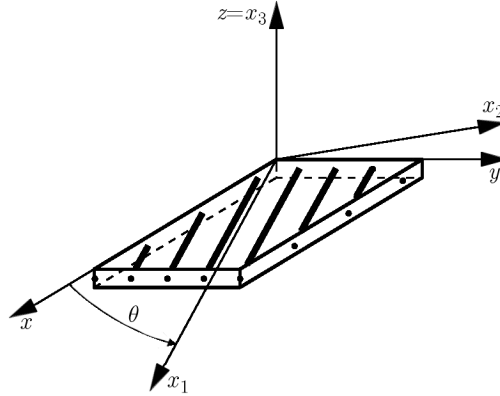


Fig. 1. Global and local coordinate systems ($x_1 \equiv x'$, $y_1 \equiv y$, $z \equiv z'$)

Usually thin plies in the laminate (Fig. 1) can be considered to be under a plane stress with all the stress components in the out-of-plane direction z being approximately zero. In the 3D case the generalized Hooke law (the local coordinate system x_1x_2z associated with fibres) is reduced to

$$\sigma'_i(x_1, x_2, z) = C'_{ij}\varepsilon'_j(x_1, x_2, z) \quad i, j = 1, 2, 6 \quad (2.1)$$

where

$$\begin{aligned} C'_{11} = Q_{11} &= \frac{E_1}{1 - \nu_{12}\nu_{21}} & C'_{12} = Q_{12} &= \frac{\nu_{12}E_2}{1 - \nu_{12}\nu_{21}} \\ C'_{22} = Q_{22} &= \frac{E_2}{1 - \nu_{12}\nu_{21}} & C'_{66} = Q_{66} &= G_{12} \end{aligned}$$

and $\boldsymbol{\sigma}'$ denotes the tensor of in-plane stress components, and $\boldsymbol{\varepsilon}'$ the tensor of in-plane strain components. Let us consider that the ply material axes are rotated by an angle θ with respect to the global reference system (xyz) – Fig. 1. In the global system, writing the Hooke law

$$\sigma_i(x, y, z) = C_{ij}\varepsilon_j(x, y, z) \quad i, j = 1, 2, 6 \quad (2.2)$$

and using the Tsai-Pagano invariant formulation, all components of the stiffness matrix \mathbf{C} can be written in the invariant form

$$\begin{aligned} C_{11} &= U_1 + U_2 \cos 2\theta + U_3 \cos 4\theta & C_{12} &= U_4 - U_3 \cos 4\theta \\ C_{22} &= U_1 - U_2 \cos 2\theta + U_3 \cos 4\theta & C_{16} &= \frac{1}{2}U_2 \sin 2\theta + U_3 \sin 4\theta \\ C_{26} &= \frac{1}{2}U_2 \sin 2\theta - U_3 \sin 4\theta & C_{66} &= U_5 - U_3 \cos 4\theta \end{aligned} \quad (2.3)$$

where

$$\begin{aligned} U_1 &= \frac{1}{8}(3Q_{11} + 3Q_{22} + 2Q_{12} + 4Q_{66}) & U_2 &= \frac{1}{2}(Q_{11} - Q_{22}) \\ U_3 &= \frac{1}{8}(Q_{11} + Q_{22} - 2Q_{12} - 4Q_{66}) & U_4 &= \frac{1}{8}(Q_{11} + Q_{22} + 6Q_{12} - 4Q_{66}) \\ U_5 &= \frac{1}{2}(U_1 - U_4) \end{aligned}$$

The above relations are developed for a single ply (lamina). The laminate can be built of N layers, see Fig. 2, so that the stresses in the l -th ply are related to the strains in the following way

$$\sigma_i^{(l)}(x, y, z) = C_{ij}^{(l)} \varepsilon_j(x, y, z) \quad i, j = 1, 2, 6 \quad l = 1, 2, \dots, N \quad (2.4)$$

assuming that all ply strains are equal to the laminate strains. The stiffness matrix coefficients $C_{ij}^{(l)}$ are defined with the use of Eq. (2.3) where the fibre orientations θ are replaced by the symbol θ_l referring to the fibre orientations of the l -th layer. From the assumption that the strains vary linearly through the laminate thickness, i.e. $\varepsilon_i(x, y, z) = \varepsilon_i^0(x, y) + z\kappa_i(x, y)$ ($i = 1, 2, 6$) one can find that relation (2.4) can be rewritten in the following form

$$\begin{aligned} N_i(x, y) &= A_{ij} \varepsilon_i^0(x, y) + B_{ij} \kappa_i(x, y) \\ M_i(x, y) &= B_{ij} \varepsilon_i^0(x, y) + D_{ij} \kappa_i(x, y) \end{aligned} \quad i, j = 1, 2, 6 \quad (2.5)$$

where the in-plane stress resultants $N_i(x, y)$ and the stress couples $M_i(x, y)$ are expressed as

$$\begin{aligned} N_i(x, y) &= \int_{-t/2}^{t/2} \sigma_i^{(l)} dz = \sum_{l=1}^N \sigma_i^{(l)} (z_l - z_{l-1}) \\ M_i(x, y) &= \int_{-t/2}^{t/2} \sigma_i^{(l)} z dz = \frac{1}{2} \sum_{l=1}^N \sigma_i^{(l)} (z_l^2 - z_{l-1}^2) \end{aligned} \quad i = 1, 2, 6 \quad l = 1, \dots, N \quad (2.6)$$

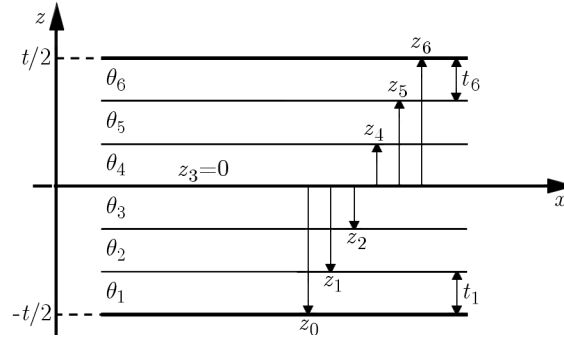
where \mathbf{A} , \mathbf{B} , \mathbf{D} are the extensional, coupling and bending stiffnesses, respectively, defined as follows

$$\begin{aligned} A_{ij} &= \sum_{l=1}^N C_{ij}^{(l)} (z_l - z_{l-1}) & B_{ij} &= \frac{1}{2} \sum_{l=1}^N C_{ij}^{(l)} (z_l^2 - z_{l-1}^2) \\ D_{ij} &= \frac{1}{3} \sum_{l=1}^N C_{ij}^{(l)} (z_l^3 - z_{l-1}^3) \end{aligned} \quad i, j = 1, 2, 6 \quad (2.7)$$

where z_l and z_{l-1} are the location coordinates of the top and the bottom surface of the lamina l . $\varepsilon_i^0(x, y)$ are the components of the in-plane (membrane) strains, and $\kappa_i(x, y)$ are the components of the vector of curvature ($i = 1, 2, 6$).

3. Definition of design variables

In the 2D approach, topological variables defining the connectivity of particular structural elements in the structure (in the paper it denotes the stacking sequence of the individual layers in the laminate) are understood in the sense of the sequence of layers having prescribed discrete fibre orientations θ_l in each individual ply. Commonly, it is assumed that the thicknesses of individual plies are identical, i.e. $t_l = t/N$ – see Fig. 2. In order to assure great flexibility and generality in the formulation of various optimisation problems, different types of the above-mentioned discrete design variables must be represented in a similar unified manner, i.e. each design variable must be coded as a finite string of digits. Let us note that the angle-ply anti-symmetric laminates are considered only, however, it can be easily extended for an arbitrary laminate configuration. Using the classical method of coding, 1 represents 0_2^0 , 2 – $\pm 45^\circ$, 3 – 90_2^0 . Each design variable s representing the fibre orientation (i.e. 1, 2 and 3) is coded as a binary number and is called as a gene. The sequence $\{1, 2, 1, 3\}$ is called a chromosome. Such a representation is not very convenient for optimisation problems since there is a lot of design variables


 Fig. 2. Cross-section of the laminate ($N = 6$)

(increasing with the total number of plies N) and, in addition, various stacking sequences are described by the identical values of the \mathbf{A} , \mathbf{B} , \mathbf{D} matrices. Therefore, we propose to adopt herein a special type of integer variables $x_r^{\{A,D\}}$ ($r = 1, 2, 3$) introduced by Muc (1997) that are completely different than those introduced by Miki (1986), Fukunaga and Vanderplaats (1991). The new design variables represent triangles in the design space, see Fig. 3. However, there is

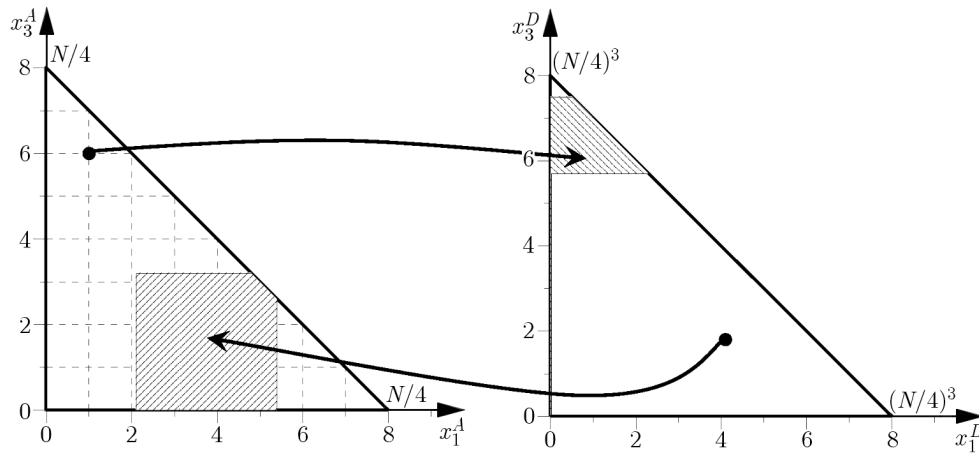


Fig. 3. Graphical representation of design variables

no unique mapping between the spaces x_r^A and x_r^D . For the assumed laminate configuration, the \mathbf{B} matrix is identically equal to zero, whereas the stiffnesses \mathbf{A} and \mathbf{D} can be written in the following way

$$\begin{aligned}
 A_{11} &= t(U_1 - U_3) + \frac{4t}{N}U_2(x_1^A - x_3^A) + \frac{8t}{N}U_3(x_1^A + x_3^A) \\
 A_{12} &= t(U_4 + U_3) - \frac{8t}{N}U_3(x_1^A + x_3^A) \\
 A_{22} &= t(U_1 - U_3) - \frac{4t}{N}U_2(x_1^A - x_3^A) + \frac{8t}{N}U_3(x_1^A + x_3^A) \\
 A_{66} &= t(U_5 + U_3) - \frac{8t}{N}U_3(x_1^A + x_3^A)
 \end{aligned} \tag{3.1}$$

and

$$D_{11} = \frac{t^3}{12}(U_1 - U_3) + \frac{1}{12}\left(\frac{4t}{N}\right)^3 U_2(x_1^D - x_3^D) + \frac{1}{6}\left(\frac{4t}{N}\right)^3 U_3(x_1^D + x_3^D)$$

$$\begin{aligned}
D_{12} &= \frac{t^3}{12}(U_4 + U_3) - \frac{1}{6}\left(\frac{4t}{N}\right)^3 U_3(x_1^D + x_3^D) \\
D_{22} &= \frac{t^3}{12}(U_1 - U_3) - \frac{1}{12}\left(\frac{4t}{N}\right)^3 U_2(x_1^D - x_3^D) + \frac{1}{6}\left(\frac{4t}{N}\right)^3 U_3(x_1^D + x_3^D) \\
D_{66} &= \frac{t^3}{12}(U_5 + U_3) - \frac{1}{6}\left(\frac{4t}{N}\right)^3 U_3(x_1^D + x_3^D)
\end{aligned} \tag{3.2}$$

where

$$\begin{aligned}
x_r^{\{A,D\}} &= \sum_{k=1}^{N/4} \{1, [3k(k-1) + 1]\} \cos(2\theta) \Xi(\alpha_r) \\
\Xi(\alpha_r) &= \begin{cases} 1 & \text{where } \alpha_r = \theta \\ 0 & \text{where } \alpha_r \neq \theta \end{cases} \\
\alpha_r &= 90^\circ \frac{r-1}{2} \quad r = 1, 2, 3
\end{aligned} \tag{3.3}$$

Let us note that using the above notation all terms in the stiffness matrix are uniquely represented by the set of four integer variables $\{x_1^A, x_3^A, x_1^D, x_3^D\}$. The terms having the index $r = 2$ are identically equal to 0 since they correspond to the plies having fibres oriented at 45° . The integer numbers x_1^A, x_3^A represent directly the number of plies with fibres oriented at 0° and 90° , respectively, since the following relation is always fulfilled

$$x_1^A + x_3^A + x_2^A = \frac{N}{4} \tag{3.4}$$

where $x_2^A = N_{45}/4$, and N_{45} denotes the total number of plies oriented at 45° . With the aid of Eqs. (3.1)-(3.4) it is possible to define feasible regions for our new design variables – the triangles presented in Fig. 3. Two sets of variables $\{x_1^A, x_3^A\}$ and $\{x_1^D, x_3^D\}$ are not independent, however, using their definition (Eq. (3.3)) it is possible to evaluate the ranges of their variations demonstrated in Fig. 3 in the form of quadrilaterals

$$\begin{aligned}
(x_1^A)^3 &= \sum_{k=1}^{x_1^A} [3k(k-1) + 1] \leq x_1^D \leq \sum_{k=N/4+1-x_1^A}^{N/4} [3k(k-1) + 1] = \left(\frac{N}{4}\right)^3 - \left(\frac{N}{4} - x_1^A\right)^3 \\
(x_3^A)^3 &= \sum_{k=1}^{x_3^A} [3k(k-1) + 1] \leq x_3^D \leq \sum_{k=N/4+1-x_3^A}^{N/4} [3k(k-1) + 1] = \left(\frac{N}{4}\right)^3 - \left(\frac{N}{4} - x_3^A\right)^3 \\
x_1^D + x_3^D &\leq \left(\frac{N}{4}\right)^3
\end{aligned} \tag{3.5}$$

Knowing the values of the $\{x_1^D, x_3^D\}$ variables, one can derive from relations (3.1), (3.2) the upper and lower bounds of the $\{x_1^A, x_3^A\}$ variables that have to be integer numbers belonging to the triangular domain shown in Fig. 3. However, in the optimisation procedure they are treated as continuous variables since they are always normalised (by the division of them by $N/4$ and $(N/4)^3$, respectively) and they belong to the interval $[0, 1]$. The normalised variables are denoted by the bar over the symbols, i.e. as $\{\bar{x}_1^A, \bar{x}_3^A\}$, $\{\bar{x}_1^D, \bar{x}_3^D\}$. The optimal solutions are completely independent of the total number of plies N and, in addition, the definition of the appropriate terms in the stiffness matrices **A** and **D** has an identical form, although they are functions of different variables. Such a definition may be also very useful for the pseudorandom generation of the design variables.

If the optimal solutions are found (in the sense of four variables $\{\bar{x}_1^A, \bar{x}_3^A\}$, $\{\bar{x}_1^D, \bar{x}_3^D\}$) the decoding procedure is required to represent the above-mentioned variables by the appropriate

stacking sequences. The decoding procedure can be easily conducted with the use of the symbolic package Mathematica. The fundamental two operations are given below

```
a = Table[3 * l * (1 - 1) + 1, l, N/4];
f = Subsets[a, L];
```

First of all, a list of values of the expression “ $3l(l - 1) + 1$ ” is generated when the natural number l runs from 1 to $N/4$ – see Eq. (2.3). Assuming $N = 16$, table “a” takes the form: {1, 7, 19, 37}. Then a finite number of subsets “f” having exactly “L” elements is constructed from the list “a”. For instance, for $L = 2$ the subsets “f” are following: {1, 7}, {1, 19}, {1, 37}, {7, 19}, {7, 37}, {19, 37}. If $L = 2$ defines the number of plies oriented at 0° (i.e. $x_1^A = 2$) then each of the subsets represents the laminates (in fact the upper part of the laminate where the symbol 0° corresponds to the pair of plies having the 0° orientation): $[0^\circ, 0^\circ, \div, \div]$, $[0^\circ, \div, 0^\circ, \div]$, $[0^\circ, \div, \div, 0^\circ]$, $[\div, 0^\circ, 0^\circ, \div]$, $[\div, 0^\circ, \div, 0^\circ]$, $[\div, \div, 0^\circ, 0^\circ]$. According to definition (3.3), all laminates have the same value $x_1^A = 2$ but different values of x_1^D equal to: 8, 20, 38, 26, 44, 56, respectively. In addition, the first laminate can be characterized by two different values of x_3^D , i.e.: $[0^\circ, 0^\circ, 45^\circ, 90^\circ] - x_3^D = 37$ or $[0^\circ, 0^\circ, 90^\circ, 45^\circ] - x_3^D = 19$. In both cases, $x_2^A = x_3^A = 1$. The example demonstrates evidently the non-uniqueness of the mapping presented in Fig. 3. However, as four design variables are known (e.g. $x_1^A = 2$, $x_3^A = 1$ and $x_1^D = 8$, $x_3^D = 19$) the lamination sequence can be derived uniquely – it corresponds to $[0^\circ, 0^\circ, 90^\circ, 45^\circ]$. Therefore, to decode the lamination sequence from the set of the normalized design variables $\{\bar{x}_1^A, \bar{x}_3^A\}$, $\{\bar{x}_1^D, \bar{x}_3^D\}$, it is necessary to conduct the following operations: Step 1) to round the values $\{\bar{x}_1^A * (N/4), \bar{x}_3^A * (N/4)\}$ to the nearest integers, Step 2) to find the subsets “f” corresponding to $x_1^A \approx \bar{x}_1^A * (N/4)$, compute the sum of each of the elements in the subsets “f” and find the nearest integer to the real number $\bar{x}_1^D * (N/4)^3$, Step 3) to repeat step 2 for the value $x_3^A \approx \bar{x}_3^A * (N/4)$, creating new subsets for the layers oriented at 90° , but selecting empty spaces only (noted as \div in the laminate in the above example), Step 4) to fill the rest of empty spaces in the laminate by the layers oriented at 45° . To verify the convergence, it is possible to increase the total number of layers N .

The decoding procedure is simple using symbolic packages. In many cases (one of them will be discussed further), the optimal design is not represented by all design variables, and the decoding method has to be slightly modified.

4. Buckling and the First-Ply-Failure of plates

Many experimental results on the buckling of composite material plates have been presented over the last years. They are summarized in Muc (1988), Muc and Gurba (2001). In general, they tend to indicate that the theory for composites is rather in good agreement with experiments. The experiments demonstrate evidently that for thin-walled flat composite plates, the loss of stability is not equivalent to the catastrophic failure of structures. The catastrophic failure in form of the limit carrying capacity may occur for thicker plates and it is associated with the First-Ply-Failure (FPF). For plates with a cutout, delaminations or stiffened, the failure mode may be in form of bifurcation buckling, but the final damage is usually associated with other modes of failure. For flat plates, the comparison between experimental and theoretical results is conducted with the use of linear prebuckling theory according to experimental observations. For more complicated plated structures, the nonlinear prebuckling and postbuckling analysis is required since the final failure mode is associated, e.g., with local buckling modes or failure of a core for sandwiches. Therefore, for flat bi-axially compressed rectangular plates, it is assumed that a critical multiplier of loading corresponding to the global loss of stability λ_b can be expressed in the following form

$$\lambda_b(s) = \frac{(m\pi/a)^2}{P_x(1+k\beta_m^2)} [D_{11} + (D_{12} + 2D_{66})\beta_m^2 + D_{22}\beta_m^4] \quad \beta_m = \frac{na}{mb} \quad k = \frac{P_y}{P_x} \quad (4.1)$$

where a , b are geometrical plate dimensions, and m , n are numbers of half-waves in two perpendicular directions corresponding to the plate co-ordinate system, and P_x is the axial compressive force in the x direction. s denotes the vector of design variables having 2 independent normalized real variables $\{\bar{x}_r^A, \bar{x}_r^D\}$ defined in the interval $[0, 1]$ representing 3 different fibre orientations and various stacking sequences in the laminate. Using the notation introduced in Eq. (4.1), the critical multiplier of loading can be written as follows

$$\lambda_b = \Omega_m(Z_1 + Z_2\bar{x}_1^D + Z_3\bar{x}_3^D) \quad (4.2)$$

where

$$\begin{aligned} \bar{x}_r^D &= \left(\frac{4}{N}\right)^3 x_r^D & \Omega_m &= \frac{(n\pi/b)^2 t^3}{P_x(1+k\beta_m^2)\beta_m^2 12} \\ Z_1 &= U_1(1 + \beta_m^2)^2 + U_3(6\beta_m^2 - 1 - \beta_m^4) & Z_2 &= U_2(1 - \beta_m^4) + 2U_3(1 - 6\beta_m^2 + \beta_m^4) \\ Z_3 &= 2U_3(1 - 6\beta_m^2 + \beta_m^4) - U_2(1 - \beta_m^4) & r &= 1, 2, 3 \end{aligned}$$

It is also worth to point out also that the validity of relation (4.1) is strictly limited by the values of $t/[\text{Min}(a, b)]$ ratio. For the ratio higher than 0.05, it is necessary to include transverse shear effects employing, for instance, the Mindlin hypothesis.

It is well-known that buckling loads (4.2) are straight lines in the convex design space (Fig. 3). Since for the known composite materials U_1 is always greater than U_3 , the coefficient Z_1 is always positive, whereas Z_2 and Z_3 may be positive, equal to zero or negative. According to the classical theory of mathematics for the prescribed mode of buckling (i.e. m and n) in the feasible domain of design variables x_1^D , x_3^D , the maximal value of the parameter λ_b defined by Eq. (4.2) may exist at the vertices of the triangle (points A , B , C – unimodal solutions) or along the lines AB and BC (e.g. points D and E , bimodal solutions – degenerated solutions since one of the variables x_1^D or x_3^D is equal to zero) – Fig. 4.

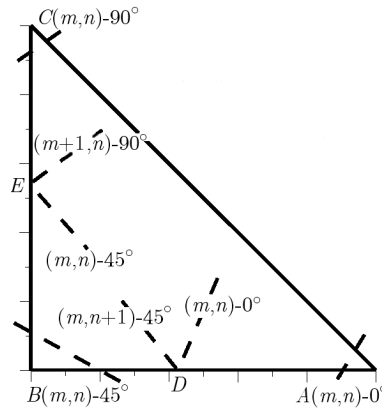


Fig. 4. Positions of the optimal buckling loads for three discrete fibre orientations

4.1. Unimodal solutions

The variations of the coefficients Z_1 , Z_2 and Z_3 with the geometrical ratios a/b are demonstrated in Fig. 5. Their values correspond directly to the location of optimal fibre orientations with respect to the a/b ratio, i.e. $\bar{x}_1^D = 1$, $\bar{x}_3^D = 0$ – orientation 0° ; $\bar{x}_1^D = 0$, $\bar{x}_3^D = 0$ – orientation 45° , $\bar{x}_1^D = 0$, $\bar{x}_3^D = 1$ – orientation 90° .

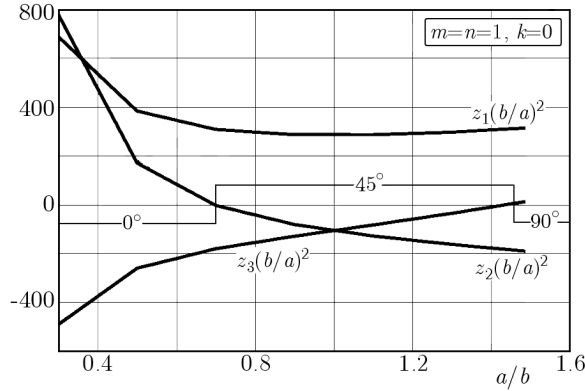


Fig. 5. Variations of the coefficients in Eq. (4.2)

With the use of the introduced design variables, the analytical unimodal optima can also be easily derived. They can be written in the following way:

— equivalent to the point *A*, $Z_2 > 0$ and $Z_3 < 0$

$$x_1^D = \left(\frac{N}{4}\right)^3 \quad x_3^D = 0 \quad \text{if} \quad \beta_m \leq \sqrt{\frac{-3\varphi + \sqrt{8\varphi^2 + 1}}{1 - \varphi}} \quad (4.3)$$

— equivalent to the point *B*, $Z_2 < 0$ and $Z_3 < 0$

$$x_1^D = 0 \quad x_3^D = 0 \quad \text{if} \quad \sqrt{\frac{-3\varphi + \sqrt{8\varphi^2 + 1}}{1 - \varphi}} \leq \beta_m \leq \sqrt{\frac{3\varphi + \sqrt{8\varphi^2 + 1}}{1 - \varphi}} \quad (4.4)$$

— equivalent to the point *C*, $Z_2 < 0$ and $Z_3 > 0$

$$x_1^D = 0 \quad x_3^D = \left(\frac{N}{4}\right)^3 \quad \text{if} \quad \beta_m \geq \sqrt{\frac{3\varphi + \sqrt{8\varphi^2 + 1}}{1 + \varphi}} \quad (4.5)$$

where $\varphi = 2U_3/U_2$.

In the above relations, the estimations are computed from the equalities:

— equivalent to $Z_1 = 0$

$$\lambda_b \left[x_1^D = \left(\frac{N}{4}\right)^3, x_3^D = 0, m, n \right] = \lambda_b \left[x_1^D = 0, x_3^D = 0, m, n \right] \quad (4.6)$$

— equivalent to $Z_3 = 0$

$$\lambda_b \left[x_1^D = 0, x_3^D = 0, m, n \right] = \lambda_b \left[x_1^D = 0, x_3^D = \left(\frac{N}{4}\right)^3, m, n \right] \quad (4.7)$$

where the first relation describes the equality of buckling loads for the laminates oriented at 0° and 45° , and the second, the equality of buckling loads for the laminates oriented at 45° and 90° .

4.2. Bimodal solutions

The bimodal solutions correspond to situations as the buckling load is identical for two neighbouring buckling modes (e.g. m and $m + 1$) – see also Muc (1988) (continuous angle-ply orientations). Let us note that the identical procedure is conducted in the buckling analysis of isotropic structures although the solutions are not called the bimodal ones. For isotropic plates constructing the classical “chain curve” for buckling loads versus the a/b ratio for different wave numbers m , it is possible to find such values of the a/b ratio that correspond to two neighbouring

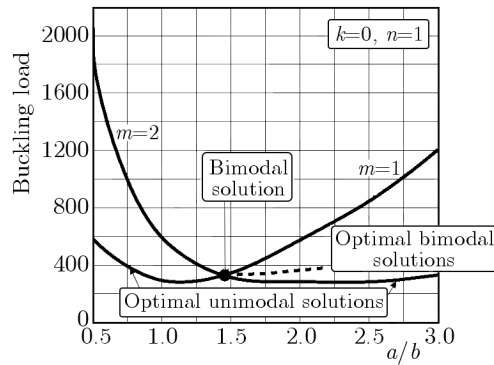


Fig. 6. Optimal unimodal and bimodal solutions

buckling modes m and $m + 1$ (e.g. for uniaxially compressed plates: $a/b = \sqrt{2}$ as $m = 1$ and 2, $a/b = \sqrt{6}$ as $m = 2$ and 3 etc.). Figure 6 shows a part of the chain curve for laminated plates as well as the optimal unimodal solutions – the lower bound envelope of buckling loads for different values of m . The dot represents the classical bimodal solutions.

For laminated plates, the critical multiplier λ_b (Eqs. (4.1) or (4.2)) is not only a function of the geometrical a/b ratio but also of the design variables s . Therefore, for the identical a/b ratio, there may exist a finite number (discrete variables) of bimodal solutions. Some of them may correspond to the higher values of buckling loads than for unimodal solutions. They will be called the optimal bimodal solutions (Fig. 6).

The bimodal solution presented as the dot in Fig. 6 demonstrates that the unimodal optimal solutions exist for two different modes of buckling $m = 2$ and $m = 1$, however, each of them corresponds to different fibre orientations ($\pm 45^\circ$ and 90° , respectively). For uniaxial compression ($k = 0$), the maximal buckling load occurs always for plies having fibres oriented at $\alpha_2 = \pm 45^\circ$. For each buckling mode (considering separately the modes $m = 1$ and $m = 2$), the buckling load at the vertex B is higher than at the vertices A and C , and it takes a lower value (for $m = 1$ and $a/b < 1.445$) than the corresponding buckling load at the vertex B for $m = 2$ – see Eq. (4.4). If $a/b = 1.445$, the optimal unimodal fibre orientations switch from $\pm 45^\circ$ to 90° for $m = 1$. However, the latter case does not satisfy the buckling criterion – it is not the lower bound with respect to buckling modes since unimodal buckling loads for plies having the orientation 90° have lower values for $m = 2$ than those for the lower buckling mode ($m = 1$). Of course, the unimodal solutions for $\pm 45^\circ$ and $m = 2$ cannot be treated as optimal ones because this orientation gives lower buckling loads for $m = 1$. Thus, the bimodal constraint becomes active.

For discrete design variables, it is possible to find two potential candidates for the optimum considering each wave numbers of buckling, i.e. (m, n) and $(m + 1, n)$. Such type of optimal solutions is represented by the points D and E in Fig. 4. The identical analysis can be carried out in the similar manner for the (m, n) and $(m, n + 1)$ buckling modes. Of course, the points D and E are not single candidates for the bimodal solutions. The equalisation of the buckling load coefficients (Eq. (4.1)) for the neighbouring buckling modes (i.e. m, n and $m + 1, n$) leads to a finite number of solutions represented by a straight line in the design space (x_1^D, x_3^D) . Using Eqs. (4.6) and (4.7), the bimodal solutions can be found at the boundaries of the triangle only since those values offer the highest buckling load among them. The proof of this conclusion is a trivial one since for each buckling mode the straight lines described by Eq. (4.1) create a family of parallel lines (parametrized by the value of buckling load) whose maximum occurs at the opposite vertices of the triangle – one vertex where the maximum occurs at the point B for the mode $(m + 1, n)$, and the second maximum located at the point C for the mode (m, n) .

The bimodal solutions can be found analytically from the following relations

$$\begin{aligned}\bar{x}_1^D &= 0 \\ \lambda_b(m, n) &= \Omega_m [Z_1(m) - \bar{x}_3^D U_2(1 - \beta_m^4) + 2\bar{x}_3^D U_3(1 - 6\beta_m^2 + \beta_m^4)] \\ &= \lambda_b(m + 1, n) = \Omega_{m+1} Z_1(m + 1)\end{aligned}\quad (4.8)$$

The relations are valid for $a/b > 0.7$. In the opposite case, the bimodal solutions are located along the line $\bar{x}_3^D = 0$.

4.3. FPF constraints

For the assumed laminate configuration and considering the membrane state only in the global coordinate system, the strain tensor is reduced to two nonzero components written in the following way (see Eq. (2.5)):

$$\varepsilon_1^0 = \frac{\lambda_{FPF} P_x (A_{22} - k A_{12})}{A_{11} A_{22} - A_{12}^2} \quad \varepsilon_2^0 = \frac{\lambda_{FPF} P_x (k A_{11} - A_{12})}{A_{11} A_{22} - A_{12}^2} \quad \varepsilon_6^0 = 0 \quad (4.9)$$

The strains in the local coordinate system of the ply having the orientation α_r take the following form

$$\varepsilon'_1 = \varepsilon_1^0 \cos^2 \alpha_r + \varepsilon_2^0 \sin^2 \alpha_r \quad \varepsilon'_2 = \varepsilon_1^0 \sin^2 \alpha_r + \varepsilon_2^0 \cos^2 \alpha_r \quad \varepsilon'_6 = (\varepsilon_2^0 - \varepsilon_1^0) \sin 2\alpha_r \quad (4.10)$$

For each individual ply, the above mentioned local strains are compared with the allowable strains along the fibres $\varepsilon_{1allowable}^{local}$, in the direction perpendicular to the fibres $\varepsilon_{2allowable}^{local}$ and with the shear strains $\gamma_{12allowable}^{local}$, respectively. Thus, for each discrete fibre orientation α_r we have three inequality FPF constraints. However, one can easily find that each FPF relation may be presented in the identical form

$$\begin{aligned}2t(U_1 + U_4)(tQ_{66} + F_2^A) - (F_1^A)^2 &= \lambda_{FPF} P_x (p_1 + p_2 F_1^A + p_3 F_2^A) \frac{1}{\varepsilon_{allowable}^{local}} \\ F_1^A &= \frac{4t}{N} U_2 \sum_{r=1}^{r_{max}+1} x_r^A \cos(2\alpha_r) \quad F_2^A = \frac{8t}{N} U_3 \sum_{r=1}^{r_{max}+1} x_r^A \cos^2(2\alpha_r)\end{aligned}\quad (4.11)$$

where $\varepsilon_{allowable}^{local}$ denotes the appropriate allowable strains for the plies, and p_i ($i = 1, 2, 3$) are appropriate constants derived from equations (4.9) and (4.10). The curves described by Eq. (4.11) represent ellipses in the design space $\{x_1^A, x_3^A\}$. It is obvious that with the aid of any of numerical packages (Mathematica, Maple, Matlab, Mathcad) it is possible to compute values of λ_{FPF} (Eq.14) for all values of x_1^A, x_3^A as well as the prescribed mechanical and geometrical properties of the plate and the loading parameter k . Such a procedure can be easily conducted for all components of strains, assuming different allowable values for tension and compression. Finally, the results are collected in a table (called as FPFTable) that is parametrized by the values of x_1^A, x_3^A and the failure mode (Eq. (4.11)).

5. Optimization problem

The optimisation problem is formulated as follows

$$\max_s (\min_{m,n} \lambda_b) \quad (5.1)$$

where λ_b denotes a critical multiplier of loading corresponding to the global loss of stability and s denotes the set of design variables $\{\bar{x}_1^D, \bar{x}_3^D\}$.

The analysed problem may be subjected to various subsidiary constraints written in the following form:

— Bimodal constraints

$$\lambda_b[m, n] \leq \lambda_b[m + 1, n] \quad \text{and} \quad \lambda_b[m, n] \leq \lambda_b[m, n + 1] \quad (5.2)$$

— FPF constraints

$$\lambda_{FPF} \leq \lambda_b \quad (5.3)$$

Constraint (5.2) presents two conditions for each wave number in buckling independently, and the values of buckling coefficients λ_b are derived from Eqs. (4.1) or (4.2).

The optimization analysis is carried out for the prescribed mechanical constants, the total number of layers N , the loading parameter k and the geometrical ratio a/b . At the beginning, the buckling loads are computed for all vertices of the triangle (Fig. 3); they correspond to the fibres oriented in all plies at 0° , 45° and 90° , respectively. Those values are collected in a table (called as UNITable) and parametrized by the values m and n (selected in the prescribed range, let say from 1 to 5). Then, the optimization is divided into four procedures described below.

I. Unimodal optimum. There are two integer numbers m and n such that for all vertices of the triangle, the values in the UNITable have the global minimum with respect to them. In addition, condition (3.5)₁ is satisfied (comparison with the values in the FPFTable). The optimal values can be computed from relations (4.3)-(4.5). The laminate stacking sequence is easily determined.

II. Bimodal optimum. There are two integer numbers m and n such that for all vertices of the triangle the values in the UNITable have not the global minimum with respect to them, i.e. the bimodal constraints become active and if condition (5.2) is not satisfied (comparison with the values in the FPFTable) then the optimal normalised design variables $\{\bar{x}_1^D, \bar{x}_3^D\}$ are computed from relations (4.8). It is necessary to decode the results to obtain the optimum in form of the laminate stacking sequence. To demonstrate it, let assume that the plate is made of $N = 64$ layers, $a/b = 0.5$ and is biaxially compressed, i.e. $k = 2$, $n = 1$. The optimum occurs for $x_1^D = 1963.307$, $x_2^D = 3899.693$, $x_3^D = 0$. The domain of possible variations of the number “L” is created with the help of inequalities (3.5), and let it be equal to 7. For each generated subset “f”, the sum of the elements in the subset is computed in the loop and compared with the rounded to two natural numbers real values of the optimal solution (1963 or 1964). Having, for instance, the subset {91, 127, 169, 217, 331, 397, 631} (the sum is equal to 1963) it is possible to recognize immediately that from the whole laminate represented by the table “a” ($N/4 = 16$) the elements having the nonzero values in the whole table, i.e. $\{\div, \div, \div, \div, \div, 91, 127, 169, 217, \div, 331, 397, \div, \div, 631, \div\}$ are replaced by the pairs oriented at 0° , whereas the symbol “ \div ” by the pairs oriented at $\pm 45^\circ$. It is worth to add that it is possible to find other 35 laminate configurations (subsets “f”) that give the same sum 1963. There is multiplicity of the solutions since the optimum is represented by two variables only.

III. Bimodal and FPF optimum. Similarly as in the previous case II, the bimodal optimum becomes active, however, the FPF load is lower than the optimum bimodal solution (condition (5.3) is satisfied) and the optimum exists inside the triangles plotted in Fig. 3. The optimum can be found from the relation

$$\lambda_b[m, n] = \lambda_b[m + 1, n] = \lambda_{FPF} \quad (5.4)$$

Using the appropriate relation for λ_b (4.2) and λ_{FPF} (4.9), it is possible to express the above equality constraint conditions in the following form: $\bar{x}_1^D = p(\bar{x}_1^A, \bar{x}_3^A)$, $\bar{x}_3^D = q(\bar{x}_1^A, \bar{x}_3^A)$ where p and q are analytical algebraic functions. Inserting those results to the definition of buckling loads (4.2), it is possible to find the maximal buckling load with respect to the values \bar{x}_1^A, \bar{x}_3^A searching for the maximum by building the table for all possible variations of the values x_1^A, x_3^A $((N/4)[(N/4) - 3] + 2$ possible values inside the half of the triangles) or using the Mathematica procedure “Maximize”. For the optimal values of x_1^A, x_3^A design variables, it is possible to derive the optimal values of \bar{x}_1^D, \bar{x}_3^D and find the optimal stacking sequences with the aid of the decoding procedure presented in Section 3. The discussed problem of both FPF and bimodal active constraints occurs, e.g. for plates: $a/b = 4$, $k = 0.25$.

IV. FPF optimum. If the FPF is the dominant failure mode (thick plates), the optimum can be found directly from relation (4.9) searching for the maximum similarity as in the previous case. Since the optimum is a function of the membrane parameters, one can observe again the multiplicity of optimal laminate configurations.

6. Concluding remarks and further works

In the paper, the proposal of a new discrete design variables that are used in the buckling and FPF optimisation problems is shown. It is demonstrated that in the buckling and FPF analysis of plates, four types of solutions may exist, i.e.:

- Unimodal buckling solutions – unique determination of optimal stacking sequences.
- Bimodal buckling solutions – multiplicity of optimal stacking sequences (bending state only).
- FPF and bimodal buckling solutions – unique determination of optimal stacking sequences (flexural and membrane design variables).
- FPF – multiplicity of optimal stacking sequences (membrane state only).

In our opinion, the new set of design variables demonstrates a lot of the advantages in comparison with the existing ones, i.e.:

- It allows us to derive unique analytical solutions.
- It explains the uniqueness and multiplicity of possible laminate configurations being a representation of laminate discrete configurations.
- It shows a simple symbolic method for the derivation of multiple optimal configurations from the used set of discrete design variables (the so-called decoding method).

The analysed example (buckling and FPF of bi-axially compressed plates) is relatively simple since the optimisation problem is characterized by flexural and membrane properties only, given by analytical formulae. The next step is connected with simultaneous application of the proposed design variables to optimisation problems characterised by analytical solutions that include both bending, membrane and coupling effects. Finally, we intend to include the proposed methodology into numerical FE codes in the similar manner as described by Muc and Gurba (2001).

Acknowledgement

The National Science Center (Poland) UMO-2013/09/B/ST8/00178 is gratefully acknowledged for the financial support.

References

1. FUKUNAGA H., VANDERPLAATS G.N., 1991, Stiffness optimization of orthotropic laminated composites using lamination parameters, *AIAA Journal*, **29**, 641-648
2. GROSSET L., LERICHE R., HAFTKA R., 2006, A double-distribution statistical algorithm for composite laminate optimization, *Structural and Multidisciplinary Optimization*, **31**, 49-59
3. IEEE Neural Network Council, Glossary of Evolutionary Computation terms, Standing Committee on Standards, IEEE, Piscataway, NY, 1996
4. KAUFFMAN S.A., 1993, *The Origins of Order: Self-Organization and Selection in Evolution*, Oxford University Press, New York
5. MIKI M., 1986, Optimum design of fibrous laminated plates subjected to axial compression, *Proceedings of 3rd Japan-US Composite Materials Conference*, Tokyo, 673-81
6. MUC A., 1988, Optimal fibre orientations for simply -supported plates under compression, *Composite Structures*, **9**, 161-172
7. MUC A., 1997, A new set of design variables in stacking sequence optimization under buckling and strength constraints, *Proceedings of WCSMO-2*, **2**, 693-698
8. MUC A., GURBA W., 2001, Genetic algorithms and finite element analysis in optimization of composite structures, *Composite Structures*, **54**, 275-281
9. MUC A., MUC-WIERZGOŃ M., 2012. An evolution strategy in structural optimization problems for plates and shells, *Composite Structures*, **94**, 1461-1470

Manuscript received May 17, 2015; accepted for print August 13, 2015

EFFECT OF HEAT TRANSFER ON THERMAL STRESSES IN AN ANNULAR HYPERBOLIC FIN: AN APPROXIMATE ANALYTICAL SOLUTION

ASHIS MALLIK, RAJIV RANJAN, PRABIR KUMAR SARKAR

Department of Mechanical Engineering, Indian School of Mines, Dhanbad, India

e-mail: mal123_us@yahoo.com

An approximate analytical solution is presented for thermal stresses in an annular convective-conductive fin of a hyperbolic profile with temperature dependent thermal conductivity. The classical thermo-elasticity theory coupled with the ADM based polynomial form of temperature field is employed for an approximate analytical solution of thermal stresses. The influence of thermal parameters, i.e. variable thermal conductivity, the thermo-geometric parameter and the non-dimensional coefficient of thermal expansion on temperature and stress fields are investigated. The results for the stress field obtained from the ADM based solution are compared with those available in literature and found to be in close agreement.

Keywords: thermal stresses, Adomian decomposition method (ADM), variable thermal conductivity

Nomenclature

r_a, r_b	– inner and outer radius, respectively
t	– thickness of the fin
h_a	– fin thickness at base
h	– convective heat transfer coefficient
C_1	– profile function, $h_a r_a$
$k(T)$	– variable thermal conductivity
k_a	– thermal conductivity at ambient temperature
κ	– parameter describing variation of thermal conductivity
β	– dimensionless parameter describing variation of thermal conductivity, $\kappa(T_a - T_\infty)$
T, T_a, T_∞	– fin, base and ambient temperature, respectively
r, ϕ	– polar coordinates
α	– linear coefficient of thermal expansion
E	– Young's modulus
$\sigma_r, \sigma_\phi, \varepsilon_r, \varepsilon_\phi$	– radial and tangential stress and strains, respectively
C, D_1, D_2, η, A, B	– constants
ψ	– thermo-geometric parameter, $\sqrt{2hr_a^2/(k_\infty h_a)}$
ξ, ξ_1	– dimensionless radius of fin, $\xi = (r - r_a)/r_a$, $\xi_1 = \xi + 1$
R	– dimensionless outer radius, $R = r_b/r_a$
θ	– dimensionless temperature, $\theta = (T - T_\infty)/(T_a - T_\infty)$
$\bar{\sigma}_r, \bar{\sigma}_\phi$	– dimensionless radial and tangential stress, σ_r/E and σ_ϕ/E
χ	– dimensionless coefficient of thermal expansion, $\alpha(T_a - T_\infty)$
ν	– Poisson's ratio
A_c, dA_s	– cross sectional area of fin and elemental surface area of fin, respectively
n	– profile parameter
A_p, B_p	– Adomian polynomials

1. Introduction

The rapid heat dissipation from a surface to the surroundings is required in many engineering and industrial applications such as heat exchangers, semiconductors, transformers, motors and many other electrical, electronical and mechanical components. A fin is an extended surface frequently used for direct heat dissipation from a hot surface to its surroundings (Kern and Kraus, 1972; Kraus *et al.*, 2001).

Thermal analyses of the fin with various geometries are presented by many researchers (Yeh, 1997; Mokheimer, 2002). However, most of the available works focus on straight fins for their ease in manufacturing and mathematical formulation. Several mathematical techniques like Adomian's Decomposition Method (ADM), Homotopy Perturbation Method (HPM), Variational Iteration Method (VIM), and Differential Transformation Method (DTM) can be found in use by many researchers to obtain semi-analytical solutions to nonlinear heat equations for fins (Miansari *et al.*, 2008; Moradi, 2011). The improvement in heat transfer is shown mainly to be associated with their surface modification. So, an enhancement in the heat transfer rate critically depends on the selection of correct fin shape. Radial shape is observed to outperform the straight fin in respect of heat transfer ability (Behnia *et al.*, 1998). A hyperbolic profile contains even larger surface area to yield more heat dissipation from the surface to the surroundings. Thus, a radial fin with a hyperbolic profile would be the most preferred shape for a better heat transfer rate with less material involved.

Recently, the heat transfer in an annular fin with a hyperbolic profile was presented by Aksoy (2013). Non-uniform temperature distributions during the heat transfer process induce thermal stresses in the fin material. Thermal stresses are responsible for various mechanical failures, i.e., crack propagation, creep and fatigue failure that can reduce the fin life. The study of thermal stresses in them is, therefore, important to prevent their early damage. So far, only few authors (Chiu and Chen, 2002; Mallick *et al.*, 2015) have reported the analysis of stresses developed due to variation of the temperature gradient in an annular fin, and these papers mainly focus on uniform thickness of the fins. A careful review of the published literature reveal that till date no work reports theoretical studies for thermal stresses in an annular radial fin of a hyperbolic profile with the consideration of variable thermal conductivity.

In this paper, a novel analytical approach is used to predict a near closed form solution for thermal stresses in an isotropic homogeneous annular fin with a hyperbolic profile. A variable thermal conductivity parameter is considered in the analysis. The temperature field is obtained by solving a non-linear steady state heat conduction-convection equation of a fin using the Adomian Decomposition Method. The solution for the temperature field is expressed in a polynomial form. The plane stress condition in a rotational symmetric geometry with respect to its axis is considered in this study. A classical thermo-elasticity relation coupled with the solution of the temperature field is employed to obtain the stress field. The study includes the affect of various non-dimensional parameters such as thermal conductivity parameter (β), the thermo-geometric fin parameter (ψ), the coefficient of thermal expansion (χ) and Poisson's ratio (ν) on the stress field. The results are compared with those given by Chiu and Chen (2002) to resolve the accuracy of the present method. The analyses presented envisage an improved fin design process.

2. Problem description and governing equations of heat transfer

An axisymmetric undeformed annular fin of a hyperbolic profile (Fig. 1) with variable thermal conductivity ($k(T)$) is considered. The fin is exposed to a conductive-convective environment at a constant ambient temperature and the tip of the fin is maintained to be well-insulated

with a traction free condition. As thickness of the fin is relatively small compared to its radial dimension, the temperature distribution and the stress field can be assumed to vary in the radial direction only.

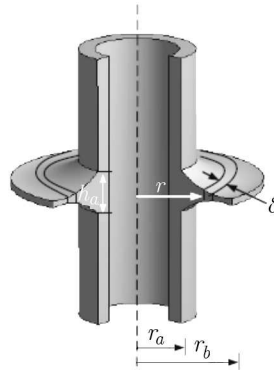


Fig. 1. Geometry of an annular fin with a hyperbolic profile

The profile function for fin tapering from the base to tip is given by

$$t = h_a \left(\frac{r}{r_a} \right)^n \quad \text{with} \quad n \geq 1 \quad (2.1)$$

where n is the profile parameter.

The steady state energy balance equation for the axisymmetric annular fin is expressed (Mokheimer, 2002) as

$$\frac{d}{dr} \left(k A_c \frac{dT}{dr} \right) - \frac{h d A_s}{dr} (T - T_\infty) = 0 \quad (2.2)$$

where $k = k_a [1 + \kappa(T - T_\infty)]$. The notations used in Eq. (2.1) and Eq. (2.2) are defined in the nomenclature.

The fin profile becomes hyperbolic when the profile parameter $n = -1$. Equation (2.2) can be expressed in the following dimensionless form

$$\frac{d^2 \theta}{d\xi^2} + \beta \theta \frac{d^2 \theta}{d\xi^2} + \beta \left(\frac{d\theta}{d\xi} \right)^2 - \psi^2 (1 + \xi) \theta = 0 \quad \text{with} \quad 0 \leq \xi \leq R - 1 \quad (2.3)$$

where

$$\theta = \frac{T - T_\infty}{T_a - T_\infty} \quad \beta = \kappa(T_a - T_\infty) \quad \xi = \frac{r - r_a}{r_a} \quad R = \frac{r_b}{r_a} \quad \psi = \sqrt{\frac{2hr_a^2}{k_a h_a}}$$

are non-dimensional parameters.

In order to evaluate the temperature distribution, the following non-dimensional boundary conditions are employed

$$\xi = \begin{cases} 0 & \text{that} \quad \theta = 1 \\ R - 1 & \text{that} \quad \frac{d\theta}{d\xi} = 0 \end{cases} \quad (2.4)$$

3. Adomian Decomposition Method to solve the heat transfer equation

Adomian Decomposition Method (ADM) is adopted to evaluate the non-dimensional temperature field. In ADM, the nonlinear ordinary and partial differential equations are represented in an operator form (Adomian, 1988)

$$Lu + Ru + Nu = g \quad (3.1)$$

where L is an n -th order invertible linear differential operator ($L = d^n/d\xi^n$), R is a linear differential operator of an order less than L , and N represents a nonlinear operator that enables Nu to be decomposed into an infinite series of Adomian polynomials.

Applying ADM, the governing equation for the temperature field (Eq. 2.3) can now be expressed as

$$L\theta = \psi^2\theta + \psi^2\xi\theta - \beta(NA) - \beta(NB) \tag{3.2}$$

where

$$NA = \theta\theta'' = \sum_{p=0}^{\infty} A_p \quad NB = (\theta')^2 = \sum_{p=0}^{\infty} B_p$$

are the nonlinear terms. The Adomian polynomials A_n and B_n are estimated as follows

$$\begin{aligned} \begin{pmatrix} A_0 \\ A_1 \\ A_2 \\ A_3 \\ A_4 \\ \cdot \\ \cdot \end{pmatrix} &= \begin{bmatrix} \theta_0 & & & & & & \\ \theta_1 & \theta_0 & & & & & \\ \theta_2 & \theta_1 & \theta_0 & & & & \\ \theta_3 & \theta_2 & \theta_1 & \theta_0 & & & \\ \theta_4 & \theta_3 & \theta_2 & \theta_1 & \theta_0 & & \\ \cdot & \cdot & \cdot & \cdot & \cdot & \cdot & \\ \cdot & \cdot & \cdot & \cdot & \cdot & \cdot & \cdot \end{bmatrix} \begin{pmatrix} \theta_0'' \\ \theta_1'' \\ \theta_2'' \\ \theta_3'' \\ \theta_4'' \\ \cdot \\ \cdot \end{pmatrix} \\ \begin{pmatrix} B_0 \\ B_1 \\ B_2 \\ B_3 \\ B_4 \\ \cdot \\ \cdot \end{pmatrix} &= \begin{bmatrix} \theta_0' & & & & & & \\ \theta_1' & \theta_0' & & & & & \\ \theta_2' & \theta_1' & \theta_0' & & & & \\ \theta_3' & \theta_2' & \theta_1' & \theta_0' & & & \\ \theta_4' & \theta_3' & \theta_2' & \theta_1' & \theta_0' & & \\ \cdot & \cdot & \cdot & \cdot & \cdot & \cdot & \\ \cdot & \cdot & \cdot & \cdot & \cdot & \cdot & \cdot \end{bmatrix} \begin{pmatrix} \theta_0' \\ \theta_1' \\ \theta_2' \\ \theta_3' \\ \theta_4' \\ \cdot \\ \cdot \end{pmatrix} \end{aligned} \tag{3.3}$$

where $(\cdot)'$ and $(\cdot)''$ are $d/d\xi$ and $d^2/d\xi^2$, respectively. An inverse operator L^{-1} can conveniently be used as a two-fold identifying integral in both sides of Eq. (3.2). Applying the Maclaurin series, yields

$$\theta = \theta(0) + \xi \frac{d\theta(0)}{d\xi} + \psi^2 \left(L^{-1} \sum_{p=0}^{\infty} \theta_p \right) + \psi^2 \left(L^{-1} \sum_{p=0}^{\infty} \xi \theta_p \right) - \beta \left(L^{-1} \sum_{p=0}^{\infty} A_p \right) - \beta \left(L^{-1} \sum_{p=0}^{\infty} B_p \right) \tag{3.4}$$

The first two terms of the right-hand side of Eq. (3.4) can be defined by

$$\theta_0 = 1 + C\xi \tag{3.5}$$

where C is the integral constant.

Considering a finite series of the order p , the higher order terms in Eq. (3.4) are obtained recursively as

$$\theta_{p+1} = \psi^2 \left(L^{-1} \sum_{p=0}^{\infty} \theta_p \right) + \psi^2 \left(L^{-1} \sum_0^p \xi \theta_p \right) - \beta \left(L^{-1} \sum_0^p A_p \right) - \beta \left(L^{-1} \sum_0^p B_p \right) \tag{3.6}$$

with $p \geq 0$.

In the present analysis, the estimation of the first four significant terms, i.e, $n = 0$ to 3, of the temperature field is now expressed in the following form

$$\begin{aligned}\theta_1 &= -\beta L^{-1}A_0 - \beta L^{-1}B_0 + \psi^2 L^{-1}[(1 + \xi)\theta_0] \\ \theta_2 &= -\beta L^{-1}A_1 - \beta L^{-1}B_1 + \psi^2 L^{-1}[(1 + \xi)\theta_1] \\ \theta_3 &= -\beta L^{-1}A_2 - \beta L^{-1}B_2 + \psi^2 L^{-1}[(1 + \xi)\theta_2] \\ \theta_4 &= -\beta L^{-1}A_3 - \beta L^{-1}B_3 + \psi^2 L^{-1}[(1 + \xi)\theta_3]\end{aligned}\quad (3.7)$$

The total temperature field can now be estimated from Eqs. (3.5) and (3.7) to yield a polynomial form

$$\theta = \sum_{i=0}^m K_i \xi^i \quad \text{with} \quad 0 \leq \xi \leq R - 1 \quad (3.8)$$

where K_i are constants. The estimation of K_i are shown in Appendix.

4. Thermal stress formulation

Using the plane stress assumption ($\sigma_z \cong 0$), the stress-displacement relations in the axisymmetric case (Timoshenko and Goodier, 1970) are

$$\begin{aligned}\sigma_r &= \frac{E}{1 - \nu^2} \left[\left(\frac{du_r}{dr} - \alpha T \right) + \nu \left(\frac{u_r}{r} - \alpha T \right) \right] \\ \sigma_\phi &= \frac{E}{1 - \nu^2} \left[\left(\frac{u_r}{r} - \alpha T \right) + \nu \left(\frac{du_r}{dr} - \alpha T \right) \right]\end{aligned}\quad (4.1)$$

Following classical theory of elasticity, the equation of equilibrium in the polar coordinate system for a variable thickness profile is given as

$$\frac{d\sigma_r}{dr} + \frac{\sigma_r}{t} \frac{dt}{dr} + \frac{\sigma_r - \sigma_\phi}{tr} = 0 \quad (4.2)$$

Equations (4.1) and (4.2) yield the equation of equilibrium in terms of the displacement field

$$\frac{d^2u}{dr^2} + \frac{1+n}{r} \frac{du}{dr} + \frac{(\nu n - 1)u}{r^2} - (1 + \nu)\alpha \left(\frac{dT}{dr} + \frac{T}{r}n \right) = 0 \quad (4.3)$$

Introducing a new non-dimensional radius, $\xi_1 = r/r_a$, the following thermo-elastic equation of equilibrium is obtained

$$\frac{d^2u}{d\xi_1^2} + \frac{1+n}{\xi_1} \frac{du}{d\xi_1} + \frac{(\nu n - 1)u}{\xi_1^2} - (1 + \nu)r_a\alpha \left[(T_a - T_\infty) \frac{d\theta}{d\xi_1} + (T_a - T_\infty)n \frac{\theta}{\xi_1} \right] = 0 \quad (4.4)$$

The temperature field in Eq. (3.8) is now modified by the new non-dimensional radius ξ_1 and can be expressed in an analogous form

$$\theta = \sum_{i=0}^m L_i \xi_1^i \quad 1 \leq \xi_1 \leq R \quad (4.5)$$

Equations (4.4) and (4.5) give together a new form of the equilibrium equation

$$\frac{d^2u}{d\xi_1^2} + \frac{1+n}{\xi_1} \frac{du}{d\xi_1} + \frac{(\nu n - 1)u}{\xi_1^2} = (1 + \nu)r_a\chi \left[\sum_{i=0}^m (i + n)L_i \xi_1^{i-1} \right] \quad (4.6)$$

where $\chi = \alpha(T_b - T_\infty)$ is a non-dimensional coefficient of thermal expansion.

The complete solution to Eq. (4.6) consists of a homogeneous and a particular solution, and is given as

$$u = D_1 \xi_1^{\eta_1} + D_2 \xi_1^{\eta_2} + \sum_{i=0}^m (1 + \nu) \chi r_a \frac{L_i(i+n)}{n(1+i+\nu) + i(i+2)} \xi_1^{i+1} \quad (4.7)$$

where D_1 , D_2 , and $\eta_{1,2} = -(n/2) \pm \sqrt{1 - \nu n + n^2/4}$ are constants. The stress field Eq. (4.1) can now be expressed in the non-dimensional form

$$\begin{aligned} \bar{\sigma}_r &= \left[\left(\frac{du}{d\xi_1} + \nu \frac{u}{\xi_1} \right) \frac{1}{r_a} - \chi(1 + \nu)\theta \right] \frac{1}{1 - \nu^2} \\ \bar{\sigma}_\phi &= \left[\left(\frac{u}{\xi_1} + \nu \frac{du}{d\xi_1} \right) \frac{1}{r_a} - \chi(1 + \nu)\theta \right] \frac{1}{1 - \nu^2} \end{aligned} \quad (4.8)$$

where $\bar{\sigma}_r = \sigma_r/E$ and $\bar{\sigma}_\phi = \sigma_\phi/E$ are non-dimensional radial and tangential stresses, respectively. The near closed form solution for the stress field is obtained by combining Eq. (4.7) and Eq. (4.8)

$$\begin{aligned} \bar{\sigma}_r &= A \xi_1^{\eta_1-1} + B \xi_1^{\eta_2-1} - \chi \sum_{i=0}^m \frac{i L_i}{n(1+i+\nu) + i(i+2)} \xi_1^i \\ \bar{\sigma}_\phi &= -\eta_2 A \xi_1^{\eta_1-1} - \eta_1 B \xi_1^{\eta_2-1} - \chi \sum_{i=0}^m \frac{i(n+i+1) L_i}{n(1+i+\nu) + i(i+2)} \xi_1^i \end{aligned} \quad (4.9)$$

where

$$A = \frac{D_1(\eta_1 + \nu)}{r_a(1 - \nu^2)} \quad B = \frac{D_2(\eta_2 + \nu)}{r_a(1 - \nu^2)}$$

are constants estimated from the boundary conditions $\bar{\sigma}_r = 0$ at $\xi_1 = 1$ and R .

5. Results and discussion

A near closed form solution for thermal stresses in the isotropic annular fin with a hyperbolic profile is derived. ADM is employed to obtain the non-dimensional temperature field represented in a polynomial form. The integral constants C are evaluated using the minimum decomposition error $J = \theta_{i+1} - \theta_i$, ($J \leq 10^{-4}$) approach. Figure 2 represents the values of the integral constant C for different values of the variable thermal conductivity parameter. The accepted C values are the x -values corresponding to the minimum decomposition error in each case. These constants directly influence the variation of local temperature distribution. The determined values of C for $\psi = 0.2$ and $\beta = 0.3$, 0 and -0.3 are -0.1737 , -0.2167 and -0.2758 , respectively.

With the best of literature search, this work is the first attempt to estimate thermal stresses in an annular fin with a hyperbolic profile along with a variable thermal conductivity. Due to this limitation, stress fields for the hyperbolic fin profile obtained from the present formulation could not be compared. However, the present formulation for stress fields can be used to obtain results for an annular fin of uniform thickness by setting $n = 0$ in Eq. (4.9). These stress field results are compared with those by Chiu and Chen (2002) shown in Fig. 3. The results in Fig. 3 take into account the same parameters, $\kappa = \pm 0.00018$, $\xi_1 = 1$ to 3, $h = 50 \text{ W}/(\text{m}^2\text{K})$, $k_\infty = 186 \text{ W}/(\text{mK})$ and $t(= h_a) = 0.004 \text{ m}$ and boundary conditions for clarity of the comparison. Both temperature and stress fields in uniform thickness obtained from Eqs. (4.5) and (4.9) visibly reveal close agreement.

Figure 4 illustrates the effect of various thermo-mechanical parameters on the non-dimensional temperature and stress field. Unless mentioned otherwise, the numerical values

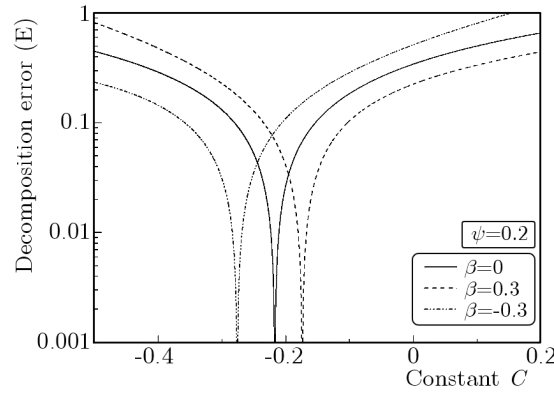


Fig. 2. Estimation of the integral constant using the minimum decomposition error approach

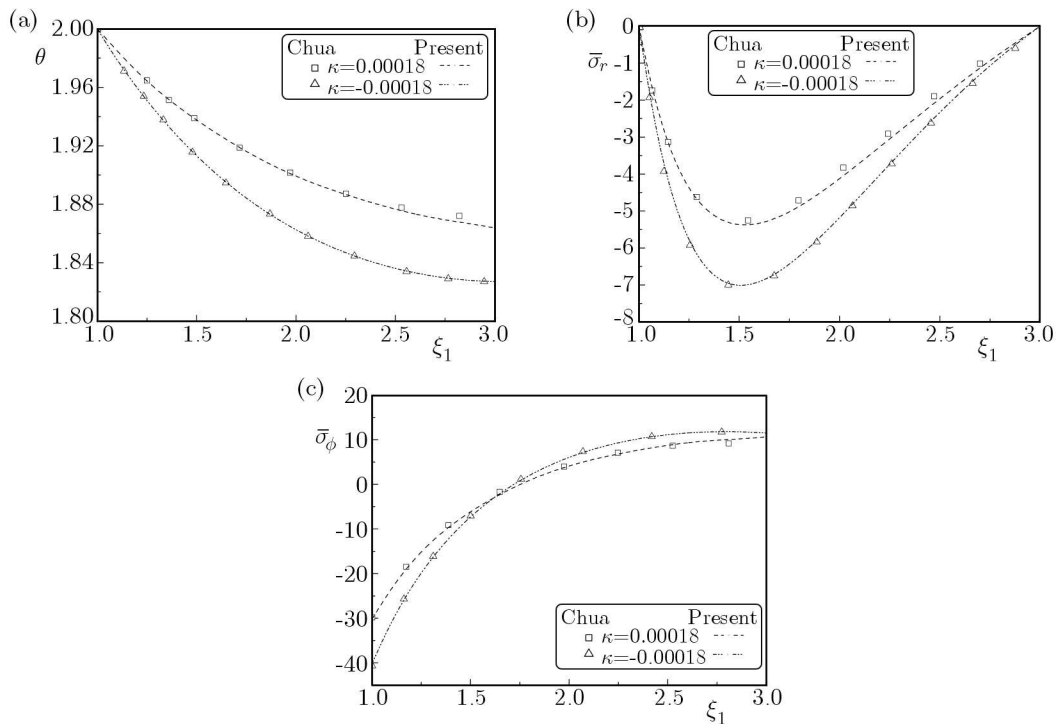


Fig. 3. Comparison of the results for (a) temperature distribution, (b) radial stress distribution and (c) tangential stress distribution for an annular fin with uniform thickness. The results have been estimated from the present closed form solution for the fin with variable thickness by setting $n = 0$

of the non-dimensional parameters are taken to be $\beta = 0$, $\psi = 0.2$, $\chi = 1$ and $\nu = 0.3$ for all the cases. In Fig. 4a, it can be seen that the steeper temperature gradient is associated with a lower variable thermal conductivity parameter β . As a result, the mean temperature difference between the base and fin tip is decreased with an increase in β . On the other hand, higher thermo-geometric parameter ψ induces higher temperature gradient. Lower thermo-geometric parameter indicates the fin as thermally thin with less thermal resistivity. Thus, the heat conduction inside the body is much faster than the heat convection away from the surface. Furthermore, it can be observed that the coefficient of thermal expansion χ and Poisson's ratio ν do not affect the temperature field. Nevertheless, the variation of stresses is influenced by all thermo-mechanical parameters. The stress field in Eq. (4.9) can be seen to vary linearly with the coefficient of thermal expansion. Consequently, the stress field can be changed with modification in the coefficient of thermal expansion by n -times. Thus, the maximum of non-dimensional radial and tangential

stress magnitudes: -0.0558 and -0.19523 increase to -0.1126 and -0.39046 , respectively, by a change in the coefficient of thermal expansion from 1 to 2 (negative value indicates compressive stress) shown in Fig. 4b and 4c. The parameters β and ψ significantly influence the variation of stress fields. The stress magnitude increases with an increment of ψ , and decreases with an increase in β . Interestingly, the stress field is very marginally affected by Poisson's ratio ν (Fig. 4). This result is reasonable for axisymmetric plane stress assumptions in the analysis of the annular fin with a hyperbolic profile.

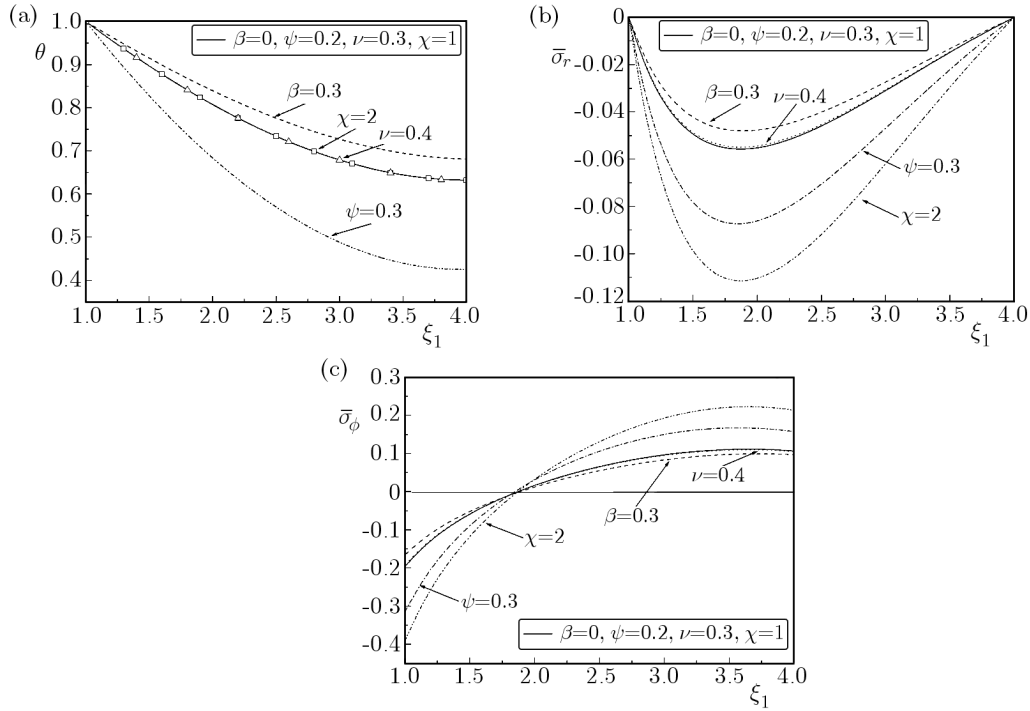


Fig. 4. Effect of various thermo-mechanical properties on (a) temperature distribution, (b) radial stress field, and (c) tangential stress field. Unless mentioned otherwise, $\beta = 0$, $\psi = 0.2$, $\chi = 1$ and $\nu = 0.3$

A comparison of the stress field between a fin of uniform thickness and that of a hyperbolic profile keeping the same material volume condition are depicted in Fig. 5a and 5b. Except for the profile geometry, all other parameters, i.e. $V = 4.0212 \cdot 10^{-5} \text{ m}^3$, $\kappa = 0$, $h = 50 \text{ W}/(\text{m}^2\text{K})$, $k_\infty = 186 \text{ W}/(\text{mK})$ (Chiu and Chen, 2002) are maintained the same in both profiles. Herein, the maximum value of $\bar{\sigma}_r$ and $\bar{\sigma}_\phi$ (compressive) are found to be less in the hyperbolic profile than in the uniform thickness condition. The $\bar{\sigma}_r$ variation with the length parameter indicates a better symmetric distribution over dimensionless radius in the hyperbolic profile than that of the uniform thickness profile.

Furthermore, the $\bar{\sigma}_\phi$ (compressive) variation in the hyperbolic profile is significantly lower compared to the uniform thickness case near to the base of the fin. A marginally higher $\bar{\sigma}_\phi$ (tensile) variation is observed in the hyperbolic profile near the fin tip. These results reveal that the fin with the hyperbolic profile is much safer from the material failure view point than that of the uniform thickness profile due to the lower stress level. Conversely, for the same stress field, the fin with the hyperbolic profile is much more compact and requires less material.

Figure 6 shows the surface plot of the temperature and stress field along the radial direction for variable β and ψ . The non-dimensional temperature surfaces (Fig. 6a) reveal that the temperature difference ($\Delta\theta = \theta_{r_a} - \theta_\infty$) from the base to tip gradually increases with a decrease in variable thermal conductivity parameters. On the other hand, the reverse nature is observed with the variation of the thermo-geometric parameter. The results obtained suggest that for a

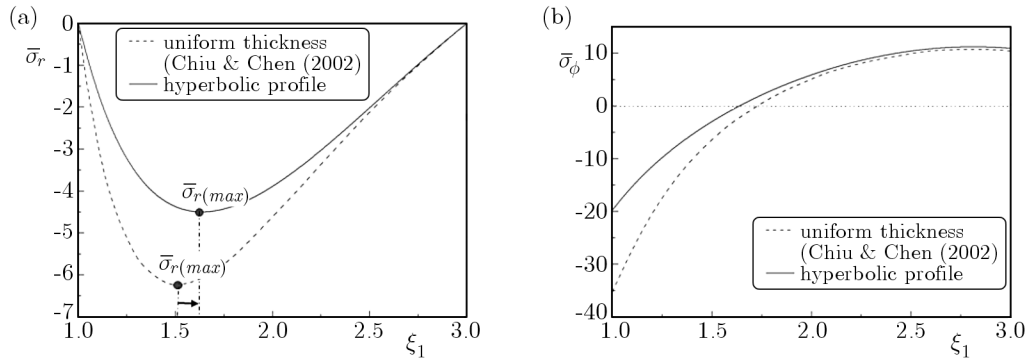


Fig. 5. Comparison of (a) radial stress field and (b) tangential stress field between the uniform and hyperbolic annular fin. The volume and other properties are the same in both cases

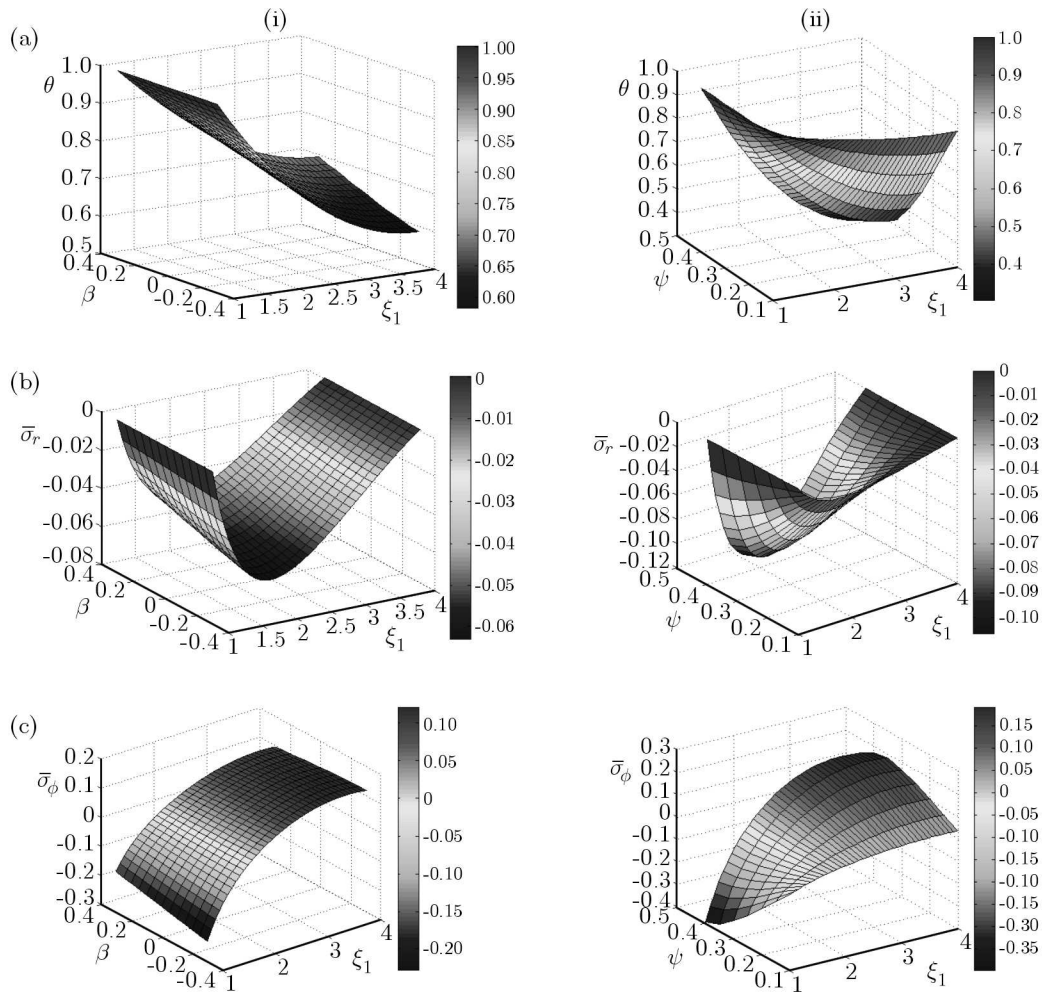


Fig. 6. Surface domain for (a) temperature field, (b) radial stress field, and (c) tangential stress field along the radial direction ξ_1 with the variation of thermal parameters (i) β and (ii) ψ

specific surface geometry the heat transfer can be enhanced either by decreasing the thermo-geometric parameter or by selecting materials with higher thermal conductivity. In addition to the heat transfer enhancement, the investigation of material failure is also an important aspect for the designer of the fin. The surface plots for $\bar{\sigma}_r$ and $\bar{\sigma}_\phi$ distribution with the variation of β and ψ are depicted in Fig. 6b and 6c, respectively. From the surface representation of stress distribution, it is apparent that the maximum $\bar{\sigma}_r$ (compressive) and $\bar{\sigma}_\phi$ (compressive or tensile)

are achievable either with a lower value of β or by the use of a higher thermo-geometric parameter ψ . The lower value of β induces high thermal resistance. As a consequence, poor heat transfer through the fin material causes a higher value of the local temperature difference between two neighbouring material points along the radial direction. Thus, a very low heat transfer can lead to the excessively induced thermal stress that reduces the fin life. Therefore, a study of the maximum limit of heat dissipation ability and the maximum limit of thermal stresses induced is necessary for better design.

6. Conclusions

A method of analysis for the determination of thermal stresses in an annular fin with a hyperbolic profile using variable thermal conductivity is presented. The ADM coupled with thermo-elasticity approach is chosen to derive an approximate analytical solution for thermal stresses. In order to validate the present analytical solution, the results are compared with the results available in literature and found to be in very good agreement. The effects of various non-dimensional parameters on the temperature field and stress fields are also investigated. Based on the present study, the remarkable outcomes are:

- i. ADM is useful and efficient to obtain a general closed form solution for the stress field in fin of a hyperbolic profile as well as of a uniform thickness with variable thermal conductivity.
- ii. The temperature field is influenced by the parameters β and ψ only, while, the stress fields are governed by all non-dimensional parameters β , ψ , χ and ν . Notably, the effect of Poisson's ratio ν on the stress field is observable only in hyperbolic fin profile. And this effect is very insignificant compared to the contribution of other parameters.
- iii. The variation of radial stress with the length parameter exhibits better symmetric distribution in the hyperbolic profile than that of the uniform thickness.
- iv. The surface plot for the temperature field and stress field with different values of β and ψ discloses the nature of thermo-parametric dependence on the temperature and stress field.
- v. Improvement in heat transfer can be attained either by increasing the thermal conductivity parameter or setting a lower thermo-geometric parameter. The lower value of local temperature difference may induce higher thermal stresses in the part. So, an appropriate combination of the heat dissipation limit and induced stress field can only be achieved with an efficient design of the fin profile. The hyperbolic section of the fin appears to be a better choice in all respects.
- vi. The present method of analysis is expected to help understanding of the heat transfer phenomena and thermal stress development in the hyperbolic fin.

Appendix

The K_i estimation (14 terms considered in this study) are given below

$$\begin{aligned}
 K_0 &= 1 & K_1 &= C \\
 K_2 &= \frac{1}{2}(-C^2\beta + \psi^2 + C^2\beta^2 - \psi^2\beta - C^2\beta^3 + \psi^2\beta^2 + C^2\beta^4 - \psi^2\beta^3) \\
 K_3 &= \frac{1}{6}(C\psi^2 + \psi^2 + 3C^3\beta^2 - 4C\beta\psi^2 - \beta\psi^2 - 6C^3\beta^3 + \beta^2\psi^2 + 7C\beta^2\psi^2 + 7C^3\beta^4 \\
 &\quad - 8C\psi^2\beta^3 - \psi^2\beta^3)
 \end{aligned}$$

$$\begin{aligned}
K_4 &= \frac{1}{24}(2C\psi^2 - 5C^2\beta\psi^2 - 6C\beta\psi^2 + \psi^4 - 15C^4\beta^3 + 28C^2\beta^2\psi^2 + 10C\beta^2\psi^2 - 5\beta\psi^4 \\
&\quad + 32C^4\beta^4 + 4C^3\beta^4 + C^2\beta^3 - 53C^2\beta^3\psi^2 - 16C\beta^3\psi^2 - \beta^2\psi^2 + 7\beta^2\psi^4) \\
K_5 &= \frac{1}{120}(-13C^2\beta\psi^2 + C\psi^4 + 4\psi^4 + 38C^3\beta^2\psi^2 + 56C^2\beta^2\psi^2 - 20C\beta\psi^4 - 18\beta\psi^4 \\
&\quad + 78C^5\beta^4 + 12C^4\beta^4 - 205C^2\beta^3\psi^2 - 120C^2\beta^3\psi^2 - 2C\beta^3\psi^2 + 96C\beta^2\psi^4 + 50\psi^4) \\
K_6 &= \frac{1}{720}(6C\psi^4 + 4\psi^4 + 120C^3\beta^2\psi^2 - 21C^2\beta\psi^4 - 86C\beta\psi^4 - 18\beta\psi^4 + \psi^6 - 116C^4\beta^3 \\
&\quad + 30C^5\beta^4 - 272C^3\beta^3 - 91C^4\beta^3\psi^2 - 156C^3\beta^3\psi^2 - 20C^2\beta^3\psi^2 + 193C\beta^2\psi^2 \\
&\quad - 48C^3\beta^2\psi^2 + 124C^2\beta^2\psi^4 + 172C\beta^2\psi^4 + 16\beta^2\psi^4 + 22\beta^2\psi^2 - 8\beta\psi^4 - 12\beta\psi^6) \\
K_7 &= \frac{1}{5040}(10C\psi^4 - 150C^2\beta\psi^4 - 128C\beta\psi^4 + C\psi^6 + 9\psi^6 - 1234C^4\beta^3\psi^2 + 329C^3\beta^2\psi^4 \\
&\quad + 1848C^2\beta^2\psi^4 + 584C\beta^2\psi^4 - 82C\beta\psi^6 - 112C^3\beta^3\psi^2 - 151\beta\psi^6) \\
K_8 &= \frac{1}{40320}(-298C^2\beta\psi^4 + 12C\psi^6 + 28\psi^6 + 5644C^3\beta^2\psi^4 + 5822C^2\beta^2\psi^4 - 243C^2\beta\psi^6 \\
&\quad - 2020C\beta\psi^6 - 1310\beta\psi^6 - 240C^4\beta^3\psi^6 + 42C^3\beta^2\psi^8 + 172C^2\beta^2\psi^8 + 36C\beta^2\psi^8 \\
&\quad - 2C\beta\psi^{10} + \psi^8) \\
K_9 &= \frac{1}{362880}(52C\psi^6 + 28\psi^6 + 6792C^3\beta^2\psi^4 + 256C^2\beta^2\psi^4 - 1055C^2\beta\psi^6 - 3022C\beta\psi^6 \\
&\quad - 686\beta\psi^6 + C\psi^8 + 16\psi^8) \\
K_{10} &= \frac{1}{1814400}(40C\psi^6 + 298C^3\beta^2\psi^4 - 3529C^2\beta\psi^6 - 2692C\beta\psi^6 + 10C\psi^8 + 50\psi^8) \\
K_{11} &= \frac{1}{19958400}(-5053C^2\beta\psi^6 - 28C\beta\psi^6 + 80C\psi^8 + 140\psi^8) \\
K_{12} &= \frac{1}{11975040}(-4C^2\beta\psi^6 + 15C\psi^8 + 7\psi^8) \\
K_{13} &= \frac{1}{7076160}C\psi^8
\end{aligned}$$

References

1. ADOMIAN G., 1988, *Non-Linear Stochastic System Theory and Application to Physics*, Kluwer Academic Publisher, Dordrecht
2. AKSOY I.G., 2013, Adomian decomposition method for heat conduction in an annular fin of hyperbolic profile with temperature dependent thermal conductivity, *Journal of Thermal Science and Technology*, **33**, 1-8
3. BEHNIA M., COPELAND D., SOODPHADAKEE D., 1998, A comparison of heat sink geometries for laminar forced convection, *Proceedings of the Sixth Intersociety Conference on Thermal and Thermomechanical Phenomena*
4. CHIU C.H., CHEN C.K., 2002, Application of the decomposition method to the thermal stresses in isotropic circular fins with temperature-dependent thermal conductivity, *Acta Mechanica*, **157**, 147-158
5. KERN Q.D., KRAUS D.A., 1972, *Extended Surface Heat Transfer*, McGraw-Hill, New York, USA
6. KRAUS A.D., AZIZ A., WELTY, J.R., 2001, *Extended Surface Heat Transfer*, John Wiley and Sons, New York
7. MALLICK A., GHOSAL S., SARKAR P.K., RANJAN R., 2015, Homotopy perturbation method for thermal stresses in an annular fin with variable thermal conductivity, *Journal of Thermal Stresses*, **38**, 110-132

8. MIANSARI M.O., GANJI D.D., MIANSARI M.E., 2008, Application of He's variational iteration method to nonlinear heat transfer equations, *Physics Letters A*, **372**, 770-785
9. MOKHEIMER E.M.A., 2002, Performance of annular fins with different profiles subject to variable heat transfer coefficient, *International Journal of Heat and Mass Transfer*, **45**, 3631-3642
10. MORADI A., 2011, Analytical solution for fin with temperature dependent heat transfer coefficient, *International Journal of Applied Science and Engineering*, **3**, 1-12
11. TIMOSHENKO S.P., GOODIER J.N., 1970, *Theory of Elasticity*, McGraw-Hill, New York
12. YEH R.H., 1997, An analytical study of the optimum dimensions of rectangular fins and cylindrical pin fins, *International Journal of Heat and Mass Transfer*, **40**, 3607-3615

Manuscript received May 29, 2015; accepted for print August 25, 2015

SOME ASPECTS OF DYNAMIC COUPLED RESPONSE OF FUNCTIONALLY GRADED THIN-WALLED COLUMNS WITH SQUARE CROSS-SECTIONS UNDER IN-PLANE PULSE COMPRESSION

ZBIGNIEW KOŁAKOWSKI

Lodz University of Technology, Department of Strength of Materials, Łódź, Poland; e-mail: zbigniew.kolakowski@p.lodz.pl

ANDRZEJ TETER

Lublin University of Technology, Department of Applied Mechanics, Lublin, Poland; e-mail: a.teter@pollub.pl

The present paper deals with a dynamic coupled response of functionally graded columns with a quadratic cross-section subjected to an in-plane pulse loading. An Al-TiC metal-ceramic material is applied. It is assumed that functionally graded materials (FGMs) are subject to Hooke's law. The thin-walled structures are simply supported at the ends. This study is devoted to the stability problem of rectangular dynamic pulse load. The effects of temperature, wave propagation and damping are neglected. In order to obtain the equations of motion of individual plates, the classic laminate plate theory (CLPT) has been modified in such a way that it additionally accounts for all components of inertial forces. A plate model is adopted for the structures. The problem of an interaction of the global mode with the local ones is concerned (i.e., a three-modes approach). Attention has been focused on some unexpected aspects related to dynamic interactive buckling of columns having two axes of the cross-section symmetry. In the present study, a new approach to the description of this phenomenon, based on Koiter's theory, has been applied.

Keywords: FGM, dynamic response, interactive buckling, thin-walled structures, compression, pulse load

1. Introduction

The dynamic buckling or dynamic response takes place when a pulse load of a mean amplitude and a pulse duration comparable to the fundamental natural flexural vibration period occurs in compression of the thin-walled column. In this case, effects of damping can be neglected in practice. When the amplitude of load is high, then the structure can vibrate very strongly or can move divergently, which is caused by dynamic buckling. One can determine the critical amplitude of load using various criteria. In the literature on this problem, a lot of criteria concerning dynamic stability have been adopted. The most widely used is the Budiansky-Hutchinson criterion (Kubiak, 2007, 2013), in which it is assumed that the dynamic stability loss occurs when the maximum structure deflection grows rapidly at a small variation in the load amplitude. Other criteria have been discussed in many papers: Ari-Gur and Simonetta (1979), Petry and Fahlbusch (2000), Kubiak (2007, 2013), Teter (2011).

Dynamic global and local buckling instabilities of component functionally graded plates (the so-called FG plates) of structures subjected to conservative loads have been taken into account. The problem of an interaction of the global mode with the local ones is very interesting. The concept of interactive buckling involves the general asymptotic theory of stability. Among all versions of the general nonlinear theory, Koiter's theory (van der Heijden, 2009) of conservative systems is the most popular one (Kołakowski *et al.*, 1999; Teter and Kołakowski, 2004; Kołakowski and Kubiak, 2005; Kołakowski and Królak, 2006).

In the present study, the classical laminate plate theory (CLPT) (Jones, 1999; Reddy, 2004) is employed to obtain the governing equations of the thin FG plate equilibrium. In order to obtain the equations of individual plates for the asymptotic analytical-numerical method, the nonlinear theory of composite plates has been modified in such a way that it additionally accounts for forces of inertia. The differential equations of motion have been obtained from Hamilton's Principle, taking into account Lagrange's description, full Green's strain tensor, the second Piola-Kirchhoff's stress tensor and all components of inertia forces. The study is based on the numerical method of the transition matrix using Godunov's orthogonalization (Kołakowski *et al.*, 1999; Teter and Kołakowski, 2004; Kołakowski and Kubiak, 2005; Kołakowski and Królak, 2006). A plate model of the column has been adopted in the study to describe global buckling, which leads to lowering the theoretical value of the limit load. The solution method assumed in this study enables analysis of interactions of all buckling modes. The nonlinear equations of dynamic instability are solved with the modified Runge-Kutta method.

The nonlinear analysis of Functionally Graded plates and shells devoted to basic types of loads is covered in the monograph by Hui-Shen (2009). The shear deformation effect is employed in the framework of Reddy's higher order shear deformation theory (HSDT) (Reddy, 2000; Reddy, 2004). Reddy (2000) presents a comparison of applications of the first order shear deformation theory (FSDT) and the classical lamination plate theory (CLPT) to functionally graded plates. The discrepancy between both theories is of 2% in the calculated deflections of the plates under analysis. The buckling and postbuckling problem of FG plates is discussed, for example, in papers by Reddy (2000), Samsam Shariata *et al.* (2005), Kołakowski *et al.* (2015). Due to the complexity of buckling problems of FG structures under compound mechanical and thermal loads, the finite element method (FEM) is the only solution possible in many cases. Therefore, in the literature, one can find many papers which present results of a solution to different problems of FG structure buckling obtained with an application of the FEM, see for example: Birman and Byrd (2007), Panda and Ray (2008), Na and Kim (2009), Kołakowski *et al.* (2015).

2. Formulation of the problem

Long thin-walled prismatic columns of length l , composed of plane rectangular plate segments interconnected along longitudinal edges and simply supported at both ends, are considered. All materials the FG plates are made of are subject to Hooke's law. The material properties are assumed to be temperature independent. A plate model is adopted for the structures. Wave propagation and damping effects have been neglected in the present study, as it is done in the majority of works devoted to dynamic stability. In the present study, the classical laminate plate theory (CLPT) (Jones, 1999; Reddy, 2004) is employed to obtain the governing equations of the thin FG structure equilibrium (Kołakowski and Królak, 2006; Panda and Ray, 2008). For the plate component, precise geometrical relationships are assumed in order to enable consideration of both out-of-plane and in-plane bending of the plate (Kubiak, 2007, 2013; Teter, 2007, 2011; Kołakowski *et al.*, 1999; Teter and Kołakowski, 2001, 2004, 2005; Kołakowski and Kubiak, 2005; Kołakowski and Królak, 2006)

$$\boldsymbol{\varepsilon} = \begin{Bmatrix} \varepsilon_x \\ \varepsilon_y \\ 2\varepsilon_{xy} \end{Bmatrix} = \begin{Bmatrix} u_{,x} + \frac{1}{2}(w_{,x}^2 + v_{,x}^2 + u_{,x}^2) \\ v_{,y} + \frac{1}{2}(w_{,y}^2 + u_{,y}^2 + v_{,y}^2) \\ u_{,y} + v_{,x} + w_{,x}w_{,y} + u_{,x}u_{,y} + v_{,x}v_{,y} \end{Bmatrix} \quad \boldsymbol{\kappa} = \begin{Bmatrix} \kappa_x \\ \kappa_y \\ \kappa_{xy} \end{Bmatrix} = \begin{Bmatrix} -w_{,xx} \\ -w_{,yy} \\ -2w_{,xy} \end{Bmatrix} \quad (2.1)$$

where u , v , w are components of the displacement vector of the plate in the x , y , z axis direction, respectively, and the plane xy overlaps the mid-plane before its buckling.

According to the rule of mixture, the properties of the functionally graded material (E – Young’s modulus, ν – Poisson’s ratio, ρ – density) can be expressed as follows

$$\begin{aligned} E(z) &= E_m + (E_c - E_m) \left(\frac{z}{h} + \frac{1}{2} \right)^q & \nu(z) &= \nu_m + (\nu_c - \nu_m) \left(\frac{z}{h} + \frac{1}{2} \right)^q \\ \rho(z) &= \rho_m + (\rho_c - \rho_m) \left(\frac{z}{h} + \frac{1}{2} \right)^q \end{aligned} \quad (2.2)$$

where the indices m and c refer to the metal and ceramic material, respectively, and q is the fraction exponent.

Using the classical laminate plate theory (CLPT) (Jones, 1999; Reddy, 2004), the stress and moment resultants ($\overline{\mathbf{N}}$, $\overline{\mathbf{M}}$) are defined as (Jones, 1999; Teter and Kołakowski, 2005, Kołakowski and Królak, 2006)

$$\begin{Bmatrix} \overline{\mathbf{N}} \\ \overline{\mathbf{M}} \end{Bmatrix} = \begin{bmatrix} \mathbf{A} & \mathbf{B} \\ \mathbf{B} & \mathbf{D} \end{bmatrix} \begin{Bmatrix} \varepsilon \\ \kappa \end{Bmatrix} \quad (2.3)$$

where \mathbf{A} , \mathbf{B} , \mathbf{D} are extensional, coupling and bending stiffness matrices, respectively, for the FG structure. Their components are listed below

$$\begin{aligned} A_{11} = A_{22} &= \int_{-h/2}^{h/2} \frac{E(z)}{1 - \nu^2(z)} dz & A_{12} = A_{21} &= \int_{-h/2}^{h/2} \frac{E(z)\nu(z)}{1 - \nu^2(z)} dz \\ A_{66} &= \int_{-h/2}^{h/2} \frac{E(z)}{2[1 + \nu(z)]} dz & A_{16} = A_{61} &= 0 \\ B_{11} = B_{22} &= \int_{-h/2}^{h/2} \frac{E(z)}{1 - \nu^2(z)} z dz & B_{12} = B_{21} &= \int_{-h/2}^{h/2} \frac{E(z)\nu(z)}{1 - \nu^2(z)} z dz \\ B_{66} &= \int_{-h/2}^{h/2} \frac{E(z)}{2[1 + \nu(z)]} z dz & B_{16} = B_{61} &= 0 \\ D_{11} = D_{22} &= \int_{-h/2}^{h/2} \frac{E(z)}{1 - \nu^2(z)} z^2 dz & D_{12} = D_{21} &= \int_{-h/2}^{h/2} \frac{E(z)\nu(z)}{1 - \nu^2(z)} z^2 dz \\ D_{66} &= \int_{-h/2}^{h/2} \frac{E(z)}{2[1 + \nu(z)]} z^2 dz & D_{16} = D_{61} &= 0 \end{aligned} \quad (2.4)$$

Due to the presence of the nontrivial submatrix \mathbf{B} , the coupling between extensional and bending deformations exists as it is in the case of unsymmetrical laminated plates (Jones, 1999; Kołakowski *et al.*, 2015). An extensional force results not only in extensional deformations, but also bending of the FG plate. Moreover, such a plate cannot be subjected to the moment without suffering simultaneously from extension of the middle surface.

The nonlinear problem of dynamic stability has been solved with the asymptotic perturbation method. Let λ be a load factor. The displacement fields $\overline{\mathbf{U}}$ and the sectional force fields $\overline{\mathbf{N}}$ (Koiter’s type expansion for the static buckling problem (van der Heijden, 2009)) have been expanded into power series with respect to the dimensionless amplitude of the r -th mode deflection ζ_r (normalized in the given case by the condition of equality of the maximum deflection to the thickness of the first component plate h_1) (Kołakowski *et al.*, 1999; Teter and Kołakowski, 2001, 2004, 2005; Teter, 2007, 2011; Kołakowski and Kubiak, 2005; Kołakowski and Królak, 2006; Kubiak, 2007, 2013; van der Heijden, 2009)

$$\begin{aligned} \overline{\mathbf{U}} &= \lambda(t) \overline{\mathbf{U}}_0 + \zeta_r(t) \overline{\mathbf{U}}_r + \zeta_r(t) \zeta_q(t) \overline{\mathbf{U}}_{qr} + \dots \\ \overline{\mathbf{N}} &= \lambda(t) \overline{\mathbf{N}}_0 + \zeta_r(t) \overline{\mathbf{N}}_r + \zeta_r(t) \zeta_q(t) \overline{\mathbf{N}}_{qr} + \dots \end{aligned} \quad (2.5)$$

where the pre-buckling static fields are $\overline{\mathbf{U}}_0$, $\overline{\mathbf{N}}_0$, the first nonlinear order fields are $\overline{\mathbf{U}}_r$, $\overline{\mathbf{N}}_r$ (the eigenvalues and eigenvectors problems) and the second nonlinear order fields – $\overline{\mathbf{U}}_{qr}$, $\overline{\mathbf{N}}_{qr}$,

respectively. The range of indexes is $[1, J]$, where J is the number of interacting modes. The summation is supposed on the repeated indexes.

If the structure contains the geometric imperfections $\bar{\mathbf{U}}^*$ (only linear initial imperfections determined by the shape of r -th buckling modes i.e., $\bar{\mathbf{U}}^* = \zeta_r^* \mathbf{U}_r$), then the total energy of the structures can be written in the form (Schokker *et al.*, 1996; Kołakowski *et al.*, 1999; Teter and Kołakowski, 2004; Teter, 2007, 2011; Kołakowski and Kubiak, 2005; Kołakowski and Królak, 2006; Kubiak, 2007, 2013)

$$\begin{aligned} \Pi = & -\frac{1}{2}\sigma^2(t)\bar{a}_0 + \frac{1}{2}\sum_{r=1}^J \bar{a}_r \zeta_r^2(t) \left(1 - \frac{\sigma(t)}{\sigma_r}\right) + \frac{1}{3}\sum_p^J \sum_q^J \sum_r^J \bar{a}_{pqr} \zeta_p(t) \zeta_q(t) \zeta_r(t) \\ & + \frac{1}{4}\sum_r^J \bar{b}_{rrrr} \zeta_r^4(t) - \sum_r^J \frac{\sigma(t)}{\sigma_r} \bar{a}_r \zeta_r^* \zeta_r(t) + \frac{1}{2}\sum_r^J m_r \zeta_{r,t}^2(t) \end{aligned} \quad (2.6)$$

Then, Hamilton's principle leads to the following Lagrange's equation (i.e. equations of motion)

$$\zeta_{r,tt} + \Omega_r^2 \zeta_r + \omega_r^2 \left(a_{pqr} \zeta_p \zeta_q + b_{rrrr} \zeta_r^3 - \frac{\sigma}{\sigma_r} \zeta_r^* + \dots \right) = 0 \quad \text{for } r = 1, \dots, J \quad (2.7)$$

where ζ_r is the dimensionless amplitude of the r -th buckling mode, σ_r , ω_r , ζ_r^* – critical stress instead of the load parameter λ_r of the r -th buckling mode, circular frequency of free vibrations and dimensionless amplitude of the initial deflection corresponding to the r -th buckling mode, respectively. In equations of motion (2.7), the inertia forces of the pre-buckling state and the second order state have been neglected (Sridharan *et al.*, 1984; Schokker, 1996; Warmiński and Teter, 2012). The coefficients in equilibrium equations (2.7) are given in papers: Sridharan *et al.* (1984), Kołakowski (1996), Schokker (1996), Kołakowski *et al.* (1999), Teter and Kołakowski (2004), Teter (2007, 2011), Kołakowski and Kubiak (2005), Kołakowski and Królak (2006), Kubiak (2007, 2013), Warmiński and Teter (2012), Kołakowski and Mania (2013). In the former parts of this paper, in relationships (2.7), λ_r has been replaced with σ_r , whereas λ with σ , correspondingly.

The initial conditions have been assumed in the form

$$\zeta_r(t=0) = 0 \quad \zeta_{r,t}(t=0) = 0 \quad (2.8)$$

In equation (2.7), the quantity Ω_r^2 depending on the values of σ/σ_r can take the following values:

- if $\sigma/\sigma_r < 1$, then $\Omega_r^2 = \omega_r^2(1 - \sigma/\sigma_r) > 0$, where Ω_r can be called the equivalent angular velocity. The linear general solution to equation (2.9) in the case of an ideal structure (that is to say, for $\zeta_r^* = 0$) are trigonometric functions;
- if $\sigma/\sigma_r = 1$, then $\Omega_r^2 = 0$;
- if $\sigma/\sigma_r > 1$, then $\Omega_r^2 < 0$, where Ω_r can be called the equivalent growing function and then the linear general solution to equation (2.7) for $\zeta_r^* = 0$ are hyperbolic functions.

The nonlinear static stability (i.e., for $\zeta_{r,tt}$ in (2.7)) of thin-walled multilayer structures in the first order approximation of Koiter's theory is solved with the modified analytical-numerical method (ANM) presented by Kołakowski and Królak (2006). The analytical-numerical method (ANM) should consider also the second order approximation of the theory in the analysis of postbuckling of elastic composite structures. The second order postbuckling coefficients were estimated with the semi-analytical method (SAM) (Kołakowski, 1996) modified by the solution method in Kołakowski and Mania (2013). In the semi-analytical method (SAM) for static problems, one postulates to determine approximated values of the coefficients b_{rrrr} in (2.7) on the

basis of the linear buckling problem. This approach allows the values of the coefficients a_{pqr} in (2.7) – according to the applied nonlinear Byskov and Hutchinson theory (Byskov and Hutchinson, 1977) – to be determined precisely. The natural frequencies have been determined analogously as in Teter and Kołakowski (2003), whereas the problem of interactive dynamic buckling (2.7) has been solved by means of the Runge-Kutta numerical method modified by Hairer and Wanner.

In the present paper, we assume that the buckling modes are the same as the vibration modes, so the solution to the eigenvalue problem is sought for various values of the m -th harmonic. Values of the natural frequencies are determined taking into account all components of inertia forces.

For static problems, Koiter and van der Neut (Kubiak, 2013) have proposed a technique in which an interaction of the overall mode with two local modes having the same wavelength (i.e., a three-mode approach $J = 3$) has been considered. The fundamental local mode is henceforth called “primary” and the nontrivial higher mode (having the same wavelength as the “primary” one), corresponding to the mode triggered by the overall long-wave mode, is called “secondary”. In total energy, the coefficients of the cubic terms $\zeta_1\zeta_2^2$, $\zeta_1\zeta_3^2$ and $\zeta_1\zeta_2\zeta_3$ (where ζ_j is the amplitude of the r -th buckling mode and the index is: 1 for the global mode, 2 for the primary local buckling mode, and 3 for the secondary local mode) are the key terms governing the interaction. In the analysis of the column with doubly symmetric cross-sections, the coefficients of $\zeta_1\zeta_2^2$ and $\zeta_1\zeta_3^2$ terms – the coefficients a_{pqr} of non-linear system of equations (2.7) – vanish.

In the paper by Kołakowski *et al.* (2015), nonlinear Koiter’s theory has been used to explain the effect of the imperfection sign (sense) on local postbuckling equilibrium paths of plates made of functionally graded materials (FGMs). In the case of the FG plate, nonzero first-order sectional inner forces that cause an occurrence of nonzero postbuckling coefficients responsible for sensitivity of the system to imperfections appear. It results in the fact that postbuckling equilibrium paths of plate structures made of FGMs are unsymmetrically stable. This explains differences in the plate response dependence on the imperfection sign (sense). On the other hand, in Kołakowski and Mania (2015), an analysis of the influence of the imperfection sign on the dynamic postbuckling equilibrium paths of the FG square plates has been continued.

In the numerical calculations of dynamic interactive buckling, a rectangular shape of the in-plane pulse loading (i.e., $\sigma(t) = \sigma_D$ for $0 \leq t \leq T_1$ and $\sigma(t) = 0$ for $T < t_1$) equal to the fundamental period of the natural frequency $T_1 = 2\pi/\omega_1$ is considered.

The prebuckling solution to the FG plate consisting of homogenous fields is assumed as in Kołakowski and Królak (2006)

$$u^{(0)} = \left(\frac{l}{2} - x\right)\Delta \quad v^{(0)} = y\Delta\frac{A_{12}}{A_{22}} \quad w^{(0)} = 0 \quad (2.9)$$

where Δ is the actual loading. This loading of the zero state is specified as a product of the unit loading and the scalar load factor Δ .

Taking into account relationship (2.3), the inner sectional forces of the prebuckling (i.e., unbending) state for the assumed homogeneous field of displacements (2.9) are expressed by the following relationships before the redistribution of forces in the plate due to plate deformations (Kołakowski *et al.*, 2015; Kołakowski and Mania, 2015; Kołakowski, 2016)

$$\begin{aligned} N_x^{(0)} &= -\left(A_{11} - \frac{A_{12}^2}{A_{22}}\right)\Delta & M_x^{(0)} &= -\left(B_{11} - B_{12}\frac{A_{12}}{A_{22}}\right)\Delta \\ N_y^{(0)} &= 0 & M_y^{(0)} &= -\left(B_{12} - B_{22}\frac{A_{12}}{A_{22}}\right)\Delta \\ N_{xy}^{(0)} &= 0 & M_{xy}^{(0)} &= 0 \end{aligned} \quad (2.10)$$

The assumed field of displacements and the field of inner forces, corresponding to it for the prebuckling state, fulfil the equilibrium equations for the zero state as an identity.

In Kołakowski and Królak (2006), an unbending, prebuckling state, i.e., a distribution field of the zero state according to (2.9), has been assumed. Dependence (2.3) for the zero state (i.e., prebuckling) takes the form

$$\bar{\mathbf{N}}_0 = \begin{Bmatrix} N_x^{(0)} \\ M_x^{(0)} \end{Bmatrix} = \begin{bmatrix} \mathbf{A} & \mathbf{B} \\ \mathbf{B} & \mathbf{D} \end{bmatrix} \begin{Bmatrix} \boldsymbol{\varepsilon}^{(0)} \\ \mathbf{0} \end{Bmatrix} \quad (2.11)$$

It results in an occurrence of the nonzero inner sectional forces (2.10) $N_x^{(0)}$, $M_x^{(0)}$, $M_y^{(0)}$ in the FG plate for the zero state. Special attention should be paid to the fact that nonzero magnitudes of the sectional moments $M_x^{(0)}$ and $M_y^{(0)}$ appear due to the effects of deformations of the middle surface (i.e., membrane deformations) resulting from the nontrivial coupling submatrix \mathbf{B} and deformations of the middle surface, and not due to an appearance of curvatures of the middle surface. These moments affect obviously the values of critical loads and the values of postbuckling coefficients (Kołakowski *et al.*, 2015; Kołakowski and Mania, 2015).

3. Analysis of the results

Prismatic thin-walled beam-columns with quadratic cross-sections subjected to an axial pulse compression have been considered. The columns are made of the same FGM subject to Hooke's law. A schematic view of the column and its dimensions are shown in Fig. 1.

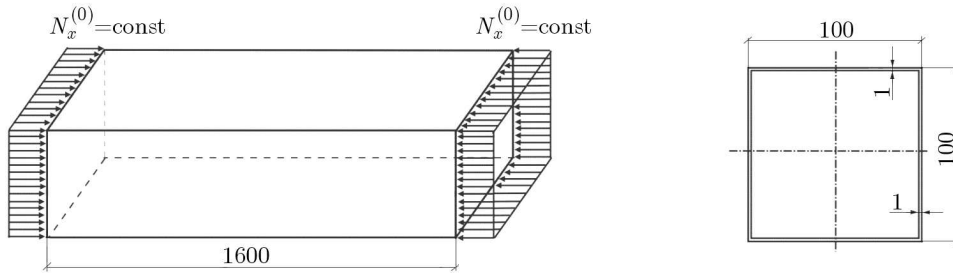


Fig. 1. Thin-walled cross-section of the beam-column

Identically as in Kołakowski *et al.* (2015), Kołakowski and Mania (2015) two different materials the columns are made of have been considered, namely:

- isotropic material – steel – with the following material properties: Young's modulus $E = 210$ GPa, Poisson's ratio $\nu = 0.3$, and density $\rho = 7850$ kg/m³;
- Al-TiC functionally graded material (FGM). The component material properties are given: Al Young's modulus: $E_m = 69$ GPa, TiC Young's modulus: $E_c = 480$ GPa, Al Poisson's ratio: $\nu_m = 0.33$, TiC Poisson's ratio: $\nu_c = 0.20$, Al density: $\rho_m = 2700$ kg/m³, TiC density: $\rho_c = 4920$ kg/m³. The fraction exponent q (2.2) is equal to 1.0.

Three variants of the beam-column structure have been considered, namely:

- variant I – isotropic column (the so-called reference variant);
- variant II – QCM FG column (ceramics inside the cross-section, metal outside);
- variant III – QMC FG column (metal inside the cross-section, ceramics – outside).

The isotropic beam-column (variant I) has symmetrical stable postbuckling local equilibrium paths, whereas the FG column (variants II and III) has nonsymmetrical stable postbuckling local

equilibrium paths (Kořakowski *et al.*, 2015; Kořakowski and Mania, 2015). Due to the above aspects, two variants of the FG beam-column – QCM and QMC – have been considered.

For each of these three structural variants, values of critical stresses σ_r : the global (Euler) buckling mode σ_1 , the lowest primary local buckling mode σ_2 and the secondary local buckling mode σ_3 have been determined, respectively. Moreover, numbers of halfwaves m corresponding to the critical loads have been given. The global mode occurs at $m = 1$ and the local modes at $m > 1$. Also, values of frequencies of free vibrations ω_r and a period of free vibrations T_r corresponding to the buckling modes under analysis have been defined as well.

An interactive dynamic response of beam-columns to the load whose duration corresponds to the fundamental period of flexural free vibrations of unloaded columns $T_1 = 2\pi/\omega_1$ has been investigated.

The assumed time of the rectangular load pulse duration corresponds to the beam-column quasi-static load for local modes (i.e., $T_2 > 2T_1$, $T_3 > 2T_1$). The tracing time of the structure dynamic response assumed as $t^* = 1.5T_1$ has been analysed. The dynamic load factor DLF is defined as a ratio of the dynamic load to the minimal critical value of the static load, $DLF = \sigma_D / \min(\sigma_1, \sigma_2, \sigma_3) = \sigma_D / \sigma_2$.

In Budiansky and Hutchinson (1966), it has been shown for the two-mode approach that when the frequencies of free vibrations differ at least twice, then in this case the dynamic term corresponding to a higher frequency of free vibrations can be neglected in the equations of motion. On the other hand, in Kořakowski (2016), attention has been paid to unexpected aspects of interactive dynamic buckling in the case of beam-columns having one axis of symmetry of the cross-section. Here, in order to show qualitatively different dynamic responses, a two- or three-mode approach could be applied. It has allowed the uncoupling of the equations of motion for the case of the inner combined resonance, when $(\omega_1 + \omega_2)/\omega_3 \approx 1$ (Nayfeh and Mook, 1979).

It is not possible to use this approach in the present study because the interaction occurs only via the coefficient of the cubic term $\zeta_1\zeta_2\zeta_3$ in total energy (2.6) governing the mode interaction. Therefore, an approach described in Budiansky and Hutchinson (1966) has been applied. The secondary local buckling mode in the case of static issues is a supplementary mode that enables one to account for the effect of the primary local mode on the global flexural buckling mode.

In the further part of the study, it has been assumed that when “complete” three dynamic equations of motion (2.7) are considered, then the case is referred to as case I. When the dynamic term is neglected for the primary local buckling mode (i.e., for $r = 2$), that is to say, when $\zeta_{2,tt} = 0$ is assumed in equations (2.7) – it is case II, whereas when the term $\zeta_{3,tt} = 0$ is neglected for the secondary local mode (i.e., for $r = 3$) – case III.

When the dynamic term is neglected in (2.7), which corresponds to case II, one of the equations is a static equation of the third order with respect to the amplitude of deflection ζ_2 , which is solved on the basis of analytical formulae. Due to this, wrong conditions in the equations could be avoided and the numerical solution could be stabilised. It means that in the formula for total energy of the system (2.6), the expression for kinetic energy $0.5m_2\zeta_{2,t}^2$ corresponding to the primary local mode (case II) could be neglected. Analogously, in case III – the expression for the energy $0.5m_3\zeta_{3,t}^2$ corresponding to the secondary local mode (i.e., ζ_3) could be omitted.

Further on in the study, the following index notations of dimensionless amplitudes of deflection have been introduced for the cases under consideration, namely: case I – ζ_r for $r = 1, 2, 3$; case II – $\hat{\zeta}_r$ for $r = 1, 2, 3$; case III – $\tilde{\zeta}_r$ for $r = 1, 2, 3$. In the calculations of dynamic stability, the following values of imperfections have been assumed: $\zeta_1^* = 1.0$, $\zeta_2^* = 0.2$, $\zeta_3^* = 0.1$. Contrary to other works by the authors (e.g., Kořakowski, 1996, 2016; Kořakowski *et al.*, 1999; Teter and Kořakowski, 2001, 2004, 2005; Teter, 2001, 2007, 2011; Kořakowski and Kubiak, 2005; Kořakowski and Królak, 2006; Kubiak, 2007; Kořakowski and Mania, 2013; Kubiak, 2013), the most unfavourable combination of initial imperfection signs ζ_r^* (for $r = 1, 2, 3$) has not been assumed

to make the effects of nonsymmetrical stable postbuckling equilibrium path and the influence of the connection between the adjacent plates of the cross-section more visible.

Values of the critical dynamic load factors DLF_{cr} have been determined from the Budiansky-Hutchinson criterion (Budiansky and Hutchinson, 1977; Kubiak 2007, 2013) in which it is assumed that the loss of dynamic stability occurs when the velocity with which the displacements grow is the highest for a certain force amplitude. The values of DLF_{cr} presented correspond with some accuracy to the maximum values of deflections $\max(\zeta_1)$ within the applicability of the assumed theory (i.e., the total maximum deflection of the column is at least a hundred times as high as the cross-section wall thickness), and not to asymptotic values (Kubiak, 2013).

3.1. Variant I – isotropic columns

Variant I has been assumed as the reference one because in the case of an isotropic column, the plates constituting the cross-section are characterized by the symmetry of cross-sectional uniformity (i.e., coupling stiffness matrix $\mathbf{B} = \mathbf{0}$ in (2.3)).

Table 1. Solutions to the eigenproblem for an isotropic column – variant I (reference)

r	σ_r [MPa]	m [-]	ω_r [rad/s]	T_r [ms]
1	1185.6	1	761	8.256
2	72.28	16	3013	2.085
3	103.66	16	3609	1.741

First, the eigenvalues of the problem given in Table 1 have been determined, namely: values of critical stresses corresponding to the global Euler buckling σ_1 , the lowest primary local buckling mode σ_2 and the secondary local buckling mode σ_3 , the frequencies of free vibrations and the periods corresponding to them, as well as a number of halfwaves m of the eigenmodes along the longitudinal direction. The ratios of frequencies of free vibrations are equal to: $\omega_2/\omega_1 = 3.96$, $\omega_3/\omega_1 = 4.74$, $\omega_3/\omega_2 = 1.197$, $(\omega_1 + \omega_2)/\omega_3 = 1.045$, respectively. In Fig. 2a, absolute values of the maximum amplitudes of global deflections (for $r=1$) (i.e., ζ_1 , $\hat{\zeta}_1$, $\tilde{\zeta}_1$) as a function of DLF for cases I-III under consideration, whereas in Fig. 2b – for local deflections of the modes ζ_2 , $\hat{\zeta}_3$ and $\tilde{\zeta}_2$ for cases I, II and III are shown, correspondingly.

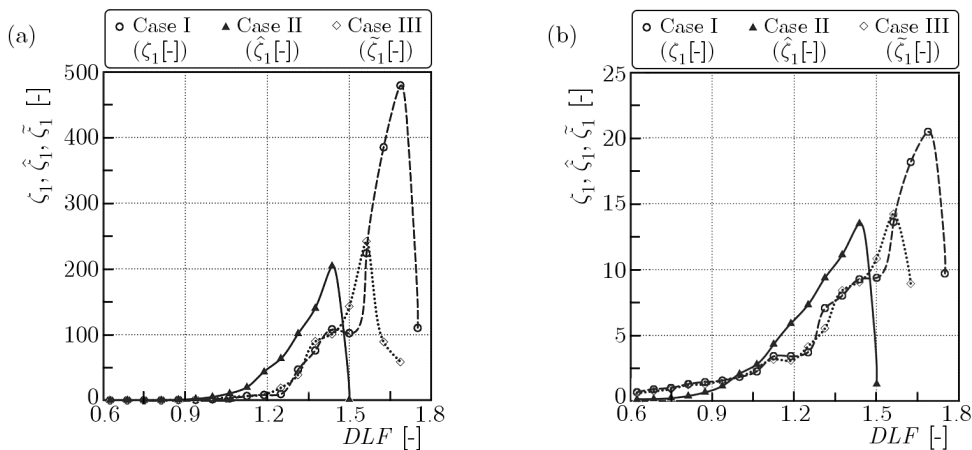


Fig. 2. Maximum dimensionless global deflections as a function of DLF for an isotropic column (variant I): (a) global modes, (b) local modes

Quantitative differences in the component amplitudes of global deflections (i.e., ζ_1 , $\hat{\zeta}_1$ and $\tilde{\zeta}_1$) and the local ones (i.e., ζ_2 , $\hat{\zeta}_3$ and $\tilde{\zeta}_2$) can be observed. As can be easily seen in these two figures, the maximum values of the amplitudes of the global and local deflection for each case under

investigation occur for the same values of DLF (i.e., $DLF \approx 1.69$ for case I, $DLF \approx 1.44$ for case II, and $DLF \approx 1.56$ for case III, respectively).

When $DLF = 1.434$, then the amplitude of dynamic load is $\sigma_D = \sigma_3$ and, moreover, $\sigma_3/\sigma_2 = 1.434$ (Table 1). When $t \leq T_1$, then for $1.0 \leq DLF < 1.434$ and $\Omega_1^2 > 0$, $\Omega_2^2 < 0$, $\Omega_3^2 > 0$, whereas for $DLF > 1.434$, $\Omega_1^2 > 0$, $\Omega_2^2 < 0$, $\Omega_3^2 < 0$, respectively.

The maximum value $\max(\zeta_1)$ is more than twice as high as $\max(\hat{\zeta}_1)$ and $\max(\tilde{\zeta}_1)$, whereas the differences between $\max(\hat{\zeta}_1)$ and $\max(\tilde{\zeta}_1)$ are equal to approx. 20%. The differences between the maximum values of local amplitudes (i.e., $\max(\zeta_2)$, $\max(\tilde{\zeta}_2)$ and $\max(\hat{\zeta}_3)$) are not so significant. The value $\max(\zeta_2)$ is more than 30% higher than the $\max(\tilde{\zeta}_2)$ and $\max(\hat{\zeta}_3)$. The maximum values of global deflections are by one order of magnitude higher than for local deflections.

As can be seen in Fig. 2 for case II, the deflections $\hat{\zeta}_1$ and $\hat{\zeta}_3$ for $DLF > 1.7$ are many times lower than the deflections in cases I and III.

For case II, the lowest value of DLF_{cr} and the lowest value $\max(\hat{\zeta}_1) \approx 200$ for $DLF \approx 1.44$ have been obtained (Fig. 2a), which correspond to: $\sigma_D \approx \sigma_3$, $\sigma_3/\sigma_2 = 1.434$ and $\Omega_3^2 \approx 0$.

When $t \leq T_1$ and for $DLF = 1.56$ in case III, we have $\max(\zeta_1) \approx 250$, $\Omega_1 = 723$, $\Omega_2 = 2259$ and $\Omega_3 = 1081$, and for $DLF = 1.69$ in case I, we have $\max(\zeta_1) < 500$, $\Omega_1 = 720$, $\Omega_2 = 2498$ and $\Omega_3 = 1518$. When $T_1 < t \leq t^*$, we have $(\omega_1 + \omega_2)/\omega_3 = 1.045$.

The critical values of DLF_{cr} , according to the Budiansky-Hutchinson criterion assumed in this study, are equal for the individual cases to: case I – $DLF_{cr} = 1.44$, case II – $DLF_{cr} = 1.31$, case III – $DLF_{cr} = 1.44$.

The duration of the rectangular load pulse is equal to $T_1 = 8.256$ ms. At the response tracing time $T_1 < t \leq t^*$, the system is not subject to load any longer and performs free unsteady vibrations in the transient period. Thus, the values of maximum amplitudes are attained in this time range for all the time functions described.

3.2. Variant II – QCM functionally graded column

Two variants of the FG column structure have been assumed. It has followed from two aspects. The first one is such that it is possible to make such columns in two ways. The ceramic surface is resistant to high temperatures. Variant II (i.e., QCM) protects the outer surface of the cross-section against high temperature, whereas variant III (QMC) protects the inner surface. The second aspect results from the fact that FG structures have nonsymmetrical stable postbuckling equilibrium paths (Kołakowski *et al.*, 2015; Kołakowski and Mania, 2015). Hence, the way the component plates of the FG column are connected exerts an influence on the postbuckling behavior of the structure. For FG columns, identical calculations have been conducted as for variant I (the reference one). For variant II (QCM), the results of calculations of the eigenproblem have been presented in Table 2. The ratios of frequencies of free vibrations are equal to: $\omega_2/\omega_1 = 3.57$, $\omega_3/\omega_1 = 4.27$, $\omega_3/\omega_2 = 1.196$, $(\omega_1 + \omega_2)/\omega_3 = 1.070$, correspondingly.

Table 2. Solutions to the eigenproblem for a QCM functionally graded column – variant II

r	σ_r [MPa]	m [-]	ω_r [rad/s]	T_r [ms]
1	1606.3	1	1273	4.935
2	79.81	16	4546	1.382
3	114.17	16	5437	1.155

Figure 3 show the absolute maximum values of global and local deflections versus DLF for the three cases under consideration, respectively. Similarly as for variant I (i.e., the reference one – isotropic), quantitative differences in the values of global (i.e., ζ_1 , $\hat{\zeta}_1$ and $\tilde{\zeta}_1$) and local (i.e., ζ_2 , $\hat{\zeta}_3$ and $\tilde{\zeta}_2$) amplitudes can be seen easily.

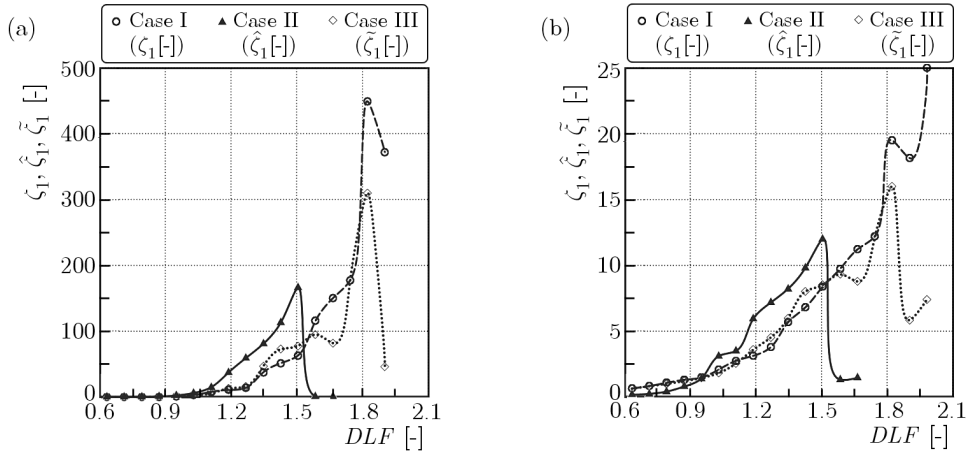


Fig. 3. Maximum dimensionless global deflections as a function of DLF for variant II: (a) global modes, (b) local modes

For each case, the maximum value of global and local deflection occurs for the same values of DLF (i.e., case I – $DLF = 1.82$, case II – $DLF = 1.51$ and case III – $DLF = 1.82$). When $DLF = 1.4307$, then we have $\sigma_3/\sigma_2 = 1.4307$. When $t \leq T_1$, then for $1.0 < DLF < 1.4307$ we have $\Omega_1^2 > 0$, $\Omega_2^2 < 0$ and $\Omega_3^2 > 0$, whereas for $DLF > 1.4307$, we have, $\Omega_1^2 > 0$, $\Omega_2^2 < 0$ and $\Omega_3^2 < 0$, correspondingly.

The maximum values $\max(\zeta_1)$ and $\max(\hat{\zeta}_1)$ are twice as high as $\max(\tilde{\zeta}_1)$, and $\max(\zeta_1)/\max(\tilde{\zeta}_1) \approx 1.5$. The differences between the maximum values of local deflections, i.e., ζ_2 , $\hat{\zeta}_3$ and $\tilde{\zeta}_2$, are not so high and they do not exceed 1.5 times. The values $\max(\zeta_1)$, $\max(\hat{\zeta}_1)$, $\max(\tilde{\zeta}_1)$ for global modes are higher by one order of magnitude than $\max(\zeta_2)$, $\max(\zeta_3)$, $\max(\tilde{\zeta}_3)$, $\max(\tilde{\zeta}_2)$ for local modes.

In Fig. 3, for the duration of load (i.e., for $t \leq T_1$), we have $\Omega_1 = 1224$, $\Omega_2 = 3235$ and $\Omega_3 = 1251$ for $DLF = 1.51$, whereas for $DLF = 1.81$ – $\Omega_1 = 1213$, $\Omega_2 = 4125$ and $\Omega_3 = 2849$, respectively. For $T_1 < t \leq t^*$, we have $(\omega_1 + \omega_2)/\omega_3 = 1.070$.

The critical values DLF_{cr} are equal to, respectively: case I – $DLF_{cr} = 1.56$, case II – $DLF_{cr} = 1.40$, case III – $DLF_{cr} = 1.69$. For $DLF = 1.11$, $DLF = 1.27$ and cases I and III, the maximum values of global deflections $\max(\zeta_1)$ and $\max(\tilde{\zeta}_1)$ are attained at $T_1 < t \leq t^*$, that is to say, after the load pulse duration. The values of local deflections $\max(\zeta_2)$, $\max(\zeta_3)$ and $\max(\tilde{\zeta}_3)$ are approximately three times lower than global deflections. For the two values of DLF under consideration in case II, the global deflections $\hat{\zeta}_1$ grow monotonously in practice and $\max(\hat{\zeta}_1)$ is twice as high as $\max(\zeta_1)$ and $\max(\tilde{\zeta}_1)$. When $DLF = 1.35$, global deflections increase monotonously during the whole response tracing time for all the three cases.

Similarly as for variant I, the maximum values of global deflections (i.e., $\max(\zeta_1)$, $\max(\hat{\zeta}_1)$, $\max(\tilde{\zeta}_1)$) are attained when the load impulse finishes for the presented time functions.

3.3. Variant III – QMC functionally graded column

In Table 3, the calculation results of the eigenproblem for variant III (QMC) are presented. The ratios of frequencies of free vibrations are equal to: $\omega_2/\omega_1 = 3.53$, $\omega_3/\omega_1 = 4.24$, $\omega_3/\omega_2 = 1.199$, $(\omega_1 + \omega_2)/\omega_3 = 1.069$, respectively. As can be easily seen, the eigenvalues for both variants of the FGM column (compare Tables 3 and 2) are very close to each other.

In Fig. 4, the absolute values of maximum amplitudes of global (i.e., ζ_1 , $\hat{\zeta}_1$ and $\tilde{\zeta}_1$) and local (i.e., ζ_2 , $\hat{\zeta}_3$ and $\tilde{\zeta}_2$) deflections versus the coefficient DLF for the three cases under consideration are presented. Analogously as for variants I and II, quantitative differences for components of global and local amplitudes can be observed. As can be easily seen in Fig. 4, the maximum value

Table 3. Solutions to the eigenproblem for a QCM functionally graded column – variant III

r	σ_r [MPa]	m [-]	ω_r [rad/s]	T_r [ms]
1	1616.6	1	1277	4.920
2	78.77	16	4516	1.391
3	113.27	16	5415	1.160

of global and local deflection occurs for the same values of DLF in cases II and III (case II – $DLF = 1.45$, case III – $DLF = 1.85$). In case I, the amplitudes of deflections grow monotonously for $DLF < 2.0$. For $DLF = 2.0$, we have $\max(\zeta_1) > 500$ and $\max(\zeta_2) > 25$. For $DLF = 1.4383$, we have $\sigma_3/\sigma_2 = 1.4383$. When $t \leq T_1$, then for $1.0 < DLF < 1.4383$, we have $\Omega_1^2 > 0$, $\Omega_2^2 < 0$ and $\Omega_3^2 > 0$, whereas at $DLF > 1.4383$, $\Omega_1^2 > 0$, $\Omega_2^2 < 0$ and $\Omega_3^2 < 0$, respectively. The lowest values of maximum deflections are for case II, that is to say, for $\max(\hat{\zeta}_1)$ and $\max(\hat{\zeta}_3)$, analogously as for variant II.

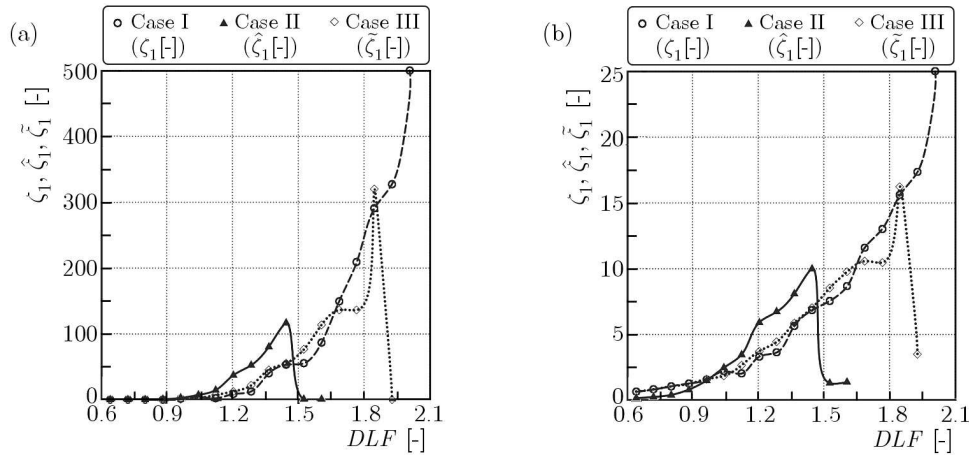


Fig. 4. Maximum dimensionless global deflections as a function of DLF for variant III: (a) global modes, (b) local modes

In Fig. 4, under the dynamic loading (for $t \leq T_1$) for $DLF = 1.45$, we have $\Omega_1 = 1231$, $\Omega_2 = 3015$ and $\Omega_3 \approx 0$, whereas for $DLF = 1.85$ – $\Omega_1 = 1218$, $\Omega_2 = 4157$ and $\Omega_3 = 28488$, respectively. At $T_1 < t \leq t^*$, we have $(\omega_1 + \omega_2)/\omega_3 = 1.069$. The critical values of DLF_{cr} are equal to: case I – $DLF_{cr} = 1.56$, case II – $DLF_{cr} = 1.69$, case III – $DLF_{cr} = 1.40$. When $t \leq T_1$, then for the assumed values of DLF , we have $\Omega_1^2 > 0$, $\Omega_2^2 < 0$ and $\Omega_3^2 > 0$. For the three values of DLF under consideration and, simultaneously, for the three cases, the maximum global deflection during the response tracing time (i.e., $0 \leq t \leq t^*$) occurs for case II – $\max(\hat{\zeta}_1)$. When the time functions for variants II and III are compared, some insignificant differences can be observed. The maximum values of global deflections (i.e., $\max(\zeta_1)$, $\max(\hat{\zeta}_1)$, $\max(\tilde{\zeta}_1)$) take place for $T_1 < t \leq t^*$.

3.4. Comparison of all variants under analysis

For all variants under consideration (i.e., I-III), diagrams of amplitudes of global deflections are similar for cases I and III, whereas significant differences can be observed for case II. It corresponds to the case when the dynamic term $\zeta_{2,tt} = 0$ is neglected in (2.7), which has a visible effect on the equations of motion. Moreover, for $DLF > 1.45$, we have $\Omega_1^2 > 0$, $\Omega_2^2 < 0$ and $\Omega_3^2 < 0$. It means that the amplitudes of local deflections grow exponentially and become dominating in a short time. A dynamic interaction of the global mode and the local ones results in a very dramatic increase in the amplitudes of deflections.

For the time functions under consideration for all variants and cases and the assumed values of load coefficients DLF , the amplitudes of global deflections attain their maximum values after the pulse load finishes (e.g., for $T_1 < t \leq t^*$). For this time range, free unsteady vibrations occur in the transient process. To the authors' knowledge, the only phenomenon that can explain this effect is the inner combined resonance which takes place accordingly to the theory of vibration (Nayfeh and Mook, 1979) for steady processes, correspondingly, in the cases when $(\omega_1 + \omega_2)/\omega_3 \approx 1.0$. The three cases under analysis comply with the above-mentioned condition. A change in the tracing time of the dynamic response t^* can exert an influence on the maximum values of amplitudes of deflections. In the study, a long enough tracing time has been assumed, as it is equal to $t^* = 1.5T_1$. However, shortening of this time (e.g., up to $t^* = 1.3T_1$) will not exert any influence on the general conclusions drawn here.

4. Conclusions

Dynamic interactive buckling of thin-walled FGM columns with a square cross-section is discussed. Three cases are considered. Case I corresponds to analysis of the dynamic response of the FG structure for "complete" equations of motion (2.7), case II refers to the situation when the dynamic effect is neglected for the primary local buckling mode (i.e., $r = 2$), whereas case III – for the secondary local mode (i.e., $r = 3$). Such an approach has been pointed out by Budiansky and Hutchinson (1966). When the structure has two axes of symmetry of the cross-section, the interactive buckling occurs only via the coefficient of the cubic term $\zeta_1\zeta_2\zeta_3$ in total potential energy (2.6). The solution method applied in this study has not been so efficient as in the case of the trapezoidal cross-section with one axis of symmetry. In Kołakowski (2016), however, a quite different approach to the solution of the problem has been assumed. Thus, the above conclusions should be subject to further, thorough investigations.

Acknowledgements

This publication is a result of the research works carried out within the project subsidized over the years 2012-2015 by the state funds designated for the National Science Centre (NCN UMO-2011/01/B/ST8/07441).

References

1. ARI-GUR J., SIMONETTA S.R., 1979, Dynamic pulse buckling of rectangular composite plates, *Composites Part B*, **28B**, 301-308
2. BIRMAN V., BYRD L.W., 2007, Modeling and analysis of functionally materials and structures, *Applied Mechanics Review*, **60**, 195-216
3. BUDIANSKY B., HUTCHINSON J.W., 1966, Dynamic buckling of imperfection-sensitive structures, *Proceedings of the 11th International Congress of Applied Mechanics*, Goetler H. (Ed.), Munich, 636-651
4. BYSKOV E., HUTCHINSON J.W., 1977, Mode interaction in axially stiffened cylindrical shells, *AIAA Journal*, **15**, 7, 941-948
5. HUI-SHEN S., 2009, *Functionally Graded Materials – Nonlinear Analysis of Plates and Shells*, CRC Press, Taylor & Francis, London
6. JONES R.M., 1999, *Mechanics of Composite Materials*, 2nd ed. Taylor & Francis, London
7. KOŁAKOWSKI Z., 1996, A semi-analytical method for the analysis of the interactive buckling of thin-walled elastic structures in the second order approximation, *International Journal of Solids Structures*, **33**, 25, 3779-3790

8. KOŁAKOWSKI Z., 2016, Some aspects of interactive dynamic stability of thin-walled trapezoidal FGM beam-columns under axial load, *Thin-Walled Structures*, **98**, 431-442
9. KOŁAKOWSKI Z., KRÓLAK M., 2006, Modal coupled instabilities of thin-walled composite plate and shell structures, *Composite Structures*, **76**, 303-313
10. KOŁAKOWSKI Z., KRÓLAK M., KOWAL-MICHALSKA K., 1999, Modal interactive buckling of thin-walled composite beam-columns regarding distortional deformations, *International Journal of Engineering Science*, **37**, 1577-1596
11. KOŁAKOWSKI Z., KUBIAK T., 2005, Load-carrying capacity of thin-walled composite structures, *Composite Structures*, **67**, 417-426
12. KOŁAKOWSKI Z., MANIA J.R., 2013, Semi-analytical method versus the FEM for analysis of the local post-buckling, *Composite Structures*, **97**, 99-106
13. KOŁAKOWSKI Z., MANIA J.R., 2015, Dynamic response of thin FG plates with a static unsymmetrical stable postbuckling path, *Thin-Walled Structures*, **86**, 10-17
14. KOŁAKOWSKI Z., MANIA R.J., GRUDZIECKI J., 2015, Local nonsymmetric postbuckling equilibrium path in thin FGM plate, *Eksploracja i Niezawodność (Maintenance and Reliability)*, **17**, 135-142
15. KUBIAK T., 2007, Criteria of dynamic buckling estimation of thin-walled structures, *Thin-Walled Structures*, **45**, 10/11, 888-892
16. KUBIAK T., 2013, *Static and Dynamic Buckling of Thin-Walled Plate Structures*, Springer
17. NA K.S., KIM J.H., 2009, Volume fraction optimization of functionally graded composite panels for stress reduction and critical temperature, *Finite Elements in Analysis and Design*, **45**, 845-851
18. NAYFEH A.H., MOOK D.T., 1979, *Nonlinear Oscillations*, Wiley, New York
19. PANDA S., RAY M.C., 2008, Nonlinear finite element analysis of functionally graded plates integrated with patches of piezoelectric fiber reinforced composite, *Finite Elements in Analysis and Design*, **44**, 493-504
20. PETRY D., FAHLBUSCH G., 2000, Dynamic buckling of thin isotropic plates subjected to in-plane impact, *Thin-Walled Structures*, **38**, 267-283
21. REDDY J.N., 2000, Analysis of functionally graded plates, *International Journal for Numerical Methods in Engineering*, **47**, 663-684
22. REDDY J.N., 2004, *Mechanics of Laminated Composite Plates and Shells*, CRC Press, London
23. SAMSAM SHARIATA B.A., JAVAHERIB R.B.A., ESLAMI B.A., 2005, Buckling of imperfect functionally graded plates under in-plane compressive loading, *Thin-Walled Structures*, **43**, 1020-1036
24. SCHOKKER A., SRIDHARAN S., KASAGI A., 1996, Dynamic buckling of composite shells, *Computers and Structures*, **59**, 1, 43-55
25. SRIDHARAN S., BENITO R., 1984, Columns: static and dynamic interactive buckling, *Journal of Engineering Mechanics ASCE*, **110**, 1, 49-65
26. TETER A., 2007, Static and dynamic interactive buckling of isotropic thin-walled closed columns with variable thickness, *Thin-Walled Structures*, **45**, 10/11, 936-940
27. TETER A., 2011, Dynamic critical load based on different stability criteria for coupled buckling of columns with stiffened open cross-sections, *Thin-Walled Structures*, **49**, 589-595
28. TETER A., KOŁAKOWSKI Z., 2001, Lower bound estimation of load-carrying capacity of thin-walled structures with intermediate stiffeners, *Thin-Walled Structures*, **39**, 8, 649-669
29. TETER A., KOŁAKOWSKI Z., 2003, Natural frequencies of thin-walled structures with central intermediate stiffeners or/and variable thickness, *Thin-Walled Structures*, **41**, 291-316
30. TETER A., KOŁAKOWSKI Z., 2004, Interactive buckling and load carrying capacity of thin-walled beam-columns with intermediate stiffeners, *Thin-Walled Structures*, **42**, 211-254

31. TETER A., KOŁAKOWSKI Z., 2005, Buckling of thin-walled composite structures with intermediate stiffeners, *Composite Structures*, **69**, 4, 421-428
32. VAN DER HEIJDEN A.M.A. (ED.), 2009, *WT Koiter's Elastic Stability of Solids and Structures*, Cambridge University Press
33. WARMIŃSKI J., TETER A., 2012, Non-linear parametric vibrations of a composite column under uniform compression, *Proceedings of the Institution of Mechanical Engineers, Part C: Journal of Mechanical Engineering Science*, **226**, 8, 1921-1938

Manuscript received July 29, 2015; accepted for print September 2, 2015

MODELLING OF SH-WAVES IN A FIBER-REINFORCED ANISOTROPIC LAYER OVER A PRE-STRESSED HETEROGENEOUS HALF-SPACE

RAJNEESH KAKAR

163, Phase-1, Chotti Baradari, Garah Road, Jalandhar, India; e-mail: rkakar_163@rediffmail.com

SHIKHA KAKAR

Department of Electronics, SBBIET, Phadiana, India; e-mail: shikha_kakar@rediffmail.com

Modelling of SH-waves in an anisotropic fiber-reinforced layer provides a great deal of support in the understanding of seismic wave propagation. This paper deals with the propagation of SH-waves in a fiber-reinforced anisotropic layer over a pre-stressed heterogeneous half-space. The heterogeneity of the elastic half-space is caused by linear variations of density and rigidity. As a special case when both media are homogeneous and stress free, the derived equation is in agreement with the general equation of the Love wave. Numerically, it is observed that the velocity of SH-waves decreases with an increase in heterogeneity-reinforced parameters and decrease in initial stress.

Keywords: heterogeneity, fiber reinforced medium, SH-waves, initial stress, anisotropy

1. Introduction

The propagation of seismic waves in anisotropic elastic media is unlike in comparison to their propagation in isotropic media. So, the study of seismic wave propagation in anisotropic elastic layered media becomes important to understand the nature of these waves in some complex media. Other types of layers which may be present in the interior of the Earth are reinforced concrete media. The reinforced layers are comprised due to excessive initial stresses present in the Earth. Fiber-reinforced composites are widely used in engineering structures, geophysical prospecting, civil engineering and mining engineering. So the investigation of shear waves in such media become obligatory with a vision to its application to geomechanics. The normal feature of a reinforced concrete medium is that its constituents, namely steel and concrete together, act as a single anisotropic unit as long as they persist in the elastic condition, i.e., the components are bound side by side so that there is no relative motion between them. There are large numbers of fiber-reinforced composite materials which exhibit anisotropic behavior, for example alumina, reinforced light alloys, fibreglasses and concrete. Spencer (1972) was the first who represented fiber-reinforced anisotropic materials with constitutive equations. Later, Belfield *et al.* (1983) presented the method of introducing a continuous self-reinforcement in an elastic solid. Chattopadhyay and Choudhury (1995) discussed some important results of propagation of seismic waves in fiber-reinforced materials. Chattopadhyay *et al.* (2012) studied propagation of SH-waves in an irregular inhomogeneous self reinforced layer lying over a self-reinforced half-space.

For seismologists, the propagation of seismic wave in elastic and reinforced layered media is useful to understand earthquake disaster prevention, oil exploration and groundwater prospecting. The geotechnical study reveals that the material properties such as heterogeneity and anisotropy of the Earth change rapidly beneath its surface, and these properties affect the propagation of seismic waves. Also, the effect of initial stresses on shear waves, which is largely present in the Earth due to a slow process of creep, temperature, pressure, and gravitation cannot be

ignored. In order to understand the underground response of seismic wave propagation towards the material properties and initial stresses of the Earth, researchers and seismologists generally prefer heterogeneous elastic models in semi-infinite domains. Due to large applications, prestressed Love/SH-waves in different media attract researchers' interests even nowadays. Li *et al.* (2004) investigated the influence of initial stresses on the Love wave propagation in piezoelectric layered structure. Du *et al.* (2008) presented an emphasis on the effect of initial stress on the Love wave propagation in a piezoelectric layer in the presence of a viscous liquid. Zakharenko (2005) studied the propagation of Love waves in a cubic piezoelectric crystal. Qian *et al.* (2004) developed a mathematical model to study the effect of Love wave propagation in a piezoelectric layered structure with initial stresses. Wang and Quek (2001) discussed propagation of Love waves in a piezoelectric coupled solid medium. Zaitsev *et al.* (2001) discussed propagation of acoustic waves in piezoelectric conductive and viscous plates. The supplement of surface wave analysis and other wave propagation problems to anisotropic elastic materials has been a subject of many studies; see for example Musgrave (1959), Crampin and Taylor (1971), Chadwick and Smith (1977), Dowaikh and Ogden (1990), Mozhaev (1995), Nair and Sotiropoulos (1999), Destrade (2001, 2003), Ting (2002), Ogden and Singh (2011, 2014).

SH-waves cause more destruction to the structure than the body waves due to slower attenuation of the energy. Many authors have studied the propagation of an SH-wave by considering dissimilar forms of asymmetry at the interface. Watanabe and Payton (2002) discussed SH-waves in a cylindrically monoclinic material with Green's function. Gupta and Gupta (2013) studied the effect of initial stress on wave motion in an anisotropic fiber reinforced thermoelastic medium. Sahu *et al.* (2014) showed the effect of gravity on shear waves in a heterogeneous fiber-reinforced layer placed over a half-space. Recently, Kundu *et al.* (2014) analyzed an SH-wave in an initially stressed orthotropic homogeneous and a heterogeneous half space. Chattopadhyay *et al.* (2014) studied the effect of heterogeneity and reinforcement on propagation of a crack due to shear waves.

The coupled effects of initial stress, heterogeneity and reinforcement on the propagation of an SH-wave in a fiber-reinforced anisotropic layer overlying a pre-stressed heterogeneous half-space are studied in this paper. The closed form of the dispersion equation for the shear wave by using the method of separation of variables and Whittaker's function is obtained. The effects of all parameters under considered geometry are discussed graphically.

2. Formulation of the problem

Let H be thickness of a steel fiber reinforced (silica fume concrete) layer placed over a prestressed heterogeneous half-space. We consider x -axis along the direction of wave propagation and z -axis vertically downwards (Fig. 1). Let the rigidity, density in the lower half-space are $\mu_2 = \mu'(1 + \varepsilon_1 z)$ and $\rho_2 = \rho'(1 + \varepsilon_2 z)$, respectively. Here ε_1 and ε_2 are heterogeneous parameters of the lower half-space and having dimensions that are inverse of length.

3. Solution of the problem

3.1. Solution for the upper layer

The constitutive equations for a fiber reinforced linearly elastic anisotropic medium with respect to a preferred direction (Belfield *et al.*, 1983) are

$$\begin{aligned} \tau_{ij} = & \lambda e_{kk} \delta_{ij} + 2\mu_T e_{ij} + \alpha(a_k a_m e_{km} \delta_{ij} + e_{kk} a_i a_j) + 2(\mu_L - \mu_T)(a_i a_k e_{kj} + a_j a_k e_{ki}) \\ & + \beta(a_k a_m e_{km} a_i a_j) \end{aligned} \quad (3.1)$$

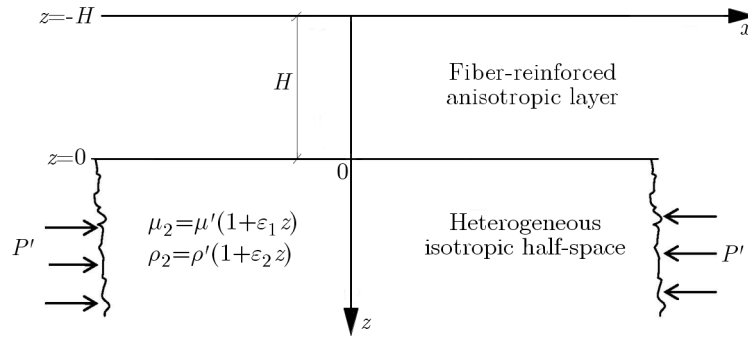


Fig. 1. Geometry of the problem

where $e_{ij} = (\mu_{i,j} + \mu_{j,i})/2$ are components of strain; are reinforced anisotropic elastic parameters with the dimension of stress; λ is an elastic parameter. The preferred direction of fibers is given by $\mathbf{a} = [a_1, a_2, a_3]$, $a_1^2 + a_2^2 + a_3^2 = 1$. If \mathbf{a} has components that are $[1, 0, 0]$ then the preferred direction is the z -axis normal to the direction of propagation. The coefficients μ_L and μ_T are the longitudinal shear and transverse shear moduli of elasticity in the tender direction, respectively.

Equation (3.1) in the presence of initial compression simplifies as given below

$$\begin{aligned}
 \tau_{11} &= (\lambda + 2\alpha + 4\mu_L + \beta - 2\mu_T)e_{11} + (\lambda + \alpha)e_{22} + (\lambda + \alpha)e_{33} \\
 \tau_{22} &= (\lambda + \alpha)e_{11} + (\lambda + 2\mu_T)e_{22} + \lambda e_{33} \\
 \tau_{33} &= (\lambda + \alpha)e_{11} + \lambda e_{22} + (\lambda + 2\mu_T)e_{33} \\
 \tau_{12} &= 2\mu_T e_{12} \quad \tau_{13} = 2\mu_T e_{13} \quad \tau_{23} = 2\mu_T e_{23}
 \end{aligned}
 \tag{3.2}$$

The equations of motion in the upper half-space are

$$\begin{aligned}
 \frac{\partial \tau_{11}}{\partial x} + \frac{\partial \tau_{12}}{\partial y} + \frac{\partial \tau_{13}}{\partial z} &= \rho_1 \frac{\partial^2 u_1}{\partial t^2} & \frac{\partial \tau_{21}}{\partial x} + \frac{\partial \tau_{22}}{\partial y} + \frac{\partial \tau_{23}}{\partial z} &= \rho_1 \frac{\partial^2 v_1}{\partial t^2} \\
 \frac{\partial \tau_{31}}{\partial x} + \frac{\partial \tau_{32}}{\partial y} + \frac{\partial \tau_{33}}{\partial z} &= \rho_1 \frac{\partial^2 w_1}{\partial t^2}
 \end{aligned}
 \tag{3.3}$$

For the SH-wave propagation along the x -axis, we have

$$u_1 = 0 \quad v_1 = v_1(x, z, t) \quad w_1 = 0
 \tag{3.4}$$

Taking transverse isotropy and setting $a_2 = 0$, we get from Eqs. (3.3)

$$\begin{aligned}
 \tau_{12} &= \mu_T \left(P \frac{\partial u_2}{\partial x} + R \frac{\partial u_2}{\partial z} \right) & \tau_{23} &= \mu_T \left(R \frac{\partial u_2}{\partial z} + Q \frac{\partial u_2}{\partial x} \right) \\
 \tau_{11} &= \tau_{22} = \tau_{33} = \tau_{23} = \tau_{13} = 0
 \end{aligned}
 \tag{3.5}$$

where

$$P = 1 + (\mu^* - 1)a_1^2 \quad Q = 1 + (\mu^* - 1)a_3^2 \quad R = (\mu^* - 1)a_1 a_3 \quad \mu^* = \frac{\mu_L}{\mu_T}
 \tag{3.6}$$

In the absence of body forces, Eq. (3.3) becomes

$$\frac{\partial \tau_{21}}{\partial x} + \frac{\partial \tau_{22}}{\partial y} + \frac{\partial \tau_{23}}{\partial z} = \rho_1 \frac{\partial^2 v_1}{\partial t^2}
 \tag{3.7}$$

where ρ_1 is density of the layer.

Using Eqs. (3.5)-(3.7), we get

$$P \frac{\partial^2 v_1}{\partial x^2} + 2R \frac{\partial^2 v_1}{\partial x \partial z} + Q \frac{\partial^2 v_1}{\partial z^2} = \frac{\rho_1}{\mu_T} \frac{\partial^2 v_1}{\partial t^2} \quad (3.8)$$

In order to solve Eq. (3.8), we take

$$v_1(x, z, t) = \xi(z) e^{ik(x-ct)} \quad (3.9)$$

Here, k is the wave number; c is the phase velocity of simple harmonic waves with a wave length $2\pi/k$.

From Eq. (3.8) and Eq. (3.9), we get

$$Q \frac{\partial^2 \xi(z)}{\partial z^2} + 2Rik \frac{\partial \xi(z)}{\partial z} + \left(\frac{\rho_1}{\mu_T} \omega^2 - Pk^2 \right) \xi(z) = 0 \quad (3.10)$$

Let the solution to Eq. (3.10) be

$$\xi(z) = A e^{-iks_1 z} + B e^{-iks_2 z} \quad (3.11)$$

where

$$s_j = \frac{1}{Q} \left[R + (-1)^{j+1} \sqrt{R^2 + Q \left(\frac{c^2}{c_1^2} - P \right)} \right] \quad j = 1, 2 \quad (3.12)$$

where A and B are arbitrary constants and $c_1 = \sqrt{\mu_T/\rho_1}$ is the shear velocity.

From Eq. (3.9) and Eq. (3.11), the equation of displacement of the upper reinforced medium is given by

$$u_2(x, z, t) = \left(A e^{-iks_1 z} + B e^{-iks_2 z} \right) e^{ik(x-ct)} \quad (3.13)$$

3.2. Solution for the lower half-space

The equation of motion for the lower half-space under initial stress P' acting along the x -axis can be written as (Love, 1911)

$$\begin{aligned} \frac{\partial \sigma_{11}}{\partial x} + \frac{\partial \sigma_{12}}{\partial y} + \frac{\partial \sigma_{13}}{\partial z} - P' \left(\frac{\partial \varpi_3}{\partial y} - \frac{\partial \varpi_3}{\partial z} \right) &= \rho_2 \frac{\partial^2 u_2}{\partial t^2} \\ \frac{\partial \sigma_{21}}{\partial x} + \frac{\partial \sigma_{22}}{\partial y} + \frac{\partial \sigma_{23}}{\partial z} - P' \left(\frac{\partial \varpi_3}{\partial x} \right) &= \rho_2 \frac{\partial^2 v_2}{\partial t^2} \\ \frac{\partial \sigma_{31}}{\partial x} + \frac{\partial \sigma_{32}}{\partial y} + \frac{\partial \sigma_{33}}{\partial z} - P' \left(\frac{\partial \varpi_3}{\partial x} \right) &= \rho_2 \frac{\partial^2 w_2}{\partial t^2} \end{aligned} \quad (3.14)$$

where σ_{11} , σ_{12} , σ_{13} , σ_{21} , σ_{22} , σ_{23} , σ_{31} , σ_{32} and σ_{33} are incremental stress components, u_2 , v_2 and w_2 are components of the displacement vector, P' is initial pressure in the lower half-space and ρ_2 is density of the lower half-space. Here, ϖ_1 , ϖ_2 and ϖ_3 are rotational components in the lower half-space, which are defined by

$$\varpi_1 = \frac{1}{2} \left(\frac{\partial w_2}{\partial y} - \frac{\partial v_2}{\partial z} \right) \quad \varpi_2 = \frac{1}{2} \left(\frac{\partial u_2}{\partial z} - \frac{\partial w_2}{\partial x} \right) \quad \varpi_3 = \frac{1}{2} \left(\frac{\partial v_2}{\partial x} - \frac{\partial u_2}{\partial y} \right) \quad (3.15)$$

Using the SH-wave conditions $u_2 = w_2 = 0$, $v_2 = v_2(x, z, t)$, Eq. (3.14) can be reduced to

$$\frac{\partial \sigma_{21}}{\partial x} + \frac{\partial \sigma_{23}}{\partial z} - \frac{P'}{2} \left(\frac{\partial^2 v_2}{\partial x^2} \right) = \rho_2 \frac{\partial^2 v_2}{\partial t^2} \quad (3.16)$$

The stress-strain relations are

$$\begin{aligned}\sigma_{11} = \sigma_{22} = \sigma_{13} = \sigma_{33} = 0 \quad \sigma_{21} = 2\mu_2 e_{xy} = 2\mu_2 \frac{1}{2} \left(\frac{\partial v_2}{\partial x} + \frac{\partial u_2}{\partial y} \right) \\ \sigma_{23} = 2\mu_2 e_{yz} = 2\mu_2 \frac{1}{2} \left(\frac{\partial w_2}{\partial y} + \frac{\partial v_2}{\partial z} \right)\end{aligned}\quad (3.17)$$

The heterogeneity of rigidity and density of the lower half-space are

$$\mu_2 = \mu'(1 + \varepsilon_1 z) \quad \rho_2 = \rho'(1 + \varepsilon_2 z) \quad (3.18)$$

Now, substituting the heterogeneity of rigidity from Eq. (3.18) into Eq. (3.17), we have

$$\sigma_{21} = \mu'(1 + \varepsilon_1 z) \frac{\partial v_2}{\partial x} \quad \sigma_{23} = \mu'(1 + \varepsilon_2 z) \frac{\partial v_2}{\partial z} \quad (3.19)$$

Equation of motion (3.16) with the help of equations (3.18) and (3.19) can be written as

$$\left(1 - \frac{P'}{2\mu'(1 + \varepsilon_1 z)}\right) \frac{\partial^2 v_2}{\partial x^2} + \frac{\partial^2 v_2}{\partial x^2} - \frac{\varepsilon_1}{1 + \varepsilon_1 z} \frac{\partial v_2}{\partial z} = \frac{\rho'}{\mu'} \left(\frac{1 + \varepsilon_2 z}{1 + \varepsilon_1 z}\right) \frac{\partial^2 v_2}{\partial t^2} \quad (3.20)$$

To solve Eq. (3.20), we take the following substitution

$$v_2 = V(z)e^{ik(x-ct)} \quad (3.21)$$

Using Eq. (3.21) in Eq. (3.20), we get

$$\frac{d^2 V(z)}{dz^2} + \frac{\varepsilon_1}{1 + \varepsilon_1 z} \frac{dV(z)}{dz} + \left[\frac{\rho'}{\mu'} \left(\frac{1 + \varepsilon_2 z}{1 + \varepsilon_1 z}\right) c^2 - \left(1 - \frac{P'}{2\mu'(1 + \varepsilon_1 z)}\right) \right] k^2 V(z) = 0 \quad (3.22)$$

After introducing $V(z) = \Phi(z)/\sqrt{(1 + \varepsilon_1 z)}$ into Eq. (3.22) in order to cancel the term $dV(z)/dz$, we have

$$\frac{d^2 \Phi(z)}{dz^2} + \left\{ \frac{\varepsilon_1^2}{4(1 + \varepsilon_1 z)^2} - k^2 \left[\left(1 - \frac{P'}{2\mu'(1 + \varepsilon_1 z)}\right) - \frac{c^2}{c_3^2} \left(\frac{1 + \varepsilon_2 z}{1 + \varepsilon_1 z}\right) \right] \right\} \Phi(z) = 0 \quad (3.23)$$

where c is the phase velocity and $c_2 = \sqrt{\mu'/\rho'}$.

Introducing non-dimensional quantities

$$r = \sqrt{1 - \frac{P'}{2\mu'(1 + \varepsilon_1 z)} - \frac{c^2}{c_2^2} \left(\frac{\varepsilon_2}{\varepsilon_1}\right)} \quad s = \frac{2rk(1 + \varepsilon_1 z)}{\varepsilon_1} \quad \omega = kc$$

in Eq. (3.23), we get

$$\frac{d^2 \Phi}{ds^2} + \left(\frac{1}{4s^2} + \frac{R}{2s^2} - \frac{1}{4} \right) \Phi(s) = 0 \quad (3.24)$$

where $R = \omega^2(\varepsilon_1 - \varepsilon_2)/(c_2^2 r k \varepsilon_1^2)$.

Equation (3.24) becomes the well known Whittaker's equation (Whittaker and Watson, 1990).

The solution to Eq. (3.24) is given by

$$\Phi(s) = DW_{\frac{r}{2}, 0}(s) + EW_{-\frac{r}{2}, 0}(-s) \quad (3.25)$$

where D and E are arbitrary constants and $W_{\frac{r}{2}, 0}(s)$, $W_{-\frac{r}{2}, 0}(s)$ are the Whittaker functions. Now considering the condition $V(z) \rightarrow 0$ as $z \rightarrow \infty$ i.e. $\Phi(s) \rightarrow 0$ as $s \rightarrow \infty$ in Eq. (3.21), the exact solution becomes

$$\Phi(s) = DW_{\frac{r}{2}, 0}(s) \quad (3.26)$$

The solution to Eq. (3.26) is given by

$$v_2 = V(z)e^{ik(x-ct)} = \frac{DW_{\frac{r}{2},0}(s)}{\sqrt{1 + \varepsilon_1 z}} e^{ik(x-ct)} \tag{3.27}$$

Equation (3.27) is the displacement for the SH-wave in the half space.

Now, expanding Eq. (3.27) up to the linear term, we have

$$v_2 = De^{\frac{-rk(1+\varepsilon_1 z)}{\varepsilon}} \sqrt{\frac{2rk}{\varepsilon_1}} \left[1 + (1 - R) \frac{2rk}{\varepsilon_1} (1 + \varepsilon_1 z) \right] e^{ik(x-ct)} \tag{3.28}$$

4. Boundary conditions

The displacement components and stress components are continuous at $z = -H$ and $z = 0$, therefore geometry of the problem leads to the following conditions:

- (1) At $z = -H$, the stress component $\tau_{23} = 0$.
- (2) At $z = 0$, the stress component of the layer and the half space is continuous, i.e. $\tau_{23} = \sigma_{23}$.
- (3) At $z = 0$, the velocity component of both layers is continuous, i.e. $v_1 = v_2$.

5. Dispersion relation

The dispersion relation for SH-waves can be obtained by using the above boundary conditions. Therefore, the displacement for the SH-waves in the in-homogeneous half-space using boundary conditions (3.1), (3.2) and (3.3) in Eq. (3.13) and Eq. (3.28) becomes (taking Whittaker’s function $W_{\frac{r}{2},0}(s)$ up to linear terms in s)

$$\begin{aligned} A(R - Q_{s1})e^{is_1kH} + B(R - Q_{s2})e^{is_2kH} &= 0 \\ ik[A(R - Q_{s1}) + B(R - Q_{s2})] \\ - D \frac{\mu'}{\mu_T \zeta} e^{-\frac{kr}{\varepsilon_1}} \sqrt{\frac{2kr}{\varepsilon_1}} \left[\frac{kr}{\varepsilon_1} (1 - R) + 1 \right] \left[\frac{(1 - R)kr}{1 + (1 - R) \frac{kr}{\varepsilon_1}} - kr \right] &= 0 \tag{5.1} \\ A + B - De^{-\frac{kr}{\varepsilon_1}} \sqrt{\frac{2kr}{\varepsilon_1}} \left[1 + (1 - R) \frac{kr}{\varepsilon} \right] &= 0 \end{aligned}$$

Now eliminating A , B and D from Eqs. (5.1), we obtain

$$\begin{bmatrix} (R - Q_{s1})e^{is_1kH} & (R - Q_{s2})e^{is_2kH} & 0 \\ ik(R - Q_{s1}) & ik(R - Q_{s2}) & -\frac{\mu'}{\mu_T \zeta} e^{-\frac{kr}{\varepsilon_1}} \sqrt{\frac{2kr}{\varepsilon_1}} \mathcal{A} \left[\frac{(1-R)kr}{\mathcal{A}} - kr \right] \\ 1 & 1 & -e^{-\frac{kr}{\varepsilon_1}} \sqrt{\frac{2kr}{\varepsilon_1}} \mathcal{A} \end{bmatrix} = 0 \tag{5.2}$$

where

$$\mathcal{A} = \frac{kr}{\varepsilon_1} (1 - R) + 1$$

On simplifying Eq. (5.2), we get

$$\tan \left[\frac{kH}{Q} \sqrt{R^2 + Q \left(\frac{c^2}{c_1^2} - P \right)} \right] = \frac{\mu'}{\mu_T} \frac{1}{\sqrt{R^2 + Q \left(\frac{c^2}{c_1^2} - P \right)}} \left[r - \frac{1 - R}{1 + (1 - R) \frac{kr}{\varepsilon_1}} \right] \tag{5.3}$$

Equation (5.3) is the dispersion equation of the SH-wave propagation in a fiber-reinforced anisotropic layer over a pre-stressed heterogeneous isotropic elastic half-space.

- *Case 1*

If we take $a_1 = 1$, $a_2 = a_3 = 0$ then $\rho_1 \rightarrow \mu_L/\mu_T$ and $\mu_L \rightarrow \mu_T \rightarrow \mu_1$, then $P \rightarrow 1$, $Q \rightarrow 1$ and $R \rightarrow 1$, therefore Eq. (5.3) reduces to

$$\tan \left(kH \sqrt{\frac{c^2}{c_1^2} - 1} \right) = \frac{\mu'}{\mu_1} \frac{1}{\sqrt{\frac{c^2}{c_1^2} - 1}} \left[r - \frac{1 - R}{1 + (1 - R) \frac{kr}{\varepsilon_1}} \right] \quad (5.4)$$

This is the dispersion equation of a homogenous reinforced medium over a pre-stressed heterogeneous half space.

- *Case 2*

When the lower half-space is homogeneous, that is $\varepsilon_1 \rightarrow 0$, $\varepsilon_2 \rightarrow 0$, which implies that $r = \sqrt{1 - \frac{P'}{2\mu'} - \frac{c^2}{c_2^2}}$, therefore Eq. (5.3) reduces to

$$\tan \left[\frac{kH}{Q} \sqrt{R^2 + Q \left(\frac{c^2}{c_1^2} - P \right)} \right] = \frac{\mu'}{\mu_T} \frac{1}{\sqrt{R^2 + Q \left(\frac{c^2}{c_1^2} - P \right)}} \sqrt{1 - \frac{P'}{2\mu'} - \frac{c^2}{c_2^2}} \quad (5.5)$$

This is the dispersion equation of an anisotropic reinforced medium over a pre-stressed homogenous half space.

- *Case 3*

When the lower half-space is stress free and homogeneous, that is $\varepsilon_1 \rightarrow 0$, $\varepsilon_2 \rightarrow 0$, $P' \rightarrow 0$, which implies that $r = \sqrt{1 - \frac{c^2}{c_2^2}}$, therefore Eq. (5.3) reduces to

$$\tan \left[\frac{kH}{Q} \sqrt{R^2 + Q \left(\frac{c^2}{c_1^2} - P \right)} \right] = \frac{\mu'}{\mu_T} \frac{1}{\sqrt{R^2 + Q \left(\frac{c^2}{c_1^2} - P \right)}} \sqrt{1 - \frac{c^2}{c_2^2}} \quad (5.6)$$

This is the dispersion equation of an anisotropic reinforced medium over a pre-stressed homogenous half space.

- *Case 4*

For a homogeneous reinforced medium over an homogeneous half space, we take $\varepsilon_1 = 0$, $\varepsilon_2 = 0$, $P' \rightarrow 0$, $a_1 = 1$, $a_2 = a_3 = 0$ then $\rho_1 \rightarrow \mu_L/\mu_T$ and $\mu_L \rightarrow \mu_T \rightarrow \mu_1$, then $P \rightarrow 1$, $Q \rightarrow 1$ and $R \rightarrow 1$ therefore Eq. (5.3) reduces to

$$\tan \left(kH \sqrt{\frac{c^2}{c_1^2} - 1} \right) = \frac{\mu'}{\mu_1} \frac{\sqrt{1 - \frac{c^2}{c_2^2}}}{\sqrt{\frac{c^2}{c_1^2} - 1}} \quad (5.7)$$

Equation (5.7) is the classical dispersion equation of SH-waves given by Love (1911) and Ewing *et al.* (1957).

6. Numerical analysis and discussion

To show the effect of heterogeneity parameters, the initial stress parameter and steel reinforced parameters on SH-wave propagation in a fiber-reinforced anisotropic layer over a heterogeneous isotropic elastic half-space, we take the data assumed by Gupta (2014) and Gubbins (1990) as shown in Table 1 and the values of parameters for figures in Table 2. We have plotted the non-dimensional phase velocity c/c_1 against the dimensionless wave number kH on the propagation of SH-wave in the fiber-reinforced anisotropic layer by using MATLAB software. The effects of reinforced parameters a_1^2 , a_3^2 , initial stress parameter $\zeta = P'/(2\mu')$ and heterogeneity parameters ε_1/k , ε_2/k are shown in Figs. 2-5. Figure 2a illustrates the effect of heterogeneity parameters in the presence of reinforced parameters and stress parameter on the propagation of SH-waves.

Table 1. Data for the fiber-reinforced anisotropic layer and the elastic medium

Symbol	Numerical value	Units
μ_T	$5.65 \cdot 10^9$	N/m ²
μ_L	$2.46 \cdot 10^9$	N/m ²
λ	$5.65 \cdot 10^9$	N/m ²
α	$-1.28 \cdot 10^{10}$	N/m ²
β	$220.09 \cdot 10^9$	N/m ²
ρ_1	7800	kg/m ³
a_3^2	0.75	–
a_1^2	0.25	–
μ'	$6.34 \cdot 10^{10}$	N/m ²
ρ'	3364	kg/m ³

Table 2. Values of parameters for the figures

Figure	a_1^2	a_3^2	ζ	ε_1/k	ε_2/k
2a	0.35	0.65	0.5	–	–
2b	0	0	0.5	–	–
3a	0.35	0.65	0	–	–
3b	0	0	0	–	–
4a	–	–	0.5	0.4	0.4
4b	–	–	0.5	0.4	0.4
5a	–	–	0	0.4	0.4
5b	–	–	0	0.4	0.4
6a	0.35	0.65	–	0.4	0.4
6b	0.35	0.65	–	0.4	0.4

It is clear from this figure that the phase velocity decreases with an increase in the heterogeneity parameters. Figure 2b represents the variation of dimensionless phase velocity with the dimensionless wave number on the propagation of SH-waves for different values of heterogeneity parameters in the absence of the reinforced parameter for the initially stressed half-space. It is observed from these curves that as the heterogeneity parameters in the half-space increase, the velocity of SH-wave decreases. From Figs. 2a and 2b, it is clear that the SH-wave propagation is more influenced by the heterogeneity parameters in comparison to reinforcement in the upper layer. It is also seen that for a large value of heterogeneity parameters, the curves of phase velocities are significantly distanced from each other.

Figure 3a shows the effect of heterogeneity parameters in the presence of reinforced parameters on the propagation of SH-waves when the lower half is stress free. It is clear from this

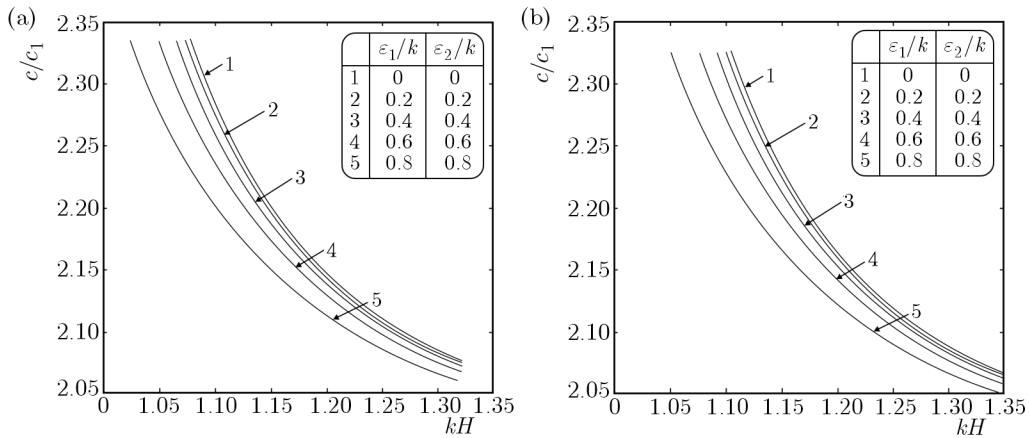


Fig. 2. Variation of the phase velocity against the wave number for different values of heterogeneity parameters in the (a) presence of the reinforced parameters and (b) absence of the reinforced parameter for the initially stressed half-space

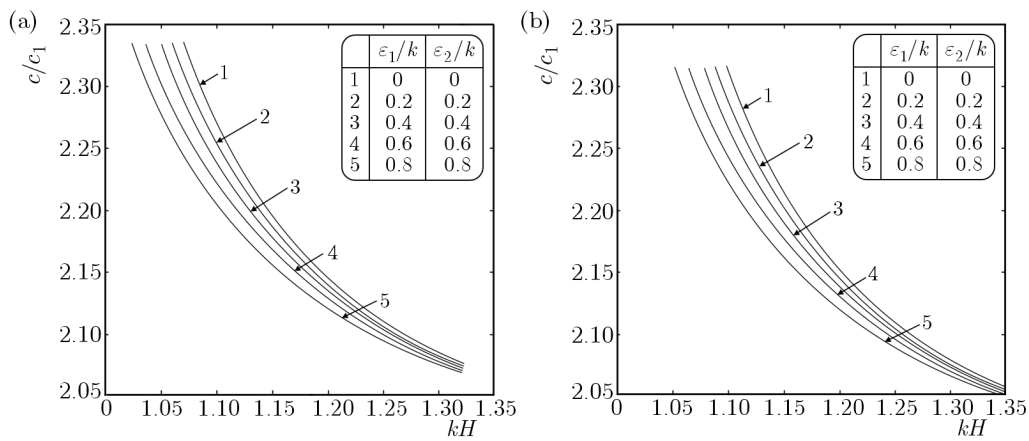


Fig. 3. Variation of the phase velocity against the wave number for different values of heterogeneity parameters in the (a) presence of the reinforced parameters and (b) absence of the reinforced parameter for the stress free half-space

figure that the phase velocity decreases with an increase in the heterogeneity parameters. Figure 3b represents the variation of dimensionless phase velocity with the dimensionless wave number on the propagation of SH-waves for different values of heterogeneity parameters in the absence of the initial stress and reinforced parameter. It is observed from these curves that as the heterogeneity parameters in the half-space increase, the velocity of SH-wave decreases.

Figure 4a shows the effect of reinforced parameters a_1^2 and a_3^2 on the propagation of SH-waves at constant stress and heterogeneity parameters. It is seen from the diagram that as a_1^2 increases as well as a_3^2 decreases, the velocity of SH-wave decreases. Figure 4b shows the effect of reinforced parameters a_1^2 and a_3^2 on the propagation of SH-waves at constant stress and heterogeneity parameters. It is seen from the diagram that as a_1^2 decreases as well as a_3^2 increases, the velocity of SH-wave decreases.

Figure 5a shows the effect of reinforced parameters a_1^2 and a_3^2 on the propagation of SH-waves at constant heterogeneity parameters in the absence of the initial stress. It is seen from the diagram that as a_1^2 increases as well as a_3^2 decreases, the velocity of SH-wave decreases. Figure 5b shows the effect of reinforced parameters a_1^2 and a_3^2 on the propagation of SH-waves at constant heterogeneity parameters in the absence of the initial stress. It is seen from the diagram that as a_1^2 decreases as well as a_3^2 increases, the velocity of SH-wave decreases.

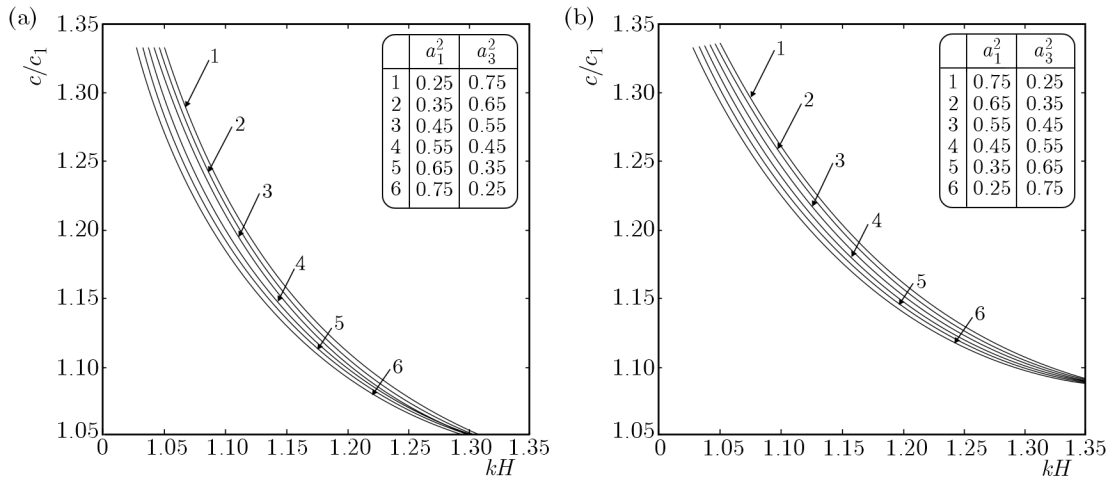


Fig. 4. Variation of the phase velocity against the wave number for different values reinforced parameters at constant stress and heterogeneity parameters

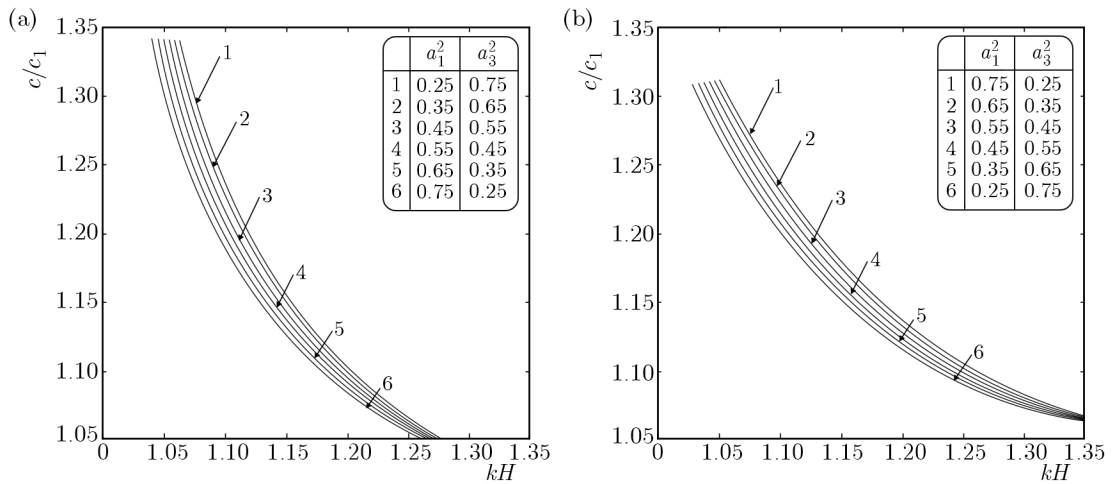


Fig. 5. Variation of the phase velocity against the wave number for different values reinforced parameters at constant heterogeneity parameters in the absence of the initial stress

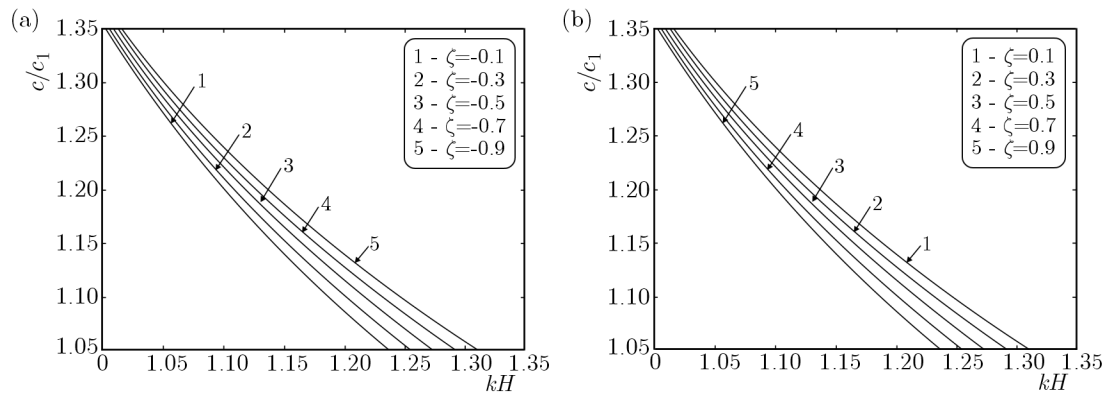


Fig. 6. Variation of the phase velocity against the wave number for different values (a) tensile stress (b) compressive stress in the presence of the heterogeneity parameter and reinforced parameters

In Fig. 6a, the curves show the effect of tensile stress $\zeta = P'/(2\mu') < 0$ on the propagation of the SH-wave in a fiber-reinforced anisotropic layer in the presence of the heterogeneity parameter in the lower half-space and reinforced parameters in the layer. It is clear from this figure that the phase velocity increases with an increase in the tensile stress. In Fig. 6b, the curves show the effect of compressive stress $\zeta = P'/(2\mu') > 0$ on the propagation of SH-waves in a fiber-reinforced anisotropic layer in the presence of the heterogeneity parameter in the lower half-space and reinforced parameters in the layer. It is clear from this figure that the phase velocity decreases with an increase in the compressive stress.

7. Conclusions

Two layers are considered in the problem analysed in this paper: a fiber-reinforced anisotropic upper layer and a pre-stressed heterogeneous lower layer with exponential variation in rigidity and density. The Whittaker function and the method of separation of variables are employed in order to find the dispersion of SH-waves in the fiber-reinforced layer placed over a pre-stressed heterogeneous elastic half-space. Displacement of the upper fiber-reinforced layer is derived in a closed form and the dispersion curves are drawn for various values of heterogeneity, stress and reinforced parameters. In a particular case, the dispersion equation coincides with the well-known classical equation of the Love wave when the upper and lower layer are homogeneous and stress free. The above results may be used to study the surface wave propagation in a fiber reinforced medium. This validates the solution.

From above numerical analysis, it may be concluded that:

- In all the figures, the dimensionless phase velocity of SH-waves decreases with an increase in the dimensionless wave number.
- The dimensionless phase velocity of SH-wave shows a remarkable change with heterogeneity and reinforced parameters.
- It is observed that the depth increases, the velocity of SH-waves decreases.
- The velocity of SH-waves decreases with an increase in the reinforced parameter of the upper layer and the inhomogeneous parameter of the lower half-space. This is the property of seismic wave propagation in the crustal layer.
- The phase velocity increases with an increase in the tensile stress but decreases with an increase in the compressive stress of the lower half-space.

Acknowledgements

The authors express their sincere thanks to the honorable reviewers for their useful suggestions and valuable comments.

Funding

This research has not received any specific grant from a funding agency in the public, commercial, or not-for-profit sectors.

References

1. BELFIELD A.J., ROGERS T.G., SPENCER A.J.M., 1983, Stress in elastic plates reinforced by fibers lying in concentric circles, *Journal of the Mechanics and Physics of Solids*, **31**, 1, 25-54
2. CHADWICK P., SMITH G.D., 1977, Foundations of the theory of surface waves in anisotropic elastic materials, *Advances in Applied Mechanics*, **17**, 303-376

3. CHATTOPADHYAY A., CHOUDHURY S., 1995, Magnetoelastic shear waves in an infinite self-reinforced plate, *International Journal for Numerical and Analytical Methods in Geomechanics*, **19**, 4, 289-304, DOI: 10.1002/nag.1610190405
4. CHATTOPADHYAY A., GUPTA S., SAHU S.A., SINGH A.K., 2012, Dispersion of horizontally polarized shear waves in an irregular non-homogeneous self reinforced crustal layer over a semi-infinite self-reinforced medium, *Journal of Vibration and Control*, DOI: 10.1177/1077546311430699
5. CHATTOPADHYAY A., SINGH A.K., DHUA S., 2014, Effect of heterogeneity and reinforcement on propagation of a crack due to shear waves, *International Journal of Geomechanics*, 10.1061/(ASCE)GM.1943-5622.0000356, 04014013
6. CRAMPIN S., TAYLOR D.B., 1971, The propagation of surface waves in anisotropic media, *Geophysical Journal of the Royal Astronomical Society*, **25**, 71-87
7. DESTRADE M., 2001, Surface waves in orthotropic incompressible materials, *Journal of the Acoustical Society of America*, **110**, 837-840
8. DESTRADE M., 2003, The explicit secular equation for surface acoustic waves in mono-clinic elastic crystals, *Journal of the Acoustical Society of America*, **109**, 1398-1402
9. DOWAIKH M.A., OGDEN R.W., 1990, On surface waves and deformations in a pre-stressed incompressible elastic solid, *IMA Journal of Mathematical Control and Information*, **44**, 261-284
10. DU J., XIAN K., WANG J., YONG Y.K., 2008, Propagation of Love waves in prestressed piezoelectric layered structures loaded with viscous liquid, *Acta Mechanica Sinica*, **21**, 542-548
11. EWING W.M., JARDETZKY W.S., PRESS F., 1957, *Elastic Waves in Layered Media*, McGraw-Hill, New York
12. GUBBINS D., 1990, *Seismology and Plate Tectonics*, Cambridge University Press, Cambridge
13. GUPTA I.S., 2014, Note on surface wave in fiber-reinforced medium, *Mathematical Journal of Interdisciplinary Sciences*, **3**, 1, 23-35
14. GUPTA R.R., GUPTA R.R., 2013, Analysis of wave motion in an anisotropic initially stressed fiber reinforced thermoelastic medium, *Earthquakes and Structures, An International Journal*, **4**, 1, 1-10
15. KUNDU S., MANNA S., GUPTA S., 2014, Propagation of SH-wave in an initially stressed orthotropic medium sandwiched by a homogeneous and an inhomogeneous semi-infinite media, *Mathematical Methods in the Applied Sciences*, DOI: 10.1002/mma.3203
16. LI X.Y., WANG Z.K., HUANG S.H., 2004, Love waves in functionally graded piezoelectric materials, *International Journal of Solids and Structures*, **41**, 7309-7328
17. LOVE A.E.H., 1911, *Some Problems of Geo-Dynamics*, London, UK, Cambridge University Press
18. MOZHAEV V.G., 1995, Some new ideas in the theory of surface acoustic waves in anisotropic media, *IUTAM Symposium on Anisotropy, Heterogeneity and Nonlinearity in Solid Mechanics: Proceedings of the IUTAM-ISIMM Symposium* (Nottingham, UK, 1994), edited by D.F. Parker and A.H. England, Kluwer, Dordrecht, 455-462
19. MUSGRAVE M.J.P., 1959, The propagation of elastic waves in crystals and other anisotropic media, *Reports on Progress in Physics*, **22**, 74-96
20. NAIR S., SOTIROPOULOS D.A., 1999, Interfacial waves in incompressible monoclinic materials with an interlayer, *Mechanical of Materials*, **31**, 225-233
21. OGDEN R.W., SINGH B., 2011, Propagation of waves in an incompressible transversely isotropic elastic solid with initial stress: Biot revisited, *Journal of Mechanics of Materials and Structures*, **6**, 453-477
22. OGDEN R.W., SINGH B., 2014, The effect of rotation and initial stress on the propagation of waves in a transversely isotropic elastic solid, *Wave Motion*, **51**, 1108-1126
23. QIAN Z., JIN F., WANG Z., 2004, Love waves propagation in a piezoelectric layered structure with initial stresses, *Acta Mechanica*, **171**, 41-57

24. TING T.C.T., 2002, An explicit secular equation for surface waves in an elastic material of general anisotropy, *Quarterly Journal of Mechanics and Applied Mathematics*, **55**, 297-311
25. SAHU S.A., SAROJ P.K., PASWAN B., 2014 Shear waves in a heterogeneous fiber-reinforced layer over a half-space under gravity, *International Journal of Geomechanics*, 10.1061/(ASCE)GM.1943-5622.0000404
26. SPENCER A.J.M., 1972, *Deformations of Fibre-Reinforced Materials*, Oxford University Press, London
27. WANG Q., QUEK S.T., 2001, Love waves in piezoelectric coupled solid media, *Smart Materials and Structures*, **10**, 380-388
28. WATANABE K., PAYTON R.G., 2002, Green's function for SH waves in a cylindrically monoclinic material, *Journal of Mechanics Physics of Solids*, **50**, 2425-2439
29. WHITTAKER E.T., WATSON G.N., 1991, *A Course of Modern Analysis*, Universal Book Stall, New Delhi, India
30. ZAITSEV B.D., KUZNETSOVA I.E., JOSHI S.G., BORODINA I.A., 2001, Acoustic waves in piezoelectric plates bordered with viscous and conductive liquid, *Ultrasonics*, **39**, 1, 45-50
31. ZAKHARENKO A., 2005, A Love-type waves in layered systems consisting of two cubic piezoelectric crystals, *Journal of Sound and Vibration*, **285**, 877-886

Manuscript received January 9, 2015; accepted for print September 4, 2015

THE ONSET OF CONVECTION IN A ROTATING MULTICOMPONENT FLUID LAYER

JYOTI PRAKASH, VIRENDER SINGH, RAJEEV KUMAR, KULTARAN KUMARI

Department of Mathematics and Statistics, Himachal Pradesh University, Shimla, India

e-mail: jpsmaths67@gmail.com

The onset of convective instability is analysed in a rotating multicomponent fluid layer in which density depends on n stratifying agents (one of them is heat) having different diffusivities. Two problems have been analysed mathematically. In the first problem, a sufficient condition is derived for the validity of the principle of the exchange of stabilities. Further, when the complement of this condition holds good, oscillatory motions of neutral or growing amplitude can exist, and thus it is important to derive upper bounds for the complex growth rate of such motions when at least one of the bounding surfaces is rigid so that exact solutions of the problem in closed form are not obtainable. Thus, as the second problem, bounds for the complex growth rates are also obtained. Above results are uniformly valid for quite general nature of the bounding surfaces.

Keywords: multicomponent convection, principle of exchange of stabilities, oscillatory motions, complex growth rate, concentration Rayleigh number, Lewis number

1. Introduction

When density of a fluid is determined by two stratifying agents, such as heat and salt diffusing at different rates, the fluid at rest can be unstable even if its density increases downward. This convective phenomenon is known as thermosolutal convection or more generally as double diffusive convection. This phenomenon has, now, been extensively studied. For review on the subject of double diffusive convection one may be referred to (Turner, 1973, 1974, 1985; Brandt and Fernando, 1996; Radko, 2013; Sekar *et al.*, 2013).

Although the subject of double diffusive convection is still an important area of research (Sekar *et al.*, 2013; Kellner and Tilgner, 2014; Nield and Kuznetsov, 2011; Schmitt, 2011), there are many fluid systems where more than two components are present (Turner, 1985; Griffiths, 1979b). Examples of such systems include the solidification of molten alloys, Earth core, geothermally heated lakes, sea water, magmas and their laboratory models. The presence of more than one salt in fluid mixtures is very often requested for describing natural phenomena such as contaminant transport, acid rain effects, underground water flow and warming of the stratosphere. The subject of more than two stratifying agents has attracted many researchers (Griffiths, 1979a,b; Pearlstein *et al.*, 1989; Rionero, 2013a,b, 2014; Lopez *et al.*, 1990; Terrones, 1993; Poliakos, 1985; Shivakumara and Naveen Kumar, 2014). In double diffusive convection (Turner, 1974) or, more generally, in multicomponent convection (Turner, 1985; Griffiths, 1979a) instability may occur in two kinds: first in form of steady (or stationary) convection which is called as ‘salt finger’ modes and the second in form of oscillatory motions of growing amplitude (or overstability) which is called as ‘diffusive convection’. When a warm and saltier fluid lies above a cold and fresh fluid then stationary convection is preferred, and when a cold and fresher fluid lies above a warm and saltier fluid then oscillatory motions are preferred. The essence of these researchers is that small concentrations of the third diffusing component with a smaller mass

diffusivity can have a significant effect upon the nature of diffusive instabilities and diffusive convection. The salt finger modes are simultaneously unstable under a wide range of conditions when the density gradients due to components with the greatest and smallest diffusivity are of the same signs even if the overall density stratification is hydrostatically stable. These researchers also notice some fundamental differences between doubly and triply diffusive convection. One is that if the gradients of two of the stratifying agents are held fixed, then three critical values of the Rayleigh number of the third agent are sometimes required to specify the linear stability criteria (in double diffusive convection only one critical Rayleigh number is required). The other difference is that the onset of convection for the case of free boundaries may occur via quassiperiodic bifurcation from the motionless basic state.

Now the triply diffusive convection despite its complexities has also been well studied. But, to the author knowledge, not many investigations have been conducted on stability theory when more than three components are present, which may be, perhaps, due to the complexities involved in mathematical calculations and numerical computations. Some worth researches which may be referred here are due to Terrones and Pearlstein (1989) who derived analytical results for n components and numerical results for $n = 5$ using dynamically free boundary conditions. Later Lopez *et al.* (1990) predicted that the results of triply diffusive convection may be extended to multicomponent convection with n components for rigid surfaces also. Further significant contributions to multicomponent convection are due to Ryzhkov and Shevtsova (2007, 2009) and Ryzhkov (2013).

The establishment of nonoccurrence of any slow oscillatory motions which may be neutral or unstable implies the validity of the principle of the exchange of stabilities (PES). The validity of this principle in stability problems eliminates unsteady terms from linearized perturbation equations which results in notable mathematical simplicity since the transition from stability to instability occurs via a marginal state which is characterized by the vanishing of both real and imaginary parts of the complex time eigenvalue associated with the perturbation. Pellew and Southwell (1940) proved the validity of PES (i.e. occurrence of stationary convection) for the classical Rayleigh-Benard instability problem. Prakash *et al.* (2014a) established such a criterion for the triply diffusive convection problem.

To study the effect of rotation on a multicomponent fluid layer is an interesting topic. Prakash *et al.* (2014b) derived a sufficient condition for the occurrence of stationary convection and upper bounds (Prakash *et al.*, 2015) for the complex growth rate of an arbitrary oscillatory motion of neutral or growing amplitude in rotatory hydrodynamic triply diffusive convection. The further extension of these results to the problem of the onset of convection in a multicomponent fluid layer in the domains of astrophysics and terrestrial physics, wherein the liquid concerned has the property of electrical conduction and the magnetic field and rotation are prevalent, is very much sought after in the present context.

In the present work, we analyse the onset of buoyancy driven convection in a multicomponent fluid layer in the presence of uniform vertical rotation. We generalize the existing results of the rotatory hydrodynamic triply diffusive convection problem concerning the validity of the principle of the exchange of stabilities (Prakash *et al.*, 2014b) and arresting the complex growth rate of oscillatory motion (when it occurs) (Prakash *et al.*, 2015) which are important especially when at least one boundary is rigid so that exact solutions in the closed form are not obtainable. To the authors knowledge, no such results have been obtained so far for the hydrodynamical systems with more than three components. The results derived herein are uniformly valid for any combination of the rigid and free boundaries and the results of doubly diffusive (Banerjee *et al.*, 1981; Gupta *et al.*, 1986) and triply diffusive convection (Prakash *et al.*, 2014a,b,c, 2015) follow as a consequence. Further, the importance of the results obtained herein lies in that these results may be used for any rotatory hydrodynamic multicomponent system where no mathematical calculation or numerical computation is possible.

2. Mathematical formulation and analysis

A viscous finitely heat conducting Boussinesq fluid of infinite horizontal extension is statistically confined between two horizontal boundaries $z = 0$ and $z = d$ which are respectively maintained at uniform temperatures T_0 and $T_1 (< T_0)$ and uniform concentrations $S_{10}, S_{20}, \dots, S_{(n-1)0}$ and $S_{11} (< S_{10}), S_{21} (< S_{20}), \dots, S_{(n-1)1} (< S_{(n-1)0})$ in the force field of gravity and in the presence of uniform vertical rotation (as shown in Fig. 1). It is assumed that the cross-diffusion effects of the stratifying agents can be neglected.

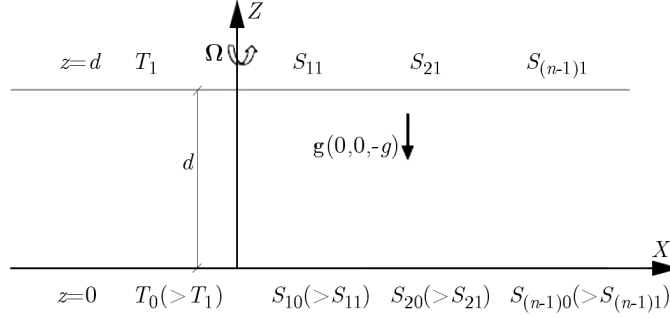


Fig. 1. Physical configuration

The basic equations that govern the motion of the rotatory hydrodynamic multicomponent fluid layer are as follows (Prakash *et al.*, 2014b; Terrones and Pearlstein, 1989)

$$\begin{aligned}
 \frac{\partial u_j}{\partial x_j} &= 0 \\
 \frac{\partial u_i}{\partial t} + u_j \frac{\partial u_i}{\partial x_j} &= -\frac{\partial}{\partial x_i} \left(\frac{P_1}{\rho_0} - \frac{1}{2} |(\mathbf{\Omega} \times \mathbf{r})|^2 \right) + \left(1 + \frac{\delta \rho}{\rho_0} + \frac{\delta \rho_1}{\rho_0} + \frac{\delta \rho_2}{\rho_0} + \dots + \frac{\delta \rho_{n-1}}{\rho_0} \right) X_i \\
 &\quad + 2\varepsilon_{ijk} u_j \Omega_k + \nu \nabla^2 u_i \\
 \frac{\partial T}{\partial t} + u_j \frac{\partial T}{\partial x_j} &= \kappa \nabla^2 T \\
 \frac{\partial S_1}{\partial t} + u_j \frac{\partial S_1}{\partial x_j} &= \kappa_1 \nabla^2 S_1 \\
 \frac{\partial S_2}{\partial t} + u_j \frac{\partial S_2}{\partial x_j} &= \kappa_2 \nabla^2 S_2 \\
 &\vdots \\
 \frac{\partial S_{n-1}}{\partial t} + u_j \frac{\partial S_{n-1}}{\partial x_j} &= \kappa_{n-1} \nabla^2 S_{n-1}
 \end{aligned} \tag{2.1}$$

where ρ is density; t is time; x_j ($j = 1, 2, 3$) are cartesian coordinates x, y, z ; u_j ($j = 1, 2, 3$) are velocity components; X_i ($i = 1, 2, 3$) are components of the external force in the x, y, z directions, respectively; P_1 is pressure; μ is viscosity; $\mathbf{\Omega}$ is angular velocity; T is temperature, κ is the coefficient of thermal diffusivity; S_1, S_2, \dots, S_{n-1} are $n - 1$ concentrations and $\kappa_1, \kappa_2, \dots, \kappa_{n-1}$ are respectively the coefficients of mass diffusivity of S_1, S_2, \dots, S_{n-1} with $\kappa_1 > \kappa_2 > \dots > \kappa_{n-1}$.

The above basic equations must be supplemented by the equation of state

$$\rho = \rho_0 [1 + \alpha(T_0 - T_1) - \alpha_1(S_{10} - S_{11}) - \alpha_2(S_{20} - S_{21}) - \dots - \alpha_{n-1}(S_{(n-1)0} - S_{(n-1)1})] \tag{2.2}$$

where $\alpha, \alpha_1, \alpha_2, \dots, \alpha_{n-1}$ are respectively the coefficients of volume expansion due to temperature variation and concentration variations for $n - 1$ concentration components S_1, S_2, \dots, S_{n-1} .

ρ_0 is the value of ρ at $z = 0$. $\nu = \mu/\rho_0$ is kinematic viscosity and $\frac{P_1}{\rho_0} - \frac{1}{2}|\mathbf{\Omega} \times \mathbf{r}|^2$ is hydrostatic pressure.

The basic state is assumed to be stationary, and the standard linear stability analysis procedure as outlined in the studies of Prakash *et al.* (2014b) is followed to obtain the following non-dimensional stability equations

$$\begin{aligned} (D^2 - a^2)\left(D^2 - a^2 - \frac{\sigma}{\text{Pr}}\right)w &= \text{Ra}a^2\theta - R_1a^2\phi_1 - R_2a^2\phi_2 - \dots - R_{n-1}a^2\phi_{n-1} + \text{Ta}D\zeta \\ (D^2 - a^2 - \sigma)\theta &= -w \\ \left(D^2 - a^2 - \frac{\sigma}{\text{Le}_1}\right)\phi_1 &= -\frac{w}{\text{Le}_1} \\ \left(D^2 - a^2 - \frac{\sigma}{\text{Le}_2}\right)\phi_2 &= -\frac{w}{\text{Le}_2} \\ &\vdots \\ \left(D^2 - a^2 - \frac{\sigma}{\text{Le}_{n-1}}\right)\phi_{n-1} &= -\frac{w}{\text{Le}_{n-1}} \end{aligned} \quad (2.3)$$

and

$$\left(D^2 - a^2 - \frac{\sigma}{\text{Pr}}\right)\zeta = -Dw \quad (2.4)$$

respectively.

Equations (2.3) and (2.4) are to be solved using the following appropriate boundary conditions:

— $w = 0 = \theta = \phi_1 = \phi_2 = \dots = \phi_{n-1}$ on both the horizontal boundaries which are at

$$z = 0 \quad \text{and} \quad z = 1 \quad (2.5)$$

— and on rigid boundary

$$Dw = \zeta = 0 \quad (2.6)$$

— or on free boundary

$$D^2w = D\zeta = 0 \quad (2.7)$$

the meaning of the symbols involved in Eqs. (2.3) and (2.4) from the physical point of view are as follows: z is the vertical coordinate, $D = d/dz$ is differentiation w.r.t. z , $a^2 > 0$ is square of the wave number, $\text{Pr} > 0$ is the thermal Prandtl number which is a measure of relative importance of heat conduction and viscosity of the fluid and varies from fluid to fluid. For air $\text{Pr} = 0.7$ (approximately), for water $\text{Pr} = 7$ (approximately), for mercury $\text{Pr} = 0.044$ (approximately) and for glycerine $\text{Pr} = 7250$. The Prandtl number of some fluids (particularly water) depends considerably on temperature. $\text{Le}_1 > 0, \text{Le}_2 > 0, \dots, \text{Le}_{n-1} > 0$ are the Lewis numbers for $n - 1$ concentrations S_1, S_2, \dots, S_{n-1} , respectively, $\text{Ta} > 0$ is the Taylor number, $\text{Ra} > 0$ is the thermal Rayleigh number, $R_1 > 0, R_2 > 0, \dots, R_{n-1} > 0$ are the concentration Rayleigh numbers for the $n - 1$ concentration components. A concentration Rayleigh number is the ratio of the buoyancy forces (which drive free convective transport of solute) to dispersive/viscous forces (which disperse solute and dissipate free convective transport). In the present problem, these have stabilizing effect on the onset of instability. w is vertical velocity, θ is temperature and $\phi_1, \phi_2, \dots, \phi_{n-1}$ are respective concentrations of the $n - 1$ components. $\sigma = \sigma_r + i\sigma_i$ is the complex growth rate where σ_r and σ_i are real constants. For $\sigma_r < 0$, the system is always stable while for $\sigma_r > 0$, the system becomes unstable. When $\sigma = 0$, the system is marginally stable

ensuring the validity of the principle of the exchange of stabilities. When $\sigma_r \geq 0$ and $\sigma_i \neq 0$, the overstability of periodic motion is possible and oscillatory motions of growing or neutral amplitude occur. It may further be noted that equations (2.3) and (2.4) describe an eigenvalue problem for p and govern rotatory hydrodynamic multicomponent convection for quite general nature of the bounding surfaces.

Theorem 1: If $(w, \theta, \phi_1, \phi_2, \dots, \phi_{n-1}, \zeta, \sigma)$, $Ra > 0$, $R_1 > 0$, $R_2 > 0, \dots, R_{n-1} > 0$, $Ta > 0$, $\sigma_r \geq 0$ is a solution to Eqs. (2.3) and (2.4) together with boundary conditions (2.5)-(2.7) and

$$\frac{R_1 Pr}{2Le_1^2 \pi^4} + \frac{R_2 Pr}{2Le_2^2 \pi^4} + \dots + \frac{R_{n-1} Pr}{2Le_{n-1}^2 \pi^4} + \frac{Ta}{\pi^4} \leq 1$$

then $\sigma_i = 0$. In particular,

$$\sigma_r = 0 \Rightarrow \sigma_i = 0 \quad \text{if} \quad \frac{R_1 Pr}{2Le_1^2 \pi^4} + \frac{R_2 Pr}{2Le_2^2 \pi^4} + \dots + \frac{R_{n-1} Pr}{2Le_{n-1}^2 \pi^4} + \frac{Ta}{\pi^4} \leq 1$$

Proof: Multiplying Eq. (2.3)₁ by w^* (the superscript * henceforth denotes complex conjugation) throughout and integrating the resulting equation over the vertical range of z , we have

$$\begin{aligned} \int_0^1 w^* (D^2 - a^2) \left(D^2 - a^2 - \frac{\sigma}{Pr} \right) w \, dz &= Ra a^2 \int_0^1 w^* \theta \, dz - R_1 a^2 \int_0^1 w^* \phi_1 \, dz \\ &- R_2 a^2 \int_0^1 w^* \phi_2 \, dz - \dots - R_{n-1} a^2 \int_0^1 w^* \phi_{n-1} \, dz + Ta \int_0^1 w^* D \zeta \, dz \end{aligned} \tag{2.8}$$

Making use of Eqs. (2.3)₂₋₆ and (2.4), we can write

$$\begin{aligned} \int_0^1 w^* (D^2 - a^2) \left(D^2 - a^2 - \frac{\sigma}{Pr} \right) w \, dz &= -Ra a^2 \int_0^1 \theta (D^2 - a^2 - \sigma^*) \theta^* \, dz \\ &+ R_1 a^2 Le_1 \int_0^1 \phi_1 \left(D^2 - a^2 - \frac{\sigma^*}{Le_1} \right) \phi_1^* \, dz + R_2 a^2 Le_2 \int_0^1 \phi_2 \left(D^2 - a^2 - \frac{\sigma^*}{Le_2} \right) \phi_2^* \, dz + \dots \\ &+ R_{n-1} a^2 Le_{n-1} \int_0^1 \phi_{n-1} \left(D^2 - a^2 - \frac{\sigma^*}{Le_{n-1}} \right) \phi_{n-1}^* \, dz + Ta \int_0^1 \zeta \left(D^2 - a^2 - \frac{\sigma^*}{Pr} \right) \zeta^* \, dz \end{aligned} \tag{2.9}$$

Integrating the various terms of Eq. (2.9) by parts for an appropriate number of times and utilizing boundary conditions (2.5)-(2.7), we obtain

$$\begin{aligned} \int_0^1 (|D^2 w|^2 + 2a^2 |Dw|^2 + a^4 |w|^2) + \frac{\sigma}{Pr} \int_0^1 (|Dw|^2 + a^2 |w|^2) \, dz \\ = Ra a^2 \int_0^1 (|D\theta|^2 + a^2 |\theta|^2 + \sigma^* |\theta|^2) \, dz - R_1 a^2 Le_1 \int_0^1 (|D\phi_1|^2 + a^2 |\phi_1|^2 + \frac{\sigma^*}{Le_1} |\phi_1|^2) \, dz \\ - R_2 a^2 Le_2 \int_0^1 (|D\phi_2|^2 + a^2 |\phi_2|^2 + \frac{\sigma^*}{Le_2} |\phi_2|^2) \, dz - \dots \end{aligned} \tag{2.10}$$

$$\begin{aligned}
 & - R_{n-1}a^2\text{Le}_{n-1} \int_0^1 \left(|D\phi_{n-1}|^2 + a^2|\phi_{n-1}|^2 + \frac{\sigma^*}{\text{Le}_{n-1}}|\phi_{n-1}|^2 \right) dz \\
 & - \text{Ta} \int_0^1 \left(|D\zeta|^2 + a^2|\zeta|^2 + \frac{\sigma^*}{\text{Pr}}|\zeta|^2 \right) dz
 \end{aligned}$$

Equating the imaginary parts of both sides of Eq. (2.10) and cancelling $\sigma_i (\neq 0)$ throughout from the resulting equation, we have

$$\begin{aligned}
 \frac{1}{\text{Pr}} \int_0^1 (|Dw|^2 + a^2|w|^2) dz &= -\text{Ra}a^2 \int_0^1 |\theta|^2 dz + R_1a^2 \int_0^1 |\phi_1|^2 dz \\
 + R_2a^2 \int_0^1 |\phi_2|^2 dz + \dots + R_{n-1}a^2 \int_0^1 |\phi_{n-1}|^2 dz &+ \frac{\text{Ta}}{\text{Pr}} \int_0^1 |\zeta|^2 dz
 \end{aligned} \tag{2.11}$$

Now, from equation (2.3)₃ we derive that

$$\int_0^1 \left(D^2 - a^2 - \frac{\sigma}{\text{Le}_1} \right) \phi_1 \left(D^2 - a^2 - \frac{\sigma^*}{\text{Le}_1} \right) \phi_1^* dz = \frac{1}{\text{Le}_1^2} \int_0^1 |w|^2 dz \tag{2.12}$$

Integrating the various terms on the left hand side of Eq. (2.12) by parts for an appropriate number of times and making use of the boundary conditions on ϕ_1 , it follows that

$$\begin{aligned}
 \int_0^1 (|D^2\phi_1|^2 + 2a^2|D\phi_1|^2 + a^4|\phi_1|^2) dz &+ \frac{2\sigma_r}{\text{Le}_1} \int_0^1 (|D\phi_1|^2 + a^2|\phi_1|^2) dz \\
 + \frac{|\sigma|^2}{\text{Le}_1^2} \int_0^1 |\phi_1|^2 dz &= \frac{1}{\text{Le}_1^2} \int_0^1 |w|^2 dz
 \end{aligned} \tag{2.13}$$

Since $\sigma_r \geq 0$, it follows from Eq. (2.13) that

$$2a^2 \int_0^1 |D\phi_1|^2 dz \leq \frac{1}{\text{Le}_1^2} \int_0^1 |w|^2 dz \tag{2.14}$$

Now, since $\phi_1, \phi_2, \dots, \phi_{n-1}$ and w satisfy the boundary conditions $\phi_1(0) = 0 = \phi_1(1)$, $\phi_2(0) = 0 = \phi_2(1), \dots, \phi_{n-1}(0) = 0 = \phi_{n-1}(1)$, $w(0) = 0 = w(1)$, we have from the Rayleigh-Ritz inequality (Schultz, 1973)

$$\begin{aligned}
 \int_0^1 |D\phi_1|^2 dz &\geq \pi^2 \int_0^1 |\phi_1|^2 dz \\
 \int_0^1 |D\phi_2|^2 dz &\geq \pi^2 \int_0^1 |\phi_2|^2 dz \\
 &\vdots \\
 \int_0^1 |D\phi_{n-1}|^2 dz &\geq \pi^2 \int_0^1 |\phi_{n-1}|^2 dz
 \end{aligned} \tag{2.15}$$

and

$$\int_0^1 |Dw|^2 dz \geq \pi^2 \int_0^1 |w|^2 dz \tag{2.16}$$

respectively.

Utilizing inequalities (2.15)₁ and (2.16) in inequality (2.14), we get

$$a^2 \int_0^1 |\phi_1|^2 dz \leq \frac{1}{2Le_1^2 \pi^4} \int_0^1 |Dw|^2 dz \tag{2.17}$$

In the same manner, we obtain from Eqs. (2.3)₄₋₆ the inequalities

$$\begin{aligned} a^2 \int_0^1 |\phi_2|^2 dz &\leq \frac{1}{2Le_2^2 \pi^4} \int_0^1 |Dw|^2 dz \\ \vdots \\ a^2 \int_0^1 |\phi_{n-1}|^2 dz &\leq \frac{1}{2Le_{n-1}^2 \pi^4} \int_0^1 |Dw|^2 dz \end{aligned} \tag{2.18}$$

respectively.

Now for the case of rigid boundaries, $\zeta(0) = 0 = \zeta(1)$, again from the Rayleigh-Ritz inequality (Schultz, 1973), we obtain

$$\int_0^1 |D\zeta|^2 dz \geq \pi^2 \int_0^1 |\zeta|^2 dz \tag{2.19}$$

Multiplying Eq. (2.4) by ζ^* and integrating over the vertical range of z , we get from the real part of the final equation

$$\begin{aligned} \int_0^1 (|D\zeta|^2 + a^2|\zeta|^2 + \sigma_r|\zeta|^2) dz &= \Re \int_0^1 \zeta^* Dw dz \leq \left| \int_0^1 \zeta^* Dw dz \right| \leq \int_0^1 |\zeta^* Dw| dz \\ &\leq \int_0^1 |\zeta^*| |Dw| dz \leq \int_0^1 |\zeta| |Dw| dz \leq \sqrt{\int_0^1 |\zeta|^2 dz} \sqrt{\int_0^1 |Dw|^2 dz} \end{aligned} \tag{2.20}$$

(using Schwartz inequality) which implies that

$$\int_0^1 |D\zeta|^2 dz \leq \sqrt{\int_0^1 |\zeta|^2 dz} \sqrt{\int_0^1 |Dw|^2 dz}$$

and thus using inequality (2.19) for the case of rigid boundaries and the result $\int_0^1 |D\zeta|^2 dz = \pi^2 \int_0^1 |\zeta|^2 dz$ for the case of free boundaries (Banerjee *et al.*, 1995), we obtain

$$\pi^2 \int_0^1 |\zeta|^2 dz \leq \sqrt{\int_0^1 |\zeta|^2 dz} \sqrt{\int_0^1 |Dw|^2 dz}$$

which gives

$$\sqrt{\int_0^1 |\zeta|^2 dz} \leq \frac{1}{\pi^2} \sqrt{\int_0^1 |Dw|^2 dz}$$

which implies that

$$\int_0^1 |\zeta|^2 dz \leq \frac{1}{\pi^4} \int_0^1 |Dw|^2 dz \quad (2.21)$$

Now using inequalities (2.17), (2.18) and (2.21) in Eq. (2.11), we obtain

$$\begin{aligned} & \left[\frac{1}{\text{Pr}} - \left(\frac{R_1}{2\text{Le}_1^2\pi^4} + \frac{R_2}{2\text{Le}_2^2\pi^4} + \dots + \frac{R_{n-1}}{2\text{Le}_{n-1}^2\pi^4} + \frac{\text{Ta}}{\pi^4} \right) \right] \int_0^1 |Dw|^2 dz \\ & + \frac{a^2}{\sigma} \int_0^1 |w|^2 dz + \text{Raa}^2 \int_0^1 |\theta|^2 dz < 0 \end{aligned} \quad (2.22)$$

which clearly implies (for $\sigma_i \neq 0$) that

$$\frac{R_1\text{Pr}}{2\text{Le}_1^2\pi^4} + \frac{R_2\text{Pr}}{2\text{Le}_2^2\pi^4} + \dots + \frac{R_{n-1}\text{Pr}}{2\text{Le}_{n-1}^2\pi^4} + \frac{\text{Ta}}{\pi^4} > 1 \quad (2.23)$$

Hence if $\frac{R_1\text{Pr}}{2\text{Le}_1^2\pi^4} + \frac{R_2\text{Pr}}{2\text{Le}_2^2\pi^4} + \dots + \frac{R_{n-1}\text{Pr}}{2\text{Le}_{n-1}^2\pi^4} + \frac{\text{Ta}}{\pi^4} \leq 1$, then we must have $\sigma_i = 0$.

This proves the theorem.

The essential content of Theorem 1 from the physical point of view is that for the problem of rotatory hydrodynamic multicomponent convection, an arbitrary neutral or unstable mode of the system is definitely non-oscillatory in character and, in particular, ‘the principle of the exchange of stabilities’ is valid if $\frac{R_1\text{Pr}}{2\text{Le}_1^2\pi^4} + \frac{R_2\text{Pr}}{2\text{Le}_2^2\pi^4} + \dots + \frac{R_{n-1}\text{Pr}}{2\text{Le}_{n-1}^2\pi^4} + \frac{\text{Ta}}{\pi^4} \leq 1$. Further, the above result is uniformly valid for quite general nature of the boundaries.

Special cases: It follows from Theorem 1 that an arbitrary neutral or unstable mode is non oscillatory in character, and in particular PES is valid for:

1. Rayleigh-Benard convection ($R_1 = R_2 = \dots = R_{n-1} = \text{Ta} = 0$) (Pellew and Southwell, 1940)
2. Rotatory Rayleigh-Benard convection ($R_1 = R_2 = \dots = R_{n-1} = 0$) if $\text{Ta}/\pi^4 \leq 1$ (Gupta *et al.*, 1986)
3. Rotatory thermohaline convection ($R_1 > 0, R_2 = \dots = R_{n-1} = 0, \text{Ta} > 0$) if $\frac{R_1\text{Pr}}{2\text{Le}_1^2\pi^4} + \frac{\text{Ta}}{\pi^4} \leq 1$ (Gupta *et al.*, 1986)
4. Thermohaline convection ($R_1 > 0, R_2 = \dots = R_{n-1} = \text{Ta} = 0$) if $\frac{R_1\text{Pr}}{2\text{Le}_1^2\pi^4} \leq 1$ (Gupta *et al.*, 1986)
5. Rotatory hydrodynamic triply diffusive convection ($R_1 > 0, R_2 > 0, R_3 = \dots = R_{n-1} = 0, \text{Ta} > 0$) if $\frac{R_1\text{Pr}}{2\text{Le}_1^2\pi^4} + \frac{R_2\text{Pr}}{2\text{Le}_2^2\pi^4} + \frac{\text{Ta}}{\pi^4} \leq 1$ (Prakash *et al.*, 2014b)
6. Triply diffusive convection ($R_1 > 0, R_2 > 0, R_3 = \dots = R_{n-1} = \text{Ta} = 0$) if $\frac{R_1\text{Pr}}{2\text{Le}_1^2\pi^4} + \frac{R_2\text{Pr}}{2\text{Le}_2^2\pi^4} \leq 1$ (Prakash *et al.*, 2014a)

Proceeding in this manner, we can obtain conditions for stationary convection for all configurations with $3, 4, \dots, n - 1$ concentration components, respectively.

Since the complement of the above result implies the occurrence of oscillatory motions, thus it is important to derive the bounds for the complex growth rate of oscillatory motions. We prove the following theorem in this direction.

Theorem 2: If $R_a > 0, R_1 > 0, R_2 > 0, \dots, R_{n-1} > 0, \text{Ta} > 0, \sigma_r \geq 0$ and $\sigma_i \neq 0$, then a necessary condition for the existence of a nontrivial solution $(w, \theta, \phi_1, \phi_2, \dots, \phi_{n-1}, \zeta, \sigma)$ to Eqs. (2.3) and (2.) together with boundary conditions (2.5)-(2.7) is that

$$|\sigma| < \max\left\{\sqrt{(R_1 + R_2 + \dots + R_{n-1})\text{Pr}}, \sqrt{\text{TaPr}}\right\}$$

Proof: Rewriting equation (2.11) for ready reference, we have

$$\begin{aligned} \frac{1}{\text{Pr}} \int_0^1 (|Dw|^2 + a^2|w|^2) dz &= -\text{Raa}^2 \int_0^1 |\theta|^2 dz + R_1 a^2 \int_0^1 |\phi_1|^2 dz \\ &+ R_2 a^2 \int_0^1 |\phi_2|^2 dz + \dots + R_{n-1} a^2 \int_0^1 |\phi_{n-1}|^2 dz + \frac{\text{Ta}}{\text{Pr}} \int_0^1 |\zeta|^2 dz \end{aligned}$$

Now since $\sigma_r \geq 0$, it follows from Eq. (2.13) that

$$\int_0^1 |\phi_1|^2 dz \leq \frac{1}{|\sigma|^2} \int_0^1 |w|^2 dz \tag{2.24}$$

Similarly, from Eqs. (2.3)₄ and (2.3)₆, by adopting the same procedure, we get

$$\begin{aligned} \int_0^1 |\phi_2|^2 dz &\leq \frac{1}{|\sigma|^2} \int_0^1 |w|^2 dz \\ \vdots & \\ \int_0^1 |\phi_{n-1}|^2 dz &\leq \frac{1}{|\sigma|^2} \int_0^1 |w|^2 dz \end{aligned} \tag{2.25}$$

respectively.

Multiply Eq. (2.4) by its complex conjugate, integrating the resulting equation by parts for an appropriate number of times and using boundary conditions (2.5)-(2.7), we have

$$\begin{aligned} \int_0^1 (|D^2\zeta|^2 + 2a^2|D\zeta|^2 + a^4|\zeta|^2) dz + \frac{2\sigma_r}{\text{Pr}} \int_0^1 (|D\zeta|^2 + a^2|\zeta|^2) dz \\ + \frac{|\sigma|^2}{\text{Pr}^2} \int_0^1 |\zeta|^2 dz = \int_0^1 |Dw|^2 dz \end{aligned} \tag{2.26}$$

Since, $\sigma_r \geq 0$, it follows from Eq. (2.26) that

$$\int_0^1 |\zeta|^2 dz \leq \frac{\text{Pr}^2}{|\sigma|^2} \int_0^1 |Dw|^2 dz \tag{2.27}$$

Now making use of inequalities (2.24), (2.25) and (2.27), in Eq. (2.11), we have

$$\begin{aligned} & \frac{1}{\text{Pr}} \left(1 - \frac{\text{TaPr}^2}{|\sigma|^2}\right) \int_0^1 |Dw|^2 dz + \frac{a^2}{\text{Pr}} \left[1 - \frac{(R_1 + R_2 + \dots + R_{n-1})\text{Pr}}{|\sigma|^2}\right] \int_0^1 |w|^2 dz \\ & + \text{Ra}a^2 \int_0^1 |\theta|^2 dz < 0 \end{aligned} \quad (2.28)$$

which clearly implies that

$$|\sigma| < \max\left\{\sqrt{(R_1 + R_2 + \dots + R_{n-1})\text{Pr}}, \sqrt{\text{TaPr}}\right\}$$

This establishes the desired result.

The above theorem may be stated in an equivalent form as: the complex growth rate of an arbitrary, neutral or unstable oscillatory perturbation of growing amplitude in a rotatory hydrodynamic multicomponent fluid layer heated from below must lie inside a semi-circle in the right half of the (p_r, p_i) -plane whose centre is at the origin and radius equals $\max\left\{\sqrt{(R_1 + R_2 + \dots + R_{n-1})\text{Pr}}, \sqrt{\text{TaPr}}\right\}$. Further, it is proved that this result is uniformly valid for quite general nature of the bounding surfaces.

Special cases: The following results may be obtained from Theorem 2 as special cases:

1. For rotatory Rayleigh-Benard convection ($R_1 = 0 = R_2 = \dots = R_{n-1} = 0$, $\text{Ta} > 0$)

$$|\sigma| < \text{TaPr}$$

(Banerjee *et al.*, 1981)

2. For thermohaline convection ($R_1 > 0$, $R_2 = \dots = R_{n-1} = \text{Ta} = 0$)

$$|\sigma| < \sqrt{R_1\text{Pr}}$$

(Banerjee *et al.*, 1981)

3. For rotatory Thermohaline convection of the Veronis type (Turner, 1985) ($R_1 > 0$, $R_2 = \dots = R_{n-1} = 0$, $\text{Ta} > 0$)

$$|\sigma| < \max\left\{\sqrt{R_1\text{Pr}}, \sqrt{\text{TaPr}}\right\}$$

(Gupta *et al.*, 1983)

4. For triply diffusive convection ($R_1 > 0$, $R_2 > 0$, $R_3 = \dots = R_{n-1} = \text{Ta} = 0$)

$$|\sigma| < \sqrt{(R_1 + R_2)\text{Pr}}$$

(Prakash *et al.*, 2014c)

Proceeding in this manner, we can obtain bounds for the complex growth rate for all configurations with 3, 4, ..., $n - 1$ concentration components, respectively.

3. Conclusions

The present analysis generalizes the previous published results for rotatory hydrodynamic singly, doubly and triply diffusive convection. The mathematical analysis carried out here yields a sufficient condition for the validity of the principle of the exchange of stabilities in rotatory hydrodynamic multicomponent convection. Since the complement of this condition implies the occurrence of oscillatory motions, the bounds for the complex growth rate are also obtained as the second problem. It is further proved that the results obtained herein are uniformly applicable for quite general nature of bounding surfaces.

Acknowledgment

The authors would like to thank the learned reviewer for his valuable comments, which helped the authors to bring the manuscript in the present form. First author (J. Prakash) also acknowledges the recently awarded financial assistance by UGC, New Delhi in the form of major research project (Grant number, 43-420/2014(SR)).

References

1. BANERJEE M.B., KATOCH D.C., DUBE G.S., BANERJEE K., 1981, Bounds for growth rate of perturbation in thermohaline convection, *Proceedings of the Royal Society of London, A*, **378**, 301-304
2. BANERJEE M.B., SHANDIL R.G., LAL P., KANWAR V., 1995, A mathematical theorem in rotatory thermohaline convection, *Journal of Mathematics Analysis and Applied*, **189**, 351-361
3. BRANDT A., FERNANDO H.J.S., 1996, Double diffusive convection, *American Geophysical Union*, Washington, DC
4. GRIFFITHS R.W., 1979a, A note on the formation of salt finger and diffusive interfaces in three component systems, *International Journal of Heat and Mass Transfer*, **22**, 1687-1693
5. GRIFFITHS R.W., 1979b, The influence of a third diffusing component upon the onset of convection, *Journal of Fluid Mechanics*, **92**, 659-670
6. GUPTA J.R., SOOD S.K., BHARDWAJ U.D., 1986, On the characterization of non-oscillatory motions in a rotatory hydromagnetic thermohaline convection, *Indian Journal of Pure and Applied Mathematics*, **17**, 1, 100-107
7. GUPTA J.R., SOOD S.K., SHANDIL R.G., BANERJEE M.B., BANERJEE K., 1983, Bounds for the growth of a perturbation in some double-diffusive convection problems, *Journal of Australian Mathematics Society, Ser. B*, **25**, 276-285
8. KELLNER M., TILGNER A., 2014, Transition to finger convection in double diffusive convection, *Physics of Fluids*, **26**, 094103
9. LOPEZ A.R., ROMERO L.A., PEARLSTEIN A.J., 1990, Effect of rigid boundaries on the onset of convective instability in a triply diffusive fluid layer, *Physics of Fluids A*, **2**, 6, 897-902
10. NIELD D.A., KUZNETSOV A.V., 2011, The onset of double-diffusive convection in a nano fluid layer, *International Journal Heat Fluid Flow*, **32**, 4, 771-776
11. PEARLSTEIN A.J., HARRIS R.M., TERRONES G., 1989, The onset of convective instability in a triply diffusive fluid layer, *Journal of Fluid Mechanics*, **202**, 443-465
12. PELLEW A., SOUTHWELL R.V., 1940, On the maintained convective motion in a fluid heated from below, *Proceedings of the Royal Society of London, A*, **176**, 312-343
13. POULIKAKOS D., 1985, The effect of a third diffusing component on the onset of convection in a horizontal porous layer, *Physics of Fluids*, **28**, 10, 3172-3174

14. PRAKASH J., BALA R., VAID K., 2014a, On the characterization of nonoscillatory motions in triply diffusive convection, *International Journal of Fluid Mechanics Research*, **41**, 5, 409-416
15. PRAKASH J., BALA R., VAID K., 2014b, On the principle of the exchange of stabilities in rotatory triply diffusive convection, *Proceeding National Academy Science, Physical Sciences, India*, **84**, 3, 433-439
16. PRAKASH J., BALA R., VAID K., 2014c, Upper limits to the complex growth rates in triply diffusive Convection, *Proceeding Indian National Science Academy*, **80**, 1, 115-122
17. PRAKASH J., BALA R., VAID K., 2015, On arresting the complex growth rates in Rotatory Triply Diffusive convection, communicated for publication
18. RADKO T., 2013, *Double-Diffusive Convection*, Cambridge university Press
19. RIONERO S., 2013a, Multicomponent diffusive-convective fluid motions in porous layers ultimately boundedness, absence of subcritical instabilities, and global nonlinear stability for any number of salts, *Physics of Fluids*, **25**, 054104, 1-23
20. RIONERO S., 2013b, Triple diffusive convection in porous media, *Acta Mechanica*, **224**, 447-458
21. RIONERO S., 2014, Onset of convection in rotating porous layers via a new approach, *Discrete and Continuous Dynamical Systems, Ser. B*, **19**, 7, 2279-2296
22. RYZHKOV I.I., 2013, Long-wave instability of a plane multicomponent mixture layer with the solet effect, *Fluid Dynamics*, **4**, 48, 477-490
23. RYZHKOV I.I., SHEVTSOVA V.M., 2007, On thermal diffusion and convection in multicomponent mixtures with application to the thermogravitational column, *Physics of Fluids*, **19**, 027101, 1-17
24. RYZHKOV I.I., SHEVTSOVA V.M., 2009, Long wave instability of a multicomponent fluid layer with the solet effect, *Physics of Fluids*, **21**, 014102, 1-14
25. SCHMITT R.W., 2011, Thermohaline convection at density ratios below one: A new regime for salt fingers, *Journal of Marine Research*, **69**, 779-795
26. SCHULTZ M.H., 1973, *Spline Analysis*, Prentice-Hall Inc. Englewood Cliffs NJ
27. SEKAR R., RAJU K., VASANTHAKUMARI R., 2013, A linear analytical study of Soret-driven Ferro thermohaline convection in an anisotropic porous medium, *Journal of Magnetism and Magnetic Materials*, **331**, 122-128
28. SHIVAKUMARA I.S., NAVEEN KUMAR S.B., 2014, Linear and weakly nonlinear triple diffusive convection in a couple stress fluid layer, *International Journal of Heat and Mass Transfer*, **68**, 542-553
29. TERRONES G., 1993, Cross-diffusion effects on the stability criteria in a triply diffusive system, *Physics of Fluids A*, **5**, 9, 2172-2182
30. TERRONES G., PEARLSTEIN A.J., 1989, The onset of convection in a multicomponent fluid layer, *Physics of Fluids A*, **1**, 5, 845-853
31. TURNER J.S., 1973, *Buoyancy Effects in Fluids*, Cambridge University Press
32. TURNER J.S., 1974, Double diffusive phenomenon, *Annual Review of Fluid Mechanics*, **6**, 37-56
33. TURNER J.S., 1985, Multicomponent convection, *Annual Review of Fluid Mechanics*, **17**, 11-44

EXPERIMENTAL INVESTIGATIONS OF ELASTIC-PLASTIC STRAIN STATES ON VARIOUS STAGES OF MATERIAL PLASTIFYING

BARBARA KOZŁOWSKA

Warsaw University of Technology, Faculty of Mechatronical Engineering, Warsaw, Poland
e-mail: b.kozłowska@mchtr.pw.edu.pl

In the paper, the possibility of application of various experimental methods to the analysis of elastic-plastic states at different levels of material plastifying is presented. For tests carried out on two-dimensional elements with different stress concentrators and loaded by tensile stresses, three experimental methods have been selected: Moiré method, method of photoelastic coating and the thermography method. On the basis of the tests results, the range of the applicability of chosen methods and their suitability to the elastic-plastic strain analysis at the development of material plastifying has been determined. The strain components distribution obtained from the Moiré method and the method of photoelastic coating has been compared. The possibility of increasing the accuracy of strain determination for the Moiré method by additional tests at the grid rotated by an angle of 45° with respect to the direction of tensile stress has been shown. The results of the investigations have been discussed.

Keywords: mechanics of solids, experimental methods, elastic-plastic states

1. Introduction and the experimental method selection

The analysis of elastic-plastic states finds many basic applications in engineering design, especially nowadays, since the economical trend towards building more lightweight and cheaper structures accepts partial material plastifying during exploitation.

Experimental studies on a great variety of non-linear problems are conducted in many research centers all over the world. These problems, like non-linear material characteristics, partial material plastifying, large deformation, material with imperfections, etc, always cause difficulties associated with the modelling of constructional materials. In such circumstances, the widely nowadays applied numerical methods as FEM still need final experimental verification. Especially the experimental methods which give information about the real object without any model simplification can be very useful as a good verification tool of theoretical and numerical design.

The experimental methods most commonly used to research work on elastic-plastic problems are: photoelasticity, especially the method of photoelastic coating (Pacey *et al.*, 2005; Foust *et al.*, 2011; Lamberson *et al.*, 2012; Diaz *et al.*, 2010), Moiré methods (Min *et al.*, 2006; Livieri and Nicoletto, 2003; Guo *et al.*, 2006), holographic interferometry (Lin, 2000; Balalov *et al.*, 2007), electronic speckle pattern interferometry method (ESPI) (Diaz *et al.*, 2001; Schajer *et al.*, 2005), digital image correlation method (DIC) (Vural *et al.*, 2011; Diaz *et al.*, 2004; Tarigopula *et al.*, 2008), strain gauge technique (Rasty *et al.*, 2007; Olmi, 2010), thermography (Pieczyńska *et al.*, 2006; Connesson *et al.*, 2011).

The selection of the experimental method to study plastic “in-plane” deformation depends on several elements: the ability and accuracy of the method, the ease of its use in practice, the character of the obtained results and the possibility of their work out, etc.

The greatest potential taking into account a variety of research techniques and a diversity of the analyzed problems, create the photoelasticity and Moiré method.

To study elastic-plastic states, much more suitable is the method of photoelastic coating than a traditional photoelasticity which requires the use of optically active materials having characteristics corresponding to material characteristics of the tested element also in the non-linear range.

Similarly, among various Moiré techniques – the best applicability to study elastic-plastic states has the classical geometric Moiré method. The frequently nowadays applied interferential Moiré method has a very high sensitivity (density of the grid is here of several thousand lines/mm) and is used to the analysis of small areas. Its additional disadvantage is the necessity of coherent (laser) light application.

Holographic interferometry, which bases on phenomena occurring during the coherent light interference, can be used directly for measurement of displacement (or shape) of the structure. It shows good accuracy (strain measurement with an accuracy of $0.1 \cdot 10^{-4}$ – $1 \cdot 10^{-4}$), but has a high mechanical sensitivity, and the result analysis is labor-consuming. It requires also laser light.

Making use of coherent light requires also one of the modern experimental methods – electronic speckle pattern interferometry (ESPI). It has a lot of advantages – non-contact measurement, high sensitivity, resolution and accuracy; it gives surface images of displacement and strain components. However, ESPI method has also very serious limitations – high susceptibility on conditions in which experiment is performed, sensitivity to even slight movements. It is also not suitable for large deformations and requires the researcher to have high skills and a lot of experience.

The second modern experimental method, the digital image correlation method (DIC) also allows non-contact measurement and gives surface images of displacement and strain components. Compared to the ESPI method, it has a bigger measurement range, but lower resolution. The surface of the element needs special preparation and the results require a lot of calculations.

In contrast to modern experimental methods, one of the oldest commonly known but still most often used experimental technique is the strain gauge measurement. It enables one to get strain values with a very high accuracy ($\sim 1 \cdot 10^{-6}$), but only in several points. That is why it is usually used in combination with other experimental methods, after determining the most loaded parts of a structure.

An auxiliary character has also usually the thermography method which is often used to detect material defects. Its accuracy is difficult to determine and depends mostly on temperature resolution of a thermovision camera and external conditions. However, the method allows one to observe thermal processes taking place in the material, what is a great advantage, especially concerning the elastic-plastic problems.

Taking into account advantages and disadvantages of various experimental methods and abilities of their application regarding to the elastic-plastic states analysis, the simplicity of their use in practice, equipment availability, etc., for further experimental testing, three methods have been selected: a method of photoelastic coating, Moiré method and the thermography method.

All the three methods give information about deformation of the whole tested area (not only at several points). They can be used to investigate real structure elements made of any material, in working conditions, even under heavy loading causing partial material plastifying. Their advantage is also excellent visualization of the process of progressive material plastifying. In particular, the methods of photoelastic coating and thermography allow direct observation of the process of formation and development of plastic zones, changes (expansion) of their boundaries and the direction of propagation.

The first two methods are optical methods, although each of them gives information about different physical quantities (method of photoelastic coating – strain, Moiré method – displacement). They are also comparable in terms of the level of accuracy (measurement or determination of strain with an accuracy $\sim 1 \cdot 10^{-4}$). The third method – thermography is based on a quite

different physical phenomenon (emission of infrared radiation from the surface of the tested element), which allows, to a certain degree, verification of the results obtained from the first two methods.

The additional advantage of the photoelastic coating method is the possibility of direct strain measurement. The disadvantage is the dependence of the obtained results on the properties of the tested material (using the analytical method of strain separation).

The Moiré method has a purely geometrical character (measurement of the displacements is direct and does not depend on the properties of the tested material), determination of strain, however, requires differentiation of the obtained displacement values.

The photoelastic coating method and the Moiré method are methods very often used in worldwide research works, thus their choice seems to be the most evident and proper. Thermography, though less precise and giving results more qualitative than quantitative, can provide a useful and interesting complement to the first two methods, particularly for solving certain elastic-plastic problems.

2. Experimental testing

The experimental investigation of elastic-plastic states has been performed on two-dimensional models of structural elements weakened by different stress concentrators (holes) and subjected to tensile stresses. The elements of this type and loaded in such a way are often used in modern structures, particularly as different construction joints. The areas of the elements weakened by cut-outs are parts of structures which require special and accurate checking (Wung *et al.*, 2001; Olmi, 2010; Foust *et al.*, 2011). Shapes of stress concentrators have been designed on the basis of literature data and engineering practice (single central holes of various shapes and groups of circular holes of various configurations). The objects of discussion presented in the work are three of the models – Fig. 1. The first two models with one central hole have the same area of the most weakened cross-section in the x axis of symmetry (the effective cross-section) and differ only in shape of the hole. The third model is weakened by five circular holes cut symmetrically not only on the axis of symmetry x .

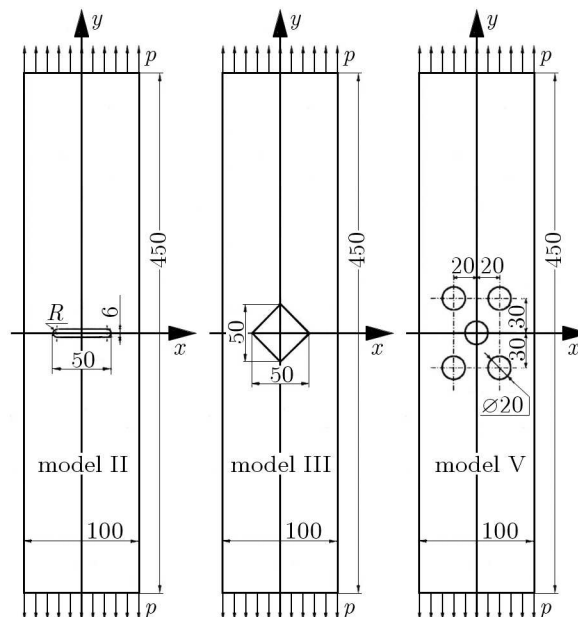


Fig. 1. Models of constructional elements

The models have been made of a duralumin sheet 3mm thick, from which stripes of 100 mm in width and 450 mm in length have been cut out. The length of the stripes was taken large enough to compensate potential non-uniformity of tensile stresses distribution applied at their ends.

The characteristic of the material (aluminum alloy EN-AW-2024) has been determined experimentally on the basis of a standard static uniaxial tensile test and it is shown in Fig. 2.

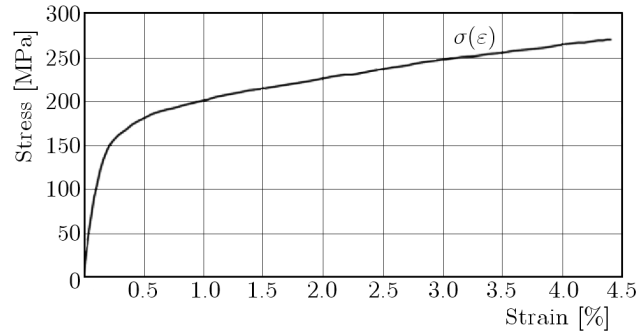


Fig. 2. Material characteristic

After mechanical working and special surface preparation, the models have been covered with: a cross-type grid of 20 lines/mm (for the Moiré method) with a 2 mm thick photoelastic coating of strain constant: $f_\varepsilon = 1.114 \cdot 10^{-3}$ 1/fringe order (for the photoelastic coating method) and with a layer of graphite (for the thermography method). Next, different holes have been cut out in the way which allowed avoiding creation of plastic strains as a result of machining.

The models have been loaded at their ends with uniformly distributed tensile stresses p . As the measure of the loading intensity, the ‘loading factor’ s has been accepted. It has been calculated as the ratio of the average tensile stresses at the cross-section weakened by the hole on the axis of symmetry perpendicular to the stretching direction in relation to the offset yield strength $R_{0.2} = 182$ MPa (taken from the material characteristic).

The loading of the models has been increased step by step within the over-elastic range of the material. At selected levels of loading, images of the Moiré pattern (for the displacement $u(x, y)$ and $v(x, y)$) and isochromatic pattern (for dark- and light-field polariscope) have been registered. For the thermography method, the loading of the models increased continuously and the temperature changes on the specimen surface have been recorded by a thermovision camera.

On the basis of the experimental data obtained from the Moiré method and the method of photoelastic coating, quantitative analysis of the elastic-plastic strain and stress around the stress concentrators has been made (Kozłowska, 2008, 2013). Due to low resolution of thermal images obtained from the infrared camera, the thermograms have given only qualitative information about deformation of the elements (Kozłowska, 2012).

3. Determination of the suitability of selected experimental methods to elastic-plastic analysis in dependence on the material plastifying level

The experiment has been performed within a wide range of the loading – from the moment of occurring first plastic deformations to the elements failure. But not at every level of loading all of the selected methods have been equally useful.

As proved by an experiment, photoelastic coating method allows analysis of the plastic strain starting from the beginning of their occurring in the material – level of about $s \approx 0.5$ (tensile stress $p \approx 45$ MPa) for the models with a single hole or $s \approx 0.3$ (tensile stress $p \approx 44$ MPa) for the model with five holes. At that loading level, the Moiré method is not very useful (to low

number of Moiré fringes). Exemplary images of isochromatic and Moiré patterns at the discussed loading level for the area around the stress concentrator of model III are shown in Fig. 3.

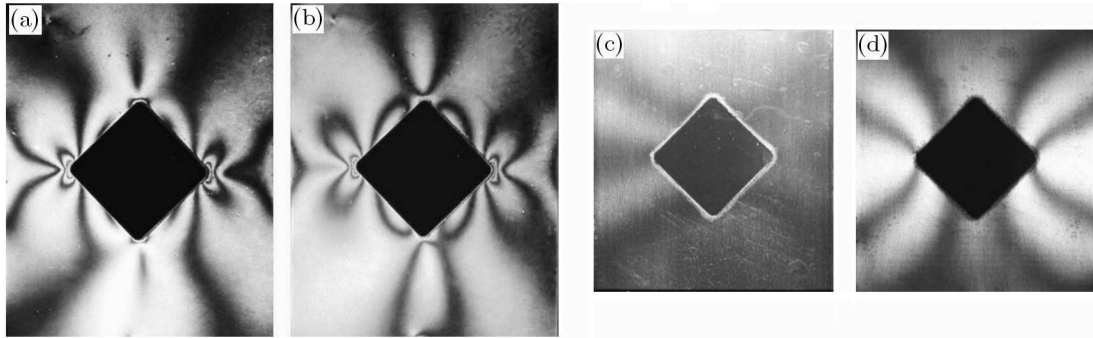


Fig. 3. Model III ($s = 0.495$) – isochromatic pattern: (a) dark-field polariscope, (b) light-field polariscope; Moiré fringe pattern: (c) $u(x, y)$ surface, (d) $v(x, y)$ surface

For significant plastic deformation, for a loading level over $s \approx 1$ (tensile stress $p \approx 91$ MPa) for the models with a single hole or $s \approx 0.8$ (tensile stress $p \approx 116$ MPa) for the model with five holes, the method of photoelastic coating is no longer useful. It is so because the photoelastic coating can crack (Fig. 4), come off the base (Fig. 5) or (in the best case) isochromatic fringes in the most plastified areas become quite unreadable (Fig. 6). The Moiré method, however, at the same loading level or even higher, enables proper analysis of elastic-plastic states (Figs. 4-6).

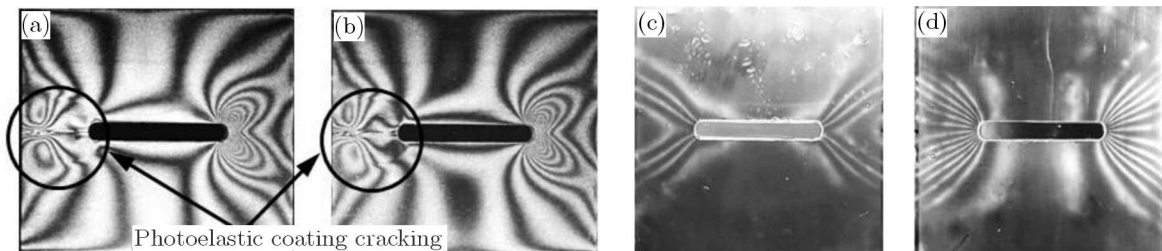


Fig. 4. Model II ($s = 1.136$) – isochromatic pattern: (a) dark-field polariscope, (b) light-field polariscope; Moiré fringe pattern: (c) $u(x, y)$ surface, (d) $v(x, y)$ surface

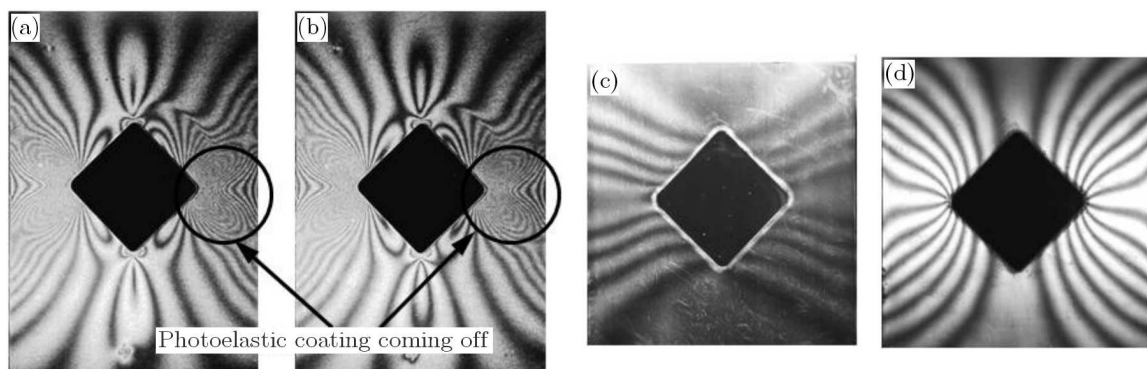


Fig. 5. Model III ($s = 1.136$) – isochromatic pattern: (a) dark-field polariscope, (b) light-field polariscope; Moiré fringe pattern: (c) $u(x, y)$ surface, (d) $v(x, y)$ surface

The discussed examples show an approximate range of the application of the Moiré method and the method of photoelastic coating depending on the level of plastic deformation of the material. This range may be changed to some extent because the sensitivity of these two methods depends on the selection of the proper “measuring element”. Greater possibilities creates here

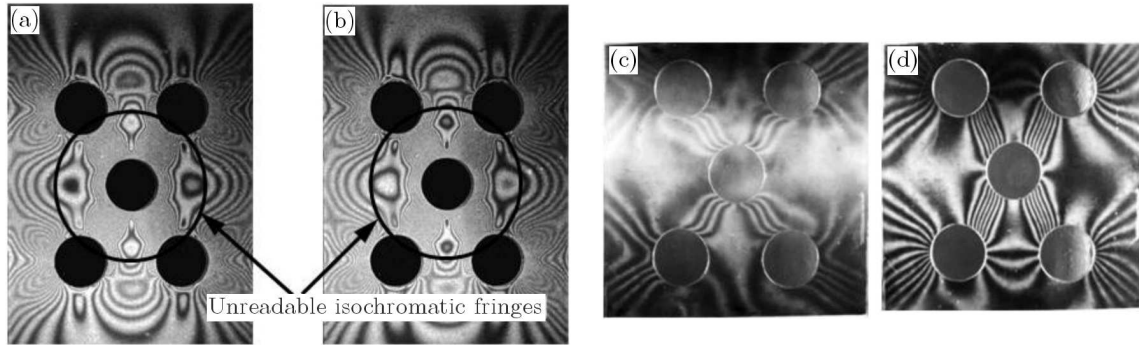


Fig. 6. Model V ($s = 0.778$) – isochromatic pattern: (a) dark-field polariscope, (b) light-field polariscope; Moiré fringe pattern: (c) $u(x, y)$ surface, (d) $v(x, y)$ surface

the Moiré method by changing density of the grids – for the geometric Moiré method, the number of lines per millimeter may vary from a few to several tens (most commonly from 20 to 40).

The change in sensitivity of the method of photoelastic coating can be achieved by variation of thickness of an optically active layer, but in a much smaller range. Usually, the thickness of the applied photoelastic coating is 1 to 3 mm, although you can find one of 0.25 mm. A thicker layer causes stiffening of the element and introduces too much of measurement inaccuracy (averaging over the thickness). The upper limit of the capabilities of the photoelastic coating method is the layer cracking or its coming off the base at higher loading levels.

This disadvantage does not apply to the Moiré method, because even if the grid is imprinted to a photographic film and is affixed to the surface of the element, it forms a flexible thin layer, very strongly connected with the base. In the case of a grid applied directly to the surface of the element (e.g. etched), the problem of the grid coming off does not exist at all.

For the grids used in experimental testing (20 lines per millimeter), the range of measured strain was $\sim 0.2\%$ to 1.5% , while for the photoelastic coating of 2 mm thick, the maximum determined plastic strain was up to $\sim 0.9\%$.

The thermal images obtained from infrared camera did not give sufficiently precise information about the temperature distribution on the surface of the tested element. The accuracy of temperature measurement by an infrared camera, however, depended mainly on its resolution, and that increases with the technical possibilities.

Even if the thermograms do not allow one to obtain the values of strain components, they show directly the full development of plastic zones, from the beginning of their creation to the failure of the element as e.g. in model III (Fig. 7)

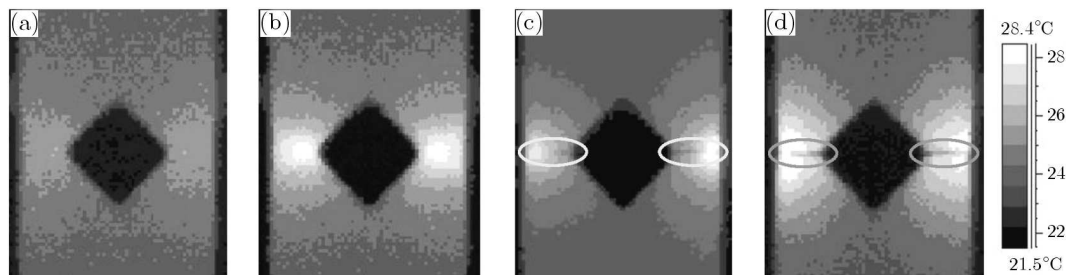


Fig. 7. Thermograms (model III) for loading levels: (a) $s = 0.989$, (b) $s = 1.172$, (c) $s = 1.304$ (first cracks), (d) $s > 1.355$ (element failure)

The method of thermography has also no limitations resulting from the properties of the layer covering model (graphite), as it is in the case of the photoelastic coating method (the optically active layer) or even in the Moiré method, when the grid is affixed to the surface of

the model. Thus, this method can be used, both as a preliminary tool to select an area of the element to be tested with a more accurate method (the formation of plastic zones) as well as a way to observe the mechanism of plastic material failure in the range already out of reach for other experimental methods.

4. The accuracy of the determination of strain components by selected experimental methods

Although the Moiré method and the method of photoelastic coating have different ranges of the best suitability for quantitative analysis of the elastic-plastic strain and stress components, there is a certain range of loading level for which both methods can be properly used.

To compare the accuracy of the Moiré method and the method of photoelastic coating, the loading levels for which both methods give results freely allowing one to determine the strain components have been chosen. The analysis of model II and III has been carried out at the loading level $s = 0.952$, which corresponds to tensile stresses $p = 87$ MPa. The average stress on the x axis was then $\sigma_{av} = 173$ MPa (average strain $-\varepsilon_{av} = 0.38\%$). For model V the loading level accepted for analysis, was $s = 0.687$ (tensile stress $p = 100$ MPa), for which the average stress on the axis of symmetry x – was $\sigma_{av} = 125$ MPa (average strain $-\varepsilon_{av} = 0.15\%$).

At the chosen loading levels, a quite significant plastification of the material already occurred around the stress concentrators, on the one hand large enough to enable measurement by the Moiré method, on the other hand, still allowing using the method of photoelastic coating.

The analysis of the elastic-plastic strain state for the models with one hole is shown on the example of model III, for which the images of isochromatic and Moiré patterns around the stress concentrator at the loading level $s = 0.952$ are presented in Fig. 8.

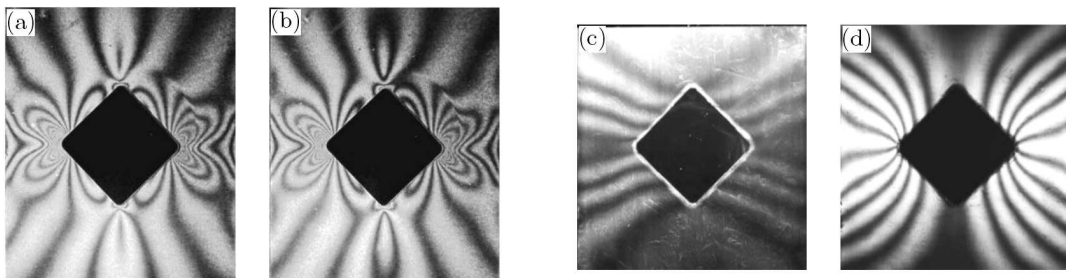


Fig. 8. Isochromatic pattern for model III – $s = 0.952$: (a) dark-field polariscope, (b) light-field polariscope; Moiré fringe pattern – (c) $u(x, y)$ surface, (d) $v(x, y)$ surface

To compare the results obtained from the Moiré method and the method of photoelastic coating, the strain components distribution on a horizontal axis of symmetry x perpendicular to the loading direction (segment AB – Fig. 1) have been assumed. In addition, on the same diagram it is also shown the distribution of strain ε_x and ε_y obtained from numerical (FEM) calculations (Fig. 9).

For model V (with five circular holes), the images of isochromatic and Moiré pattern around the stress concentrators at the loading level $s = 0.687$ are shown in Fig. 10.

To compare the results obtained from the Moiré method and the method of photoelastic coating, the strain components distribution in the horizontal axis of symmetry x perpendicular to the loading direction (segment AB – Fig. 1) has been assumed (Fig. 11). For this model, FEM calculations have not been performed.

As follows from the presented diagrams, the strain components ε_x and ε_y distribution in the axis of symmetry x (segment AB) for the chosen loading level obtained from the Moiré method and the method of photoelastic coating are approximate. The differences between the calculated

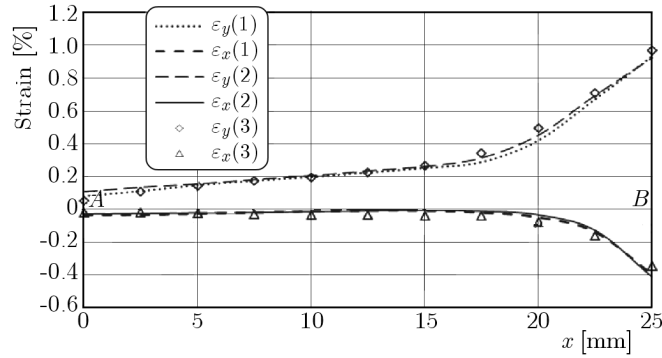


Fig. 9. Strain components distribution in the axis of symmetry x for model III – $s = 0.952$: (1) Moiré method, (2) method of photoelastic coating, (3) FEM calculations

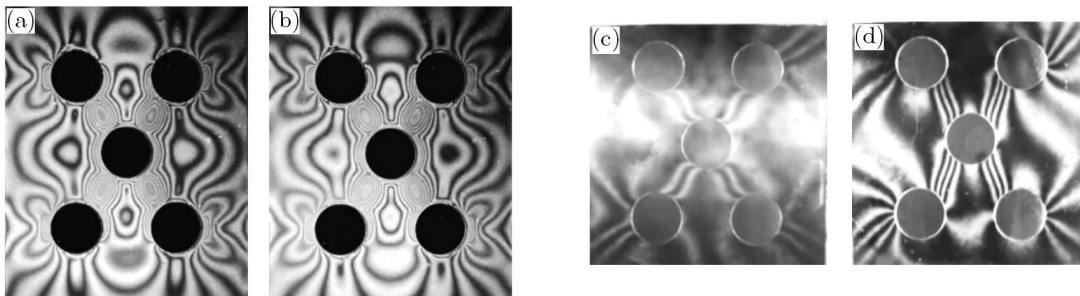


Fig. 10. Isochromatic pattern for model V – $s = 0.687$: (a) dark-field polariscope, (b) light-field polariscope; Moiré fringe pattern – (c) $u(x, y)$ surface, (d) $v(x, y)$ surface

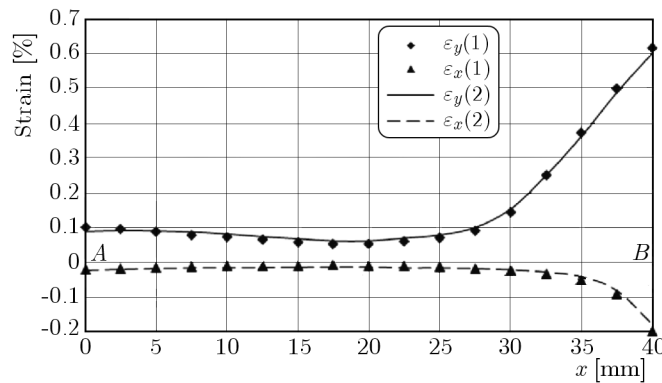


Fig. 11. Strain components distribution in the axis of symmetry x for model V – $s = 0.687$: (1) Moiré method, (2) method of photoelastic coating

values of strain components do not exceed a few percent (6% to 8%). A higher divergence occurs between the experimental results and numerical calculations, but even there it does not exceed 10% to 12%.

5. The influence of grid configuration on the accuracy of determination of strain components distribution

The strain components obtained on the basis of the Moiré fringes at the traditionally affixed grid (in accordance with the axes of symmetry of the model – the direction of tension) can be determined accurately not in every part of the tested model. Where the surfaces of deformation are not much diversified in the direction of the axis of the coordinate system (directions of differentiation), the derivatives can be calculated with a certain error.

As it has been said, the measurement sensitivity of the Moiré method may be increased by changing density of used grids. It is not always convenient, when the increasing of the accuracy is needed only in the part of the tested element. In such a case, an improvement of the measurement accuracy may be achieved by performing additional tests with grids rotated with respect to the direction of the basic grid by a certain angle.

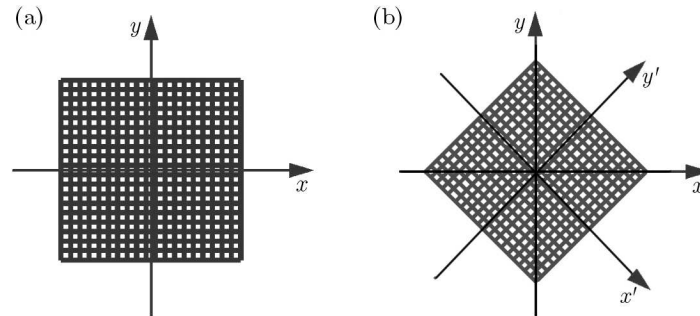


Fig. 12. The grid affixed according to the direction of tensile stresses (a), grid rotated by an angle of 45° (b)

In order to verify the possibility of increasing accuracy of determination of the elastic-plastic strain distribution around stress concentrators, additional tests have been performed at the grid rotated by an angle of 45° with respect to the direction of tensile stress (coordinate system $x-y$) – Fig. 12.

An exemplary comparison of the strain components obtained by grids arranged in different ways is shown for model V with five holes at the loading level $s = 0.778$, for which, the strain state has been already determined using a traditionally affixed grid (Kozłowska, 2008).

The images of Moiré fringes at the grids affixed in different ways are shown in Fig. 13, where one can see a larger number of Moiré fringes in selected areas at the rotated grid than at the grid affixed in the direction of tensile stress.

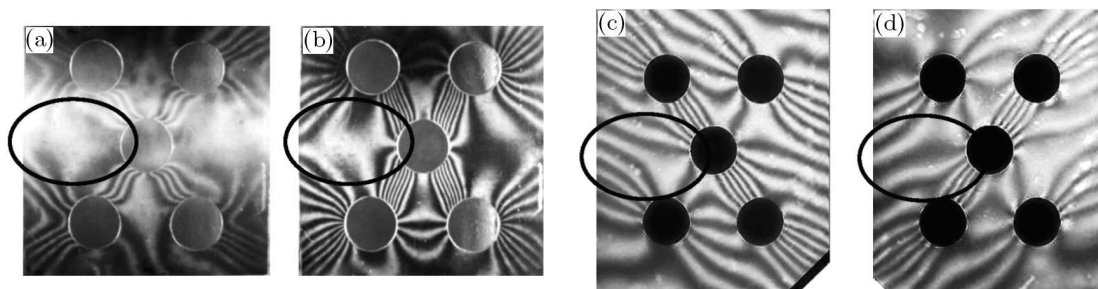


Fig. 13. Moiré pattern for model V ($s = 0.778$) – grid affixed according to the direction of tension: (a) $u(x, y)$, (b) $v(x, y)$; grid rotated by an angle of 45°: (c) clockwise, (d) counter-clockwise

The analysis for the rotated grid has been carried out as in previous cases (because of the double symmetry of the model and loading) for one-quarter of the tested area (Kozłowska, 2007) – Fig. 14.

For strain analysis, the coordinate system $x-y$ associated with an element under tension and a traditionally affixed grid has been rotated by an angle of 45° to form a coordinate system $x'-y'$ associated with a rotated grid (Fig. 12).

On the basis of the displacement obtained from Moiré fringes at the rotated grid, the strain components have been determined in the new coordinate system (x', y') by means of analytical differentiation.

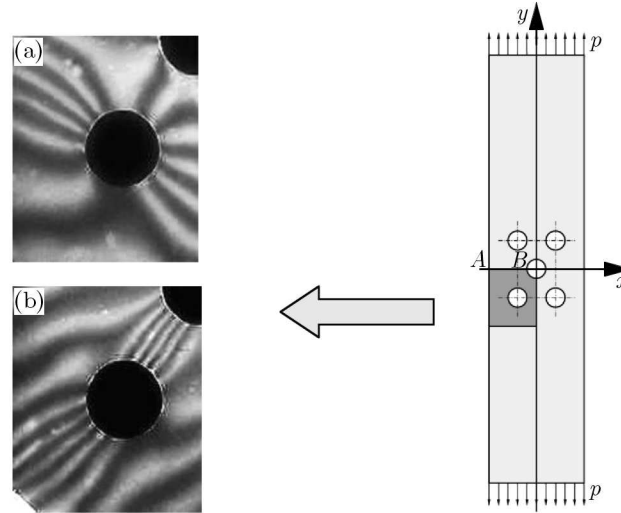


Fig. 14. Moiré pattern for the analyzed area of model V ($s = 0.778$) – grid rotated by an angle of 45° :
(a) clockwise, (b) counter-clockwise

Then the values of strain ε_x and ε_y in the basic coordinate system (x, y) have been calculated by making use of formulas enabling converting the strain state described in one coordinate system to another (rotated) one (1), where $\alpha = 45^\circ$, Fig. 15

$$\begin{aligned}\varepsilon_x &= \varepsilon_{x'} \cos^2 \alpha + \varepsilon_{y'} \sin^2 \alpha + \gamma_{x'y'} \sin \alpha \cos \alpha \\ \varepsilon_y &= \varepsilon_{x'} \sin^2 \alpha + \varepsilon_{y'} \cos^2 \alpha - \gamma_{x'y'} \sin \alpha \cos \alpha \\ \frac{1}{2} \gamma_{xy} &= (\varepsilon_{x'} - \varepsilon_{y'}) \sin \alpha \cos \alpha + \frac{1}{2} \gamma_{x'y'} (\sin^2 \alpha - \cos^2 \alpha)\end{aligned}\quad (5.1)$$

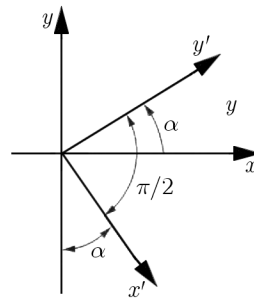


Fig. 15. Strain state transformation

To compare the obtained results with those from the analysis of Moiré images at the grid affixed according to the direction of the tensile stresses, the strain components distribution in the horizontal axis of symmetry x has been assumed (Fig. 16). In the diagram, the correction of strain components calculation resulting from the larger number of Moiré fringes (selected areas) is shown.

The analysis of strain components for model V (model with five holes) shows that in its horizontal axis of symmetry x , where the data obtained at the grid affixed traditionally are relatively inaccurate (low number of Moiré fringes), the information found from the rotated grid allows one to increase the accuracy of strain determination and to correct errors resulting from differentiation of surfaces of deformation.

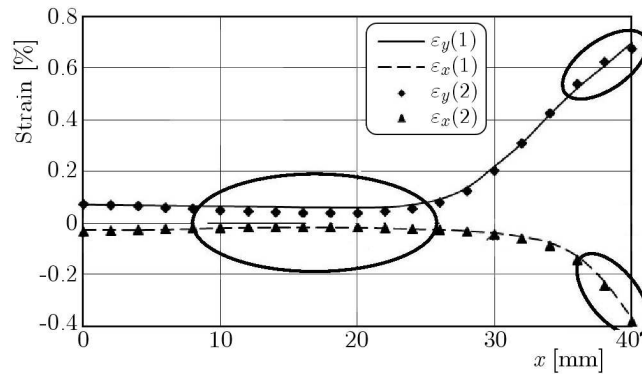


Fig. 16. Strain distribution in the axis of symmetry x (model V – $s = 0.778$): (1) grid affixed according to the direction of tension, (2) grid rotated by an angle of 45°

6. Conclusions

The review of experimental methods used in mechanics of solids carried out in terms of elastic-plastic analysis resulted in the selection of three of them for further investigations: the Moiré method, the method of photoelastic coating and the method of thermography. The choice has been dictated not only by their measuring capabilities in the over-elastic range of the material characteristics, but also by the simplicity of their use in practice and the availability of the equipment.

The main advantage of all three methods is the ability to conduct an experiment on real structures in working conditions, also under loading causing partial plastifying of the material and to obtain information about the strain state of the whole tested object. An additional advantage of the chosen methods (especially the method of photoelastic coating and the thermography method) is excellent visualization of the process of progressive material plastifying. The advantage of the Moiré method is also the simplicity of measurements and the work out of the experimental results.

The Moiré method and the method of photoelastic coating enable a relatively easy and quick quantitative analysis of the strain state around stress concentrators on the basis of experimental data. Thermographic tests have shown that this method allows rather getting a general view of the distribution of plastic strain components than their precise quantitative determination.

The conducted tests and detailed analysis of experimental data enabled definition of the range of applicability of each of the selected methods and determination of their capabilities in terms of the accuracy of calculation of strain components at various stages of material plastifying.

The range of application of the method of photoelastic coating (for an 2 mm thick optically active layer used in the testing of duralumin elements) is up to the maximum plastic strain $\sim 0.9\%$.

The Moiré method allows testing of the elements in a wider range of the material plastifying. For the used grids of 20 lines per millimeter, plastic strain can be measured up to $\sim 1.5\%$, while determination of the strain less than $\sim 0.2\%$ causes difficulties due to the low number of Moiré fringes. The measurement sensitivity of the Moiré method can be locally increased by affixing the grids at different angles. Such a possibility has been verified by additional tests performed at the grid rotated by an angle of 45° to the axis of symmetry of the model. That gave an effect similar to applying the rosette of strain gauges and showed that the accuracy of the elastic-plastic strain distribution around stress concentrators could be increased in the areas where the number of Moiré fringes is low.

The comparison of the strain components distribution in the horizontal axis of symmetry x (perpendicular to the direction of tension) obtained from the Moiré method and the method of

photoelastic coating for the range of material plastifying, for which both of them are applicable, shows that the differences between results are about a few percent. The comparison with numerical calculations (FEM) also shows good agreement of the results.

The quantitative analysis of strain and stress components in the whole area around stress concentrators proves that the Moiré method is a little more useful. The method of photoelastic coating is more labor-consuming due to the necessity of analytical strain separation (solving of the system of partial differential equations, Kozłowska, 2013) and converting the obtained results from irregular grid nodes to the rectangular grid.

The thermography method, although not enough accurate for quantitative strain analysis, gives an opportunity of observing plastic zones developing in elements in the full range of loading until their complete failure, so it seems to be useful for the study of elastic-plastic states in cooperation with other experimental methods (e.g., Moiré method and the method of photoelastic coating).

References

1. BALALOV V.V., PISAREV V.S., MOSHENSKY V.G., 2007, Combined implementing the hole drilling method and reflection hologram interferometry for residual stresses determination in cylindrical shells and tubes, *Optics and Lasers in Engineering*, **45**, 5, 661-676
2. CONNESSON N., MAQUIN F., PIERRON F., 2011, Experimental energy balance during the first cycles of cyclically loaded specimens under the conventional yield stress, *Experimental Mechanics*, **51**, 1, 23-44
3. DIAZ F.A., PATTERSON E.A., SIEGMANN P., 2010, A novel experimental approach for calculating stress intensity factors from isochromatic data, *Experimental Mechanics*, **50**, 2, 273-281
4. DIAZ F.V., ARMAS A.E., KAUFMANN G.H., GALIZZI G.E., 2004, Fatigue damage accumulation around a notch using a digital image measurement system, *Experimental Mechanics*, **44**, 3, 241-246
5. DIAZ F.V., KAUFMANN G.H., MOLLER O., 2001, Residual stresses determination using blind-hole drilling and digital speckle pattern interferometry with automated data processing, *Experimental Mechanics*, **41**, 4, 319-323
6. GUO Z., XIE H., LIU B., DAI F., CHEN P., ZHANG Q., HUANG F., 2006, Study on deformation of polycrystalline aluminum alloy using Moiré interferometry, *Experimental Mechanics*, **46**, 6, 699-711
7. FOUST B.E., LESNIAK J.R., ROWLANDS R.E., 2011, Determining individual stresses throughout a pinned aluminum joint by reflective photoelasticity, *Experimental Mechanics*, **51**, 9, 1441-1452
8. KOZŁOWSKA B., 2007, Effect of grid pattern arrangement on the accuracy of determination of strain distribution (in Polish), *Theoretical Foundations of Civil Engineering, Polish-Ukrainian-Lithuanian Transactions*, **15**, 309-312
9. KOZŁOWSKA B., 2008, Strain and stress analysis in two-dimensional elastic-plastic state by Moiré method, *Transactions of FAMENA*, **XXXII**, 1, 19-26
10. KOZŁOWSKA B., 2012, Application of thermography method to the investigation of two-dimensional elastic-plastic states, *The Archive of Mechanical Engineering*, **LIX**, 3, 297-312
11. KOZŁOWSKA B., 2013, Two-dimensional experimental elastic-plastic strain and stress analysis, *Journal of Theoretical and Applied Mechanics*, **51**, 2, 419-430
12. LAMBERSON L., ELIASSON V., ROSAKIS A.J., 2012, In situ optical investigations of hypervelocity impact induced dynamic fracture, *Experimental Mechanics*, **52**, 2, 161-170
13. LIN S.T., 2000, Blind-hole residual stresses determination using optical interferometry, *Experimental Mechanics*, **40**, 1, 60-67
14. LIVIERI P., NICOLETTO G., 2003, Elastoplastic strain concentration factors in finite thickness plates, *Journal of Strain Analysis*, **38**, 1, 31-36

15. MIN Y., HONG M., XI Z., LU J., 2006, Determination of residual stresses by use of phase shifting Moiré interferometry and hole drilling methods, *Optics and Lasers in Engineering*, **44**, 1, 68-79
16. OLMÍ G., 2010, In-field experimental stress analysis in the elastic and plastic fields on motorbike handlebar clamped joints, *Proceedings of 27th DANUBIA-ADRIA Symposium on Advances in Experimental Mechanics*, Wrocław, 161-162
17. PACEY M.N., JAMES M.N., PATTERSON E.A., 2005, A new photoelastic model for studying fatigue crack closure, *Experimental Mechanics*, **45**, 1, 42-52
18. PIECZYSKA E.A., GADAJ S.P., NOWACKI W.K., TOBUSHI H., 2006, Phase-transformation fronts evolution for stress- and strain-controlled tension tests in TiNi shape memory alloy, *Experimental Mechanics*, **46**, 4, 531-542
19. RASTY J., LE X., BAYDOGAN M., CÁRDENAS-GARCA J.F., 2007, Measurement of residual stresses in nuclear-grade Zircaloy-4(R) tubes effect of heat treatment, *Experimental Mechanics*, **47**, 2, 185-199
20. SCHAJER G.S., STEINZIG M., 2005, Full-field calculation of hole drilling method residual stresses from electronic speckle pattern interferometry data, *Experimental Mechanics*, **45**, 6, 526-532
21. TARIGOPULA V., HOPPERSTAD O.S., LANGSETH M., CLAUSEN A.H., HILD F., LADEMO O.-G., ERIKSSON M., 2008, A study of large plastic deformations in dual phase steel using digital image correlation and FE analysis, *Experimental Mechanics*, **48**, 2, 181-196
22. TIMOSHENKO S., GOODIER J.N., 1962, *Teoria sprężystości*, Wyd. Arkady, Warszawa
23. VURAL M., MOLINARI A., BHATTACHARYYA N., 2011, Analysis of slot orientation in shear-compression specimen (SCS), *Experimental Mechanics*, **51**, 3, 263-273
24. WUNG P., WALSH T., OURCHANE A., STEWART W., JIE M., 2001, Failure of spot welds under in-plane static loading, *Experimental Mechanics*, **41**, 1, 100-106

Manuscript received July 31, 2015; accepted for print September 11, 2015

ANALYSIS OF THE PROCESS OF WOOD PLASTICIZATION BY HOT ROLLING

MARIAN DUDZIAK, IRENEUSZ MALUJDA, KRZYSZTOF TALAŚKA,
TOMASZ ŁODYGOWSKI, WOJCIECH SUMELKA

Politechnika Poznańska

*e-mail: marian.dudziak@put.poznan.pl; ireneusz.malujda@put.poznan.pl; krzysztof.talaska@put.poznan.pl;
tomasz.lodygowski@put.poznan.pl; wojciech.sumelka@put.poznan.pl*

In this research, a mathematical model is derived to enable analytical determination of effective ultimate forces in the process of plasticization of the surface layer of wood. The experimentally determined thermo-mechanical properties of the material subjected to the process of plasticization are used in defining the structure of the model. The analysis of plastic strain in the layer in consideration is based on a generalised model of an ideally rigid-plastic medium, including certain modifications. Considering the anisotropic properties of wood, the Azzi-Tsai-Hill (ATH) strength criterion is applied which takes into account variation in the response of the loaded material depending on the direction. The article presents also results of FEM analysis of the same process of hot rolling of wood.

Keywords: yield point, temperature, moisture content, porosity, orthotropy

1. Properties of porous anisotropic natural polymers

The focus is on designing machines and devices of newly developed techniques for modification of the internal structure and surface characteristics of products made of various engineered materials. These materials include wood, which is considered the oldest structural material, through generally used metals to the cutting edge composites. The inspiration to undertake this research are the machines designed to improve properties of natural wood veneered furniture components by application of hot rolling technique. Wood has been used to analyse the complex process of plasticisation of superficial layers of such materials with the objective to improve their quality as well as their strength and functional performance.

The efficiency of plasticisation and densification of such materials depends on the desired ultimate load values (Ashby and Jones, 1996). Hence, an extensive testing program has been carried out to determine mechanical properties of wood and their dependence on temperature and moisture content. The results were used to set up constitutive equations of plasticity and to build models describing these processes. This was the basis to determine the effective ultimate load values used to define the machine design criteria (Mackenzie-Helnwein *et al.*, 2005; Malujda, 2006).

Properties of natural polymers are defined by specific and unique characteristics of the plant tissue of which they are made (Forest Products Laboratory, 1999; Kokociński, 2004). Some of them may be determined with organoleptic methods, others require highly specialised test apparatus to measure often mutually dependent physical quantities (Malujda and Marlewski, 2011). The values depend on several factors and phenomena which occur inside these materials exposed simultaneously to mechanical and thermal loading. Considering the number and complexity of characteristics of natural polymers such as wood, for the sake of clarity, a few important groups of properties and physical quantities have been identified, as schematically illustrated in Fig. 1.

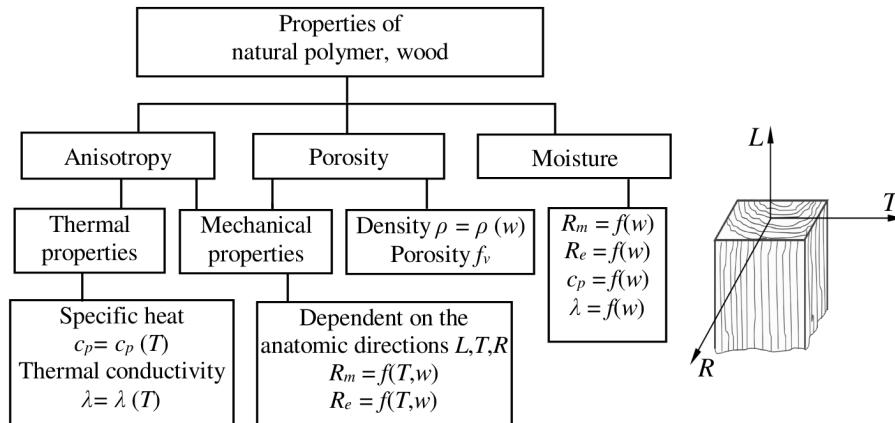


Fig. 1. The main thermo-mechanical properties of wood dependent on temperature and moisture content. R_m is the ultimate strength and R_e is the yield point, both in the three orthotropic directions: longitudinal L , tangential T and radial R

There is a number of important complex biochemical phenomena involved in plasticization processes highly relevant to the desired modification of geometrical parameters of their surfaces and internal structures. These phenomena have not been analysed in detail, as this would exceed the scope of this study. However, it can be assumed that the effect of these phenomena on the thermo-mechanical properties is reflected in the material functions determined experimentally through tests carried out on a macroscopic scale (Sumelka *et al.*, 2013).

The structural component of wood is cellulose, and it is the specific anatomical structure of cellulose that is responsible for the completely different structure and appearance of wood depending on the cutting direction. Skeleton-forming substances are based on cellulose and owe it its strength.

2. Experimental motivation

2.1. Compression test

The test specimens were subjected to compression load in the direction parallel to the grain and two perpendicular directions: tangential and radial. The specimens were made of beech wood (*Fagus sylvatica*). The dimensions of test specimens are presented in Fig. 2. Fig. 3 shows the annual growth rings. The tests specimens were produced in sufficient number for the planned tests.

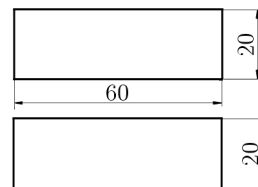


Fig. 2. Dimensions of the compression test specimen

The specimens were made of selected wood logs to obtain representative and reproducible results of testing as per Polish Standard PN-81/D-04107 (Kokociński, 2004). Specimens including structural features such as snags were rejected.

The specimens were compressed in the respective directions (L , T , R) and the output results enabled relating the determined strength to temperature and moisture gradients. The tests were carried out at three temperatures: 20°C, 50°C, 80°C and three moisture contents: 9%, 18% and 27%. The highest test temperature was 80°C because above that point chemical reactions

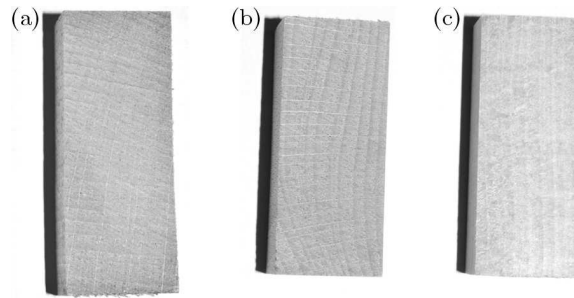


Fig. 3. Specimens: (a) radial direction, (b) tangential direction, (c) longitudinal direction

take place in beech wood, which brings unrecoverable changes in the composition and structure of wood. The moisture content was limited to 27%, which in the case of wood is the practical limit for absorption of moisture from air. The testing program for one fibre direction is presented in Table 1.

Table 1. Testing program for one fibre direction

		Temperature		
		20°C	50°C	80°C
Percent moisture	9%	3	3	3
	18%	3	3	3
	27%	3	3	3

Before the test, the specimens were conditioned in a climatic chamber (Fig. 4b) to attain the equilibrium moisture content. After subsequent storage in ambient conditions at the laboratory, the moisture content of specimens was 9%. The threshold values of 18% and 27% were achieved by placing the specimens in the desiccator above the saturated solution of NaCl and water respectively (Fig. 4a). The moisture content was checked by weighing of samples during conditioning until the desired value was obtained. The percent moisture at the point when the sample weight has stabilised is called the saturation moisture content. The weight was checked on a moisture balance with 0.001 g accuracy. Before each test, specimens of a specific percent moisture were heated up to the specified test temperature. The compression tests were carried out using a strength tester with 50 kN load cell and MTS mechanical extensometer resistant to high temperature and moisture. The strength tester was integrated with the climatic chamber placed within the MTS working space to maintain the specified ambient conditions. The strength tester incorporating the climatic chamber is presented in Figs. 5 and 6.

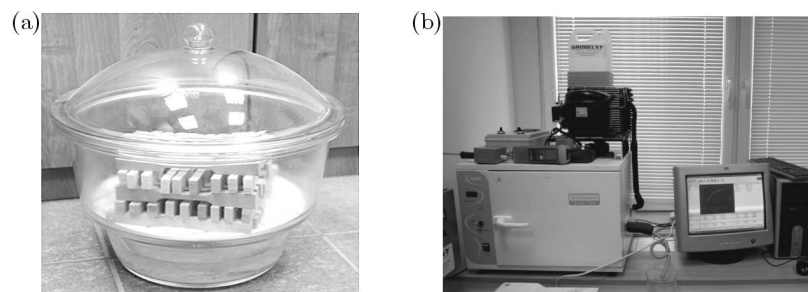


Fig. 4. (a) Desiccator with specimens placed inside, (b) stationary climatic chamber

The stress-strain curves were obtained for each compression test on the basis of extensometer displacement. The cross-sectional area of the specimen was determined before the test. The other input parameters, namely temperature and percent moisture, were measured right after the test.

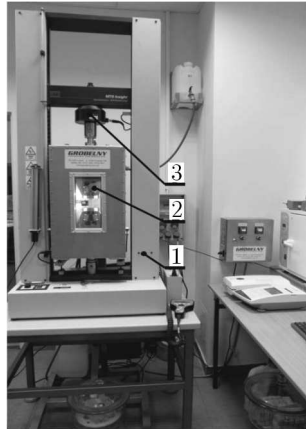


Fig. 5. MTS strength tester incorporating climate chamber 1 – strength tester, 2 – climate chamber, 3 – load cell (measuring the applied force)

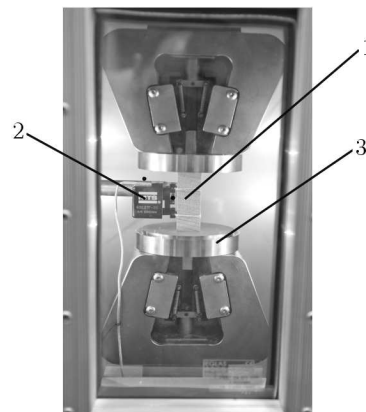


Fig. 6. Climatic chamber with holding jaws assembly designed for compression test: 1 – specimen placed between holding jaws, 2 – extensometer, 3 – force/ specimen alignment fixture to ensure that the force is applied perpendicular to the specimen cross-section

An example of a typical curve obtained from a compression test carried out on a specimen of beech wood in the tangential direction is presented in Fig. 7.

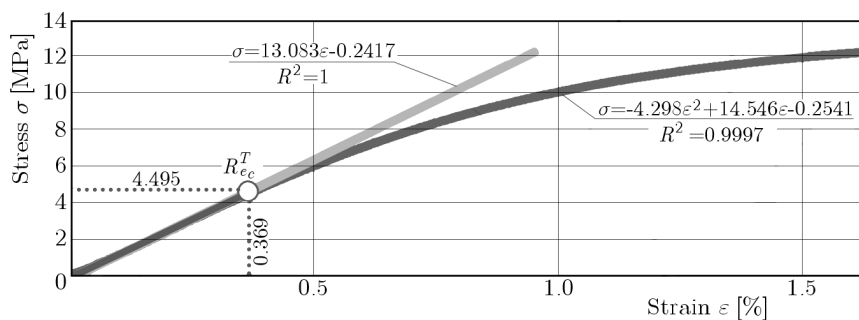


Fig. 7. The stress-strain curve for beech compressed in the tangential direction

The yield point values R_e in the respective orthotropic directions L , T , R were taken as the wood strength criterion used to set up constitutive equations describing the plasticization model of wood. For the compression test, those parameters were designated $R_{e_c}^L$, $R_{e_c}^R$, $R_{e_c}^T$, respectively. Their values were determined by the point where the tangent “departs” from the curve by more than 1% of the ultimate strength value. This point, in turn, was determined by

solving a system of equations comprising an equation of a straight line tangent to the stress-strain curve in tension and an equation of the actual stress-strain curve in compression (Fig. 7).

The results of each test type were recorded in single test record sheets and test logs which included all the relevant strength test information. Table 2 presents an example of a single test record sheet from a compression test carried out on a beech wood specimen with 9% moisture at 20°C. The test logs include the results obtained for the whole test series and accompany the respective test descriptions. An example of such a test log is presented in Table 3.

Table 2. Single test record sheet (compression of beech in the tangential direction, 9% moisture, 20°C)

Wood variety	beech	
Direction	tangential	
Moisture content [%]	9	
Temperature [^{circ} C]	20	
Cross-section area [mm ²]	402	
Young's modulus E [MPa]	1282.857	
Breaking force [M]	4894.27	
Ultimate strength R_c^T [MPa]	12.175	Test No. 1
Shortening at R_c^T [mm]	0.407	
Strain at R_c^T	0.016	
Yield point $R_{e_c}^T$ [MPa]	4.495	
Shortening at $R_{e_c}^T$ [mm]	0.09225	
Strain at $R_{e_c}^T$	0.00369	
$R_{e_c}^T/R_c^T$	0.369	
Gauge length l_0 [mm]	25	

Table 3. One series of tests: beech – tangential direction

	Test No.			
	1	2	3	avg.
Wood variety	beech			
Direction	tangential			
Moisture content [%]	9			
Temperature [°C]	20			
Cross-section area [mm ²]	402	406	404	404
Young's modulus E [MPa]	1282.857	1244.392	1267.786	1265.01
Breaking force [N]	4894.27	5309.5	5239.05	5147.60
Ultimate strength R_c^T [MPa]	12.175	13.078	12.969	12.7406
Shortening at R_c^T [mm]	0.407	0.565	0.475	0.48233
Strain at R_c^T	0.016	0.023	0.019	0.01929
Yield point $R_{e_c}^T$ [MPa]	4.495	3.541	4.21	4.082
Shortening at $R_{e_c}^T$ [mm]	0.09225	0.073	0.08675	0.084
Strain at $R_{e_c}^T$	0.00369	0.00292	0.00347	0.00336
$R_{e_c}^T/R_c^T$	0.369	0.271	0.325	0.32152

Having all the results, it was possible to define the relation between strength and temperature for the respective moisture content levels.

An example of the test results is presented in form of curves in Fig. 8. They relate the yield point R_e to the effect of temperature for three different moisture content levels in the tangential direction.

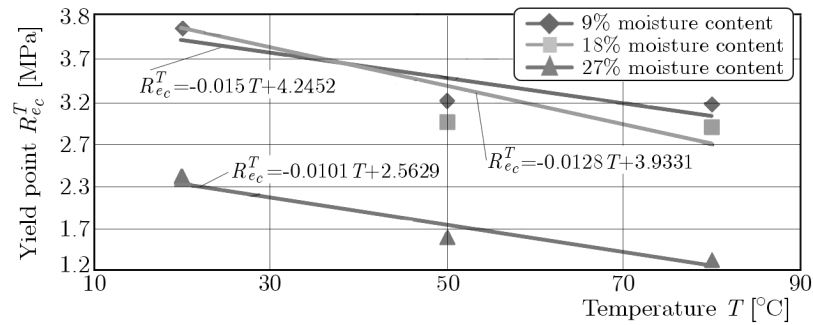


Fig. 8. Yield point R_{ec}^T vs. temperature T for different moisture content levels (beech wood, tangential direction)

2.2. Experimental determination of thermal conductivity

The thermal tester used in the determination of the thermal conductivity of wood was designed specifically for testing materials of low thermal conductivity (Fig. 9a). As the first step, specimens of the same density and thickness were prepared. The test set-up components were aligned coaxially and then load was applied to the top of the heat sink. Then the whole set-up was thermally isolated and the remaining parts, namely temperature sensors, power supply unit and the measuring device were connected. The system was energised and the heat sink switched on. Measurements were taken upon reaching the test temperature and thermal equilibrium.

The measurements were carried out on beech wood (Fig. 9b) in the three directions in relation to the grain: L , T , R (longitudinal, tangential and radial) at test temperatures of 40, 60, 80, 100, 120, 140 and 150°C to obtain arithmetic average of five measurement results for each test point.

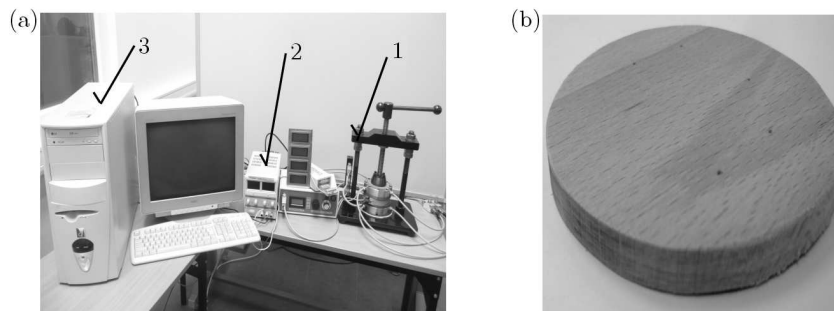


Fig. 9. (a) Experimental set-up for measuring thermal conductivity: 1 – thermal conductivity tester, 2 – amplifier, 3 – recording computer; (b) specimens of beech wood used for thermal conductivity measurement tests

The measurement results for beech wood were used to derive the curves (Fig. 10) relating the thermal conductivity coefficient λ to temperature for the three directions in relation to the grain: L , T , R .

The relationship between the thermal conductivity and temperature is described with application of an arctan approximation model λ_{arctan} , specially developed for this purpose by the authors. This description is consistent with the approximation methods developed by several researchers working in different research centres (Harada *et al.*, 1998; Gu and Zink-Sharp, 2005; Yang, 2001). Malujda and Marlewski (2011) demonstrated that the arctan approximation model provided more accurate approximation than the methods proposed by other researchers.

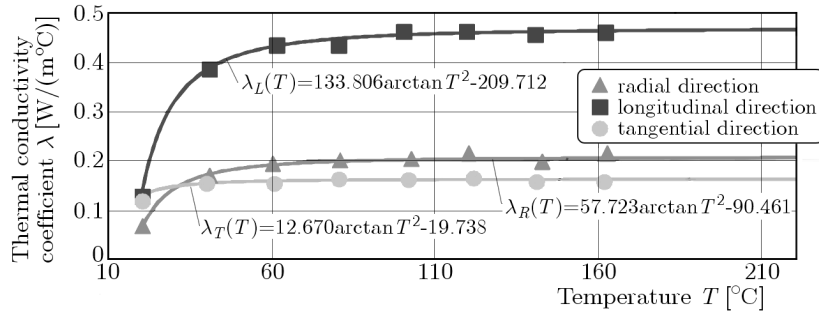


Fig. 10. Thermal conductivity vs. temperature for different fibre directions, approximation with the arctan model

3. Analysis of plasticization of an anisotropic material

In anisotropic materials, specific directions can be found in which plastic properties reach the extreme values. If these directions are oriented orthogonally one to another, we call it orthotropy, and the material with such characteristics is referred to as an orthotropic material (German, 2001). Wood is an example of such an orthotropic material.

The problem of defining the yield criterion of the surface layer of wood is approached as a two-dimensional problem (Fig. 11).

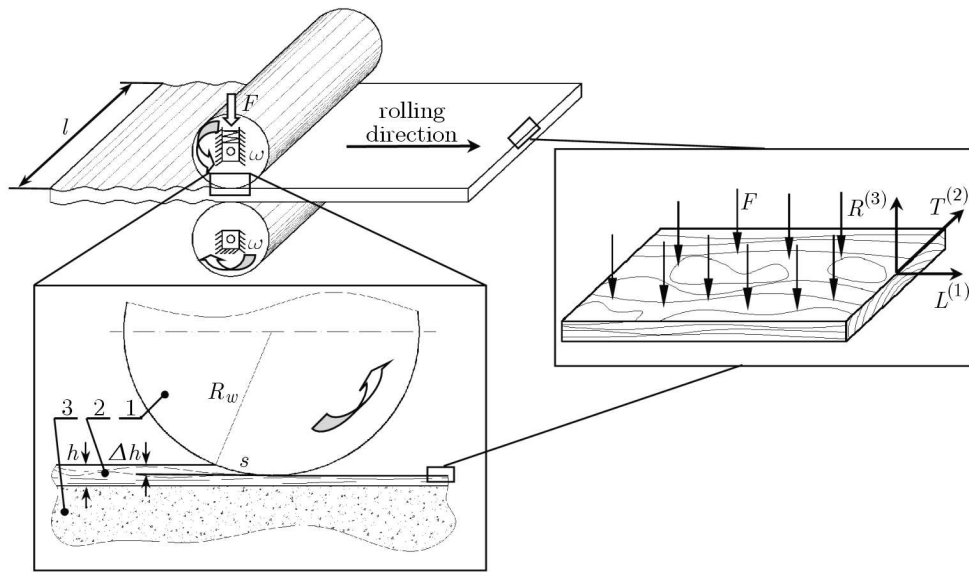


Fig. 11. Treatment to improve properties of the surface layer of the natural material by hot rolling: 1 – adjustable upper roller, 2 – layer of wood, 3 – chipboard, R_w – roller radius, s – roller/material contact length, h – depth of the layer of wood, l – board width, Δh – compression degree, directions: $L^{(1)}$ – longitudinal, $T^{(2)}$ – tangential, $R^{(3)}$ – radial

Let us use the anisotropic yield criterion of Azzi-Tsai-Hill (ATH) to analyse the ultimate stress-strain state of the analysed layer of wood, which considers its multi-directional reactions resulting from the components of the complex stress state. Hill (1956) generalized the HMH yield criterion to make it hold true for orthotropic materials. Wood is a natural polymer for which the reference system of co-ordinates can be set up so that the directions of axes coincide with the orthotropic directions L , T , R (Fig. 11). Having taken this assumption, the yield criterion may be represented by

$$(M + N)\sigma_{11}^2 + (L + N)\sigma_{22}^2 + (L + M)\sigma_{33}^2 - 2N\sigma_{11}\sigma_{22} - 2M\sigma_{11}\sigma_{33} - 2L\sigma_{22}\sigma_{33} + 2P\sigma_{23}^2 + 2Q\sigma_{31}^2 + 2R\sigma_{12}^2 = 1 \quad (3.1)$$

where L, M, N are the proportional limits with the values depending on the orthotropic direction and P, Q, R are the respective shear strength proportional limits.

The yield criterion formulated in this way is the strength criterion of an anisotropic material, and the critical strength is reached at the proportional limit. It is a characteristic feature of brittle materials, such as wood, for which these limits coincide with the yield and elasticity limits, and this has been confirmed by the results of experimental research.

The process of plasticization of natural materials having such complex properties as, for example, wood has not yet been described by non-linear models. Thus, the engineers cannot use a mathematical model whose structure is built of complex engineering constants, typical for natural polymers.

Now, let us take the process of hot rolling of wood (Fig. 11) and try to derive constitutive relations for natural materials by analytical method, assuming applicability of the theory of plasticity taking into account the plastic compressibility mechanism and allowing for the effect of heat and moisture (Bordia *et al.*, 2006; Fujii *et al.*, 2003; Malujda, 2006; Müllner *et al.*, 2004; Nairn, 2005).

The key parameter for the modelling of the process in consideration is the ultimate stress corresponding to the lower limit of statically determined strength of the layer subjected to loading (Ashby and Jones, 1996). At this point, having in hand the mathematical model, we shall try to determine the ultimate load resulting in plasticization of the material. The value of this load is of primary importance to the efficiency of the analysed process.

The establishing of a model can be defined as the identification of the process occurring in the material. Therefore, it is necessary to carry out in-depth analysis of these elements of the model which are critical to obtaining a satisfactory solution thereof. In the case of wood, these are: complex thermo-mechanical properties, porosity and process parameters including in particular the ultimate force F which depends on temperature and process duration (Malujda, 2006). Wood is a highly porous material and, for this reason, the ultimate stress depends not only on the second but also on the first invariant of the stress tensor. This effect must be considered in the final form of the yield criterion, similarly to the effect of direction in relation to the grain (Tsai and Wu, 1971). For this reason, the Huber von Mises-Hencky yield criterion for isotropic materials was used (German, 2001; Hill, 1956; Malujda and Talaška, 2010), generalized by Azzi-Tsai-Hill (ATH) to hold true for anisotropic materials.

Scalar functions of porosity, temperature and moisture are then fitted into this yield criterion formula, generalised to hold true for anisotropic materials. Subsequent analyses are carried out for the assumed physical model of the unsupported rigid-plastic medium.

Now, let us formulate the general yield criterion expressing the yield criterion for an anisotropic and porous material allowing for the effect of temperature and moisture content expressed generally as a function describing the yield surface

$$F(\sigma, f_v, T, w) = 0 \quad (3.2)$$

where σ is the stress tensor and the other terms are scalar functions of porosity f_v , temperature T and moisture content w (Malujda and Talaška, 2010). The structure of the yield criterion formulated in this way is created by interrelated physical quantities which have direct effect on the value of the ultimate yield force. Wood features porosity (Malujda and Talaška, 2010), which affects its yield point. This effect has been allowed for in the formulated mathematical model by introducing the following scalar functions of porosity

$$A = \frac{f_v}{1 - f_v} \quad B = 1 - f_v \quad (3.3)$$

which, while meeting the following limit conditions:

$$\begin{aligned} \text{if } f_v \rightarrow 0, \quad A \rightarrow 0, \quad \text{then } B \rightarrow 1 \\ \text{if } f_v \rightarrow 1, \quad A \rightarrow \infty, \quad \text{then } B \rightarrow 0 \end{aligned}$$

reduce criterion (3.2) to HMM criterion.

Introducing porosity functions (3.3) according to equation (3.2), we obtain

$$A(\sigma_1 + \sigma_2)^2 + (\sigma_1 - \sigma_2)^2 = BY_1^2 \quad (3.4)$$

where σ_1 and σ_2 are the principal stresses in the orthotropic directions (L - T).

In yield criterion (3.4), the complex ultimate stress-strain state is equated to the stress-strain state expressed by the non-zero main stress determined during a uniaxial compression test as a function of temperature and moisture content $Y_1 = R_{ec}^L$. At the critical state, this stress obtains a constant value at the strength limit of wood. The compressive yield strength has been taken as the parameter defining the critical stress of a natural polymer, i.e. the stress created by application of the ultimate force. This parameter is used as the basis for evaluating the characteristics of composite materials, such as wood, and its value depends on temperature and moisture content as well as on the direction of load application in relation to the grain.

In the first phase of pressure application to the thin layer of wood, permanent strains are produced without a significant effect of heat. Nevertheless, they are necessary in order to obtain the roller/ surface contact time sufficient to increase the temperature to approximately 120°C depending on the wood variety. As it has been demonstrated in the experimental research, this process takes very little time, namely ca 0.04-0.1 s. During that time, heat penetrates into the thin layer of wood by ca 0.1-0.12 mm which is the key element of the process of improving the material properties.

Hence, the process in consideration may be divided into two stages. The first stage concerns permanent strains created upon exceeding the proportional limit and it is related to densification of the structure of wood. In the second stage, smoothing and consolidation of the structure of the heated surface layer takes place. The yield load is reduced as a result of a decreased strength of wood resulting from an increase in temperature in the processing zone.

Introducing the orthotropy coefficients $\alpha = (Y_1/Y_2)^2$ and $\beta = (Y_1/Y_3)^2$, established on the basis of experimentally determined strength of wood Y_1, Y_2, Y_3 into equation (3.4), gives the following yield criterion

$$\sigma_1^2 + \alpha\sigma_2^2 - (1 + \alpha - \beta)\sigma_1\sigma_2 + A\sigma_1^2 + A\sigma_2^2\alpha + 2A(1 + \alpha - \beta)\sigma_1\sigma_2 = BY_1^2 \quad (3.5)$$

which is then rearranged to

$$\sigma_1^2(1 + A) + \alpha\sigma_2^2(1 + A) - (1 - 2A)(1 + \alpha - \beta)\sigma_1\sigma_2 = BY_1^2 \quad (3.6)$$

Some additional assumptions have been taken and simplifications have been made due to complexity of the process of hot rolling of wood. This process concerns plasticization of a thin layer of the processed material in the case when two dimensions are much higher than the third one. The depth of this layer h is small (Fig. 11) as compared to the lateral dimensions and hence the process is analysed in the in-plane strain state. The high value of the width to depth ratio of $l/h > 10$ and porosity of the material structure allow us to consider the strain in the tangential direction $T^{(2)}$ ignorable ($d\varepsilon_{22} = 0$) (Bednarski, 1995). This is supported by the approach used in real-life industrial applications. The second of the important simplifications is leaving out the stress σ_1 justified by the low value of the rolling resistance (ca 2% of the normal force) in the rolling direction $L^{(1)}$ (Bednarski, 1995). This is due to a very small contact angle (large diameter of the roller is required for process-related reasons) and hence it is justified to assume that the

roller pressure $p = F/(sl)$ (Fig. 11) is almost entirely directed on the component perpendicular to the plane $L^{(1)}-T^{(2)}$ (Fig. 11).

In the next step of building up the model, we shall use the associated plastic flow rule which relates the strain increase deviator $d\varepsilon_{ij}$ to the plastic potential function $F(\sigma_{ij})$ represented by the following relationship

$$d\varepsilon_{ij} = d\varsigma \frac{\partial F(\sigma_{ij})}{\partial \sigma_{ij}} \quad (3.7)$$

where ς is a coefficient determined from the increase of work of plastic strain.

Hence, with the assumed value of $d\varepsilon_{ij} = 0$, the associated plastic flow rule is expressed by the following formula

$$d\varepsilon_{22} = d\varsigma \frac{\partial F}{\partial \sigma_{22}} = 0 \quad (3.8)$$

Differentiating equation (3.5)

$$\frac{\partial F}{\partial \sigma_2} = 2\alpha\sigma_2(1+A) - (1-2A)(1+\alpha-\beta)\sigma_1 = 0 \quad (3.9)$$

yields

$$\sigma_2 = \frac{(1-2A)(1+\alpha-\beta)}{2\alpha(1+A)}\sigma_1 \quad (3.10)$$

Substituting expression (3.10) described by equation (3.6) to get rid of σ_2 , we get

$$\begin{aligned} \sigma_1^2(1+A) + \alpha(1+A) \left[\frac{(1-2A)(1+\alpha-\beta)}{2\alpha(1+A)} \right]^2 \sigma_1^2 \\ - (1-2A)(1+\alpha-\beta) \frac{(1-2A)(1+\alpha-\beta)}{2\alpha(1+A)} = BY_1^2 \end{aligned} \quad (3.11)$$

Rearranging equation (3.11), we get the following relationship for calculating the stress σ_1

$$\sigma_1^2 = \frac{B}{(1+A) - \frac{(1-2A)^2(1+\alpha-\beta)}{4\alpha(1+A)}} Y_1^2 \quad (3.12)$$

Now let us use yield criterion (3.6) in order to determine the isotropic state stress

$$Ap^2 + A\alpha p^2 + 2A(1+\alpha-\beta)p^2 + \beta p^2 = BY_1^2 \quad (3.13)$$

and thus, upon rearranging equation (3.13), we obtain

$$p^2 = \frac{B}{A(3+3\alpha-2\beta) + \beta} Y_1^2 \quad (3.14)$$

If $A \rightarrow 0$ then $p \rightarrow \infty$, where $f_v \rightarrow 0$ means incompressibility of the analysed material.

Finally, we get the following equation describing the yield criterion, expressing the ultimate stress state derived through transition from the in-plane strain state to the equivalent in-plane stress state

$$p = \sqrt{\left[\frac{B}{(1+A) - \frac{(1-2A)^2(1+\alpha-\beta)}{4\alpha(1+A)}} - \frac{B}{A(3+3\alpha-2\beta) + \beta} \right] Y_1^2} \quad (3.15)$$

The above expression, describing the ultimate roller pressure applied to the processed layer of wood allows for the porosity and anisotropic properties of the analysed material. Experimental determination of the compressive yield strength in the longitudinal direction $Y_1 = R_{ec}^L$ takes into account the effect of heat and moisture content.

4. Analytical and numerical solutions of the model of the thin layer plasticization process

In the obtained analytical model, functions of material characteristics are applied including the arctangent thermal conductivity function. The relevant data are given in Table 1. Since all the functions of material characteristics required for the determination of the critical stress according to (3.15) depend on the temperature, the values calculated with equation (3.15) are compared to the results of FEM analysis by determining the stress value for a given temperature at a given point during the rolling process modelled with the FEM software. The process parameters assumed as the input for calculations correspond to the values applied in wood improvement processes in furniture manufacturing applications. Figure 12 illustrates geometry of the model derived for the purpose of FEM analysis.

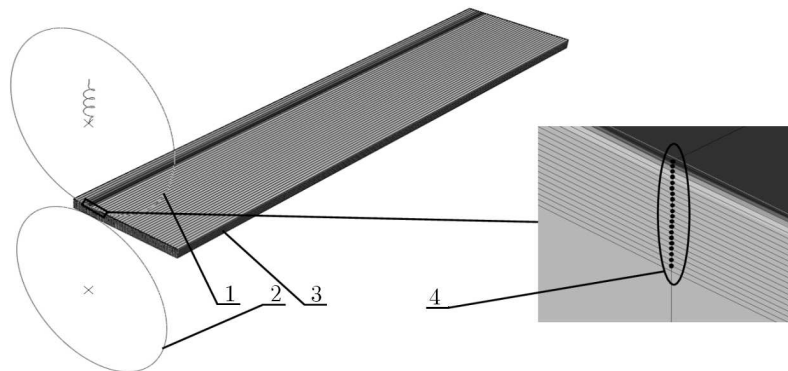


Fig. 12. Model derived for the purpose of FEM analysis: 1 – adjustable upper roller, 2 – lower roller, 3 – processed material, processed layer of wood showing nodes in the depth-wise direction

A 0.8 mm deep surface layer of the processed material is sub-divided into twenty finite elements. The entire model comprising of the roller and processed material is “encases” with air at temperature of 20°C. The purpose is to imitate the real-life ambient temperature of the surrounding air which is about 20°C. The roller/material contact parameters are defined assuming that the exchange of heat between these surfaces is close to ideal. The abutting surfaces of the roller and the processed material are assumed to have the same temperature, namely 220°C.

The duration of contact between each point located in the thin surface whose location is defined by the co-ordinates of the node of a rectangular grid component, and the roller is assumed at ca 0.06 s. This time corresponds to ca 6 m/min linear speed of the roller (process parameter). The thermo-mechanical properties of beech wood and geometric parameters of the analysed wood improvement process are presented in Tables 4 and 5.

The curves in Figs. 13a,b,c represent the relation between the stress value and the depth below the surface of the rolled material determined with the use of analytically determined relationship (3.15) and FEM analysis. Figure 14 presents the relative percent difference between the values calculated with equation (3.15) and the results of FEM analysis.

5. Conclusions

The processes of plasticization of natural polymers in real-life conditions are governed by several parameters. The relevant factors include external mechanical loads, temperature, moisture content and process duration. Consequently, the established constitutive relations have a more general form.

The analysis of plastic strain in the analysed layer of wood is based on a generalised model of an ideally rigid-plastic medium with certain simplifications and modifications. Taking account

Table 4. Material characteristics – thermo-mechanical properties of beech

Physical quantity	Designation	Unit	Value/function
Arctangent thermal conductivity in the L, T, R directions in relation to the grain	$\lambda_{\text{arctan}}^L$ $\lambda_{\text{arctan}}^R$ $\lambda_{\text{arctan}}^T$	W/(m°C)	$\lambda_{\text{arctan}}^L = 133.806 \arctan T^2 - 209.712$ $\lambda_{\text{arctan}}^R = 57.723 \arctan T^2 - 90.462$ $\lambda_{\text{arctan}}^T = 12.67 \arctan T^2 - 19.739$
Elastic constant	$E_{c-9\%}^{L,R,T}$ $E_{c-18\%}^{L,R,T}$ $E_{c-27\%}^{L,R,T}$	MPa	$E_{c-9\%}^L = -78.48T + 17809$ $E_{c-18\%}^L = -21.514T + 11574$ $E_{c-27\%}^L = -34.454T + 8530.9$ $E_{c-9\%}^R = -8.363T + 2047.2$ $E_{c-18\%}^R = -7.757T + 2022$ $E_{c-27\%}^R = -1.3884T + 1114$ $E_{c-9\%}^T = -4.0966T + 1256.5$ $E_{c-18\%}^T = -5.775T + 1278.2$ $E_{c-27\%}^T = -3.598T + 832.78$
Yield strength	$Y_1 = R_{e_c}^L$ $Y_2 = R_{e_c}^T$ $Y_3 = R_{e_c}^R$	MPa	$R_{e_c-9\%}^L = -0.06T + 17.451$ $R_{e_c-18\%}^L = -0.047T + 13.213$ $R_{e_c-27\%}^L = -0.0312T + 9.5012$ $R_{e_c-9\%}^R = -0.0201T + 6.0151$ $R_{e_c-18\%}^R = -0.014T + 4.6398$ $R_{e_c-27\%}^R = -0.0102T + 3.4249$ $R_{e_c-9\%}^T = -0.015T + 4.2452$ $R_{e_c-18\%}^T = -0.0128T + 3.9331$ $R_{e_c-27\%}^T = -0.0101T + 2.5629$
Specific heat capacity of dry wood	c_{po}	kJ/(kg K)	$c_{po} = 0.1031 + 0.003867T$
Specific heat capacity allowing for the effect of moisture content	c_p	kJ/(kg K)	$c_p = \frac{c_{po} + 0.01w c_{pw}}{1 + 0.01w + A_k}$ w – moisture content (9%, 18%, 27%) c_{pw} – specific heat of water A_k – coefficient $A_k = -0.07592$ (9%) $A_k = -0.17338$ (18%) $A_k = -0.29238$ (27%)
Density	ρ	kg/m ³	810
Moisture content	m	%	9, 18, 27

the anisotropic properties of wood, the Azzi-Tsai-Hill (ATH) strength criterion is used as it allows for the variation of reaction to the loading depending on the direction. The strength criterion is based on the experimentally determined compressive yield strength allowing for the effect of temperature and moisture content. The ultimate load determined in this way depends on the established strength criterion as well as factors defining porosity and orthotropic properties of the material which relate the yield strength values in the respective orthotropic directions.

Table 5. Geometric parameters of the analysed wood improvement process

Physical quantity	Designation	Unit	Value
Roller radius	R_w	m	0.1565
Thickness of layer before rolling	h_1	m	0.0008
Linear speed	v	m/s	0.1
Roller temperature	T	°C	220

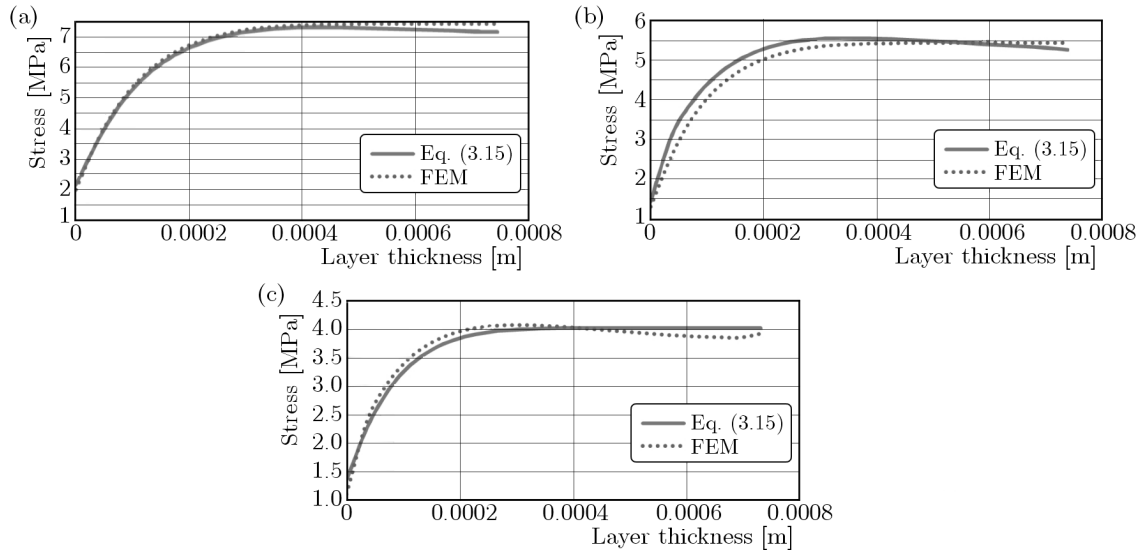


Fig. 13. Stress depending on depth inwards the processed material with (a) 9%, (b) 18%, (c) 27% moisture content

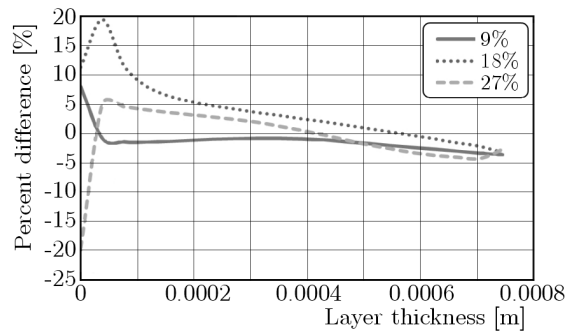


Fig. 14. Percent difference between the results of analytical and numerical calculations as a function of depth of the layer of the plasticized material

The ultimate stresses determined with the above-mentioned model are used in simulations and numerical calculations. The equations presented herein may be used to ensure the desired properties and dimensions of products and to define input assumptions and design machines used to realise the process in consideration and other similar processes.

According to the results of the process lasting ca 0.06 s, the calculated stresses generated by the roller in the plasticized layer of wood decrease nearly two times. This is due to an increase in temperature up to the range of 110-130°C at which plasticization of the surface layer of wood to ca 0.1 mm in depth occurs.

It can be seen that an increase in the moisture content results in a decrease in the value of stress. With the moisture content of 27%, the stress values are almost two times lower at the same depth.

The percent differences between the results obtained by FEM analysis and calculated using the ultimate roller pressure formula are small. This confirms that the assumptions and simplifications made in the process of deriving constitutive relationships relating to the rolling process are appropriate.

References

1. ASHBY M.F., JONES D.R.H., 1996, *Engineering Materials* (in Polish), WNT, Warszawa
2. BEDNARSKI T. 1995, *Mechanics of Plastic Flow at a Glance* (in Polish), PWN, Warszawa 1995
3. BORDIA R.K., ZUO R., GUILLON O., SALAMONE S.M., RODEL J., 2006, Anisotropic constitutive laws for sintering bodies, *Acta Materialia*, **54**, 111-118
4. FUJII Y., OKUMURA S., INOUE M., ADACHI K., 2003, FE-analysis of roll pressing of wood, *Proceedings of 16th International Wood Machining Seminar*, Matsue, Japan, 410-413
5. Forest Products Laboratory, 1999, Wood as an engineering material, Gen. Tech. Rep. FPL-GTR-113, Madison, WI: U.S. Department of Agriculture, Forest Service
6. GERMAN J., 2001, *Fundamentals of Mechanics of Fiber Composites* (in Polish), Publishing House of Cracow University of Technology, Kraków
7. GU H.M., ZINK-SHARP A., 2005, Geometric model for softwood transverse thermal conductivity. Part I, *Wood and Fiber Science*, **37**, 4, 699-711
8. HARADA, T., HATA, T., ISHIHARA SH. 1998, Thermal constants of wood during the heating process measured with the laser flash method, *Journal of Wood Science*, **44**, 425-431
9. HILL R., 1956, *The Mathematical Theory of Plasticity*, Clarendon Press, Oxford
10. KOKOCIŃSKI W., 2004, *Wood: Measurement of Physical and Mechanical Properties*, Poznań
11. MACKENZIE-HELNWEIN P., EBERHARDSTEINER J., MANG H.A., 2005, Rate-independent mechanical behavior of biaxially stressed wood: experimental observations and constitutive modelling as an orthotropic two-surface elasto-plastic material, *Holzforschung*, **59**, 3, 311-321
12. MALUJDA I., 2006, Plasticization of a bounded layer of anisotropic and loose material, *Machine Dynamics Problems*, **30**, 4, 48-59
13. MALUJDA I., MARLEWSKI A., 2011, On the heat conduction in natural porous and anisotropic materials, *Proceedings of World Congress on Engineering WCE*, London, Vol. I, 261-265, 37-39, Hung To Road, Hong Kong, IAENG International Association of Engineering, ISBN: 978-988-18210-6-5, ISSN: 2078- 0958
14. MALUJDA I., TALAŚKA K., 2010, Modeling of yielding processes in porous and anisotropic natural materials, *Machine Dynamics Research*, **34**, 4, 40-50
15. MÜLLNER H.W., MACKENZIE-HELNWEIN P., EBERHARDSTEINER J., 2004, Constitutive modelling of biaxially stressed wood for the analysis of layered wooden shells, *Proceedings of 3rd International Conference of the Europe Society for Wood Mechanics*, 277-284
16. NAIRN J.A., 2005, Numerical simulations of transverse compression and densification in wood, *Material Science and Engineering*, University of Utah, Salt Lake City, Utah
17. SUMELKA W., ŁODYGOWSKI T., 2013, Reduction of the number of material parameters by ANN approximation, *Computational Mechanics*, **52**, 2, 287-300
18. TSAI S.W., WU E.M., 1971, A general theory of strength for anisotropic materials, *Journal of Composite Materials*, **5**, 58-80
19. YANG Q.X., 2001, Theoretical expressions of thermal conductivity of wood, *Journal of Forestry Research*, **12**, I, 43-46

THERMAL AND FLUID ANALYSIS ON EFFECTS OF A NANOFLUID OUTSIDE OF A STRETCHING CYLINDER WITH MAGNETIC FIELD USING THE DIFFERENTIAL QUADRATURE METHOD

S.E. GHASEMI

*Young Reseachers and Elite Club, Sari Branch, Islamic Azad University, Sari, Iran
e-mail: s.ebrahim.ghasemi@gmail.com*

M. HATAMI

Department of Mechanical Engineering, Esfarayen University of Technology, Esfarayen, North Khorasan, Iran

ARMIA SALARIAN, G. DOMAIRRY

Department of Mechanical Engineering, Babol University of Technology, Babol, Iran

In this paper, magnetohydrodynamic flow (MHD) of a nonofluid over a stretching cylinder is investigated numerically. The Differential Quadrature Method (DQM) is applied for solving the governing equations. The influence of relevant parameters such as the magnetic parameter, the solid volume fraction of nanoparticles and the type of nanofluid on the flow, heat transfer, Nusselt number and skin friction coefficient is discussed. Also, comparison with the published results is presented. The results show that the Nusselt number increases with growth in the volume fraction coefficient and Reynolds number but decreases with the magnetic parameter.

Keywords: nanofluids, Differential Quadrature Method (DQM), heat transfer, stretching cylinder, magnetic field

1. Introduction

Magnetohydrodynamics can be regarded as a combination of fluid mechanics and electromagnetism, that is, behaviour of an electrically conducting fluid in the presence of magnetic and electric fields. The study of magnetohydrodynamic (MHD) flow has received a great deal of research interest due to its importance in many engineering applications such as plasma studies, MHD power generators, petroleum industries, cooling of nuclear reactors, boundary layer control in aerodynamics and crystal growth (Harada and Tsunoda, 1998; Shang, 2001).

Many investigations have been done on the flow past a moving flat plate or a stretching sheet in the presence of a transverse magnetic field, and a good amount of literature has been generated on this problem (Ishak *et al.*, 2006; Mahapatra and Gupta, 2001).

Examples of such technological applications are hot rolling, wire drawing, glass-fibre and paper production, drawing of plastic films, metal and polymer extrusion and metal spinning (Magyari and Keller, 1999). In all these cases, a study of the flow field and heat transfer can be of significant importance since the quality of the final product depends to a large extent on the skin friction coefficient and the surface heat transfer rate. The heat removal strategies in many engineering applications such as cooling of electronic components rely on natural convection heat transfer due to its simplicity, minimum cost, low noise, smaller size and reliability. In most natural convection studies, the base fluid has a low thermal conductivity, which limits the heat transfer enhancement. However, the continuing miniaturization of electronic devices requires further heat transfer improvements from the energy saving viewpoint (Aminossadati and Ghasemi, 2009). An innovative technique which uses a mixture of nanoparticles and the base

fluid was first introduced by Choi (1995) in order to develop advanced heat transfer fluids with substantially higher conductivities. The resulting mixture of the base fluid and nanoparticles having unique physical and chemical properties is referred to as a nanofluid. It is expected that the presence of nanoparticles in the nanofluid will increase the thermal conductivity and, therefore, substantially enhance the heat transfer characteristics of the nanofluid. Convective heat transfer fluids, including oil, water, and ethylene glycol mixture are poor heat transfer fluids, since the thermal conductivity of these fluids plays an important role in determining the coefficient of heat transfer between the heat transfer medium and the heat transfer surface (Ho *et al.*, 2008).

Mathematical modelling is a vantage point to reach a solution in an engineering problem, so the accurate modelling of nonlinear engineering problems is an important step to obtain accurate solutions (Zolfagharian *et al.*, 2014a,b,c, 2015; Misagh *et al.*, 2014).

Most differential equations of engineering problems do not have exact analytical solutions, so approximation and numerical methods must be used. Recently, some different methods have been introduced to solving these equations, such as the Variational Iteration Method (VIM) (Ghasemi *et al.*, 2012), Homotopy Perturbation Method (HPM) (Ghasemi *et al.*, 2013; Mohammadian *et al.*, 2015), Parameterized Perturbation Method (PPM) (Ghasemi *et al.*, 2015c), Differential Transformation Method (DTM) (Ghasemi *et al.*, 2014a,c; Hatami *et al.*, 2015), Homotopy Analysis Method (HAM) (Ziabakhsh and Domairry, 2009; Ziabakhsh *et al.*, 2010), Adomian Decomposition Method (Ghasemi *et al.*, 2012), Modified Homotopy Perturbation Method (MHPM) (Ghasemi *et al.*, 2014d), Least Square Method (LSM) (Ghasemi *et al.*, 2014c, 2015b; Darzi *et al.*, 2015), Collocation Method (CM) (Ghasemi *et al.*, 2015a; Atouei *et al.*, 2015), Galerkin Method (GM) (Ghasemi *et al.*, 2015d), and Optimal Homotopy Asymptotic Method (OHAM) (Vatani *et al.*, 2014; Valipour *et al.*, 2015). Also, the Differential Quadrature Method (DQM) is a numerical technique for solving differential equations. It was first developed by Bellman *et al.* (1972). Afterwards, it was improved by Shu (2000). The magnetohydrodynamic natural convection boundary-layer flow on a sphere in a porous medium was studied numerically using the Differential Quadrature Method (DQM) by Moghimi *et al.* (2011). The boundary-layer natural convection flow on a permeable vertical plate with thermal radiation and mass transfer was investigated when the plate moved in its own plane by Talebizadeh *et al.* (2011). They solved the governing equations by means of an excellent analytical method called Homotopy Analysis Method (HAM) and a higher-order numerical method, namely the Differential Quadrature Method (DQM). Hatami and Ganji (2014) applied the Differential Transformation Method with the Padé approximation (DTM-Padé) and the Differential Quadrature Method (DQM) for the motion of a particle in a forced vortex. They showed that the results of the DQM were in excellent agreement with the numerical fourth-order Runge-Kutta solution.

Ghasemi *et al.* (2016a) applied the Differential Quadrature Method (DQM) to find an accurate solution for blood flow analysis in femoral and coronary arteries. They showed that the results of the DQM were in excellent agreement with the numerical Crank Nicholson Method (CNM).

Application of the Differential Quadrature Method (DQM) for boundary layer flow over a flat plate with slip flow and constant heat flux surface condition was studied by Moghimi *et al.* (2013). Wang (1988) studied the steady flow of a viscous and incompressible fluid outside of a stretching hollow cylinder in an ambient fluid at rest. Ishak *et al.* (2008) investigated the flow and heat transfer of a viscous and incompressible electrically conducting fluid outside of a stretching cylinder in the presence of a constant transverse magnetic field. The problem is governed by a third-order nonlinear ordinary differential equation that leads to exact similarity solutions of the Navier-Stokes equations.

The main aim of this paper is to simulate the problem of the flow of a nanofluid outside of a stretching cylinder in the presence of magnetic field by DQM and to compare the obtained

results with those of Ishak *et al.* (2008), which represent the influence of adding nanoparticles to the base fluid. Also, the effects of some parameters such as the solid volume fraction of nanoparticles, type of the nanofluid and the magnetic parameter on velocity and temperature profiles are examined.

2. Formulation of the problem

Consider a steady laminar flow of an incompressible electrically conducting fluid (with electrical conductivity σ) caused by a stretching tube of radius a in the axial direction in the fluid at rest as shown in Fig. 1, where the z -axis is measured along the axis of the tube and the r -axis is measured in the radial direction. It is assumed that the surface of the tube is at constant

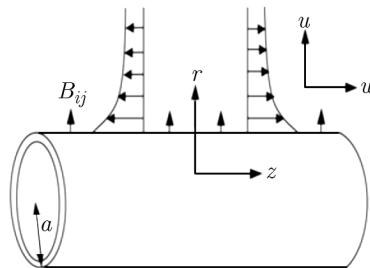


Fig. 1. Physical model and coordinate system

temperature T_w and the ambient fluid temperature is T_1 , where $T_w > T_1$. We also assume that the uniform magnetic field of intensity B_0 acts in the radial direction and that the effect of the induced magnetic field is negligible, which is valid when the magnetic Reynolds number is small. The viscous dissipation, Ohmic heating and Hall effects are neglected as they are also assumed to be small. The fluid is a water based nanofluid containing different types of nanoparticles: Cu, Al_2O_3 and TiO_2 . It is assumed that the base fluid and the nanoparticles are in thermal equilibrium and no slip occurs between them. The thermo physical properties of the nanofluid are given in Table 1

Table 1. Thermo-physical properties of water and nanoparticles (Oztop and Abu-Nada, 2008)

	ρ [kg/m ³]	C_p [J/(kgK)]	k [W/(mK)]	β [1/K]
Pure water	997.1	4179	0.613	21
Copper (Cu)	8933	385	401	1.67
Silver (Ag)	10500	235	429	1.89
Alumina (Al_2O_3)	3970	765	40	0.85
Titanium Oxide (TiO_2)	4250	686.2	8.9538	0.9

(see Oztop and Abu-Nada, 2008). On the above assumptions, the boundary layer equations governing the flow, and the concentration field can be written in dimensional form as

$$\begin{aligned}
 \frac{\partial(ru)}{\partial r} + \frac{\partial(rw)}{\partial z} &= 0 & u \frac{\partial w}{\partial r} + w \frac{\partial w}{\partial z} &= \frac{\mu_{nf}}{\rho_{nf}} \left(\frac{\partial^2 w}{\partial r^2} + \frac{1}{r} \frac{\partial w}{\partial r} \right) - \frac{\sigma B_0^2}{\rho_{nf}} w \\
 u \frac{\partial u}{\partial r} + w \frac{\partial u}{\partial z} &= -\frac{1}{\rho_{nf}} \frac{\partial p}{\partial r} + \frac{\mu_{nf}}{\rho_{nf}} \left(\frac{\partial^2 u}{\partial r^2} + \frac{1}{r} \frac{\partial u}{\partial r} - \frac{u}{r^2} \right) \\
 (\rho C_p)_{nf} \left(w \frac{\partial T}{\partial z} + u \frac{\partial T}{\partial r} \right) &= k_{nf} \left(\frac{\partial^2 T}{\partial r^2} + \frac{1}{r} \frac{\partial T}{\partial r} \right)
 \end{aligned}
 \tag{2.1}$$

Subject to the following boundary conditions

$$\begin{aligned} u = 0 & & w = W_w & & T = T_w & & \text{at } r = a \\ w \rightarrow 0 & & T \rightarrow T_\infty & & & & \text{as } r \rightarrow \infty \end{aligned} \quad (2.2)$$

where u and w are the velocity components along the r and z axes, respectively, $W_w = 2cz$ where c is a positive constant, and a is a constant. Further, ν , ρ , T and α are the kinematic viscosity, fluid density, fluid temperature and thermal diffusivity, respectively. It is necessary to mention that the magnetic term in Eq. (2.1)₃ (in the r direction) is neglected because it does not affect the flow dynamics in perpendicular situations and can be absorbed by the pressure term.

The effective density ρ_{nf} , the effective dynamic viscosity μ_{nf} , the heat capacitance $(\rho C_p)_{nf}$ and the thermal conductivity k_{nf} of the nanofluid are given as (see Aminossadati and Ghasemi, 2009)

$$\begin{aligned} (\rho C_p)_{nf} &= (\rho C_p)_f(1 - \varphi) + (\rho C_p)_s\varphi & \frac{k_{nf}}{k_f} &= \frac{k_s + 2k_f - 2\varphi(k_f - k_s)}{k_s + 2k_f + \varphi(k_f - k_s)} \\ \rho_{nf} &= \rho_f(1 - \varphi) + \rho_s\varphi & \mu_{nf} &= \frac{\mu_f}{(1 - \varphi)^{2.5}} \end{aligned} \quad (2.3)$$

Here, φ is the solid volume fraction, μ_f is the dynamic viscosity of the basic fluid, ρ_f and ρ_s are the densities of the pure fluid and nanoparticle, respectively. $(\rho C_p)_f$ and $(\rho C_p)_s$ are the specific heat parameters of the base fluid and nanoparticle, k_f and k_s are the thermal conductivities of the base fluid and nanoparticle, respectively. Following Wang (1988), we take the similarity transformation

$$u = -ca \frac{f(\eta)}{\sqrt{\eta}} \quad w = 2cf'(\eta)z \quad \eta = \left(\frac{r}{a}\right)^2 \quad \theta = \frac{T - T_\infty}{T_w - T_\infty} \quad (2.4)$$

where the prime denotes differentiation with respect to η . Substituting Eq. (14) into Eqs. (2.1)₂ and (2.1)₄, we get the following ordinary differential equations

$$\begin{aligned} \frac{1}{(1 - \varphi)^{2.5}} \frac{1}{1 - \varphi + \frac{\rho_s}{\rho_f}\varphi} (f''' \eta + f'') - \frac{M}{1 - \varphi + \frac{\rho_s}{\rho_f}\varphi} f' - \text{Re} f'^2 + \text{Re} f f'' &= 0 \\ \theta'' \eta + \theta' + f \theta' \text{Re Pr} \frac{1 - \varphi + \frac{(\rho C_p)_s}{(\rho C_p)_f}\varphi}{\frac{k_s + 2k_f - 2\varphi(k_f - k_s)}{k_s + 2k_f + \varphi(k_f - k_s)}} &= 0 \end{aligned} \quad (2.5)$$

where $\text{Re} = ca^2/(2\nu_{nf})$ is the Reynolds number and $M = \sigma B_0^2 a^2/(4\nu_{nf}\rho_{nf})$ is the magnetic parameter. ν_{nf} is the kinematic viscosity of nanofluid. Boundary conditions (2.2) become

$$\begin{aligned} f(1) = 0 & & f'(1) = 1 & & \theta(1) = 1 \\ f(\infty) \rightarrow 0 & & \theta(\infty) \rightarrow 0 \end{aligned} \quad (2.6)$$

The pressure can now be determined from Eq. (2.1)₃ in the following form

$$\frac{p - p_\infty}{\rho c v} = -\frac{\text{Re}}{\eta} f^2(\eta) - 2f'(\eta) \quad (2.7)$$

The physical quantities of interest are the skin friction coefficient and the Nusselt number, which are defined as follows

$$C_f = \frac{\tau_w}{\rho W_w/2} \quad \text{Nu} = \frac{aq_w}{k(T_w - T_\infty)} \quad (2.8)$$

Furthermore, τ_w and q_w are the skin friction and the heat transfer from the surface of the tube, respectively, and are given as

$$\tau_w = \mu \left(\frac{\partial w}{\partial r} \right)_{r=a} \quad q_w = -k \left(\frac{\partial T}{\partial r} \right)_{r=a} \tag{2.9}$$

where k is the thermal conductivity. Considering variables (2.4), we get

$$C_f \frac{\text{Re}z}{a} = f''(1) \quad \text{Nu} = -2\theta'(1) \tag{2.10}$$

3. Differential Quadrature Method (DQM)

The differential quadrature method (DQM) is a rather efficient numerical method for rapid solution of linear and nonlinear partial differential equations (Bellman *et al.*, 1972). Compared with the conventional methods such as the finite element and finite difference methods, the DQM requires less computer time and storage.

In this study, a polynomial expansion based differential quadrature, as introduced by Quan and Chang (1989), is applied for solving the problem. Several attempts have been made by researchers to develop polynomial based differential quadrature methods. One of the most useful approaches is the one that uses the following Lagrange interpolation polynomials as test functions

$$g_k = \frac{M(x)}{(x - x_k)M^{(1)}(x_k)} \quad k = 1, 2, \dots, N \tag{3.1}$$

where

$$M(x) = (x - x_1)(x - x_2) \cdots (x - x_N) \quad M^{(1)}(x_i) = \prod_{\substack{k=1 \\ k \neq i}}^N (x_i - x_k) \tag{3.2}$$

By applying the above equation at N grid points, the following algebraic formulations to compute the weighting coefficients are developed

$$A_{ij}^{(1)} = \frac{1}{x_j - x_i} \prod_{\substack{k=1 \\ k \neq i,j}}^N \frac{x_i - x_k}{x_j - x_k} \quad i \neq j \tag{3.3}$$

$$A_{ij}^{(1)} = \sum_{\substack{k=1 \\ k \neq i}}^N \frac{1}{x_i - x_k} \quad A_{ij}^{(2)} = \sum_{k=1}^N A_{ik}^{(1)} A_{kj}^{(1)}$$

where $A^{(1)}$ and $A^{(2)}$ denote the weighting coefficients of the first and second order derivatives of the function $f(r)$ with respect to the r direction. N is the number of grid points chosen in the r direction. The differential quadrature approximation can be easily extended from the above formulation to other coordinates. The first order derivatives in the two-dimensional formulation are approximated by

$$\left. \frac{\partial f}{\partial r} \right|_{ij} \approx \sum_{l=1}^N A_{il}^{(1)} f_{lj} \quad \left. \frac{\partial f}{\partial z} \right|_{ij} \approx \sum_{m=1}^M B_{jm}^{(1)} f_{im} \tag{3.4}$$

And the second order derivatives can be approximated by:

$$\begin{aligned}
 \left. \frac{\partial f}{\partial r} \right|_{ij} &\approx \sum_{l=1}^N A_{il} f_{lj} & \left. \frac{\partial^2 f}{\partial r^2} \right|_{ij} &\approx \sum_{l=1}^N A_{il}^{(2)} f_{lj} \\
 \left. \frac{\partial f}{\partial z} \right|_{ij} &\approx \sum_{m=1}^P B_{jm} f_{im} & \left. \frac{\partial^2 f}{\partial z^2} \right|_{ij} &\approx \sum_{n=1}^P B_{kn}^{(2)} f_{ijn} \\
 \left. \frac{\partial^2 f}{\partial r \partial z} \right|_{ij} &\approx \sum_{l=1}^N A_{il}^{(1)} \sum_{m=1}^P B_{jm}^{(1)} f_{lm}
 \end{aligned} \tag{3.5}$$

where $A^{(1)}$ and $B^{(1)}$ denote the weighting coefficients of the first order derivatives; $A^{(2)}$ and $B^{(2)}$ denote the weighting coefficients of the second order derivatives of the function $f(r, z)$ with respect to the r and z -directions, respectively; N and P are the number of grid points chosen in the r and z -directions, respectively.

4. Results and discussion

Equations (2.5) along with their boundary conditions are solved numerically by using the DQM. After applying this method, the influence of several non-dimensional parameters, namely the Reynolds number Re , Prandtl number Pr , nanoparticles volume fraction φ and magnetic parameter M , have been investigated. Validating the numerical results obtained in this study, the case when the volume fraction coefficient is zero ($\varphi = 0$) has been considered and compared with the previously published results in Tables 2 and 3. These tables present numerical values of the skin friction coefficient in terms of $f''(1)$ and the Nusselt number Nu in terms of $-\theta'(1)$ along with the results reported by Ishak *et al.* (2008), which show an excellent agreement with the achieved results in the present study.

Table 2. Values of the skin friction coefficient for several values of M and Re at $Pr = 6.2$

M	$Re = 1$		$Re = 5$	
	Present work	Ishak <i>et al.</i> (2008)	Present work	Ishak <i>et al.</i> (2008)
0	-1.17849	-1.1780	-2.41745	-2.4174
0.01	-1.18431	-1.1839	-2.41990	-2.4199
0.05	-1.20708	-1.2068	-2.42965	-2.4296
0.10	-1.23454	-1.2344	-2.44174	-2.4417
0.50	-1.42693	-1.4269	-2.53523	-2.5352

Table 3. Values of the Nusselt number for several values of M and Re at $Pr = 6.2$

M	$Re = 1$		$Re = 5$	
	Present work	Ishak <i>et al.</i> (2008)	Present work	Ishak <i>et al.</i> (2008)
0	2.05857	2.0587	19.1185	19.1587
0.01	2.05715	2.0572	19.1184	19.1586
0.05	2.05158	2.0516	19.1179	19.1581
0.10	2.04487	2.0449	19.1174	19.1576
0.50	1.99806	1.9978	19.1129	19.1530

Figure 2 shows the effect of volume fraction coefficient φ on velocity distribution for $Re = 5$. It is noticed that the Prandtl number Pr gives no effect to the velocity as can be seen from

Eq. (2.5)₁. The velocity curves show that the rate of transport is considerably reduced with an increase of φ . In all cases, the velocity vanishes at some large distance from the surface of the tube.

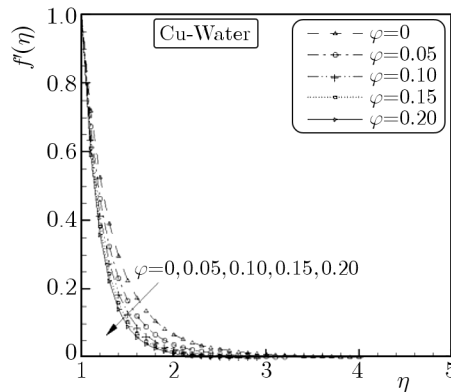


Fig. 2. Velocity profiles for various values of φ ($Re = 5, M = 5, Pr = 6.2$)

Figure 3 presents temperature profiles for various values of φ when $Pr = 6.2$ and $Re = 5$, and the nanoparticle is Copper. It is obvious that the temperature increases as φ increases, but it decreases as the distance from the surface increases, and finally vanishes at a some large distance from the surface. Consider that $\varphi = 0$ represents pure water like what is presented by Ishak *et al.* (2008). It is clear that the heat transfer in the present case is more than the case when the fluid is pure water.

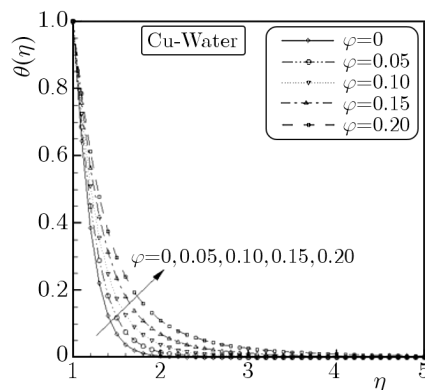


Fig. 3. Temperature profiles for various values of φ ($Re = 5, M = 5, Pr = 6.2$)

Figure 4a exhibits the skin friction coefficient profiles C_f for various values of the Reynolds number Re as M is constant. It is observed that the magnitude of the skin friction coefficient increases as Re increases. Figure 4b represents the skin friction coefficient profiles C_f for various values of M when the Reynolds number Re is constant. It can be seen that the magnitude of the skin friction coefficient grows as M increases.

Furthermore, it is clear from both Figs. 4a,b that the skin friction coefficient increases with an increase in the volume fraction coefficient. The same behavior can be observed for the Nusselt number, i.e. growing Re increases the temperature gradient and, in turn, increases the Nusselt number. And an increase in M decreases the Nusselt number, which is obvious from Figs. 5a,b. Also, it is clear that the Nusselt number increases with an increase in the volume friction coefficient.

After the velocity $f'(\eta)$ is obtained, the pressure p in terms of $(p - p_\infty)/(\rho cv)$ can be found by using Eq. (2.7). The numerical results are shown in Fig. 6a for $M = 2, \varphi = 0.1$ and $Re = 1, 5$

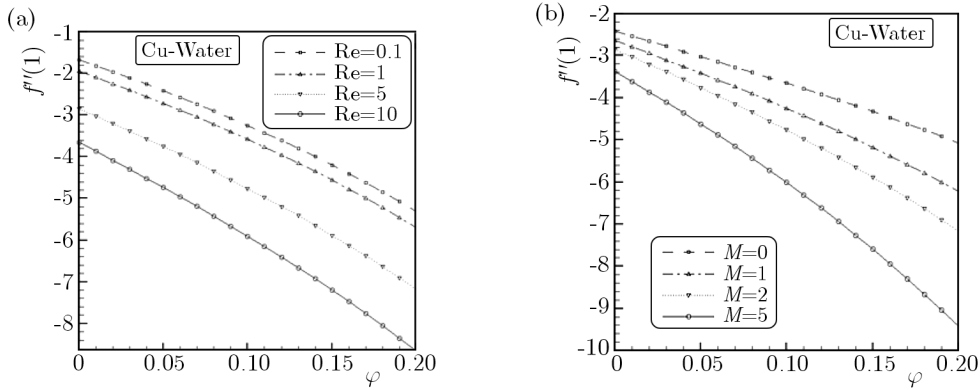


Fig. 4. Skin friction coefficient for various values of (a) Re and ϕ ($M = 2$, $Pr = 6.2$), (b) M and ϕ ($Re = 5$, $Pr = 6.2$)

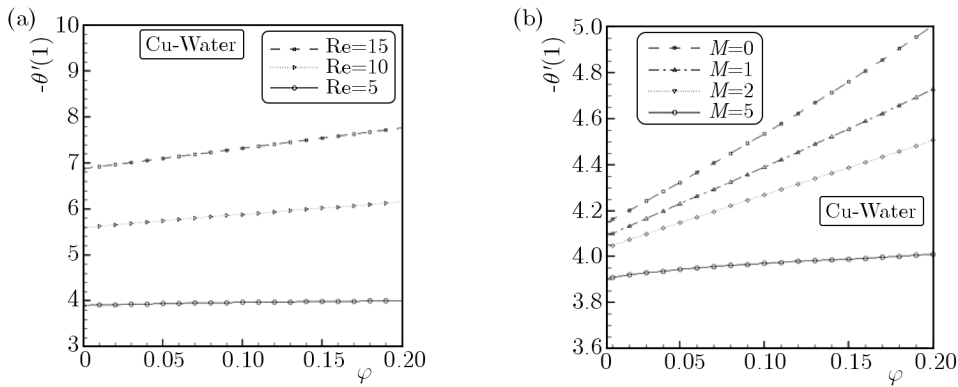


Fig. 5. Nusselt number for various values of (a) Re and ϕ ($M = 2$, $Pr = 6.2$), (b) M and ϕ ($Re = 5$, $Pr = 6.2$)

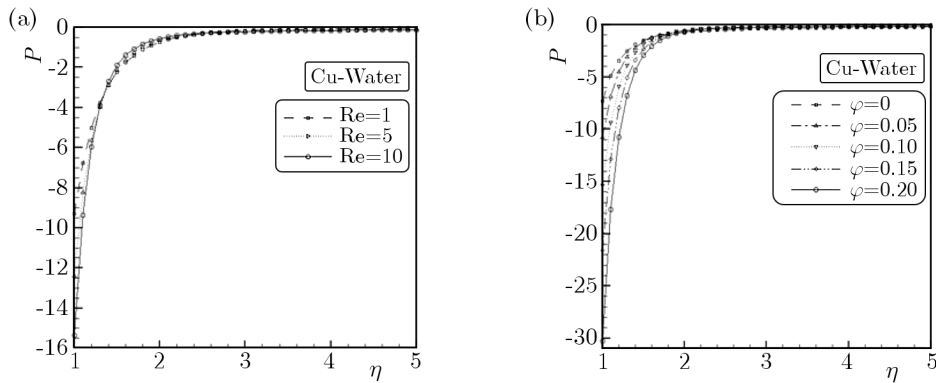


Fig. 6. Pressure distribution obtained from Eq. (2.7) for various values of (a) Re ($\phi = 0.1$, $M = 2$, $Pr = 6.2$), (b) ϕ ($Re = 10$, $M = 2$, $Pr = 6.2$)

and 10. All curves show that $p \rightarrow p_\infty$ far away from the surface $\eta \rightarrow \infty$. Further, Fig. 6b shows the pressure curve for different values of ϕ when $Re = 10$ and $M = 2$. It is clear from this figure that bigger values of ϕ result in slower algebraic decay. In other words, if $\phi = 0.2$, sufficient decay of $(p - p_\infty)$ takes place at higher values of η than the case when $\phi = 0$.

Figures 7a and 7b represent $f'(\eta)$ and $\theta(\eta)$ curves, respectively, for different types of nanoparticles, namely, Cu, Al_2O_3 and TiO_2 when $\phi = 0.1$, $M = 5$, $Pr = 6.2$, and $Re = 5$. The figure shows that by using different types of nanofluids, values of the velocity and temperature change, i.e. we can say that the shear stress and the rate of heat transfer change by using different

types of nanofluids. This means that the nanofluids will be important in the cooling and heating processes.

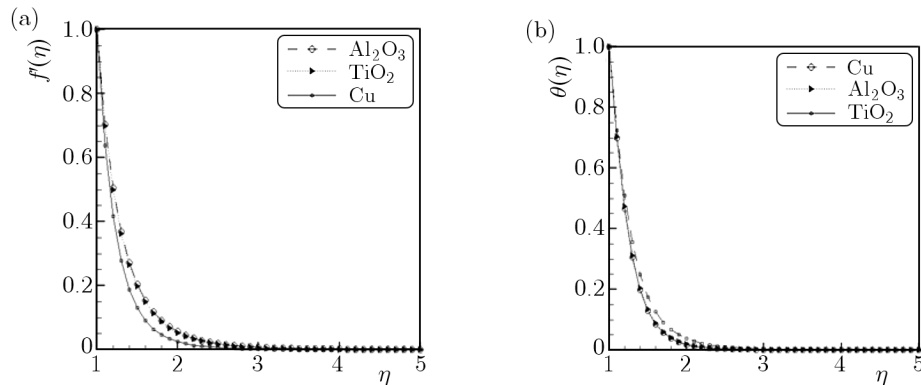


Fig. 7. (a) Velocity profiles and (b) temperature profiles for various values of nonparticles ($\varphi = 0.1$, $\text{Re} = 5$, $M = 5$, $\text{Pr} = 6.2$)

5. Conclusions

A steady two dimensional flow of an electrically conducting incompressible nanofluid due to stretching cylindrical tube is studied in the present work. Similarity solutions are obtained for a linearly stretching tube with a constant surface temperature, and the achieved ordinary differential equations are solved numerically by applying the Differential Quadrature Method (DQM). Effects of the volume fraction coefficient, magnetic parameter and Reynolds number on the flow and heat transfer characteristics have been examined. It can be concluded that the magnitude of the skin friction coefficient increases with the volume fraction coefficient, magnetic parameter and Reynolds number, while it is constant with the Prandtl number. The Nusselt number, also, increases with the volume fraction coefficient and Reynolds number but decreases with the magnetic parameter.

References

1. AMINOSADATI S.M., GHASEMI B., 2009, Natural convection cooling of a localised heat source at the bottom of a nanofluid-filled enclosure, *European Journal of Mechanics – B/Fluids*, **28**, 630-640
2. ATOUEI S.A., HOSSEINZADEH KH., HATAMI M., GHASEMI SEIYED E., SAHEBI S.A.R., GANJI D.D., 2015, Heat transfer study on convective-radiative semi-spherical fins with temperature-dependent properties and heat generation using efficient computational methods, *Applied Thermal Engineering*, **89**, 299-305
3. BELLMAN R.E., KASHEF B.G., CASTI J., 1972, Differential quadrature: A technique for the rapid solution of nonlinear partial differential equations, *Journal of Computational Physics*, **10**, 40-52
4. CHOI S.U.S., 1995, Enhancing thermal conductivity of fluids with nanoparticles, *ASME Fluids Engineering Division*, **231**, 99-105
5. DARZI M., VATANI M., GHASEMI S.E., GANJI D.D., 2015, Effect of thermal radiation on velocity and temperature fields of a thin liquid film over a stretching sheet in a porous medium, *European Physical Journal Plus*, **130**, 100
6. GHASEMI S.E., HATAMI M., GANJI D.D., 2013, Analytical thermal analysis of air-heating solar collectors, *Journal of Mechanical Science and Technology*, **27**, 11, 3525-3530

7. GHASEMI S.E., HATAMI M., GANJI D.D., 2014a, Thermal analysis of convective fin with temperature-dependent thermal conductivity and heat generation, *Case Studies in Thermal Engineering*, **4**, 1-8
8. GHASEMI S.E., HATAMI M., HATAMI J., SAHEBI S.A.R., GANJI D.D., 2016a, An efficient approach to study the pulsatile blood flow in femoral and coronary arteries by Differential Quadrature Method, *Physica A*, **443**, 406-414
9. GHASEMI S.E., HATAMI M., KALANI SAROKOLAIE A., GANJI D.D., 2015a, Study on blood flow containing nanoparticles through porous arteries in presence of magnetic field using analytical methods, *Physica E*, **70**, 146-156
10. GHASEMI S.E., HATAMI M., MEHDIZADEH AHANGAR GH.R., GANJI D.D., 2014b, Electrohydrodynamic flow analysis in a circular cylindrical conduit using Least Square Method, *Journal of Electrostatics*, **72**, 47-52
11. GHASEMI S.E., JALILI PALANDI S., HATAMI M., GANJI D.D., 2012, Efficient analytical approaches for motion of a spherical solid particle in plane couette fluid flow using nonlinear methods, *The Journal of Mathematics and Computer Science*, **5**, 2, 97-104
12. GHASEMI S.E., VALIPOUR P., HATAMI M., GANJI D.D., 2014c, Heat transfer study on solid and porous convective fins with temperature-dependent heat generation using efficient analytical method, *Journal of Central South University*, **21**, 4592-4598
13. GHASEMI S.E., VATANI M., GANJI D.D., 2015b, Efficient approaches of determining the motion of a spherical particle in a swirling fluid flow using weighted residual methods, *Particuology*, **23**, 68-74
14. GHASEMI S.E., VATANI M., HATAMI M., GANJI D.D., 2016b, Analytical and numerical investigation of nanoparticles effect on peristaltic fluid flow in drug delivery systems, *Journal of Molecular Liquids*, **215**, 88-97
15. GHASEMI S.E., ZOLFAGHARIAN A., GANJI D.D., 2014d, Study on motion of rigid rod on a circular surface using MHPM, *Propulsion and Power Research*, **3**, 3, 159-164
16. GHASEMI S.E., ZOLFAGHARIAN A., HATAMI M., GANJI D.D., 2015c, Analytical thermal study on nonlinear fundamental heat transfer cases using a novel computational technique, *Applied Thermal Engineering*, <http://dx.doi.org/10.1016/j.applthermaleng.2015.11.120>
17. HARADA N., TSUNODA K., 1998, Study of a disk MHD generator for nonequilibrium plasma generator (NPG) system, *Energy Conversion and Management*, **39**, 493-503
18. HATAMI M., GANJI D.D., 2014, Motion of a spherical particle in a fluid forced vortex by DQM and DTM, *Particuology*, **16**, 206-212
19. HATAMI M., GHASEMI S.E., SAHEBI S.A.R., MOSAYEBIDORCHEH S., GANJI D.D., HATAMI J., 2015d, Investigation of third-grade non-Newtonian blood flow in arteries under periodic body acceleration using multi-step differential transformation method, *Applied Mathematics and Mechanics*, **36**, 11, 1449-1458
20. HO C.J., CHEN M.W., LI Z.W., 2008, Numerical simulation of natural convection of nanofluid in a square enclosure: effects due to uncertainties of viscosity and thermal conductivity, *International Journal of Heat and Mass Transfer*, **51**, 4506-4516
21. ISHAK A., NAZAR R., POP I., 2006, Magnetohydrodynamic stagnation-point flow towards a stretching vertical sheet, *Magnetohydrodynamics*, **42**, 17-30
22. ISHAK A., NAZAR R., POP I., 2008, Magnetohydrodynamic (MHD) flow and heat transfer due to a stretching cylinder, *Energy Conversion and Management*, **49**, 3265-3269
23. MAGYARI E., KELLER B., 1999, Heat and mass transfer in the boundary layers on an exponentially stretching continuous surface, *Journal of Physics D: Applied Physics*, **32**, 577-585

24. MAHAPATRA T.R., GUPTA A.S., 2001, Magneto hydrodynamic stagnation-point flow towards a stretching sheet, *Acta Mechanica*, **152**, 191-196
25. MISAGH IMANI S., GOUDARZI A.M., GHASEMI S.E., KALANI A., MAHDINEJAD J., 2014, Analysis of the stent expansion in a stenosed artery using finite element method: Application to stent versus stent study, *Proceedings of the Institution of Mechanical Engineers, Part H: Journal of Engineering in Medicine*, **228**, 10, 996-1004
26. MOGHIMI M.A., TABAEI H., KIMIAEIFAR A., 2013, HAM and DQM solutions for slip flow over a flat plate in the presence of constant heat flux, *Mathematical and Computer Modelling*, **58**, 1704-1713
27. MOGHIMI M.A., TALEBIZADEH P., MEHRABIAN M.A., 2011, Heat generation/absorption effects on magneto hydrodynamic natural convection flow over a sphere in a non-Darcian porous medium, *Proceedings of the Institution of Mechanical Engineers, Part E: Journal of Process Mechanical Engineering*, **225**, 29-39
28. MOHAMMADIAN E., GHASEMI S.E., POORGASHTI H., HOSSEINI M. AND GANJI D.D., 2015, Thermal investigation of Cu-water nanofluid between two vertical planes, *Proceedings of the Institution of Mechanical Engineers, Part E: Journal of Process Mechanical Engineering*, **229**, 1, 36-43
29. OZTOP H.F., ABU-NADA E., 2008, Numerical study of natural convection in partially heated rectangular enclosures filled with nanofluids, *International Journal of Heat and Fluid Flow*, **29**, 1326-1336
30. QUAN J.R., CHANG C.T., 1989, New insights in solving distributed system equations by quadrature methods – I. Analysis, *Computers and Chemical Engineering*, **13**, 779-788
31. SHANG J.S., 2001, Recent research in magneto-aerodynamics, *Progress in Aerospace Sciences*, **37**, 1-20
32. SHU C., 2000, *Differential Quadrature and its Application in Engineering*, Springer
33. TALEBIZADEH P., MOGHIMI M.A., KIMIAEIFAR A., AMERI M., 2011, Numerical and analytical solution for natural convection flow with thermal radiation and mass transfer past a moving vertical porous plate by DQM and HAM, *International Journal of Computational Methods*, **8**, 611-631
34. VALIPOUR P., GHASEMI S.E., VATANI M., 2015, Theoretical investigation of micropolar fluid flow between two porous disks, *Journal of Central South University*, **22**, 2825-2832
35. VATANI M., GHASEMI S.E., GANJI D.D., 2014, Investigation of micropolar fluid flow between a porous disk and a nonporous disk using efficient computational technique, *Proceedings of the Institution of Mechanical Engineers, Part E: Journal of Process Mechanical Engineering*, DOI:10.1177/0954408914557375
36. WANG C.Y., 1988, Fluid flow due to a stretching cylinder, *Physics of Fluids*, **31**, 466-468
37. ZIABAKHSH Z., DOMAIRRY G., MOZAFFARI M., MAHBOBIFAR M., 2010, Analytical solution of heat transfer over an unsteady stretching permeable surface with prescribed wall temperature, *Journal of the Taiwan Institute of Chemical Engineers*, **41**, 169-177
38. ZIABAKHSH Z., DOMAIRRY G., 2009, Solution of the laminar viscous flow in a semi-porous channel in the presence of a uniform magnetic field by using the homotopy analysis method, *Communications in Nonlinear Science and Numerical Simulation*, **14**, 1284-1294
39. ZOLFAGHARIAN A., GHASEMI S.E., MISAGH I., 2014a, A multi-objective, active fuzzy force controller in control of flexible wiper system, *Latin American Journal of Solids and Structures*, **11**, 9, 1490-1514
40. ZOLFAGHARIAN A., NOSHADI A., GHASEMI S.E., MD. ZAIN M.Z., 2014b, A nonparametric approach using artificial intelligence in vibration and noise reduction of flexible systems, *Proceedings of the Institution of Mechanical Engineers, Part C, Journal of Mechanical Engineering Science*, **228**, 8, 1329-1347

41. ZOLFAGHARIAN A., NOSHADI A., KHOSRAVANI M.R., MD. ZAIN M.Z., 2014c, Unwanted noise and vibration control using finite element analysis and artificial intelligence in flexible wiper system, *Applied Mathematical Modelling*, **38**, 2435-2453
42. ZOLFAGHARIAN A., VALIPOUR P., GHASEMI S.E., 2015, Fuzzy force learning controller of flexible wiper system, *Neural Computing and Application*, **26**, 2, DOI: 10.1007/s00521-015-1869-0

Manuscript received October 25, 2014; accepted for print September 15, 2015

LONGITUDINAL SHEAR OF A BI-MATERIAL WITH FRICTIONAL SLIDING CONTACT IN THE INTERFACIAL CRACK

HEORHIY SULYM

Bialystok University of Technology, Bialystok, Poland; e-mail: h.sulym@pb.edu.pl

IAROSLAV PASTERNAK

Lutsk National Technical University, Lutsk, Ukraine; e-mail: pasternak@ukrpost.ua

LYUBOV PISKOZUB, YOSYF PISKOZUB

Ukrainian Academy of Printing, Pidgolosko, L'viv, Ukraine; e-mail: pisko Zub@pancha.lviv.ua

We construct an analytical solution to the anti-plane problem of an inhomogeneous bi-material medium with the interfacial crack considering sliding friction. The medium is exposed to an arbitrary normal and shear loading in the longitudinal direction. Using the jump function method, the problem is reduced to a solution to singular integral equations for the jumps of displacements and stresses in the areas with sliding friction. Explicit expressions for displacements, stress intensity factors and energy dissipation are obtained. Critical load values for determination of the onset of slippage are investigated. The effect of friction and loading parameters on the size of the slip zone, stress intensity factors and energy dissipation is numerically analyzed.

Keywords: friction, interfacial crack, stress intensity factor, longitudinal shear, jump functions

1. Introduction

Contact problems have received much attention in the literature as a result of their practical importance. The study of contact phenomena considering friction is one of the most pressing problems in engineering (Arhipenko and Kriviy, 2008; Goryacheva, 2001; Comninou, 1977; Ostryk and Ulitko, 2006; Sulym and Pisko Zub, 2004; Hills *et al.*, 1993; Johnson, 1985; Kalker, 1977) and others. To a greater or lesser extent, but contact phenomena are always accompanied by friction at both macroscopic and microscopic levels. Mechanical, electrical, thermal, chemical processes and vibration that can simultaneously occur due to friction significantly affect degradation of materials, duration of their wave processes, reliability and durability of structural elements, etc. The effect of friction can be both harmful and helpful, when causing dissipation of the accumulated strain energy in the body and thus reduce stress.

However, the problem of contact interaction between adjacent surfaces of a crack has not received sufficient attention. Major achievements in this area include the study of theory of cracks at the interface of two media assuming the elimination of physically incorrect oscillating features singularity by a widely used model of local contact directly near the vicinity of the crack end (Comninou, 1977; Comninou *et al.*, 1980; Comninou and Dundurs, 1980; Kundrat and Sulym, 2003; Cherepanov, 1966; Herrmann and Loboda, 1999; Kharun and Loboda, 2003). A wide class of problems on the effect of friction forces on the contact stresses between the half-planes was examined by Martynyak and Kryshatfovych (2000), Aravas and Sharma (1991), Weertman *et al.* (1983). Growth of cracks (in fact, the relative slip of materials) on the verge of a hard fibrous inclusion considering friction between the components was studied by Brussat and Westmann (1974).

This paper proposes a novel technique for obtaining the analytical solution of the anti-plane problem (longitudinal shear) for a bi-material with a closed interfacial crack accounting for friction between surfaces. Therefore, all characteristics of the stress-strain state, such as displacements, stresses, energy dissipation, slip zone size, etc., are exactly calculated. Note that the frictional slippage is essentially an incremental process and, therefore, the solution to the contact problem depends on the load history. We assume that the magnitude and direction of the external force factors that generate longitudinal shear change quasi-statically (so slowly that it is not necessary to consider the inertial member) by a certain law, which may be different. Thus, no incremental formulation is necessary for solving this problem because of quasi-statically way of the initial step loading.

2. Formulation of the problem

Consider an infinite isotropic matrix consisting of two half-spaces with elastic constants E_k, ν_k ($k = 1, 2$). The half-spaces are mutually pressed to the interface by external normal stresses $\sigma_{yy}(x) < 0$. Here, $Oxyz$ are the Cartesian coordinates and xOz is the contact plane of the half-spaces.

We study the stress-strain state (SSS) of the body section by the plane xOy perpendicular to the direction of its longitudinal shear. This section forms two half-planes S_k ($k = 1, 2$), and the interface between them corresponds to the x -axis L . Under the action of the applied loads, the cracks may slip at intervals forming the line $L' = \cup_{n=1}^N L'_n = \cup_{n=1}^N [b_n^-; b_n^+]$ as indicated in Fig. 1. The normal stress in the body is generated by uniform compression at infinity $\sigma_{yy}^\infty < 0$ and two balanced concentrated forces $P_k = \mp iP$ at the points $z_k \in S_k$. The same traditional notation for the axis z and a complex variable $z = x + iy$ should not cause misunderstanding in the solution of the problem.

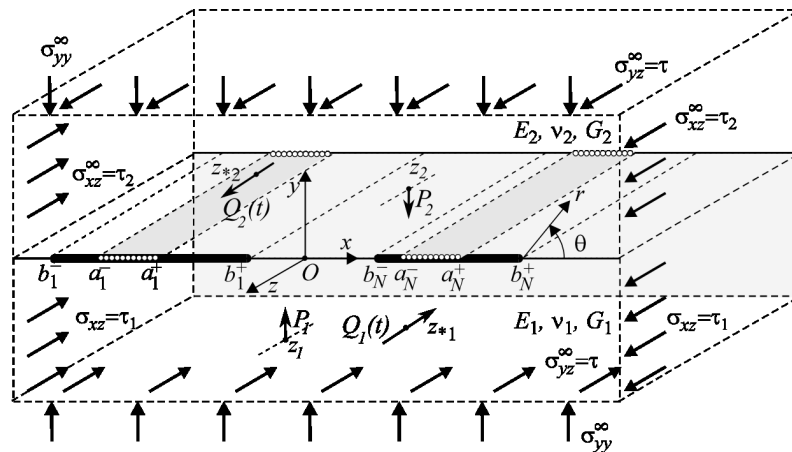


Fig. 1. Geometry and loading scheme of the problem

Suppose that the external loading increases or decreases monotonically and consists of a uniformly distributed at the infinity shear stress $\sigma_{yz}^\infty = \tau(t)$, $\sigma_{xz}^\infty = \tau_k(t)$, concentrated forces with magnitude $Q_k(t)$, screw dislocations with Burger's vector $b_k(t)$ at the points $z_{*k} \in S_k$ ($k = 1, 2$), t denotes the time as parameter. Note that the positive direction of the forces and Burgers vectors is chosen along the axis as opposed to implicitly accepted in some studies the opposite direction. According to Eq. (20.5) (Sulym, 2007), stresses at infinity must always satisfy the conditions $\tau_2(t)G_1 = \tau_1(t)G_2$, which provides straightness of the matrix interface at infinity.

Contact between the half-spaces is assumed mechanically perfect omitting L' where it is more complicated. The contact in L' we assume mechanically perfect until the moment when

relative sliding of the crack surfaces may start in some areas $\gamma_n \subset L'_n$ (Johnson, 1985; Pasternak *et al.*, 2010; Piskozub, 2014; Piskozub *et al.*, 2014).

Thus, we formulate the problem of longitudinal shear with possible slip in the interfacial cracks under the action of an inhomogeneous distribution of compressive normal stresses and frictional forces on the surfaces of contact (line section L). These forces may cause in these apriority unknown slip zones heat emission, energy dissipation, wear, etc.

3. The problem solution

The presence of such slip zones in the cracks can be simulated by jumps of traction and displacement vectors at L'_n (Piskozub, 2014; Piskozub *et al.*, 2014; Sulym, 2007; Sulym and Piskozub, 2004; Piskozub and Sulim, 2008)

$$[[\Xi]] \equiv \Xi^- - \Xi^+ = \mathbf{f}^n(x, t) \quad x \in L'_n \tag{3.1}$$

where $\Xi(z, t) = [\sigma_{yz}, \partial t / \partial x](z, t)$ is the state vector; $\mathbf{f}^n(x, t) = [f_3^n, f_6^n](x, t)$ is the jump vector. Hereinafter, the following notation is used: $[[\varphi]]_L = \varphi(x, -0) - \varphi(x, +0)$, $\langle \varphi \rangle_L = \varphi(x, -0) + \varphi(x, +0)$; symbols “+” and “-” correspond to the threshold function on the top and bottom edges of the line L .

Based on Hooke’s law, expression (3.1) results in

$$\begin{aligned} [[\sigma_{yz}]]_{L'_n} &\equiv \sigma_{yz}^- - \sigma_{yz}^+ = f_3^n(x, t) \\ \left[\frac{\partial w}{\partial x} \right]_{L'_n} &\equiv \frac{\partial w^-}{\partial x} - \frac{\partial w^+}{\partial x} = \left[\frac{\sigma_{xz}}{G} \right]_{L'_n} \equiv \frac{\sigma_{xz}^-}{G_1} - \frac{\sigma_{xz}^+}{G_2} = f_6^n(x, t) \quad x \in \gamma_n \subset L'_n \\ f_3^n(x, t) &= f_6^n(x, t) = 0 \quad \text{if } x \notin \gamma_n \end{aligned} \tag{3.2}$$

The boundary conditions at L'_n provide that the slipping starts at some zones $\gamma_n = [a_n^-; a_n^+] \subset L'_n$ when reaching the tangent stress σ_{yz} of a certain critical value τ_{yz}^{max} , moreover, this threshold shear stress σ_{yz} can not exceed τ_{yz}^{max} . Confining with classic Amonton’s law of friction (Goryacheva, 2001; Hills *et al.*, 1993; Johnson, 1985), consider the contact problem which states that everywhere in γ_n , the shear stresses (friction force) are equal

$$\begin{aligned} \sigma_{yz}^\pm(x) &= -\text{sgn}[[w]]\tau_{yz}^{max}(x) \quad \tau_{yz}^{max}(x) = -\alpha\sigma_{yy}(x) \\ \sigma_{yy} &< 0 \quad |w^- - w^+| \neq 0 \end{aligned} \tag{3.3}$$

where α denotes the coefficient of sliding friction. Outside the domains γ_n , there is no slippage, and the magnitude of shear stresses does not exceed the maximum allowable level

$$|\sigma_{yz}(x)| \leq \tau_{yz}^{max}(x) \tag{3.4}$$

The sign (direction of action) of shear stresses is chosen depending on the sign of the difference in the mutual displacement $[[w]]$ at the source point of L'_n .

The general case of normal pressing gives

$$\tau_{yz}^{max}(x) = 4\alpha \left(-\frac{\sigma_{yy}^\infty}{4} + \sum_{k=1}^2 E_j \eta_k \text{Re} \frac{N_k}{x - z_k} \right) \quad j = 3 - k \tag{3.5}$$

where

$$\begin{aligned} N_k &= \frac{P_k}{e_{jk}} - \frac{\kappa_k \bar{P}_k - P_k}{e_{kj}} & \kappa_k &= 4 - 3\nu_k \\ \eta_k &= \frac{1}{8\pi(1 - \nu_k)} & e_{kj} &= 2 \frac{G_k + \kappa_k G_j}{(1 - \nu_1)(1 - \nu_2)} \end{aligned}$$

Amonton’s law of friction in classical form (3.3) provides, of course, simplification of the boundary conditions for the basic problem, but making use of more complex models of friction (Johnson, 1985; Sulym and Piskozub, 2004; Comninou *et al.*, 1980), taking into account the wear, does not essentially complicate the process of solving

$$\begin{aligned}
 \sigma_{yz}^\pm(x, t) &= \mp p_k f_3^n(x, t) - C g_6^n(x, t) + \sigma_{yz}^{0\pm}(x, t) \\
 \sigma_{xz}^\pm(x, t) &= \mp C f_6^n(x, t) + p_k g_3^n(x, t) + \sigma_{xz}^{0\pm}(x, t) \\
 g_r^n(z, t) &\equiv \frac{1}{\pi} \int_{L'_n} \frac{f_r^n(x, t)}{x - z} dx \quad p_k = \frac{G_k}{G_1 + G_2} \quad C = G_{3-k} p_k \\
 \sigma_{yz}(z, t) + i\sigma_{xz}(z, t) &= \sigma_{yz}^0(z, t) + i\sigma_{xz}^0(z, t) + ip_k g_3^n(z, t) - C g_6^n(z, t)
 \end{aligned} \tag{3.6}$$

where $z \in S_k$, $r = 3, 6$, $k = 1, 2$.

The superscript “+” refers to $k = 2$; “-” – $k = 1$. The superscript “0” denotes the corresponding values in the solid body model without heterogeneity (cracks) under the same external loading (homogeneous solution). Hereinafter, the following notations (Piskozub *et al.*, 2014; Sulym, 2007; Piskozub and Sulim, 2008) are used

$$\begin{aligned}
 \sigma_{yz}^0(z, t) + i\sigma_{xz}^0(z, t) &= \tau(t) + i[\tau_k(t) + D_k(z, t) + (p_k - p_j)\overline{D}_k(z, t) + 2p_k D_j(z, t)] \\
 D_k(z, t) &= -\frac{Q_k(t) + iG_k b_k(t)}{2\pi(z - z_{*k})} \quad z \in S_k \quad k = 1, 2 \quad j = 3 - k
 \end{aligned} \tag{3.7}$$

Using (3.6), (3.7) and boundary conditions (3.2), (3.3) at the domains γ_n , the problem reduces to a system of $2N$ singular integral equations

$$\begin{aligned}
 f_3^n(x, t) &= 0 \\
 g_6^n(x, t) &= \frac{1}{2C} \left(\langle \sigma_{yz}^0(x, t) \rangle + 2 \operatorname{sgn} [w] \tau_{yz}^{max}(x) \right)
 \end{aligned} \tag{3.8}$$

whose solution is known (Sulym, 2007).

For a more detailed analysis of the problem solution, consider the partial case of the presence of a single ($N = 1$) crack $L'_1 = [-b; b]$ with a symmetric zone of slippage $\gamma_1 = [-a; a]$ ($a \leq b$) that can occur when symmetric load acts about the vertical axis.

The solution to (3.8) in this case, after calculating the corresponding integrals, have the exact form

$$\begin{aligned}
 f_6(x, t) &= \frac{1}{\pi C \sqrt{a^2 - x^2}} \left\{ \pi [\tau(t) - \alpha \operatorname{sgn} [w] \sigma_{yy}^\infty] x \right. \\
 &\quad \left. + \sum_{k=1}^2 p_j \operatorname{Im} \left[[Q_k(t) + iG_k b_k(t)] \left(\frac{\sqrt{z_{*k}^2 - a^2} x - z_{*k}}{+} 1 \right) \right] \right\} \\
 &\quad + \frac{4\alpha \operatorname{sgn} [w]}{C \sqrt{a^2 - x^2}} \sum_{k=1}^2 E_j \eta_k \operatorname{Re} \left[N_k \left(\frac{\sqrt{z_k^2 - a^2}}{x - z_k} + 1 \right) \right] \quad j = 3 - k \quad x \in [-a; a]
 \end{aligned} \tag{3.9}$$

Here the function $\sqrt{z^2 - a^2}$ is the branch which satisfies the condition $\sqrt{z^2 - a^2}/z \rightarrow 1$ $z \rightarrow \infty$. Similar arguments are used to select the branches $\sqrt{z_{*k}^2 - a^2}$ and $\sqrt{\overline{z_{*k}^2} - a^2}$, $k = 1, 2$.

Thus, the expression for the jump displacement $[[w]]$ is obtained by integration of Eq. (3.9)

$$\begin{aligned}
 [[w]](x, t) &= \int_{-a}^x f_{6(1)}(x, t) dx = -\frac{\tau(t) - \alpha \operatorname{sgn} [[w]] \sigma_{yy}^\infty}{C} \sqrt{a^2 - x^2} \\
 &+ \sum_{k=1}^2 \frac{p_j}{\pi C} \operatorname{Im}\{[Q_k(t) + iG_k b_k(t)]I_2(x, a, z_{*k})\} \\
 &+ \frac{4\alpha \operatorname{sgn} [[w]]}{C} \sum_{k=1}^2 E_j \eta_k \operatorname{Re}[N_k I_2(x, a, z_k)] \quad j = 3 - k \quad |x| \leq a
 \end{aligned} \tag{3.10}$$

and

$$\begin{aligned}
 I_2(x, a, z) &= \frac{\pi}{2} + \arcsin \frac{x}{a} + I(x, a, z) \\
 I(x, a, z) &\equiv \sqrt{z^2 - a^2} \int_{-a}^x \frac{dx}{\sqrt{a^2 - x^2}(x - z)} = i \operatorname{sgn}(\operatorname{Im}z) \ln \frac{a(z - x)}{a^2 - xz - i\sqrt{a^2 - x^2}\sqrt{z^2 - a^2}}
 \end{aligned} \tag{3.11}$$

Introducing mode 3 stress intensity factor (SIF) by expression $K_3 = \lim_{r \rightarrow 0(\theta=0)} \sqrt{\pi r}(\sigma_{yz})$, it is easy to obtain the analytical form for SIF in the case of the crack slip zone $[-a; a] \subset L'$

$$\begin{aligned}
 K_3^\pm(t) &= \frac{1}{2\sqrt{\pi a}} \int_{-a}^a \sqrt{\frac{a \pm x}{a \mp x}} [\langle \sigma_{yz}^0(x, t) \rangle + 2 \operatorname{sgn} [[w]] \tau_{yz}^{max}(x)] dx = \sqrt{\pi a} [\tau(t) - \alpha \operatorname{sgn} [[w]] \sigma_{yy}^\infty] \\
 &+ \frac{1}{\sqrt{\pi a}} \sum_{k=1}^2 p_j \operatorname{Im} \left[[Q_k(t) + i b_k(t) G_k] \left(\frac{\sqrt{z_{*k}^2 - a^2}}{a \mp z_{*k}} \pm 1 \right) \right] \\
 &+ 4\alpha \operatorname{sgn} [[w]] \sqrt{\frac{\pi}{a}} \sum_{k=1}^2 E_j \eta_k \operatorname{Re} \left[N_k \left(\frac{\sqrt{z_k^2 - a^2}}{a \mp z_k} \pm 1 \right) \right] \quad j = 3 - k
 \end{aligned} \tag{3.12}$$

Now it is time to discuss the question about the apriority unknown size of the slip zone a . While increasing the magnitude of shear load from zero to maximum, there are three phases that are fundamentally different in view of slipping:

- 1) The combination of compressive and increasing shear load always fulfills condition (3.4). There is no slippage at all, and the cracks have no effect on SSS of the matrix.
- 2) The magnitude of shear load at the time point t^* becomes sufficient for the occurrence of conditions (3.3) at least in a limited area $\gamma_1 = [-a; a]$ ($a \leq b$). The magnitude of the load when the slippage first appears, will be called the first critical. To determine this critical value and the current size of the slip zone, one can put SIF (3.12) equal to zero (Cherepanov, 1966; Piskozub, 2014; Piskozub *et al.*, 2014).
- 3) The magnitude of shear load at the time t^{**} makes the size of the slip zone coincide with the crack size $a = b$. Further growth will not lead to an increase in the slip zone, but singular stress occurs in the crack tip and, therefore, non-zero SIF exists. The magnitude of the load, when the size of the slip zone coincides with the crack size for the first time, will be called the second critical.

It is also possible that such a combination of the shear and compressing loading make conditions (3.3) arise instantly along the whole L' or along the L' , except for the area γ_1 . This shear load value will be called the threshold value.

The analytical form of solution for all SSS components allows obtaining an analytical expression for the work of friction forces at the slip zone γ_1 for arbitrary loading

$$\begin{aligned}
 W^d(t) = & - \int_{-a}^a |\tau_{yz}^{max}(x)[w](x, t)| dx = -\frac{4\alpha}{C} \int_{-a}^a \left| \left(-\frac{\sigma_{yy}^\infty}{4} + \sum_{k=1}^2 E_j \eta_k \operatorname{Re} \frac{N_k}{x - z_k} \right) \right. \\
 & \cdot \left(-[\tau(t) - \alpha \operatorname{sgn} [w] \sigma_{yy}^\infty] \sqrt{a^2 - x^2} + \sum_{k=1}^2 \frac{p_j}{\pi} \operatorname{Im} \{ [Q_k(t) + iG_k b_k(t)] I_2(x, a, z_{*k}) \} \right. \\
 & \left. \left. + 4\alpha \operatorname{sgn} [w] \sum_{k=1}^2 E_j \eta_k \operatorname{Re} [N_k I_2(x, a, z_k)] \right) \right| dx \quad j = 3 - k \quad (3.13)
 \end{aligned}$$

Suppose that the loading of the matrix is symmetric about the vertical axis: the focus points of the applied concentrated force are $z_k = \pm ih \in S_k$ and $z_{*k} = \pm id$ ($k = 2, 1$). Thus, simplifying expressions (3.5), (3.9) and (3.10), one can write expressions for the most important components of SSS

$$\begin{aligned}
 [w](x, t) = & -\frac{\tau(t) - \alpha \operatorname{sgn} [w] \sigma_{yy}^\infty}{C} \sqrt{a^2 - x^2} \\
 & + \sum_{k=1}^2 \frac{p_{3-k}}{2\pi C} \left[(-1)^k Q_k(t) \ln \frac{\sqrt{a^2 + d^2} - \sqrt{a^2 - x^2}}{\sqrt{a^2 + d^2} + \sqrt{a^2 - x^2}} + G_k b_k(t) \left(\frac{\pi}{2} + \arcsin \frac{x}{a} \right) \right] \\
 & + \frac{2\alpha \operatorname{sgn} [w]}{C} P\gamma^+ \ln \frac{\sqrt{a^2 + h^2} - \sqrt{a^2 - x^2}}{\sqrt{a^2 + h^2} + \sqrt{a^2 - x^2}} \quad |x| \leq a \\
 K_3^\pm(t) = & \sqrt{\pi a} [\tau(t) - \alpha \operatorname{sgn} [w] \sigma_{yy}^\infty] \\
 & + \frac{1}{\sqrt{\pi a}} \sum_{k=1}^2 p_{3-k} \left(\frac{(-1)^k Q_k(t) a}{\sqrt{a^2 + d^2}} \pm G_k b_k(t) \frac{\sqrt{a^2 + d^2} - d}{\sqrt{a^2 + d^2}} \right) + \sqrt{\pi a} \frac{4\alpha \operatorname{sgn} [w] P\gamma^+}{\sqrt{a^2 + h^2}} \quad (3.14)
 \end{aligned}$$

$$\begin{aligned}
 W^d(t) = & -\frac{\alpha}{C} \left| 4\pi [\tau(t) - \alpha \operatorname{sgn} [w] \sigma_{yy}^\infty] \left[\frac{a^2 \sigma_{yy}^\infty}{8} - P\gamma^+ (\sqrt{h^2 + a^2} - h) \right] \right. \\
 & + \sigma_{yy}^\infty (\sqrt{d^2 + a^2} - d) \sum_{k=1}^2 (-1)^k p_{3-k} Q_k(t) \\
 & - 2P\gamma^+ \ln \frac{\sqrt{h^2 + a^2} \sqrt{d^2 + a^2} + hd + a^2}{\sqrt{h^2 + a^2} \sqrt{d^2 + a^2} + hd - a^2} \sum_{k=1}^2 (-1)^k p_{3-k} Q_k(t) \\
 & \left. - 8\alpha\pi \operatorname{sgn} [w] P^2 \gamma^{+2} \ln \frac{h^2 + a^2}{h^2} + 4\sigma_{yy}^\infty \alpha\pi \operatorname{sgn} [w] P\gamma^+ (\sqrt{h^2 + a^2} - h) \right|
 \end{aligned}$$

Substituting $P_k = P = 0$ in expressions (3.14), we obtain the known special case of the half-spaces compressed only by a uniform load $\sigma_{yy}^\infty < 0$ at infinity (Piskozub, 2014; Piskozub *et al.*, 2014). More interesting is the special case of normal pressing by the concentrated forces $P_k = \mp iP$ only. Below we analyze expressions (3.14) for various special cases of shear loading. Hereinafter, τ^* , Q_k^* denotes the first critical load values; τ^{**} , Q_k^{**} – the second critical load values, τ^{***} , Q_k^{***} – threshold load values.

1) Suppose that there are only tangential shear stresses at infinity $\tau(t) > 0$. Given that with an increasing load $\operatorname{sgn} [w] = -1$, we get

$$K_3(t) = \sqrt{\pi a} [\tau(t) - \alpha \operatorname{sgn} [w] \sigma_{yy}^\infty] + \sqrt{\pi a} \frac{4\alpha \operatorname{sgn} [w] P\gamma^+}{\sqrt{a^2 + h^2}} \quad (3.15)$$

From expression (3.15), we obtain the condition for the start of slipping

$$\sqrt{\pi a} [\tau(t) + \alpha \sigma_{yy}^\infty] - \sqrt{\pi a} \frac{4\alpha P\gamma^+}{\sqrt{a^2 + h^2}} = 0 \quad (3.16)$$

Thus, the first critical value τ^* and size of the slip zone a become

$$\tau^* = \alpha \left(\frac{4P\gamma^+}{h} - \sigma_{yy}^\infty \right) \quad a(t) = \sqrt{\frac{16\alpha^2 P^2 \gamma^{+2}}{[\tau(t) + \alpha\sigma_{yy}^\infty]^2} - h^2} \quad (3.17)$$

Substituting $a = b$ in (3.17) gives us the second critical value and the condition of non-zero SIF nascence

$$\tau^{**} = \alpha \left(\frac{4P\gamma^+}{\sqrt{b^2 + h^2}} - \sigma_{yy}^\infty \right) \quad (3.18)$$

Analysis of Eqs. (3.17) and (3.18) shows however that $\tau^* > \tau(t) > \tau^{**}$, which is devoid of physical meaning. This fact is easily explained since in this case of loading $\tau_{yz}^{max}(x)$ achieves its own maximum at the point $x = 0 \in L'_1$ and, therefore, the uniform growth of magnitude $\tau(t)$ will exceed the value $\tau_{yz}^{max}(0)$ at the last time point having generated the pre-slippage at the remotest location. This case of loading leads to the following conclusion: geometry of the problem must be changed by introducing into consideration two slip zones.

2) There is only one concentrated force $Q_2(t)$ growing from zero to Q_{max} and acting at the point $z_{*2} = id$ in the upper half-space. And given the fact that with the increasing load, $\text{sgn}[[w]] = -1$ using (3.14)_{1,2}, we obtain

$$\begin{aligned} [[w]](x, t) = & -\frac{\alpha\sigma_{yy}^\infty}{C} \sqrt{a^2 - x^2} + \frac{p_1 Q_2(t)}{\pi C} \ln \frac{\sqrt{a^2 + d^2} - \sqrt{a^2 - x^2}}{\sqrt{a^2 + d^2} + \sqrt{a^2 - x^2}} \\ & - \frac{\alpha P \gamma^+}{2\pi C} \ln \frac{\sqrt{a^2 + h^2} - \sqrt{a^2 - x^2}}{\sqrt{a^2 + h^2} + \sqrt{a^2 - x^2}} \quad |x| \leq a \end{aligned} \quad (3.19)$$

and

$$K_3(t) = \sqrt{\pi a} \alpha \sigma_{yy}^\infty + \sqrt{\frac{a}{\pi}} \frac{p_1 Q_2(t)}{\sqrt{a^2 + d^2}} - \sqrt{\pi a} \frac{4\alpha P \gamma^+}{\sqrt{a^2 + h^2}} \quad (3.20)$$

By equating SIF (3.20) to zero, we obtain the first critical value

$$Q_2^* = \frac{\pi \alpha d}{p_1} \left(\frac{4\gamma^+ P}{h} - \sigma_{yy}^\infty \right) \quad (3.21)$$

and the condition when slippage appears at the first time. The slip zone size is determined from the equation

$$\alpha \sigma_{yy}^\infty + \frac{p_1 Q_2(t)}{\pi \sqrt{a^2 + d^2}} - \frac{4\alpha P \gamma^+}{\sqrt{a^2 + h^2}} = 0 \quad (3.22)$$

Without the component σ_{yy}^∞ , one can obtain the exact solution

$$a(t) = \sqrt{\frac{h^2 d^2 [Q_2(t)^2 - Q_2^{*2}]}{h^2 Q_2^{*2} - d^2 Q_2(t)^2}} \quad (3.23)$$

It is clear that there is no slippage when $Q_{max(1)} < Q_2^*$. Substituting $a = b$ in Eq (3.22) gives us the second critical value and the condition of non-zero SIF nascence

$$Q_2^{**} = \frac{\pi \alpha \sqrt{d^2 + b^2}}{p_1} \left(\frac{4\gamma^+ P}{\sqrt{h^2 + b^2}} - \sigma_{yy}^\infty \right) \quad (3.24)$$

or when the component σ_{yy}^∞ is absent

$$Q_2^{**} = \frac{4\pi \alpha \gamma^+ P}{p_1} \frac{\sqrt{d^2 + b^2}}{\sqrt{h^2 + b^2}} = Q_2^* \frac{h \sqrt{d^2 + b^2}}{d \sqrt{h^2 + b^2}} \quad (3.25)$$

So, taking $Q_{max} \geq Q_2^{**}$ in general, we get the following scenario of changing the SSS:

- when $Q_2^* \leq Q_2(t) \leq Q_2^{**}$, the jump of displacements $[[w]](x, t)$ and the slip zone size $a(t)$ are defined from Eqs. (3.19), (3.23), thus expression (3.14)₃ for calculating the energy dissipation takes form

$$\begin{aligned} W^d(t) = & -\frac{\alpha}{C} \left| 4\pi\alpha\sigma_{yy}^\infty \left(\frac{a^2\sigma_{yy}^\infty}{8} - P\gamma^+(\sqrt{h^2 + a^2} - h) \right) \right. \\ & + \sigma_{yy}^\infty(\sqrt{d^2 + a^2} - d)p_1Q_2(t) - 2P\gamma^+p_1Q_2(t) \ln \frac{(h+d)[4\pi\alpha\gamma^+P - p_1Q_2(t)]}{(h-d)[4\pi\alpha\gamma^+P + p_1Q_2(t)]} \\ & \left. + 8\alpha\pi P^2\gamma^{+2} \ln \frac{16\pi^2\alpha^2\gamma^{+2}P^2(h^2 - d^2)}{h^2[16\pi^2\alpha^2\gamma^{+2}P^2 - p_1^2Q_2^2(t)]} - 4\sigma_{yy}^\infty\alpha\pi P\gamma^+(\sqrt{h^2 + a^2} - h) \right| \end{aligned} \quad (3.26)$$

- when $Q_2^{**} \leq Q_2(t) \leq Q_{max}$, the size $a(t)$ in formulas (3.19), (3.20) and (3.26) should be replaced by b instead of (3.23), then we have $a = b$ and (3.20) defines a non-zero SIF.

To determine the threshold load, it is enough to direct $a \rightarrow \infty$ in formula (3.25)

$$Q_2^{***} = \frac{4\pi\alpha\gamma^+P}{p_1} \quad (3.27)$$

For a more detailed analytical analysis, we suppose that the component σ_{yy}^∞ is absent. Having found that for the considered problem statement which provides a single sliding zone $\gamma_1 = [-a; a]$ ($a \leq b$), the condition $h > d$ must consider the increasing load magnitude $Q_2(t) \geq Q_2^*$. Thus, noting the correlation $1 \leq (h\sqrt{d^2 + b^2})/(d\sqrt{h^2 + b^2}) \leq h/d$, one can conclude that the size of the slip zone will coincide with the crack size before the time when the ratio $Q_2(t)/Q_2^*$ reaches the value h/d . Taking the value $h = d$, we obtain the threshold case of the third phase: $Q_2^* = Q_2^{**} = Q_2^{***}$. The choice of parameter values $h < d$ requires changing the geometry of the considered problem to the case with the arising slip zone along the L' , except for the area $\gamma_1 = [-a; a]$ ($a \leq b$).

Similar reasoning for such cases of shear loading as that for the concentrated force acting at the point $z_{*1} = -id$ in lower half-space, a pair of mutually opposite or collinear balanced concentrated forces acting in different semi-spaces and simultaneously increasing from zero to Q_{max} etc., provides similar to Eq (3.19)-(3.27) expressions for the components of SSS.

When the materials of the half-spaces are identical ($G_1 = G_2 = G$), it is enough to assume in the above formulas $C = G/2$, $p_1 = p_2 = 1/2$. For smooth contact between the half-spaces one should put $\alpha = 0$ in the above formulas. This immediately gives an instant increase of the slip size to the whole area L' for any asymmetric shear loading.

Note that the superposition of the obtained above solutions for different kinds of loading can not be used because of nonlinearity of the problem.

4. Numerical analysis

Using the above-mentioned approach, we determine the dependence of the slip zone size, shape of the displacement jump, energy dissipation and SIF on the basic parameters of SSS (distance and magnitude of the applied force, friction coefficient, ratio of elastic properties) in the most illustrative example of loading No. 2. To apply formulas (3.20)-(3.27), we introduce dimensionless values: size of the slip zone a/b , the coordinate and distance from the crack of the points of application of the shear and pressing forces respectively x/b , d/b , h/b ; $Q_2(t)/Q_2^{***}$ and $Q_2(t)/Q_2^*$ – the absolute and relative intensity of shear magnitude; $[[w]](x)C/(2\alpha\gamma^+P)$, $W^d(t)C/(8\pi\gamma^{+2}P^2)$ and $K_3\sqrt{b}/(4\sqrt{\pi}\alpha\gamma^+P)$ – the displacement jump, energy dissipation and SIF, respectively.

The dependence of size a/b on the relative magnitude of the applied force $Q_2(t)/Q_2^{***}$ is shown in Fig. 2a for different values d/b , h/b . It is noticeable that the growth rate of the size increases when d/b approaches h/b . Growing distance from the crack position of the coordinate h/b also leads to an increase in the rate of growth a/b .

Note that while $Q_2(t)/Q_2^* \leq 1$, there is no slippage. The slippage area increases monotonically and simultaneously with an increase in the load.

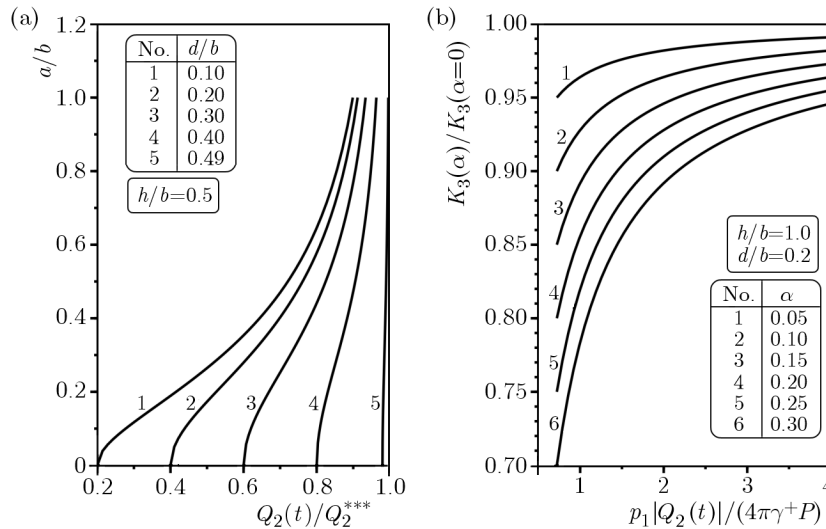


Fig. 2. (a) Dependence of the slip zone size on the coordinates of points of application of concentrated forces; (b) influence of friction in the slip zone on SIF

When the loading force magnitude exceeds the second critical value (phase 3), then non-zero SIF in the vicinity of the crack tip appears. The calculated SIF is compared with the known SIF for an interfacial crack in the absence of friction, and it is shown in Fig. 2b. The presence of friction allows significant reduction of SIF (decline by 30%).

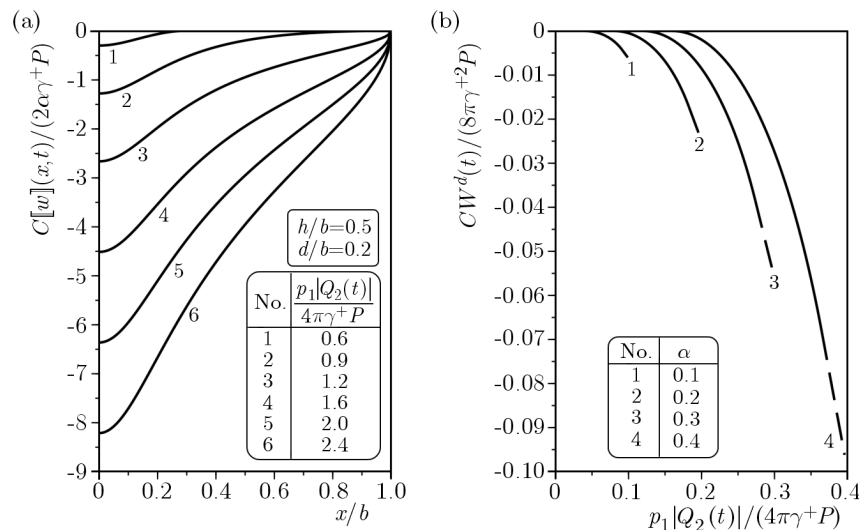


Fig. 3. (a) Shape of the displacement jump depending on the shear magnitude; (b) changes of the energy dissipation vs. load and coefficient of friction

Figure 3a depicts the influence of different settings on the shape of the displacement jump. It is noticeable that the highest sensitivity to the changing of the shape of the displacement jump is observed when placing the shear force application point closer to the crack. Approaching the

points of application of normal forces lessens the effect on the shape of the displacement jump, but significantly changes its amplitude.

Figure 3b indicates the energy dissipation during the second phase of loading by solid lines and by the dotted line – energy dissipation during the third phase of shear loading after reaching the maximum size of the slip zone. One observes the tendency of increasing the dissipation of energy when the coefficient of friction grows, or when approaching the point of force application to the crack position, or when the points of application of clamping forces are withdrawn.

5. Conclusions

We build an effective solution to the problem of a bi-material with a closed interfacial crack where sliding friction is possible. Different ways of loading of the solid body by arbitrary normal compression and monotonically increasing loading in the longitudinal direction is taken into account. This solution allows obtaining explicit expressions for displacements, stress intensity factors and energy dissipation. The dependence of the contact zone size on the loading parameters at different stages is analyzed. The critical load values for determination of the onset of slipping are investigated. Upon reaching the second critical value of the load when the slip zone size matches the size of the crack, the singular stresses in the vicinity of the ends of the crack and non-zero values of stress intensity factors appear.

We numerically analyze the effect of friction and loading parameters on the size of the slip zone, energy dissipation and stress intensity factors. It is discovered that the slip zone appears and grows fastest when the pressing normal stresses are minimal. The growth rate of the slip zone also promotes the increase of the distance of the application point of concentrated loading factors from it. The growth of the coefficient of friction significantly reduces the intensity of stresses at the vicinity of the ends of cracks at the third stage of loading. Energy dissipation for the examined cases of loading is calculated. The energy dissipation becomes more intense when the point of force application is closer to the sliding zone.

References

1. ARAVAS N., SHARMA S.M., 1991, An elastoplastic analysis of the interface crack with contact zones, *Journal of the Mechanics and Physics of Solids*, **39**, 311-344
2. ARHIPENKO K.M., KRIVYI O.F., 2008, Interphase beam at different types of contact interaction of heterogeneous anisotropic plane (in Ukrainian), *Mashynoznavstvo*, **3**, (129), 16-21
3. BRUSSAT T.R., WESTMANN R.A., 1974, Interfacial slip around rigid fiber inclusion, *Journal of Composite Materials*, **8**, 4, 364-377
4. CHEREPANOV G.P., 1966, On the development of cracks in compressed bodies (in Russian), *Priladnaya Matematika i Mehanika*, **30**, 1, 82-93
5. COMNINOU M., 1977, The interface crack, *Journal of Applied Mechanics*, **44**, 631-636
6. COMNINOU M., DUNDURS J., 1980, Effect of friction on the interface crack loaded in shear, *Journal of Elasticity*, **10**, 2, 203-212
7. COMNINOU M., SCHMUESER D., DUNDURS J., 1980, Frictional slip between a layer and a substrate caused by a normal load, *International Journal of Engineering Science*, **18**, 131-137
8. GORYACHEVA I.G., 2001, *Mechanics of Friction Interaction* (in Russian), Moscow, Nauka
9. HERRMANN K.P., LOBODA V.V., 1999, On interface crack models with contact zones situated in an anisotropic bimaterial, *Archive of Applied Mechanics*, **69**, 317-335

10. HILLS D.A., NOWELL D., SACKFIELD A., 1993, *Mechanics of Elastic Contact*, Butterworth-Heinemann, Oxford
11. JOHNSON K.L., 1985, *Contact Mechanics*, Cambridge etc., Cambridge University Press
12. KALKER J.J., 1977, A survey of the mechanics of contact between solid bodies, *Zeitschrift für Angewandte Mathematik und Mechanik*, **57**, 5, T3-T17
13. KHARUN I.V., LOBODA V.V., 2003, A set of interface cracks with contact zones in combined tension-shear field, *Acta Mechanica*, **166**, 43-56
14. KUNDRAT M.M., SULYM H.T., 2003, Prefracture zone in the composition of high-modulus elastic inclusion in the symmetric and antisymmetric load (in Ukrainian), *Matematychni Problemy Mehaniky Neodnorodnyh Struktur*, Lviv, 322-324
15. MARTYNYAK R., KRYSHTAFOVYCH A., 2000, Friction contact of two elastic half-planes with local recesses in boundary, *Journal of Friction and Wear*, **21**, 4, 6-15
16. OSTRYK V.I., ULITKO A.F., 2006, *Wiener-Hopf Method in Contact Problems of Elasticity Theory* (in Russian), Kiev, Naukova Dumka
17. PASTERNAK YA.M., SULYM H.T., PISKOZUB L.G., 2010, Models of thin inclusion with the account of imperfect contact with the medium (in Russian), *Proceedings of VI International Symposium on Tribo-Fatigue ISTF 2010*, Part 2, Minsk, BGU, 399-404
18. PISKOZUB L.G., 2014, Longitudinal shear by concentrated force of bi-material with taking into account friction in the interfacial crack (in Ukrainian), *Physic-Mathematical Modeling and Informational Technologies*, **20**, 160-172
19. PISKOZUB J.Z., SULIM G.T., 2008, Thermoelastic equilibrium of piecewise homogeneous solids with thin inclusions, *Journal of Engineering Mathematics. Special Issue Thermomechanics*, **61**, 315-337
20. PISKOZUB L.G., SULYM H.T., PASTERNAK YA.M., 2014, Influence of friction on hysteresis under cycling loading of solid with interface crack by the longitudinal shear (in Ukrainian), *Applied Problems of Mechanics and Mathematics*, **12**, 184-191
21. SULYM H.T., 2007, *Bases of Mathematical Theory of Thermo-Elastic Equilibrium of Solids Containing Thin Inclusions* (in Ukrainian), L'viv, Research and Publishing center of NTSh
22. SULYM G.T., PISKOZUB J.Z., 2004, Contact conditions (a survey) (in Ukrainian), *Mat. Metody i Fiz.-Meh. Polya (Journal of Mathematical Science)*, **47**, 3, 110-125
23. WEERTMAN J., LIN I.-H., THOMSON R., 1983, Double slip plane crack model, *Acta Metallurgica*, **31**, 4, 473-482

ON THE INVESTIGATION OF WHEEL FLANGE CLIMB DERAILMENT MECHANISM AND METHODS TO CONTROL IT

HABIBOLLAH MOLATEFI, AMIN MAZRAEH

School of Railway Engineering, Iran University of Science And Technology, Tehran, Iran
e-mail: molatefi@iust.ac.ir; amin.mazraeh.me@gmail.com

In this research, investigations are focused on the study of railway vehicle wheel flange climb derailment. A three dimensional nonlinear dynamic model of the wheel-set and suspension system is developed. Having validated the model through field tests, the effect of friction coefficient, wheel-set AOA, vehicle suspension system and running speed on the wheel flange climb derailment are investigated. In addition, different rail lubrication methods are studied and their effects on the wheel flange climb derailment are compared in the case of two point contact for nonlinear wheel-rail profiles. The results are debated and recommendations proposed to improve running safety against derailment.

Keywords: modified Nadal criterion, wheel flange climb derailment, wheel-rail angle of attack, rail lubrication

1. Introduction

Due to ever growing demand especially for an increase in running speed and keeping up with required running safety regulations, investigation on the derailment phenomenon and its mechanism have been of interest. More and more researches are done to find parameters affecting this phenomenon, particularly the wheel flange climb derailment. Parameters influencing the wheel flange climb derailment are often related to wheel-rail interaction geometry, dynamic and tribo features according to available literature. To address the demand for running safety, efforts were devoted to develop formulas that predict running safety criterion for wheel on an outer rail at curves. A very famous one was the work published by Nadal which was developed later by numerous researchers (Iwnicki, 2006). In the 19th century he developed a relation between wheel-rail geometry properties and friction coefficient to predict the maximum ratio of wheel lateral to vertical forces (L/V) at which the wheel flange climb derailment occurs. He assumed that in this condition, forces acting on the outer wheel are in equilibrium, hence the problem was considered as a two dimensional problem with quasi-static presumption. The formula depends on the coefficient of friction and the rail side-wheel flange contact angle.

Figures 1a to 1d show the wheel-set angle of attack (AOA) for different cases in addition to the wheel-rail experiencing two point contact. With respect to Nadal's formula, the wheel-set AOA is not considered. That is why the effects of this parameter on the wheel flange climb derailment with quasi static presumption are ignored just the same as the effect of the other wheel on the inner rail at curves.

Regarding to Nadal limit as shown in Fig. 2, field tests showed different limit values for derailment when the wheel-set AOA was considered. The difference is highlighted when the wheel-set AOA contains negative values or does not have considerable positive values. Therefore, improved Nadal theories have been introduced to present a better insight into the wheel-set derailment criterion.

Reviewing the available literature, there have been efforts to study the effects of wheel-rail geometry and dynamic features on the wheel flange climb derailment and, hence, mathematical

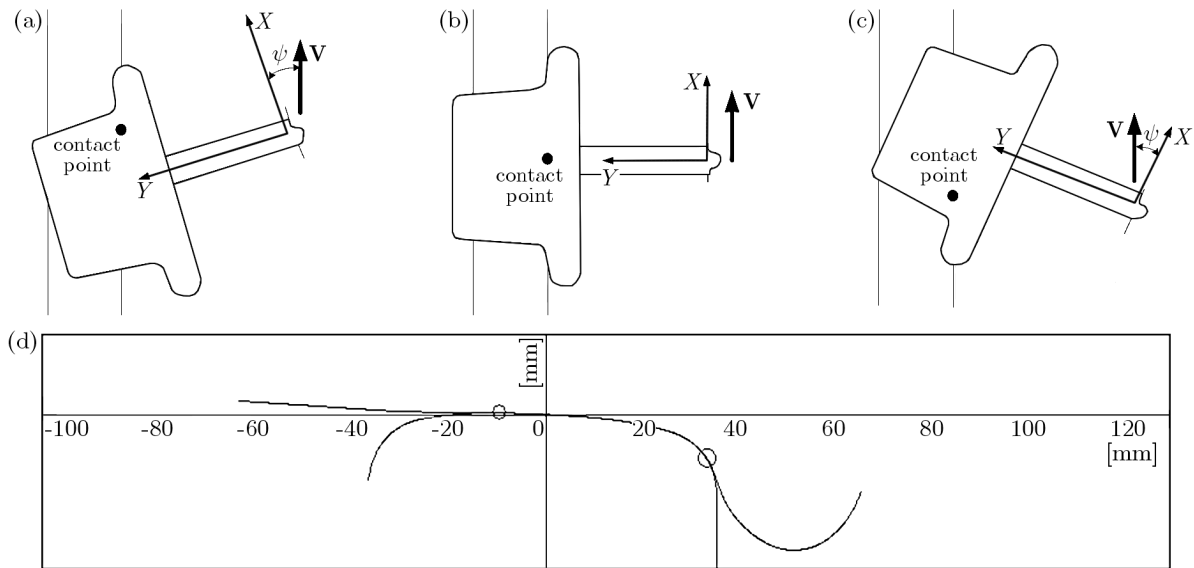


Fig. 1. Wheel-set AOA in rail-wheel flange contact (Santamaria *et al.*, 2009) in addition to demonstration of the wheel-rail two point contact; (a) positive wheel-set angle of attack, (b) zero angle of attack, (c) negative angle of attack, (d) wheel-rail two point contact

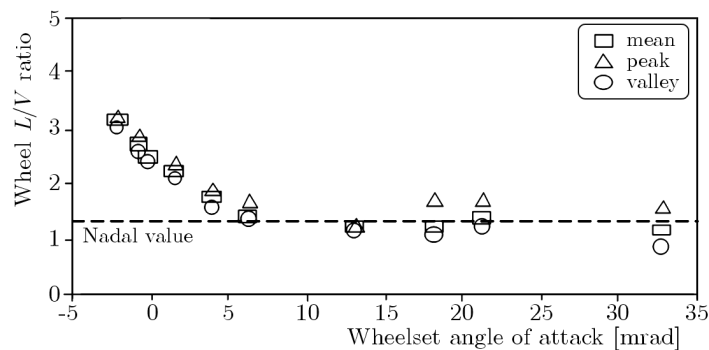


Fig. 2. Results of the wheel lateral to vertical forces ratio by field tests (Shust *et al.*, 1997)

relations have been developed. Yokose (1965, 1966) investigated the effect of wheel-set AOA on the wheel flange climb derailment. He suggested a mathematical model in which the lateral creep force is derived as a function of the friction coefficient, wheel-set AOA and wheel flange angle. Weinstock (1984) suggested a formula in which the effects of both wheels (the term friction coefficient of the inner rail was added up to Nadal equation) of wheel-set on the wheel flange climb derailment were considered. TCRP (TCRP report 71, 2005) performed investigations to determine the parameters which affect the wheel flange climb derailment as well. Moreover, Elkins and Wu (2000) also studied efficient parameters in the wheel derailment mechanism in addition to introduction of new derailment criteria.

More recently, studies have been devoted to the development of mathematical models validated through field tests with the aid of commercial software or developed codes. Wilson *et al.* (2011) compared and investigated different methods of safety against derailment and debated some issues on validation of derailment simulations. Also some researches were conducted by Brabie and Andersson (2007), Yamashita and Sugiyama (2012) on simulation and study methodology of wheel derailment.

A method suggested, in which the wheel-rail interaction can be improved especially in curves in aspect of derailment, was the proposal for wheel-rail lubrication which has been investigated by some researchers (Heavy haul conference, 2001; Eadie *et al.*, 2002). Also some investigations

on the effects of lower rail lubrication in improving running safety were performed by Ishida *et al.* (2008). They investigated the effects of lubrication on the traction coefficient and change in lateral forces exerted on the wheel-set in aspect of derailment safety in curves.

Many lubrication methods (friction management which can lead to change in slip-friction coefficient diagram) have been proposed and utilized in various railway networks. Those common methods include outer rail side lubrication, outer rail side-rail head lubrication, in addition to the inner rail head and rail side lubrication. Iran railway network is currently using the outer-rail side lubrication method with unknown efficiency with regard to practical service conditions and numerous derailments in curves and turnouts which have been reported (reports are confidential). Also the wheel-rail interaction for Iran railway network is exposed to two point contact due to using S1002 and UIC60 standards for the wheel-rail profile with rail inclination 1:20. In this case, not so considerable research works have been done.

Considering the scientific research studies which have been done to examine the wheel flange climb derailment, further investigations are necessary to be performed in order to understand the derailment mechanism and increase rolling stock transportation safety. Thus it is the purpose of this research to develop a model validated through field tests to study the effects of parameters affecting the wheel flange climb derailment. In this research, the effects of wheel-set AOA and the wheel-rail coefficient of friction on the wheel flange climb derailment are studied. In addition, a study on an appropriate wheel-rail contact algorithm is done. In the case of achieving an improvement in the wheel-rail interaction in curves and considering various lubrication methods currently in use in railway networks, it is necessary to compare the efficiency of various lubrication methods in railway operation and choose the appropriate one. The large number of parameters included in the wheel-rail tribo system in aspect of lubrication, affect the friction coefficient. Therefore, in this research, the effects of change in the friction coefficient on running safety are investigated for both rails.

2. Modeling

In the first step, it is required to find a proper wheel-rail contact algorithm among those suggested and currently in use. Indeed, those algorithms should be compared to field tests as shown in Fig. 2 to determine the appropriate method to be used in the wheel-rail contact problem investigation.

A single 5 degree of freedom wheel-set with a frame is modeled in Universal Mechanism software on elastic rails (Euler beams on foundation) which are shown in Fig. 3a,b. The frame contains longitudinal, vertical, lateral, yaw and roll degrees of freedom. The roll movement of the frame is considered in the case the effect of the other wheel in the wheel-set in addition to different lubrication methods are investigated in curve. During the simulations, the frame is laterally displaced (0.002 m/s to 0.008 m/s). Lateral displacement of the wheel-set at such speeds will not result in applying impulsive loads to the wheel. Simulations are performed on a straight track. A constant wheel-set AOA is applied to the wheel-set for investigation on the wheel flange climb derailment criterion as a function of the wheel-set AOA (control parameter).

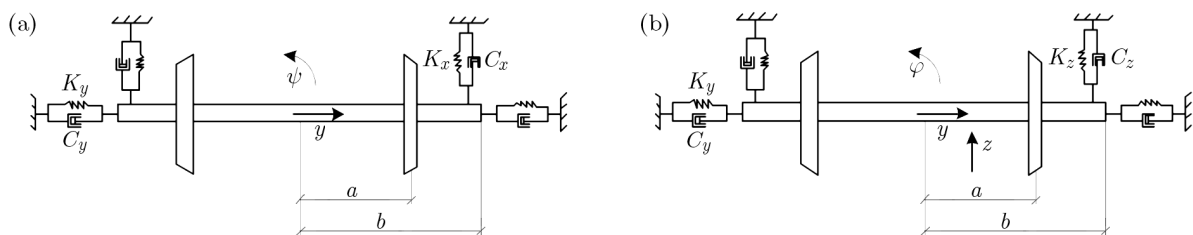


Fig. 3. Single wheel-set model with the frame and illustration of the suspension system; (a) top view, (b) front view

The wheel-rail contact algorithms studied in this research include FastSim, FastSim A, Muller, Minov, non elliptic and simplified. The L/V ratio (maximum value at which derailment occurs) is gained as a function of the wheel-set AOA. the results are presented for rail inclinations 0.05 rad (1:20) and 0.025 rad (1:40) with the track gauge of 1435 mm. the rails are considered elastic with constant and continuous lateral stiffness of $18E+06$ N/m, vertical stiffness $44E+06$ N/m with lateral damping of $1E+05$ N·s/m and vertical damping of $4E+05$ N·s/m. the rail surfaces are considered even. In addition, the information about the S1002 wheel profile rolling radius difference (RRD) and contact points distribution on UIC60 rail profile considering both rail inclinations is shown in Fig. 4a and 4b in addition to Fig. 5a and 5b. These diagrams show the nonlinear relation between wheel-set lateral displacement and wheel rolling radius in addition to wheel-rail contact points. The information of loads on the wheel-set, wheel-set mass and the suspension system is given in Table 1. The bushing elements including rotational and torsion damping and stiffness on both wheel ends are not shown in Fig. 3 for simplicity.

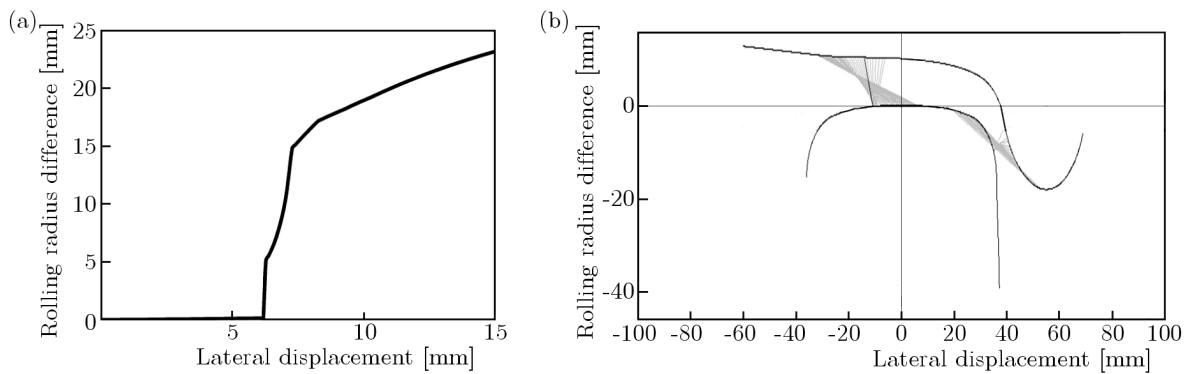


Fig. 4. Wheel-rail contact points and wheel-set rolling radius difference with rail inclination 0.05 rad (1:20); (a) wheel rolling radius difference (RRD), (b) wheel-rail contact points distribution

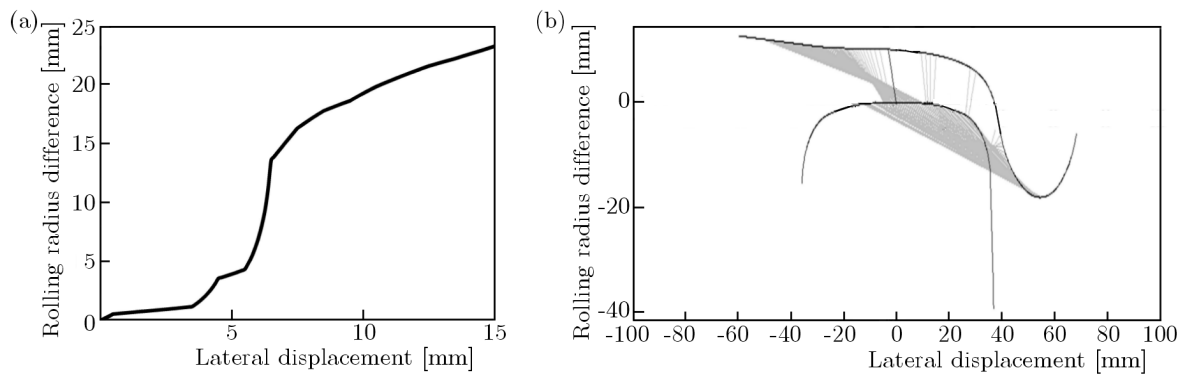


Fig. 5. Wheel-rail contact points and wheel-set rolling radius difference with rail inclination 0.025 rad (1:40); (a) wheel rolling radius difference (RRD), (b) wheel-rail contact points distribution

Also in the case of investigation on the efficiency of various lubrication methods with the wheel-rail two point contact in curves, the rail lubrication efficiency assessment in this research is conducted for the inner rail head and outer rail head-rail side lubrication. The effect of lubrication in curves for the outer wheel in the case of one point contact has already been investigated by many researchers. Here, two different lubrication zones are considered for the rail. As it is shown in Fig. 6, the angles β_r and β_s which are measured with respect to the vertical axis are used to determine the transition zone boundaries. The distance between the two angles is equal to

Table 1. Wheel-set and suspension system parameters

Parameter	Value	Parameter	Value
Wheel-set mass	1500 kg	Longitudinal stiffness	2E+05 N/m
M_x	1200 m ⁴	Lateral stiffness	1E+07 N/m
M_y	300 m ⁴	Vertical stiffness	5E+04 N/m
M_z	1200 m ⁴	Wheel tape circle distance	1500 mm
Vertical damping	4.5E+04 N·s/m	Lateral damping	2E+04 N·s/m

M_k – moment of inertia about k axis, $k = x, y, z$

the transition zone between one friction zone to another. The friction coefficient variation in the transition zone is considered to be linear. The friction coefficient at the right and left side of the transition zones is constant with known values.

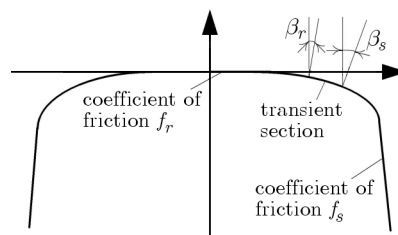


Fig. 6. A schematic view of the rail with three different friction coefficient zones (UM software, User manuals)

As has been mentioned before, the investigations are performed on straight tracks while the lab tests are often performed on rollers. In order to perform simulations, some aspects of the research are necessary to be considered. Firstly, a significant change in gravitational stiffness of the wheel-set is inevitable. This happens to be since the wheel-roller contact surface normal vector may not be parallel to the vertical axis. Secondly, as a result of the use of rollers, considering general normal (Hertz theory) and tangential wheel-rail contact algorithms, a change in creep forces during wheel-roller interaction is inevitable (Iwnicki, 2006). For more information about the effect of rollers on wheel-rail contact forces and dynamic behavior of the wheel-set in curves (especially wheel-set gravitational stiffness) the papers by Iwnicki (2006), Yaschinski (1990), De Pater (1993), Dukkipati (2000) are recommended. Thus in order to gain more realistic results and avoid dealing with the mentioned problems, investigations are performed on a straight path.

3. Results

The maximum L/V value is shown in Fig. 7 which demonstrates a gradual increase in the lateral force to the maximum amount. Then, as the wheel flange climbs the rail, a sudden decrease in the L/V ratio is observed. Moreover, from Fig. 7 it is seen that as the wheel flange climbs the rail, the wheel flange will move on the rail head surface for a while before derailment occurs. In addition, the RMS method is used for the case where there is perturbation in values at the top of the diagram as shown in Fig. 7.

The maximum L/V ratios for different contact algorithms as a function of the wheel-set AOA are shown in Fig. 8 and Fig. 9 for different rail inclinations. Comparing the results from simulations to test results, the FastSim algorithm is appropriate to be used for numerical simulation. Also, comparing the results from different rail inclinations, it is concluded that for the rail inclination 1:40, the maximum L/V values will be larger compared to the case with rail

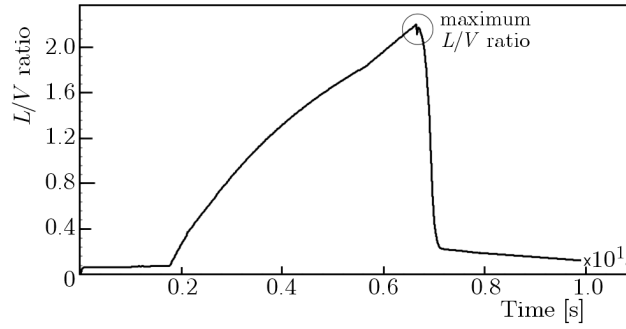


Fig. 7. Diagram of the L/V forces ratio

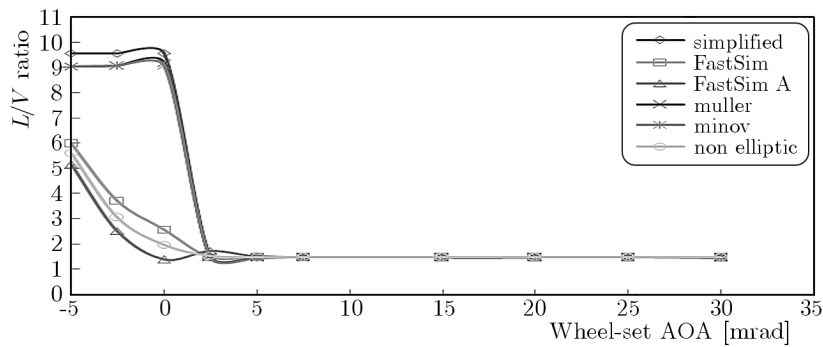


Fig. 8. Comparison between wheel-rail contact theories with rail inclination 1:20

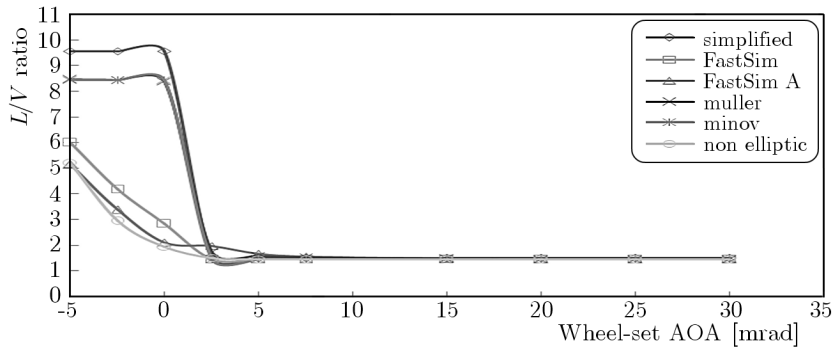


Fig. 9. Comparison between wheel-rail contact theories with rail inclination 1:40

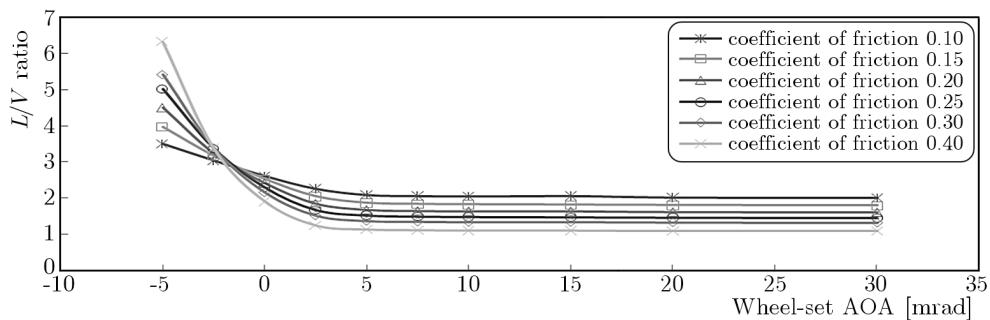


Fig. 10. L/V values as a function of the coefficient of friction with rail inclination 1:20

inclination 1:20. Then the effects of the outer rail coefficient of friction on derailment considering different angles of attack are studied. No lubrication for the outer rail has been considered, thus the rail side and rail head friction coefficient values are similar. The results are shown in Fig. 10 and Fig. 11 for rail inclinations 1:20 and 1:40 using FastSim algorithm.

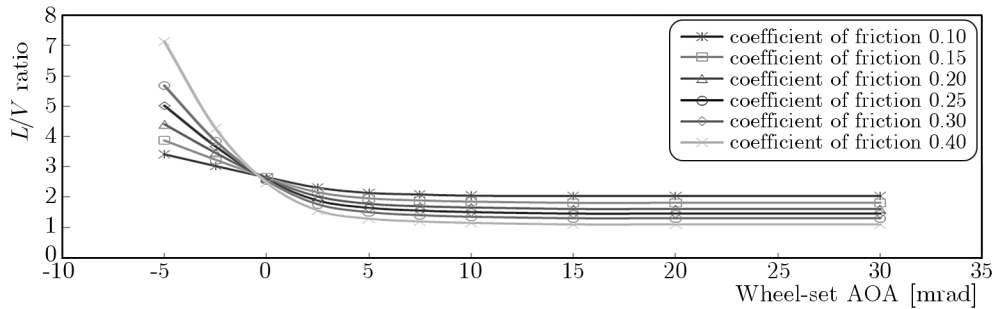


Fig. 11. L/V values as a function of the coefficient of friction with rail inclination 1:40

With regard to the results for the positive wheel-set AOA, as the coefficient of friction increases, the wheel L/V criteria would decrease. But the L/V limit diagram after 10 mrad will converge to a constant value for each coefficient of friction diagram. In the negative wheel-set AOA, as the coefficient of friction increases, the wheel L/V values criterion would increase. It is seen that the friction coefficient has different influence on the wheel flange climb derailment criterion at positive and negative wheel-set AOAs, and the diagrams would cross each other approximately at the zero angle of attack. This means that in such a case near the zero wheel-set AOA, the friction coefficient variation will not have considerable effect on the L/V ratio. The effect of the friction coefficient on the maximum L/V ratio at both positive and negative wheel-set AOAs is different, which is related to the direction and magnitude of creep forces.

Also the effect of lateral stiffness (vehicle primary suspension system) on the wheel L/V ratio as a function of the wheel-set AOA has been investigated as shown in Fig. 12. The coefficient of friction and rail inclination are considered to be 0.28 and 1:20, respectively. It is seen that L/V values are not very sensitive to the lateral suspension system. The differences are highlighted at the negative wheel-set AOA. Therefore, it is concluded that in the case of the wheel flange climb derailment, the suspension system affects the wheel flange climb criterion by making a change to the wheel-set yaw angle (or AOA). This means that in the lab tests, the exact suspension system, particularly the lateral one, would not be necessary to be used for the wheel flange climb derailment investigation where the wheel-set AOA is controlled.

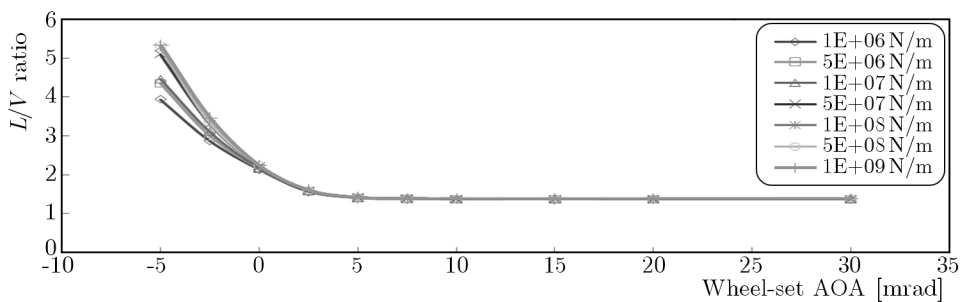


Fig. 12. L/V values as a function of the suspension system lateral stiffness

Next, the effects of vehicle running speed on the L/V ratio are studied. The simulations are performed for rail inclination 1:20 on the condition that the lateral stiffness and coefficient of friction would be constant. According to the results shown in Fig. 13, the running speed does not affect L/V values considering an even rail surface. This means that for lab test applications, the operational running speed is not necessary to be applied to the wheel-set in the case of wheel flange climb derailment investigations.

In the next step, the effects of lubrication methods on wheel-rail interaction in curves are studied. The results for the inner and outer rails are shown in Tables 2 and 3. Friction coefficient values vary from 0.1 to 0.4 which have been reported from field measurements and tests per-

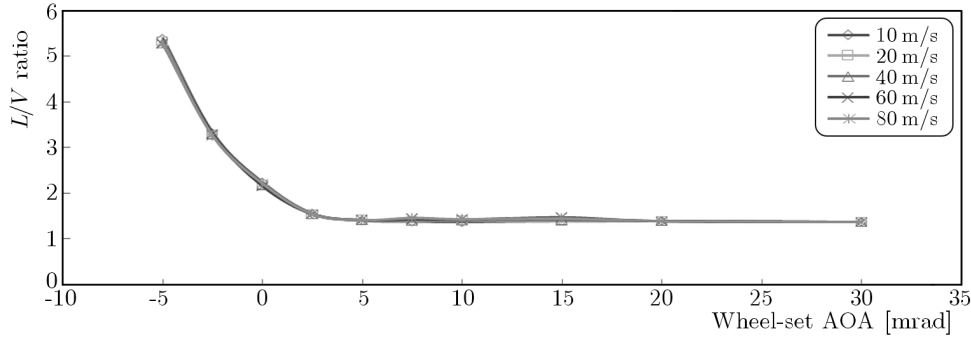


Fig. 13. L/V values as a function of the dynamic system running velocity

formed in labs (Lewis and Olofsson, 2009). Simulations were performed for a curve with radius of 300 m and super elevation of 130 mm with constant running speed of 16 m/s. For the case of investigations on the effects of the outer rail head lubrication on running safety, the outer rail side and inner rail head friction coefficient was 0.3. Also for the case of inner rail head lubrication, the outer rail friction coefficient was 0.3. It is be noted that due to rail inclination of 1:20 during the wheel-set curving, two point contact exists between the outer wheel and the rail.

Table 2. L/V values for the outer rail as a function of the inner rail friction coefficient

Friction coefficient	L/V value
0.20	0.22
0.25	0.28
0.30	0.33
0.35	0.37
0.40	0.41

Table 3. L/V values for the outer rail as a function of the outer rail-head friction coefficient

Friction coefficient	L/V value	AOA [mrad]
0.10	0.26	2.4
0.15	0.26	2.6
0.20	0.28	3.2
0.25	0.30	3.9
0.30	0.33	4.6
0.35	0.38	5.2
0.40	0.40	5.5

The results show that decreasing the inner rail head friction coefficient by means of lubrication will improve vehicle safety at curves. It is shown that the wheel-rail two point contact will decrease the wheel-set steer ability since the resultant creep force for both points do not lie in the same direction, and even they can be in opposite direction (TCRP report 71, 2005). Therefore, in order to decrease the second contact point influence on the wheel-set steer ability, the outer rail head friction modification has been investigated. The results show that as the friction coefficient for the outer rail head increases, the risk of derailment would increase. In addition, decreasing the friction coefficient results in an increase in running safety. In order to monitor the wheel-set curving performance in much more detail, the wheel-set AOA has been monitored as well. As shown in Table 3, decreasing the outer rail head friction coefficient will decrease the wheel-set AOA. This will result in a better wheel-set steer ability in curves. Moreover, it

is seen that the inner rail lubrication has better effect in comparison with the outer rail head lubrication.

The important point in lubrication of the outer rail is that the high difference (rail head friction coefficient is much larger than the rail side friction coefficient) between the flange and wheel tread friction coefficient (while wheel flange lubrication is interested for the wheel-rail wear purposes) will increase the risk of derailment, which can be seen in Table 3.

4. Conclusions

In this investigation, effects of the friction coefficient, wheel-set AOA, rail lubrication, lateral suspension and longitudinal velocity on the wheel flange climb derailment are studied in order to have a better insight into the derailment mechanism and parameters which affect this phenomenon. Thus, a model has been developed and validated by field test results. The main results are presented as follows:

- As the wheel-set AOA sign changes from positive to negative values, the friction coefficient would have different effects on the maximum L/V ratio. Moreover, it is shown that as the wheel-set AOA reaches the zero value, the friction coefficient approximately loses its effect on the maximum L/V .
- It is shown that the wheel-set running velocity and primary suspension system (in the case the wheel-set AOA is controlled) would not have a noticeable effect on the maximum L/V . Thus, conducting further research on wheel flange climb derailments at labs, it is not necessary to apply the exact primary suspension and running speed.
- Derailment would not take place right after the wheel flange climb. The wheel flange will continue moving on the rail head surface for a while. This will give a better insight, particularly in cases where investigations on derailed trains are of interest. In the cases where the wheel flange climb is the main cause of the derailment, it is very likely to see the trace of the wheel flange on the rail head surface at the derailment area.
- It is shown that by means of the inner rail head lubrication, the vehicle safety would improve. In addition, the outer rail head lubrication in the case of two point contact will enhance safety of the vehicle. But the inner rail head lubrication has a better effect on the wheel-set safety. Moreover, it has been found that a high friction coefficient difference between the outer rail side and rail head will increase the risk of derailment. Therefore, this must be considered while the outer rail lubrication at curves is of interest.
- Conducting research on the effects of the outer rail head lubrication on safety revealed that in the case of two point contact, a considerable decrease in the wheel-set AOA and, as a result, an improvement in the safety margin is possible.

For current railway conditions with two point contact for the outer wheel-rail in curve, in the case of improving safety against derailment, low rail lubrication is suggested. In addition, the method including simultaneous outer rail lubrication along with the inner rail lubrication is proposed. It must be considered that in the case of outer rail side lubrication, the outer rail head friction coefficient must be close to the rail side friction coefficient and moreover, traction obligations must be regarded as well.

Acknowledgment

This research was supported by Iran University of Science and Technology Center of Excellence.

References

1. BRABIE D., ANDERSSON E., 2006, Dynamic simulation of derailments and its consequences, *Journal of Vehicle System Dynamics*, **44**, 652-662
2. DUKKIPATI R.V., 2000, *Vehicle Dynamics*, Alpha Science International, Ltd.
3. DE PATER A.D., 1993, The motion of a railway wheel-set supported by a pair of rollers as compared with the motion of such a wheel-set along a tangent track, *Delft University of Technology, Laboratory for Engineering Mechanics, Report*, **1012**
4. EADIE D.T., KALOUSEK J., CHIDDICK K.C., 2002, The role of high positive friction (HPF) modifier in the control of short pitch corrugations and related phenomena, *Journal of Wear*, **253**, 185-192
5. ELKINS J., WU H., 2000, New criteria for flange climb derailment, *IEEE/ASME Joint Railroad Conference*, Newark, NJ, April 4-6
6. International Heavy Haul Association, 2001, Guidelines to best practices for heavy haul railway operations: wheel and rail interface issues, 2808 Forest Hills Court Virginia Beach, Virginia 23454, USA
7. ISHIDA M., BAN T., IIDA K., ISHIDA H., AOKI F., 2008, Effect of moderating friction of wheel/rail interface on vehicle/track dynamic behavior, *Journal of Wear*, **265**, 1497-1503
8. IWNICKI S., 2006, *Handbook of Railway Vehicle Dynamics*, CRC Press, Taylor & Francis Group, LLC
9. LEWIS R., OLOFSSON U., 2009, *Wheel Rail Interface Handbook*, CRC, Whodhead Publishing Limited, Abington Hall, Granta Park, Great Abington, Cambridge CB21 6AH, UK
10. SANTAMARIA J., VADILLO E.G., GOMEZ J., 2009, Influence of creep forces on the risk of derailment of railway vehicles, *Journal of Vehicle System Dynamics*, **47**, 721-752
11. SHUST W.C., ELKINS J.A., KALAY S., EL-SIBAIE M., 1997, Wheel-climb derailment tests using AAR's track loading vehicle, *Association of American Railroads Report*, **R-910**
12. TCRP Report 71 Vol. 5, 2005, Flange climb derailment criteria and wheel/rail profile management and maintenance guidelines for transit operations, track related research, transit cooperative research program
13. WEINSTOCK H., 1984, Wheel climb derailment criteria for evaluation of rail vehicle safety, *Proceedings of ASME Winter Annual Meeting*, 84-WA/RT-1, New Orleans, LA
14. WILSON N., FRIES R., HAIGERMOSER A., MRANG M., EVANS J., ORLAVA A., 2011, Assessment of safety against derailment using simulations and vehicle acceptance tests: a worldwide comparison of state-of-the-art assessment methods, *Journal of Vehicle System Dynamics*, **49**, 1113-1157
15. YAMASHITA S., SUGIYAMA H., 2012, Numerical procedure for dynamic simulation of two-point contact wheel-rail contact and flange climb derailment of railroad vehicles, *Journal of Computational and Nonlinear Dynamics*, **7**, 1012-1019
16. YASCHINSKI A., 1990, On the application of similarity laws to a scaled railway bogie model, PhD Thesis, TU Delft University
17. YOKOSE K., 1965, On the theory (sic) of derailment of one-axle wheel (in Japanese), *Railway Technical Research Report*, **504**
18. YOKOSE K., 1966, A theory of the derailment of wheel-set, *Quarterly Report RTRI*, **7**, 3

IMPROVING MECHANICAL PROPERTIES OF EPOXY BY ADDING MULTI-WALL CARBON NANOTUBE

BASIM M. FADHIL, PAYMAN SAHBAH AHMED

Manufacturing Engineering Department, Koya University, Koyseinjaq, Irak
e-mail: basim.fadhil@koyauniversity.org

AVA ALI KAMAL

Engineering and Projects Directorate, Salahadin University, Erbil, Irak
e-mail: avaali@yahoo.com

In this research, multi-walled carbon nanotubes (MWCNTs) are used as the reinforcement in an epoxy resin with weight percentages (0, 0.2, 0.4, 0.6, 0.8, 1) wt%, respectively, by using both direct (nonhomogeneous) and homogeneous dispersion mixing processes to prepare (epoxy/MWCNTs) nanocomposites. Tensile and drop weight impact tests are used to evaluate mechanical properties of the composites. Results show that homogeneous dispersion has a great effect on enhancing mechanical properties of multi-wall carbon nanotube reinforced composites. Adding 0.2 wt% of MWCNTs enhances and increases tensile properties, and adding 0.6 wt% of MWCNTs enhances impact properties.

Keywords: multi-wall carbon nanotubes, mechanical properties and nanocomposites

1. Introduction

CNT/polymer composites are increasingly used for engineering applications under hard working conditions due to unique mechanical properties of CNTs, such as high elastic modulus, tensile strength and strain to fracture, ability to withstand cross-sectional and twisting distortions and compression without fracture combined with a low specific weight and high resistance to degradation in order to ensure safety and economic efficiency (Du *et al.*, 2007; Walter *et al.*, 1997).

Epoxy based Multi-Walled Carbon Nanotubes (MWCNTs) reinforced composites are synthesized by Samal (2009) by the method of sonication. The variation of nature of the reinforcement (aligned and randomly oriented MWNTS) has resulted in the improvement of mechanical properties like flexural modulus, tensile strength and hardness. A small change in chemical treatment of the nanotubes has a great effect in the mechanical and morphological properties of the nanocomposites due to the effective load transfer mechanism and state of dispersion. The change in properties has been verified by optical microscopy and scanning electron microscopy. Apart from that the prepared composites have been treated under different temperatures (like hot water, room temperature and liquid nitrogen temperature) and the change in mechanical as well as morphological nature has been verified by SEM of fractographic surface, this proved the elasticity and ductility of the composites.

Multi-walled carbon nanotubes (MWCNTs) were used by Nema *et al.* (2014) to enforce the blend of epoxy/polysulfide and then tensile and wear behavior of this reinforcement were evaluated. For achieving this goal, different weight percentages of MWCNT (0.2-0.6 wt%) were dispersed in the epoxy resin, then polysulfide resin was added and mixed with two curing

agents. Experimental results have shown significant difference between epoxy/polysulfide and CNT/epoxy/polysulfide in mechanical properties. With 0.2-0.6% MWCNTs we observed an increase in Young's modulus from 245 to 273 MPa, tensile strength from 30.5 to 38.9 MPa and fracture strain from 12.4% to 14.2%. For understanding the structure and morphology of nanocomposite, the dispersion states were studied using scanning electron microscopy (SEM) and field emission electron microscopy (FESEM).

Different types of Multi-Walled Carbon Nanotubes (MWCNTs) long and short were used by Al-Rawi *et al.* (2014) as the reinforcement in an epoxy resin with weight percentages (0.1, 0.2, 0.5, 1.0, 1.5, 2.0, 2.5, 3.0, 3.5, 4.0, 4.5, 5) wt%, respectively, by using direct mixing processes to prepare (epoxy/MWCNTs) nanocomposites. The ultrasonic mixing process was used to disperse the nanotubes into the epoxy resin system. The results show improvement of the mechanical properties with an increase in the percentage weight less than 2% and then a decrease with a further increase in the MWCNTs content. The results show that long carbon nanotubes have mechanical properties better than short carbon nanotubes.

A systemic evaluation was done by Ci and Bai (2006), for different reinforcement roles of carbon nanotubes in those nanocomposites with different matrix stiffnesses while the curing process were controlled. Both mechanical tests and microscope observations indicated that such a reinforcement would gradually reduce while increasing the stiffness of matrix. However, in soft and ductile composites, carbon nanotubes show a significant reinforcement without fracture strain growth. The interface interaction is poor between carbon nanotubes and matrix in the stiff composite, and therefore, they have little contribution to the mechanical properties of the composite.

In this research, Multi-Walled Carbon Nanotubes (MWCNTs) are used as the reinforcement in an epoxy resin with weight percentages (0, 0.2, 0.4, 0.6, 0.8, 1) wt%, respectively, by using direct and homogeneous dispersion mixing processes to prepare (epoxy/MWCNTs) nanocomposites. Tensile and drop weight impact tests are used to evaluate the mechanical properties of the composites.

2. Experimental part

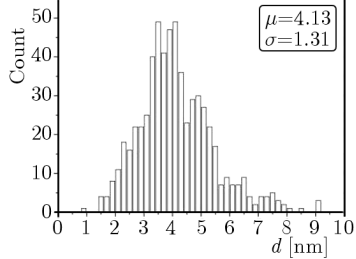
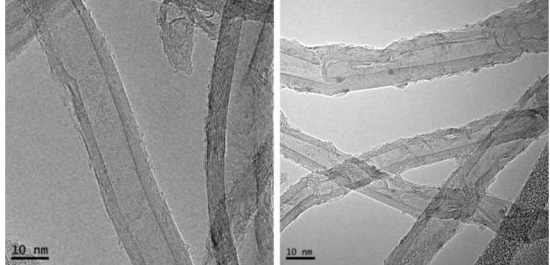
Epoxy resin of a trade mark (Quickmast 105 base) is used as the matrix which is a liquid of low viscosity as compared with other thermosets, and it is converted to solid state by adding a hardener (Quickmast 105 hardener) at ratio of 3:1, the technical properties of Quickmast 105 according to the data sheet of DCP company are listed in Table 1; while the nanoparticle reinforcements are MWCNTs manufactured by Henan Huier Nano Technology Co. Ltd. Their technical properties are listed in Table 2.

Table 1. Technical properties of Quickmast 105 (provided by the supplier)

Compressive strength BS6319	Flexural strength BS6319	Tensile strength BS6319	Pot life	Specific gravity	Viscosity
> 72 MPa 7 days	> 50 MPa 25°C	> 20 MPa	60 min 25°C	1.1	3-5 poise 25°C
					1-2 poise 35°C

To prepare a carbon nanotubes/epoxy composite, the nanotube powder (with a content of 0, 0.2, 0.4, 0.6, 0.8, and 1 wt%) was added into the liquid epoxy in two ways:

Table 2. Technical properties of multi-wall carbon nanotube (provided by the supplier)

Length of the carbon tube	Outer diameter of tubes	Tube wall thickness	Number of layer
3-12 nm	12.9 nm	4.1 nm	8-15
Tube thickness distribution		TEM image	
			

1. Nonhomogeneous dispersion: the resin and carbon nanotube solution was manually stirred for 5 min to form a homogeneous suspension. And then an epoxy hardener was mixed into the carbon nanotubes/epoxy suspension, and softly stirred for about 2 min. Finally, the composite suspension was poured into the impact and dog-bone-like steel tensile mould and left to be cured at room temperature for 7 days.
2. Homogeneous dispersion: the resin and carbon nanotube solution was manually stirred for 10 min to form a homogeneous suspension. And then an epoxy hardener was mixed into the carbon nanotubes/epoxy suspension, softly stirred for about 10 min, and the mixture was left for 2hrs to get homogeneous dispersion. Finally, the composite suspension was poured one corner into the impact and dog-bone-like steel tensile mould (to avoid bubble formation which causes cast damage) and left to be cured at room temperature for 7 days.

Samples without carbon nanotube addition (matrix samples) were also fabricated for comparison.

Mechanical tests were done according to ASTM D638 [3] for a tensile test and ISO 6603 [10] for an impact test. Instron 5982 tensile test machine was used to measure tensile behavior of the samples at strain rate of 2 mm/s. The specimen was fixed straightly by using two jaws with 100 kN maximum load. The machine started to elongate the specimen at a constant rate, and to continuously and simultaneously measure the instantaneous applied load and the resulting extension. Instron Ceast 9350 instrumented with the Drop weight impact tester was used to measure the resistance to failure of a material subjected to a suddenly falling object (weight=5.8 kg) from a level of 700 mm. The machine started to continuously and simultaneously measure the instantaneous impact load and the resulting deformation and impact energy (absorbed energy).

3. Results and discussion

During the study, multi-walled carbon nanotubes (MWCNTs) were used as the reinforcement in the epoxy resin with weight percentages (0, 0.2, 0.4, 0.6, 0.8, 1) wt%, respectively, by using direct and homogeneous dispersion mixing processes to prepare (epoxy/MWCNTs) nanocomposites. Tensile and drop weight impact test were carried out used to evaluate the mechanical properties of the composites. The relationships of stress-strain, impact force-time, impact force-deformation, impact energy-time and impact energy-deformation were obtained from experimental data as follows.

3.1. Tensile test results

Figure 1 shows the stress-strain results of the composites used in this study with different multi-walled carbon nanotubes (MWCNTs) reinforcement in the epoxy: 0, 0.2, 0.4, 0.6, 0.8, and 1 wt% for two mixing techniques, i.e. nonhomogeneous and homogeneous dispersion.

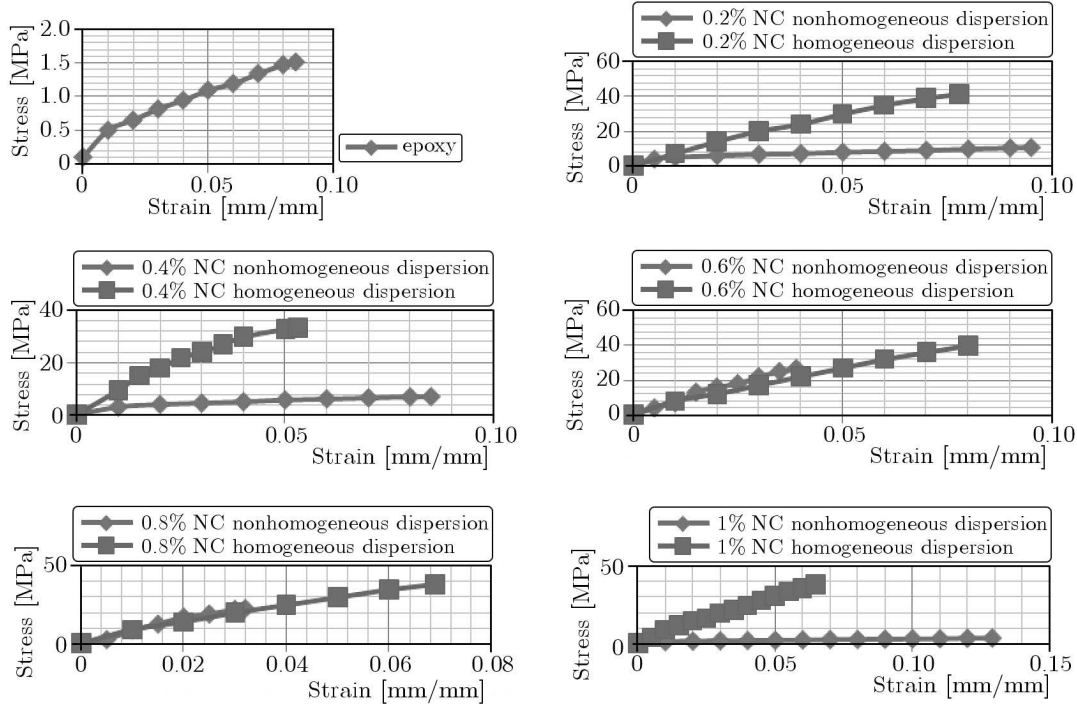


Fig. 1. Stress-strain curves of the composites with different percentages of multi-wall carbon nanotube: 0, 0.2, 0.4, 0.6, 0.8, and 1 wt%

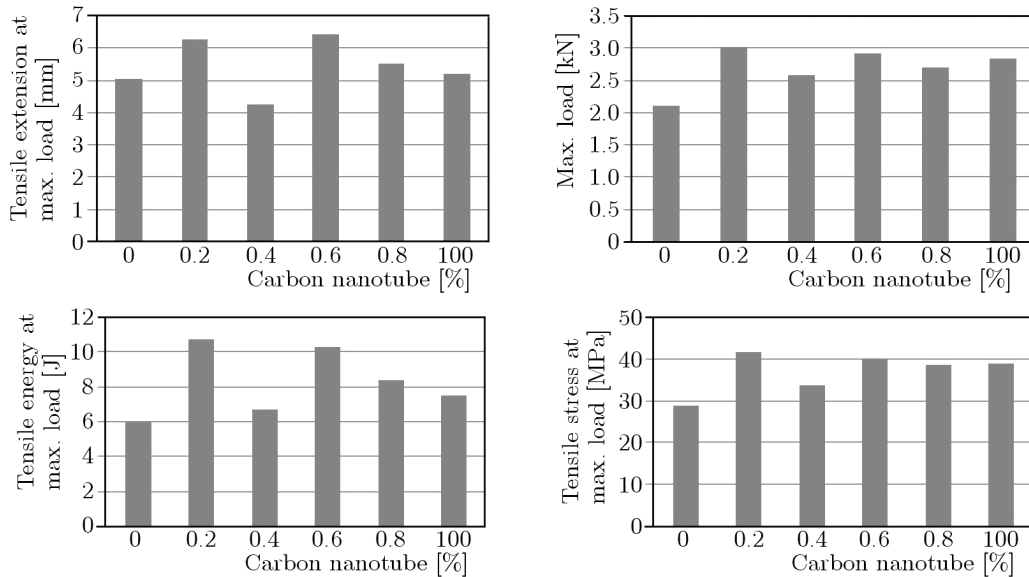


Fig. 2. Tensile stress, extension and energy at maximum load in the composites with different percentages of MWCNTs reinforcement in the epoxy: 0, 0.2, 0.4, 0.6, 0.8, and 1 wt%

It can be seen that the dispersion has a great effect on the stress and strain values for all composites. Such low reinforcing ability of the nanotubes in epoxy nanocomposites, which is sometimes observed, can be explained by a number of reasons: one is lack of interfacial adhesion,

which is critical for load transfer in composites. Indeed, carbon nanotube surfaces are atomically smooth, which may limit the transfer of load from the matrix to nanotubes reinforcement (Cooper *et al.*, 2000; Bokobza, 2007). Another reason is poor dispersion of nanotubes in the polymer matrix, which is also significant for fabrication of reinforced nanocomposites (Gojny *et al.*, 2004). Due to their high aspect ratio and huge surface area, CNTs have strong tendency to agglomerate, which leads to inhomogeneous dispersion in the polymer matrix (Smutisikha, 2010).

Figure 2 shows tensile properties and results of the composites used with different percentages of Multi-Walled Carbon Nanotubes (MWCNTs) reinforcement in the epoxy: 0, 0.2, 0.4, 0.6, 0.8, and 1 wt%.

It can be seen that the content of MWCNTs (0.2-1 wt%) enhances and increases the tensile properties and reaches the maximum values for 0.2% NT composite: tensile stress at maximum load from 28.6 MPa for epoxy resin to 41.4 MPa, maximum load from 2.1 kN for epoxy resin to 2.9 kN, tensile extension at maximum load from 5.04 mm for epoxy resin to 4.2 mm and tensile energy at maximum load from 5.9 J for epoxy resin to 10.6 J. Creating attractive polar forces, and Van der-Waals bonding between chains and nanotubes leads to an increase in the constraint between tubes/epoxy chains and epoxy chains, complicates epoxy chains which approach one another, reduces free volume space. This effect of MWCNTs make the epoxy chains bear extra loading (Park *et al.*, 2004). A 0.4% wt of MWCNTs is better than that of epoxy, but lower than other percentages due to formation of agglomerates of nanotubes in the polymer matrix that reduce the reinforcing effects of the CNTs.

3.2. Impact test results

3.2.1. Impact force – time behavior

Figure 3 shows time histories of the impact force in the composites used with different percentages of MWCNTs reinforcement in the epoxy: 0, 0.2, 0.4, 0.6, 0.8, and 1 wt% for two mixing techniques, i.e. nonhomogeneous and homogeneous dispersion.

It can be seen that dispersion has a great effect on the force values for all composites which is attributed to good dispersions of the nanotubes in the matrix and good reactions between the epoxy and grafted nanotubes. The investigation of the fracture surface in nanocomposites revealed that narrower crack-tips underneath the advancing cracks were more efficiently bridged by the nanotubes in epoxy/MWCNTs resulting in an increased resistance against crack propagation (Ajayan *et al.*, 2006).

3.2.2. Impact force – deformation behavior

Figure 4 shows the impact force vs. deformation results of composites with different percentages of MWCNTs reinforcement in the epoxy: 0, 0.2, 0.4, 0.6, 0.8, and 1 wt% for two mixing techniques. It can be seen that dispersion has a great effect on the force values for all composites which is attributed to the formation of a network structure which can take more mechanical loading from the matrix when the matrix is under stress. This means that when the applied loading is over the elastic deformation stress, the carbon nanotubes transfer the stress (Qi *et al.*, 2006), which enhances the strength of the resin matrix.

3.2.3. Impact energy – time behavior

Figure 5 shows the impact energy vs. time of composites with different percentages of MWCNTs reinforcement in the epoxy: 0, 0.2, 0.4, 0.6, 0.8, and 1 wt% for two mixing techniques. It can be seen that dispersion has a great effect on the force values for all composites which is attributed to the weak van der Waals bonding between the reinforcement and the matrix, which

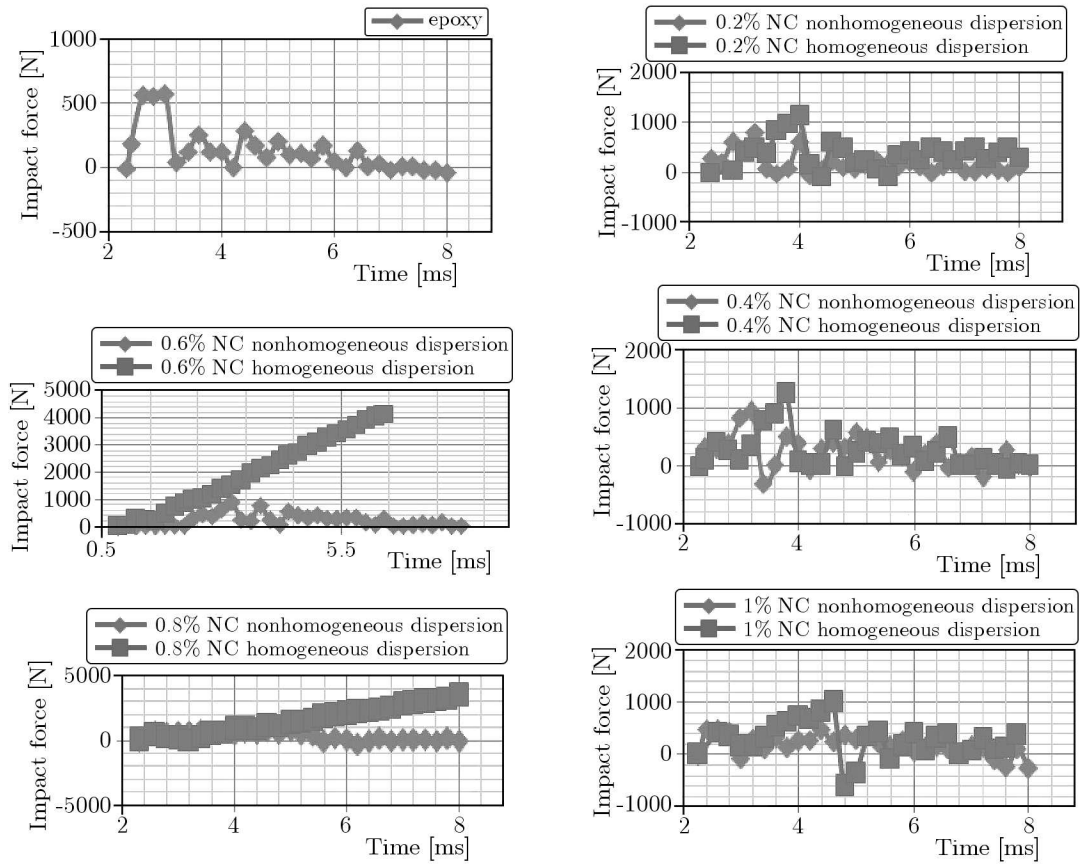


Fig. 3. Impact force vs. time in composites used with different percentages of MWCNTs reinforcement in the epoxy: 0, 0.2, 0.4, 0.6, 0.8, and 1 wt%

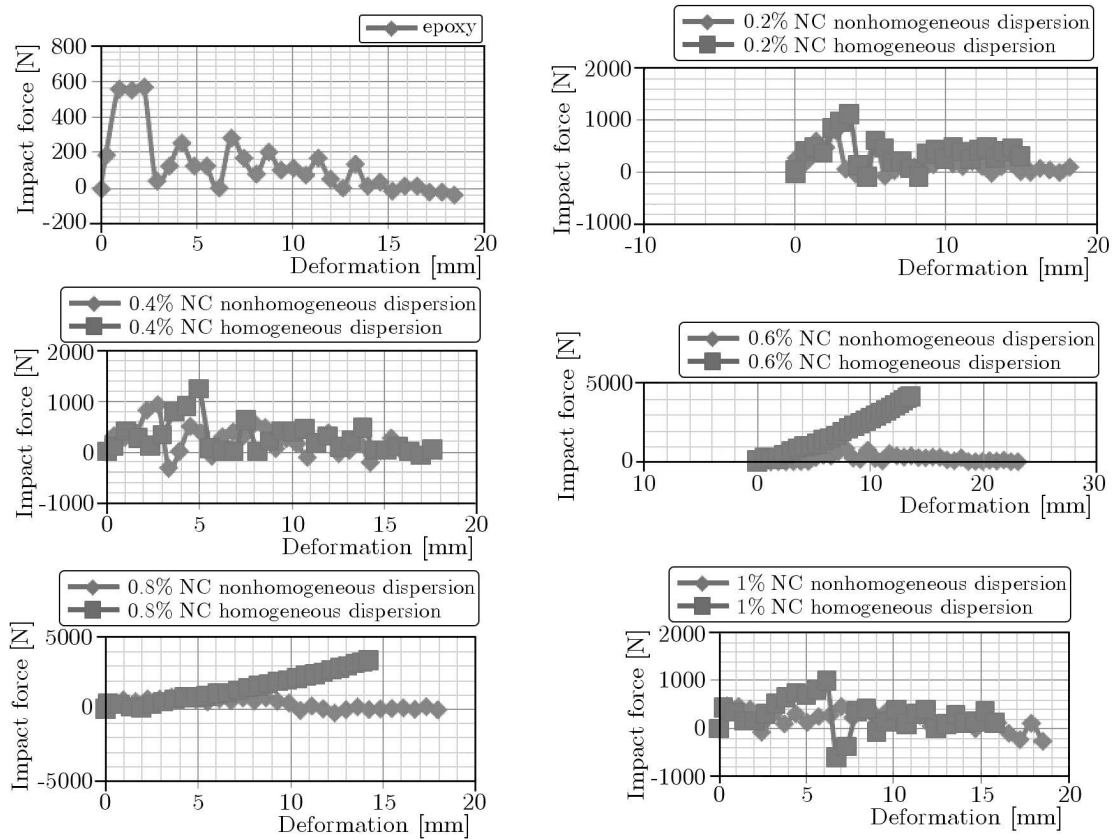


Fig. 4. Impact force vs. deformation of composites with different percentages of MWCNTs reinforcement in the epoxy: 0, 0.2, 0.4, 0.6, 0.8, and 1 wt%

is the main load transfer mechanism for CNT/polymer composites where the interfacial energies normally amount to $\sim 50\text{-}350\text{ mJ/m}$ (Nardin and Schultz, 1993).

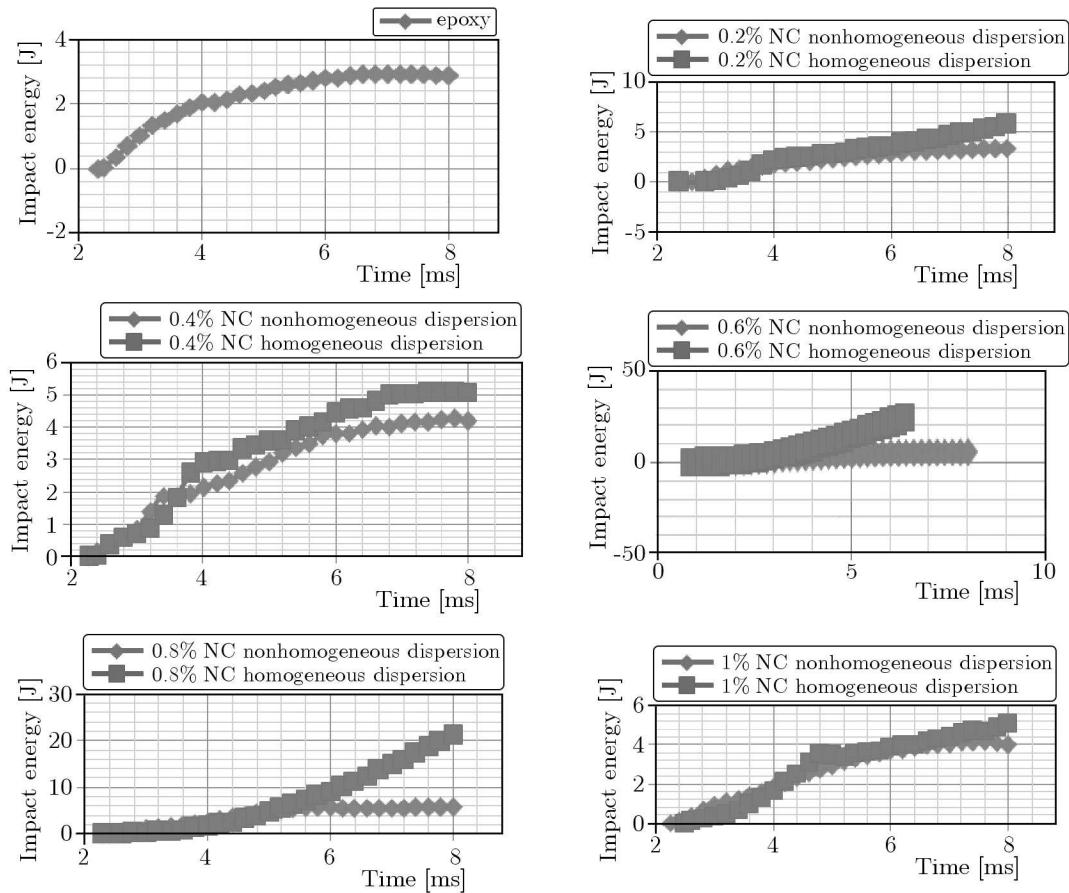


Fig. 5. Impact energy vs. time of composites with different percentages of MWCNTs reinforcement in the epoxy: 0, 0.2, 0.4, 0.6, 0.8, and 1 wt% for two mixing techniques

3.2.4. Impact energy – deformation behavior

Figure 6 shows the impact energy vs. deformation of composites with different percentages of MWCNTs reinforcement in the epoxy: 0, 0.2, 0.4, 0.6, 0.8, and 1 wt% for two mixing techniques. It can be seen that dispersion has a great effect on the force values for all composites which is attributed to the micromechanical interlocking, which can be marginal in CNT/polymer composites if CNTs have atomically smooth surface. The van der Waals bonding is increased by using small size reinforcement and close contact at the interface. CNTs are strong enough and inter-connected or long enough to block the movement of polymer chains (Du *et al.*, 2007; Lu, 1997; Meguid and Sun, 2004).

3.2.5. Effect of multi-wall carbon nanotube percentages on impact properties of the composites

Figure 7 shows a summary of the effect of adding multi-wall carbon nanotube percentages on impact properties: energy, force and deformation of the composites in this study. It can be seen that both energy and force values are increased up to 0.6% multi-wall carbon nanotube then they decrease, which is due to critical CNT content in the matrix. This can be found when the CNT strengthening effect on randomly oriented CNT/polymer composites are investigated. Below this content, the strengthening effect for randomly oriented CNT/polymer composites increases with

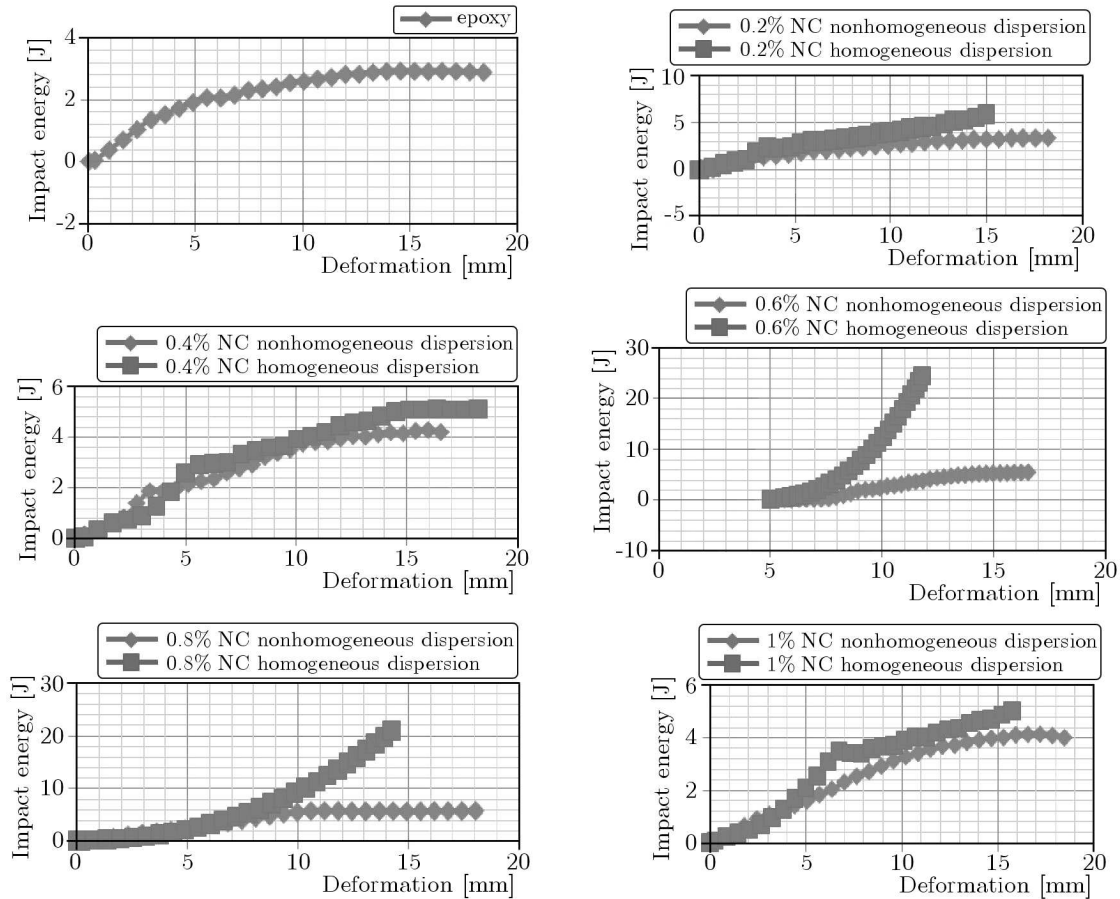


Fig. 6. Impact energy vs. deformation of composites with different percentages of MWCNTs reinforcement in the epoxy: 0, 0.2, 0.4, 0.6, 0.8, and 1 wt% for two mixing techniques

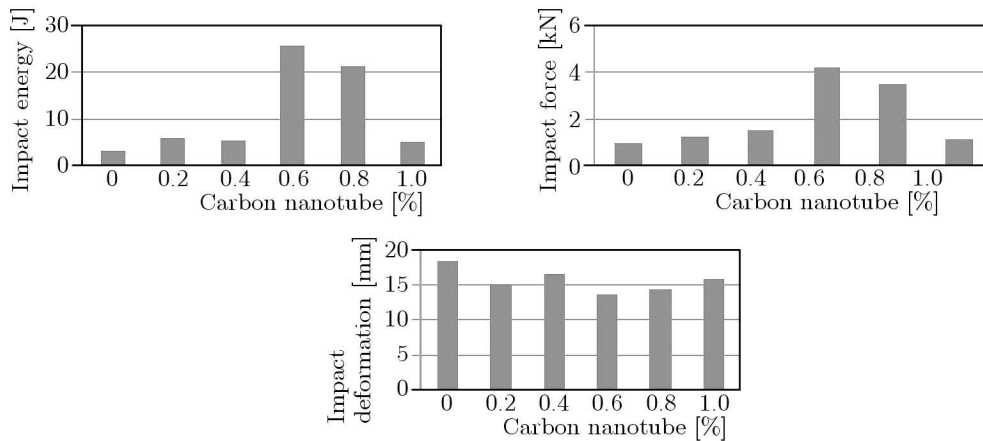


Fig. 7. Effect of adding multi-wall carbon nanotube percentages on impact properties: energy, force and deformation of the studied composites

growing CNT content. Above this content, the strength of CNT/polymer composites decreases. The work of Bai (2003) shows that the critical CNT loading percentage is about 0.5 wt% for CNT/epoxy composites. The same tendency was reported by Meguid and Sun (2004) in their work on the tensile and shear strength of nano-reinforced composite interfaces. The excess of CNTs increases the viscosity of polymers and can also cause some surface of the CNTs not be completely covered by the polymer matrix due to the large specific surface area of the CNTs. This makes uniform dispersion and load transfer more difficult. Moreover, it is very difficult

for high quantity of polymers to intercalate among CNTs when the CNT content becomes high (Du *et al.*, 2007). Impact energy and force increases from 2.9 J and 0.92 kN for the epoxy to its maximum value 25.5 J and 4.16 kN in 0.6% NT composites, and the impact deformation decreases from 18.4 mm for the epoxy to its minimum value 13.6 mm in 0.6% NT composites.

4. Conclusions

- Homogeneous dispersion has a great effect on enhancing mechanical properties of multi-wall carbon nanotube reinforced composites.
- Adding 0.2 wt% of MWCNTs enhances and increases tensile properties to reach their maximum values as follows: tensile stress at maximum load from 28.6 MPa for epoxy resin to 41.4 MPa, maximum load from 2.1 kN for epoxy resin to 2.9 kN, tensile extension at maximum load from 5.04 mm for epoxy resin to 4.2 mm and tensile energy at maximum load from 5.9 J for epoxy resin to 10.6 J.
- The impact energy and force increase from 2.9 J and 0.92 kN for the epoxy to their maximum values of 25.5 J and 4.16 kN, respectively, in 0.6% NT composites. The impact deformation decreases from 18.4 mm for the epoxy to its minimum value 13.6 mm in 0.6% NT composites.

References

1. AL-RAWI K.R., HEDAR A.J., AND OLFATA.MAHMOOD O.A., 2014, Effect different multi-walled carbon nanotubes MWCNTs type on mechanical properties of epoxy resin nanocomposites, *International Journal of Application or Innovation in Engineering and Management (IJAIEM)*, **3**, 8, ISSN 2319-4847
2. AJAYAN P.M., SUHR J., KORATKAR N., 2006, Utilizing interfaces in carbon nanotube reinforced polymer composites for structural damping, *Journal of Materials Science*, **41**, 23, 7824-7829
3. *Annual Book of ASTM Standard*, vol.08.01, 1989
4. BAI J.B., 2003, Evidence of the reinforcement role of CVD multi-walled carbon nanotubes in a polymer matrix, *Carbon*, **41**, 1331-1334
5. BOKOBZA L., 2007, Mechanical properties and interfacial characteristics of carbon nanotube reinforced epoxy, *Journal of Applied Polymer Science*, **48**, 15, 4907
6. CI L., BAI J.-B., 2006, The reinforcement role of carbon nanotubes in epoxy composites with different matrix stiffness, *Composites Science and Technology*, **66**, 599-603
7. COOPER C.A., YOUNG R.J., HALSALL M., 2000, Mechanical properties of carbon nanotube, *Composites Part A: Applied Science and Manufacturing*, **32**, 5, 401
8. DU J.-H., BAI J., CHENG H.-M., 2007, The present status and key problems of carbon nanotube – based polymer composites, *Express Polymer Letters*, **1**, 5, 253-273
9. GOJNY F.H., WICHMANN M.H.G., KÖPKE U., FIEDLER B., SCHULTE K., 2004 Carbon nanotube-reinforced epoxy-composites: enhanced stiffness and fracture toughness at low nanotube content, *Composites Science and Technology*, **64**, 2363-2371
10. ISO 6603-2:2000: International Standard, Plastics – Determination of puncture impact behaviour of rigid plastics – Part 2: Instrumented impact testing Second edition 2000-10-01
11. LU J.P., 1997, Elastic properties of carbon nanotubes and nanoropes, *Physical Review Letters*, **79**, 1297-1300
12. MEGUID S.A., SUN Y., 2004, On the tensile and shear strength of nano-reinforced composite interfaces, *Materials and Design*, **25**, 289-296

13. NARDIN M., SCHULTZ J., 1993, Effect of elastic-moduli and interfacial adhesion energy on the critical fiber aspect ratio in single-fiber composites, *Journal of Materials Science Letters*, **12**, 1245-1247
14. NEMAA A., AL-RAZAQ I.A., KADER E.E., 2014, Characteristics and properties of epoxy/polysulfide composite materials reinforced by carbon nanotubes, *Diyala Journal of Engineering Sciences*, **7**, 3, 106-119, ISSN 1999-8716
15. PARK S.J., JEONG H.J., NAH C., 2004, A study of oxyfluorination of multi-walled carbon nanotubes on mechanical interfacial properties of epoxy matrix nanocomposites, *Materials Science and Engineering A*, **385**, 13-16
16. QI H.J., JOYCE K., BOYCE M.C., 2006, Durometer hardness and the stress-strain behavior of elastomeric materials, *Rubber Chemistry and Technology*, **76**, 2, 419-435
17. SAMAL S.S., 2009, Role of temperature and carbon nanotube reinforcement on epoxy based nanocomposites, *Journal of Minerals and Materials Characterization and Engineering*, **8**, 1, 25-36
18. SMUTISIKHA B., 2010, Dispersion and reinforcing mechanism of carbon nanotubes in epoxy nanocomposites, *Bulletin of Materials Science*, **33**, 1, 27-31
19. WALTER R., FRIEDRICH K., PRIVALKO V., SAVADORI A., 1997, On modulus and fracture toughness of rigid particulate filled high density polyethylene, *The Journal of Adhesion*, **64**

Manuscript received July 20, 2015; accepted for print September 22, 2015

PROFILE DESIGN OF NONCIRCULAR BELT PULLEYS

PIOTR KRAWIEC

*Poznań University of Technology, Chair of Basics of Machine Design, Poznań, Poland
e-mail: piotr.krawiec@put.poznan.pl*

ADAM MARLEWSKI

Poznań University of Technology, Institute of Mathematics, Poznań, Poland; e-mail: adam.marlewski@put.poznan.pl

During design of the envelope of a noncircular belt pulley one should take into account several conditions resulting from kinematics and geometry of the uneven-running strand transmission. Design of proper values of pitches for a belt pulley, which enable good cooperation between the belt pulley and the belt, should be carefully done. In available Polish literature and catalogues offered by belt manufacturers, one can find only detailed dimensions of belts with a trapezoidal profile. Information on other profiles is insufficient for full description of geometrical features of belt pulley teeth as well as to design tools for machining belt pulleys. Manufacturers of belt pulleys and belts give only necessary data to submit a purchase order. The paper presents a digitization process (scanning) of geometry of the envelope of circular belt pulleys with non-standard profiles; this scanning has been done with the application of coordinate measuring machines. The obtained information on geometrical features of tooth profiles has been numerically analysed. As a result of this analysis, the mathematical description has been obtained. Finally, noncircular belt pulleys with different tooth profiles have been designed and manufactured.

Keywords: reverse engineering, tooth profile, numerical modelling

1. Reverse engineering: definition, historical notes and basic techniques

Many definitions of the reverse engineering exist nowadays. In (Eilam, 2005), it is said that it is a process of extracting the knowledge or design information from anything a man made. Thus what makes the difference between the reverse engineering and conventional scientific research is that with the reverse engineering the artifact being investigated is man-made unlike in the scientific research – there is taken into account a natural phenomenon. According to Schreve and Basson (2005), the reverse engineering encompasses the set of activities aiming at (re)discovering the functional, structural and behavioural semantics of a given artifact with the aim of leveraging this information for the efficient usage or adaptation of that artifact or the creation of related artifacts. In (Ülker, 2013), the reverse engineering is defined as a process of duplicating an item, i.e., its functionality and dimensions by physically examining and measuring the existing parts to develop technical data (physical and material characteristics) required for competitive procurement.

In (Eilam, 2005), the reverse engineering is dated back to the era of the industrial revolution, the transition to new manufacturing processes. Then, in the years 1760-1840, new machines entered to the manufactures, and the reverse engineering was a way of an espionage aiming at acquiring information about modern machines, to have a commercial or military advantage of having them. In fact, the espionage reverse engineering was practiced in the Antiquity: Egypt built its power on Assyrian chariots copied around 1600 BC, in the 3rd century BC Romans gained the domination on Mediterranean thanks to capturing Carthaginian quinquiremes. More

recent examples of the analogous activities concern the Soviet piston-engine bomber Tupolev Tu-4 (it was developed in late 1940's as a copy of American Boeing B-29 aircrafts landed in Vladivostok after completing combat missions to the Japanese mainland; see e.g. Fitzpatrick and DiLullo (2006), also for juridical aspects of the reverse engineering) and decoding the Nazi German encryption machine Enigma made by Polish and British cryptographers.

All four above examples concern directly military issues. In industrial practice, the reverse engineering deals with recovering information on objects which disappeared or were damaged (during the standard use or in experiments), with creation and completing of documentation for an existing product or device, with product analysis, interoperability or re-designing.

Nowadays, the reverse engineering is applied in various branches of science and industry, and it is still the most popular in recognition of the machine element shape (e.g. Baier *et al.*, 2012; Boyer and Petitjean, 2000; Kotlyar, 1991; Kumar, 2013; Kumar *et al.*, 2014; Prautzsch *et al.*, 2002; Schreve and Basson, 2005; US Army Reverse Engineering, 2006). Obviously, the reverse engineering comprises fitting, approximation and numerical optimization techniques, so it is located within the applied mathematics. Thus, an reverse engineer can not be unfamiliar with numerical methods and techniques (presented e.g. in Burden and Faires, 1985; Chapra and Canale, 1990). In industrial applications, B-splines (including NURBS and Bézier splines) are dominant representations of shape description – the reverse engineering very often applies these techniques, see. e.g. Hoschek (2001), Sarfraz *et al.* (2013), Weiss (2001), Xia (2014), Yin and Jiang (2010) as well as (Ray and Ray, 2013) and (Tsay and Fong, 2005) where genetic algorithms are in use. It also concerns the search for the description of non-typical gears. Such gears are discussed in many papers in both theoretical and implementation aspects – see e.g. Bär (2009), Krawiec and Marlewski (2011), Laczik (2008), Liu and Chen (2008), Liu *et al.* (2013), Lovasz *et al.* (2007), Telea (2012).

In this paper, we aim at simplifying and efficient describing the shape of a tooth which is known by a point cloud only (the coordinates of these points are obtained with the digitalization done by the CMM – coordinate measuring machine, see, e.g., Chajda *et al.* (2008)). The tooth shape is described by circles (determined by carefully chosen points) and an appropriate parabola which joins the circles smoothly. This parabola can be presented as a Bézier arc (so it is the graph of a Bernstein polynomial; these polynomials were found in 1912 and are still investigated, see e.g. Farouki (2012), Pobegailo (2014), Prautzsch *et al.* (2002)). This type of the description can not be produced by the existing software (such as Rhinoceros from Robert McNeel & Associates, ZAR products from HEXAGON Software, EXCEL-LENT from Excel Gear, Inc., MITCalc – Worm Gear Calculation 1.16, GearTeq from Camnetics Inc., GearEngineer from DEPO).

2. Reverse engineering in design of belt pulleys with a noncircular envelope

Information on geometrical features of belt pulleys with non-standard profiles can be achieved by methods of *reverse engineering*. In general, these methods consist of numerical discretization of elements or machines, and conversion of the obtained graphical information (points or surfaces) into two or three dimensional models (Marciniec *et al.*, 2010). For the described example, the process of reverse engineering consisted of four stages:

- scanning of the envelope profile of a circular belt pulley with the application of the CMM,
- numerical analysis of the obtained results,
- designing of the tooth profile geometry of belt pulleys,
- manufacturing of a prototype of the noncircular belt pulley.

During the measurements, the belt pulley was mounted on the table of the CMM, and the measuring head was moved according to the assigned parameters. An essential restriction of this

method is the possibility to scan cylindrical surfaces which are circumscribed for angles between 0° and 45° . However, for the presented task, this range was sufficient owing to the repeatability of belt pulley profiles. As a result of the measurement, the geometrical features of the belt pulley were obtained in form of the Cartesian coordinates. The geometrical centre of the belt pulley was taken as an origin of the coordinate system. This fact has improved the design process of the geometry of noncircular belt pulleys during the next stage.

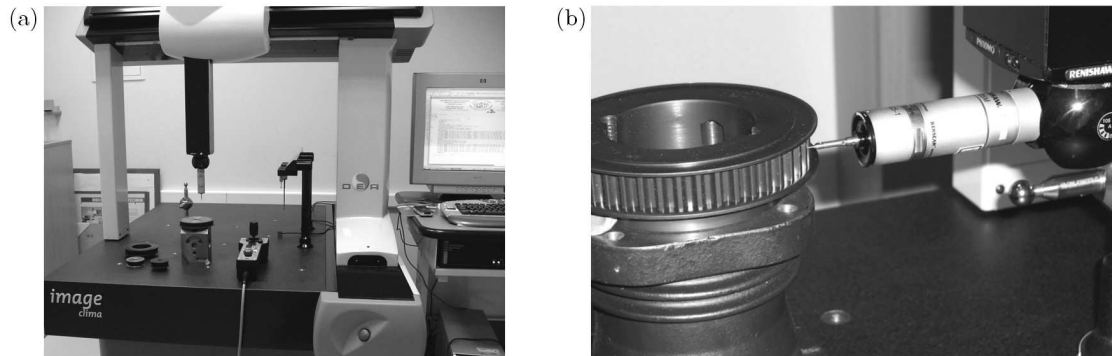


Fig. 1. Measurement of geometrical features of non-standard belt pulleys: (a) test stand, (b) belt pulley measurement

The measurement of belt pulley profiles was performed by the CMM CNC DEA Global Image Clima (Fig. 1). This machine was placed in an air-conditioned room, and this fact was essential to ensure the correctness of the measuring procedure. The measurement consisted of a continuous scanning with the use of a gauge plunger. Sampling density was equal to 100 points/mm, scanning speed – 5 mm/s, ball diameter of the gauge plunger SP 25M Reinshaw was equal to 1 mm. The measurements were performed for two variants. The first one consisted of automatic application of the “offset” function – it took into account the ball dimension which was placed at the end of the gauge plunger. In application of the second variant, a fragment of the envelope profile of the belt pulley was obtained and the correction due to the ball radius was taken. The scanning process allowed one to get a set of coordinates written in a txt file. On the basis of these coordinates, the profile of the half of the belt pulley tooth was determined. The analysis of curvatures of the obtained profile allowed one to restrict the number of coordinates which are describing the profile to the value 36 (Table 1).

Table 1. Points coordinates accepted to the design of the tooth profile

j	x_j	y_j	j	x_j	y_j	j	x_j	y_j
1	-7.7752	55.1300	2	-7.5779	55.1470	3	-7.4664	55.1457
4	-7.4419	55.1429	5	-7.3921	55.1449	6	-7.3104	55.1346
7	-7.2542	55.1288	8	-7.1365	55.1013	9	-7.0037	55.0567
10	-6.9057	55.0085	11	-6.7908	54.9337	12	-6.7082	54.8588
13	-6.6734	54.8090	14	-6.6342	54.7239	15	-6.5970	54.6489
16	-6.5699	54.5646	17	-6.5449	54.4684	18	-6.5250	54.3727
19	-6.4728	54.1592	20	-6.4334	53.9815	21	-6.3991	53.8119
22	-6.3340	53.6141	23	-6.3032	53.5276	24	-6.2763	53.4198
25	-6.2224	53.2729	26	-6.1293	53.1231	27	-6.0630	53.0405
28	-6.0164	52.8889	29	-5.8621	52.6834	30	-5.6769	52.5085
31	-5.3631	52.2537	32	-5.0184	52.0408	33	-4.6800	51.8986
34	-4.1830	51.7606	35	-3.9972	51.7398	36	-3.7887	51.7423

The obtained profile of the half of the tooth is presented in Fig. 2. This figure shows a square with the coordinates $\langle -8, -3 \rangle \times \langle 51, 56 \rangle$ and the points obtained as a result of the scanning process. Five points which have a significant impact on the design process of the tooth profile are distinguished by indexes (1, 10, 20, 34, 36).

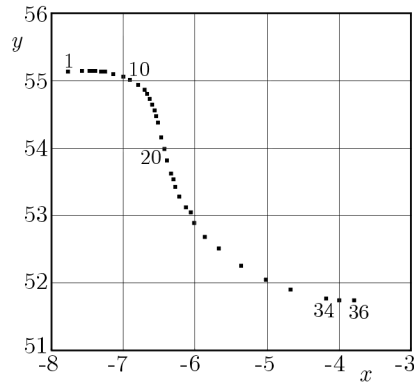


Fig. 2. Points describing the half of the tooth profile of the belt pulley

3. Numerical determination of the tooth profile

The points obtained during the scanning process are called measuring points, and the points which are laying on the nominal tooth profile are called nominal points.

The presented task consists in determination of mathematical description of the edge of the perfect tooth – this description should be relatively simple. According to the accepted criterion of the simplicity, the description should consist of a small number of equations and every equation should describe a “simple” curve. The simple curve is a curve which can be simply described on the basis of mathematical notation (without the application of any advanced computer programs), e.g. low degree polynomial curves (straight line, parabola and n -degree polynomial curves where n is a small natural number – it is generally accepted that $n \leq 4$), second degree curves (circle, ellipse and hyperbola), spirals (logarithmic spiral, spiral of Archimedes) and other curves applied in mechanical engineering (e.g., cycloid, cardioid). The next research task is to find and select the so-called transition curves such as Cornu’s spiral (also called as a clothoid). These curves determine a standard way of transition from a circular arc to a straight segment where the curve continuity is kept at the transition point.

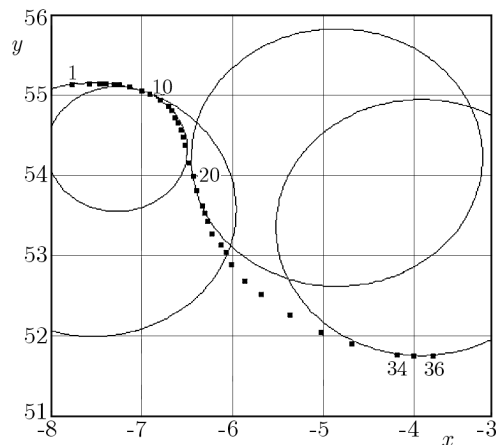


Fig. 3. Four circles which are drawn through three successive measuring points: 1–2–3, 10–11–12, 20–21–22 and 34–35–36

Taking into account the descriptions presented in literature concerning the analysis of the measurement results of scanning (Filipowski, 2002; Filipowski *et al.*, 2005) and information from manufacturers of belt pulleys, we decided to approximate the analysed distribution of points by arcs of tangent circles or polynomial curves of a low degree (line segments) in the case when the tangency could not be modelled. Within the framework of the preliminary analysis, the circles were drawn through every three successive measuring points. The examples of these circles are presented in Fig. 3.

On the basis of the analysis of circles position and the measuring points, we can accept that circle 10–11–12, i.e. drawn through the measuring point No. 10 and two successive points, is a good approximation of the shape in its vicinity (in the range from point No. 8 to point No. 18). Circle 34–35–36 is a satisfying approximation of the searched shape only in the vicinity of these points. Figure 4 presents nine circles which are drawn through three successive measuring points.

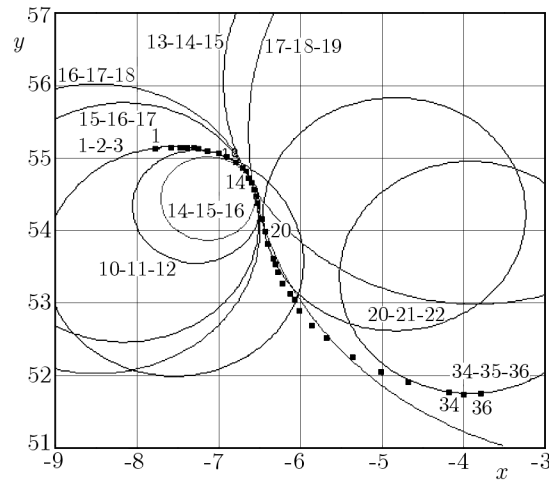


Fig. 4. Nine exemplary circles which are drawn through three successive measuring points

Radii of all 34 circles (circle No. k passes through the points $k, k + 1, k + 2$, where $k = 1, 2, \dots, 34$) are presented in Fig. 5. We can see that the variation of the radius r has not any visible monotonicity (interval monotonicity). The interval monotonicity guarantees the fulfillment of the condition of smooth transition between elements of the tooth profile.

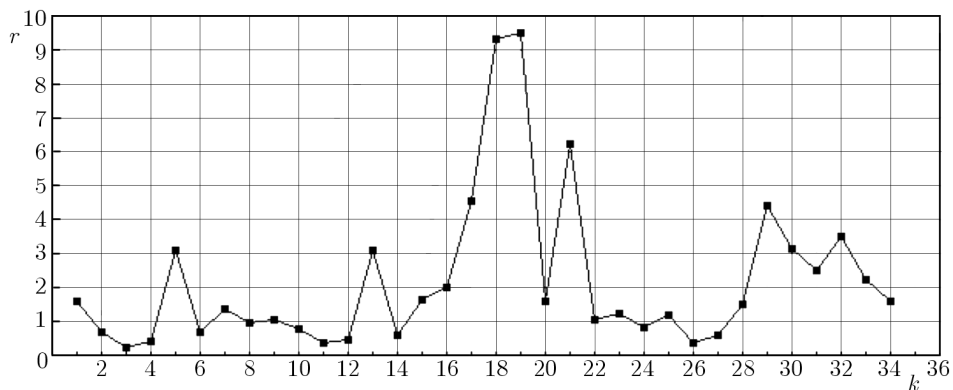


Fig. 5. Radii r of circles No. k for $k = 1, 2, \dots, 34$. On the basis of Fig. 2, we can conclude that the radius value r should be equal to 0 for point No. 16 or its vicinity; in the case of a perfect profile (when it consists of two circles) the radius values r should be constant for k from 1 to ca. 15 and (higher than the previous values) for k from ca. 17 to 34

The interval monotonicity characterizes circles (radius r is constant for any three points laying on the circle), straight lines ($r = 0$), parabolas (these curves have only one point where the

increasing function becomes the decreasing function or vice versa), etc. For spirals, the radius r is constantly increasing (or constantly decreasing), and for a standard cycloid, the radius r is decreasing from the infinity first (it is decreasing to the value 0, but it does not achieve it) and next it is increasing to the infinity. The lack of the monotonicity is not a result of the reading quality of the results from the CMM (monotonicity disturbance caused by work precision of the CMM is not high – in practice this disturbance is negligible and is a part of the so-called device error), but is a result of teeth manufacturing. Due to the lack of the monotonicity, the circles have been drawn through two nonadjacent points. An idea of this approach is visualized in Fig. 6 generated by points

$$A = (6, 7) \quad B = (7, 6.82842) \quad S = (10, 4.21252) \quad T = (10.6832, 4.10557)$$

The configuration of these points is intentionally similar to that exhibiting by measured 36 points (numbered from 1 to 36, see Fig. 3). They determine two circles which are tangent at the point M . The centres of the these circles are

$$L = (6, 4) \quad \text{and} \quad R = (10.6832, 6.34164)$$

and radii of these circles are equal to 3 and $\sqrt{5} = 2.23606$, respectively (all calculations have been performed exactly with the assistance of program Derive 5 from Texas Instruments, Inc., and the results have been then rounded to six significant digits).

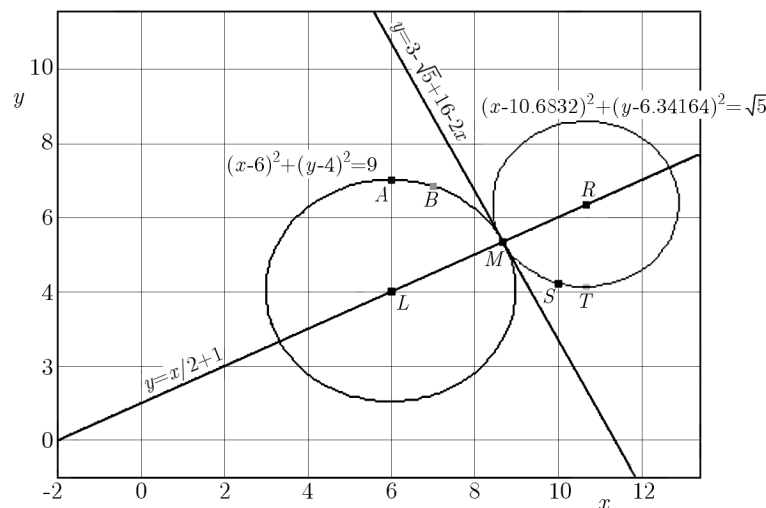


Fig. 6. Two tangent circles; the left circle is drawn through points A and B , and the right one passes through points S and T

The left circle has its highest point A , and the point T is the lowest point of the right circle.

The application of this method does not allow one to find the tangent circles where one circle is drawn through the selected points from the beginning of the list (e.g. through points No. 1 and 10) and the other circle is drawn through the end points (e.g. points No. 20 and 36). The tangent circles are not found either for the case when measuring points No. 1 and 2 have not been taken into considerations. The reason of this practice is the following observation: the ordinates of these two points are smaller than the ordinates of measuring point No. 3, so (by the assumption: the reading from the CMM does not produce any significant errors) these points lay on the other side of the tooth profile than the analysed one. These points are presented in Table 1 with the measurement results, because the starting point and the end point of the reading have been imprecisely indicated.

After successive searching, it turned out that the best fitting for the end points is the circle with the lowest point No. 36, and it goes through point No. 26. The equation of this circle is

$$(x + 3.7887)^2 + (y - 54.4144)^2 = 7.14017$$

and, as seen in Fig. 7, on this circle the points numbered as $P_{20}, P_{21}, \dots, P_{36}$ sit up to a high accuracy. The tangent to the circle (see Fig. 8) at the point P_{20} has the equation

$$y = 14.6779 - 6.10928x$$

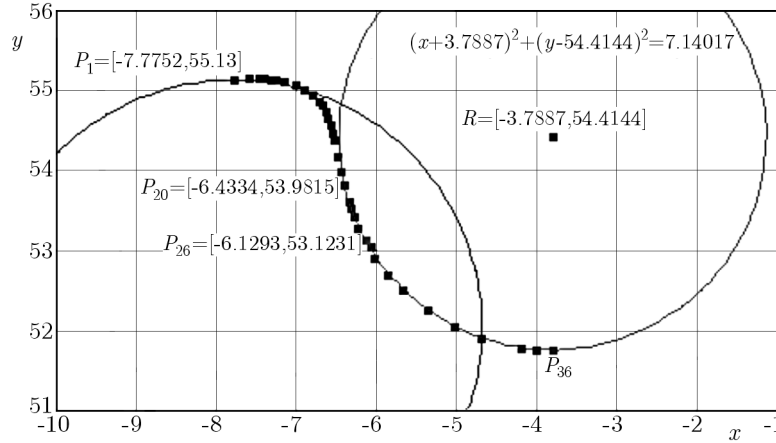


Fig. 7. Circle with the lowest point P_{36} which is drawn through the point P_{26}

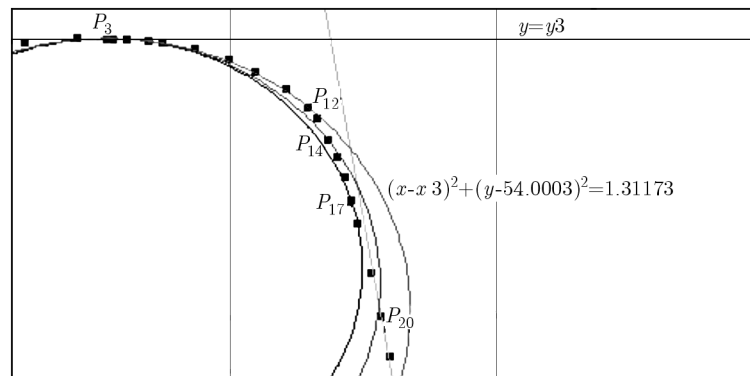


Fig. 8. Tangent line at the point P_{20} and three circles for which the highest point is P_3 . On the left side of the point P_3 , one can see points No. 1 and 2, and these ones are not taken into account

Searching for a circle with the highest point P_3 and a circle which passes really close to successive points is finished when the circle is drawn through the point P_{12} . Figure 8 shows this circle and two other circles which pass through points No. 14 and No. 17, respectively. It is clearly seen that these two other circles are worse approximations with respect to points which are close to the point P_3 than the circle which goes through the point P_{12} . This circle, passing through P_3 and P_{12} , is covered by the equation

$$(x + 7.4664)^2 + (y - 54.0003)^2 = 1.31173$$

and the line which at P_{12} is tangential to this circle has the equation

$$y = 48.9341 - 0.883171x$$

The curve between the points P_{12} and P_{20} is found by an inverse search for the Bernstein polynomial B_2 of degree 2. Here, we know points the wanted polynomial passes through (the points P_{12} and P_{20}) and slopes of tangent lines at these points (respectively -0.883171 and -6.10928), so we can find coefficients c_0, c_1 and c_2 of the polynomial

$$x \rightarrow B_2(t) := c_0t^2 + 2c_1t(1 - t) + c_2(1 - t)^2$$

where the variable

$$t = 3.63901x + 24.4112$$

is introduced in order to transform the interval $\langle x_{12}, x_{20} \rangle = \langle -6.7082, -6.4334 \rangle$ in the standard interval $\langle 0, 1 \rangle$ which is used to define the Bernstein polynomial B_2 . It results with the equation

$$y = -7.18927x^2 - 97.6709x - 276.821$$

It describes the parabola which joins smoothly (i.e. with continuous derivatives at points P_{12} and P_{20}) the arc P_3P_{12} of the left circle and the arc $P_{20}P_{36}$ of the right circle.

As we see, the application the Bernstein interpolation (let us call so what we did: we joined two circular arcs by a parabola arc fitted in form of the Bernstein polynomial) resulted with a polynomial curve (of the lowest possible degree here, 2). This is a non typical use of the Bernstein polynomials (by their nature they serve to approximate points, and not to interpolate them). A standard procedure to get a curve connecting two other curves is to deal with an Hermite interpolating polynomial or with a spline function; in our case they have to be found for the curvilinear segment with ends in P_{12} and P_{20} , and we obtain a polynomial of the third degree. Thus, our non-typical Bernstein interpolation produced a polynomial of a lower degree (2); it means we obtained a description we looked for, namely the one of degree 2 only. It is important because the lower degree the less sensitivity to data, and the data are measured quantities (so they are always approximate values) as well as to the roundings executed in both the calculation process and the final form (here it embraces 6 significant digits). Therefore, the arc of the polynomial curve of the third degree satisfies the imposed requirements worse than the polynomial curve $y = B_2(x)$ – especially in relation to the value y_{12} . The obtained approximation satisfies (even in excess) the limits of manufacturing tolerances for the belt pulley teeth.

To verify the correctness of the conducted scanning process, numerical data processing and CAD modelling, a few of sets of noncircular belt pulleys were manufactured. Due to the low manufacturing costs and relatively high manufacturing accuracy, the FDM (*fused deposition modelling*) method of *rapid prototyping* was applied (Fig. 9).



Fig. 9. Noncircular belt pulleys with nonstandard tooth profiles manufactured with the use of the rapid prototyping method

The manufactured belt pulleys were subjected to metrological analysis in the scope of geometrical features. The assessment of the correctness of the coupling between the belt and the belt pulleys was also done with the test stand. The results of these analyses show that the presented methodology can be applied with success to determine tooth profiles which are not defined in standards.

4. Summary

The reverse engineering presented in this paper starts with a cloud of points laying in the plane, the coordinates of these points are obtained by the CMM (coordinate measuring machine), and aims at producing a simple mathematical description of the object points. In the reported case, the digitalized points are taken from a recently produced belt pulley which has not any geometrical specification. The obtained description consists of three equations: for the arcs of two circles and the parabola which smoothly joins them. This description is worked out via examination of several other ones, and the paper shows how the final result has been obtained. This method serves as an exemplary approach to the reverse engineering which can be applied in analogous situations when, due to the definition of the shape, standard procedures are not applicable or these ones give formulas which do not fulfil the requirement for the simplicity. A positive result of the discussed procedure confirms that the reverse engineering can be successfully used to retrieve, as well as to design, the teeth geometry of non-typical gears. It also shows the specificity of finding of an appropriate mathematical description; this process is inventory (it has to be carefully fitted to the point cloud at hand) and time-consuming, it is troublesome to execute it with no computer assistance. It also suggests that it is worthy to undertake research on the automatization of forming of the mathematical description of profiles, and such a description is necessary for numerical control of producing machines.

References

1. BAIER M., BOGUICKI R., BAIER A., 2012, Reverse engineering as a tool in process of gear reconstruction, *Selected Engineering Problems*, **3**, 9-14
2. BÄR G.F., 2009, Two synthesis methods for non-circular cylindrical gears, *Journal of Geometry and Graphics*, **13**, 1, 101-112
3. BOYER E., PETITJEAN S., 2000, Curve and surface reconstruction from regular and non-regular point sets, *Proceedings of Conference on Computer Vision and Pattern Recognition*, Hilton Head Island, **2**, 659-665
4. BURDEN R.L., FAIRES J.D., 1985, *Numerical Analysis*, PWS Publishers, Boston
5. CHAPRA S.C., CANALE R.P., 1990, *Numerical Methods for Engineers*, McGraw Hill International Editions
6. CHAJDA J., ET AL., 2008, Coordinate measurement of complicated parameters like roundness, cylindricity, gear teeth or free-form surface, *8 International Conference of Advanced Manufacturing Operations Kranevo*, 225-231
7. EILAM E., 2005, *Reversing – Secrets of Reverse Engineering*, John Wiley & Sons
8. FAROUKI R.T., 2012, The Bernstein polynomial basis: a centennial retrospective, *Computer Aided Geometric Design*, **29**, 379-419
9. FITZPATRICK W.M., DiLULLO S.A., 2006, Attack of the clones: reverse engineering, R&D and the law, *Competition Forum*, **4**, 2, 501-515
10. FILIPOWSKI R., 2002, *Generating and Processing of Offset Curves and Machine Element Surfaces with the Application of CAD/CAM* (in Polish), Warsaw, Publishing House of Poznan University of Technology
11. FILIPOWSKI R., DĄBROWSKI L., ZAWORA J., 2005, New method of offset points generation for scanning with CMM (in Polish), *Pomiary Automatyka Kontrola*, **11**, 5-8
12. HOSCHEK J., 2001, Mathematical methods in reverse engineering, [In:] *Multivariate Approximation and Applications*, N. Dyn, D. Leviatan, D. Levin, A. Pinkus (Edit.), Cambridge University Press, 252-284

13. KOTLYAR Y., 1991, Gear fundamentals reverse engineering, *Gear Technology*, **7**, 34-38
14. KRAWIEC P., MARLEWSKI A., 2011, Spline description of not typical gears for belt transmissions, *Journal of Theoretical and Applied Mechanics*, **49**, 2, 355-367
15. KUMAR B.R., 2013, Polygonal approximation and scale-space analysis of closed digital curves, *Apple Academic Press*, 388
16. KUMAR A., JAIN P.K., PATHAK P.M., 2014, Curve reconstruction of digitized surface using K-means algorithm, *Procedia Engineering*, **69**, 544-549
17. LACZIK B., 2008, *Design and Manufacturing of Non-circular Gears by Given Transfer Function*, HEXAGON Industriesoftware GmbH <http://www.hexagon.de/pdf/noncgear.pdf>; also Laczik B. – *Analytic Design of Non-circular Gears by Maple*, <http://www.maplesoft.com/applications/view.aspx?SID=6885&view=html>
18. LIU G., CHANG K., LIU Z., 2013, Reverse engineering of machine-tool settings with modified roll for spiral bevel pinions, *Chinese Journal of Mechanical Engineering*, **26**, 3, 573-584
19. LIU J., CHEN Y., 2008, A design for the pitch curve of noncircular gears with function generation, *International MultiConference of Engineers and Computer Scientists*, **II**, 1681-1686
20. LOVASZ E.C., PERJU D., MODLER K.-H., MARGINEANU D.T., ZABAVA E.S., 2007, Non-circular gear wheels in the geared-linkages mechanisms, *12th IFToMM World Congress*, Besançon, paper A394, p. 6
21. MARCINIEC A., BOROWIAK M., DZIUBEK K., 2010, Reconstruction of gear geometry with application of CMM and CAD system (in Polish), *Pomiary Automatyka Kontrola*, **56**, 1, 60-61
22. POBEGAILO A.P., 2014, Interpolating Bézier spline curves with local control, *Buletinul Academiei de Stiinta a Republicii Moldova Moldova, Matematica*, **75**, 2, 18-28
23. PRAUTZSCH H., BOEHM W., PALUSZNY M., 2002, *Bézier- and B-spline Techniques*, Springer-Verlag, 304
24. RAY K.S., RAY B.K., 2013, Polygonal approximation of digital curve based on reverse engineering concept, *International Journal of Image and Graphics*, **13**, 1350017
25. SARFRAZ M., IRSHAD M., HUSSAIN M.Z., 2013, Reverse engineering of planar objects using GAs, *Sains Malaysiana*, **48**, 2, 1167-79
26. SCHREVE K., BASSON A.H., 2005, Edge detection in reverse engineering using a scanning approach. Part I: Scanning algorithm, *International Journal of Advanced Manufacturing Technology*, **26**, 1048-1054
27. TELEA A.C., 2012, *Reversing. Reverse Engineering. Recent Advances and Applications*, In Tech
28. TSAY M., FONG Z., 2005, Study on the generalized mathematical model of noncircular gears, *Mathematical and Computer Modelling*, **41**, 555-569
29. ÜLKER E., 2013, B-spline curve approximation using Pareto envelope-based selection algorithm – PESA, *International Journal of Computer and Communication Engineering*, **2**, 1, 60-63
30. *US Army Reverse Engineering*, 2006, Military Handbook MIL-HDBK-115A
31. WEISS V., 2001, Reverse engineering free-form shapes, PhD dissertation presented at University of Technology and Economics, Budapest, 106
32. XIA Z., 2014, Application of reverse engineering based on computer in product design, *International Journal of Multimedia and Ubiquitous Engineering*, **9**, 5, 343-354
33. YIN Z., JIANG S., 2010, Automatic segmentation and approximation of digitized data for reverse engineering, *International Journal of Production Research*, **41**, 13, 3045-58

EFFECTS OF PIEZOELECTRICITY ON BULK WAVES IN MONOCLINIC PORO-ELASTIC MATERIALS

VISHAKHA GUPTA

Dyal Singh College, Department of Mathematics, Karnal, India

ANIL K. VASHISHTH

Kurukshetra University, Department of Mathematics, Kurukshetra, India

e-mail: vi_shu85@yahoo.co.in

Piezoelectric materials are materials which produce electric field when stress is applied and get strained when electric field is applied. Piezoelectric materials are acting as very important functional components in sonar projectors, fluid monitors, pulse generators and surface acoustic wave devices. Wave propagation in porous piezoelectric material having crystal symmetry 2 is studied analytically. The Christoffel equation is derived. The phase velocities of propagation of all these waves are described in terms of complex wave velocities. The effects of phase direction, porosity, wave frequency and piezoelectric interaction on the phase velocities are studied numerically for a particular model.

Keywords: piezoelectricity, porous, monoclinic

1. Introduction

Piezoelectric materials have widespread applications in many branches of science and technology such as electronics, navigation, mechatronics and micro-system technology. In recent years, piezoelectric materials have been integrated with structural systems to form a class of smart structures and embedded as layers or fibers into multifunctional composites. The survey of literature can be found in many related texts and books (Arnau, 2008; Auld, 1973). A short survey of the piezoelectric wave propagation and resonance were described by Auld (1981). Both, theoretical and experimental studies on wave propagation in piezoelectric materials have attracted attention of scientists and engineers during the last two decades. Nayfeh and Chien (1992) made a study on ultrasonic wave interaction with fluid-loaded anisotropic piezoelectric substrates and derived an analytical expression for reflection and transmission coefficients for monoclinic materials. Zinchuk and Podlipenents (2001) obtained dispersion equations for the acousto-electric Rayleigh wave in a periodic layer piezoelectric half-space in a study for a 6 mm crystal class.

Porous piezoelectric materials (PPM) are widely used for applications such as low frequency hydrophones, miniature, accelerometers, vibratory sensors and contact microphones. Experimental studies (Qian *et al.*, 2004; Praveenkumar *et al.*, 2005; Piazza *et al.*, 2006) related to properties of porous piezoelectric materials and influence of porosity on its properties have been made by different authors. Gupta and Venkatesh (2006) developed a finite element model to study the effect of porosity on the electromechanical response of piezoelectric materials. Craciun *et al.* (1998) and Gomez *et al.* (2000) made an experimental study on wave propagation in porous piezoceramics. Vashishth and Gupta (2009a) derived constitutive equations for anisotropic porous piezoelectric materials. Wave propagation in transversely isotropic porous piezoelectric materials was studied analytically and numerically by Vashishth and Gupta (2009b).

In this paper, the wave propagation in porous piezoelectric materials having crystal symmetry 2 is studied. The constitutive equations are formulated for porous piezoelectric materials

having crystal symmetry 2. The Christoffel equation is derived analytically and its solutions are obtained numerically. The variation of phase velocities with the direction of propagation, porosity, piezoelectricity and viscosity is studied numerically for a particular model.

2. Governing equations and their solution

The constitutive equations for anisotropic porous piezoelectric materials (Vashishth and Gupta, 2009a) are

$$\begin{aligned} \sigma_{ij} &= c_{ijkl}\varepsilon_{kl} + m_{ij}\varepsilon^* + e_{kij}\phi_{,k} + \zeta_{kij}\phi_{,k}^* & \sigma^* &= m_{ij}\varepsilon_{ij} + R\varepsilon^* + \tilde{\zeta}_i\phi_{,i} + e_i^*\phi_{,i}^* \\ D_i &= e_{ijk}\varepsilon_{jk} + \tilde{\zeta}_i\varepsilon^* - \xi_{ij}\phi_{,j} - A_{ij}\phi_{,j}^* & D_i^* &= \zeta_{ijk}\varepsilon_{jk} + e_i^*\varepsilon^* - A_{ij}\phi_{,j} - \xi_{ij}^*\phi_{,j}^* \end{aligned} \quad (2.1)$$

where σ_{ij}/σ^* are the stress components acting on the solid/fluid phase of a porous aggregate. $\varepsilon_{ij}/\varepsilon^*$ are strain tensor components for the solid/fluid phase, respectively. ϕ/ϕ^* and D_i/D_i^* are electric potentials and electric displacement components for the solid/fluid phase of the porous bulk material, respectively. c_{ijkl} are elastic stiffness constants. The elastic constant R measures the pressure to be exerted on the fluid to push its unit volume into the porous matrix. e_{kij}/e_i^* , ξ_{ij}/ξ_{ij}^* are piezoelectric and dielectric constants for the solid/fluid phase, respectively. m_{ij} ; ζ_{kij} , $\tilde{\zeta}_i$; A_{ij} are the parameters which take into account the elastic; piezoelectric; dielectric coupling between the two phases of the porous aggregate.

The coefficient matrix for porous piezoelectric materials, having crystal symmetry 2 (Auld, 1973) is

$$\begin{bmatrix} c_{11} & c_{12} & c_{13} & 0 & 0 & c_{16} & m_{11} & 0 & 0 & -e_{31} & 0 & 0 & -\zeta_{31} \\ c_{12} & c_{22} & c_{23} & 0 & 0 & c_{26} & m_{11} & 0 & 0 & -e_{32} & 0 & 0 & -\zeta_{32} \\ c_{13} & c_{23} & c_{33} & 0 & 0 & c_{36} & m_{33} & 0 & 0 & -e_{33} & 0 & 0 & -\zeta_{33} \\ 0 & 0 & 0 & c_{44} & c_{45} & 0 & 0 & -e_{14} & -e_{24} & 0 & -\zeta_{14} & -\zeta_{24} & 0 \\ 0 & 0 & 0 & c_{45} & c_{55} & 0 & 0 & -e_{15} & -e_{25} & 0 & -\zeta_{15} & -\zeta_{25} & 0 \\ 0 & 0 & 0 & 0 & 0 & c_{66} & m_{12} & 0 & 0 & -e_{36} & 0 & 0 & -\zeta_{36} \\ m_{11} & m_{11} & m_{33} & 0 & 0 & m_{12} & R & 0 & 0 & -\tilde{\zeta}_3 & 0 & 0 & -e_3^* \\ 0 & 0 & 0 & e_{14} & e_{15} & 0 & 0 & \xi_{11} & \xi_{12} & 0 & A_{11} & A_{12} & 0 \\ 0 & 0 & 0 & e_{24} & e_{25} & 0 & 0 & \xi_{12} & \xi_{22} & 0 & A_{12} & A_{22} & 0 \\ e_{31} & e_{32} & e_{33} & 0 & 0 & e_{36} & \tilde{\zeta}_3 & 0 & 0 & \xi_{33} & 0 & 0 & A_{33} \\ 0 & 0 & 0 & \zeta_{14} & \zeta_{15} & 0 & 0 & A_{11} & A_{12} & 0 & \xi_{11}^* & \xi_{12}^* & 0 \\ 0 & 0 & 0 & \zeta_{24} & \zeta_{25} & 0 & 0 & A_{12} & A_{22} & 0 & \xi_{12}^* & \xi_{22}^* & 0 \\ \zeta_{31} & \zeta_{32} & \zeta_{33} & 0 & 0 & 0 & e_3^* & 0 & 0 & A_{33} & 0 & 0 & \xi_{33}^* \end{bmatrix} \quad (2.2)$$

The equations of motion for a fluid-saturated porous piezoelectric medium, in the absence of body forces, are (Vashishth and Gupta, 2009a)

$$\begin{aligned} \sigma_{ij,j} &= \rho_{11}\ddot{u}_j + \rho_{12}\ddot{U}_j^* & \sigma_{,i}^* &= \rho_{12}\ddot{u}_j + \rho_{22}\ddot{U}_j^* \\ D_{i,i} &= 0 & D_{,i}^* &= 0 \end{aligned} \quad (2.3)$$

where u_i/U_i^* are the components of mechanical displacement for the solid/fluid phase of the porous aggregate. ρ_{11} , ρ_{12} and ρ_{22} are dynamical coefficients.

For the propagation of plane waves, let us assume that

$$\begin{aligned} u_j &= B_j \exp[i\omega(p_k x_k - t)] & U_j^* &= F_j \exp[i\omega(p_k x_k - t)] \\ \phi &= G \exp[i\omega(p_k x_k - t)] & \phi^* &= H \exp[i\omega(p_k x_k - t)] \end{aligned} \quad (2.4)$$

where $i = \sqrt{-1}$, p_k are the components of the slowness vector \mathbf{p} . These can be written as $p_k = n_k/V$ in terms of phase velocity v , where n_k are components of the unit vector normal to the wave surface. ω is the circular frequency of waves and t is the time. Making use of equations (2.1)-(2.4), we obtain a system of equations in unknowns B_j , F_j ($j = 1, 2, 3$), G and H , which is given as follows

$$\begin{aligned}
& (c_{11}n_1^2 + c_{55}n_3^2 - \rho_{11}v^2)B_1 + (c_{16}n_1^2 + c_{45}n_3^2)B_2 + [(c_{13} + c_{55})n_1n_3]B_3 \\
& \quad + (m_{11}n_1^2 - \rho_{12}v^2)F_1 + (m_{11}n_1n_3)F_3 + [(e_{31} + e_{15})n_1n_3]G + [(\zeta_{31} + \zeta_{15})n_1n_3]H = 0 \\
& (c_{16}n_1^2 + c_{45}n_3^2)B_1 + (c_{66}n_1^2 + c_{44}n_3^2 - \rho_{11}v^2)B_2 + [(c_{36} + c_{45})n_1n_3]B_3 + (m_{12}n_1^2)F_1 \\
& \quad + (m_{12}n_1n_3)F_3 + [(e_{36} + e_{14})n_1n_3]G + [(\zeta_{36} + \zeta_{14})n_1n_3]H = 0 \\
& [(c_{13} + c_{55})n_1n_3]B_1 + [(c_{36} + c_{45})n_1n_3]B_2 + (c_{55}n_1^2 + c_{33}n_3^2 - \rho_{11}v^2)B_3 + (m_{33}n_1n_3)F_1 \\
& \quad + (m_{33}n_3^2 - \rho_{12}v^2)F_3 + (e_{15}n_1^2 + e_{33}n_3^2)G + (\zeta_{15}n_1^2 + \zeta_{33}n_3^2)H = 0 \\
& (m_{11}n_1^2 - \rho_{12}v^2)B_1 + (m_{12}n_1^2)B_2 + (m_{33}n_1n_3)B_3 + (Rn_1^2 - \rho_{22}v^2)F_1 \\
& \quad + (Rn_1n_2)F_2 + (Rn_1n_3)F_3 + (\tilde{\zeta}_3n_1n_3)G + (e_3^*n_1n_3)H = 0 \\
& \rho_{12}B_2 + \rho_{22}F_2 = 0 \\
& (m_{11}n_1n_3)B_1 + (m_{12}n_1n_3)B_2 + (m_{33}n_3^2 - \rho_{12}v^2)B_3 + (Rn_1n_3)F_1 \\
& \quad + (Rn_3^2 - \rho_{22}v^2)F_3 + (\tilde{\zeta}_3n_3^2)G + (e_3^*n_3^2)H = 0 \\
& [(e_{15} + e_{31})n_1n_3]B_1 + [(e_{14} + e_{36})n_1n_3]B_2 + (e_{15}n_1^2 + e_{33}n_3^2)B_3 + (\tilde{\zeta}_3n_1n_3)F_1 \\
& \quad + (\tilde{\zeta}_3n_3^2)F_3 - (\xi_{11}n_1^2 + \xi_{33}n_3^2)G - (A_{11}n_1^2 + A_{33}n_3^2)H = 0 \\
& [(\zeta_{15} + \zeta_{31})n_1n_3]B_1 + [(\zeta_{14} + \zeta_{36})n_1n_3]B_2 + (\zeta_{15}n_1^2 + \zeta_{33}n_3^2)B_3 + (e_3^*n_1n_3)F_1 \\
& \quad + (e_3^*n_3^2)F_3 - (A_{11}n_1^2 + A_{33}n_3^2)G - (\xi_{11}n_1^2 + \xi_{33}n_3^2)H = 0
\end{aligned} \tag{2.5}$$

The condition of existence of a non-trivial solution of the system leads to

$$x_1V^8 + x_2V^6 + x_3V^4 + x_4V^2 + x_5 = 0 \tag{2.6}$$

where x_1, x_2, x_3, x_4, x_5 are coefficients which have been calculated symbolically.

On solving equation (2.6), we obtain 4 complex roots V_j ($j = 1, 2, 3, 4$). Corresponding to these 4 complex roots, we get 4 complex wave velocities v_j of four waves. Thus we obtain four plane harmonic waves propagating along the given phase direction in the monoclinic porous piezoelectric material. The wave with the largest phase velocity is termed as stiffened quasi- P_1 wave, and the wave with the smallest phase velocity is termed as quasi- P_2 wave. The other two waves are termed as quasi- S_1 and quasi- S_2 waves.

3. Numerical discussion

The analytical expressions of the phase velocity of propagation and the attenuation quality factor of stiffened quasi P_1, P_2 and S_1, S_2 waves are computed numerically for a particular model Barium Sodium Niobate. Following Auld (1973), the elastic, piezoelectric and dielectric constants for the monoclinic crystal are given in Table 1.

Figure 1 exhibits the variation of phase velocities of quasi waves in porous piezoelectric materials saturated with a viscous fluid for the crystal class 2, respectively with the direction of propagation (θ, ϕ) . It is seen from these figures that the range of variation of the velocities of four waves are different. The elevations and depressions of phase velocity surfaces from the horizontal plane in the figures measure the extent of velocity anisotropy in the medium. The effects of azimuth variation on the phase velocities of qP_1 and qP_2 waves are negligible for small

Table 1. Elastic constants, piezoelectric constants and dielectric constants of Barium Sodium Niobate crystal

Elastic constants [GPa]	Piezoelectric constants [C/m ²]	Dielectric constants [nC/(Vm)]
$c_{11} = 150.4$	$e_{15} = 11.4$	$\xi_{11} = 10.8$
$c_{12} = 60.63$	$e_{24} = 15.4$	$\xi_{13} = 9.8$
$c_{13} = 65.94$	$e_{31} = -4.32$	$\xi_{22} = 14.8$
$c_{22} = 160.4$	$e_{32} = -6.32$	$\xi_{33} = 13.1$
$c_{23} = 75.94$	$e_{33} = 17.4$	$\xi_{11}^* = 0.038$
$c_{33} = 145.5$	$e_{36} = 0.8$	$\xi_{13}^* = 0.09$
$c_{44} = 40.86$	$\zeta_{15} = 0.456$	$\xi_{22}^* = 0.055$
$c_{55} = 43.86$	$\zeta_{24} = 0.356$	$\xi_{33}^* = 0.049$
$c_{66} = 50.37$	$\zeta_{31} = -1.728$	$A_{11} = 0.018$
$m_{11} = 8.8$	$\zeta_{32} = -0.2728$	$A_{13} = 0.04$
$m_{13} = 11.5$	$\zeta_{33} = 0.696$	$A_{22} = 0.031$
$m_{22} = 16.8$	$\zeta_{36} = 0.08$	$A_{33} = 0.015$
$m_{33} = 5.2$	$e_3^* = -3.6$	
$R = 20$	$\zeta_3 = -7.5$	

values of θ but noticeable for large values of θ . The phase velocity of qP_1 wave increases with increase in θ but the phase velocity of qP_2 wave decreases with an increase in θ . The phase velocity of qS_1 wave first decreases with an increase in θ and attain local minima at $\theta = 30^\circ$ and after that it increases with θ . Contrary to this, V_4 increases first and then decreases having the minimum at 45° and then increases further.

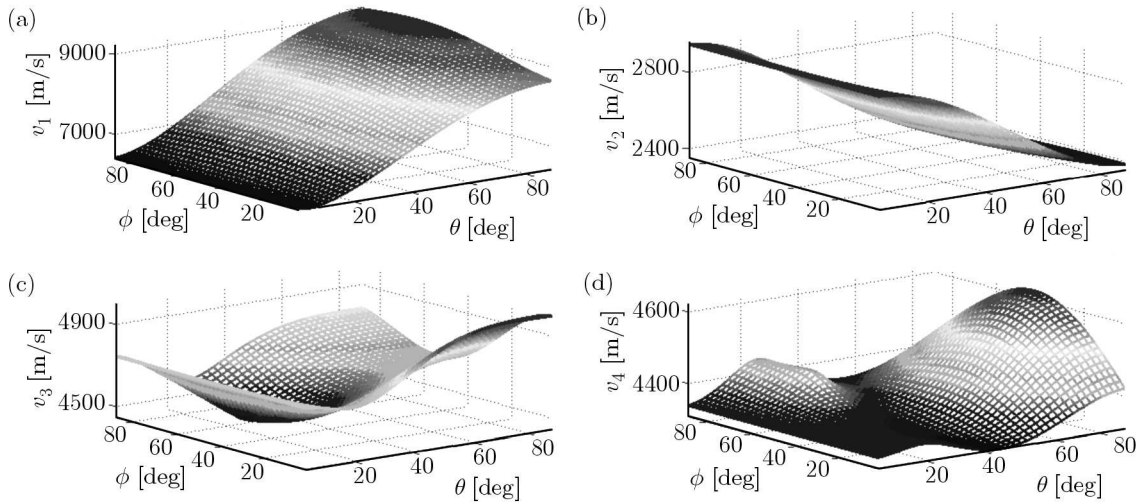


Fig. 1. Variation of phase velocities of quasi waves with the propagation directions (θ, ϕ) for Barium Sodium Niobate crystal of class 2; (a) qP_1 wave, (b) qP_2 wave, (c) qS_1 wave, (d) qS_2 wave

Figure 2a depicts the variation of phase velocities with the direction of propagation in PPM saturated with a non-viscous fluid, for the crystal class 2. The waves are not attenuated in such a medium. Figures 2b and 2c exhibit the variation of phase velocities in PPM saturated with the viscous fluid in the low frequency range (LFR) and high frequency range (HFR), respectively. It is observed that all waves slow down due to the viscous effects of the pore fluid. It is also observed that the faster the wave is, the larger are effects of viscosity. It is also interesting to note that the effects of viscosity are not significant in the HFR which reveals the fact that viscosity

dominates in LFR. Comparison of Figs. 2b and 2c shows that the velocities of all the quasi waves increase as the frequency shifts from LFR to HFR. The pattern of variation of phase velocities with the phase directions remain unaffected in either case.

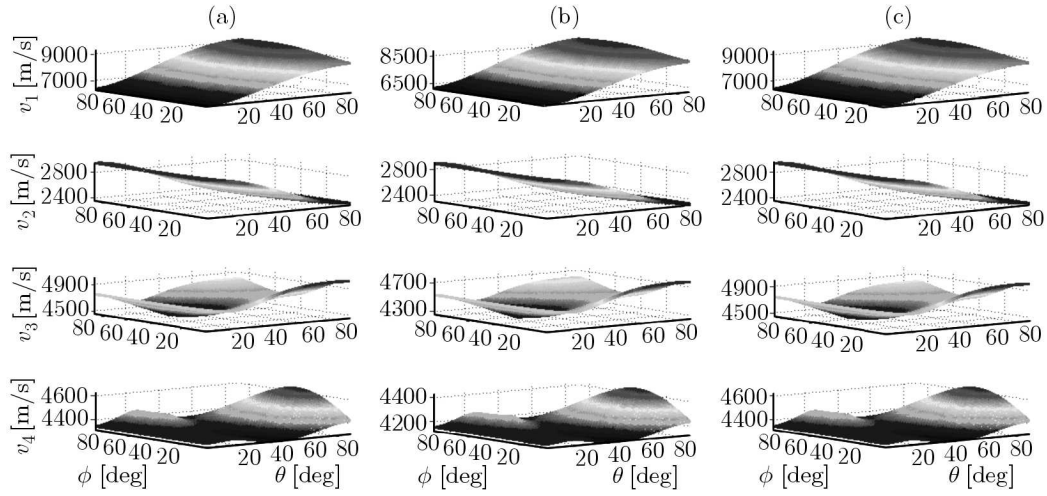


Fig. 2. Effects of viscosity of the pore fluid on the variation of phase velocities of quasi waves with the direction of propagation (θ, ϕ) for Barium Sodium Niobate crystal of class 2; (a) without viscous effects, (b) with viscous effects in the low frequency range, (c) with viscous effects in the high frequency range

The effects of electro-elastic interactions on the phase velocities of quasi waves are observed for class 2 in Fig. 3. The phase velocity of qP_2 wave increases due to piezoelectric interaction while the effects are not significant in the case of other three waves.

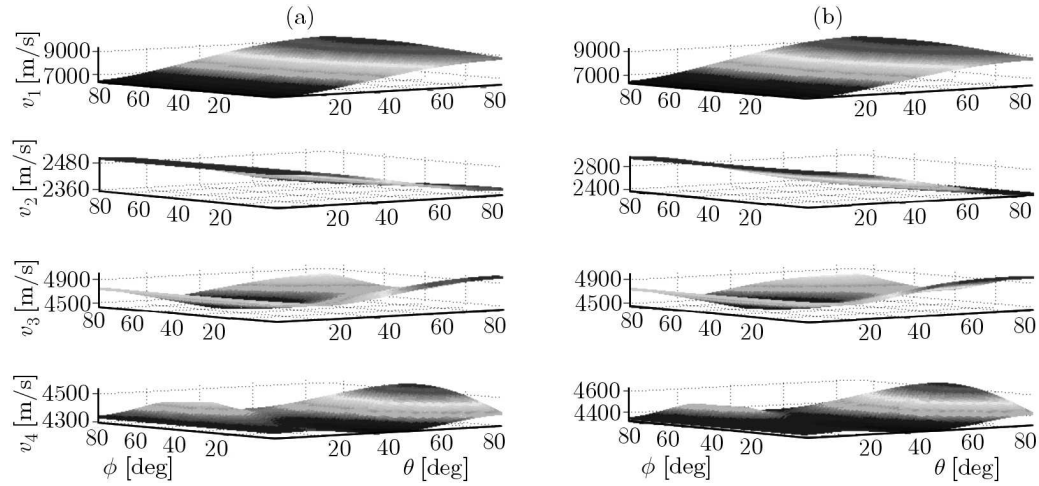


Fig. 3. Effects of piezoelectricity on the variation of phase velocities of quasi waves with the direction of propagation (θ, ϕ) for Barium Sodium Niobate crystal of class 2; (a) without effects of piezoelectricity, (b) with effects of piezoelectricity

Figure 4 shows the variation of phase velocities of qP_1 , qP_2 , qS_1 and qS_2 waves with the pore volume fraction in LFR and HFR, respectively, for class 2. It is observed that in the LFR, the phase velocities of all waves decrease with an increase in porosity while they increase monotonically by a very small amount with porosity in the HFR. The phase velocities of qP_1 , qS_1 and qS_2 waves in the LFR become almost constant when the porosity is greater than 60%. However, phase velocity of qP_2 wave decreases even when the porosity is greater than 60%. Thus the slowest wave is found to be more sensitive to the porosity of the medium.

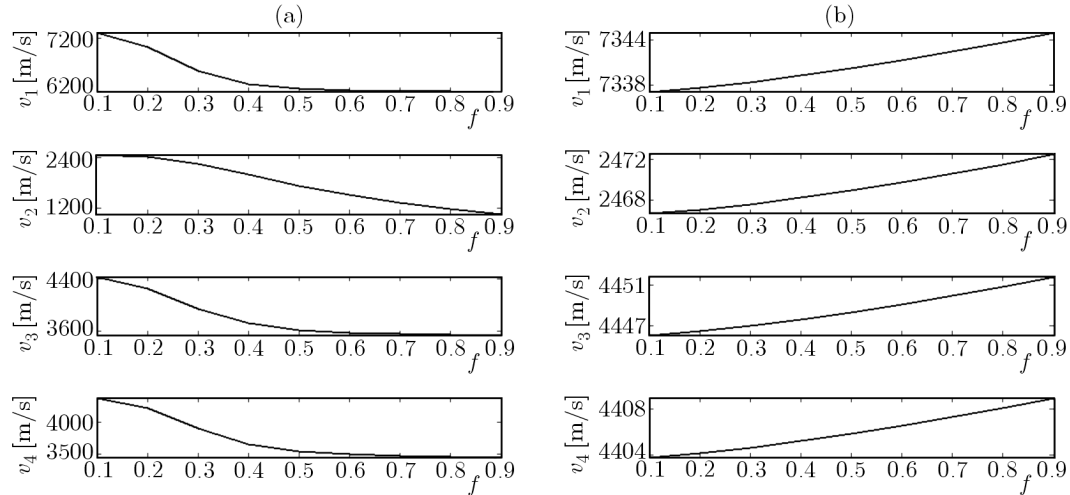


Fig. 4. Variation of phase velocities of quasi waves with porosity f for Barium sodium Niobate crystal of class 2; (a) LFR, (b) HFR

4. Conclusion

In the present paper, wave propagation in a monoclinic porous piezoelectric material is studied both analytically and numerically. The four complex roots of the obtained Christoffel equation define the phase velocities of propagation of four stiffened quasi waves propagating in such a medium. The variation of phase velocities of these waves with frequency, phase direction and the porosity is observed numerically for a particular crystal Barium Sodium Niobate. The phase velocities of all four waves increase with frequency. The phase velocities of all four waves decrease with porosity in LFR which can be explained on the basis of percolation theory. The electric-elastic interaction does not affect the behavior of phase velocities with porosity but the magnitude of quasi P2 wave increases significantly.

References

1. ARNAU A. (EDS.), 2008, *Piezoelectric Transducers and Applications*, Springer
2. AULD B.A., 1973, *Acoustic Fields and Waves in Solids*, Vol. 1, John Wiley & Sons, Inc.
3. AULD B.A., 1981, Wave propagation and resonance in piezoelectric materials, *Journal of Acoustic Society of America*, **70**, 6, 1577-1585
4. CRACIUN F., GUIDARELLI G., GALASSI C., RONCARI E., 1998, Elastic wave propagation in porous piezoelectric ceramics, *Ultrasonic*, **36**, 427-430
5. GOMEZ T.E., MULHOLLAND A.J., HAYWARD G., GOMATAM J., 2000, Wave propagation in 0-3/3-3 connectivity composites with complex microstructure, *Ultrasonics*, **38**, 897-907
6. GUPTA R.K., VENKATESH T.A., 2006, Electromechanical response of porous piezoelectric materials, *Journal Acta Materialia*, 4063-4078
7. NAYFEH A.H., CHIEN H.T., 1992, Wave propagation interaction with free and fluid loaded piezoelectric substrates, *Journal of Acoustic Society of America*, **91**, 3126-3135
8. PIAZZA D., STOLERIU L., MITOSERIU L., STANCU A., GALASSI C., 2006, Characterization of porous PZT ceramics by first order reversal curves (FORC) diagrams, *Journal of the European Ceramic Society*, **26**, 2959-2962
9. PRAVEENKUMAR B., KUMAR H.H., KHARAT D.K., 2005, Characterization and microstructure of porous lead zirconate titanate ceramics, *Bulletin Material Sciences*, **28**, 5, 453-455

10. QIAN Z., JIN F., KISHIMOTO K., WANG Z., 2004, Effect of initial stress on the propagation behavior of SH waves in multilayered piezoelectric composite structures, *Sensor and Actuators A*, **112**, 368-375
11. VASHISHTH A.K., GUPTA V., 2009a, Vibration of porous piezoelectric plates, *Journal of Sound and Vibration*, **325**, 781-797
12. VASHISHTH A.K., GUPTA V., 2009b, Wave propagation in transversely isotropic porous piezoelectric materials, *International Journal of Solids and Structures*, **46**, 3620-3632
13. ZINCHUK L.P., PODLIPENETS A.N., 2001, Dispersion equations for Rayleigh waves in a piezoelectric periodically layered structure, *Journal of Mathematical Sciences*, **103**, 3, 398-403

Manuscript received February 10, 2015; accepted for print September 29, 2015

P-WAVE INTERACTION WITH A PAIR OF RIGID STRIPS EMBEDDED IN AN ORTHOTROPIC STRIP

SANJOY BASU

Haldia Institute of Technology, Department of Applied Science, Haldia, India; e-mail: basu1982@gmail.com

S.C. MANDAL

Jadavpur University, Department of Mathematics, Kolkata, India; e-mail: scmandal@math.jdvu.ac.in

The present paper is concerned with the problem of scattering of the P-wave by two co-planer finite rigid strips placed symmetrically in an infinitely long orthotropic strip. Using the Hilbert transform technique, the mixed boundary value problem has been reduced to the solution of dual integral equations which has finally been reduced to the solution of a Fredholm integral equation of the second kind. Solving this integral equation numerically, stress intensity factors have been calculated at the inner and outer edges of the rigid strips, and the vertical displacement outside the strips has been calculated and plotted graphically to show the effect of material orthotropy.

Keywords: P-wave, Fourier transform, Hilbert transform, Fredholm integral equation, stress intensity factor

1. Introduction

The dynamic interaction of rigid strips with an elastic isotropic or orthotropic medium is a subject of considerable interest in mechanics. Dynamical analysis of this kind is of importance to earth-quake engineering, machine, vibrations and seismology. The performance of engineered systems is affected by inhomogeneities such as cracks and inclusions present in the material. Cracks and rigid inclusions in an elastic material have become the subject of investigations. Presently, the use of anisotropic materials is increasing due to their strength. The increasing use of anisotropic media demands that the study should be extensive. A detailed reference of work done on the determination of the dynamic stress field around a crack or inclusion in an elastic solid was given by Sih (1977), Sih and Chen (1981), Chen (1978), Cinar (1983). However, in the presence of finite boundaries, the problem becomes complicated since they involve additional geometric parameters, describing the dimension of the solids. Forced vertical vibration of a single strip was treated by Wickham (1977). Singh *et al.* (1983) solved the problem of diffraction of a torsional wave by a circular rigid disc at the interface of two bonded dissimilar elastic solids. In that paper, they discussed an iterative method to solve the Fredholm integral equation of the second kind and described the stress intensity factor with the wave number. Mandal *et al.* (1997, 1998) solved the problem of forced vibration of two and four rigid strips on a semi-infinite elastic medium. Mandal *et al.* (1998) also treated the diffraction problem by four rigid strips in an orthotropic medium. Interaction of elastic waves with a periodic array of the coplanar Griffith crack in an orthotropic medium was discussed by Mandal *et al.* (1994). Das *et al.* (1998) solved the problem of determining the stress intensity factor for an interfacial crack between two orthotropic half planes bonded to a dissimilar orthotropic layer with a punch. They reduced the problem to a system of simultaneous integral equations which were solved by Chebyshev polynomials. The problem of two perfectly bonded dissimilar orthotropic strips with an interfacial crack was studied by Li (2005). He derived the analytical expression for the

stress intensity factor. Sarkar *et al.* (1995) solved the problem of diffraction of elastic waves by three coplanar Griffith cracks in an orthotropic medium. Das (2002) solved the problem of interaction between line cracks in an orthotropic layer. An elastostatic problem of an infinite row of parallel cracks in an orthotropic medium was analyzed by Sinharoy (2013). Monfared and Ayatollahi (2013) investigated the problem of determining the dynamic stress intensity factors of multiple cracks in an orthotropic strip with a functionally graded materials coating. They solved the problem by reducing it to a singular integral equation of the Cauchy type. The problem of interaction of three interfacial Griffith cracks between bonded dissimilar orthotropic half planes was studied by Mukherjee and Das (2007). Das *et al.* (2008) solved the problem of determining the stress intensity factors due to symmetric edge cracks in an orthotropic strip under normal loading. They derived an analytical expression for the stress intensity factor at the crack tip. The problem of finding the stress intensity factors for two parallel interface cracks between a nonhomogeneous bonding layer and two dissimilar orthotropic half-planes under tension was studied by Itou (2012). Shear wave interaction with a pair of rigid strips in elastic strip was analyzed by Pramanick *et al.* (1999). WU Da-zhi *et al.* (2006) considered the torsional vibration problem of a rigid circular plate on a transversely isotropic saturated soil. Very recently Morteza *et al.* (2010a,b) considered the vibration problem of a rigid circular disc on transversely isotropic media. Diffraction of elastic waves by two parallel rigid strips in an infinite orthotropic medium was analyzed by Sarkar *et al.* (1995).

In this paper, the diffraction of the elastic P-wave by two rigid strips embedded in an infinite orthotropic strip is analyzed. Using the Hilbert transform technique, the mixed boundary value problem has been reduced to the Fredholm integral equation of the second kind which has been solved numerically by the Fox and Goodwin method (1953). Stress intensity factors at both the edges of the strips have been calculated and shown graphically for different parameters and materials. Finally, vertical displacement has been calculated outside the strips and shown by 3D-graphs.

2. Formulation of the problem

Let us consider an infinitely long orthotropic elastic strip of width $2h$ containing two coplanar rigid strips embedded in it. The location of the strips are $b \leq |X| \leq a$, $Y = 0$, $|Z| < \infty$, with reference to the cartesian co-ordinate axes (X, Y, Z) . Normalizing all lengths with respect to a and putting $X/a = x$, $Y/a = y$, $Z/a = z$, $b/a = c$, the locations of the rigid strips are defined by $c \leq |x| \leq 1$, $y = 0$, $|z| < \infty$ (Fig. 1).

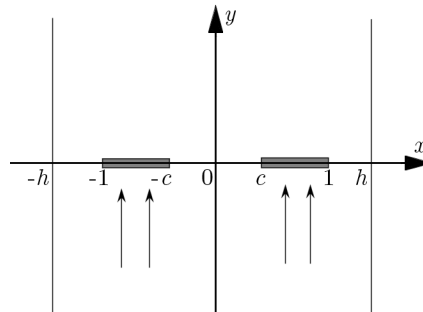


Fig. 1. Geometry of the strips

Let a time harmonic wave given by $u = 0$ and $v = v_0 e^{i(ky - \omega t)}$, where $k = a\omega / (c_s \sqrt{c_{22}})$, $c_s = \sqrt{\mu_{12}/\rho}$ with ρ being the density of the material, ω the circular frequency and v_0 a constant, travelling in the direction of the positive y -axis and be incident normally on the strips.

The non-zero stress components τ_{yy} , τ_{xy} and τ_{xx} are given by

$$\frac{\tau_{yy}}{\mu_{12}} = c_{12} \frac{\partial u}{\partial x} + c_{22} \frac{\partial v}{\partial y} \quad \frac{\tau_{xy}}{\mu_{12}} = \frac{\partial u}{\partial y} + \frac{\partial v}{\partial x} \quad \frac{\tau_{xx}}{\mu_{12}} = c_{11} \frac{\partial u}{\partial x} + c_{12} \frac{\partial v}{\partial y} \quad (2.1)$$

where u and v are displacement components and c_{ij} ($i, j = 1, 2$) are non-dimensional parameters related to the engineering elastic constants E_i , μ_{ij} and ν_{ij} ($i, j = 1, 2, 3$) by the relations

$$\begin{aligned} c_{11} &= \frac{E_1}{\mu_{12}} \left(1 - \frac{\nu_{12}^2 E_2}{E_1}\right) & c_{22} &= \frac{E_2}{\mu_{12}} \left(1 - \frac{\nu_{12}^2 E_2}{E_1}\right) = c_{11} \frac{E_2}{E_1} \\ c_{12} &= \frac{\nu_{12} E_2}{\mu_{12}} \left(1 - \frac{\nu_{12}^2 E_2}{E_1}\right) = \nu_{12} c_{22} = \nu_{21} c_{11} \end{aligned} \quad (2.2)$$

for the generalized plane stress and

$$\begin{aligned} c_{11} &= \frac{E_1}{\Delta \mu_{12}} (1 - \nu_{23} \nu_{32}) & c_{22} &= \frac{E_2}{\Delta \mu_{12}} (1 - \nu_{13} \nu_{31}) \\ c_{12} &= \frac{E_1}{\Delta \mu_{12}} \left(\nu_{21} + \frac{\nu_{13} \nu_{32} E_2}{E_1}\right) = \frac{E_2}{\Delta \mu_{12}} \left(\nu_{12} + \frac{\nu_{23} \nu_{31} E_1}{E_2}\right) \end{aligned} \quad (2.3)$$

where

$$\Delta = 1 - \nu_{12} \nu_{21} - \nu_{23} \nu_{32} - \nu_{31} \nu_{13} - \nu_{12} \nu_{23} \nu_{31} - \nu_{13} \nu_{21} \nu_{32}$$

for the plane strain. The constants E_i and ν_{ij} satisfy Maxwell's relation

$$\frac{\nu_{ij}}{E_i} = \frac{\nu_{ji}}{E_j} \quad (2.4)$$

Therefore, substituting $u(x, y, t) = u(x, y)e^{-i\omega t}$ and $v(x, y, t) = v(x, y)e^{-i\omega t}$, our problem reduces to the solution of the equations

$$\begin{aligned} c_{11} \frac{\partial^2 u}{\partial x^2} + \frac{\partial^2 u}{\partial y^2} + (1 + c_{12}) \frac{\partial^2 v}{\partial x \partial y} + k_s^2 u &= 0 \\ c_{22} \frac{\partial^2 v}{\partial y^2} + \frac{\partial^2 v}{\partial x^2} + (1 + c_{12}) \frac{\partial^2 u}{\partial x \partial y} + k_s^2 v &= 0 \end{aligned} \quad (2.5)$$

where $k_s^2 = a^2 \omega^2 / c_s^2$.

Thus the problem is to find the stress distribution near the edges of the strips subject to the following boundary conditions

$$v(x, 0+) = v(x, 0-) = -v_0 \quad c \leq |x| \leq 1 \quad (2.6)$$

$$\tau_{yy}(x, 0) = 0 \quad |x| < c \quad 1 < |x| < h \quad (2.7)$$

$$u(x, 0) = 0 \quad |x| < h \quad (2.8)$$

$$\tau_{xx}(\pm h, y) = 0 \quad \tau_{xy}(\pm h, y) = 0 \quad (2.9)$$

Henceforth, the time factor $e^{-i\omega t}$ which is common to all field variables will be omitted in the sequel.

The solution to equations (2.5) can be taken as

$$\begin{aligned}
 u(x, y) &= \frac{2}{\pi} \int_0^{\infty} [A_1(\xi)e^{-\nu_1|y|} + A_2(\xi)e^{-\nu_2|y|}] \sin(\xi x) d\xi \\
 &+ \frac{2}{\pi} \int_0^{\infty} [A_3(\zeta) \sinh(\nu_3 x) + A_4(\zeta) \sinh(\nu_4 x)] \sin(\zeta y) d\zeta \\
 v(x, y) &= \frac{2}{\pi} \int_0^{\infty} \frac{1}{\xi} [\alpha_1 A_1(\xi)e^{-\nu_1|y|} + \alpha_2 A_2(\xi)e^{-\nu_2|y|}] \cos(\xi x) d\xi \\
 &+ \frac{2}{\pi} \int_0^{\infty} \frac{1}{\zeta} [\alpha_3 A_3(\zeta) \cosh(\nu_3 x) + \alpha_4 A_4(\zeta) \cosh(\nu_4 x)] \cos(\zeta y) d\zeta
 \end{aligned} \tag{2.10}$$

where $A_i(\xi)$ ($i = 1, 2, 3, 4$) are the unknown functions to be determined, ν_1^2 and ν_2^2 are the roots of the equation

$$c_{22}\nu^4 + \{(c_{12}^2 + 2c_{12} - c_{11}c_{22})\xi^2 + (1 + c_{22})k_s^2\}\nu^2 + (c_{11}\xi^2 - k_s^2)(\xi^2 - k_s^2) = 0 \tag{2.11}$$

and ν_3^2, ν_4^2 are the roots of the equation

$$c_{11}\nu^4 + \{(c_{12}^2 + 2c_{12} - c_{11}c_{22})\zeta^2 + (1 + c_{11})k_s^2\}\nu^2 + (c_{22}\zeta^2 - k_s^2)(\zeta^2 - k_s^2) = 0 \tag{2.12}$$

where

$$\alpha_i = \begin{cases} \frac{c_{11}\xi^2 - k_s^2 - \nu_i^2}{(1 + c_{12})\nu_i} & i = 1, 2 \\ \frac{\zeta^2 - k_s^2 - c_{11}\nu_i^2}{(1 + c_{12})\nu_i} & i = 3, 4 \end{cases} \tag{2.13}$$

From boundary condition (2.11), it is found that

$$A_2(\xi) = -A_1(\xi) \tag{2.14}$$

Therefore, the displacements u, v and stresses $\tau_{yy}, \tau_{xy}, \tau_{xx}$ can be finally written as

$$\begin{aligned}
 u(x, y) &= \frac{2}{\pi} \int_0^{\infty} [e^{-\nu_1|y|} - e^{-\nu_2|y|}] A_1(\xi) \sin(\xi x) d\xi \\
 &+ \frac{2}{\pi} \int_0^{\infty} [A_3(\zeta) \sinh(\nu_3 x) + A_4(\zeta) \sinh(\nu_4 x)] \sin(\zeta y) d\zeta \\
 v(x, y) &= \frac{2}{\pi} \int_0^{\infty} \frac{1}{\xi} [\alpha_1 e^{-\nu_1|y|} - \alpha_2 e^{-\nu_2|y|}] A_1(\xi) \cos(\xi x) d\xi \\
 &+ \frac{2}{\pi} \int_0^{\infty} \frac{1}{\zeta} [\alpha_3 A_3(\zeta) \cosh(\nu_3 x) + \alpha_4 A_4(\zeta) \cosh(\nu_4 x)] \cos(\zeta y) d\zeta
 \end{aligned} \tag{2.15}$$

and

$$\begin{aligned}
 \frac{\tau_{yy}}{\mu_{12}} &= \frac{2}{\pi} \left\{ \int_0^\infty \left[\left(c_{12}\xi - \operatorname{sgn}(y) \frac{c_{22}\alpha_1\nu_1}{\xi} \right) e^{-\nu_1|y|} - \left(c_{12}\xi - \operatorname{sgn}(y) \frac{c_{22}\alpha_2\nu_2}{\xi} \right) e^{-\nu_2|y|} \right] \right. \\
 &\quad \cdot A_1(\xi) \cos(\xi x) \, d\xi + \int_0^\infty [(c_{12}\nu_3 - c_{22}\alpha_3)A_3(\zeta) \cosh(\nu_3x) \\
 &\quad \left. + (c_{12}\nu_4 - c_{22}\alpha_4)A_4(\zeta) \cosh(\nu_4x)] \sin(\zeta y) \, d\zeta \right\} \\
 \frac{\tau_{xy}}{\mu_{12}} &= -\frac{2}{\pi} \left\{ \int_0^\infty [(\nu_1 + \alpha_1)e^{-\nu_1y} - (\nu_2 + \alpha_2)e^{-\nu_2y}] A_1(\xi) \sin(\xi x) \, d\xi \right. \\
 &\quad + \int_0^\infty \left[\left(\zeta + \frac{\nu_3\alpha_3}{\zeta} \right) A_3(\zeta) \sinh(\nu_3x) \right. \\
 &\quad \left. \left. + \left(\zeta + \frac{\nu_4\alpha_4}{\zeta} \right) A_4(\zeta) \sinh(\nu_4x) \right] \cos(\zeta y) \, d\zeta \right\} \quad y > 0 \tag{2.16} \\
 \frac{\tau_{xx}}{\mu_{12}} &= \frac{2}{\pi} \left\{ \int_0^\infty \left[\left(c_{11}\xi - \frac{c_{12}\alpha_1\nu_1}{\xi} \right) e^{-\nu_1|y|} - \left(c_{11}\xi - \frac{c_{12}\alpha_2\nu_2}{\xi} \right) e^{-\nu_2|y|} \right] A_1(\xi) \cos(\xi x) \, d\xi \right. \\
 &\quad + \int_0^\infty [(c_{11}\nu_3 - c_{12}\alpha_3)A_3(\zeta) \cosh(\nu_3x) \\
 &\quad \left. + (c_{11}\nu_4 - c_{12}\alpha_4)A_4(\zeta) \cosh(\nu_4x)] \sin(\zeta y) \, d\zeta \right\} \quad y > 0
 \end{aligned}$$

Boundary conditions (2.6) and (2.7) yield the following pair of dual integral equations

$$\begin{aligned}
 \int_0^\infty \frac{1}{\xi} [1 + H(\xi)] A(\xi) \cos(\xi x) \, d\xi &= p(x) \quad c \leq |x| \leq 1 \\
 \int_0^\infty A(\xi) \cos(\xi x) \, d\xi &= 0 \quad |x| < c \quad 1 < |x| < h
 \end{aligned} \tag{2.17}$$

where

$$\begin{aligned}
 A(\xi) &= \frac{\alpha_1\nu_1 - \alpha_2\nu_2}{\xi} A_1(\xi) \\
 H(\xi) &= \left(\frac{\alpha_1 - \alpha_2}{\alpha_1\nu_1 - \alpha_2\nu_2} \right) \frac{\xi}{d} - 1 \rightarrow 0 \quad \text{as } \xi \rightarrow \infty \\
 p(x) &= -\frac{\pi}{2c} v_0 - \frac{1}{c} \int_0^\infty \frac{1}{\zeta} [\alpha_3 A_3(\zeta) \cosh(\nu_3x) + \alpha_4 A_4(\zeta) \cosh(\nu_4x)] \, d\zeta \\
 d &= \frac{c_{11} + N_1 N_2}{N_1 N_2 (N_1 + N_2)}
 \end{aligned} \tag{2.18}$$

and

$$\begin{aligned}
 N_1^2 &= \frac{1}{2c_{22}} \left[-(c_{12}^2 + 2c_{12} - c_{11}c_{22}) + \sqrt{(c_{12}^2 + 2c_{12} - c_{11}c_{22})^2 - 4c_{11}c_{22}} \right] \\
 N_2^2 &= \frac{1}{2c_{22}} \left[-(c_{12}^2 + 2c_{12} - c_{11}c_{22}) - \sqrt{(c_{12}^2 + 2c_{12} - c_{11}c_{22})^2 - 4c_{11}c_{22}} \right]
 \end{aligned} \tag{2.19}$$

Using boundary conditions (2.9), $A_3(\zeta)$ and $A_4(\zeta)$ are expressed in terms of the function $A(\xi)$ as

$$\begin{aligned} M(\zeta)A_3(\zeta) &= \left(\zeta + \frac{\alpha_4\nu_4}{\zeta}\right)i_1(\zeta)\sinh(\nu_4h) - (c_{11}\nu_4 - c_{12}\alpha_4)i_2(\zeta)\cosh(\nu_4h) \\ M(\zeta)A_4(\zeta) &= -\left(\zeta + \frac{\alpha_3\nu_3}{\zeta}\right)i_1(\zeta)\sinh(\nu_3h) + (c_{11}\nu_3 - c_{12}\alpha_3)i_2(\zeta)\cosh(\nu_3h) \end{aligned} \quad (2.20)$$

where

$$\begin{aligned} M(\zeta) &= \left(\zeta + \frac{\alpha_4\nu_4}{\zeta}\right)(c_{11}\nu_3 - c_{12}\alpha_3)\cosh(\nu_3h)\sinh(\nu_4h) \\ &\quad - \left(\zeta + \frac{\alpha_3\nu_3}{\zeta}\right)(c_{11}\nu_4 - c_{12}\alpha_4)\sinh(\nu_3h)\cosh(\nu_4h) \end{aligned} \quad (2.21)$$

and

$$\begin{aligned} i_1(\zeta) &= \frac{2}{\pi} \int_0^\infty \left\{ \frac{\zeta[c_{11}\xi^2 + c_{12}(k_s^2 + \nu_1^2)]}{\nu_1^2 + \zeta^2} - \frac{\zeta[c_{11}\xi^2 + c_{12}(k_s^2 + \nu_2^2)]}{\nu_2^2 + \zeta^2} \right\} \frac{A(\xi)\cos(\xi h)}{\nu_1^2 - \nu_2^2} d\xi \\ i_2(\zeta) &= -\frac{2}{\pi} \int_0^\infty \left(\frac{c_{12}\nu_1^2 + c_{11}\xi^2 - k_s^2}{\nu_1^2 + \zeta^2} - \frac{c_{12}\nu_2^2 + c_{11}\xi^2 - k_s^2}{\nu_2^2 + \zeta^2} \right) \frac{\xi A(\xi)\sin(\xi h)}{\nu_1^2 - \nu_2^2} d\xi \end{aligned} \quad (2.22)$$

3. Method of solution

In order to reduce dual integral equations (2.17) to a single Fredholm integral equation, let us assume that

$$A(\xi) = \int_c^1 \frac{h(t^2)}{t} [1 - \cos(\xi t)] dt \quad (3.1)$$

where the unknown function $h(t^2)$ is to be determined.

Substituting $A(\xi)$ from (3.1) into equations (2.17)₂, we note that

$$\int_0^\infty A(\xi)\cos(\xi x) d\xi = \pi \int_c^1 \frac{h(t^2)}{t} \left[\delta(x) - \frac{1}{2}\delta(x+t) - \frac{1}{2}\delta(|x-t|) \right] dt$$

so that equation (2.17)₂ is automatically satisfied.

Again, the substitution of the value of $A(\xi)$ from (3.1) into equation (2.17)₁ yields

$$\frac{1}{2} \int_c^1 \frac{h(t^2)}{t} \log \left| \frac{x^2 - t^2}{x^2} \right| dt = p(x) - \int_c^1 \frac{h(t^2)}{t} dt \int_0^\infty \xi^{-1} H(\xi)\cos(\xi x)[1 - \cos(\xi t)] d\xi \quad (3.2)$$

Differentiating both sides of equation (3.2) with respect to x and subsequently multiplying by $(-2x/\pi)$, we obtain

$$\begin{aligned} &\frac{2}{\pi} \int_c^1 \frac{th(t^2)}{t^2 - x^2} dt \\ &= \frac{2x}{\pi} \int_c^1 \frac{h(t^2)}{t} dt \left\{ \frac{1}{d} \int_0^\infty \frac{1}{\zeta} [\alpha_3\nu_3 A_5(\zeta)\sinh(\nu_3x) + \alpha_4\nu_4 A_6(\zeta)\sinh(\nu_4x)] d\zeta \right. \\ &\quad \left. - \int_0^\infty H(\xi)\sin(\xi x)[1 - \cos(\xi t)] d\xi \right\} \quad c \leq |x| \leq 1 \end{aligned} \quad (3.3)$$

Using the Hilbert transform technique, the solution to integral equation (3.3) is given by

$$h(u^2) + \int_c^1 \frac{h(t^2)}{t} [k_1(u^2, t^2) + k_2(u^2, t^2)] dt = \frac{D}{\sqrt{(u^2 - c^2)(1 - u^2)}} \tag{3.4}$$

where

$$k_1(u^2, t^2) = \frac{4}{\pi^2 d} \sqrt{\frac{u^2 - c^2}{1 - u^2}} \int_c^1 \sqrt{\frac{1 - x^2}{x^2 - c^2}} \frac{x^2}{x^2 - u^2} dx$$

$$\cdot \left\{ \int_0^\infty \frac{1}{\zeta} [\alpha_3 \nu_3 A_5(\zeta) \sinh(\nu_3 x) + \alpha_4 \nu_4 A_6(\zeta) \sinh(\nu_4 x)] d\zeta \right\}$$

$$k_2(u^2, t^2) = -\frac{4}{\pi^2} \sqrt{\frac{u^2 - c^2}{1 - u^2}} \int_c^1 \sqrt{\frac{1 - x^2}{x^2 - c^2}} \frac{x^2 dx}{x^2 - u^2} \int_0^\infty H(\xi) \sin(\xi x) [1 - \cos(\xi t)] d\xi \tag{3.5}$$

$$A_5(\zeta) = \frac{1}{M(\zeta)} \left[\left(\zeta + \frac{\alpha_4 \nu_4}{\zeta} \right) i_3(\zeta) \sinh(\nu_4 h) - (c_{11} \nu_4 - c_{12} \alpha_4) i_4(\zeta) \cosh(\nu_4 h) \right]$$

$$A_6(\zeta) = -\frac{1}{M(\zeta)} \left[\left(\zeta + \frac{\alpha_3 \nu_3}{\zeta} \right) i_3(\zeta) \sinh(\nu_3 h) + (c_{11} \nu_3 - c_{12} \alpha_3) i_4(\zeta) \cosh(\nu_3 h) \right]$$

and

$$i_3(\zeta) = \frac{2}{\pi} \int_0^\infty \left\{ \frac{\zeta [c_{11} \xi^2 + c_{12} (k_s^2 + \nu_1^2)]}{\nu_1^2 + \zeta^2} - \frac{\zeta [c_{11} \xi^2 + c_{12} (k_s^2 + \nu_2^2)]}{\nu_2^2 + \zeta^2} \right\} \frac{[1 - \cos(\xi t)] \cos(\xi h)}{\nu_1^2 - \nu_2^2} d\xi$$

$$i_4(\zeta) = -\frac{2}{\pi} \int_0^\infty \left(\frac{c_{12} \nu_1^2 + c_{11} \xi^2 - k_s^2}{\nu_1^2 + \zeta^2} - \frac{c_{12} \nu_2^2 + c_{11} \xi^2 - k_s^2}{\nu_2^2 + \zeta^2} \right) \frac{\xi [1 - \cos(\xi t)]}{\nu_1^2 - \nu_2^2} \sin(\xi h) d\xi \tag{3.6}$$

In order to determine the arbitrary constant D , multiplying equation (3.2) by $x/\sqrt{(x^2 - c^2)(1 - x^2)}$ and integrating from c to 1 with respect to x , we obtain

$$\int_c^1 \frac{h(u^2)}{u} du = -\frac{\pi v_0}{c \log \left| \frac{1-c}{1+c} \right|} - \frac{4}{\pi \log \left| \frac{1-c}{1+c} \right|} \left[\int_c^1 \frac{x B_1(x, t^2)}{\sqrt{(x^2 - c^2)(1 - x^2)}} dx \right.$$

$$\left. + \int_c^1 \frac{h(t^2)}{t} dt \int_c^1 \frac{x B_2(x, t^2)}{\sqrt{(x^2 - c^2)(1 - x^2)}} dx \right] \tag{3.7}$$

where

$$B_1(x, t^2) = \frac{1}{d} \int_0^\infty \frac{1}{\zeta} [\alpha_3 A_5(\zeta) \cosh(\nu_3 x) + \alpha_4 A_6(\zeta) \cosh(\nu_4 x)] d\zeta$$

$$B_2(x, t^2) = \int_0^\infty \frac{1}{\xi} H(\xi) \cos(\xi x) [1 - \cos(\xi t)] d\xi \tag{3.8}$$

Again, substituting $h(u^2)$ from equation (3.4) into equation (3.7) and simplifying, we obtain

$$D = -\frac{2v_0 c}{d \log \left| \frac{1-c}{1+c} \right|} - \frac{8c}{\pi^2 \log \left| \frac{1-c}{1+c} \right|} \int_c^1 \frac{h(t^2)}{t} dt \int_c^1 \frac{x [B_1(x, t^2) + B_2(x, t^2)]}{\sqrt{(x^2 - c^2)(1 - x^2)}} dx$$

$$+ \frac{2c}{\pi} \int_c^1 \frac{h(t^2)}{t} dt \int_c^1 \frac{1}{u} [k_1(u^2, t^2) + k_2(u^2, t^2)] du \tag{3.9}$$

Eliminating D from equations (3.4) and (3.9) and simplifying, we obtain

$$\begin{aligned} & \sqrt{(u^2 - c^2)(1 - u^2)}h(u^2) + \int_c^1 \frac{h(t^2)}{t} [k_a(u^2, t^2) + k_b(u^2, t^2) + k_c(u^2, t^2)] dt \\ &= -\frac{2v_0c}{d \log \left| \frac{1-c}{1+c} \right|} \end{aligned} \quad (3.10)$$

where

$$\begin{aligned} k_a(u^2, t^2) &= \frac{4}{\pi^2} (u^2 - c^2) \int_c^1 \sqrt{\frac{1-x^2}{x^2-c^2}} \frac{x^2}{x^2-u^2} \left\{ \frac{\partial}{\partial x} [B_1(x, t^2) + B_2(x, t^2)] \right\} dx \\ k_b(u^2, t^2) &= \frac{8c}{\pi^2 \log \left| \frac{1-c}{1+c} \right|} \int_c^1 \frac{x[B_1(x, t^2) + B_2(x, t^2)]}{\sqrt{(x^2-c^2)(1-x^2)}} dx \\ k_c(u^2, t^2) &= -\frac{8c}{\pi^3 u} \sqrt{\frac{u^2-c^2}{1-u^2}} \int_c^1 \sqrt{\frac{1-x^2}{x^2-c^2}} \frac{x^2}{x^2-u^2} \left\{ \frac{\partial}{\partial x} [B_1(x, t^2) + B_2(x, t^2)] \right\} dx \end{aligned} \quad (3.11)$$

Next, for further simplification, we put

$$\sqrt{(u^2 - c^2)(1 - u^2)}h(u^2) = H(u^2)$$

and make the substitution

$$u^2 = c^2 \cos^2 \phi + \sin^2 \phi \quad t^2 = c^2 \cos^2 \theta + \sin^2 \theta$$

into equation (3.10) which then reduces to the form

$$G(\phi) + \int_0^{\frac{\pi}{2}} \frac{G(\theta)}{c^2 \cos^2 \theta + \sin^2 \theta} [k'_a(\phi, \theta) + k'_b(\phi, \theta) + k'_c(\phi, \theta)] d\theta = -\frac{2v_0c}{d \log \left| \frac{1-c}{1+c} \right|} \quad (3.12)$$

where

$$\begin{aligned} G(\phi) &= H(c^2 \cos^2 \phi + \sin^2 \phi) \\ G(\theta) &= H(c^2 \cos^2 \theta + \sin^2 \theta) \\ k'_a(\phi, \theta) &= k_a(c^2 \cos^2 \phi + \sin^2 \phi, c^2 \cos^2 \theta + \sin^2 \theta) \\ k'_b(\phi, \theta) &= k_b(c^2 \cos^2 \phi + \sin^2 \phi, c^2 \cos^2 \theta + \sin^2 \theta) \\ k'_c(\phi, \theta) &= k_c(c^2 \cos^2 \phi + \sin^2 \phi, c^2 \cos^2 \theta + \sin^2 \theta) \end{aligned} \quad (3.13)$$

When h tends to infinity ($h \rightarrow \infty$), the medium becomes infinite. In this case, the expression for $p(x)$ given by equation (2.18)₃ becomes $p(x) = -(\pi/2c)v_0$, since $A_3(\zeta)$ and $A_4(\zeta)$ given by equations (2.20)-(2.22) become zero.

$A_3(\zeta)$ can be written as

$$A_3(\zeta) = \frac{1}{2M(\zeta)} \left[\left(\zeta + \frac{\alpha_4 \nu_4}{\zeta} \right) i_1(\zeta) (e^{\nu_4 h} - e^{-\nu_4 h}) - (c_{11} \nu_4 - c_{12} \alpha_4) i_2(\zeta) (e^{\nu_4 h} + e^{-\nu_4 h}) \right]$$

where

$$\begin{aligned} M(\zeta) &= \frac{1}{4} \left[\left(\zeta + \frac{\alpha_4 \nu_4}{\zeta} \right) (c_{11} \nu_3 - c_{12} \alpha_3) (e^{\nu_3 h} + e^{-\nu_3 h}) (e^{\nu_4 h} - e^{-\nu_4 h}) \right. \\ &\quad \left. - \left(\zeta + \frac{\alpha_3 \nu_3}{\zeta} \right) (c_{11} \nu_4 - c_{12} \alpha_4) (e^{\nu_3 h} - e^{-\nu_3 h}) (e^{\nu_4 h} + e^{-\nu_4 h}) \right] \end{aligned}$$

Therefore,

$$A_3(\zeta) = \frac{1}{M_1(\zeta)} \left[\left(\zeta + \frac{\alpha_4 \nu_4}{\zeta} \right) i_1(\zeta) (1 - e^{-2\nu_4 h}) - (c_{11} \nu_4 - c_{12} \alpha_4) i_2(\zeta) (1 + e^{-2\nu_4 h}) \right]$$

and

$$M_1(\zeta) = \frac{e^{\nu_3 h}}{2} \left[\left(\zeta + \frac{\alpha_4 \nu_4}{\zeta} \right) (c_{11} \nu_3 - c_{12} \alpha_3) (1 + e^{-2\nu_3 h}) (1 - e^{-2\nu_4 h}) - \left(\zeta + \frac{\alpha_3 \nu_3}{\zeta} \right) (c_{11} \nu_4 - c_{12} \alpha_4) (1 - e^{-2\nu_3 h}) (1 + e^{-2\nu_4 h}) \right]$$

As $h \rightarrow \infty$, $M_1(\zeta) \rightarrow \infty$ and therefore $A_3(\zeta) \rightarrow 0$. Similarly, $A_4(\zeta) \rightarrow 0$.

So in this case, dual integral equations (2.17)₁ and (2.17)₂ become

$$\int_0^\infty \frac{1}{\xi} [1 + H(\xi)] A(\xi) \cos(\xi x) d\xi = -\frac{\pi}{2c} v_0 \quad c \leq |x| \leq 1$$

$$\int_0^\infty A(\xi) \cos(\xi x) d\xi = 0 \quad |x| < c \quad |x| > 1$$

This problem has been analyzed in detail by Sarkar *et al.* (1995).

4. Quantities of physical interest

The stress $\tau_{yy}(x, y)$ for $y \rightarrow 0$ in the neighbourhood of the strip can be found from equation (2.16)₁, and is given by

$$\tau_{yy}(x, 0\pm) = \mp \frac{2\mu_{12}c_{22}}{\pi} \int_0^\infty A(\xi) \cos(\xi x) d\xi \quad c \leq |x| \leq 1 \tag{4.1}$$

Now

$$\Delta\tau_{yy}(x, 0) = \tau_{yy}(x, 0+) - \tau_{yy}(x, 0-) \tag{4.2}$$

then

$$\Delta\tau_{yy}(x, 0) = -\frac{4}{\pi} \mu_{12}c_{22} \int_0^\infty A(\xi) \cos(\xi x) d\xi \tag{4.3}$$

Substituting the value of $A(\xi)$ from equation (3.1) into equation (4.3), we get

$$\Delta\tau_{yy}(x, 0) = 2\mu_{12}c_{22} \frac{h(x^2)}{x} \tag{4.4}$$

Since

$$h(x^2) = \frac{1}{\sqrt{(x^2 - c^2)(1 - x^2)}} H(x^2) \quad x^2 = c^2 \cos^2 \phi + \sin^2 \phi$$

equation (4.4) becomes

$$\Delta\tau_{yy}(x, 0) = \frac{2\mu_{12}c_{22} G(\phi)}{x \sqrt{(x^2 - c^2)(1 - x^2)}} \tag{4.5}$$

So the stress intensity factors N_c and N_1 at the two tips of the strip can be expressed as

$$N_c = \lim_{x \rightarrow c^+} \left[\frac{\Delta\tau_{yy}(x, 0)}{\pi c_{22}\mu_{12}} \sqrt{x - c} \right] = \frac{2}{\pi} \frac{G(0)}{c\sqrt{2c(1 - c^2)}} \quad (4.6)$$

and

$$N_1 = \lim_{x \rightarrow 1^-} \left[\frac{\Delta\tau_{yy}(x, 0)}{\pi c_{22}\mu_{12}} \sqrt{1 - x} \right] = \frac{2}{\pi} \frac{G\left(\frac{\pi}{2}\right)}{\sqrt{2(1 - c^2)}} \quad (4.7)$$

Making c tend to zero, the two strips merge into one, and in that case

$$N_1 = \frac{\sqrt{2}}{\pi} G\left(\frac{\pi}{2}\right)$$

Now from equation (2.15)₂ after substituting the value of $A_1(\xi)$ and using equation (3.1), we get the vertical displacement outside the strip as

$$v(x, y) = \frac{2}{\pi} \int_c^1 \frac{h(t^2)}{t} dt \left\{ \int_0^\infty (\alpha_1 e^{-\nu_1 y} - \alpha_2 e^{-\nu_2 y}) \frac{[1 - \cos(\xi t)] \cos(\xi x)}{\alpha_1 \nu_1 - \alpha_2 \nu_2} d\xi \right. \\ \left. + \int_0^\infty \frac{1}{\zeta} [\alpha_3 A_5(\zeta) \cosh(\nu_3 x) + \alpha_4 A_6(\zeta) \cosh(\nu_4 x)] \cos(\zeta y) d\zeta \right\} \quad (4.8)$$

5. Numerical calculations and discussions

It is important to choose a numerical method of solving the Fredholm integral equation. The Fox and Goodwin methods require that the definite integrals should be calculable by numerical quadrature, using known formulae in the theory of finite differences, and Fredholm equations are conveniently treated by solving simultaneous equations. The methods enable accurate solutions to be obtained without a prohibitive expenditure of time and energy. The choice of an interval is of course rather arbitrary. We want to keep to a minimum number of linear equations, but the interval must not be large that the finite-difference equations are meaningless. Since the differences are examined, the method guards against the possibility of obtaining wrong results from this case. It also ensures that neither too few nor too many differences are retained in the quadrature formulae.

The method of Fox and Goodwin (1953) has been used to solve integral equation (3.12) numerically for different values of the dimensionless frequency k_s , material strip width $2h$ and separating distance of the strips c . The integral in (3.12) has been represented by a quadrature formula involving values of the desired function G at pivotal points in the range of integration, which leads to a set of algebraic linear simultaneous equations. The solution of the set of linear algebraic equations gives the first approximation of the required pivotal values of G which has been improved by the use of the difference correction technique. After solving integral equation (3.12) for different values of engineering elastic constants of several orthotropic materials listed in Table 1, the stress intensity factors (SIF), k_c and k_1 at both ends of the strip given by equations (4.6) and (4.7) has been plotted against k_s for different values of h and c and for different materials. Instead of the real part of SIF, its mod value is taken because both shows the same type of results.

In Fig. 2a and 4a, N_c (SIF, at the inner edge of the strip) and N_1 (SIF, at the outer edge of the strip) have been plotted against k_s for $h = 2.0$ and $h = 2.5$ and for different strip lengths ($c = 0.2, 0.4, 0.6$) for material type I. In Fig. 3a and 5a, N_c and N_1 have been plotted against

Table 1. Engineering elastic constants

		E_1 [Pa]	E_2 [Pa]	μ_{12} [Pa]	ν_{12}
Type I	E-type glass-epoxi composite	$9.79 \cdot 10^9$	$42.3 \cdot 10^9$	$3.66 \cdot 10^9$	0.063
Type II	Stainless steel-aluminium composite	$79.76 \cdot 10^9$	$85.91 \cdot 10^9$	$30.02 \cdot 10^9$	0.31

k_s for $c = 0.4$ and $c = 0.6$ and for different material strip widths ($h = 2.0, 2.5, 3.0$) for material type I. The same set of parameters stated above for the graphs of N_c and N_1 have been plotted in Figs. 2b, 4b, 3b, 5b for material type II. For a particular value of material strip width h ($=2.0, 2.5$), the value of N_c decreases initially and, after increasing again, it decreases with an increase in k_s for material type I (Fig. 2a), whereas for material type II, it is slowly decreasing with an increase in k_s (Fig. 2b) for different values of strip length c ($=0.2, 0.4, 0.6$). It is also observed that with an increase in c , the value of N_c increases. When strip length c is fixed, the value of N_c is higher for higher values of h ($=2.0, 2.5, 3.0$) (Fig. 3a and Fig. 3b) for both types of materials. Figure 4 and 5 show that N_1 has initial decreasing tendency and then increases with an increase in k_s for both the materials. For fixed c , N_c is higher when material strip width h is higher. In all the cases, it is seen that as the length of the strip increases the value of N_1 decreases.

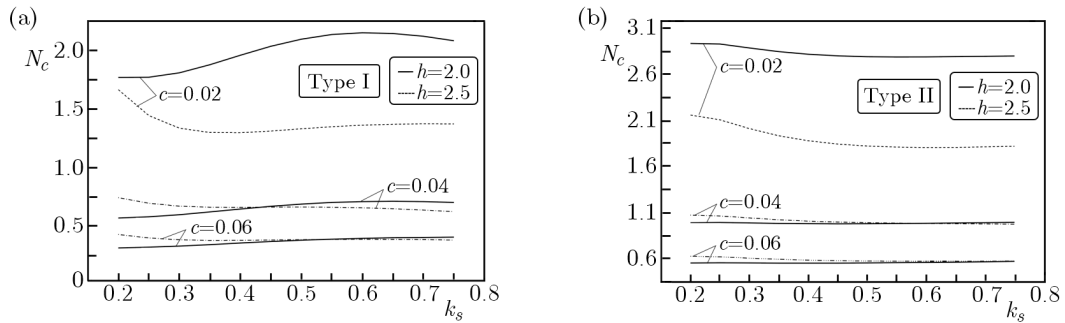


Fig. 2. Stress intensity factor N_c verses frequency k_s

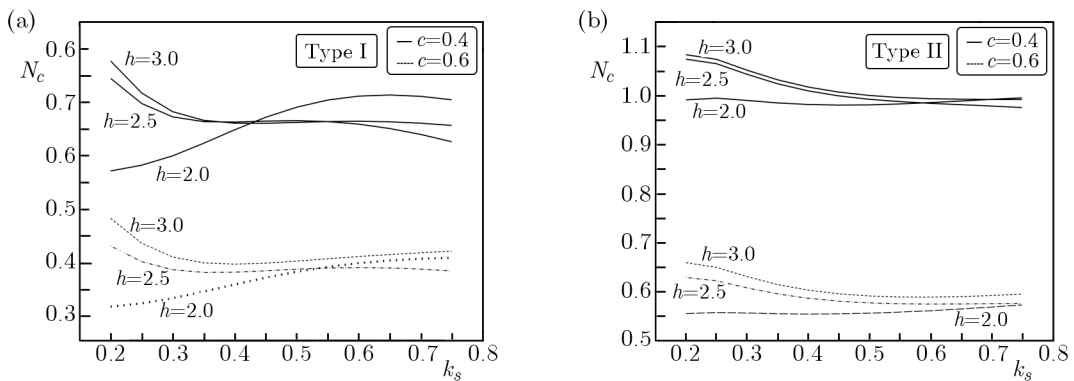


Fig. 3. Stress intensity factor N_c verses frequency k_s

Finally, in Fig. 6 and 7 the vertical displacement $v(x, y)$ has been plotted outside the strips ($0 < x < c, 1 < x < h$) for fixed values of $h = 2.5, k_s = 0.4$ and $c = 0.6$ for both the materials. In Fig. 6, $v(x, y)$ has been plotted for the inner side of the strip ($0 < x < c$) and in Fig. 7 for the outer side of the strip ($1 < x < h$). In Fig. 6a and 7a, it is observed that the vertical displacement $v(x, y)$ increases initially with an increment of the values of x and y , then it decreases for material I. But in the case of Fig. 6b and 7b, it is seen that the vertical displacement $v(x, y)$ increases slowly with an increase in the values of x and y , then it decreases

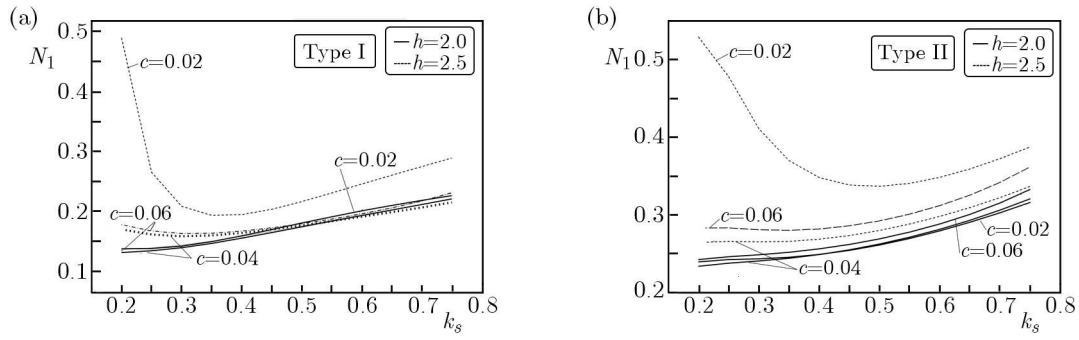


Fig. 4. Stress intensity factor N_1 versus frequency k_s

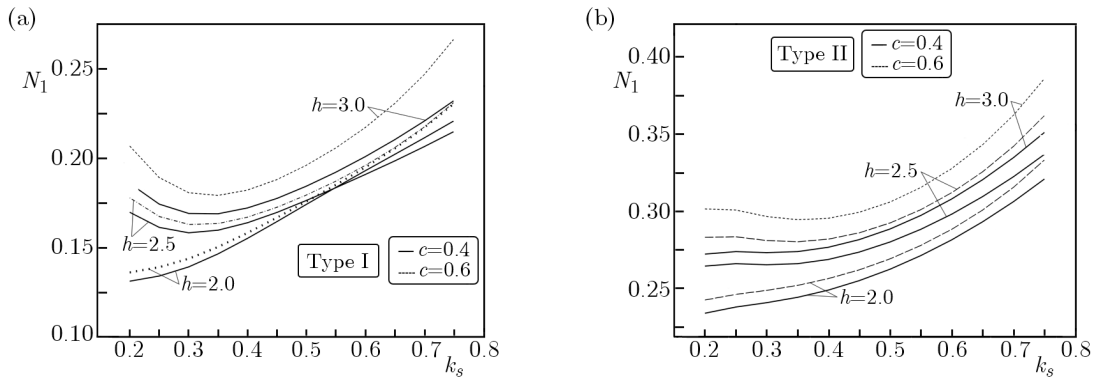


Fig. 5. Stress intensity factor N_1 versus frequency k_s

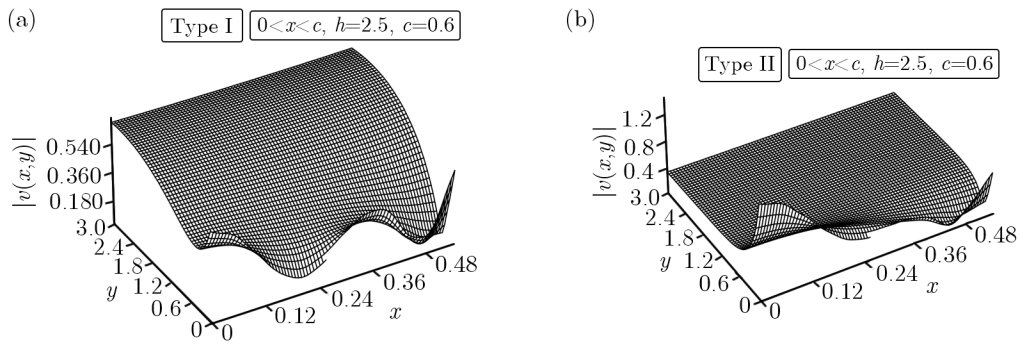


Fig. 6. Displacement $|v(x,y)|$ versus distances (x,y)

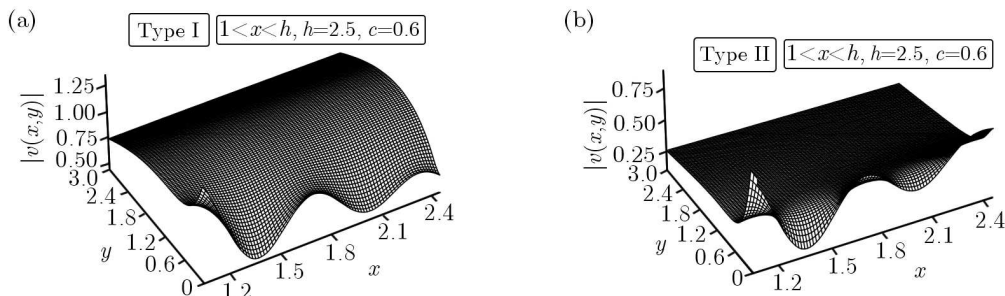


Fig. 7. Displacement $|v(x,y)|$ versus distances (x,y)

for material II. In all cases, the wave like nature has been observed, and finally the displacement tends to zero as $(x, y) \rightarrow \infty$, which satisfies the radiation condition.

6. Conclusions

The diffraction of the elastic P -wave by two rigid strips embedded in an infinite orthotropic strip is investigated on two types of materials by using the integral equation technique. The governing differential equation with constant coefficients with the boundary conditions becomes a mixed boundary value problem. Then, the mixed boundary value problem is transformed into a pair of dual integral equations with an unknown constant $A(\xi)$. To reduce the dual integral equations (2.17)₁ and (2.17)₂ to a single Fredholm integral equation, we assume the unknown constant $A(\xi)$ in the form of equation (3.1), so that equation (2.17)₂ can be automatically satisfied. Also, it has been found that the normal stress component $\tau_{yy}(x, 0)$ at the two tips of the strip has a square root singularity at $x = c$ and $x = 1$. The form of (3.1) has a square root type singularity in it, which can be utilized to find stress singularities at the tips of the strips.

From all the graphs of SIF, it can be concluded that the SIF decreases gradually with an increment of the frequency (k_s), after reaching the minimum value, it increases slowly. In all suggested cases, it is noted that the maximum value of the SIF at both tips of the strip for material II is little higher than that for material I. The SIF can be arrested within a certain range, which is very important with respect to growth of the crack. Finally, the vertical displacement $v(x, y)$ has been calculated outside the strips for both the materials. It has been observed the wave like nature from all the 3D figures, which finally decreases as the distance increases.

Acknowledgement

This research has been supported by the project "Mobile Computing and Innovative Applications" under UPE-II Programme of Jadavpur University. Also we thank the referees for their valuable comments to improve our paper.

References

1. CHEN E.P., 1978, Sudden appearance of a crack in a stretched finite strip, *Journal of Applied Mechanics*, **45**, 2, 277-280
2. CINAR A., ERDOGAN F., 1983, The crack and wedging problem for an orthotropic strip, *International Journal of Fracture*, **19**, 83-102
3. DAS S., 2002, Interaction between line cracks in an orthotropic layer, *International Journal Mathematics and Mathematical Sciences*, **29**, 2, 31-42
4. DAS S., CHAKRABORTY S., SRIKANTH N., GUPTA M., 2008, Symmetric edge cracks in an orthotropic strip under normal loading, *International Journal of Fracture*, **153**, 77-84
5. DAS S., PATRA B., DEBNATH L., 1998, Stress intensity factors for an interfacial crack between an orthotropic half-plane bonded to a dissimilar orthotropic layer with a punch, *Computers and Mathematics with Applications*, **35**, 12, 27-40
6. FOX L., GOODWIN E.T., 1953, The numerical solution of non-singular linear integral equations, *Philosophical Transactions A*, **245**, 501-534
7. ITOU S., 2012, Stress intensity factors for two parallel interface cracks between a nonhomogeneous bonding layer and two dissimilar orthotropic half-planes under tension, *International Journal of Fracture*, **175**, 187-192
8. LI X.L., 2005, Two perfectly-bonded dissimilar orthotropic strips with an interfacial crack normal to the boundaries, *Applied Mathematics and Computation*, **163**, 961-975

9. MANDAL S.C., GHOSH M.L., 1992, Forced vertical vibration of two rigid strips on a semi-infinite elastic solid, *Journal of Sound and Vibration*, **158**, 1, 169-179
10. MANDAL S.C., GHOSH M.L., 1994, Interaction of elastic waves with a periodic array of coplanar Griffith crack in an orthotropic medium, *International Journal of Engineering Science*, **32**, 1, 167-178
11. MANDAL S.C., PAL S.C, GHOSH M.L., 1997, Forced vertical vibration of four rigid strips on semi-infinite elastic solid, *International Journal of Solids and Structures*, **34**, 1017-1033
12. MANDAL S.C., PAL S.C, GHOSH M.L., 1998, Diffraction of elastic waves by four coplanar rigid strips embedded in an infinite orthotropic medium, *Journal of Engineering Mathematics*, **33**, 47-60
13. MONFARED M.M., AYATOLLAHI M., 2013, Dynamic stress intensity factors of multiple cracks in an orthotropic strip with FGM coating, *Engineering Fracture Mechanics*, **109**, 45-57
14. MORTEZA E.G., AMMAR M., AZIZOLLAH A.B., 2010a, Rocking vibration of a rigid circular disc in a transversely isotropic full-space, *International Journal for Numerical and Analytical Methods in Geomechanics* (Wiley online Library)
15. MORTEZA E.G., MORTEZA F., AZIZOLLAH A.B., 2010b, Forced vertical vibration of rigid circular disc on a transversely isotropic half-space, *Journal of Engineering Mechanics*, **136**, 913-922
16. MUKHERJEE S., DAS S., 2007, Interaction of three interfacial Griffith cracks between bonded dissimilar orthotropic half planes, *International Journal of Solids and Structures*, **44**, 5437-5446
17. PRAMANICK R.K., PAL S.C., GHOSH M.L., 1999, Shear wave interaction with a pair of rigid strips embedded in an infinitely long elastic strip, *Journal of Technical Physics*, **39**, 31-44
18. SARKAR J., GHOSH M.L., MANDAL S.C., 1995, Diffraction of elastic waves by two parallel rigid strips embedded in an infinite orthotropic medium, *International Journal of Engineering Science*, **33**, 13, 1943-1958
19. SARKAR J., MANDAL S.C., GHOSH M.L., 1995, Diffraction of elastic waves by three coplanar Griffith cracks in an orthotropic medium, *International Journal of Engineering Science*, **33**, 2, 163-177
20. SIH G.C., 1977, *Elastodynamic Crack Problems in Mechanics of Fracture*, Noordhoff Leyden, **4**
21. SIH G.C., CHEN E.P., 1981, *Cracks in Composite Materials*, Martinus Nijhoff Publishers, **6**
22. SINGH B.M., ROKNE J., DHALIWAL R.S., 1983, Diffraction of torsional wave by a circular rigid disc at the interface of two bonded dissimilar elastic solids, *Acta Mechanica*, **49**, 139-146
23. SINHAROY S., 2013, Elastostatic problem of an infinite row of parallel cracks in an orthotropic medium under general loading, *International Journal of Physics and Mathematical Sciences*, **3**, 1, 96-108
24. WICKHAM G.R., 1977, The forced two dimensional oscillations of a rigid strip in smooth contact with a semi-infinite elastic solid, *Mathematical Proceedings of the Cambridge Philosophical Society*, **81**, 291-311
25. WU D., CAI Y., XU C., ZHAN H., 2006, Torsional vibrations of rigid circular plate on transversely isotropic saturated soil, *Applied Mathematics and Mechanics*, **27**, 1541-1548

THE THERMOELASTIC PROBLEM FOR A PENNY-SHAPED ANTICRACK WITH HEAT CONDUCTIVITY IN A TRANSVERSELY ISOTROPIC SPACE

ANDRZEJ KACZYŃSKI

*Warsaw University of Technology, Faculty of Mathematics and Information Science, Warsaw, Poland
e-mail: akacz@mini.pw.edu.pl*

BOHDAN MONASTYRSKYI

Protein Structure Prediction Center, University of California Davis, Davis, CA USA; e-mail: bmonast@gmail.com

An analytical solution of a 3D transversely isotropic thermoelastic problem of a uniform heat flow disturbed by a penny-shaped rigid sheet-like inclusion (anticrack) with some small conductivity is obtained by using the potential theory method. The behaviour of thermal stresses near the edge of the disc is analysed from the standpoint of the mechanics of fracture initiation.

Keywords: transversely isotropic space, circular anticrack, heat flow, singular integral equations, thermal stress singularities

1. Introduction

The study of thermal stresses in solids containing foreign inhomogeneities has great importance for the evaluation of the strength of materials and structures which operate under thermal actions. The rapid development of high-strength composite materials has driven researches to take into account the influence of anisotropy in thermomechanical fields for fractured bodies. In addition to cracks, rigid lamellate inclusions (also called anticracks, for brevity) are objects around which stress concentrations occur, which will stimulate failure of materials. Most of research works discuss 2D problems dealing with these defects. Owing to mathematical complexity, only few publications on the subject within 3D statement of thermoelastic anticrack problems can be found in the literature (see Kit and Khay, 1989; Stadnyk, 1994, 2011; Podil'chuk, 2001; Chaudhuri, 2003; Kaczyński and Kozłowski, 2009; Kaczyński and Monastyrskyy, 2013).

This work treats a rigid penny-shaped inclusion obstructing a uniform perpendicular heat flow in a transversely isotropic space. It may be regarded as a sequel to our papers (Kaczyński and Monastyrskyy, 2009; Kaczyński, 2014; see also extensive references therein) in which a classical condition of thermal insulation of the inclusion faces was assumed. The present contribution focuses on the determination of a stationary temperature field with more general thermal condition by taking into account certain conductivity of a rigid inclusion. The associated problem of induced thermal stresses is reduced to a two-dimensional singular equation with the unknown normal stress discontinuity across inclusion faces, a closed-form solution to which is found by use of Dyson and Galin theorems. Relations for the evaluation of stresses near the inclusion edge are presented and interpreted from a fracture perspective. Moreover, thermal and mechanical fields for thermally conductive and insulated anticracks are compared.

2. Thermoelastostatics of transversely isotropic materials

Let us recall the basic relations of uncoupled thermoelasticity for homogeneous transversely isotropic materials. Referring to a Cartesian coordinate system (X_1, X_2, X_3) and denoting the

temperature, fluxes, displacements and stresses by T , q_i , u_i , σ_{ij} , respectively, the governing equations for an infinite transversely isotropic thermoelastic solid whose isotropic plane is perpendicular to the X_3 -axis and, in absence of body forces and heat sources, are (Ding *et al.*, 2006; Kaczyński, 2014)

$$\begin{aligned}
 T_{,\gamma\gamma} + k_0^{-2}T_{,33} &= 0 \\
 q_\alpha &= -k_1T_{,\alpha} & q_3 &= -k_3T_{,3} \\
 \frac{1}{2}(c_{11} + c_{12})u_{\gamma,\gamma\alpha} + \frac{1}{2}(c_{11} - c_{12})u_{\alpha,\gamma\gamma} + c_{44}u_{\alpha,33} + (c_{13} + c_{44})u_{3,3\alpha} &= \beta_1T_{,\alpha} \\
 (c_{13} + c_{44})u_{\gamma,\gamma 3} + c_{44}u_{3,\gamma\gamma} + c_{33}u_{3,33} &= \beta_3T_{,3} \\
 \sigma_{3\alpha} &= c_{44}(u_{\alpha,3} + u_{3,\alpha}) \\
 \sigma_{33} &= c_{13}u_{\gamma,\gamma} + c_{33}u_{3,3} - \beta_3T \\
 \sigma_{12} &= \frac{1}{2}(c_{11} - c_{12})(u_{1,2} + u_{2,1}) \\
 \sigma_{11} &= c_{11}u_{1,1} + c_{12}u_{2,2} + c_{13}u_{3,3} - \beta_1T \\
 \sigma_{22} &= c_{12}u_{1,1} + c_{11}u_{2,2} + c_{13}u_{3,3} - \beta_1T
 \end{aligned} \tag{2.1}$$

Moreover,

$$k_0 = \sqrt{\frac{k_1}{k_3}} \quad \beta_1 = (c_{11} + c_{12})\alpha_1 + c_{13}\alpha_3 \quad \beta_3 = 2c_{13}\alpha_1 + c_{33}\alpha_3 \tag{2.2}$$

In the equations given above, $k_1(\alpha_1)$ and $k_3(\alpha_3)$ denote the coefficients of conductivity (of thermal expansion) in the plane isotropy and along the X_3 -axis of rotational material symmetry, respectively, and c_{11} , c_{12} , c_{13} , c_{33} , c_{44} are five independent elastic constants. Indices i, j run over 1, 2, 3 while indices α, γ run over 1, 2. Summation convention holds unless otherwise stated. Subscripts preceded by a comma indicate partial differentiation with respect to the corresponding coordinates.

3. Formulation of the anticrack problem

Consider a transversely isotropic space weakened by a penny-shaped rigid inclusion (anticrack) subjected to a uniform steady-flow of heat q_0 in the direction of the negative X_3 -axis as shown in Fig. 1. The anticrack region S on the mid-plane of transverse isotropy $x_3 = 0$ is denoted as $r \equiv \sqrt{x_1^2 + x_2^2} \leq a$.

We are faced with the boundary-value problem: find the fields T and u_i suitable smooth on $R^3 - S$ such that Eqs. (2.1) hold, subject to the following boundary conditions:

- thermal conditions taking into account the thermal conductivity within the anticrack S
- mechanical conditions for $(x_1, x_2, x_3 = 0^\pm) \in S$ with a small constant ε characterizing the rigid vertical translation

$$u_1 = u_2 = 0 \quad u_3 = \varepsilon \tag{3.1}$$

- thermal and mechanical conditions at infinity

$$\begin{aligned}
 q_1 = q_2 &= 0 & q_3 &= -q_0 & (q_0 > 0) \\
 \sigma_{ij} &= 0
 \end{aligned} \tag{3.2}$$

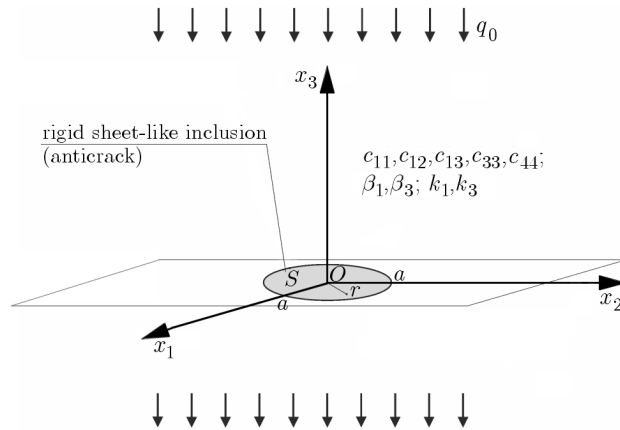


Fig. 1. A transversely isotropic space with a penny-shaped conductive anticrack subjected to a perpendicular uniform flow

4. Solution

By means of the superposition principle, it is convenient to represent the solution to the anticrack boundary-value problem as a sum of two components, namely

$$T = T^{(0)} + \tilde{T} \quad u_i = u_i^{(0)} + \tilde{u}_i \quad \sigma_{ij} = \sigma_{ij}^{(0)} + \tilde{\sigma}_{ij} \tag{4.1}$$

where the components attached by 0 describe the basic state of the defect-free solid, and the components with the tilde represent perturbations due to the anticrack.

The results for the first 0-problem are found to be given by Kaczyński (2014)

$$\begin{aligned} T^{(0)} &= \frac{q_0}{k_3} x_3 \\ u_\alpha^{(0)} &= \frac{\beta_3 q_0}{k_3(2c_{13} + c_{33})} x_\alpha x_3 \quad u_3^{(0)} = \frac{\beta_3 q_0}{2k_3(2c_{13} + c_{33})} (x_3^2 - x_1^2 - x_2^2) \\ \sigma_{ij}^{(0)} &= 0 \end{aligned} \tag{4.2}$$

Attention will be next drawn to the corrective solution of the perturbed problem. The disturbing thermal field \tilde{T} , decaying at infinity, is determined by solving quasi-Laplace equation (2.1)₁ with applying the following model expressions related to the rigid disc S , given from Kaczyński and Monastyrskyy (2009)

$$\begin{aligned} \tilde{T}_{,3}(x_1, x_2, x_3 = 0^+) - \tilde{T}_{,3}(x_1, x_2, x_3 = 0^-) &= 0 \\ \tilde{T}(x_1, x_2, 0^+) - \tilde{T}(x_1, x_2, 0^-) - k_3 R(x_1, x_2) \tilde{T}_{,3}(x_1, x_2, 0^+) &= q_0 R(x_1, x_2) \end{aligned} \tag{4.3}$$

where $R(x_1, x_2)$ is interpreted as the thermal anticrack resistance.

From the potential theory (Kellogg, 1953), the solution is expressed as follows

$$\tilde{T}(x_1, x_2, x_3) = \left. \frac{\partial \tilde{\omega}(x_1, x_2, z_0)}{\partial z_0} \right|_{z_0=k_0 x_3} \tag{4.4}$$

with

$$\tilde{\omega}(x_1, x_2, z_0) = -\frac{1}{2\pi} \iint_S \frac{\omega(\xi_1, \xi_2) d\xi_1 d\xi_2}{\sqrt{(x_1 - \xi_1)^2 + (x_2 - \xi_2)^2 + z_0^2}} \tag{4.5}$$

Using the well-known property of a simple layer potential, the satisfaction of Eq. (4.3)₂ leads to an integro-differential singular equation of the Newton type for the unknown density of the potential of the single layer $\omega(\xi_1, \xi_2)$

$$2\omega(x_1, x_2) - \frac{\sqrt{k_1 k_3} R(x_1, x_2)}{2\pi} \Delta \iint_S \frac{\omega(\xi_1, \xi_2) d\xi_1 d\xi_2}{\sqrt{(x_1 - \xi_1)^2 + (x_2 - \xi_2)^2}} = q_0 R(x_1, x_2) \tag{4.6}$$

in which $\Delta \equiv \frac{\partial^2}{\partial x_1^2} + \frac{\partial^2}{\partial x_2^2}$ stands for the two-dimensional Laplace operator. Assuming next that

$$R(x_1, x_2) = \tilde{R}(r) = R_0 \sqrt{a^2 - r^2} \quad R_0 > 0 \tag{4.7}$$

an analytical solution to Eq. (4.6) is achieved in the form

$$\omega(x_1, x_2) = \tilde{\omega}(r) = \frac{2\tilde{q}}{\pi \sqrt{k_1 k_3}} \sqrt{a^2 - r^2} \tag{4.8}$$

with

$$\tilde{q} = q_0 \left(1 + \frac{4}{\pi \sqrt{k_1 k_2} R_0} \right)^{-1} \leq q_0 \tag{4.9}$$

Inserting Eq. (4.8) into (4.5) and after integration we arrive at the following elementary formulas for the main thermal potential $\tilde{\omega}$ for $x_3 \geq 0$ (see Fabrikant, 1989)

$$\tilde{\omega}(x_1, x_2, z_0) = -\frac{\tilde{q}}{2\pi \sqrt{k_1 k_3}} \left[(2a^2 + 2z_0^2 - r^2) \sin^{-1} \frac{a}{l_{20}} - \frac{2a^2 - 3l_{10}^2}{a} \sqrt{l_{20}^2 - a^2} \right] \tag{4.10}$$

and, in view of Eqs. (4.4) and (2.1)₂, for the temperature \tilde{T} and heat fluxes \tilde{q}_i

$$\begin{aligned} \tilde{T}(x_1, x_2, x_3) &= -\frac{2\tilde{q}}{\pi \sqrt{k_1 k_3}} \left(k_0 x_3 \sin^{-1} \frac{a}{l_{20}} - \sqrt{a^2 - l_{10}^2} \right) \\ \tilde{q}_\alpha &= \frac{2\tilde{q} a^2}{\pi} \sqrt{\frac{k_1}{k_3}} \frac{x_\alpha \sqrt{a^2 - l_{10}^2}}{l_{20}^2 (l_{20}^2 - l_{10}^2)} \quad \tilde{q}_3 = \frac{2\tilde{q}}{\pi} \left(\sin^{-1} \frac{a}{l_{20}} - \frac{a \sqrt{l_{20}^2 - a^2}}{l_{20}^2 - l_{10}^2} \right) \end{aligned} \tag{4.11}$$

Here

$$\begin{aligned} l_1 = l_1(x_3) &= \frac{1}{2} \left[\sqrt{(r+a)^2 + x_3^2} - \sqrt{(r-a)^2 + x_3^2} \right] & l_{10} &= l_1(z_0) \\ l_2 = l_2(x_3) &= \frac{1}{2} \left[\sqrt{(r+a)^2 + x_3^2} + \sqrt{(r-a)^2 + x_3^2} \right] & l_{20} &= l_2(z_0) \end{aligned} \tag{4.12}$$

In the inclusion plane $x_3 = 0^\pm$ (making use of the relations $l_{10}|_{x_3=0} = \min(a, r)$, $l_{20}|_{x_3=0} = \max(a, r)$), we obtain

$$\begin{aligned} T(r, 0^\pm) &= \begin{cases} \pm \frac{2\tilde{q}}{\pi \sqrt{k_1 k_3}} \sqrt{a^2 - r^2} & 0 \leq r \leq a \\ 0 & r > a \end{cases} \\ q_r(r, 0^\pm) = -k_1 \frac{\partial T(r, 0^\pm)}{\partial r} &= \begin{cases} \pm \frac{2\tilde{q}}{\pi} \sqrt{\frac{k_1}{k_3}} \frac{r}{\sqrt{a^2 - r^2}} & 0 \leq r \leq a \\ 0 & r > a \end{cases} \\ q_3(r, 0^\pm) = -k_3 T_{,3}(r, 0^\pm) &= \begin{cases} \tilde{q} - q_0 & 0 \leq r < a \\ \frac{2\tilde{q}}{\pi} \left(\sin^{-1} \frac{a}{r} - \frac{a}{\sqrt{r^2 - a^2}} \right) - q_0 & r > a \end{cases} \end{aligned} \tag{4.13}$$

It follows from these formulas that the rigid inclusion acts as an obstruction to the given heat flow, producing thermal local disturbances such as the jump of temperature T across the inclusion plane and the infinite increase of the heat fluxes in the interior vicinity of the inclusion edge.

Now we pass to the non-trivial perturbed elastic problem, affixed by the tilde and connected with the determination of the induced state of stress and deformation resulting from the known disturbed temperature $\tilde{T} = (\partial\tilde{\omega}/\partial z_0)|_{z_0=k_0x_3}$. Because of the anti-symmetry of the temperature and stress system, and bearing in mind Eqs. (3.1), (4.1) and (4.2), it reduces to that of the half space $x_3 \geq 0$ subjected to the following mixed boundary conditions

$$\begin{aligned} \tilde{u}_\alpha(x_1, x_2, x_3 = 0^+) &= 0 & (x_1, x_2) \in R^2 \\ \tilde{u}_3(x_1, x_2, x_3 = 0^+) &= \frac{\beta_3 q_0}{2k_3(2c_{13} + c_{33})}(x_1^2 + x_2^2) + \varepsilon & (x_1, x_2) \in S \end{aligned} \tag{4.14}$$

and

$$\begin{aligned} \tilde{\sigma}_{33}(x_1, x_2, x_3 = 0^+) &= 0 & (x_1, x_2) \in R^2 - S \\ \tilde{u}_i &= O(|x|^{-1}) & |x| = \sqrt{x_1^2 + x_2^2 + x_3^2} \rightarrow \infty \end{aligned} \tag{4.15}$$

Moreover, having found the distribution of the normal stress $\tilde{\sigma}_{33}|_{S^+} \equiv q(x_1, x_2)$ in the region S , the unknown rigid translation ε can be calculated from the equilibrium condition

$$\iint_S q(x_1, x_2) dx_1 dx_2 = 0 \tag{4.16}$$

A solution to this problem was given by Kaczyński (2014). Here only the main idea and final results with some modifications will be presented.

An efficient approach is based on the construction of harmonic potentials that satisfy governing equations (2.1)_{3,4} and are well suited to the above-mentioned anticrack boundary conditions. We take the following displacement representation expressed by potentials $\tilde{\phi}_\alpha \equiv \tilde{\phi}_\alpha(x_1, x_2, z_\alpha)$, $z_\alpha = t_\alpha x_3$, $\alpha = 1$ or $\alpha = 2$

$$\tilde{u}_\alpha = \left(\tilde{\phi}_1 + \tilde{\phi}_2 + c_1 \int_{z_0}^{\infty} \tilde{\omega}(x_1, x_2, z_0) dz_0 \right)_{,\alpha} \quad \tilde{u}_3 = m_\alpha t_\alpha \frac{\partial \tilde{\phi}_\alpha}{\partial z_\alpha} + c_2 k_0 \tilde{\omega} \tag{4.17}$$

with the potentials satisfying the harmonic equations

$$\left(\Delta + \frac{\partial^2}{\partial z_\alpha^2} \right) \tilde{\phi}_\alpha = 0 \quad \alpha = 1, 2 \quad (\text{no sum on } \alpha) \tag{4.18}$$

Here the constants m_α , c_α , t_α are given in Appendix A of Kaczyński (2014). Note that the general case $t_1 \neq t_2$, $t_\alpha \neq k_0$ is considered.

Next we put

$$\tilde{\phi}_\alpha = (-1)^\alpha \tilde{f}(x_1, x_2, z_\alpha) + a_\alpha \int_{z_\alpha}^{\infty} \tilde{\omega}(x_1, x_2, z_\alpha) dz_\alpha \quad \alpha = 1, 2 \quad (\text{no sum on } \alpha) \tag{4.19}$$

where

$$\left(\Delta + \frac{\partial}{\partial x_3^2} \right) \tilde{f}(x_1, x_2, x_3) = 0 \tag{4.20}$$

and choose the constants a_α in order to satisfy a part of boundary conditions (3.1). In this way, the perturbed anticrack problem reduces to the determination of a potential function \tilde{f} in the upper half-space, decaying at infinity and satisfying the following mixed conditions on the X_1X_2 -plane

$$\begin{aligned} \left. \frac{\partial \tilde{f}(x_1, x_2, x_3)}{\partial x_3} \right|_{x_3=0^+} &= \frac{1}{m_2 t_2 - m_1 t_1} f_0(x_1, x_2) & (x_1, x_2) \in S \\ \left. \frac{\partial^2 \tilde{f}(x_1, x_2, x_3)}{\partial x_3^2} \right|_{x_3=0^+} &= 0 & (x_1, x_2) \in R^2 - S \end{aligned} \quad (4.21)$$

where

$$f_0(x_1, x_2) = \tilde{f}_0(r) = -\beta^* \tilde{\omega}(r, 0) + Ar^2 + \varepsilon = \frac{\beta^* \tilde{q} a^2}{2\sqrt{k_1 k_3}} + \varepsilon + \left(A - \frac{\beta^* \tilde{q}}{4\sqrt{k_1 k_3}} \right) r^2 \quad (4.22)$$

with the following constants

$$\begin{aligned} \beta^* &= c_2 k_0 - a_\alpha m_\alpha t_\alpha & a_1 &= \frac{c_1(1+m_2) - \frac{\delta_3}{c_{44}}}{m_1 - m_2} & a_2 &= \frac{-c_1(1+m_1) + \frac{\delta_3}{c_{44}}}{m_1 - m_2} \\ \delta_3 &= \beta_3 - c_1 c_{13} - c_2 c_{33} k_0^2 & A &= \frac{\beta_3 q_0}{2k_3(2c_{13} + c_{33})} \end{aligned} \quad (4.23)$$

It is known from the potential theory (Kellogg, 1953) that the solution to this problem is represented by the Newton potential of a simple layer distributed over the region S as

$$\tilde{f}(x_1, x_2, x_3) = \frac{1}{2\pi c_{44}(m_1 - m_2)} \iint_S q(\xi_1, \xi_2) \ln\left(\sqrt{(x_1 - \xi_1)^2 + (x_2 - \xi_2)^2 + x_3^2} + x_3\right) d\xi_1 d\xi_2 \quad (4.24)$$

where the unknown layer density q can be identified as the normal stress $\tilde{\sigma}_{33}|_{S^+}$. Taking consideration of the first condition in Eq. (4.21), the following governing two-dimensional singular integral equation (similar to that arising in classical contact mechanics) is obtained

$$\tilde{H} \iint_S \frac{q(\xi_1, \xi_2) d\xi_1 d\xi_2}{\sqrt{(x_1 - \xi_1)^2 + (x_2 - \xi_2)^2}} = -f_0(x_1, x_2) \quad (x_1, x_2) \in S \quad (4.25)$$

with f_0 given by Eq. (4.22) and \tilde{H} defined by

$$\tilde{H} = \frac{m_2 t_2 - m_1 t_1}{2\pi c_{44}(m_2 - m_1)} = \frac{\sqrt{c_{11} c_{33}} + c_{44}}{2\pi \sqrt{c_{44} c_{33}} \sqrt{(\sqrt{c_{11} c_{33}} - c_{13})(\sqrt{c_{11} c_{33}} + c_{13} + 2c_{44})}} \quad (4.26)$$

Taking a solution to this equation in the form (using Dyson's and Galin's theorems)

$$q(x_1, x_2) = \tilde{q}(r) = \frac{\tilde{p}_0 a^2 - \tilde{p}_2 r^2}{\tilde{H} \pi^2 \sqrt{a^2 - r^2}} \quad 0 \leq r < a \quad (4.27)$$

and substituting it into Eq. (4.25), after appropriate calculations and utilizing Eq. (4.16), we find the unknown coefficients \tilde{p}_0 and \tilde{p}_2 as well as the rigid vertical displacement ε

$$\tilde{p}_2 = 4A - \frac{\beta^* \tilde{q}}{\sqrt{k_1 k_3}} \quad \tilde{p}_0 = \frac{2}{3} \tilde{p}_2 \quad \varepsilon = -a^2 \left(2A - \frac{1}{3} \tilde{p}_2 \right) \quad (4.28)$$

The primary harmonic potential to the thermoelastic perturbed problem is obtained by calculating integral (4.24) with the use of Eq. (4.27). From the results given in Fabrikant (1989, 1991), it is found that for $x_3 \geq 0$

$$\begin{aligned} \tilde{f}(r, x_3) = & -\frac{\tilde{p}_2}{3\pi^2(m_2t_2 - m_1t_1)} \left[x_3 \sin^{-1} \frac{a}{l_2} \left(a^2 - \frac{3}{2}r^2 + x_3^2 \right) \right. \\ & \left. + \sqrt{a^2 - l_1^2} \left(\frac{5}{2}r^2 + \frac{1}{3}a^2 - l_2^2 - \frac{11}{6}l_1^2 \right) \right] \end{aligned} \tag{4.29}$$

The expressions for the full-space stress-displacement field can then be obtained from Eq. (4.29) by simple differentiation, with all results being in terms of elementary functions. As easily seen, the solution is axially symmetric. In particular, let us focus on some quantities in the anticrack plane which are presented below

$$\begin{aligned} u_1(r, 0^\pm) = u_2(r, 0^\pm) = 0 & \quad 0 \leq r < \infty \\ u_3(r, 0^\pm) = \begin{cases} \varepsilon & 0 \leq r < a \\ \frac{2}{\pi}(\varepsilon + Ar^2) \sin^{-1} \frac{a}{r} - \frac{2Aa}{\pi} \sqrt{r^2 - a^2} - Ar^2 & r > a \end{cases} \\ \sigma_{33}(r, 0^\pm) = \begin{cases} \pm \frac{\tilde{p}_2}{3\tilde{H}\pi^2} \frac{2a^2 - 3r^2}{\sqrt{a^2 - r^2}} & 0 \leq r < a \\ 0 & r > a \end{cases} \\ \sigma_{3r}(r, 0^\pm) = \begin{cases} \tilde{\beta}r & 0 \leq r < a \\ \frac{2}{\pi} \left(\tilde{\beta}r \sin^{-1} \frac{a}{r} - \frac{\tilde{\beta}_0 a^3}{r\sqrt{r^2 - a^2}} - \frac{\tilde{\beta}a\sqrt{r^2 - a^2}}{r} \right) & r > a \end{cases} \end{aligned} \tag{4.30}$$

where

$$\begin{aligned} \tilde{\beta}_0 = \tilde{p}_2 \frac{c_{44}(\sqrt{c_{11}c_{33}} - c_{13})}{3(\sqrt{c_{11}c_{33}} + c_{44})} & \quad \tilde{\beta} = \frac{c_{44}}{2} \left[3\tilde{\beta}_0 - q_0 \frac{\tilde{\delta} + (c_1 - c_2)k_0}{\sqrt{k_1k_2}} \right] \\ \tilde{\delta} = \frac{(\sqrt{c_{11}c_{33}} - c_{13})(2c_1c_{44} - \delta_3)}{c_{33}c_{44}(t_1 + t_2)} & - c_1(t_1 + t_2) \end{aligned} \tag{4.31}$$

5. Analysis of the results and conclusions

The analytical results obtained in the previous Section are useful in interpreting the mechanics of fracture initiation at the rim of the rigid inclusion. In view of linear fracture mechanics, two failure mechanisms are possible: mode II (edge-sliding) of fracture deformation characterized by the stress intensity factor

$$K_{II} = \lim_{r \rightarrow a^+} \sqrt{2\pi(r - a)} \sigma_{3r}(r, 0) = -\frac{2\tilde{\beta}_0 a \sqrt{a}}{\sqrt{\pi}} \tag{5.1}$$

and the possible detachment of the material from the inclusion surface described by the stress intensity coefficients

$$S_I^\pm = \lim_{r \rightarrow a^-} \sqrt{2\pi(a - r)} \sigma_{33}(r, 0^\pm) = \mp \frac{\tilde{p}_2 a \sqrt{a}}{3\pi \sqrt{\pi} \tilde{H}} \tag{5.2}$$

These parameters can be used in conjunction with a suitable failure criterion.

In conclusion, by taking into account some interior conductivity of the anticrack, we have pointed out that by letting $R_0 \rightarrow \infty$ (see Eqs. (4.6) and (4.7)) the present solution with

$\tilde{q} = q_0$ (cf. Eq. (4.9)) reduces to that dealing with the case of a thermally insulated rigid circular inclusion obtained in Kaczyński (2014). Moreover, comparison between thermally conductive and insulated anticracks in a transversely isotropic (in particular, isotropic) space has shown only quantitative changes in the temperature and stress distributions.

References

1. CHAUDHURI R.A., 2003, Three-dimensional asymptotic stress field in the vicinity of the circumference of a penny-shaped discontinuity, *International Journal of Solids and Structures*, **40**, 3787-3805
2. DING H., CHEN W., ZHANG L., 2006, *Elasticity of Transversely Isotropic Materials*, Solid Mechanics and its Applications, **126**, Springer, The Netherlands
3. FABRIKANT V.I., 1989, *Applications of Potential Theory in Mechanics: A Selection of New Results*, Kluwer Academic Publishers, Dordrecht
4. FABRIKANT V.I., 1991, *Mixed Boundary Value problems of Potential Theory and their Applications*, Kluwer Academic Publishers, Dordrecht
5. KACZYŃSKI A., 2014, Thermal stress analysis of a three-dimensional anticrack in a transversely isotropic solid, *International Journal of Solids and Structures*, **51**, 2382-2389
6. KACZYŃSKI A., KOZŁOWSKI W., 2009, Thermal stresses in an elastic space with a perfectly rigid flat inclusion under perpendicular heat flow, *International Journal of Solids and Structures*, **46**, 1772-1777
7. KACZYŃSKI A., MONASTYRSKYY B., 2009, On the thermoelastic problem of uniform heat flow disturbed by a circular rigid lamellate inclusion, *Archives of Mechanics*, **61**, 3/4, 309-324
8. KACZYŃSKI A., MONASTYRSKYY B., 2013, A rigid inclusion in an elastic space under the action of a uniform heat flow in the inclusion plane, *International Journal of Solids and Structures*, **50**, 2631-2640
9. KELLOGG O.D., 1953, *Foundation of Potential Theory*, Dover, New York
10. KIT H.S., KHAY M.V., 1989, *Method of Potentials in Three-Dimensional Thermoelastic Problems of Bodies with Cracks* (in Russian), Naukova Dumka, Kiev
11. PODIL'CHUK YU.,N., 2001, Exact analytical solutions of three-dimensional static thermoelastic problems for a transversally isotropic body in curvilinear coordinate systems, *International Applied Mechanics*, **37**, 6, 728-761
12. STADNYK M.M., 1994, Method for the solution of the three-dimensional thermoelasticity for bodies with thin inclusions, *Materials Science*, **30**, 6, 643-653
13. STADNYK M.M., 2011, Elastic-ellipsoidal heat-conducting inclusion in a body under the action of a heat flux applied at infinity, *Materials Science*, **47**, 3, 284-293

Manuscript received February 22, 2015; accepted for print October 9, 2015

INFLUENCE OF UNCERTAINTY IN AERODYNAMIC PERFORMANCE ON THE DYNAMIC RESPONSE OF A TWO STAGE GEAR SYSTEM

MANEL TOUNSI, MOEZ BEYAOUI, KAMEL ABBOUDI, NABIH FEKI,
LASSAAD WALHA, MOHAMED HADDAR

*Laboratory of Mechanics, Modelling and Manufacturing (LA2MP), National School of Engineers of Sfax, Sfax, Tunisia
e-mail: manelt@yahoo.fr; moez.beyaoui@yahoo.fr; kamalo1982@yahoo.fr; fekinabih@gmail.com; walhalassaad@yahoo.fr;
mohamed.haddar@enis.rnu.tn*

In this paper, the nonlinear dynamic response in a wind turbine system is considered and the quantification of uncertainty effects on the variability of this nonlinear response is investigated. Under dynamic conditions, a lumped model with 12 degrees of freedom is proposed taking into account the uncertainty associated to the power coefficient of the input aerodynamic torque. The dynamic response of the two-stage spur gear system is obtained using ODE45 solver of Matlab. The Polynomial Chaos (PC) method is used to introduce the uncertainties on the proposed model. A comparison between the two dynamic responses given by the proposed lumped dynamic model takes into account the uncertainty. It is performed on the existed model without uncertainty. Thus, the efficiency and robustness of the proposed new methodology is evaluated.

Keywords: gearbox, uncertainty, power coefficient, random parameter, polynomial chaos

1. Introduction

Recently, due to increasing demand for energy, there has been a rapid development of wind turbines all over the world. This constant growth in energy consumption and polluting effects associated are in the heart of the issue of the environmental care, so that an increasing attention is being paid to wind energy. Generally, wind turbines are one of the machines that take advantage of wind energy to generate electrical power.

During preliminary design of dynamic systems, many physical parameters can have a significant effect on the vibration response of the system. Indeed, some features can generate nonlinear responses need to be taken into account. The aerodynamic complexities are involved in optimisation of wind turbine systems in an attempt to maximise its performance. Their aerodynamic and dynamic properties have a decisive influence on the entire system. These properties are responsible of rotor capability to convert wind energy into mechanical energy. Thus, the overall efficiency of the energy conversion in the wind turbine is determined.

Several studies have been developed to study the dynamic behaviour of wind turbines (Abboudi *et al.*, 2011; Helsen *et al.*, 2011; Zhu *et al.*, 2014). However, the modelling of these mechanical systems admits strong dispersions and uncertainties. In this context, design parameters may vary in an uncertain way during the manufacturing monitoring or operation. Thus, the response may change in some uncertain way. Therefore, the formulation of dynamical systems requires introducing uncertainties into input parameters. In this field, Wei *et al.* (2015) studied the dynamic response of a geared transmission system of a wind turbine with uncertainty.

To take into account the uncertainties, different methods are reported in the literature, such as Monte Carlo simulations (Rubinstein, 1981; Kalos and Whitlock, 1986), Polynomial Chaos Expansion (Wiener, 1938; Ghanem and Spanos, 1991; Fisher and Bhattacharya, 2008).

The main idea of the polynomial chaos methods is to transform the stochastic differential equations by means of an intrusive Galerkin projection (Ghanem and Spanos, 1991; Jakerman and Roberts, 2009) into a deterministic set of differential equations. Moreover, mechanical systems operate under parametric and external excitation uncertainties. Such as reported in the literature, the Polynomial Chaos approach is the efficient method comparing to the Monte Carlo approach for quantifying the effects of such uncertainties on the system response.

The capabilities of polynomial chaos have been illustrated in numerous fields, such as environmental and biological problems (Isukapalli *et al.*, 1998a,b), fluid dynamics (Pettersson *et al.*, 2009; Chantrasmı *et al.*, 2066), multibody dynamic systems (Sandu *et al.*, 2006a,b).

In this study, the main originality is that the treatment of uncertainties in the dynamic analysis of a wind turbine system is proposed. The dynamic behaviour of nonlinear systems is investigated in order to analyse the robustness and reliability. For that, a dynamic lumped model of a two-stage gear system is developed in this paper. Three-bladed horizontal-axis wind turbines are considered with 12 degrees of freedom in the presence of the aerodynamic torque that is highlighted by an uncertain coefficient of performance belonging to a well-defined interval. Finally, the main goal of this work is to determine the dynamic behaviour of the gearbox transmission system of the wind turbine generated by uncertainty parameters.

2. Dynamic modelling

The studied system is a wind turbine. The increased speed mechanism is a two-stage gear system. It is composed by two trains of gearings supposed without manufacturing defects. In order to make this system more reliable, resistant and sustainable, a numerical analysis of the mechanical system is developed to study the dynamic response.

Figure 1 shows the dynamic model of the two stages gear system. The power transmission of the wind turbine is composed of the two-stage spur gear system. It is presented by three main blocks. The first block ($j = 1$) includes wheel 11 representing the turbine, main shaft and gear 12. The second block ($j = 2$) includes gear 21, intermediate flexible shaft and gear 22. Finally, the third block ($j = 3$) is composed by gear 31, intermediate shaft and wheel 32 which is the representative wheel of the electrical generator.

Every block j is supported by a flexible bearing having two stiffnesses: the bending stiffness k_{xj} and the traction-compression stiffness k_{yj} . Each intermediate flexible shaft has a negligible mass compared to the turbine and the generator. It admits some torsional stiffness $k_{\theta j}$. Wheels (11) and (32) characterise respectively the motor side (inertia I_{11}) and the receiving side (inertia I_{32}). Angular displacements of each wheel about their rotation axes are denoted by θ_{ji} . The indices $j = 1$ to 3 designates the number of the block and the indices $i = 1$ to 2 designates the two wheels of each block.

Besides, the linear displacements of the bearing denoted by x_j and y_j are measured in the plane which is orthogonal to the axes of rotation of the wheels. Each pair of wheels is linked through flexible teeth. This flexibility causes displacements. The gear-mesh contacts are modelled by a linear time varying stiffness $k(t)$ along the lines of action in the spur gear stage.

The gear mesh stiffness can be modelled by a sinusoid wave or by a square wave depending on the type of gear employed (for spur gear the stiffness function is a square wave, for helical gear it is a sinusoid wave function). So the periodic square wave form is the most representative for description of operation of gear systems (Fig. 2).

The terms ε_α are the contacts ratio corresponding to the two gear mesh contacts and T_e is the mesh period.

The teeth deflection, denoted by $\delta_i(t)$, is projected along the line of action because the gear mesh stiffness is defined along this direction.

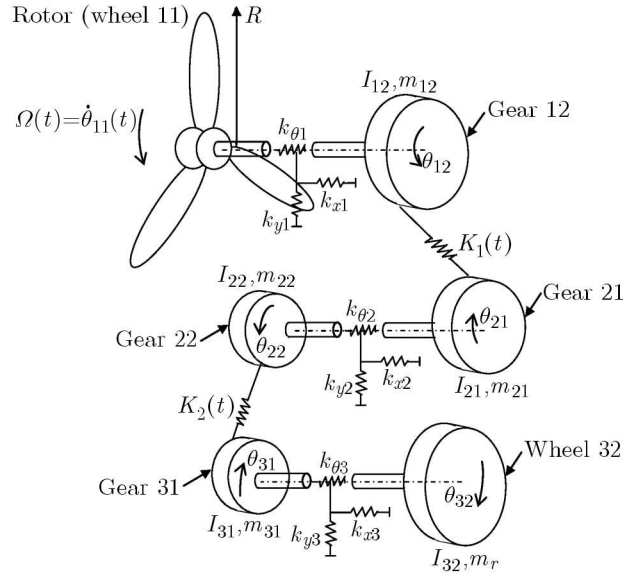


Fig. 1. Components of the wind turbine system

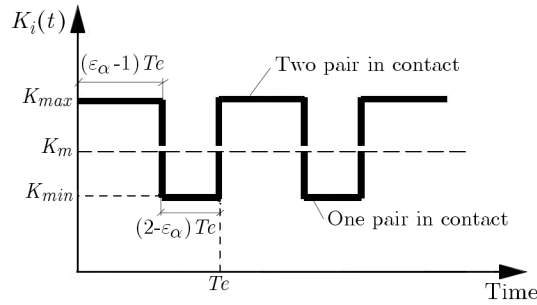


Fig. 2. Modelling of the mesh stiffness fluctuation

The first deflection $\delta_1(t)$ along the first gear-mesh contact is given by

$$\delta_1(t) = (x_1 - x_2) \sin \alpha_1 + (y_1 - y_2) \cos \alpha_1 + rb_{12}\theta_{12} + rb_{21}\theta_{21} \tag{2.1}$$

while the deflection $\delta_2(t)$ can be written by

$$\delta_2(t) = (x_2 - x_3) \sin \alpha_2 + (-y_2 + y_3) \cos \alpha_2 + rb_{22}\theta_{22} + rb_{31}\theta_{31} \tag{2.2}$$

while α_n represents the pressure angle (generally equal to 20°) and rb_{ji} are the base radii of the wheels.

3. Aerodynamic torque

The maximisation of the power coefficient presents a fundamental role in the wind turbine design to optimise the extraction of energy and to increase the efficiency (Beltran *et al.*, 2011; Buckspan, 2012). The power coefficient is defined by the ratio of power available on the primary shaft and the power of wind. The optimum design of the aerodynamic unit of a wind turbine can be achieved from considering uncertainty of the power coefficient.

For the wind turbine system studied in this paper, we consider that the rotor is composed of three blades removed by an angle of 120° (Gebreslassie *et al.*, 2013) and connected by a hub, which houses the system for regulating the angular speed.

The rotor is presented by wheel (11) rotating with some angular velocity and have an input aerodynamic torque to the power transmission system such as shown in Fig. 1.

Sloth *et al.* (2011) considered that the power in the wind depends on the wind speed, air density, and the swept area. Here, the aerodynamic torque is expressed by the following equation (Lei *et al.*, 2013)

$$C_{aero} = \rho_{air} A R^3 \Omega^2 C_p \quad (3.1)$$

where ρ_{air} represents the air density, A and R are the area and the radius of the rotor, respectively, Ω is the angular velocity and C_p is the power coefficient.

The power coefficient for the existing model is assumed deterministic by the following empirical expression (Abboudi *et al.*, 2011)

$$C_p = 0.44 \left(\frac{125}{\lambda} - 6.94 \right) e^{-\frac{16.5}{\lambda}} \quad (3.2)$$

where $\lambda = \Omega R / V(t)$ and $V(t)$ is the wind velocity.

4. Formulation of equations of motion

The Lagrange formalism leads to the set of differential equations governing the system motion

$$\mathbf{M}\ddot{\mathbf{X}} + (\mathbf{K}_s + \mathbf{K}(t))\mathbf{X} = \mathbf{F}(C_p) \quad (4.1)$$

The generalised vector of coordinates \mathbf{X} is defined by

$$\mathbf{X}(t) = [x_1, y_1, x_2, y_2, x_3, y_3, \theta_{11}, \theta_{12}, \theta_{21}, \theta_{22}, \theta_{31}, \theta_{32}]^T \quad (4.2)$$

The matrix \mathbf{M} representing the global mass matrix is expressed by

$$\mathbf{M} = \begin{bmatrix} \mathbf{M}_L & \mathbf{0} \\ \mathbf{0} & \mathbf{M}_A \end{bmatrix} \quad (4.3)$$

$$\mathbf{M}_L = \text{diag}(m_1, m_1, m_2, m_2, m_3, m_3) \quad \mathbf{M}_A = \text{diag}(I_{11}, I_{12}, I_{21}, I_{22}, I_{31}, I_{32})$$

where m_j is the mass of the block j and I_{ji} is the inertia.

The matrix \mathbf{K}_s is the average stiffness matrix of the structure defined by

$$\mathbf{K}_s = \begin{bmatrix} \mathbf{K}_p & \mathbf{0} \\ \mathbf{0} & \mathbf{K}_\theta \end{bmatrix} \quad (4.4)$$

where \mathbf{K}_p represents the bearing stiffness and \mathbf{K}_θ represents the torsional stiffness matrix of shafts

$$\mathbf{K}_p = \text{diag}(k_{x1}, k_{y1}, k_{x2}, k_{y2}, k_{x3}, k_{y3})$$

$$\mathbf{K}_\theta = \begin{bmatrix} k_{\theta 1} & -k_{\theta 1} & 0 & 0 & 0 & 0 \\ -k_{\theta 1} & k_{\theta 1} & 0 & 0 & 0 & 0 \\ 0 & 0 & k_{\theta 2} & -k_{\theta 2} & 0 & 0 \\ 0 & 0 & -k_{\theta 2} & k_{\theta 2} & 0 & 0 \\ 0 & 0 & 0 & 0 & k_{\theta 3} & -k_{\theta 3} \\ 0 & 0 & 0 & 0 & -k_{\theta 3} & k_{\theta 3} \end{bmatrix} \quad (4.5)$$

The matrix $\mathbf{K}(t)$ is the gear mesh stiffness matrix

$$\mathbf{K}(t) = \mathbf{K}_m + \mathbf{K}_v(t) \quad (4.6)$$

Each gear mesh stiffness variation is approximately modelled by the function $K(t)$. It is composed of an average component K_m and a variable component $K_v(t)$

$$K_v(t) = \begin{cases} K_{min} & \text{if } t < t_a \\ K_{max} & \text{else} \end{cases} \quad \text{where } t_a = (2 - \varepsilon_\alpha)T_e \quad (4.7)$$

The external force vector \mathbf{F} can be written by

$$\mathbf{F} = [0, 0, 0, 0, 0, 0, C_{aero}, 0, 0, 0, 0, -C_r]^T \quad (4.8)$$

where C_r presents the receiving torque. It is defined by the aerodynamic torque C_{aero} divided by the gear ratio GR expressed by

$$GR = \left(\frac{Z_{12}Z_{22}}{Z_{21}Z_{31}} \right) \quad (4.9)$$

5. Modal analysis and dynamic response

The technological and dimensional parameters of the two-stage gear system (Abboudi *et al.*, 2011) are summarised in Table 1.

Table 1. System parameters

Description	Symbol	Value	Units
Gear material density (42CrMo4)	ρ	7860	Kg/m ³
Rotor diameter	D	12	m
Bending stiffness	k_{xj}	$7 \cdot 10^8$	N/m
Traction stiffness – compression	k_{yj}	$6 \cdot 10^8$	N/m
Average mesh stiffness	k_m	$2 \cdot 10^8$	N/m
Torsional stiffness of the shaft	$k_{\theta j}$	$5 \cdot 10^6$	N m/rad
Number of teeth	$Z(12), Z(21)$	72, 18	–
	$Z(22), Z(31)$	54, 18	–
Module of teeth	m	0.016	m
Contact ratio	$\varepsilon_{\alpha 1} - \varepsilon_{\alpha 2}$	1.67-1.64	–

In this contribution, the modal analysis focuses on the dynamic properties of system under vibrational excitation is considered. The goal of the modal analysis is to determine the natural mode vibration and frequencies of a structure. Thus, the stiffness matrix of the model is assumed to be the average matrix in order to determine the eigenvalue and modal vibration of the system. The dynamic system response is different at each natural frequency. A null eigenvalue indicates rigid body motion. The dashed lines indicate the initial wheel positions.

Figure 3 represents the reference position and some eigen modes of the two-stage gear system. The fifth mode (mode of pure translation) is relative to the fifth eigen value $w_{p5} = 4600$ rad/s. The first mode (mode of pure rotation) characterises the rigid body motion. Finally, the tenth mode is relative to the tenth eigen value $w_{p10} = 40700$ rad/s, in fact this mode is a combined mode of translation and rotation.

In order to compare the two models with and without uncertainty, the power coefficient of the aerodynamic torque is considered without uncertainty in this Section. The Newmark method is employed to resolve the equations of motion obtained by the Lagrange formalism.

Figure 4 presents evolution of the displacements of the first (input) and the third (output) bearings. The figures show that the bearing dynamic behaviour is symmetric according to the y direction as a function of the x direction: $y = f(x)$.

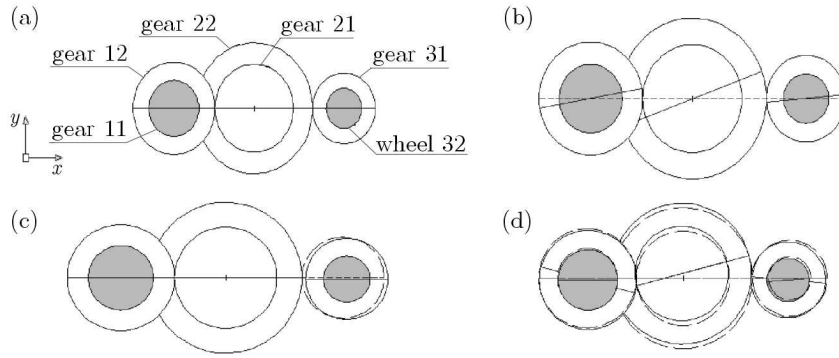


Fig. 3. Mode shapes of the gear system; (a) reference position, (b) pure rotation mode (rigid body motion), (c) pure translation mode ($f_5 = 740$ Hz), (d) combined mode ($f_{10} = 6460$ Hz)

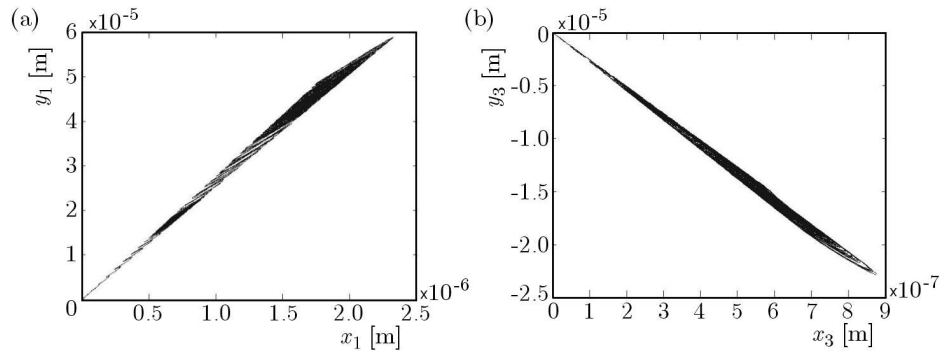


Fig. 4. Displacements of the first and third bearing; (a) first bearing, (b) third bearing

Figure 5 presents the fluctuation of deflections of the first and second tooth. These deflections are due to teeth flexibility. The deflection has an amplitude in the order of 10^{-5} m.

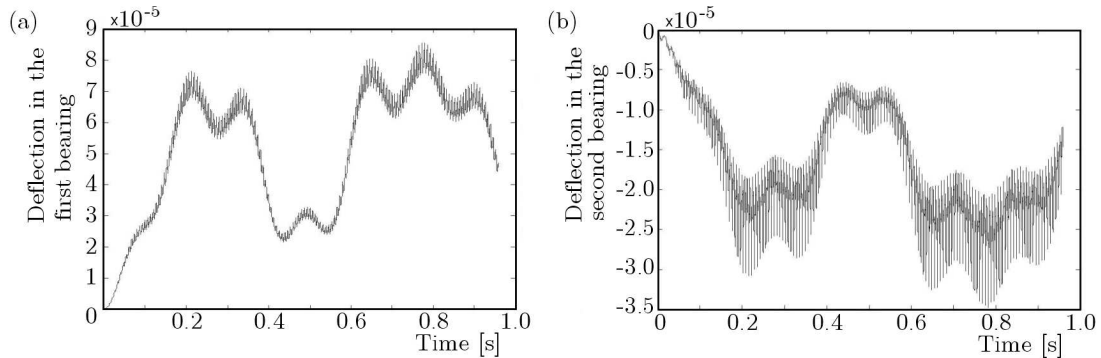


Fig. 5. Fluctuation of deflections in the first and second stage; (a) First stage; (b) second stage

6. Application of the polynomial chaos method

The fundamental idea of this approach is to establish a separation between the stochastic components of a random function and its deterministic components. The random process of interest is approximated by sums of orthogonal polynomial chaos of random independent variables. In this context, any uncertain parameter can be viewed as a second order random process. Therefore, the second order random process z can be expanded in terms of orthogonal polynomial chaos as (Nechak *et al.*, 2011)

$$z = \sum_{j=0}^{\infty} \bar{z}_j \phi_j(\xi) \quad (6.1)$$

where ξ is a vector of standard normal random variables with the known joint density function $W(\xi)$, \bar{z}_j are stochastic modes of the random process z and ϕ_j are orthogonal polynomial functions satisfying the orthogonally relation

$$\langle \phi_i \phi_j \rangle = \int \phi_i(\xi) \phi_j(\xi) W(\xi) d\xi \quad (6.2)$$

where $\langle \cdot \rangle$ means the internal product operator and $W(\xi)$ is the probability density function (PDF) of random variables that make up the vector ξ . The PDF (Xiu and Karniadakis, 2002) acts as a weighting function in the orthogonally relation for $\phi_j(\xi)$. Therefore, the type of orthogonal expansion polynomials depends on the nature of the stochastic process through the PDF of the random variables that describe the probability space. In practice, the generalised polynomial chaos expansion is truncated to a finite number of terms P . The truncation of the infinite series is necessary to keep the problem computationally feasible. In this work, we will truncate the series in such a way that all expansion polynomials up to a certain maximum degree, denoted by p , are included. The number of terms ($P+1$) in the expansion now follows from this maximum degree r and the dimensionality n of the random vector according to

$$P = \frac{(r+n)!}{r!n!} \quad (6.3)$$

Then, the computing of z is transformed into the problem of finding the coefficients \bar{z}_j of its truncated expansion. The intrusive and non-intrusive approaches are defined to calculate these coefficients called stochastic modes. The non-intrusive approach is shown to be more efficient than the intrusive approach. This approach requires simulations that correspond to particular samples of the random variables and needs no modifications of the stochastic model, contrary to the instructive approach.

The system in this work is equivalently expressed as follows

$$\mathbf{M}\ddot{\mathbf{Q}} + \mathbf{K}(t)\mathbf{Q} = \mathbf{F}(C_p) \quad (6.4)$$

A representation in the state space can reduce the order of the system to get a first order system, and it can be written as follows

$$\dot{\mathbf{q}}(t) = \mathbf{A}\mathbf{q}(t) + f(\mathbf{q}(t), C_p) \quad (6.5)$$

The robust analysis is based on the system representation in the phase space defined by the displacements and velocities

$$\mathbf{q}(t) = [\theta_{11}, \dot{\theta}_{11}, \theta_{12}, \dot{\theta}_{12}, \theta_{21}, \dot{\theta}_{21}, \theta_{22}, \dot{\theta}_{22}, \theta_{31}, \dot{\theta}_{31}, \theta_{32}, \dot{\theta}_{32}, x_1, \dot{x}_1, x_2, \dot{x}_2, x_3, \dot{x}_3, y_1, \dot{y}_1, y_2, \dot{y}_2, y_3, \dot{y}_3]^T \quad (6.6)$$

The coefficient of performance of the aerodynamic torque is supposed a random variable according to a uniform distribution law defined as follows

$$C_p(\xi) = \frac{b+a}{2} + \frac{b-a}{2}\xi \quad (6.7)$$

According to the state of the art, the Legendre polynomials are the best suited to deal with uniform uncertainties. Here ξ is distributed uniformly within the orthogonally interval $[-1, 1]$ of the Legendre polynomials. It models the uncertainty of the parameter C_p in the interval $[a, b] = [0.35, 0.45]$.

The Legendre polynomials calculated using the recurrence relation are as follows

$$(n + 1)L_{n+1}(x) = (2n + 1)xL_n(x) - nL_{n-1}(x) \quad L_0(x) = 1 \quad L_1(x) = x \quad (6.8)$$

The decomposing of the random in the Legendre polynomial basis using the Galerkin projection allows generating a non-linear deterministic differential equation system

$$\begin{aligned} \ddot{\bar{\theta}}_{11,l} &= -\frac{k_{\theta 1}}{\text{Im}}(\bar{\theta}_{11,l} - \bar{\theta}_{12,l}) + \frac{1}{\langle L_l^2(\xi) \rangle} \frac{\rho AR^3}{\text{Im}} \sum_{j=0}^p \sum_{k=0}^p \dot{\bar{\theta}}_{11,j} \dot{\bar{\theta}}_{11,k} \langle Cp(\xi), L_j(\xi), L_k(\xi), L_l(\xi) \rangle \\ \ddot{\bar{\theta}}_{12,l} &= \frac{k_{\theta 1}}{I_1}(\bar{\theta}_{11,l} - \bar{\theta}_{12,l}) - \frac{Rb_1}{I_1} K_1(t) \delta_{1,l} \\ \ddot{\bar{\theta}}_{21,l} &= \frac{k_{\theta 2}}{I_2}(-\bar{\theta}_{21,l} + \bar{\theta}_{22,l}) - \frac{Rb_2}{I_2} K_1(t) \delta_{1,l} \\ \ddot{\bar{\theta}}_{22,l} &= \frac{k_{\theta 2}}{I_3}(\bar{\theta}_{21,l} - \bar{\theta}_{22,l}) + \frac{Rb_3}{I_3} K_2(t) \delta_{2,l} \\ \ddot{\bar{\theta}}_{31,l} &= \frac{k_{\theta 3}}{I_4}(-\bar{\theta}_{31,l} + \bar{\theta}_{32,l}) + \frac{Rb_4}{I_4} K_2(t) \delta_{2,l} \\ \ddot{\bar{\theta}}_{32,l} &= \frac{k_{\theta 3}}{I_r}(\bar{\theta}_{31,l} - \bar{\theta}_{32,l}) - \frac{1}{\langle L_l^2(\xi) \rangle} \frac{\rho AR^3}{I_r} \\ &\quad \sum_{j=0}^p \sum_{k=0}^p \dot{\bar{\theta}}_{11,j} \dot{\bar{\theta}}_{11,k} \langle Cp(\xi) L_j(\xi) L_k(\xi) L_l(\xi) \rangle \frac{1}{GR} \end{aligned} \quad (6.9)$$

and

$$\begin{aligned} \ddot{\bar{x}}_1 &= -\frac{k_{x1}}{M_1} \bar{x}_{1,l} + \frac{\sin \varphi_1}{M_1} K_1(t) \delta_{1,l} \\ \ddot{\bar{x}}_2 &= -\frac{k_{x2}}{M_2} \bar{x}_{2,l} - \frac{\sin \varphi_1}{M_2} K_1(t) \delta_{1,l} - K_2(t) \frac{\sin \varphi_2}{M_2} \delta_{2,l} \\ \ddot{\bar{x}}_3 &= -\frac{k_{x3}}{M_3} \bar{x}_{3,l} + K_2(t) \frac{\sin \varphi_2}{M_3} \delta_{2,l} \\ \ddot{\bar{y}}_1 &= -\frac{k_{y1}}{M_1} \bar{y}_{1,l} - \frac{\cos \varphi_1}{M_1} K_1(t) \delta_{1,l} \\ \ddot{\bar{y}}_2 &= -\frac{k_{y2}}{M_2} \bar{y}_{2,l} + \frac{\cos \varphi_1}{M_2} K_1(t) \delta_{1,l} + \frac{\cos \varphi_2}{M_2} K_2(t) \delta_{2,l} \\ \ddot{\bar{y}}_3 &= -\frac{k_{y3}}{M_3} \bar{y}_{3,l} - \frac{\cos \varphi_2}{M_3} K_2(t) \delta_{2,l} \end{aligned} \quad (6.10)$$

7. Uncertainty in the dynamic response of the two stages gear system

In this Section, the dynamic behaviour of the two stage gear transmission system is investigated. The results are presented using the polynomial chaos method. The PC results are compared with the results of the deterministic system derived in Section 5.

Figures 6 and 7 represent the mean value and standard deviation of the input angular displacement $\theta_{11}(t)$ and the linear displacement $x_1(t)$, respectively. The signal is random and it fluctuates around the boundary conditions (zero value). The standard deviation allows predicting the variation domain around the average value of the response. The mean value and the standard deviation of the dynamic displacement have the same order of amplitude.

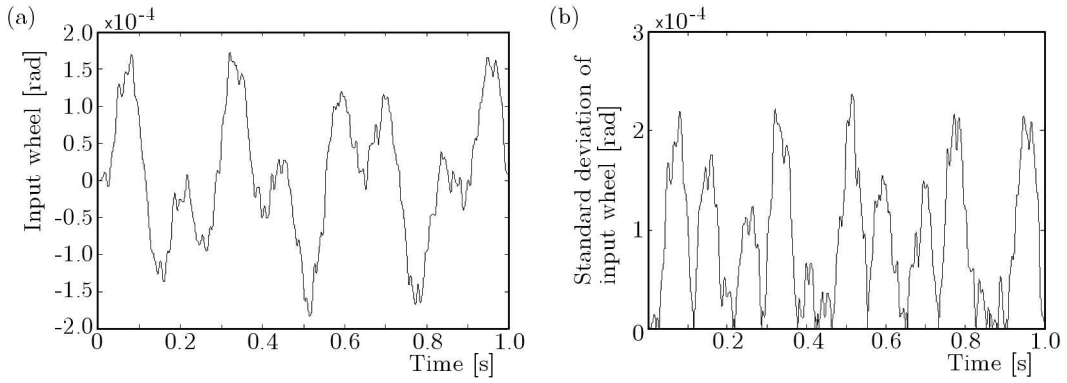


Fig. 6. Instantaneous mean value and standard deviation of $\theta_{11}(t)$; (a) mean value, (b) standard deviation

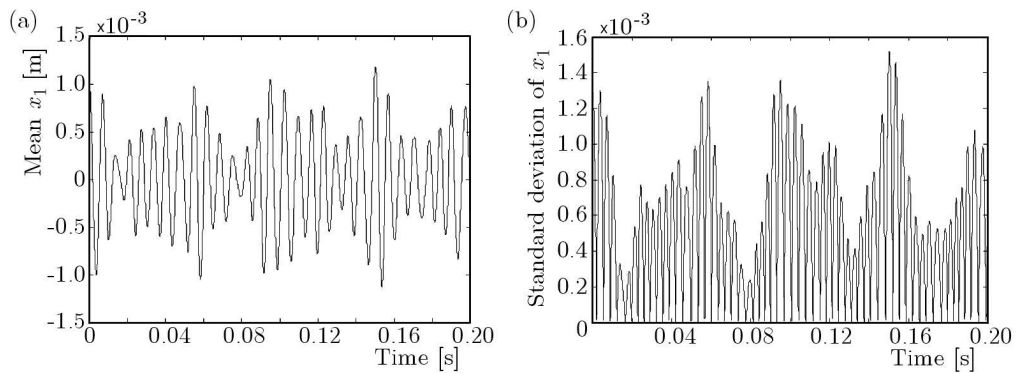


Fig. 7. Instantaneous mean value and standard deviation of $x_1(t)$; (a) mean value, (b) standard deviation

Figure 8 represents deflection of the first and the second tooth. The signal fluctuates around the zero value with an amplitude of the in order to 10^{-3} . The signal is sinusoidal and have the same form of the deterministic model (Fig. 5), therefore, the polynomial chaos results provide a very good accuracy. In the case of uncertainty, at each time t , the performance coefficient varies randomly in the range of $[0.35, 0.45]$. By contrast, it is constant in the case without uncertainty (deterministic model). So, there are many curves of teeth deflection relative to each performance coefficient. Here, Fig. 8, including Fig. 5, presents a more accurate range.

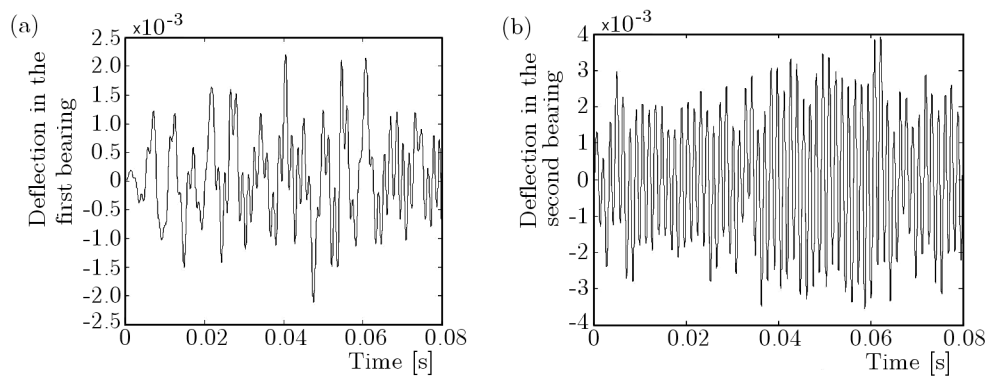


Fig. 8. Fluctuation of teeth deflection; (a) first bearing, (b) second bearing

The fluctuation of the aerodynamic torque with consideration of the uncertainty according to the power coefficient is plotted in Fig. 9. The signal is sinusoidal and the amplitude is increasing between 0 and 60 N m.

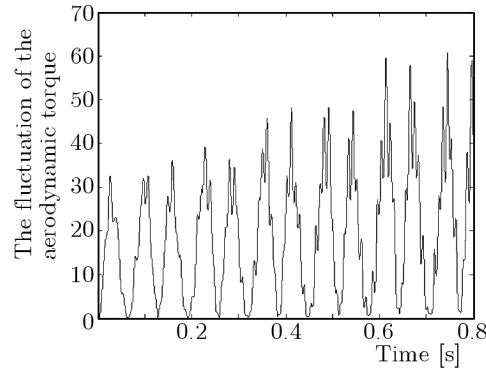


Fig. 9. Fluctuation of the aerodynamic torque

The results presented in Fig. 10 are found through orbits of the shaft. The orbits are constructed by using displacements in the x - and y -directions. Figure 10 shows the evolution of orbits for the first and third bearing with a set of the random parameter defined previously. The bearings behave in an arbitrary way, which is not observed in the case in the model without uncertainty (Fig. 4).

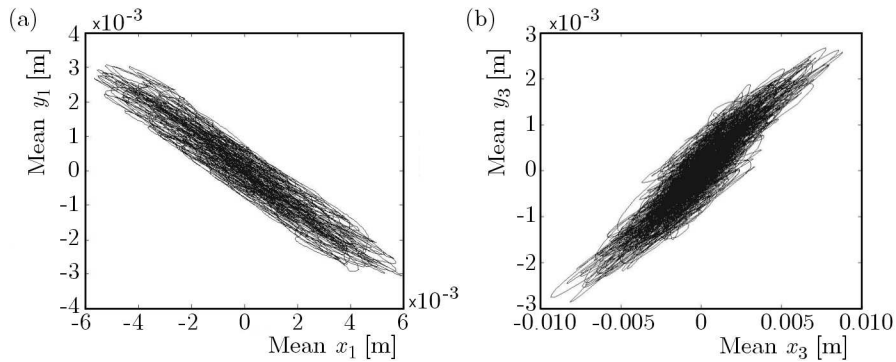


Fig. 10. Evolutions of bearings displacements $y = f(x)$; (a) first bearing, (b) third bearing

8. Conclusions

The probabilistic dynamic response of a wind turbine system with a two-stage gearbox transmission system generated by an uncertain input aerodynamic torque has been investigated. A new application of the polynomial chaos (PC) method is derived to study the influence of the input uncertainty parameter. The system structural dynamic response is presented using the polynomial chaos theory. Therefore, a set of mathematical equations is developed in order to predict the dynamic behavior of the two-stage spur gear system. Results of the uncertain model using the PC method are compared with the deterministic model.

The results suggest that the polynomial chaos method takes into account the uncertainty with a good efficiency. So, the PC approach can be considered as an efficient tool to take into account uncertainties in the study of dynamic behaviour of gearbox systems.

References

1. ABBOUDI K., WALHA L., DRISS Y., MAATAR M., FAKHFAKH T., HADDAR M., 2011, Dynamic behavior of a two-stage gear train used in a fixed-speed wind turbine, *Journal of Mechanism and Machine Theory*, **46**
2. BELTRAN B., BENBOUZID M.E.H., MOHAMED-ALI T., 2011, Second-order sliding mode power control and grid fault-tolerance a dfig-based wind turbine, *Revue des Sciences et de la Technologie*, **2**, 75-91
3. BUCKSPAN A., 2012, Nonlinear control of a wind turbine, *Journal of Undergraduate Research*, **13**, 2, 1-5
4. CHANTRASMI T., CONSTANTINE P., ETEMADIZ N., IACCARINO G., WANG Q., 2006, Uncertainty quantification in simple linear and non-linear problems, *Annual Research Briefs*
5. FISHER J., BHATTACHARYA R., 2008, Stability analysis of stochastic systems using polynomial chaos, *American Control Conference*, 4250-4255
6. GEBRESLASSIE M.G., TABOR G.R., BELMONT M.R., 2013, Numerical simulation of a new type of cross flow tidal turbine using OpenFOAM – Part I: Calibration of energy extraction, *Renewable Energy*, **50**, 994-1004
7. GHANEM R., SPANOS P.D., 1991, *Stochastic Finite Elements. A Spectral Approach*, Springer-Verlag, New York
8. HELSEN J., VANHOLLEBEKE F., MARRANT B., VANDEPITTE D., DESMET W., 2011, Multibody modelling of varying complexity for modal behaviour analysis of wind turbine gearboxes, *Renewable Energy*, **36**, 11, 3098-113
9. ISUKAPALLI S.S., ROY A., GEORGOPOULOS P.G., 1998a, Development and application of methods for assessing uncertainty in photochemical air quality problems, Interim Report for U.S.EPA National Exposure Research Laboratory
10. ISUKAPALLI S.S., ROY A., GEORGOPOULOS P.G., 1998b, Stochastic response surface methods (SRSMs) for uncertainty propagation: application to environmental and biological systems, *Risk Analysis*, **18**, 351-363
11. JAKERMAN J.D., ROBERTS S.G., 2009, Stochastic Galerkin and collocation methods for quantifying uncertainties in differential equation, a review, *ANZIAM Journal*, **50**, 815-830
12. KALOS M.H., WHITLOCK P.A., 1986, Monte Carlo methods, *Basics*, Wiley-Interscience, **1**, New York
13. LEI Y., BAI Y., XU Z., GAO Q., ZHAO C., 2013, An experimental investigation on aerodynamic performance of a coaxial rotor system with different rotor spacing and wind speed, *Experimental Thermal and Fluid Science*, **44**, 779-785
14. NECHAK L., BERGER S., AUBRY E., 2011, A polynomial chaos approach to the robust analysis of the dynamic behavior of friction systems, *European Journal of Mechanics A/Solids*, 594-607
15. PETERSSON P., IACCARINO G., NORDSTROM J., 2009, Numerical analysis of the Burgersequation in the presence of uncertainty, *Journal of Computational Physics*, **228**, 8394-8412
16. RUBINSTEIN R.Y., 1981, *Simulation and the Monte Carlo Method*, John Wiley & Sons Inc. New York
17. SANDU A., SANDU C., AHMADIAN M., 2006a, Modeling multibody dynamic systems with uncertainties. Part I: numerical application, *Multibody System Dynamic*, **15**, 369-391
18. SANDU C., SANDU A., AHMADIAN M., 2006b, Modeling multibody dynamic systems with uncertainties. Part II: theoretical and computational aspects, *Multibody System Dynamic*, **15**, 241-262
19. SLOTH C., ESBENSEN T., STOUSTRUP J., 2011, Robust and fault-tolerant linear parameter-varying control of wind turbines, *Mechatronics*, **21**

20. WEI S., ZHAO J., HAN Q., CHU F., 2015, Dynamic response analysis on torsional vibrations of wind turbine geared transmission system with uncertainty, *Renewable Energy*, **78**, 60-67
21. WIENER N., 1938, The homogeneous chaos, *American Journal of Mathematics*, **60**, 4, 897-936
22. XIU D., KARNIADAKIS G., 2002, The Wiener-Askey polynomial chaos for stochastic differential equations, *SIAM Journal on Scientific Computing*, **24**, 2, 619-644
23. ZHU C., XU X., LIU H., LUO T., ZHAI H., 2014, Research on dynamical characteristics of wind turbine gearboxes with flexible pins, *Renewable Energy*, **68**, 724-32

Manuscript received February 3, 2015; accepted for print October 15, 2015

ON THE BUCKLING AND VIBRATIONAL RESPONSE OF CARBON NANOTUBES WITH SPIRAL DEFORMATION

SADEGH IMANI YENGEJEH

Department of Solid Mechanics and Design, Faculty of Mechanical Engineering, Universiti Teknologi Malaysia – UTM, Skudai, Johor, Malaysia; e-mail: imani.sd@gmail.com

SEYEDEH ALIEH KAZEMI

Department of Mechanical Engineering, The University of Birjand, Birjand, Iran; e-mail: sa.kazemi83@gmail.com

ANDREAS ÖCHSNER

*School of Engineering, Griffith University, Gold Coast Campus, Southport, Australia, and
School of Engineering, The University of Newcastle, Callaghan New South Wales, Australia
e-mail: andreas.oechsner@gmail.com*

Perfect and spiral models of carbon nanotubes (CNTs) have been simulated based on the finite element method and their vibrational and buckling behavior has been investigated. In order to evaluate their natural frequency and critical buckling load, computational tests have been conducted. It has been concluded that the existence of any geometrical modification in the configuration of perfect CNTs results in a remarkable reduction in the natural frequency and critical buckling load of CNTs. It has been also revealed that the analytical solutions are in good agreement with the finite element simulation results in the cases of perfect and spiral CNTs.

Keywords: finite element method, carbon nanotubes, natural frequency, critical buckling load, spiral shape

1. Introduction

The industrial application of carbon nanotubes (CNTs) is continuously increasing due to their outstanding physical properties. Since their discovery (Iijima, 1991), these nanostructures have attracted worldwide attention. CNTs are unique because of their outstanding mechanical and physical properties such as strength, lightness and good conductivity (Dai *et al.*, 1996; Saito *et al.*, 1997; Niu *et al.*, 1997). The investigation of CNTs can be divided into two groups, i.e. experimental and computational approaches. Molecular dynamics (MD) and continuum mechanics techniques such as the finite element method (FEM) have been the most popular approaches to study the mechanical behavior of these nano-materials. In the following, the results of several studies on vibrational characteristics and buckling behavior of CNTs are presented.

Previous investigations (Arghavan and Singh, 2011) conducted a numerical study on free and forced vibrations of single-walled carbon nanotubes (SWCNTs). They applied a simple approach so that the proximity of the mathematical model to the actual atomic structure of the CNT was considerably retained. Their results revealed that the appearance of these modes of vibration in the eigenvectors and eigenvalues were indistinguishable. It was concluded that in the case of zigzag nanotubes, the axial bending and torsional modes appeared to be decoupled whereas the armchair nanotubes showed coupling between such modes. Then, the vibrational behavior of two- and three-junctioned CNTs was investigated with different geometries and boundary conditions (Seyyed Fakhrabadi *et al.*, 2012). The authors applied a molecular mechanics approach to analyze

the mentioned CNTs. They finally obtained natural frequencies and their corresponding mode shapes of two-junctioned CNTs with different diameters and lengths. After that, the natural frequency of CNTs was investigated (Ghavamian and Öchsner, 2013). They simulated numerous forms of CNTs from single to 5-walled ones in their perfect form based on the FEM. Then, they evaluated natural frequencies of the CNTs analytically and through the FEM and compared their findings. Then, some specific defects were introduced to the perfect models and their vibrational behavior and the influence of these defects on the vibrational stability of CNTs were studied. They finally concluded that the existence and development of any type of defects in the configuration of CNTs reduce the natural frequency and vibrational stability of perfect CNTs. A study on the impact of vacancy defects on critical buckling loads and strains in CNTs was conducted under axial compression (Parvaneh *et al.*, 2009). Their results showed that vacancy defects in CNTs can most likely be modeled as cutouts of the shells. They finally compared their results of the structural model with those from MD simulations in which the outputs were in good agreement with the present model. The buckling characteristics of several curved forms of SWCNTs was investigated performing MD simulations (Wong and Vijayaraghavan, 2012). They concluded that the performance of the CNT under compression can be changed by an inclusion of a curvature along the tube axis. The effect of defects on the buckling behavior of CNTs was investigated by Ghavamian and Öchsner (2012). Their study was based on the FEM. In detail, they modeled two basic CNTs in their perfect form. Then the buckling behavior of CNTs was evaluated by comparing their critical loads obtained from the simulation and analytical calculations. They concluded that the existence of any curvature in the structure of nanotubes decreases their buckling strength. The aim of the actual research is to continue the previous investigations and to study vibrational and buckling behavior of spiral CNTs.

As most of the investigations have been performed on perfect CNTs, it is necessary to pay more attention to geometrical imperfections, e.g. twists and spirals of CNTs, in order to realistically examine their mechanical properties (see Fig. 1). Spiral deformations were reported in (Faria *et al.*, 2013; Liuyue *et al.*, 2013; Faria *et al.*, 2013) where the CNTs revealed a shape similar to a spring which is deformed around its longitudinal axis. The purpose of this research is to derive computational models of CNTs and investigate their vibrational and buckling behavior.

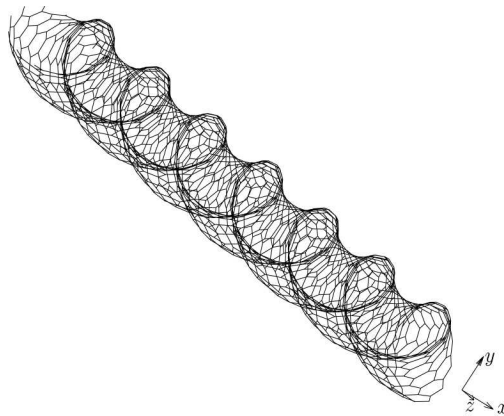


Fig. 1. General view of a spiral CNT

2. Methodology

2.1. Geometric definition

The atomic structure of CNTs can be imagined as a graphene sheet that has been rolled into a tube. The thickness of the tube wall is generally considered to be 0.34 nm, which is very

close to that of a graphene sheet (Li and Chou, 2003; To, 2006). These nano-particles possess a length of over $10\ \mu\text{m}$ and diameters ranging from 0.4 to 3.0 nm.

We followed the modeling method which was first proposed by Li and Chou (2003) where the theory of classical structural mechanics was extended to the modeling of CNTs. It was assumed that CNTs, when subjected to loading, behave like space-frame structures. Based on Fig. 2, the bonds between carbon atoms are considered as connecting load-carrying generalized beam members, while the carbon atoms act as joints of the members.

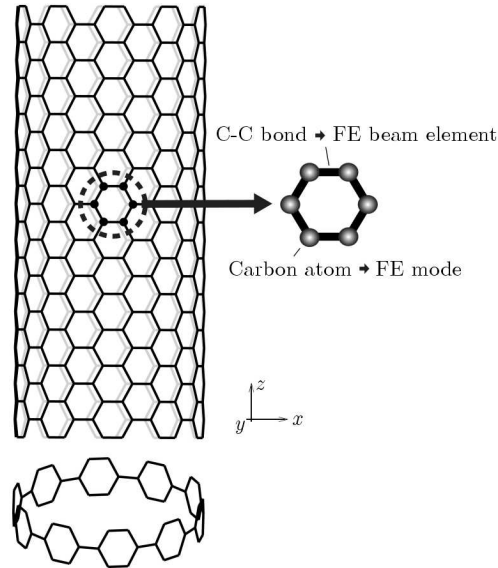


Fig. 2. Front view and single ring of a SWCNT as a space-frame structure

The configuration of CNTs in this study has been generated by the CoNTub software (Melchor and Dobado, 2004; Melchor *et al.*, 2011), a computer program for determining the coordinates of CNTs. Then, the finite element analyses have been conducted in order to investigate the vibrational and buckling behavior of different types of perfect and spiral CNTs.

2.2. Boundary conditions

Vibrational and buckling behavior of perfect and spiral CNTs under cantilevered boundary conditions are investigated, where for the vibrational behavior one end is fully fixed and the other end is completely free; and for the buckling behavior one end is fully fixed and the other end is exposed to a compressive axial load. Different angles for spiral CNTs have been taken into consideration, as shown in Fig. 3.

3. Results and discussion

In order to evaluate the critical buckling load of CNTs, the numerical finite element approach allows the introduction of arbitrary compressive point loads to one of the CNT's ends. The simulation of the vibrational behavior does not require the introduction of any loads. The obtained numerical finite element results are compared to simple analytical predictions to check if these simple design equations provide reasonable values.

3.1. Analytical approach to the vibrational behavior

The natural frequency is the frequency of a vibrating system at which the system oscillates at a greater amplitude. This phenomenon occurs because of the existence of resonance. The natural

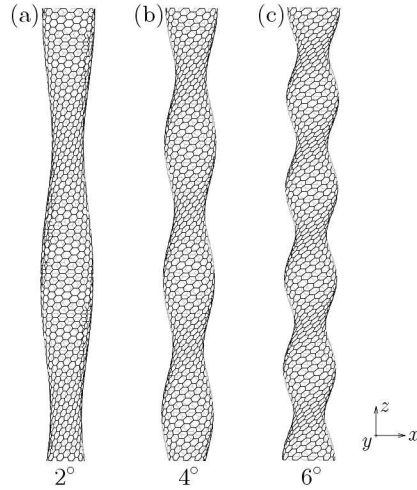


Fig. 3. Spiral CNT with (a) 2°, (b) 42° and (c) 62° twisting angle

frequency is mostly investigated to examine the vibrational response of structural members. The first natural frequency of a fixed-free helical spring is defined by the following analytical equation (Renno and Mace, 2012)

$$f_n = \frac{1}{4} \sqrt{\frac{k}{\bar{m}}} \quad (3.1)$$

where \bar{m} and k are the value of mass per unit of the spring and the spring rate, respectively. In the case of spiral CNTs, we assumed an average value for the diameter as the whole structure does not possess a constant diameter along its length. The value of the mass per unit length \bar{m} can be obtained from the following equation

$$\bar{m} = \frac{m_{total}}{l_{total}} \quad (3.2)$$

where m_{total} is the total mass of the CNT carbon atoms and l_{total} is the total length of the nanotube. Figure 4 illustrates the first five natural frequencies of a spiral CNT obtained from the numerical finite element simulation.

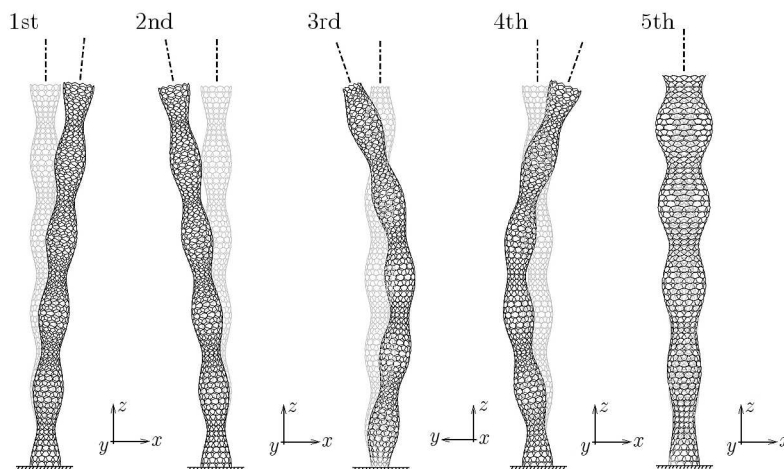


Fig. 4. First five eigenmodes of a spiral CNT

3.2. Analytical approach to the buckling behavior

The phenomenon of buckling is in its simplest form a particular kind of elastic instability in a slender configuration that occurs under certain compressive loads. In the basic theory of elasticity, the critical buckling deflection of a compressive spring is presented by Eq. (3.3) (Pearson, 1982) as

$$\frac{\delta_{cr}}{L_f} = 0.812 \left[1 \pm \sqrt{1 - 6.87 \left(\frac{2D_m}{L_f} \right)^2} \right] \quad (3.3)$$

where L_f is the free length or unloaded length of the spring, D_m is the mean diameter of the spring, and δ_{cr} is the critical deflection of the spring.

Figure 5 shows a spiral CNT under the cantilevered boundary condition in its original and buckled shape obtained from the numerical finite element calculation.

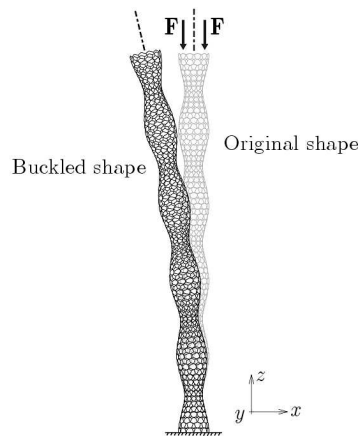


Fig. 5. A spiral CNT's first mode under buckling load in the original and buckled form with the cantilevered boundary condition

It should be indicated that the proposed approach in this paper deals with the evaluation of mechanical properties, i.e. vibrational and buckling behavior of spiral CNTs, whereby the CNTs are deformed as a spring around their axis. By manipulating the twisting angle of these spiral CNTs from 02° to 102° , the behavior of different models with different conditions could be studied. This study tried to continue and broaden the investigations on only slightly twisted CNTs around their straight vertical axis.

It could be shown that the computational and analytical values of the natural frequency as well as critical buckling load of perfect CNTs are reduced by introducing spiral imperfections to the configuration of these perfect nano-structures, as illustrated in Fig. 6. Comparing all cases, it is clear that a decrease in the natural frequency and the critical buckling load is more visible in the case of armchair spiral CNTs. Figure 6a-c shows a decrease in the natural frequency of armchair, zigzag and chiral CNTs as a result of increasing the twisting angle of spiral configurations. It is clear that the natural frequency of all CNTs reduces to less than 12 GHz at the angle of 102° . Figure 6d-f illustrates a significant change in the critical buckling load of armchair, zigzag and chiral models by increasing the twisting angle of spiral CNTs. Based on the obtained calculations, it is concluded that the finite element values are in good agreement with analytical results, where the maximum difference for the natural frequency and critical buckling load is 17 and 23%, respectively.

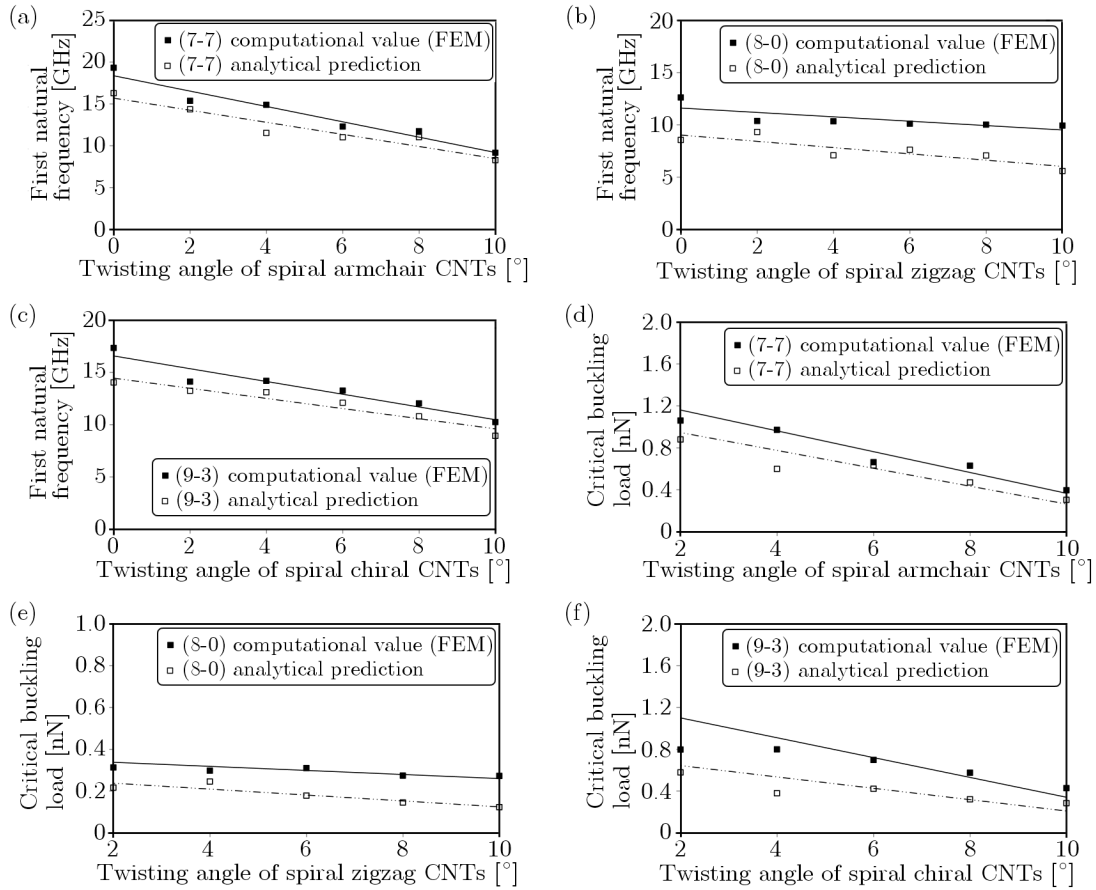


Fig. 6. Change in the natural frequency with different twisting angles for (a) armchair, (b) zigzag and (c) chiral spiral CNTs. Change in the critical buckling load with different twisting angles for (d) armchair, (e) zigzag and (f) chiral spiral CNTs

4. Conclusions

In this study, perfect and spiral CNTs (armchair, zigzag and chiral) have been simulated and their vibrational and buckling behavior has been studied through performing computational tests with cantilevered boundary condition. Both computational and analytical calculations have been compared in the cases of perfect and spiral CNTs. It has been shown that the finite element simulation are in good agreement with the analytical solutions in the case of perfect and spiral CNTs. It has been shown that in all cases, the analytical values are slightly smaller than the computational results. It has been also concluded that the existence of any spiral imperfection in the configuration of perfect CNTs results in a significant reduction in the natural frequency and critical buckling load of these nano-configurations.

References

1. ARGHAVAN S., SINGH A.V., 2011, On the vibrations of single-walled carbon nanotubes, *Journal of Sound and Vibration*, **330**, 3102-3122
2. DAI H., WONG E.W., LIEBER C.M., 1996, Probing electrical transport in nanomaterials: conductivity of individual carbon nanotubes, *Science*, **272**, 523-526
3. FARIA B., SILVESTRE N., 2013, Canongia Lopes JN: Induced anisotropy of chiral carbon nanotubes under combined tension-twisting, *Mechanics of Materials*, **58**, 97-109

4. FARIA B., SILVESTRE N., CANONGIA LOPES J.N., 2013, Tension-twisting dependent kinematics of chiral CNTs, *Composites Science and Technology*, **74**, 211-220
5. GHAVAMIAN A., ÖCHSNER A., 2012, Numerical investigation on the influence of defects on the buckling behavior of single-and multi-walled carbon nanotubes, *Physica E*, **46**, 241-249
6. GHAVAMIAN A., ÖCHSNER A., 2013, Numerical modeling of the eigenmodes and eigen frequencies of carbon nanotubes under the influence of defects, *Journal of Nano Research*, **21**, 159-164
7. IJIMA S., 1991, Helical microtubules of graphitic carbon, *Nature*, **354**, 56-58
8. LI C., CHOU T.W., 2003, A structural mechanics approach for the analysis of carbon nanotubes, *International Journal of Solids and Structures*, **40**, 2487-2499
9. LIUYUE C., YANG L., HONGBO L., YUXI C., XIAOHONG X., HAIBO Z., 2013, Investigation of graphite/carbon spiral nanoribbons using FeCl₃-CuCl₂-graphite intercalation compounds as precursors, *Materials Letters*, **108**, 196-199
10. MELCHOR S., DOBADO J.A., 2004, CoNTub: An algorithm for connecting two arbitrary carbon nanotubes, *Journal of Chemical Information and Computer Sciences*, **44**, 1639-1646
11. MELCHOR S., MARTIN-MARTINEZ F.J., DOBADO J.A., 2011, CoNTub v2. 0-algorithms for constructing c 3-symmetric models of three-nanotube junctions, *Journal of Chemical Information and Modeling*, **51**, 1492-1505
12. NIU C., SICHEL E.K., HOCH R., 1997, High power electrochemical capacitors based on carbon nanotube electrodes, *Applied Physics Letters*, **70**, 1480-1482
13. PARVANEH V., SHARIATI M., MAJDSABETI A.M., 2009, Investigation of vacancy defects effects on the buckling behavior of SWCNTs via a structural mechanics approach, *European Journal of Mechanics A/Solids*, **28**, 1072-1078
14. PEARSON D., 1982, The transfer matrix method for the vibration of compressed helical springs, *Journal of Mechanical Engineering Science*, **24**, 163-171
15. RAHMANDOUST M., ÖCHSNER A., 2011, Buckling behavior and natural frequency of zigzag and armchair single-walled carbon nanotubes, *Journal of Nano Research*, **16**, 153-160
16. RENNO J.M., MACE B.R., 2012, Vibration modelling of helical springs with non-uniform ends, *Journal of Sound and Vibration*, **331**, 2809-2823
17. SAITO Y., HAMAGUCHI K., HATA K., 1997, Conical beams from open nanotubes, *Nature*, **389**, 554-555
18. SEYYED FAKHRABADI M.M., AMINI A., RASTGOO A., 2012, Vibrational properties of two and three junctioned carbon nanotubes, *Computational Materials Science*, **65**, 411-425
19. TO C.W.S., 2006, Bending and shear moduli of single-walled carbon nanotubes, *Finite Elements in Analysis and Design*, **42**, 404-413
20. WONG C.H., VIJAYARAGHAVAN V., 2012, Nanomechanics of imperfectly straight single walled carbon nanotubes under axial compression by using molecular dynamics simulation, *Computational Materials Science*, **53**, 268-277

INVESTIGATION ON A QUASI-ZERO-STIFFNESS VIBRATION ISOLATOR UNDER RANDOM EXCITATION

YONG WANG, SHUNMING LI, CHUN CHENG

*College of Energy and Power Engineering, Nanjing University of Aeronautics and Astronautics, Nanjing, China
e-mail: wangy1921@126.com*

The dynamic response and isolation performance of a Quasi-Zero-Stiffness (QZS) vibration isolator using inclined springs as negative stiffness correctors under random excitation are presented in this paper. The probabilistic linearization method is employed to determine the dynamic response of the QZS vibration isolator and compared with the exact solution based on the Fokker-Planck-Kolmogorov (FPK) equation and the equivalent linearization method. Two performance indexes (Mean Square Relative Displacement (MSRD) and Mean Square Acceleration (MSA)) are considered to evaluate the isolation performance of the QZS vibration isolator under random excitation and compared with the equivalent linear vibration isolator. The results show that the MSRD of the QZS vibration isolator is always lower than the equivalent linear vibration isolator, while the MSA of the QZS vibration isolator can be larger or lower than the equivalent linear vibration isolator based on the values of damping ratio and spectral density of the random excitation.

Keywords: vibration isolator, quasi-zero-stiffness, random excitation, dynamic analysis, performance analysis

1. Introduction

Nonlinear vibration isolators with Quasi-Zero-Stiffness (QZS) characteristic (Ibrahim, 2008) have been developed to improve the vibration isolation performance of passive linear vibration isolators and have drawn much attention in the engineering industry since they can provide lower vibration isolation frequency without sacrificing the load bearing capacity. The QZS vibration isolator usually comprises of a load bearing elastic element providing positive stiffness and special mechanisms providing negative stiffness named as negative stiffness correctors. Alabuzhev *et al.* (1989) investigated the effect of negative stiffness correctors and summarized many prototypes of QZS vibration isolators. Carrella *et al.* (2007), Kovacic *et al.* (2008) and Hao and Cao *et al.* (2014) considered a QZS vibration isolator by using inclined springs as negative stiffness correctors and studied the static and dynamic characteristics theoretically. Le and Ahn (2011) built a QZS vibration isolator composed of a positive stiffness mount and two symmetric negative stiffness structures for improving vibration isolation performance of the vehicle seat. Robertson *et al.* (2009), Zhou and Liu (2010) and Xu *et al.* (2013) used electromagnetic springs or magnetic springs as negative stiffness correctors to build a QZS vibration isolator and studied the static and dynamic characteristics detailedly. Liu *et al.* (2013) designed a QZS vibration isolator by using Euler buckled beams as negative stiffness correctors and analyzed the dynamic behavior theoretically. Shaw *et al.* (2013) used bistable composite plates as negative stiffness correctors to form a QZS vibration isolator and investigated the dynamic response theoretically and experimentally.

In most of the above mentioned researches, the dynamic response and vibration isolation performance of the QZS vibration isolators under harmonic excitation have been investigated in detail. The QZS vibration isolator can also endure shock excitation or random excitation, which

are common in the practical engineering. Liu *et al.* (2013) and Wang *et al.* (2014) considered the performance of the QZS vibration isolators under shock excitation systematically. But the performance of the QZS vibration isolator subjected to random excitation has been rarely discussed in detail. Linear vibration isolators under random excitation were studied fully by Harris and Piersol (2002). Lyon (1960, 1961) investigated vibration statistics of a randomly excited hard-spring oscillator and obtained an expression of the joint density of displacement and velocity. Klein (1964) considered the random excitation of a nonlinear system with tangent elasticity characteristics and studied the dynamic behavior of the nonlinear system in detail. Kirk (1988) compared dynamic performances of three different kinds of nonlinear vibration isolators with cubic hard, cubic soft and tangent stiffness comprehensively. Shin (2014) did experimental investigation of the vibration transmissibility of a magnet-spring vibration isolator under random excitation.

A number of approximated analytic methods have been developed to study the dynamic response of nonlinear vibration isolators under random excitation, such as the method based on the Fokker-Planck-Kolmogorov (FPK) equation (Lin, 1967), equivalent linearization method (Caughey, 1963), partial linearization method (Elishakoff and Cai, 1993), dissipation energy balancing and weighted residuals method (Cai and Lin, 1988), and cumulant-neglect closure method (Wu and Lin, 1984). In this paper, the probabilistic linearization method (Polidori and Beck, 1996; Polidori *et al.*, 2000) is used. The probabilistic linearization method finds a linear vibration system which best approximates the true nonlinear vibration system and minimizes the error of the FPK equation rather than the stochastic differential equation, it can yield simple expressions to determine the desired probabilistic characteristics of the dynamic response of the nonlinear vibration system.

The organization of this paper is as follows. A QZS vibration isolator using inclined springs as negative stiffness correctors (Carrella *et al.*, 2007) is presented and a brief static analysis of the QZS vibration isolator is shown in Section 2. In Section 3, a brief description of the probabilistic linearization method is introduced, the dynamic response of the QZS vibration isolator under random excitation using this method is obtained and compared with the exact solution based on the FPK equation and the equivalent linearization method. In Section 4, two performance indexes are considered to evaluate the isolation performance of the QZS vibration isolator and compared with an equivalent linear vibration isolator. Conclusions are drawn in Section 5.

2. Static analysis of a QZS vibration isolator

A QZS vibration isolator comprised of a vertical spring used as the load bearing element and inclined springs used as negative stiffness correctors is shown in Fig. 1. Figure 1 also shows when loading a mass m , the system is balanced at the static equilibrium position, and the inclined springs are in the horizontal position. The stiffness of the vertical and inclined springs are K_v and K_h ; the initial length of the inclined springs is l_0 and the length when they are in the horizontal position is l ; the damping coefficient of the damper is c ; x is the displacement of the mass from the static equilibrium position and y is the base excitation with random input.

The force-displacement and stiffness-displacement relationships of the QZS vibration isolator are given as

$$F = K_v(x - y) + 2K_h \left(1 - \frac{l_0}{\sqrt{x^2 + l^2}}\right)(x - y) \quad K = K_v + 2K_h - \frac{2K_h l_0 l^2}{\sqrt{[(x - y)^2 + l^2]^3}} \quad (2.1)$$

Equation (2.1) can be written in non-dimensional form as

$$\hat{F} = z + 2k \left(1 - \frac{1}{\sqrt{z^2(1 - \hat{l}^2) + \hat{l}^2}}\right)z \quad \hat{K} = 1 + 2k - \frac{2k\hat{l}^2}{\sqrt{[z^2(1 - \hat{l}^2) + \hat{l}^2]^3}} \quad (2.2)$$

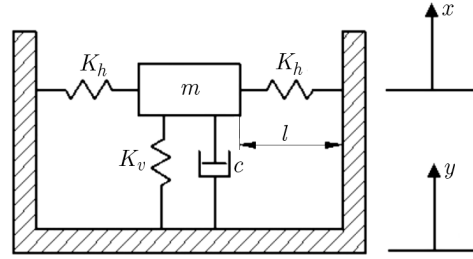


Fig. 1. Model of a QZS vibration isolator

where $z = (x - y)/x_s$, $\hat{F} = F/(K_v x_s)$, $\hat{l} = l/l_0$, $k = K_h/K_v$, $\hat{K} = K/K_v$, $x_s = \sqrt{l_0^2 - l^2}$ is the static equilibrium displacement.

The non-dimensional stiffness of the QZS vibration isolator at the static equilibrium position can be obtained by substituting $z = 0$ into Eq. (2.2)₂

$$\hat{K}_s = 1 + 2k \left(1 - \frac{1}{\hat{l}}\right) \quad (2.3)$$

If the stiffness of the QZS vibration isolator is zero at the static equilibrium position, the QZS characteristic can be achieved and then the value of \hat{l} is given as

$$\hat{l}_{QZS} = \frac{2k}{1 + 2k} \quad (2.4)$$

The non-dimensional force-displacement and stiffness-displacement curves of the QZS vibration isolator for various values of \hat{l} when $k = 1$ are shown in Fig. 2. It can be seen that when $\hat{l} = \hat{l}_{QZS}$, the positive stiffness of the vertical spring is balanced by the negative stiffness provided by the inclined springs at the static equilibrium position, then the QZS characteristic can be achieved. When $\hat{l} < \hat{l}_{QZS}$, the stiffness of the QZS vibration isolator is negative in the neighborhood of the static equilibrium position which is an undesirable condition in the engineering practice. When $\hat{l} > \hat{l}_{QZS}$, the stiffness of the QZS vibration isolator maintains a small positive value at the static equilibrium position. So in order to keep the stiffness positive, \hat{l} should be greater than or equal to \hat{l}_{QZS} .

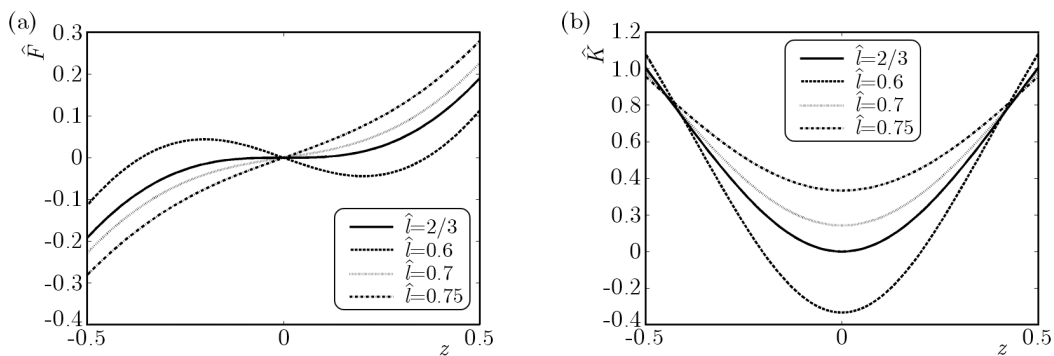


Fig. 2. Non-dimensional force-displacement and stiffness-displacement curves

When the amplitude of the displacement is small, the non-dimensional force and stiffness can be expanded as a Taylor series at the static equilibrium position $z = 0$ for simplicity

$$\begin{aligned} \hat{F}_a(z) &= \left(1 - 2k \frac{1 - \hat{l}}{\hat{l}}\right)z + k \frac{1 - \hat{l}^2}{\hat{l}^3}z^3 = \alpha z + \gamma z^3 & \hat{K}_a(\hat{x}) &= \alpha + 3\gamma z^2 \\ \alpha &= 1 - 2k \frac{1 - \hat{l}}{\hat{l}} & \gamma &= k \frac{1 - \hat{l}^2}{\hat{l}^3} \end{aligned} \quad (2.5)$$

The dynamic equation of the QZS vibration isolator under random base excitation using a third-order Taylor series expansion is given as

$$m\ddot{x} + c(\dot{x} - \dot{y}) + \alpha K_v(x - y) + \gamma K_v \frac{(x - y)^3}{x_s^2} = 0 \quad (2.6)$$

where the dots denote derivatives with respect to time t . Equation (2.6) can be written in non-dimensional form as

$$z'' + 2\zeta z' + z + \lambda z^3 = f(T) \quad (2.7)$$

where $\zeta = c/(2mw_n)$, $\lambda = \gamma/\alpha$, $w_n = \sqrt{\alpha K_v/m}$, $T = w_n t$, $f(T) = -y''/x_s$. The primes denote derivatives with respect to T . When the base excitation is random excitation, the mathematical expression of the non-dimensional function $f(T)$ can be expressed as

$$f(T) = \sqrt{S_0}n(T) \quad (2.8)$$

where $n(T)$ is a stationary zero-mean Gaussian white noise with $E[n(T)n(T + \tau)] = \delta(\tau)$ and S_0 is the spectral density. Then, Eq. (2.7) can be written as

$$z'' + 2\zeta z' + z + \lambda z^3 = \sqrt{S_0}n(T) \quad (2.9)$$

3. Response of the QZS vibration isolator under random excitation

The response of the QZS vibration isolator under random excitation is obtained by using the probabilistic linearization method. The probabilistic linearization method finds an equivalent linear vibration system whose stationary probability density function best fits the FPK equation of the nonlinear vibration system. Consider the Itô stochastic differential equation

$$dz(T) = g(z, T)dT + h(z, T)dw(T) \quad (3.1)$$

where $z \in R^n$, $g(z, T) \in R^n$, $h(z, T) \in R^{n \times m}$ and $w(T) \in R^m$ is a normalized Wiener process with $E[(w_i(T_1) - w_i(T_2))(w_j(T_1) - w_j(T_2))] = |T_1 - T_2|\delta_{ij}$. The FPK equation is a linear equation governing the evolution of the state transition probability density function $p(z, T|z_0, T_0)$ of the system, which is given as

$$\frac{\partial}{\partial T}p(z, T|z_0, T_0) = L(z, T)p(z, T|z_0, T_0) \quad (3.2)$$

where $L(z, T)$ is the forward Kolmogorov operator expressed as

$$L(z, T)\varphi(z, T) = -\sum_{i=1}^n \frac{\partial}{\partial z_i}(g_i(z, T)\varphi(z, T)) + \frac{1}{2} \sum_{i=1}^n \sum_{j=1}^n \frac{\partial}{\partial z_i} \frac{\partial}{\partial z_j}(b_{ij}(z, T)\varphi(z, T)) \quad (3.3)$$

where $b(z, T) = h(z, T)h^T(z, T) \in R^{n \times n}$. The equivalent linear vibration system used to approximate Eq. (3.1) is defined as

$$dz(T) = A_{eq}(\sigma)z(T)dT + B_{eq}(\sigma)dw(T) \quad (3.4)$$

where $A_{eq}(\sigma)$ and $B_{eq}(\sigma)$ are the matrices of appropriate dimensions and σ is a parameter vector of the equivalent linear vibration system.

Define $L_{nl}(z)$ and $L_{lin}(z|\sigma)$ as the forward Kolmogorov operators of the nonlinear vibration system and equivalent linear vibration system respectively. Let $p_{nl}(z)$ and $p_{lin}(z|\sigma)$ be stationary solutions of their corresponding FPK equations, then gives

$$L_{nl}(z)p_{nl}(z) = 0 \quad L_{lin}(z|\sigma)p_{lin}(z|\sigma) = 0 \quad (3.5)$$

where $p_{lin}(z|\sigma)$ is the Gaussian probability density function of the equivalent linear vibration system and depends on the parameter vector σ . The main objective of the probabilistic linearization method is to find a probability density $p_{lin}(z|\sigma)$ to satisfy the following condition

$$L_{nl}(z)p_{lin}(z|\sigma) \approx 0 \quad (3.6)$$

The criterion for making this condition is chosen as

$$\min_{\sigma} \|L_{nl}(z)p_{lin}(z|\sigma)\| \quad (3.7)$$

where the norm is a standard or weighted \mathfrak{R}^2 norm. For any two functions: $f(z), g(z) : R^n \rightarrow R$, the standard \mathfrak{R}^2 inner product of these two functions is defined as

$$\langle f, g \rangle = \int_{R^n} f(z)g(z) dz \quad (3.8)$$

For any weighted function $\mu(z) > 0$, a weighted inner product of these two functions is defined as

$$\langle f, g \rangle_{\mu} = \int_{R^n} f(z)g(z)\mu(z) dz \quad (3.9)$$

So a standard \mathfrak{R}^2 norm and weighted \mathfrak{R}^2 norm of the criterion can be obtained

$$\begin{aligned} \|L_{nl}(z)p_{lin}(z|\sigma)\|_{\mathfrak{R}^2}^2 &= \int_{R^n} (L_{nl}(z)p_{lin}(z|\sigma))^2 dz \\ \|L_{nl}(z)p_{lin}(z|\sigma)\|_{\mathfrak{R}^2(\mu)}^2 &= \int_{R^n} (L_{nl}(z)p_{lin}(z|\sigma))^2 \mu(z) dz \end{aligned} \quad (3.10)$$

The weighted function $\mu(z)$ is chosen to put emphasis in the approximations to the tails of the probability density function of the nonlinear vibration system, which is known to be non-Gaussian for the nonlinear vibration system.

The exact probability density function of the nonlinear vibration system based on the FPK equation expressed by Eq. (2.9) is given by

$$p(z_1, z_2) = \frac{\sqrt{4\zeta\lambda/(\pi S_0)}}{e^{\varepsilon} K_{1/4}(\varepsilon)} \exp\left[-\frac{4\zeta}{S_0}\left(\frac{1}{2}z_1^2 + \frac{1}{4}\lambda z_1^2 + \frac{1}{2}z_2^2\right)\right] \quad (3.11)$$

where $z_1 = z$, $z_2 = z'$, $\varepsilon = \zeta/(2\lambda S_0)$ and $K_{1/4}$ is a modified Bessel function of the second kind.

Rewriting Eq. (2.9) in form of Eq. (3.1), gives

$$\begin{bmatrix} dz_1(T) \\ dz_2(T) \end{bmatrix} = \begin{bmatrix} z_2 \\ -2\zeta z_2 - z_1 - rz_1^3 \end{bmatrix} dT + \begin{bmatrix} 0 \\ \sqrt{S_0} \end{bmatrix} dw(T) \quad (3.12)$$

The associated equivalent linear vibration system is obtained as

$$\begin{bmatrix} dz_1(T) \\ dz_2(T) \end{bmatrix} = \begin{bmatrix} 0 & 1 \\ -w_{eq}^2 & -2\zeta_{eq} \end{bmatrix} \begin{bmatrix} z_1 \\ z_2 \end{bmatrix} dT + \begin{bmatrix} 0 \\ \sqrt{S_0} \end{bmatrix} dw(T) \quad (3.13)$$

The stationary probability density function of the equivalent linear vibration system can be obtained as the following two terms

$$\begin{aligned} p_{lin}(z|w_{wq}^2, \zeta_{eq}) &= \frac{4\zeta_{eq}w_{eq}}{2\pi S_0} \exp\left[-\left(\frac{2\zeta_{eq}w_{eq}^2}{S_0}z_1^2 + \frac{2\zeta_{eq}}{S_0}z_2^2\right)\right] \\ p_{lin}(z|\sigma, \sigma_{z_2}) &= \frac{1}{2\pi\sigma\sigma_{z_2}} \exp\left[-\left(\frac{z_1^2}{2\sigma^2} + \frac{z_2^2}{2\sigma_{z_2}^2}\right)\right] \end{aligned} \quad (3.14)$$

Since the damping ratio of the nonlinear vibration system is linear, the probability density function of $p_{nl}(z_2)$ is a Gaussian probability density function, then Eq. (3.14)₂ can be obtained as a function of the parameter σ

$$p_{lin}(z|\sigma) = \frac{1}{2\pi\sigma\sigma_{z_2}} \exp\left[-\left(\frac{z_1^2}{2\sigma^2} + \frac{z_2^2}{2\sigma_{z_2}^2}\right)\right] \quad (3.15)$$

where $\sigma_{z_2}^2 = S_0/(4\zeta)$. The forward Kolmogorov operators of the nonlinear vibration system and the probabilistic linearization method criterion are given by

$$\begin{aligned} L_{nl}(z)p(z) &= \frac{S_0}{2} \frac{\partial^2 p(z)}{\partial z_2^2} - \frac{\partial}{\partial z_1} [z_2 p(z)] + \frac{\partial}{\partial z_2} [(2\zeta z_2 + z_1 + \lambda z_1^3)p(z)] \\ \min_{\sigma} \|L_{nl}(z)p_{lin}(z|\sigma)\| & \end{aligned} \quad (3.16)$$

Using the standard \mathfrak{R}^2 norm, Eqs. (3.16) can be written as

$$\begin{aligned} L_{nl}(z)p_{lin}(z|\sigma) &= \left[\left(\frac{S_0}{2\sigma_{z_2}^4} - \frac{2\zeta}{\sigma_{z_2}^2}\right)z_2^2 + \left(\frac{z_1}{\sigma_{z_1}^2} - \frac{z_1}{\sigma_{z_2}^2} - \frac{\lambda z_1^3}{\sigma_{z_2}^2}\right)z_2 + 2\zeta - \frac{S_0}{2\sigma_{z_2}^2}\right]p_{lin}(z|\sigma) \\ \min_{\sigma} \|L_{nl}(z)p_{lin}(z|\sigma)\|_{\mathfrak{R}^2}^2 &= \frac{15\lambda^2}{64\pi\sigma_{z_2}^3}\sigma^5 + \frac{3\lambda}{16\pi\sigma_{z_2}^3}\sigma^3 + \frac{1}{16\pi}\left(-\frac{3\lambda}{\sigma_{z_2}} + \frac{1}{\sigma_{z_2}^3}\right)\sigma \\ &+ \left[\left(\frac{3}{4\pi}\zeta^2 - \frac{1}{8\pi}\right)\frac{1}{\sigma_{z_2}} - \frac{3\zeta S_0}{8\pi\sigma_{z_2}^3} + \frac{3S_0^2}{64\pi\sigma_{z_2}^5}\right]\frac{1}{\sigma} + \frac{\sigma_{z_2}}{16\pi\sigma^3} \end{aligned} \quad (3.17)$$

To minimize the criterion, let $\partial \min_{\sigma} \|L_{nl}(z)p_{lin}(z|\sigma)\|_{\mathfrak{R}^2}^2 / \partial \sigma = 0$, then σ can be obtained numerically.

σ_z can also be obtained by using the equivalent linearization method, then it gives

$$\sigma_z^2 = \frac{\sqrt{\zeta^2 + 3\zeta\lambda S_0} - \zeta}{6\zeta\lambda} \quad (3.18)$$

Figure 3 shows the probability density function $p(z)$ of the QZS vibration isolator using different analytical methods. It can be seen that both the probabilistic linearization method and equivalent linearization method give good results in the tails of the probability density function, but the errors become larger in the peak value areas of the probability density function and the probabilistic linearization method gives better results than the equivalent linearization method. When \hat{l} increases, the parameter α increases and γ decreases, which indicates that the nonlinear parameter λ becomes smaller, the errors of both methods become smaller in the peak value areas of the probability density function.

4. Performance of the QZS vibration isolator under random excitation

The performance of the QZS vibration isolator under random excitation is evaluated by two performance indexes, which are defined as follows:

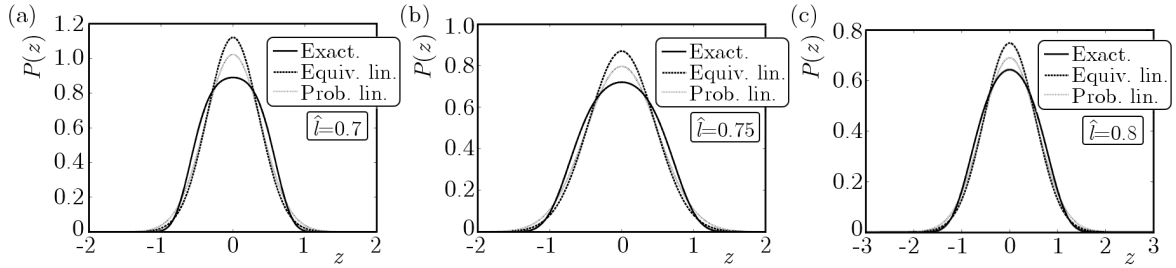


Fig. 3. Probability density function $p(z)$ of the QZS vibration isolator using different analytic methods ($\zeta = 0.02$, $S_0 = 0.05$)

- (1) Mean square relative displacement (MSRD) $E(z^2)$,
- (2) Mean square acceleration (MSA) $E(z''^2)$.

It is also of interest to compare the isolation performance of the QZS vibration isolator with an equivalent linear vibration isolator with the same load bearing capacity. Since the QZS vibration isolator is comprised of the load bearing element and negative stiffness correctors, the equivalent linear vibration isolator is the QZS vibration isolator with the negative stiffness correctors removed, then the natural frequency and damping ratio of the equivalent linear vibration isolator can be obtained

$$w_l = \frac{w_n}{\sqrt{\alpha}} \quad \zeta_l = \sqrt{\alpha}\zeta \quad (4.1)$$

4.1. Mean square relative displacement (MSRD)

The MSRD can be obtained by using both the probabilistic linearization method and equivalent linearization method, which can be clearly seen in Eq. (3.17) and Eq. (3.18). The MSRD obtained by the probabilistic linearization method can be improved by using a weighted function. The weighted function $\mu(z) = 1 + z^2$ is used in calculating $E(z^2)$. Although the chosen weighted function can be arbitrary, this particular function is chosen for three reasons:

- (1) Give more weight to the tails of the probability density function $p(z)$, as the probability density function $p(z)$ for small values of z is not as important when calculating MSRD.
- (2) The weighted function should not significantly increase the computation complexity.
- (3) It seems reasonable to include a z^2 term in calculating $E(z^2)$. Then the weighted \mathfrak{R}^2 norm of the criterion combining Eq. (3.10)₂ and Eq. (3.17)₁ can be obtained

$$\begin{aligned} \min_{\sigma} \|L_{nl}(z)p_{lin}(z|\sigma)\|_{\mathfrak{R}^2(\mu)}^2 &= \frac{105\lambda^2}{128\pi\sigma_{z_2}^3}\sigma^7 + \frac{15(\lambda^2+2\lambda)}{64\pi\sigma_{z_2}^3}\sigma^5 + \frac{1}{32\pi}\left(-\frac{15\lambda}{\sigma_{z_2}} + \frac{3+6\lambda}{\sigma_{z_2}^3}\right)\sigma^3 \\ &+ \left[\left(\frac{3}{8\pi}\zeta^2 - \frac{3\lambda}{16\pi} - \frac{3}{16\pi}\right)\frac{1}{\sigma_{z_2}} + \left(\frac{1}{16\pi} - \frac{3}{16\pi}\zeta S_0\right)\frac{1}{\sigma_{z_2}^3} + \frac{3S_0^2}{128\pi\sigma_{z_2}^5}\right]\sigma \\ &+ \left[\frac{3\sigma_{z_2}}{32\pi} + \left(\frac{3}{4\pi}\zeta^2 - \frac{1}{8\pi}\right)\frac{1}{\sigma_{z_2}} - \frac{3\zeta S_0}{8\pi\sigma_{z_2}^3} + \frac{3S_0^2}{64\pi\sigma_{z_2}^5}\right]\frac{1}{\sigma} + \frac{\sigma_{z_2}}{16\pi\sigma^3} \end{aligned} \quad (4.2)$$

To minimize the criterion, let $\partial \min_{\sigma} \|L_{nl}(z)p_{lin}(z|\sigma)\|_{\mathfrak{R}^2(\mu)}^2 / \partial \sigma = 0$, then σ can be obtained numerically.

Figure 4 shows the MSRD curves of the QZS vibration isolator using different analytical methods. The exact solutions can be determined by integrating Eq. (3.11) directly using the numerical method. It can be seen that the probabilistic linearization method overestimates the MSRD, while the equivalent linearization method underestimates it. The weighted probabilistic

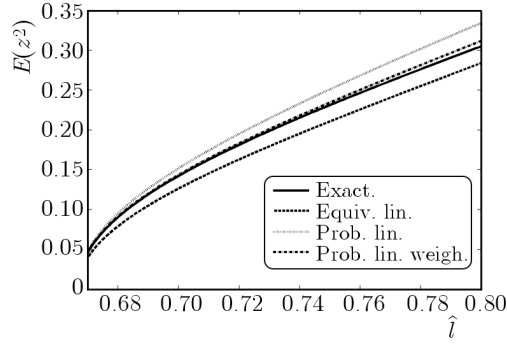


Fig. 4. MSR D curves of the QZS vibration isolator using different analytical methods ($\zeta = 0.02$, $S_0 = 0.05$)

linearization method gives better results with the numerical results than the other two analytical methods.

The MSR D curves of the QZS vibration isolator for different values of damping ratio and spectral density of the random excitation using the weighted probabilistic linearization method are shown in Fig. 5. The MSR D curves of the equivalent linear vibration isolator are also plotted in the same figure for comparison, which are plotted in the thinner lines. The MSR D of the equivalent linear vibration isolator is given as

$$\sigma_{z_l}^2 = \frac{S_0}{4\zeta_l} = \frac{S_0}{4\sqrt{\alpha}\zeta} \quad (4.3)$$

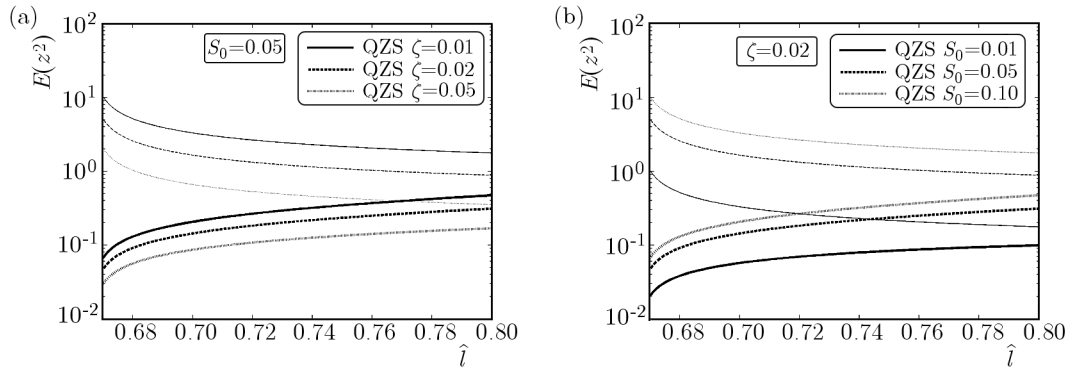


Fig. 5. MSR D curves of the QZS vibration isolator for different values of damping ratio and spectral density of the random excitation

The MSR D of the QZS vibration isolator is always lower than the equivalent linear vibration isolator, which indicates that the QZS vibration isolator can achieve a better isolation performance for the MSR D case. With an increase in the damping ratio ζ or a decrease in the spectral density S_0 , the MSR D of both vibration isolators decreases. Also when the length ratio \hat{l} increases, the parameter α increases, γ decreases and the nonlinear parameter λ becomes smaller, then the MSR D of the equivalent linear vibration isolator decreases, while the MSR D of the QZS vibration isolator increases with an increase in the length ratio \hat{l} .

4.2. Mean square acceleration (MSA)

The MSA is an important index for investigating the overall effects of various parameters on the response of the vibration isolator. The MSA can be obtained from Eq. (2.9)

$$E(z''^2) = 4\zeta^2 E(z'^2) + E(z^2) + 2\gamma E(z^4) + \gamma^2 E(z^6) \quad (4.4)$$

The MSA can be determined by using both the probabilistic linearization method and equivalent linearization method. Using these two methods, Eq. (4.4) can be transformed as

$$E(z''^2) = \zeta S_0 + \sigma^2 + 6\gamma\sigma^4 + 15\gamma^2\sigma^6 \quad (4.5)$$

where $E(z^2) = \sigma^2$ is determined differently for these two methods. The MSA obtained by the probabilistic linearization method can be improved by using a weighted function. In this case, the weighted function $\mu(z) = 1 + (x_1z + x_2z^3)^2$ is chosen in calculating $E(z''^2)$, where x_1 and x_2 are larger values in order to put more weight to the tails of the probability density function because of the σ^2 , σ^4 and σ^6 terms exist when it determines $E(z''^2)$. Then the weighted \mathfrak{R}^2 norm of the criterion can be obtained

$$\begin{aligned} \min_{\sigma} \|L_{nl}(z)p_{lin}(z|\sigma)\|_{\mathfrak{R}^2(\mu)}^2 &= \frac{10395\lambda^2x_2^2}{512\pi\sigma_{z_2}^3}\sigma^{11} + \frac{945(\lambda^2x_1x_2 + \lambda x_2^2)}{128\pi\sigma_{z_2}^3}\sigma^9 \\ &+ \frac{105}{128\pi} \left(-\frac{9\lambda x_2^2}{\sigma_{z_2}} + \frac{\lambda^2x_1^2 + 4\lambda x_1x_2 + x_2^2}{\sigma_{z_2}^3} \right) \sigma^7 + \frac{15}{64\pi} \left[(6x_2^2\zeta^2 - 14\lambda x_1x_2 - 7x_2^2) \frac{1}{\sigma_{z_2}} \right. \\ &+ \left. (-3x_2^2\zeta S_0 + \lambda^2 + 2\lambda x_1^2 + 2x_1x_2) \frac{1}{\sigma_{z_2}^3} + \frac{3x_2^2S_0^2}{8\sigma_{z_2}^5} \right] \sigma^5 \\ &+ \left[\frac{105x_2^2\sigma_{z_2}}{128\pi} + \left(\frac{9x_1x_2\zeta^2}{8\pi} - \frac{15x_1x_2}{16\pi} - \frac{15x_1^2\lambda}{32\pi} \right) \frac{1}{\sigma_{z_2}} \right. \\ &+ \left. \frac{3}{16\pi\sigma_{z_2}^3} \left(-3x_1x_2\zeta S_0 + \lambda + \frac{x_1^2}{2} \right) + \frac{9x_1x_2S_0^2}{128\pi\sigma_{z_2}^5} \right] \sigma^3 \\ &+ \left[\frac{15x_1x_2\sigma_{z_2}}{32\pi} + \left(\frac{3}{8\pi}x_1\zeta^2 - \frac{3\lambda}{16\pi} - \frac{3x_1^2}{16\pi} \right) \frac{1}{\sigma_{z_2}} + \left(\frac{1}{16\pi} - \frac{3x_1}{16\pi}\zeta S_0 \right) \frac{1}{\sigma_{z_2}^3} + \frac{3x_1S_0^2}{128\pi\sigma_{z_2}^5} \right] \sigma \\ &+ \left[\frac{3x_1^2\sigma_{z_2}}{32\pi} + \left(\frac{3}{4\pi}\zeta^2 - \frac{1}{8\pi} \right) \frac{1}{\sigma_{z_2}} - \frac{3\zeta S_0}{8\pi\sigma_{z_2}^3} + \frac{3S_0^2}{64\pi\sigma_{z_2}^5} \right] \frac{1}{\sigma} + \frac{\sigma_{z_2}}{16\pi\sigma^3} \end{aligned} \quad (4.6)$$

To minimize the criterion, let $\partial \min_{\sigma} \|L_{nl}(z)p_{lin}(z|\sigma)\|_{\mathfrak{R}^2(\mu)}^2 / \partial \sigma = 0$, then σ can be obtained numerically.

Figure 6 shows the MSA curves of the QZS vibration isolator using different analytical methods. The exact solutions can be determined by integrating Eq. (4.4) directly using the numerical method combined with Eq. (3.11). It can be seen that both the equivalent linearization method and the probabilistic linearization method overestimate the MSA. The weighted probabilistic linearization method gives better results with the numerical results than the other two analytical methods.

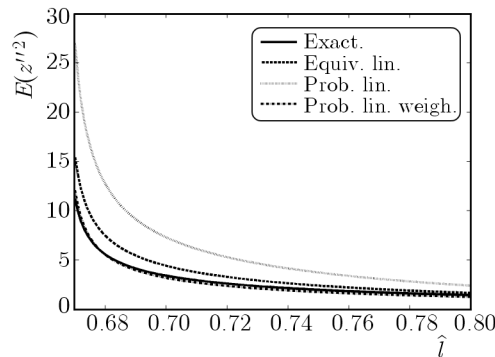


Fig. 6. MSA curves of the QZS vibration isolator using different analytical methods ($\zeta = 0.02$, $S_0 = 0.05$)

The MSA curves of the QZS vibration isolator for different values of damping ratio and spectral density of the random excitation using the weighted probabilistic linearization method

are shown in Fig. 7. The MSA curves of the equivalent linear vibration isolator are also plotted in the same figure for comparison, which are plotted in the thinner lines. The MSA of the equivalent linear vibration isolator is given as

$$E(z''^2_l) = (1 + 4\zeta_l^2)\sigma_{z_l}^2 = (1 + 4\alpha\zeta^2)\frac{S_0}{4\sqrt{\alpha\zeta}} \quad (4.7)$$

It is more complicated for the MSA case. With an increase in ζ or a decrease in S_0 , the MSA of both vibration isolators decrease. For smaller values of ζ , the MSA of the QZS vibration isolator is larger than the linear one, which indicates the isolation performance of the QZS vibration isolator is inferior to the linear one; when ζ continues to increase, the MSA is more or less the same for both vibration isolators; when ζ reaches a higher value, the MSA of the QZS vibration isolator is smaller than the linear one, which indicates that the QZS vibration isolator can achieve a better isolation performance. For smaller values of S_0 , the MSA of the QZS vibration isolator is smaller than the linear one; when S_0 continues to increase, the MSA is more or less the same for both vibration isolators; when S_0 reaches a higher value, the MSA of the QZS vibration isolator is larger than the linear one, then the isolation performance of the QZS vibration isolator is inferior to the linear one. Also when the length ratio \hat{l} increases, the MSA of both vibration isolators decrease.

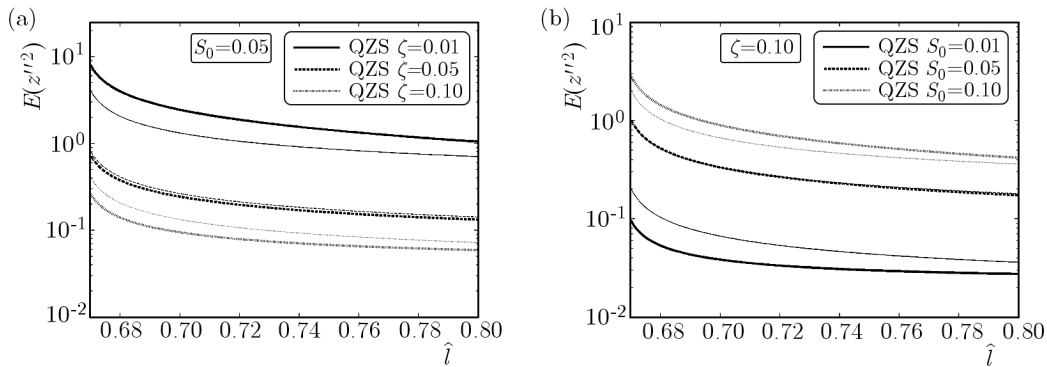


Fig. 7. MSA curves of the QZS vibration isolator for different values of damping ratio and spectral density of the random excitation

5. Conclusions

In this paper, the dynamic response and isolation performance of the QZS vibration isolator under random excitation are investigated. The QZS vibration isolator is comprised of a vertical spring providing positive stiffness and inclined springs used as negative stiffness correctors. The probability density function of the relative displacement of the mass is obtained by using probabilistic linearization method, and compared with the exact solution based on the FPK equation and the equivalent linearization method. The compared results show that both the probabilistic linearization method and equivalent linearization method give very good results in the tails of the probability density function, but the errors become larger in the peak value areas of the probability density function and the probabilistic linearization method gives better results than the equivalent linearization method. When the length ratio increases, which indicates that the nonlinear parameter λ decreases, the errors of both methods become smaller in the peak value areas of the probability density function.

Two performance indexes (MSRD and MSA) are defined to evaluate the isolation performance of the QZS vibration isolator. The weighted probabilistic linearization method is employed to improve the accurate results of the two performance indexes by adding a weighted function to

the criterion. The two performance indexes obtained by the weighted probabilistic linearization method are also compared with the numerical method, the equivalent linearization method and the probabilistic linearization method. The weighted probabilistic linearization method gives better results with the numerical results than the other two analytical methods.

The isolation performance of the QZS vibration isolator is also compared with an equivalent linear vibration isolator. The MSRDR of the QZS vibration isolator is always lower than the equivalent linear vibration isolator, which indicates that the QZS vibration isolator can achieve a better isolation performance for this case. The MSA of the QZS vibration isolator can be larger or lower than the equivalent linear vibration isolator based on the values of damping ratio and spectral density of the random excitation, which is different from the MSRDR case. For the MSA case, the spectral density of the random excitation should be considered first, and choose an appropriate damping ratio for the QZS vibration isolator to provide a better random isolation performance than the equivalent linear vibration isolator.

Acknowledgments

This work was supported by China Scholarship Council (CSC) and also supported by Funding of Jiangsu Innovation Program for Graduate Education (grant number KYLX_0243) and the Fundamental Research Funds for the Central Universities.

References

1. ALABUZHEV P., GRITCHIN A., KIM L., MIGIRENKO G., CHON V. AND STEPANOV P., 1989, *Vibration Protecting and Measuring Systems with Quasi-Zero Stiffness*, Hemisphere Publishing, Taylor & Francis Group, New York
2. CAI G.Q., LIN Y.K., 1988, A new approximate solution technique for randomly excited non-linear oscillators, *International Journal of Non-Linear Mechanics*, **23**, 5, 409-420
3. CARRELL A., BRENNAN M.J., WATERS T.P., 2007, Static analysis of a passive vibration isolation with quasi zero-stiffness characteristic, *Journal of Sound and Vibration*, **301**, 3, 678-689
4. CAUGHEY T.K., 1963, Equivalent linearization techniques, *The Journal of the Acoustical Society of America*, **35**, 11, 1706-1711
5. ELISHAKOFF I., CAI G.Q., 1993, Approximate solution for nonlinear random vibration problems by partial stochastic linearization, *Probabilistic Engineering Mechanics*, **8**, 3, 233-237
6. HAO Z., CAO Q., 2014, A novel dynamical model for GVT nonlinear supporting system with stable-quasi-zero-stiffness, *Journal of Theoretical and Applied Mechanics*, **52**, 1, 199-213
7. HARRIS C.M., PIERSOL A.G., 2002, *Shock and Vibration Handbook*, McGraw-Hill, New York
8. IBRAHIM R.A., 2008, Recent advances in nonlinear passive vibration isolators, *Journal of Sound and Vibration*, **314**, 3, 371-452
9. KIRK C.L., 1988, Non-linear random vibration isolators, *Journal of Sound and Vibration*, **124**, 1, 157-182
10. KLEIN G.H., 1964, Random excitation of a nonlinear system with tangent elasticity characteristics, *The Journal of the Acoustical Society of America*, **36**, 11, 2095-2105
11. KOVACIC I., BRENNAN M.J., WATERS T.P., 2008, A study of a nonlinear vibration isolator with a quasi-zero stiffness characteristic, *Journal of Sound and Vibration*, **315**, 3, 700-711
12. LE T.D., AHN K.K., 2011, A vibration isolation system in low frequency excitation region using negative stiffness structure for vehicle seat, *Journal of Sound and Vibration*, **330**, 26, 6311-6335
13. LIN Y.K., 1967, *Probabilistic Theory of Structural Dynamics*, McGraw-Hill, New York

14. LIU X., HUANG X., HUA H., 2013, On the characteristics of a quasi-zero stiffness isolator using Euler buckled beam as negative stiffness corrector, *Journal of Sound and Vibration*, **332**, 14, 3359-3376
15. LIU X., HUANG X., HUA H., 2014, Performance of a zero stiffness isolator under shock excitations, *Journal of Vibration and Control*, **20**, 14, 2090-2099
16. LYON R.H., 1960, On the vibration statistics of a randomly excited hard-spring oscillator, *The Journal of the Acoustical Society of America*, **32**, 6, 716-719
17. LYON R.H., 1961, On the vibration statistics of a randomly excited hard-spring oscillator II, *The Journal of the Acoustical Society of America*, **33**, 10, 1395-1403
18. POLIDORI D.C., BECK J.L., 1996, Approximate solutions for non-linear random vibration problems, *Probabilistic Engineering Mechanics*, **11**, 3, 179-185
19. POLIDORI D.C., BECK J.L., PAPADIMITRIOU C., 2000, A new stationary PDF approximation for non-linear oscillators, *International Journal of Non-linear Mechanics*, **35**, 4, 657-673
20. ROBERTSON W.S., KINDER M.R.F., CAZZOLATO B.S., ZANDER A.C., 2009, Theoretical design parameters for a quasi-zero stiffness magnetic spring for vibration isolation, *Journal of Sound and Vibration*, **326**, 1/2, 88-103
21. SHAW A.D., NEILD S.A., WAGG D.J., 2013, A nonlinear spring mechanism incorporating a bi-stable composite plate for vibration isolation, *Journal of Sound and Vibration*, **332**, 24, 6265-6275
22. SHIN K., 2014, Experimental investigation of the vibration transmissibility of a magnet-spring vibration isolator under random excitation, *Journal of Vibroengineering*, **16**, 4, 1745-1752
23. WANG Y., LI S.M., LI J.Y., 2014, Response and performance of a nonlinear vibration isolator with high-static-low-dynamic-stiffness under shock excitations, *Journal of Vibroengineering*, **16**, 7, 3382-3398
24. WU W.F., LIN Y.K., 1984, Cumulant-neglect closure for non-linear oscillators under random parametric and external excitations, *International Journal of Non-Linear Mechanics*, **19**, 4, 349-362
25. XU D., YU Q., ZHOU J., 2013, Theoretical and experimental analyses of a nonlinear magnetic vibration isolator with quasi-zero-stiffness characteristic, *Journal of Sound and Vibration*, **332**, 14, 3377-3389
26. ZHOU N., LIU K., 2010, A tunable high-static low-dynamic stiffness vibration isolator, *Journal of Sound and Vibration*, **329**, 9, 1254-1273

Manuscript received March 9, 2015; accepted for print October 16, 2015

NUMERICAL SIMULATION OF FLOW AND HEAT TRANSFER IN HYDROMAGNETIC MICROPOLAR FLUID BETWEEN TWO STRETCHABLE DISKS WITH VISCOUS DISSIPATION EFFECTS

KASHIF ALI, SHAHZAD AHMAD, MUHAMMAD ASHRAF

Centre for Advanced Studies in Pure and Applied Mathematics, Bahauddin Zakariya University, Multan, Pakistan
e-mail: muhammadashraf@bzu.edu.pk

A study of magnetohydrodynamic (MHD) flow with viscous dissipation and heat transfer in an electrically conducting laminar steady viscous incompressible micropolar fluid between two infinite uniformly stretching disks is presented. The transformed self similar nonlinear ODEs are first linearized using a quasi linearization method and then solved by employing a combination of a direct and an iterative method. The study may be beneficial to flow and thermal control of polymeric processing.

Keywords: MHD, micropolar fluid, stretchable disk, viscous dissipation, couple stress, heat transfer rate

1. Introduction

The exploration in the field of flow over a stretching surface has attracted attention of the research community due to its significant applications in different industries such as extrusion paper production, extrusion of polymers sheet, metal and plastic industries (Altan *et al.*, 1979; Fisher, 1976; Tadmor and Klein, 1970). The problem of fluid flow between parallel disks is also important due to its applications in many technological and engineering processes. These applications include semiconductor-manufacturing processes with rotating wafers, magnetic storage devices, gas turbine engines, hydrodynamical machines and apparatus, crystal growth processes, rotating machinery, biomechanics, geothermal, geophysical, heat and mass exchanges, computer storage devices, viscometry, lubrication, oceanography radial diffusers, etc. Robert *et al.* (2010) presented the analytical solution of axi-symmetric flow between two infinite stretching disks whereas Fang and Zhang (2008) found the exact solution for the axi-symmetric flow between two stretchable infinite disks. Munawar *et al.* (2011) studied flow of an incompressible viscous fluid between two continuously stretching coaxial disks by employing the optimal HAM. Xinhui *et al.* (2012) studied asymmetric flow and heat transfer of a viscous fluid between contracting/expanding rotating disks by using the homotopy analysis method.

All the above cited researchers are, however, confined to the flow and heat transfer problems of classical Newtonian fluids. The Newtonian model is, however, inadequate to completely describe some modern scientific, engineering and industrial processes which involve materials possessing an internal structure. The scope of non-Newtonian fluids has significantly increased mainly due to their connection with applied sciences. The governing equations of motion for non-Newtonian fluids are highly nonlinear and complicated as compared to those for Newtonian fluids. The flow problems of non-Newtonian fluids are challenging for researchers due to their inherent complexity. Hoyt and Fabula (1964) predicted experimentally that fluids having polymeric additives display a significant reduction of shear stress and polymeric concentration (see Eringen, 1965). Deformation of such materials can be well explained by the theory of micropolar fluids given by Eringen (1964, 1966). Micropolar fluids have applications in colloidal fluids flow,

blood flows, dumbbell molecules or short rigid cylindrical elements, liquid crystals, lubricants, turbulent shear flow and flow in capillaries, fluid suspensions, animal blood, fluid with bar like elements, heat and mass exchangers, etc. The steady laminar incompressible flow of a micropolar fluid between two parallel disks in which the lower disk is taken to be impermeable while the upper one is permeable was discussed numerically by Ashraf *et al.* (2009a). The magnetohydrodynamics (MHD) has attracted the research community due to its novel industrial applications. Rashidi *et al.* (2014) investigated velocity and temperature profiles as well as entropy generation in magnetohydrodynamic (MHD) and slip flow over a rotating porous disk with different properties using numerical methods. Neetu (2014) found the analytical solution to magnetohydrodynamic flow problem of an incompressible micropolar fluid between two eccentric disks. MHD steady and axisymmetric flow of an incompressible viscous fluid between two radially stretching sheets was analyzed by Hayat and Nawaz (2010). Hayat *et al.* (2011) examined a time dependent magnetohydrodynamic (MHD) flow problem of a micropolar fluid between two radially stretching infinite sheets.

The above cited researchers did not take the effects of viscous dissipation in their investigations. Therefore, the aim of the present study is to investigate MHD steady viscous incompressible electrically conducting micropolar fluid flow and heat transfer between two stretching disks in the presence of a transverse magnetic field and viscous dissipation effects.

2. Problem formulation

Consider hydromagnetic steady laminar viscous flow and heat transfer of an incompressible electrically conducting micropolar fluid between two stretchable infinite disks located at $z = -L$ and $z = L$ as shown in Fig. 1. A uniform transverse magnetic field \underline{B} is applied perpendicularly at the disks. The geometry of the problem suggests that the cylindrical polar coordinate system is most suitable for the study. Both the disks are stretched uniformly with the velocity proportional to the r coordinate. The magnetic Reynolds number is assumed to be small, and hence the induced magnetic field can be neglected as compared to the imposed magnetic field (Shercliff, 1965). We assume that there is no applied polarization voltage, so the electric field is zero. The components of velocity (u, v, w) and microrotation (v_1, v_2, v_3) along the radial, transverse and axial directions can be written respectively as

$$\begin{aligned} u_r &= u_r(r, z) & u_\theta &= 0 & u_z &= u_z(r, z) \\ v_1 &= 0 & v_2 &= v_2(r, z) & v_3 &= 0 \end{aligned} \quad (2.1)$$

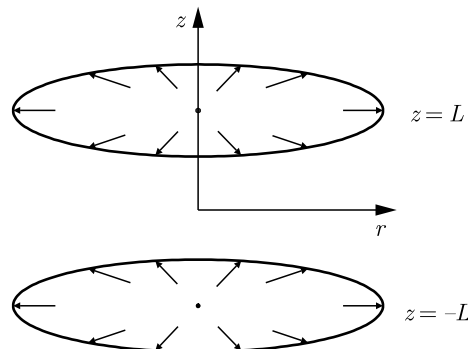


Fig. 1. Physical configuration

Following the work of Eringen (1964, 1966) and in view of Eq. (2.1), the governing equations of the problem under consideration can be written as

$$\frac{u_r}{r} + \frac{\partial u_r}{\partial r} + \frac{1}{L} \frac{\partial u_z}{\partial \eta} = 0 \tag{2.2}$$

and

$$\begin{aligned} \rho \left(u_r \frac{\partial u_r}{\partial r} + \frac{u_z}{L} \frac{\partial u_r}{\partial \eta} \right) &= -\frac{\partial p}{\partial r} - \frac{\kappa}{L} \frac{\partial v_2}{\partial \eta} + (\mu + \kappa) \left(\frac{\partial^2 u_r}{\partial r^2} + \frac{1}{r} \frac{\partial u_r}{\partial r} - \frac{u_r}{r^2} + \frac{1}{L^2} \frac{\partial^2 u_r}{\partial \eta^2} \right) - \sigma_e B_0^2 u_r \\ \rho \left(u_r \frac{\partial u_z}{\partial r} + \frac{u_z}{L} \frac{\partial u_z}{\partial \eta} \right) &= -\frac{1}{L} \frac{\partial p}{\partial \eta} + \kappa \left(\frac{\partial v_2}{\partial r} + \frac{v_2}{r} \right) + (\mu + \kappa) \left(\frac{\partial^2 u_z}{\partial r^2} + \frac{1}{r} \frac{\partial u_z}{\partial r} + \frac{1}{L^2} \frac{\partial^2 u_z}{\partial \eta^2} \right) \\ \rho j \left(u_r \frac{\partial v_2}{\partial r} + \frac{u_z}{L} \frac{\partial v_2}{\partial \eta} \right) &= \kappa \left(\frac{1}{L} \frac{\partial u_r}{\partial \eta} - \frac{\partial u_z}{\partial r} \right) - 2\kappa v_2 + \gamma \left(\frac{\partial^2 v_2}{\partial r^2} - \frac{v_2}{r^2} + \frac{1}{r} \frac{\partial v_2}{\partial r} + \frac{1}{L^2} \frac{\partial^2 v_2}{\partial \eta^2} \right) \end{aligned} \tag{2.3}$$

where $\eta = z/L$ is the similarity variable, ρ is density, p is pressure, μ is dynamic viscosity of the fluid, κ is vortex viscosity, j is microinertia, γ is spin gradient viscosity, σ_e is electrical conductivity, B_0 is strength of the magnetic field. Including viscous dissipation effects, the energy equation for the problem of flow between two stretching disks can be written as

$$\rho c_p \left(u_r \frac{\partial T}{\partial r} + \frac{u_z}{L} \frac{\partial T}{\partial \eta} \right) - k_0 \left(\frac{1}{L^2} \frac{\partial^2 T}{\partial \eta^2} + \frac{\partial^2 T}{\partial r^2} + \frac{1}{r} \frac{\partial T}{\partial r} \right) - \frac{\mu}{L^2} \left(\frac{\partial u_r}{\partial \eta} \right)^2 = 0 \tag{2.4}$$

where T is temperature, c_p is specific heat capacity and k_0 is thermal conductivity of the fluid. The boundary conditions for the problem may be written as,

$$\begin{aligned} u_r(r, -L) = rE & \quad u_r(r, L) = rE & \quad u_z(r, -L) = 0 & \quad u_z(r, L) = 0 \\ \nu_2(r, -L) = 0 & \quad \nu_2(r, L) = 0 & \quad T(r, -L) = T_1 & \quad T(r, L) = T_2 \end{aligned} \tag{2.5}$$

where E is the parameter determining stretching strength of both the upper and lower disks, having units of $1/t$.

Partial differential Eqs. (2.3) and (2.4) can be converted into ordinary ones by using the following similarity transformations

$$u_r = -\frac{rE}{2} f'(\eta) \quad u_z = ELf(\eta) \quad v_2 = -\frac{Er}{2L^2} g(\eta) \quad \theta(\eta) = \frac{T - T_2}{T_1 - T_2} \tag{2.6}$$

where T_1 and T_2 are temperatures at the lower and upper disks, respectively. We see that the velocity field given in Eq. (2.6) identically satisfies continuity Eq. (2.1), and hence represents possible fluid motion. By using Eq. (2.6) in Eqs. (2.3) and (2.4), we get the following nonlinear ordinary differential equations in dimensionless form

$$\begin{aligned} (1 + C_1) f'''' - C_1 g'' - \text{Re} f f''' - \text{Re} M^2 f'' &= 0 \\ C_3 g'' + C_1 (f'' - 2g) + \text{Re} C_2 \left(\frac{f'g}{2} - fg' \right) &= 0 \\ \theta'' + \frac{1}{4} \text{PrEc} f''^2 - \text{RePr} f \theta' &= 0 \end{aligned} \tag{2.7}$$

where $\text{Re} = (\rho EL^2)/\mu$ is the stretching Reynolds number, $M = \sqrt{(\sigma_e B_0^2)/(\rho E)}$ is the magnetic parameter, $C_1 = \kappa/\mu$ is the vortex viscosity parameter, $C_2 = j/L^2$ is the microinertia density parameter, $C_3 = \gamma/\mu L^2$ is the spin gradient viscosity parameter, $\text{Pr} = (\mu c_p)/k_0$ is the Prandtl number and $\text{Ec} = (r^2 E^2)/[c_p(T_1 - T_2)]$ is the Eckert number.

Boundary conditions given in Eq. (2.7)₂ also get the form

$$\begin{aligned} f(-1) = f(1) = 0 & \quad f'(-1) = -2 & \quad f'(1) = -2 \\ g(-1) = 0 & \quad g(1) = 0 & \quad \theta(-1) = 1 & \quad \theta(1) = 0 \end{aligned} \tag{2.8}$$

3. Computational procedure

In this paper, we discuss the approach based on quasi-linearization of nonlinear ODEs.

3.1. Quasi-linearization

We use quasi-linearization to construct sequences of vectors $\{f^{(k)}\}$, $\{g^{(k)}\}$, and $\{\theta^{(k)}\}$, which converge to the numerical solutions to Eqs. (2.7), respectively. To construct $\{f^{(k)}\}$, we linearize Eq. (2.7)₁ by retaining only the first order terms as follows:

We set

$$G(f, f', f'', f''', f''') \equiv (1 + C_1)f'''' - C_1g'' - \text{Re}f f'' - \text{Re}M^2 f''$$

and

$$\begin{aligned} G(f^{(k)}, f'^{(k)}, f''^{(k)}, f'''^{(k)}, f''''^{(k)}) + (f^{(k+1)} - f^{(k)}) \frac{\partial G}{\partial f^{(k)}} + (f'^{(k+1)} - f'^{(k)}) \frac{\partial G}{\partial f'^{(k)}} \\ + (f''^{(k+1)} - f''^{(k)}) \frac{\partial G}{\partial f''^{(k)}} + (f'''^{(k+1)} - f'''^{(k)}) \frac{\partial G}{\partial f'''^{(k)}} + (f''''^{(k+1)} - f''''^{(k)}) \frac{\partial G}{\partial f''''^{(k)}} = 0 \end{aligned}$$

which simplifies to

$$(1 + C_1)f''''^{(k+1)} - \text{Re}f''''^{(k+1)} f^{(k)} - \text{Re}M^2 f''^{(k+1)} - \text{Re}f'''^{(k)} f^{(k+1)} = C_1g''^{(k)} - \text{Re}f'''^{(k)} f^{(k)} \quad (3.1)$$

Now Eq. (3.1) gives a system of linear differential equations with f^k being the numerical solution vector of the k^{th} equation. To solve the linear ODEs, we replace the derivatives with their central difference approximations, giving rise to the sequence $\{f^{(k)}\}$ generated by the following linear system

$$Bf^{(k+1)} = C \quad \text{with} \quad B \equiv B_{n \times n}(f^{(k)}) \quad \text{and} \quad C \equiv C_{n \times 1}(f^{(k)}) \quad (3.2)$$

where n is the number of grid points. On the other hand, Eqs. (2.7)_{2,3} are linear in g and θ respectively and, therefore, in order to generate the sequences $\{g^{(k)}\}$ and $\{\theta^{(k)}\}$, we write

$$\begin{aligned} C_3g''^{(k+1)} + C_1(f''^{(k+1)} - 2g^{(k+1)}) + \text{Re}C_2 \left(\frac{f'^{(k+1)}g^{(k+1)}}{2} - g'^{(k+1)}f^{(k+1)} \right) = 0 \\ \theta''^{(k+1)} + \frac{1}{4}\text{PrEc}f''^{(k+1)2} - \text{RePr}f^{(k+1)}\theta'^{(k+1)} = 0 \end{aligned} \quad (3.3)$$

Importantly, $f^{(k+1)}$ is considered to be known in the above equation and its derivatives are approximated by the central differences.

We outline the computational procedure as follows:

- Provide the initial guess $f^{(0)}$, $g^{(0)}$ and $\theta^{(0)}$, satisfying the boundary conditions given in Eq. (2.8)
- Solve the linear system given by Eq. (3.2) to find $f^{(1)}$
- Use $f^{(1)}$ to solve the linear system arising from the FD discretization of Eqs. (3.3), to get $g^{(1)}$ and $\theta^{(1)}$
- Take $f^{(1)}$, $g^{(1)}$ and $\theta^{(1)}$ as the new initial guesses and repeat the procedure to generate the sequences $\{f^{(k)}\}$, $\{g^{(k)}\}$ and $\{\theta^{(k)}\}$ which, respectively, converge to f , g and θ (the numerical solutions to Eqs. (2.7))

- The three sequences are generated until

$$\max \left\{ \|f^{(k+1)} - f^{(k)}\|_{L_\infty}, \|g^{(k+1)} - g^{(k)}\|_{L_\infty}, \|\theta^{(k+1)} - \theta^{(k)}\|_{L_\infty} \right\} < 10^{-6}$$

It is important to note that the coefficient matrix B in Eq. (3.2) will be pentadiagonal and not diagonally dominant, and hence the iterative method (like SOR) may fail or work very poorly. Therefore, some direct method like LU factorization or Gaussian elimination with full pivoting (to ensure stability) may be employed. On the other hand, Eqs. (3.3) will give a rise to the diagonally dominant algebraic system when discretized using the central differences, which allows us to use the SOR method. Lastly, we may also improve the order of accuracy of the solution by using the polynomial extrapolation scheme.

4. Results and discussion

In this Section, the results are presented in tabular and graphical forms together with their discussion and interpretations. Our objective is to develop a better understanding of the effects of the micropolar structure of fluids on flow and heat transfer characteristics. The parameters of the study are the Reynolds number Re , the magnetic parameter M , the micropolar parameters C_1 , C_2 , and C_3 , the Eckert number Ec and the Prandtl number Pr . The physical quantities of our interest are the shear stress, the couple stress and the heat transfer rate at the disks which are, respectively, proportional to $f'(-1)$, $g'(-1)$, $\theta'(-1)$ and $\theta'(1)$. It is important to note that $f''(-1) = f''(1)$, $g'(-1) = g'(1)$ and $\theta'(-1) = \theta'(1)$ for $Ec = 0$ due to symmetry of the problem. But in the case when $Ec \neq 0$, the symmetry of temperature profiles no longer exists, and thus $\theta'(-1) \neq \theta'(1)$ as C_3 affects the temperature distribution only (clear from decoupled Eqs. (2.7)). Therefore, in the presence of viscous dissipation, we will consider $f''(-1)$, $g'(-1)$, $\theta'(-1)$ and $\theta'(1)$ as well. We shall study the effects of the parameters described above on $f''(-1)$, $g'(-1)$, $\theta'(-1)$ and $\theta'(1)$ as well as on the velocity profiles $f(\eta)$, $f'(\eta)$, the microrotation profile $g(\eta)$ and the temperature profile $\theta(\eta)$.

The sets of values of the dimensionless micropolar parameters C_1 , C_2 and C_3 used in the present work are given in Table 1. In order to establish the validity of our numerical computations and to improve the order of accuracy of the solutions, numerical values of radial velocity $f'(\eta)$ are computed for three grid sizes h , $h/2$ and $h/4$ and then Richardson extrapolation is used as presented in Table 2. It also shows the convergence of our numerical results as the step size decreases. Table 3 shows that the shear and couple stresses increase, where the heat transfer rate increases at the upper disk and decreases at the lower disk as the stretching Reynolds number increases. The increased stretching rate of the disks forces the fluid to move rapidly towards the disks, thus increasing both the shear and couple stresses. Moreover, the fluid is carrying away the heat from the flow region, resulting in an increase in the temperature difference and, hence, the heat transfer rate.

Table 1. Five cases of values of micropolar parameters C_1 , C_2 and C_3

Case No.	C_1	C_2	C_3
1(Newtonian)	0	0	0
2	0.5	0.1	0.2
3	1	0.3	0.4
4	3	0.5	0.6
5	5	0.7	0.8

Table 2. Dimensionless radial velocity $f'(\eta)$ on three grid sizes and extrapolated values for $Re = 15$, $M = 1.5$, $C_1 = 3$, $C_2 = 0.5$, $C_3 = 0.6$, $Pr = 0.7$, $Ec = 0.5$

$f'(\eta)$				
η	1 st grid ($h = 0.02$)	2 nd grid ($h = 0.01$)	3 rd grid ($h = 0.005$)	Extrapolated values
-1	-1.995047	-1.998750	-1.999686	-1.999998
-0.6	0.092943	0.093467	0.093599	0.093642
-0.2	0.606570	0.607070	0.607195	0.607237
0	0.652236	0.652728	0.652851	0.652892
0.2	0.606570	0.607070	0.607195	0.607237
0.6	0.092943	0.093467	0.093599	0.093642
1	-1.995047	-1.998750	-1.999686	-1.999998

Table 3. The effect of the stretching Reynolds number on the shear and couple stresses as well as the heat transfer rate with $M = 1.5$, $C_1 = 3$, $C_2 = 0.5$, $C_3 = 0.6$, $Pr = 0.7$, $Ec = 0.5$

R	$f''(-1)$	$g'(-1)$	$\theta'(-1)$	$-\theta'(1)$
0	5.245037	5.710461	0.556018	1.556018
5	6.656467	6.023234	0.515410	2.005796
10	7.898473	6.213057	0.453647	2.412162
15	8.998815	6.329128	0.385683	2.777904
20	9.986100	6.399389	0.317821	3.110079

Table 4 shows that the magnetic parameter increases both the shear and couple stresses while reducing the heat transfer rate at the disks. From the mechanical point of view, the magnetic field exerts a friction like force, called the Lorentz force, which tends to drag the fluid

Table 4. The effect of the magnetic parameter on the shear and couple stresses as well as the heat transfer rate with $Re = 15$, $C_1 = 3$, $C_2 = 0.5$, $C_3 = 0.6$, $Pr = 0.7$, $Ec = 0.5$

M	$f''(-1)$	$g'(-1)$	$\theta'(-1)$	$-\theta'(1)$
0	6.270359	5.982139	0.798720	3.468070
0.4	6.509053	6.014097	0.721225	3.365199
0.8	7.172924	6.101533	0.558495	3.132747
1.2	8.142989	6.225003	0.427947	2.903393
1.6	9.300534	6.364672	0.382388	2.746286

towards the disks. This not only results in increasing the shear stress at the disks but also causes greater spinning of the micro fluid particles, and hence increases the couple stress as well. Furthermore, the frictional force tends to raise the fluid temperature and thus decreases the temperature difference between the fluid and the disks. Therefore, the heat transfer rate, which is directly proportional to the temperature difference, also decreases. The influence of the micropolar parameters C_1 , C_2 and C_3 on the shear and couple stresses is given in Table 5. The first case corresponds to the Newtonian fluid whereas the remaining ones are taken arbitrarily to investigate their influence on the flow as chosen in the literature (Ashraf and Batool, 2013; Ali *et al.*, 2014, 2009b). It may be concluded that the micropolar structure of the fluid tends to decrease the shear stress, which is in accordance with the experimental prediction of Hoyt and Fabula (1964) that the micro fluid particles cause significant reduction in the shear stress near a rigid body. Moreover, the particles also cause microrotation in the fluid, which is responsible for the couple stress at the disks, as shown in Table 5. It is also clear from the table that the role

Table 5. The effect of micropolar parameters on the shear and couple stresses as well as the heat transfer rate with $Re = 1, M = 1.5, Pr = 2, Ec = 0.2$

Cases	$f''(-1)$	$g'(-1)$	$\theta'(-1)$	$-\theta'(1)$
1	7.014810	0.000000	0.697019	1.960602
2	6.473276	3.912051	0.698798	1.973223
3	6.190115	3.896368	0.704141	1.984454
4	5.478203	6.449680	0.729788	2.024384
5	5.183083	7.439771	0.745661	2.046135

of microfluid particles in increasing the heat transfer rate is not as pronounced as compared to its effect on the shear and couple stresses. Table 6 shows that the viscous dissipation may cause thermal reversal at the lower disk, thus decreasing the temperature of the fluid which, in turn, increases the temperature difference between the fluid and the upper disk, and hence the heat transfer rate at the upper disk.

Table 6. The effect of viscous dissipation on the heat transfer rate with $Re = 20, M = 1.5, C_1 = 3, C_2 = 0.5, C_3 = 0.6, Pr = 0.3$

Ec	$-\theta'(-1)$	$-\theta'(1)$
0.0	0.844799	0.844799
0.2	0.608888	1.080710
0.4	0.372977	1.316622
0.6	0.137066	1.552533
0.8	-0.098845	1.788444

Now we present a graphical interpretation of our results. Streamlines for the present problem are given in Fig. 2. It is obvious that the streamlines near the walls are very close to each other showing larger gradients of the stream function which, in turn, predicts a greater fluid velocity

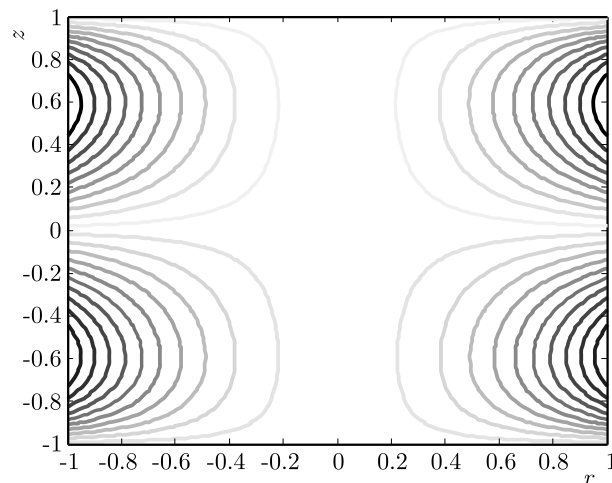


Fig. 2. Variation of streamlines for $Re = 5, M = 1.5, C_1 = 3, C_2 = 0.5, C_3 = 0.6$

closer to the disks. In order to further validate the presented solution method, we consider the case when the distance between the disks is infinite and the upper disk is at rest. In this situation, the problem reduces to the micropolar fluid flow over a stretchable disk which was studied by Ashraf and Batool (2013). Figure 3 shows an excellent comparison of our numerical results with those of Ashraf and Batool (2013).

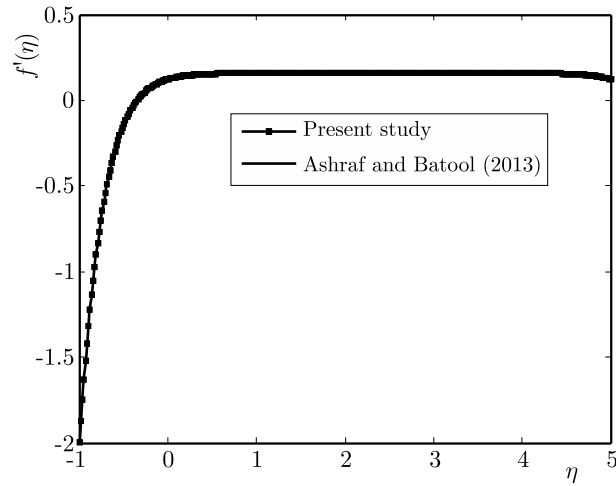


Fig. 3. Comparison with the results by Ashraf and Batool (2013)

Figures 4-6 show the influence of the magnetic parameter M for typical values of the stretching Reynolds number, the micropolar parameters, the Eckert number and the Prandtl number. The magnetic parameter decreases the velocity as well as the microrotation distribution across the disks (Fig. 4 and 5). On the other hand, the external magnetic field decreases the thermal

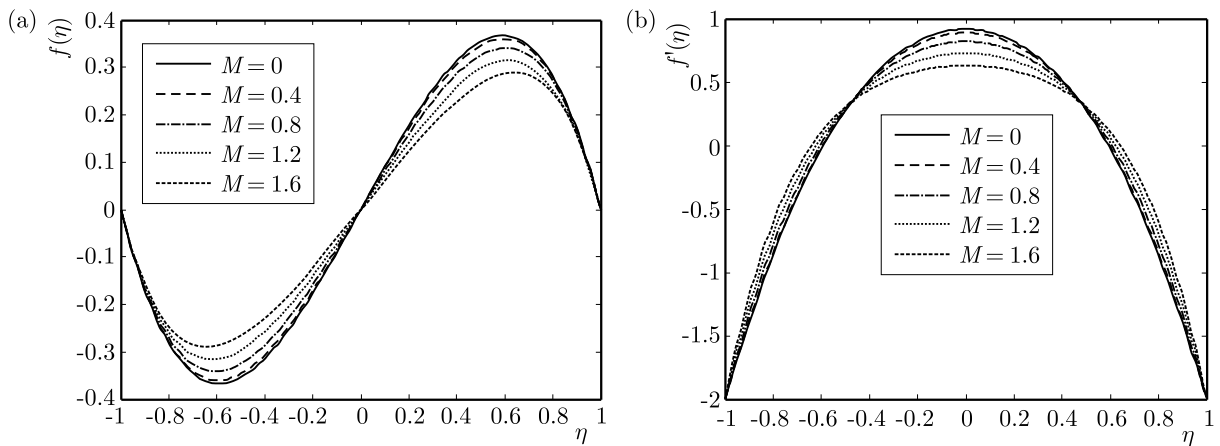


Fig. 4. Variation of (a) axial, (b) radial velocity for $Re = 15$, $C_1 = 3$, $C_2 = 0.5$, $C_3 = 0.6$, $Pr = 0.7$, $Ec = 0.5$ and various M

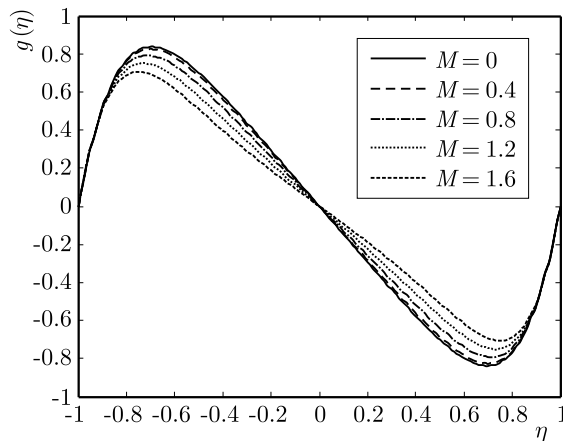


Fig. 5. Variation of microrotation for $Re = 15$, $C_1 = 3$, $C_2 = 0.5$, $C_3 = 0.6$, $Pr = 0.7$, $Ec = 0.5$ and various M

reversal by decreasing the temperature distribution across the disks, whether we consider the viscous dissipation effects or not, as shown in Fig. 6a.

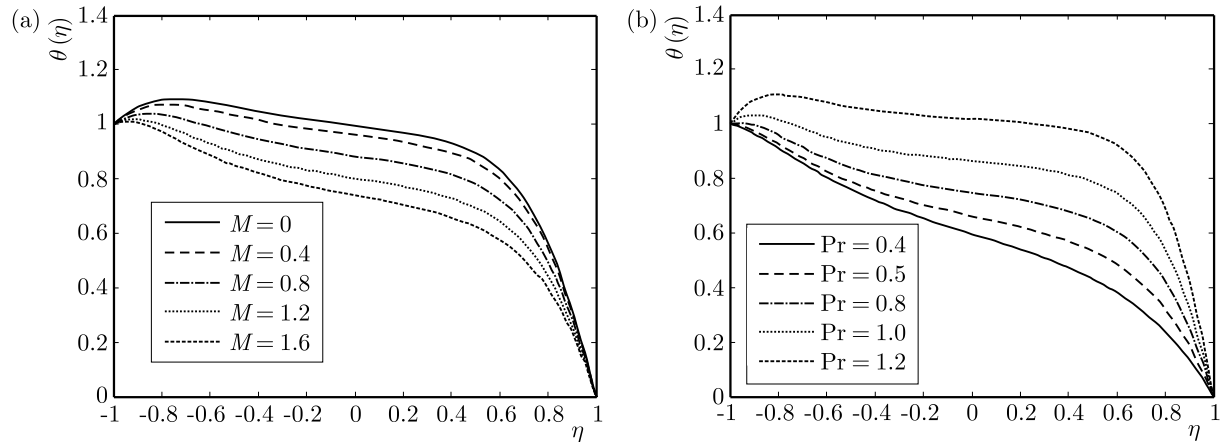


Fig. 6. Variation of temperature for (a) $Re = 15$, $C_1 = 3$, $C_2 = 0.5$, $C_3 = 0.6$, $Pr = 0.7$, $Ec = 0.5$ and various M , (b) $Re = 15$, $M = 1.5$, $C_1 = 3$, $C_2 = 0.5$, $C_3 = 0.6$, $Ec = 0.4$ and various Pr

We have noted that the effect of Re on the velocity and microrotation distribution is similar to that of M . The Reynolds number always tends to flatten the temperature profiles almost in the middle of the two disks, thus developing an equi-temperature region. On the other hand, it discourages thermal reversal near the lower disk, for the case $Ec \neq 0$.

The effect of the micropolar structure of the fluid on the velocity, microrotation and temperature profiles is opposite to that of the magnetic field. Thus, the external magnetic field tends to balance the effect of micropolar parameters. The viscous dissipation tends to eliminate the symmetry of temperature profiles by raising them near the lower disks, thus causing the thermal reversal. Viscous dissipation plays a vital role like an internal heat generation source in the energy transfer, which depends on the temperature distributions and heat transfer rates. This heat source is caused by the shearing of fluid layers. The merit of the effect of the viscous dissipation depends on whether the disks walls are hot or cold. Finally, the Prandtl number increases the thermal reversal by increasing the temperature distribution across the disks in the presence of viscous dissipation (Fig. 6b).

Table 7. The effect of the Prandtl number on the heat transfer rate with $Re = 20$, $M = 1$, $C_1 = 2$, $C_2 = 0.2$, $C_3 = 0.3$

Pr	Ec = 0.0		Ec = 0.3	
	$-\theta'(-1)$	$-\theta'(1)$	$-\theta'(-1)$	$-\theta'(1)$
0.0	0.500000	0.500000	0.500000	0.500000
0.2	0.719813	0.719813	0.494006	0.945619
0.4	0.976928	0.976928	0.482008	1.471849
0.6	1.254718	1.254718	0.426965	2.082470
0.8	1.536267	1.536267	0.278411	2.794123

On comparison of our results with those given by Khan *et al.* (2015) (where the classical Newtonian fluid has been taken into consideration between the two stretchable disks), we notice that the role of the external magnetic field and the disk stretching remains the same, even when the micropolar fluid is introduced in place of the classical Newtonian fluid. That is, both the factors increase the shear stresses at the disks. Micropolar fluids however show a remarkable reduction in the shear stress but introduce couple stresses at the disks due to the spinning of the fluid particles.

5. Conclusions

In this paper, we numerically study how the governing parameters affect the flow and heat transfer characteristics of a steady laminar incompressible electrically conducting micropolar fluid between two stretchable infinite disks. The following conclusions can be drawn.

Micropolar fluids exhibit significant reduction in the shear stress at the disks compared to Newtonian ones, which may be beneficial for many industrial processes (e.g. in flow and thermal control of polymeric processing). The external magnetic field is responsible for a remarkable rise in both the shear and couple stresses while reduction the heat transfer rate at the two disks. We, therefore, conclude that the external magnetic field may serve as a controlling agent to neutralize the effects of the micropolar structure of the fluid. Thus, in experimental setups involving micropolar flows caused by moving disks, the possibility of interference of the external magnetic field should be eliminated in order to obtain accurate and reliable data.

Acknowledgement

The authors are extremely grateful to the Higher Education Commission of Pakistan for the financial support to carry out this research. The authors are also very thankful to the learned reviewer for his remarks to improve the quality of the present work.

References

1. ALI K., ASHRAF M., JAMEEL N., 2014, Numerical simulation of MHD micropolar fluid flow and heat transfer in a channel with shrinking walls, *Canadian Journal of Physics*, **92**(2), 987-996
2. ALTAN T., OH S., GEGEL H.L., 1979, *Metal Forming Fundamentals and Applications*, American Society of Metals, Metals Park, OH
3. ASHRAF M., BATOOL K., 2013, MHD flow of a micropolar fluid over a stretching disk, *Journal of Theoretical and Applied Mechanics*, **51**(1), 25-38
4. ASHRAF M., KAMAL M.A., SYED K.S., 2009a, Numerical simulation of a micropolar fluid between a porous disk and a non-porous disk, *Journal of Applied Mathematics and Modelling*, **33**, 1933-1943
5. ASHRAF M., KAMAL M.A., SYED K.S., 2009b, Numerical study of asymmetric laminar flow of micropolar fluids in a porous channel, *Computers and Fluids*, **38**, 1895-1902
6. ERINGEN A.C., 1964, Simple micropolar fluids, *International Journal of Engineering Science*, **2**, 205-217
7. ERINGEN A.C., 1965, *Theory of Micropolar Continua*, Proceedings of the Ninth Midwestern Conference
8. ERINGEN A.C., 1966, Theory of micropolar fluids, *Journal of Mathematics and Mechanics*, **16**, 1-18
9. FANG T., ZHANG J., 2008, Flow between two stretchable disks – An exact solution of the Navier-Stokes equations, *International Communications in Heat and Mass Transfer*, **35**, 892-895
10. FISHER E.G., 1976, *Extrusion of Plastics*, Wiley New York
11. HAYAT T., NAWAZ M., 2010, Effect of heat transfer on magnetohydrodynamic axisymmetric flow between two stretching sheets, *Zeitschrift für Naturforschung*, **65**, 961-968
12. HAYAT T., NAWAZ M., OBAIDAT S., 2011, Axisymmetric magnetohydrodynamic flow of a micropolar fluid between unsteady stretching surfaces, *Applied Mathematics and Mechanics*, **32**, 361-374
13. HOYT J.W., FABULA A.G., 1964, The effect of additives on fluid friction, *US Naval Ordinance Test Station Report*

14. KHAN N., SAJID M., MAHMOOD T., 2015, Heat transfer analysis for magnetohydrodynamics axisymmetric flow between stretching disks in the presence of viscous dissipation and Joule heating, *AIP Advances*, **5**, 057115
15. MUNAWAR S., MEHMOOD A., ALI A., 2011, Effects of slip on flow between two stretchable disks using optimal homotopy analysis method, *Canadian Journal of Applied Sciences*, **1**(2), 50-68
16. NEETU S., 2014, MHD flow of the micropolar fluid between eccentrically rotating disks, *International Scholarly Research Notices*, Article ID-317075
17. RASHIDI M.M., KAVYANI N., ABELMAN S., 2014, Investigation of entropy generation in MHD and slip flow over a rotating porous disk with variable properties, *International Journal of Heat and Mass Transfer*, **70**, 892-917
18. ROBERT A., GORDER V., SWEET E., VAJRARELU K., 2010, Analytical solutions of a coupled nonlinear system arising in a flow between stretching disks, *Applied Mathematics and Computation*, **216**, 1513-1523
19. SHERCLIFF J.A., 1965, *A Text Book of Magnetohydrodynamics*, Pergamon Press Oxford
20. TADMOR Z., KLEIN I., 1970, *Engineering Principles of Plasticating Extrusion*, Polymer Science and engineering series, Van Norstrand Reinhold New York
21. XINHUI S., LIANCUN Z., XINXIN Z., XINYI S., 2012, Homotopy analysis method for the asymmetric laminar flow and heat transfer of viscous fluid between contracting rotating disks, *Applied Mathematical Modeling*, **36**, 1806-1820

Manuscript received January 30, 2015; accepted for print October 19, 2015

CABLE-SUSPENDED CPR-D TYPE PARALLEL ROBOT

MIRJANA FILIPOVIC

Mihajlo Pupin Institute, University of Belgrade, Belgrade, Serbia; e-mail: mira@robot.imp.bg.ac.rs

ANA DJURIC

Wayne State University, Detroit, U.S.A; e-mail: ana.djuric2@wayne.edu

This paper deals with the analysis and synthesis of a newly selected Cable-suspended Parallel Robot configuration, named CPR-D system. The camera carrier workspace has the shape of a parallelepiped. The CPR-D system has a unique Jacobian matrix that maps the relationship between internal and external coordinates. This geometric relationship is a key solution for the definition of the system kinematic and dynamic models. Because of the CPR-D system complexity, the Lagrange principle of virtual work has been adapted. Two significant Examples have been used for the CPR-D system analysis and validation.

Keywords: cable-suspended parallel robot, camera observation, kinematics, dynamics

1. Introduction

A system for observation of a workspace with moving objects has been developed to some extent and widely analyzed in various research areas as well as for different applications. Similar systems have been analyzed and modeled as presented by numerous publications.

The kinematic design of a planar three-degree-of-freedom parallel manipulator was considered by Gosselin and Grenier (2011). Four optimal different design criteria were established and analyzed. A trajectory planning approach for cable-suspended parallel mechanisms was presented by Gosselin *et al.* (2012). A planar two-degree-of-freedom parallel mechanism was used in the analysis. Carricato (2011) studied the kinematics and statics of under-constrained cable-driven parallel robots with less than six cables in crane configuration. A motion controller for a six DOF tendon-based parallel manipulator (driven by seven cables) which moves a platform with high speed was introduced by Fang *et al.* (2004). A control design of the CPR systems was investigated by Kraus *et al.* (2013), and Avci *et al.* (2014). The workspace conditions and the dynamics of the manipulator were described in details. Borgstrom *et al.* (2007) presented algorithms that enabled precise trajectory control of the Networked Info Mechanical Systems (NIMS), and under constrained three-dimensional (3D) cabled robot intended for use in actuated sensing. Several prototypes of the wire-driven parallel robots with different actuation schemes were presented by Merlet (2010). Two of them were evaluated through extensive tests and showed unexpected kinematic problems. The determination of this workspace was an important issue by Gouttefarde *et al.* (2006) since the cables can only pull and not push on the mobile platform.

Parallel cable-driven Stewart-Gough platforms consist of an end-effector which is connected to the machine frame by motor driven cables. Since the cables can transmit only tension forces, at least $m = n + 1$ cables are needed to tense a system having n -degrees-of-freedom. This will cause a kinematical redundancy and leads to an $(m - n)$ -dimensional solution space for the cable force distribution presented by Bruckmann *et al.* (2007). The recent result from a newly designed parallel wire robot which is currently under construction was presented by Pott (2008). It is used for developing a new technique for computation and transfer of its workspace to the available CAD software. An auto-calibration method for over constrained cable-driven parallel

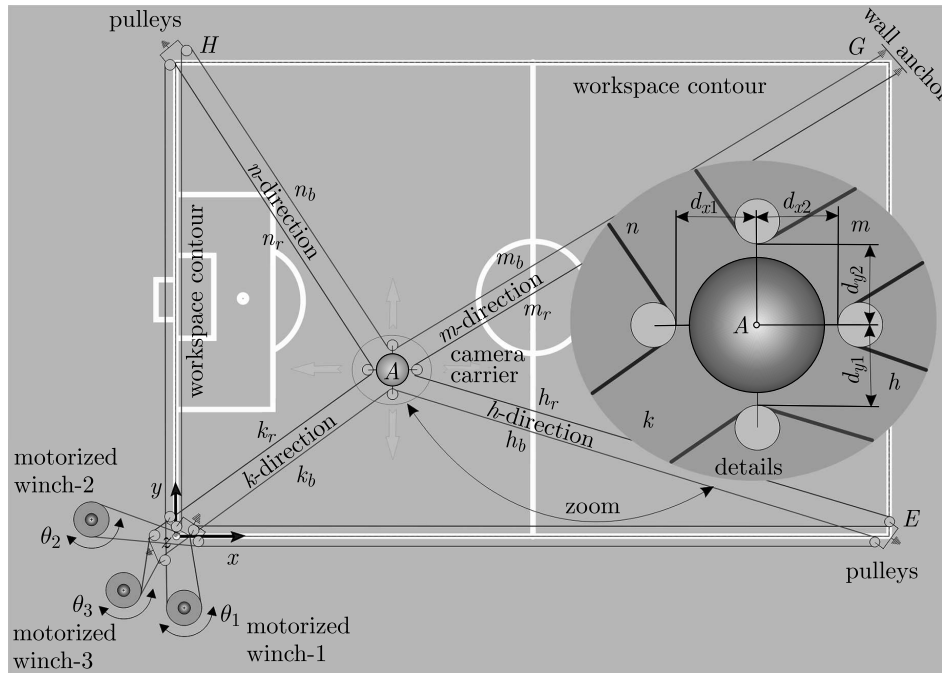


Fig. 2. CPR-D, top view

regardless of the size of the observed space. Motion of the ropes which carry the camera is controlled. The ropes can uncoil or coil, which allow the camera to reach any position in the space. The control system provides three-dimensional motion of the camera. The commands for synchronized motion of each winch are provided by controlling the motion of each motor which ultimately provides the three-dimensional continuous camera carrier motion. The gyroscopic sensor that is installed in the camera carrier is stabilized to the horizon. The nature of this system requires development of a new methodology for calculation of its kinematic and dynamic models, which will be used for building the system.

This work will be extended by implementing elastic properties of the ropes in the kinematic and dynamic models. The research of elasticity dynamics for nonlinear systems was done by the following authors: Raskovic (1965), Rega (2004a,b), Hedrih (2010, 2012). In this paper, the CPR model has been generated using the following assumptions: transverse vibrations of the ropes are neglected and the ropes are unstretchable.

In Section 2, a detailed description of a selected CPR system type and its mathematical model is given. Most of that Section is devoted to its kinematic model, which is directly involved in the development of its dynamic model. Two cases of the system responses are analyzed for different conditions in Section 3, while in Section 4 concluding remarks are presented.

2. Mathematical model of CPR-D system

In this research, one subsystem of the CPR family has been selected and analyzed in depth. A graphical representation of that system, named CPR-D, is shown in Figs. 1 and 2. The camera carrier of the CPR-D structure is guided through the work area of the parallelepiped shape with two ropes connected with three winches, each powered by a motor. The ropes coil or uncoil on the winches of radius R_1 , R_2 and R_3 . The motors rotate the winches directly, and the motor shafts angular positions after gear boxes are θ_1 , θ_2 , θ_3 . This motion moves the camera in the x , y , z Cartesian coordinates.

The first step towards the dynamical model of the CPR-D is the development of its kinematic model. The geometrical relationship between the lengths k , h , m , n and Cartesian coordinates x , y , z is defined by the following equations

$$\begin{aligned} k &= \sqrt{x^2 + y^2 + z^2} & h &= \sqrt{(d-x)^2 + y^2 + z^2} \\ m &= \sqrt{(d-x)^2 + (s-y)^2 + z^2} & n &= \sqrt{x^2 + (s-y)^2 + z^2} \end{aligned} \quad (2.1)$$

In Fig. 3, motions of motors 1 and 2 are depicted. Motor 1 (motor 2 as well) works so that it winds its corresponding rope from one side and unwinds from other side.

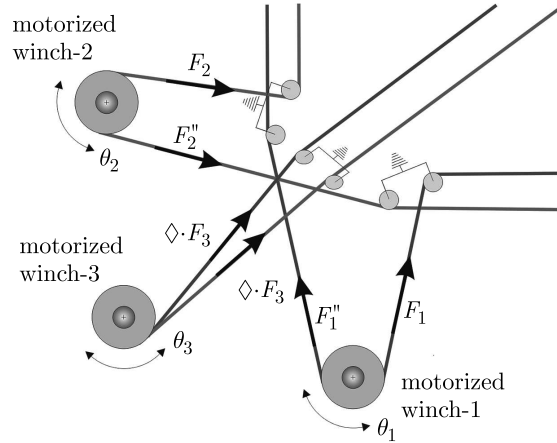


Fig. 3. Rope forces before motor 1, 2 and 3 and after motor 1 and 2

Motions of motors 1 and 2 toward the wall anchors (we call this line “before” motor) are expressed with the following equations respectively

$$\frac{\Delta\theta_1}{\Delta t} R_1 = \frac{\Delta h}{\Delta t} + \frac{\Delta m}{\Delta t} \quad \frac{\Delta\theta_2}{\Delta t} R_2 = \frac{\Delta m}{\Delta t} + \frac{\Delta n}{\Delta t} \quad (2.2)$$

The third motor is used to wind up the two ropes about coil 3 in the k , h , m , n directions. This motion produces winding or unwinding of both ropes at the same time. This can be seen in Figs. 2 and 3. The winch used for winding the ropes has radius R_i , $i = 1, 2, 3$. The relation between the third motor motion changes $\Delta\theta_3$, and the lengths change Δk , Δh , Δm , Δn can be expressed either with equation (2.3)₁ or (2.3)₂

$$\frac{\Delta\theta_3}{\Delta t} R_3 = \frac{\Delta k}{\Delta t} + \frac{\Delta h}{\Delta t} + \frac{\Delta\theta_2}{\Delta t} R_2 \quad \frac{\Delta\theta_3}{\Delta t} R_3 = \frac{\Delta k}{\Delta t} + \frac{\Delta n}{\Delta t} + \frac{\Delta\theta_1}{\Delta t} R_1 \quad (2.3)$$

Equation (2.4) is obtained by substituting equation (2.2)₂ into (2.3)₁, or equation (2.2)₁ into (2.3)₂

$$\frac{\Delta\theta_3}{\Delta t} R_3 = \frac{\Delta k}{\Delta t} + \frac{\Delta h}{\Delta t} + \frac{\Delta m}{\Delta t} + \frac{\Delta n}{\Delta t} \quad (2.4)$$

If the sampling time Δt is small enough then equations (2.2) and (2.4) can be expressed, respectively, as

$$\dot{\theta}_1 R_1 = \dot{h} + \dot{m} \quad \dot{\theta}_2 R_2 = \dot{m} + \dot{n} \quad \dot{\theta}_3 R_3 = \dot{k} + \dot{h} + \dot{m} + \dot{n} \quad (2.5)$$

By differentiating equations (2.1) and substituting them into equations (2.5), the relationship between the velocities of the camera carrier in the Cartesian space $\dot{\mathbf{p}} = [\dot{x}, \dot{y}, \dot{z}]^T$ and the velocities of the internal coordinates $\dot{\boldsymbol{\phi}} = [\dot{\theta}_1, \dot{\theta}_2, \dot{\theta}_3]^T$ can be obtained as following

$$\dot{\boldsymbol{\phi}} = \mathbf{J}_d \dot{\mathbf{p}} \quad (2.6)$$

This procedure is named KinCPRD-Solver (Kinematic Cable Parallel Robot D-type Solver). It is clear that the Jacobian matrix \mathbf{J}_d [1/m] is a full matrix, and its elements beyond the diagonal show strong coupling between the external and internal coordinates.

The kinetic energy E_k and the potential energy E_p of the camera carrier motion with mass m_c are given in the following equations

$$E_k = \frac{1}{2}m_c\dot{x}^2 + \frac{1}{2}m_c\dot{y}^2 + \frac{1}{2}m_c\dot{z}^2 \quad E_p = m_cgz \quad (2.7)$$

The gravitational acceleration is $g = 9.81 \text{ m/s}^2$. The CPR-D system has three motors, and their mathematical model is expressed with vector equation (2.8) (Vukobratovic, 1989)

$$\mathbf{u} = \mathbf{G}_v\ddot{\phi} + \mathbf{L}_v\dot{\phi} + \mathbf{S}_v\mathbf{M}_d \quad (2.8)$$

where $\mathbf{u} = [u_1, u_2, u_3]^T$ is voltage, $\mathbf{G}_v = \text{diag}(G_{vi})$ – motor inertia characteristic, $\mathbf{L}_v = \text{diag}(L_{vi})$ – motor damping characteristic, $\mathbf{S}_v = \text{diag}(S_{vi})$ – motor geometric characteristic, \mathbf{M}_d – motor load torque

$$G_{vi} = \frac{J_{ri}R_{ri}}{C_{Mi}} \quad L_{vi} = \frac{R_{ri}B_{Ci}}{C_{Mi}} + C_{Ei} \quad S_{vi} = \frac{R_{ri}}{C_{Mi}} \quad (2.9)$$

where: R_{ri} [Ω] is rotor circuit resistance, C_{Ei} [V/(rad/s)] – back electromotive force constant, C_{Mi} [Nm/A] – constant of torque proportionality, B_{Ci} [Nm/(rad/s)] – coefficient of viscous friction, J_{ri} [kg m^2] – moment of inertia for the rotor and the gear box.

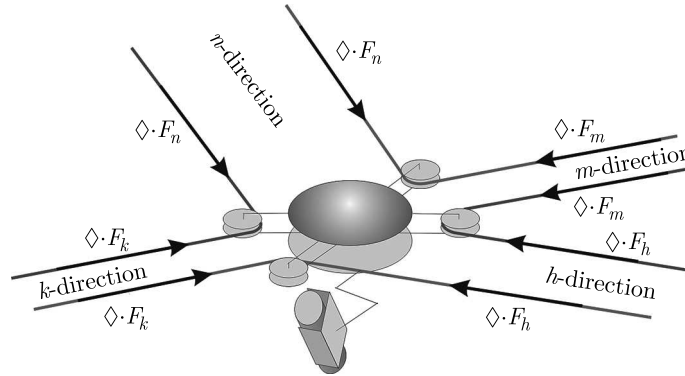


Fig. 4. Rope forces carrying the camera

Vector equation (2.8) is based on Lagrange's equation of motion. The angular positions of the motors shafts $\theta_1, \theta_2, \theta_3$ are selected as generalized coordinates.

The motor load torque \mathbf{M}_d is defined with vector equation

$$\mathbf{M}_d = [F_1R_1, F_2R_2, F_3R_3]^T \quad (2.10)$$

The load force \mathbf{F}_d includes three components expressed in a vector form as $\mathbf{F}_d = [F_1, F_2, F_3]^T$. This force is acting on the shaft of each motor, and its value depends on the external force \mathbf{F} . The external force $\mathbf{F} = [F_x, F_y, F_z]^T$ represents the sum of the camera inertial force \mathbf{F}_p which is acting on the camera carrier described in equation (2.11)₂ and the perturbation force \mathbf{P}_p which is disturbing the camera motion

$$\mathbf{F} = \mathbf{F}_p + \mathbf{P}_p \quad \mathbf{F}_p = m(\ddot{\mathbf{p}} + \mathbf{a}_{cc}) \quad (2.11)$$

The vector $\mathbf{a}_{cc} = [0, 0, -g]^T$ represents the gravitational acceleration. The next step is to describe the dynamic balance between the force \mathbf{F}_m in the m rope direction and the external force \mathbf{F} , see

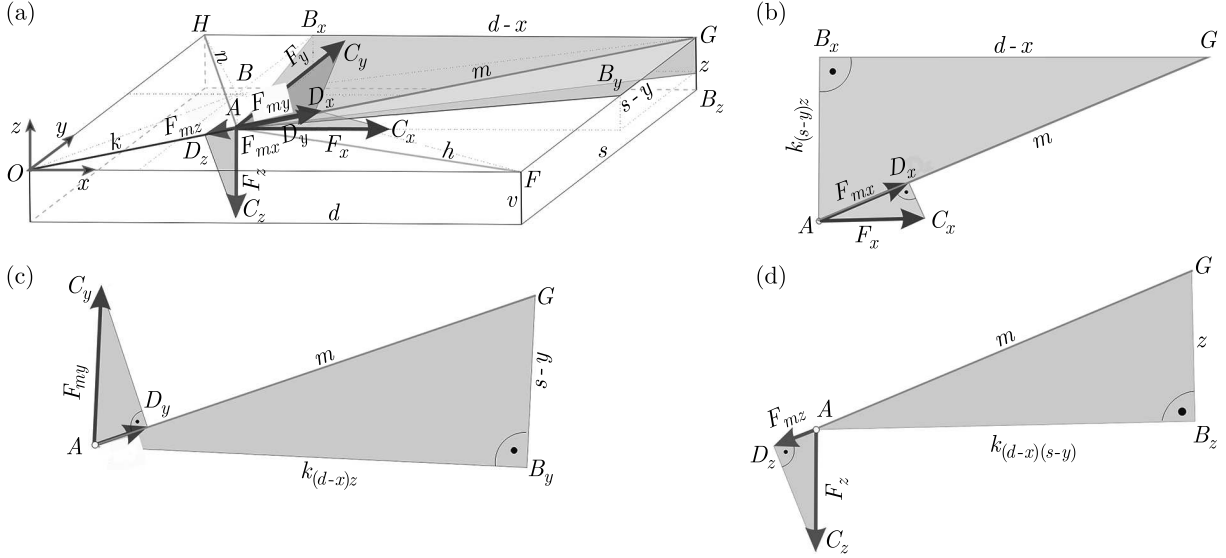


Fig. 5. (a) Characteristic triangles in 3D space, (b) characteristic triangle in the $(d-x)$ - m plane, (c) characteristic triangle in the $(s-y)$ - m plane, (d) characteristic triangle in the z - m plane

Figs. 5a-5d. Two similar right-angle triangles in the $(d-x)$ - m plane, in the $(s-y)$ - m plane, and in the z - m plane are presented in 2D space, see Figs. 5b-5d, respectively. All of these triangles can be seen in 3D space, which is shown in Fig. 5a. The hypotenuses of the GAB_x , GAB_y , GAB_z triangles has length m , which is changeable during motion of the camera. The other two sides of the GAB_x , GAB_y , GAB_z triangles have sizes $d-x$ and $k_{(s-y)z} = \sqrt{(s-y)^2 + z^2}$, $s-y$ and $k_{(d-x)z} = \sqrt{(d-x)^2 + z^2}$, z and $k_{(d-x)(s-y)} = \sqrt{(d-x)^2 + (s-y)^2}$, respectively. The component of the external force \mathbf{F} in the x direction is F_x , in the y direction is F_y , in the z direction is F_z . The projection forces F_x , F_y , F_z on the m direction are F_{mx} , F_{my} , F_{mz} , respectively, which can be seen in Figs. 5b-5d. The similarities of the two triangles in Fig. 5 produce the following relations

$$\begin{aligned} \frac{d-x}{m} &= \frac{F_{mx}}{F_x} & F_{mx} &= \frac{d-x}{m} F_x & \frac{s-y}{m} &= \frac{F_{my}}{F_y} \\ F_{my} &= \frac{s-y}{m} F_y & \frac{z}{m} &= \frac{F_{mz}}{F_z} & F_{mz} &= \frac{z}{m} F_z \end{aligned} \quad (2.12)$$

The force F_m is a sum of the previously defined components and it is expressed in the following equation

$$F_m = F_{mx} + F_{my} + F_{mz} = \frac{d-x}{m} F_x + \frac{s-y}{m} F_y + \frac{z}{m} F_z \quad (2.13)$$

The Lagrange principle of virtual work has been used to find the relation between the motor load torque \mathbf{M}_d and the external force \mathbf{F}

$$(\mathbf{M}_d)^T \dot{\boldsymbol{\phi}} = \mathbf{F}^T \dot{\mathbf{p}} \quad (2.14)$$

By substituting equations (2.6) into (2.14), the following equations are generated

$$(\mathbf{M}_d)^T \mathbf{J}_d \dot{\mathbf{p}} = \mathbf{F}^T \dot{\mathbf{p}} \quad (\mathbf{J}_d)^T \mathbf{M}_d = \mathbf{F} \quad (2.15)$$

From (2.15)₂, equation (2.16) can be expressed as

$$\mathbf{M}_d = \left((\mathbf{J}_d)^T \right)^{-1} \mathbf{F} \quad (2.16)$$

Equation (2.16) cannot be directly applied to the system from Figs. 1 and 2 because of the following reasons:

- The system has two ropes in each direction. Equation (2.16) has been corrected using the factor $\diamond = 0.5$.
- Motor 3 is used to synchronize winding or unwinding of the two ropes.

These will produce the adopted Jacobian matrix $J_{x\diamond d}$. The matrix \mathbf{O}_d [m] is generated, which represents the torque mapping matrix, as defined below

$$\mathbf{O}_d = \left((J_{x\diamond d})^T \right)^{-1} \quad (2.17)$$

The adapted Lagrange's principle of virtual work has been used for solving the complex relation between the motor load torque \mathbf{M}_d (acting as a load on the first, second and third motor shaft) and external forces \mathbf{F} (acting on the camera carrier)

$$\mathbf{M}_d = \mathbf{O}_d \mathbf{F} \quad \mathbf{u} = \mathbf{G}_v \ddot{\phi} + \mathbf{L}_v \dot{\phi} + \mathbf{S}_v \mathbf{O}_d \mathbf{F} \quad (2.18)$$

The torque mapping matrix \mathbf{O}_d [m] indicates that the system is highly coupled. The control law is selected by the local feedback loop for the position and velocity of the motor shaft in the following form

$$u_i = K_{lpi}(\theta_i^o - \theta_i) + K_{lvi}(\dot{\theta}_i^o - \dot{\theta}_i) \quad (2.19)$$

where K_{lpi} is a position constant, and K_{lvi} is a velocity constant for the motion control.

The comparison between previously published papers and this research is summarized as in the following:

- The novel KinCPRD-Solver gives a relation between the internal and external coordinates through the unique Jacobian matrix \mathbf{J}_d .
- All three motors in this system are differently integrated in comparison with the previously published systems.
- Most of the previously published papers do not involve dynamics of the motor. The CPR-D system includes the motors which significantly influence the total system response.
- The CPR-D system construction requires a novel dynamic relation between the load forces which are acting on the camera and the forces in the m direction.
- The previously published systems used Lagrange's principle of virtual work for calculating the relation between the external and internal forces in the original form. This system has double ropes in all four directions, which requires an adaptation of the Lagrange principle of virtual work.

3. Simulation results

The CPR-D system presented in Figs. 1 and 2 is modeled and analyzed by the software package AIRCAMD. The software package AIRCAMD is used for validation of applied theoretical contributions. This software includes three essential modules which are kinematic, dynamic and motion control law solvers for the CPR-D system. The most important element of the CPR-D system is the mathematical model of the motor which is an integral part of the software package AIRCAMD. Through the simulation results, it is shown that the dynamic characteristics of the motor significantly affect the response of the system and its stability. In order to make the results comparable, simulation is made for the same desired system parameters. The camera carrier motion dynamics directly depends on the mechanism dynamic parameters. The camera moves in the 3D space (x, y, z directions). The workspace is characterized by length $d = 3.2$ m, width $s = 2.2$ m and height $v = 2.0$ m of the recorded field. The position of the camera carrier

in the Cartesian space is $\mathbf{p} = [x, y, z]$ [m]. The starting point is $\mathbf{p}_{start}^o = [0.3 \text{ m}, 1.8 \text{ m}, -0.2 \text{ m}]$, and the end point $\mathbf{p}_{end}^o = [0.9 \text{ m}, 1.2 \text{ m}, -0.9 \text{ m}]$, They are presented in Fig. 6a, while their reference velocities are shown in Fig. 6c. In Fig. 6b, we show the reference composite velocity of the camera carrier. The shape of the composite velocity is trapezoidal.

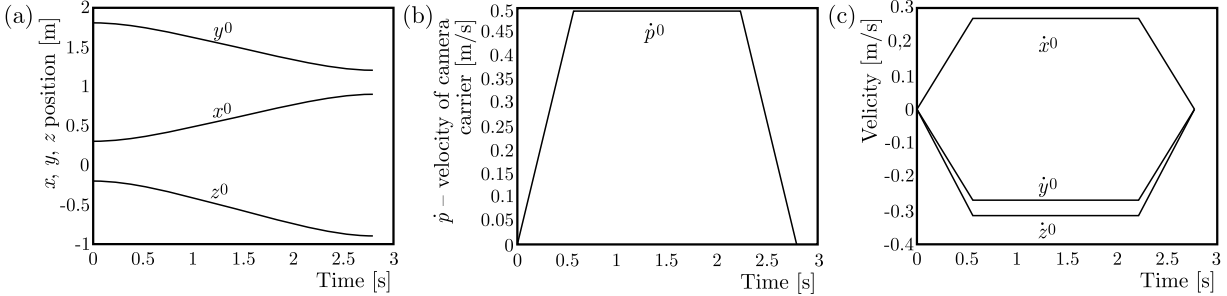


Fig. 6. The reference trajectory motion of the camera carrier (a) position x^o , y^o , z^o , (b) velocity (maximum value: $p_{max}^o = 0.494 \text{ m/s}$, (c) velocity components \dot{x}^o , \dot{y}^o , \dot{z}^o (Examples 1, 2)

The motors are Heinzman SL100F type and gears are HFUC14-50-2A-GR+belt type. The characteristics of the motors are: $R_{ri} = 0.917 \Omega$ – rotor circuit resistance, $C_{Ei} = 3.3942 \text{ V}/(\text{rad/s})$ – back electromotive force constant, $C_{Mi} = 2.5194 \text{ Nm/A}$ – constant of torque proportionality, $B_{Ci} = 0.0670 \text{ Nm}/(\text{rad/s})$ – coefficient of viscous friction, $J_{ri} = 1.5859 \text{ kg m}^2$ – moment of inertia for the rotor and the gear box.

The sample time is $dt = 0.0001 \text{ s}$. The positional and velocity motion controller parameters are $K_{lpi} = 4200$ and $K_{lvi} = 130$, respectively. Winches radii are $R_i = 0.15 \text{ m}$. The system responses are comparable and therefore are shown in Table 1. The results for Example 1 are presented in Figs. 7 and 10a, while for Example 2 are presented in Figs. 8 and 10b. Figure 7 (and Fig. 8 as well) has six pictures related to:

- camera carrier position at the reference and the real frames,
- motor shaft position at the reference and the real frames,
- load force at the reference and the real frames,
- deviation between the real and the reference trajectory of the camera carrier,
- deviation between the real and the reference trajectory of the motor shaft positions,
- control signals at the reference and the real frames.

Table 1. Comparison of two selected Examples

Example	1	2
Figure	7, 10a	8, 10b
Mathematical model of the system at the reference frame is defined by equations	(2.1)-(2.19)	(3.1)-(3.5)
Camera carrier is under the influence of the disturbance force	yes	yes
System at the reference frame is coupled	yes	no

The CPR-D system is designed for outdoor use. Because of that, we analyzed the system behavior under the influence of wind impacts, determined as the force $\mathbf{F}_p = [100(\sin(4\pi t) + \sin(32\pi t)), 0, 0]^T$, see Fig. 9. The force has a sine shape and operates only in the x direction, while the components in the y and z directions are zero.

Example 1: The motion response of the camera carrier has oscillatory characteristics and angular positions of all three motors are caused by the sinusoidal disturbance force. There is a very good

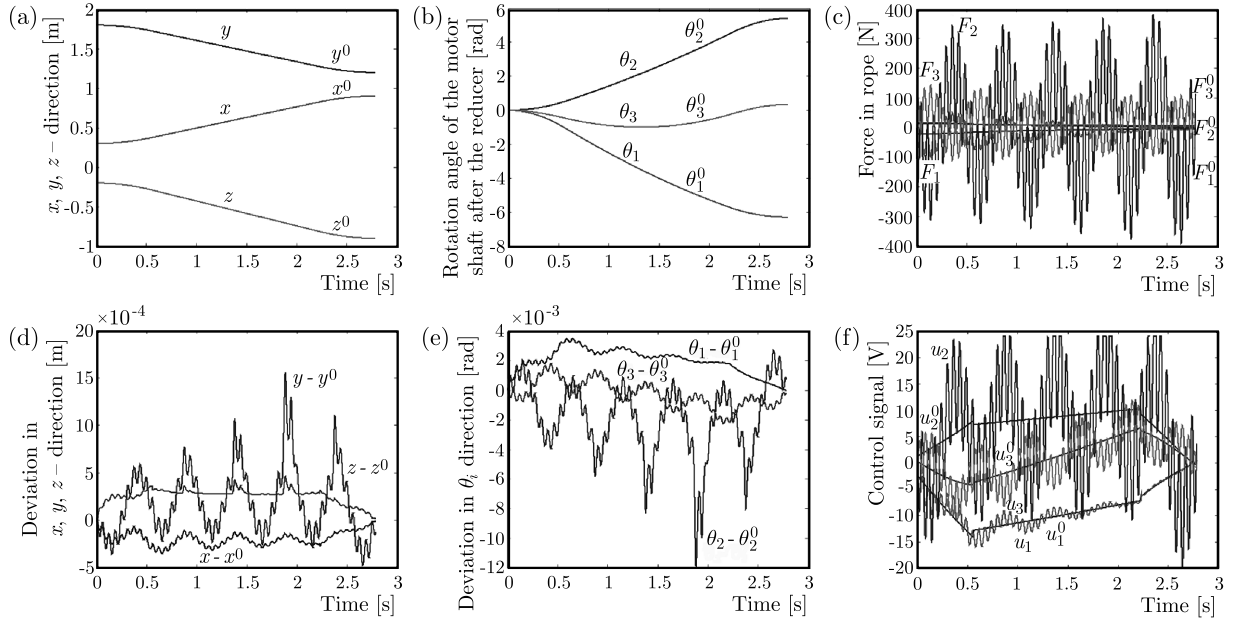


Fig. 7. Example 1

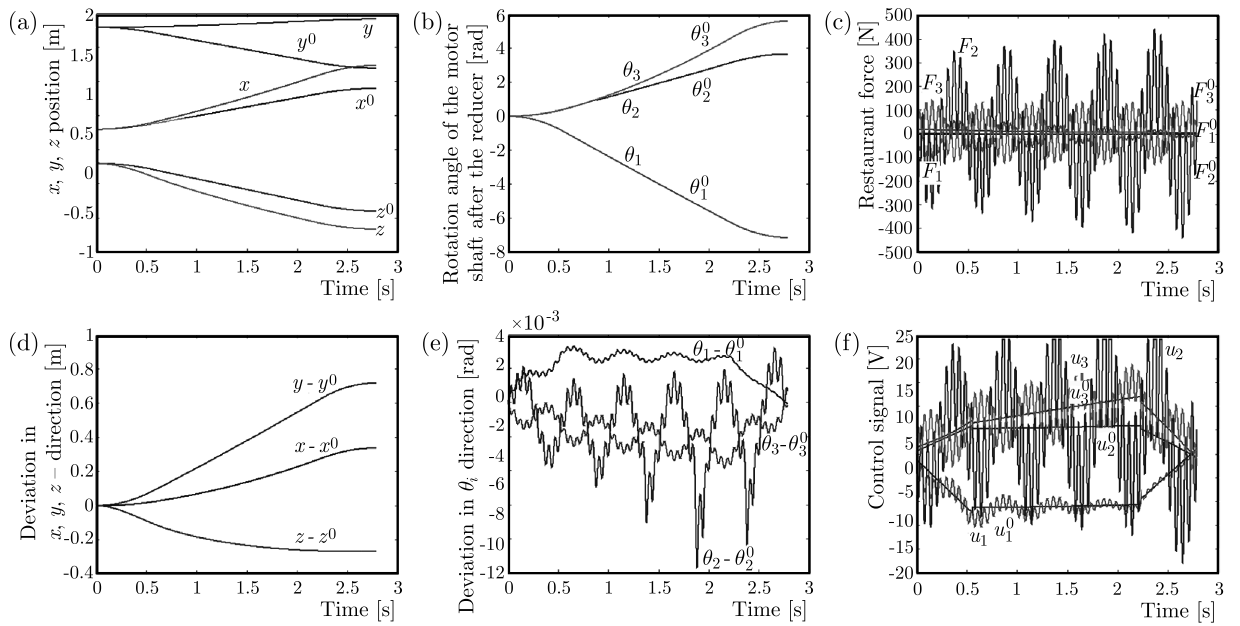


Fig. 8. Example 2

tracking of the desired trajectory at the camera carrier real frame and at the motor motion real frame, until the moment when motor 2 enters the saturation in oscillatory manner, see Fig. 7f. The first and the third motor do not enter the saturation at all. The force F_m has two components of the same magnitude $F_{m1} = F_{m2}$ acting in each rope in the m direction at the reference and the real frames, which is presented in Fig. 10a.

Example 2: All system and control parameters are the same as in Example 1. This Example is done with one illogical assumption, which is that the system at the reference frame is uncoupled. In that case, the Jacobian matrix $\mathbf{J}_{d\oplus}$ has the diagonal form

$$\dot{\phi} = \mathbf{J}_{d\oplus} \dot{\mathbf{p}} \quad (3.1)$$

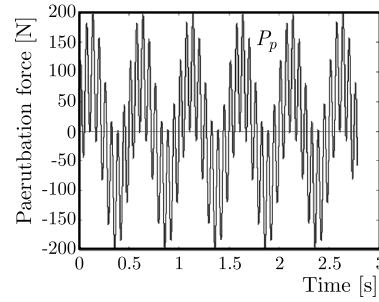


Fig. 9. Perturbation force at the camera carrier (Examples 1, 2)

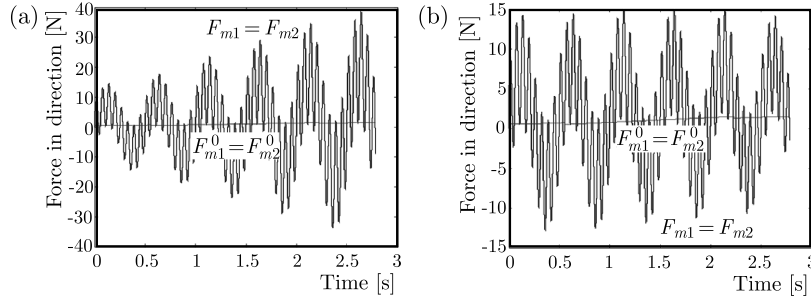


Fig. 10. Components of the force F_m acting in the m direction at the reference and the real frames, (a) Example 1, (b) Example 2

The mathematical model of the system has the following form

$$\mathbf{u} = \mathbf{G}_v \ddot{\boldsymbol{\phi}} + \mathbf{L}_v \dot{\boldsymbol{\phi}} + \mathbf{S}_v \mathbf{M}_{d\oplus} \quad (3.2)$$

Using the adapted Lagrange principle of virtual work, the relationship between the motor load torque $\mathbf{M}_{d\oplus}$ and the external force \mathbf{F} has been given below

$$\mathbf{M}_{d\oplus} = \mathbf{O}_{d\oplus} \mathbf{F} \quad (3.3)$$

The diagonal adopted Jacobian matrix is $\mathbf{J}_{x\triangleleft d\oplus}$. The matrix $\mathbf{O}_{d\oplus}$ is generated, which represents the torque mapping matrix, as defined below

$$\mathbf{O}_{d\oplus} = \left((\mathbf{J}_{x\triangleleft d\oplus})^T \right)^{-1} \quad (3.4)$$

The torque mapping matrix $\mathbf{O}_{d\oplus}$ is diagonal like the Jacobian matrix $\mathbf{J}_{d\oplus}$. Substituting (3.3) into equation (3.2) produces a dynamic model of the uncoupled CPR-D system at the reference frame

$$\mathbf{u} = \mathbf{G}_v \ddot{\boldsymbol{\phi}} + \mathbf{L}_v \dot{\boldsymbol{\phi}} + \mathbf{S}_v \mathbf{O}_{d\oplus} \mathbf{F} \quad (3.5)$$

In this case, the mathematical model of the CPR-D system at the reference frame is defined by equations (3.1)-(3.5). At the real frame, the system is coupled and its kinematic and dynamic models are defined by equations (2.1)-(2.19), see Fig. 8. The coupling characteristics are not taken into the consideration at the reference frame. Due to that fact, the tracking of the referent trajectory in the Cartesian space is not satisfactory, see Figs. 8a and 8d.

The position control law produces the ideal response of the motor angular motion, see Figs. 8b and 8e.

The forces $F_{m1} = F_{m2}$ acting in each rope in the m direction at the reference and real frames are presented in Fig. 10b. Example 2 has an important theoretical meaning, because it confirms the strong coupling between the external and internal coordinates.

The presented results imply that the dynamics of the individual motor significantly depends of the selection of the CPR-D structure and its parameters. The CPR-D is modeled and analyzed by the software package AIRCAMD.

4. Conclusion

The highly authentic general mathematical model for the CPR-D system has been developed. This model represents novel kinematic and dynamic solutions of the complex Cable suspended Parallel Robot structure. The CPR-D system is selected to carry the camera through four pivot points which produce a 3D workspace of a parallelepiped shape. The camera carrier is controlled by two ropes in each of the three directions, and driven by three motors. The kinematic model is defined for the monitored system via the Jacobian matrix. The generalized coordinates selected for the CPR-D model are angular positions of the motors $\theta_1, \theta_2, \theta_3$ named internal coordinates. Camera motion is defined in the Cartesian space, described with the x, y, z coordinates, named the external coordinate system. The relation between the internal and external coordinate systems is described by the Jacobian matrix \mathbf{J}_d . This relation represents the kinematic model of the CPR-D system. The solution for the CPR-D kinematic structure has been found through a novel procedure named KinCPRD-Solver (Kinematic Cable Parallel Robot D-type Solver) which is developed and validated using two selected Examples. The relation between the motor load torque and the force acting at the camera carrier is described by the Lagrange principle of virtual work. This calculation shows that in this relation, the Jacobian matrix is involved. Because of the construction complexity of this system, the Lagrange principle of virtual work had to be adapted for two reasons. The software package AIRCAMD has been developed and used for individual analysis of the CPR-D model from various aspects such as selecting different workspace dimensions, camera carrier mass, external disturbances, choice of the control law, reference trajectory, avoidance of singularity and many other characteristics.

The future research will involve elastic ropes (type of nonlinear dynamic elasticity as defined by Filipovic *et al.* (2007), Filipovic and Vukobratovic (2008a,b), Filipovic (2012) in the mathematical model of the CPR system. Different CPR models previously developed will be unified according to their similarities into a single reconfigurable model, using the methodology presented by Djuric *et al.* (2010, 2012). Stability conditions, sensitivity analysis and singularity analysis of the CPR-D system will be done in the future research.

Acknowledgment

This research has been supported by the Ministry of Education, Science and Technological Development, Government of the Republic of Serbia through the following two projects: Grant TR-35003 „Ambientally intelligent service robots of anthropomorphic characteristics”, by Mihajlo Pupin Institute, University of Belgrade, Serbia, and partially supported by the project SNSF Care-robotics project No. IZ74Z0-137361/1 by Ecole Polytechnique Federale de Lausanne, Switzerland.

We are grateful to Prof. Dr. Katica R. (Stevanovic) Hedrih from the Mathematical Institute, Belgrade for helpful consultations during preparation of this paper.

References

1. AVCI E., KENMOCHI M., KAWANISHI M., NARIKIYO T., KAWAKAMI S., SAITOH Y., 2014, Vibration Control of 3P(S)4 class parallel mechanisms for high speed applications using quantitative feedback design, *IROS 2014 – IEEE/RSJ International Conference on Intelligent Robots and Systems*, Chicago, IL, USA
2. BORGSTROM P.H., BORGSTROM N.P., STEALEY M.J., JORDAN B., SUKHATME G., BATALIN M.A., KAISER W.J., 2007, Discrete trajectory control algorithms for NIMS3D, an autonomous

- underconstrained three-dimensional cabled robot, *Proceedings of the 2007 IEEE/RSJ International Conference on Intelligent Robots and Systems*, San Diego, CA, USA
3. BRUCKMANN T., MIKELSONS L., SCHRAMM D., HILLER M., 2007, Continuous workspace analysis for parallel cable-driven Stewart-Gough platforms, *Special Issue: Sixth International Congress on Industrial Applied Mathematics (ICIAM07) and GAMM Annual Meeting*, Zürich, **7**, 1
 4. CARRICATO M., 2011, Under-constrained cable-driven parallel robots, [In:] *Quarta giornata di studio Ettore Funaioli*, 16 luglio 2010, Asterisco, 443-454
 5. DJURIC A.M., SAIDI R.AL, ELMARAGHY W.H., 2010 Global kinematic model generation for n-DOF reconfigurable machinery structure, *6th IEEE Conference on Automation Science and Engineering, CASE 2010*, Toronto, Canada
 6. DJURIC A., SAIDI R.AL, ELMARAGHY W.H., 2012, Dynamics solution of n-DOF global machinery model, *Robotics and Computer Integrated Manufacturing (CIM) Journal*, **28**, 5, 621-630
 7. DUAN B.Y., 1998, A new design project of the line feed structure for large spherical radio telescope and its nonlinear dynamic analysis, *Mechatronics*, **9**, 53-64
 8. FANG S., FRANITZA D., TORLO M., BEKES F., HILLER M., 2004, Motion control of a tendon-based parallel manipulator using optimal tension distribution, *IEEE/ASME Transactions of Mechatronics*, **9**, 3, 561-568
 9. FILIPOVIC M., 2012, Relation between Euler-Bernoulli equation and contemporary knowledge in robotics, *Robotica*, **30**, 1-13
 10. FILIPOVIC M., POTKONJAK V., VUKOBRATOVIC M., 2007, Humanoid robotic system with and without elasticity elements walking on an immobile/mobile platform, *Journal of Intelligent and Robotic Systems*, **48**, 157-186
 11. FILIPOVIC M., VUKOBRATOVIC M., 2008a, Complement of source equation of elastic line, *Journal of Intelligent and Robotic Systems*, **52**, 2, 233-261
 12. FILIPOVIC M., VUKOBRATOVIC M., 2008b, Expansion of source equation of elastic line, *Robotica*, **26**, 6, 739-751
 13. GOSSELIN C., GRENIER M., 2011, On the determination of the force distribution in overconstrained cable-driven parallel mechanisms, *Meccanica*, **46**, 1, 3-15
 14. GOSSELIN C., REN P., FOUCAULT S., 2012, Dynamic trajectory planning of a two-DOF cable-suspended parallel robot, *International Conference on Robotics and Automation RiverCentre*, Saint Paul, Minnesota, USA, May 14-18
 15. GOUTTEFARDE M., MERLET J.-P., DANAY D., 2006, Determination of the wrench-closure workspace of 6-DOF parallel cable-driven mechanisms, *Advances in Robot Kinematics*, **5**, 315-322
 16. HEDRIH (STEVANOVIC) K., 2010, Energy analysis in the hybrid system forced regimes, *Proceeding of Institute of Mathematics NANU Ukraine*, **7**, 3, 90-107
 17. HEDRIH (STEVANOVIC) K., 2012, Energy and nonlinear dynamics of hybrid system, [In:] *Dynamical Systems and Methods*, Albert Luo (Edit.), Springer, **1**, 29-83
 18. HIGUCHI T., MING A., JIANG-YU J., 1988, Application of multi-dimensional wire crane in construction, *5th International Symposium on Robotics in Construction*, Tokyo, June, 6/8, 661-668
 19. HILLER M., FANG S.Q., 2005, Design, analysis and realization of tendon-base parallel manipulators, *Mechanism and Machine Theory*, **40**, 429-445
 20. KOZAK K., ZHOU Q.J., WANG J., 2006, Static Analysis of Cable-driven manipulators with non-negligible cable mass, *IEEE Transaction on Robotics*, **22**, 2, 425-433
 21. KRAUS W., SCHMIDT V., RAJENDRA P., POTT A., 2013, Load identification and compensation for a Cable-Driven parallel robot, *ICRA 2013, IEEE International Conference on Robotics and Automation*, Karlsruhe, Germany, 2485-2490

22. MERLET J.P., 2010, MARIONET, A family of modular wire-driven parallel robots, *Advances in Robot Kinematics: Motion in Man and Machine*, **1**, 53-61
23. MIERMEISTER P., POTT A., VERL A., 2012, Auto-calibration method for overconstrained cable-driven parallel robots, *ROBOTIK 2012 – 7th German Conference on Robotics*, Munich, Germany
24. OH S.-R., AGRAWAL S.K.A., 2005, Reference governor-based controller for a cable robot under input constraints, *IEEE Transaction on Control Systems Technology*, **13**, 4, 639-645
25. POTT A., 2008, Forward kinematics and workspace determination of a wire robot for industrial applications, *Advances in Robot Kinematics: Analysis and Design*, **7**, 451-458
26. RASKOVIC D., 1965, *Theory of Oscillations*, Scientific Book, Belgrade, Serbia
27. REGA G., 2004a, Nonlinear vibrations of suspended cables. Part I: Modeling and analysis, *Applied Mechanics Reviews, ASME*, **57**, 6, 443-478
28. REGA G., 2004b, Nonlinear vibrations of suspended cables, Part II: Deterministic phenomena, *Applied Mechanics Reviews, ASME*, **57**, 6, 479-514
29. SHIANG W.-J., CANNON D., GORMAN J., 2000, Optimal force distribution applied to a robotic crane with flexible cables, *Proceedings of the 2000 IEEE International Conference on Robotics and Automation*, San Francisco, Ca, 1948-1954
30. SU X.Y., DUAN B.Y., 2000a, The application of the stewart platform in large spherical radio Telescopes, *Journal of Robotic Systems*, **17**, 7, 375-383
31. SU X.Y., DUAN B.Y., 2000b, The mathematical design and kinematics accuracy analysis of a fine tuning stable platform for the large spherical radio telescope, *Mechatronics*, **10**, 819-834
32. VUKOBRATOVIC M., 1989, *Introduction to Robotics*, Springer-Verlag
33. YAO R., TANG X., WANG J., HUANG P., 2010, Dimensional optimization design of the four-cable driven parallel manipulator, *FAST, IEEE/ASME Transaction on Mechatronics*, **15**, 6, 932-941
34. ZI B., DUAN B.Y., DU J.L., BAO H., 2008, Dynamic modeling and active control of a cable-suspended parallel robot, *Mechatronics*, **18**, 1, 1-12

Manuscript received February 10, 2014; accepted for print October 21, 2015

WAVELETS AND PRINCIPAL COMPONENT ANALYSIS METHOD FOR VIBRATION MONITORING OF ROTATING MACHINERY

HOCINE BENDJAMA

Research Center in Industrial Technologies (CRTI), Cheraga, Algiers; e-mail: hocine_bendjama@daad-alumni.de

MOHAMAD S. BOUCHERIT

Department of Automatic, Polytechnic National School (ENP), El-Harrach, Algiers; e-mail: ms_boucherit@yahoo.fr

Fault diagnosis is playing today a crucial role in industrial systems. To improve reliability, safety and efficiency advanced monitoring methods have become increasingly important for many systems. The vibration analysis method is essential in improving condition monitoring and fault diagnosis of rotating machinery. Effective utilization of vibration signals depends upon effectiveness of applied signal processing techniques. In this paper, fault diagnosis is performed using a combination between Wavelet Transform (WT) and Principal Component Analysis (PCA). The WT is employed to decompose the vibration signal of measurements data in different frequency bands. The obtained decomposition levels are used as the input to the PCA method for fault identification using, respectively, the Q-statistic, also called Squared Prediction Error (SPE) and the Q-contribution. Clearly, useful information about the fault can be contained in some levels of wavelet decomposition. For this purpose, the Q-contribution is used as an evaluation criterion to select the optimal level, which contains the maximum information. Associated to spectral analysis and envelope analysis, it allows clear visualization of fault frequencies. The objective of this method is to obtain the information contained in the measured data. The monitoring results using real sensor measurements from a pilot scale are presented and discussed.

Keywords: vibration, fault diagnosis, wavelet analysis, principal component analysis, squared prediction error

1. Introduction

Growing demand for higher performance, safety and reliability of industrial systems has increased the need for condition monitoring and fault diagnosis. During the two past decades, various monitoring methods have been developed, including dynamics, vibration, tribology and non-destructive techniques (Altmann, 1999; Yang, 2004).

The vibration analysis is one of the most important methods used for condition monitoring and fault diagnosis, because it always carries the dynamic information of a system. Effective utilization of vibration signals depends upon the effectiveness of applied signal processing techniques. The analysis of stationary vibration signals has largely been based on well-known spectral techniques such as: Fourier Transform (FT) and Short Time Fourier Transform (STFT) (Seker and Ayaz, 2002; Shibata *et al.*, 2000). Unfortunately, these methods are not suitable for non-stationary signal analysis (Wu and Liu, 2008). In order to solve this problem, Wavelet Transform (WT) has been developed. WT is used to extract approximations and detail coefficients of measurements data with different frequency bands by using successive low-pass and high-pass filtering. This makes the application of WT for non-stationary signal processing an area of active research over the past decade. An overview of the WT used in vibration signal analysis was provided by Litak and Sawicki (2009), Al-Badour *et al.* (2011) and Yan *et al.* (2014).

The original signal using WT can be decomposed into approximations and details versions with different resolutions. The decomposed levels will not change their information in the time domain (Gaing, 2004). However, useful information can be contained in some sub-bands. So, the fault can be detected from a given level of resolution. This is based on the choice of an indicator to determine the optimal level where failure can occur. The selection of the most reliable indicator has been studied by several authors. A large number of applications have been reviewed, e.g. Prabhakar *et al.* (2002) selected periodic impulses of bearing faults in the time domain based on the low and high frequency nature of decomposed levels. Similar analyses were carried out by Purushotham *et al.* (2005) in order to extract periodic impulses from time signals using discrete wavelet transform at Mel-frequency scales. Chinmaya and Mohanty (2006) used sidebands of gear meshing frequencies as an evaluation criterion for gear faults diagnosis. Djebala *et al.* (2008) analyzed vibration of faults inducing periodical impulsive forces by selecting the kurtosis as indicator. In another study, Gavrovska *et al.* (2009) described the optimal selection of decomposition levels in the wavelet transform used for both high-frequency and low-frequency filtering of the ECG signal. Yaqub *et al.* (2011) estimated the bandwidth of the resonant frequency band of vibration data by adaptive selection of wavelet decomposition levels. The adaptive criterion was based on saturated dissemination of the signal energy over the wavelet decomposition nodes.

In this work, we propose to use a combination between WT and PCA for improving the vibration monitoring. PCA is a multivariate analysis technique, also a dimension reduction technique. It finds the directions of significant variability in the data by forming linear combinations of variables. Its application for vibration analysis is suggested in several papers (De Moura *et al.*, 2011; Shao *et al.*, 2014).

The aim of the proposed combined method is to provide a solution to the fault diagnosis problem. WT is used to extract approximations and details vectors in order to obtain multiple data series at different resolutions. Clearly, useful information is contained in some decomposition levels. The obtained levels are used as the input to the PCA method for identifying abnormal situations in different frequency bands using the Q-statistic or Squared Prediction Error (SPE) and Q-contributions. In order to extract useful information, the Q-contribution is used as the principal criterion to select the optimal level of resolution. Associated to spectral analysis and envelope analysis, it allows clear visualization of the frequencies faults. The proposed method is evaluated using the experimental measurements data in the cases of mass unbalance and gear fault.

The remainder of this paper is structured as follows. Section 2 presents the fault diagnosis method using WT and PCA along with its formulations. The experimental setup is discussed in Section 3. The monitoring results and discussion are presented in Section 4. Finally, Section 5 concludes our work and contributions.

2. Fault diagnosis method

2.1. Wavelet transform

Wavelet Transform (WT) is a relatively new signal processing tool. Due to its strong capability in the time and frequency domain analysis, it is applied by many researchers in diverse applications (see, for example, Litak *et al.*, 2009; Sen *et al.*, 2010). WT describes a signal by using the correlation with translation and dilatation of a function called mother wavelet; it includes Continuous Wavelet Transform (CWT) and Discrete Wavelet Transform (DWT). Let $s(t)$ be the signal, then the CWT of $s(t)$ is defined as

$$CWT(a, b) = \frac{1}{\sqrt{|a|}} \int_{-\infty}^{\infty} s(t) \psi^* \left(\frac{t-b}{a} \right) dt \quad (2.1)$$

where $\psi^*(t)$ is the conjugate function of the mother wavelet $\psi(t)$, a and b are the dilation (scaling) and translation (shift) parameters, respectively.

DWT is derived from discretization of CWT. The most common discretization is dyadic. DWT is found to yield fast computation of the WT. It is given by

$$DWT(j, k) = \frac{1}{\sqrt{2^j}} \int_{-\infty}^{\infty} s(t) \psi^* \left(\frac{t - 2^j k}{2^j} \right) dt \quad (2.2)$$

where a and b are replaced by 2^j and $2^j k$, j is an integer.

A very useful implementation of DWT, called multiresolution analysis (Mallat, 1989), is demonstrated in Fig. 1. The DWT analyzes the signal at different frequency bands with different resolutions by decomposing the signal into several levels; approximations (A1, A2, A3, ...) and details (D1, D2, D3, ...). The signal is decomposed at the expected level. DWT employs two sets of functions, called scaling function and wavelet function (Mallat, 1989), which are associated with Low-pass (L) and High-pass (H) filters, respectively. The approximations are the high-scale, low-frequency components and the details are the low-scale, high-frequency components of the signal.

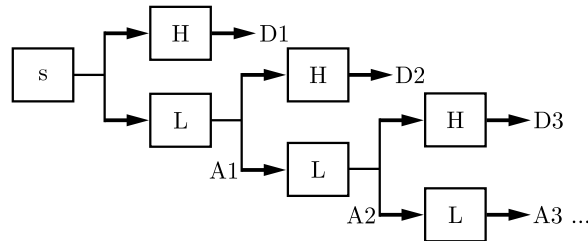


Fig. 1. Principle of DWT decomposition

Selection of an appropriate wavelet is very important in signal analysis. There are many functions available that can be used, such as Haar, Daubechies, Meyer, and Morlet functions (Chui, 1992; Daubechies, 1988). In this application, we use the Daubechies wavelet for fault diagnosis of the mass unbalance and gear fault.

2.2. Principal Component Analysis

Principal Component Analysis (PCA) (Chiang *et al.*, 2001; Jolliffe, 2002) is a projection statistical method used for dimensionality reduction. It produces a lower-dimensional representation in a way that preserves the correlation structure between the variables. Given a set of n observations or samples and m variables stacked into a matrix \mathbf{X} , whose variance-covariance matrix has eigenvalue-eigenvector pairs

$$(\lambda_1, p_1), (\lambda_2, p_2), \dots, (\lambda_m, p_m) \quad (2.3)$$

where $\lambda_1 \geq \lambda_2 \geq \lambda_3 \geq \dots \geq \lambda_m \geq 0$.

The principal decomposition component of \mathbf{X} can be represented as

$$\mathbf{X} = \mathbf{TP}^T + \mathbf{E} = \sum_{i=1}^l t_i p_i^T + \mathbf{E} \quad l < m \quad (2.4)$$

where $\mathbf{T} = [t_1, t_2, \dots, t_l]$ is defined to be the matrix of principal component scores, $\mathbf{P} = [p_1, p_2, \dots, p_l]$ is the matrix of principal component loadings, \mathbf{E} is the residual matrix in the sense of the minimum Euclidean norm and l is the index of the Principal Components (PCs).

The identification of the PCA model thus consists in estimating its parameters by an eigenvalue-eigenvector decomposition and determining the number of PCs l to retain. Many procedures have been proposed for selecting the number of PCs to be retained (Kano and Hasebe, 2001). In this study, we use the experiential method (Nomikos and MacGregor, 1995) which judges that the cumulative sum contribution of the anterior l PCs is higher than 0.85, as follows

$$100 \cdot \frac{\sum_{i=1}^l \lambda_i}{\sum_{i=1}^m \lambda_i} > 85\% \quad (2.5)$$

The basic idea of the process of fault detection using PCA is to collect normal observation data to establish the PCA model. When a new observation data is subject to fault, these new data can be compared to the PCA model and its threshold. In order to detect the abnormal changes of the new data, the Q-statistic or SPE is used as follows

$$\text{Q-statistic} = \text{SPE} = \mathbf{e}^T \mathbf{e} = \|\mathbf{x}(\mathbf{I} - \mathbf{P}\mathbf{P}^T)\|^2 \quad (2.6)$$

The process is considered normal if

$$\text{Q-statistic} \leq \delta_Q^2 \quad (2.7)$$

where δ_Q^2 denotes the confidence limit or threshold for the Q-statistic. It can be calculated from its approximate distribution (Jackson and Mudholkar, 1979)

$$\delta_Q^2 = \theta_1 \left[C_\alpha \frac{\sqrt{2\theta_2 h_0^2}}{\theta_1} + 1 + \frac{\theta_2 h_0 (h_0 - 1)}{\theta_1^2} \right] \quad (2.8)$$

where $\theta_i = \sum_{j=k+1}^m \lambda_j^i$, $i = 1, 2, 3$ and $h_0 = 1 - 2\theta_1\theta_3/(3\theta_2^2)$, and λ_j is the eigenvalue, C_α is the critical value of the normal distribution and m is the number of all PCs.

The threshold is used to determine whether the data is within range of the model. To compare the new data to the PCA model, a confidence limit of $\alpha = 95\%$ is used. Any point below the confidence limit line is considered to have a normal variance from the selected number of PCs, and any point above this line is considered to have an abnormally high level of variance.

After the fault is detected, i.e. the new observation data exceed the threshold line of the PCA model but can not be assure in what place the fault appears in the process. An assignable cause is determined by the contribution plot. The contribution plots are bar graphs of the Q-residual contribution of each variable calculated as in equation (2.9) (Xu *et al.*, 2008). The variable having the largest residual produces the worst compliance to the PCA model, and indicates the source of the fault

$$\text{Q-contribution} = \text{cont}_i = \frac{\|e_i\|^2}{\text{Q-statistic}} \quad (2.9)$$

where e_i presents the i -th element of the residual vector \mathbf{e} and cont_i is the contribution of the i -th variable to the total sum of variations in the residual space.

By using the WT, the time domain information will not be lost when the signal is decomposed. In order to extract useful information in different decomposition levels, the contribution plots are used as an evaluation criterion for selecting the optimal level which contains the maximum information about the fault. A flowchart of the fault detection and diagnosis method based on WT and PCA is illustrated in Fig. 2.

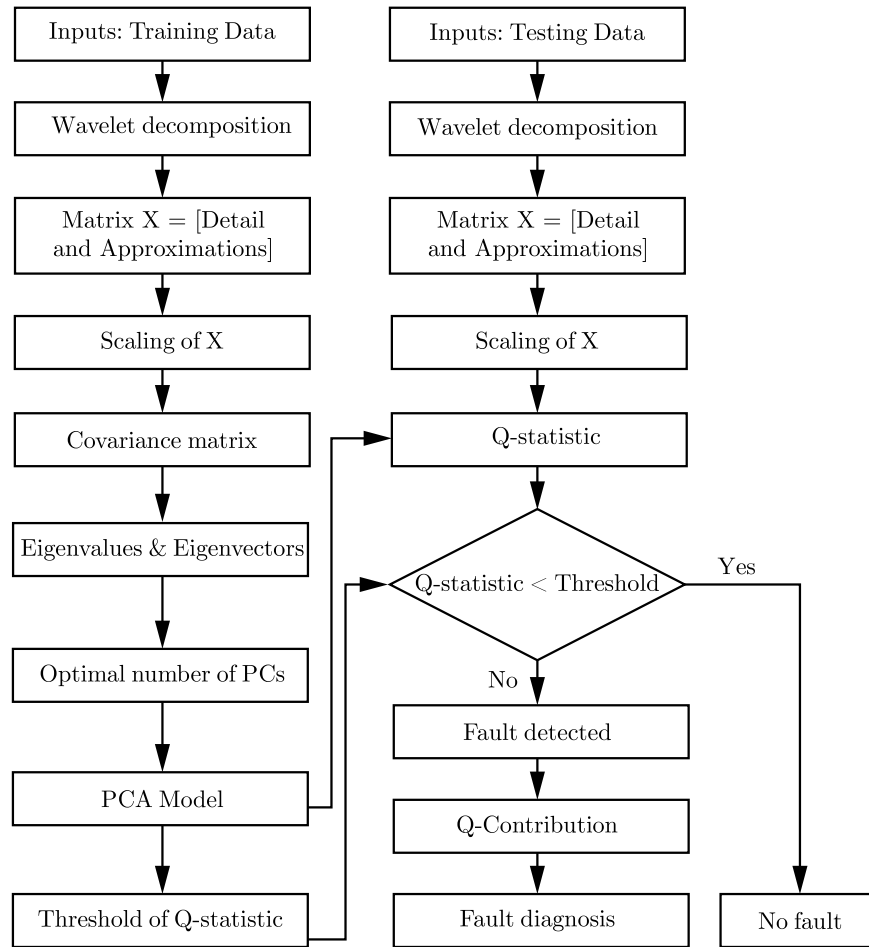


Fig. 2. Flowchart of the fault diagnosis method

3. Experimental setup

The problem of diagnosing the degradation of working conditions of rotating machinery is extremely important in industries to reduce the productivity loss. The measurement of vibration applied to the condition monitoring and fault diagnosis requires different types and levels of equipment and techniques. In the present study, an experimental system is used and the vibration response for mass unbalance and gear fault are obtained.

3.1. System description

The experimental system consists of a test rig built by S'tell Diagnostic (France), a data acquisition system (OROS OR25, 4 channels), piezoelectric accelerometers (PCB Piezotronics 353B34) and a PC (see Fig. 3). The system is driven by a 0.18 kW induction motor giving an output of 0-1500 rpm, controlled by a variable speed drive. To confirm the feasibility of the proposed method, we collect real vibration signals using the experimental test rig illustrated in Fig. 3, where 1 and 2 are gears with 60 and 48 teeth, respectively, H1, H2, H3 and H4 are the bearing housings.

The vibration signals are taken on bearing housing H1 by means of two piezoelectric accelerometers measuring radial vibration, i.e. in the Vertical Direction (VD) and Horizontal Direction (HD). These measurements are repeated for different states at different rotation speeds. The data acquisition is performed using the OR25 software. The vibration signals measured have

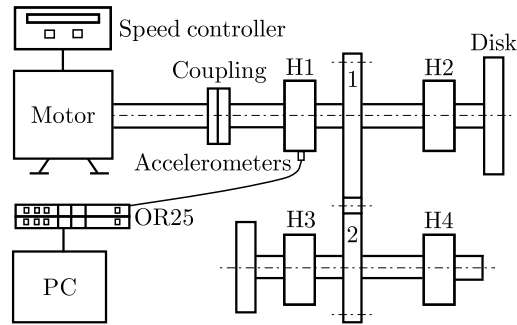


Fig. 3. Illustration of the experimental system

length of acquisition of 400 milliseconds. The sampling frequency is 5120 Hz and each signal has 2048 samples.

3.2. Faults description

The experiment described in this paper, performs the condition monitoring of rotating machinery to predict some anomalies that may occur under different measurement conditions such as: mass unbalance and gear fault.

3.2.1. Mass unbalance

Mass unbalance is one of the most common causes of vibration. It is a condition when the center of mass does not coincide with the center of rotation, due to unequal distribution of mass about the center of rotation. It is simulated in this study by an additional weight on the disk. The mass unbalance creates a vibration frequency exactly equal to the rotational speed, with an amplitude proportional to the amount of unbalance (Tandon and Parey, 2006).

Figure 4 represents the measured signals of the mass unbalance at a speed of 900 rpm in VD and HD.

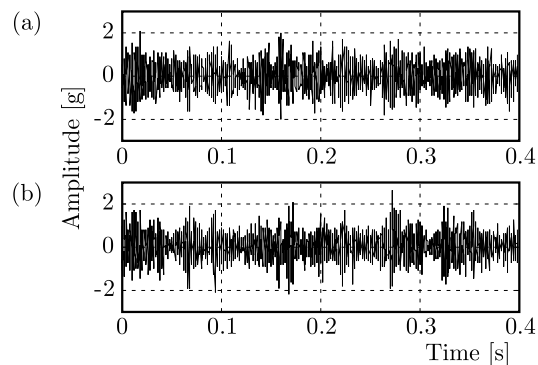


Fig. 4. Vibration signals of the mass unbalance collected at 900 rpm: (a) VD and (b) HD

3.2.2. Gear fault

Vibrations of a gear are mainly produced by the shock between teeth of the two wheels. Gear fault is simulated with a gap between teeth. The vibration monitored on a faulty gear generally exhibits a significant level of vibration at the tooth mesh frequency (i.e. the number of teeth on the gear multiplied by its rotational speed) and its harmonics (Tandon and Parey, 2006).

Figure 5 represents the measured signals of the gear fault at a speed of 900 rpm in VD and HD.

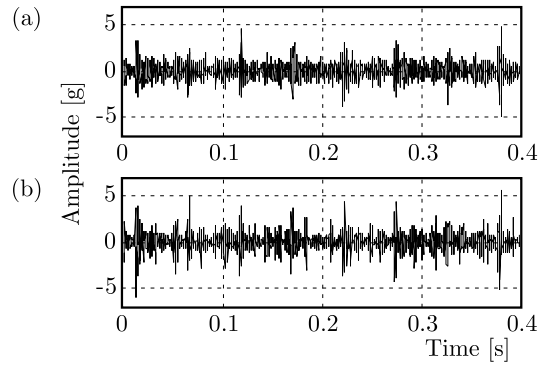


Fig. 5. Vibration signals of the gear fault collected at 900 rpm: (a) VD and (b) HD

4. Results and discussion

The structure of proposed fault diagnosis technique involves two parts: the first one is development and training of the PCA model; the second is testing the process fault based on the trained model (see Fig. 2). The measurements used in training phase represent the normal operating conditions of the system, i.e. system without fault.

The vibration signals used in this work have been gained through the practical measurement, including a normal state, mass unbalance and gear fault. The data collection has been carried out according to the following routine: vibration signals used in the training are taken in VD and HD at seven different rotating speeds between 300 and 1425 rpm. In the testing phase, each fault of the process has been measured in the radial direction at five different rotating speeds: 675, 900, 1125, 1275 and 1425 rpm which, respectively, correspond to 11.25, 15, 18.75, 21.25 and 23.75 Hz.

The multiresolution analysis is applied by using the Daubechies wavelet of the order 4 (db4) and level 4. It may be noted that the same wavelet with the same level of decomposition is applied to each signal for the training and testing phases. The results of db4 decomposition of the vibration signals of the mass unbalance and gear fault collected at 900 rpm in the radial direction are given respectively in Figs. 6 and 7.

After decomposition with db4, the approximations and details vectors of each signal measured at the same rotation speed in the radial direction are collected in a matrix. Thus the input matrices of the PCA method are formed. During the training phase, seven matrices are collected for identifying the PCA model. Through PCA method, the anterior 8 PCs accumulation sum contribution rate is 92.46%, as shown in Table 1. These first 8 PCs are selected for the fault identification.

The detection threshold of Q-statistic is calculated according to equation (2.8), which is 2.2414. To evaluate the fault detection method, the detection ratio is used. It is defined as the number of samples whose Q-statistic values go beyond the threshold to the total samples. If the detection ratio is less than 20%, the fault is not successfully detected (Xuet *et al.*, 2008). In normal operating conditions, 2.83% of the Q-statistic samples are above the threshold value. It implies that the model has captured the major correlation and variance among the system variables.

In the testing phase, five matrices of each fault are collected for validating the PCA method. The new data are compared to the PCA model and its threshold. The evaluation results of fault detection rate are summarized in Tables 2 and 3. We show clearly that the majority samples of the Q-statistic at different rotation speeds are above the threshold value. By comparing these values to 2.83% obtained in the normal state, it is also clear that an abnormal situation has occurred in the process.

The objective of the proposed method is to demonstrate the effectiveness of the Q-contribution as a principal criterion for selecting the optimal level of wavelet decomposition.

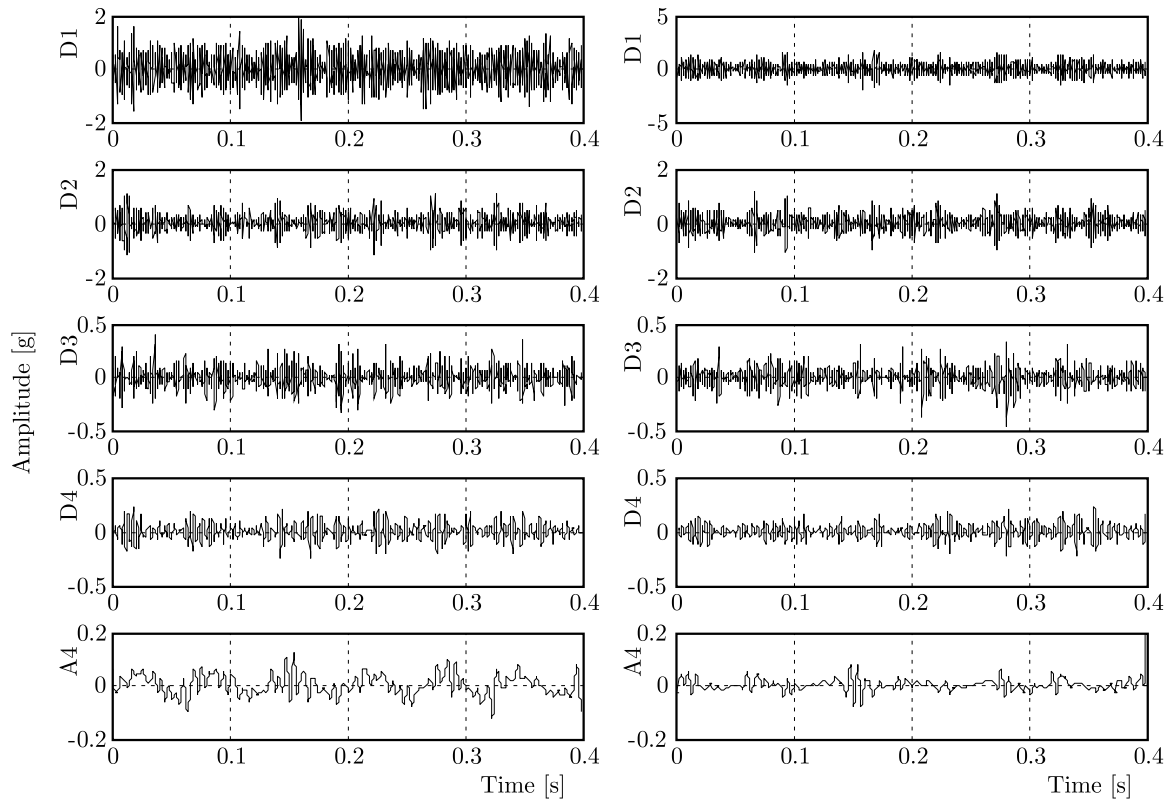


Fig. 6. Decomposition results of the measured signals of the mass unbalance at 900 rpm in VD (left) and HD (right)

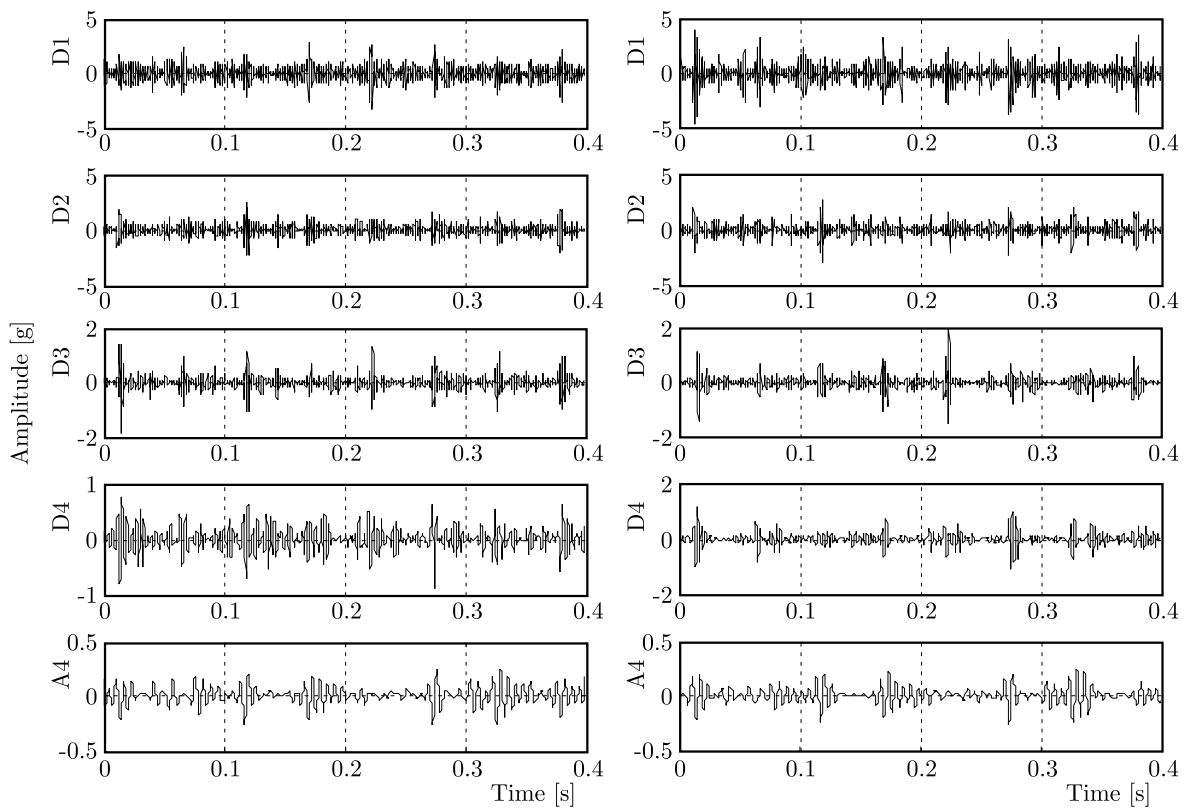


Fig. 7. Decomposition results of the measured signals of the gear fault at 900 rpm in VD (left) and HD (right)

Table 1. PCs values

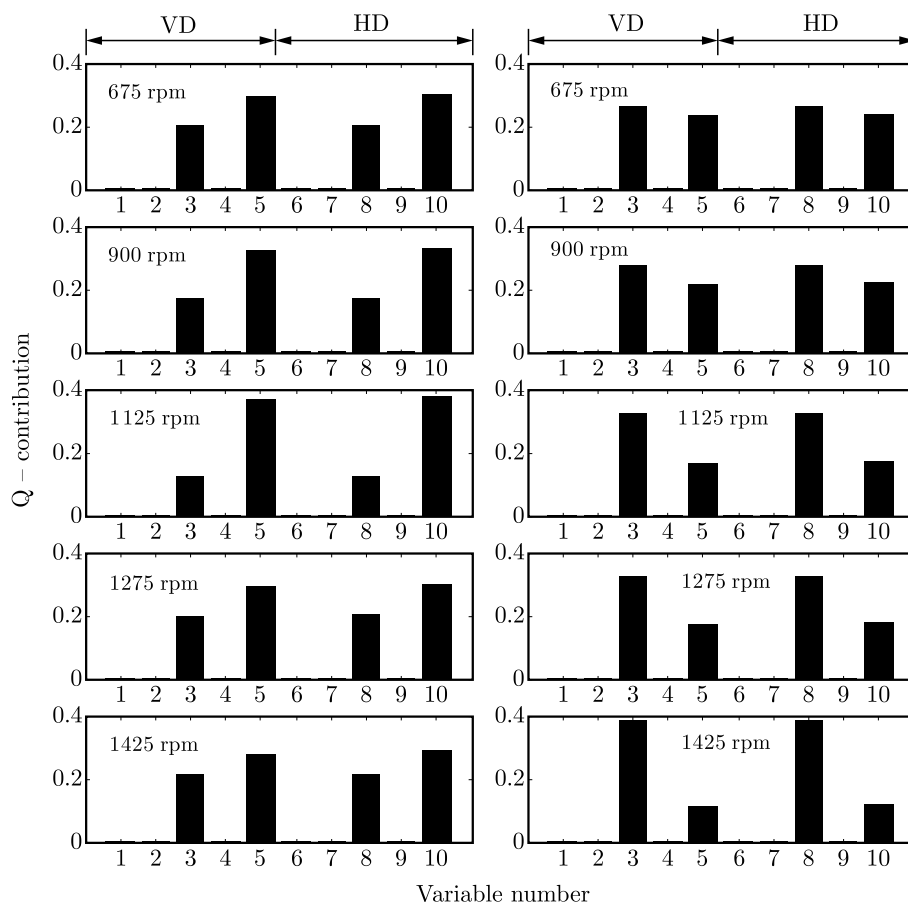
PCs	Eigenvalues	Variance [%]
1	1.6459	16.46
2	1.6159	16.16
3	1.2381	12.38
4	1.1741	11.74
5	1.0642	10.64
6	0.9358	9.36
7	0.8259	8.26
8	0.7458	7.46
9	0.3934	4.13
10	0.3611	3.54

Table 2. Evaluation results of the mass unbalance detection rate

rpm	675	900	1125	1275	1425
SPE [%]	35.59	67.91	79.00	83.30	85.40

Table 3. Evaluation results of the gear fault detection rate

rpm	675	900	1125	1275	1425
SPE [%]	70.94	81.59	76.36	80.17	87.50

**Fig. 8.** Contribution plots of the mass unbalance (left) and the gear fault (right)

The contribution plots are bar graphs of the Q-residual contribution of each variable or decomposed vector (Fig. 8). The level having the largest value produces the worst compliance to the PCA model and indicates the desired level of decomposition. As shown in Fig. 8, decomposition levels 1 to 4 and 6 to 9 present respectively the detail vectors for VD and HD, and levels 5 and 10 stand respectively for the approximation vectors. It shows an obvious difference between the levels. From Fig. 8 (left), it can be seen that levels 5 and 10 have the largest values. We show also in Fig. 8 (right), that the contribution plot using db4 occurs in the third level. So our choice is attached to approximation A4 for the mass unbalance and detail D3 for the gear fault.

In order to diagnose the mass unbalance and the gear fault from the selected level we use, respectively, spectral analysis and envelope analysis. Figure 9 (left) shows the spectra of fourth approximations (A4). Frequency peaks at 11.25, 15, 18.75, 21.25 and 23.75 Hz are present, which could be related to a mass unbalance fault. Figure 9 (right) illustrates the FT of the envelopes of the selected details. It can be seen from this figure that the peaks at the rotation frequencies of the shaft (11.25, 15, 18.75, 21.25 and 23.75 Hz) and their multiples ($\times 2, \times 3, \dots$) are present in the frequency spectra. This clearly indicates a gear fault.

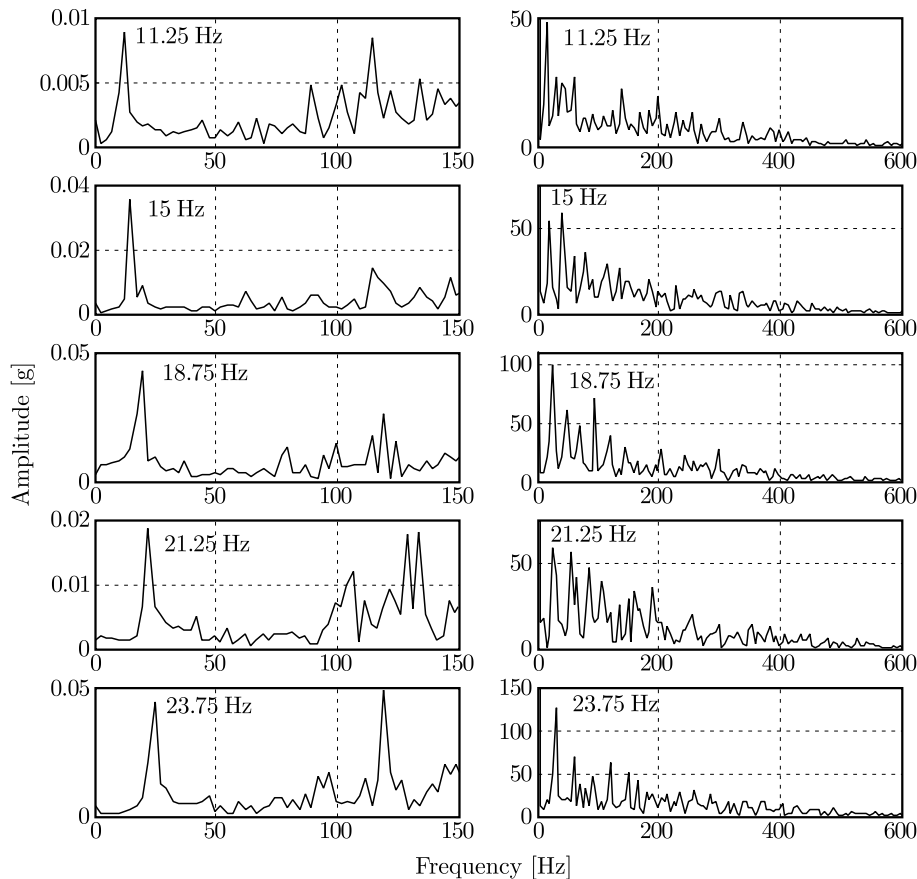


Fig. 9. Spectra of selected levels of the mass unbalance (left) and the gear fault (right)

5. Conclusion

This paper presents a combined approach based on the WT and PCA method to improve the condition monitoring and fault diagnosis of rotating machinery. It is adapted to obtain multiple data series at different levels using wavelet decomposition and reduce the number of variables needed to monitor the process through PCA. The detection method is based on a confidence limit estimated from normal conditions. The aim is to select the optimal level of resolution using the

residual contribution of each decomposed vector, for a possible diagnosis. The proposed method has been tested on real measurement signals collected from a vibration system containing mass unbalance and gear fault. Better experimental results have been obtained by identifying the type of fault. Hence the WT combined with the PCA method is a successful approach to vibration monitoring.

References

1. AL-BADOUR F., SUNAR M., CHEDED L., 2011, Vibration analysis of rotating machinery using time-frequency analysis and wavelet techniques, *Mechanical Systems and Signal Processing*, **25**, 2083-2101
2. ALTMANN J., 1999, Application of discrete wavelet packet analysis for the detection and diagnosis of low speed rolling-element bearing faults, Ph.D. thesis, Monash University, Melbourne, Australia
3. CHIANG L.H., RUSSELL E.L., BRAATZ R.D., 2001, *Fault Detection and Diagnosis in Industrial Systems*, Springer-Verlag, London
4. CHINMAYA K., MOHANTY A.R., 2006, Monitoring gear vibrations through motor current signature analysis and wavelet transform, *Mechanical Systems and Signal Processing*, **20**, 1, 158-187
5. CHUI CH.K., 1992, *An Introduction to Wavelets*, Academic Press, New York
6. DAUBECHIES I., 1988, Orthonormal bases of compactly supported wavelets, *Communication on Pure and Applied Mathematics*, **41**, 909-996
7. DE MOURA E.P., SOUTO C.R., SILVA A.A., IRMÃO M.A.S., 2011, Evaluation of principal component analysis and neural network performance for bearing fault diagnosis from vibration signal processed by RS and DF analyses, *Mechanical Systems and Signal Processing*, **25**, 5, 1765-1772
8. DJEBALA A., OUELAA N., HAMZAOU N., 2008, Detection of rolling bearing defects using discrete wavelet analysis, *Meccanica*, **43**, 339-348
9. GAING Z.L., 2004, Wavelet-based neural network for power disturbance recognition and classification, *IEEE Transactions on Power Delivery*, **19**, 1560-1568
10. GAVROVSKA A.M., JEVTIC D.R., RELJIN B.D., 2009, Selection of wavelet decomposition levels in ECG filtering, *Proceedings of the International Conference on Telecommunication in Modern Satellite, Cable and Broadcasting Services TELSIKS*, Niš-Serbia, DOI: 10.1109/TELSKS.2009.5339423, 221-224
11. JACKSON J.E., MUDHOLKAR G.S., 1979, Control procedures for residuals associated with principal components analysis, *Technometrics*, **21**, 341-349
12. JOLLIFFE I.T., 2002, *Principal Component Analysis*, Springer-Verlag, New York
13. KANO M., HASEBE S., 2001, A new multivariate statistical process monitoring method using principal component analysis, *Computers and Chemical Engineering*, **25**, 1103-1113
14. LITAK G., SAWICKI J.T., 2009, Intermittent behaviour of a cracked rotor in the resonance region, *Chaos, Solitons and Fractals*, **42**, 1495-1501
15. LITAK G., SEN A.K., SYTA A., 2009, Intermittent and chaotic vibrations in a regenerative cutting process, *Chaos, Solitons and Fractals*, **41**, 2115-2122
16. MALLAT S.G., 1989, A theory for multiresolution signal decomposition: the wavelet representation, *IEEE Transactions on Pattern Analysis and Machine Intelligence*, **11**, 7, 674-693
17. NOMIKOS P., MACGREGOR J.F., 1995, Multivariate SPC charts for monitoring batch processes, *Technometrics*, **37**, 1, 41-59
18. PRABHAKAR S., MOHANTY A.R., SEKHAR A.S., 2002, Application of discrete wavelet transform for detection of ball bearings race faults, *Tribology International*, **35**, 793-800

19. PURUSHOTHAM V., NARAYANAN S., PRASAD S.A.N., 2005, Multi-fault diagnosis of rolling bearing elements using wavelet analysis and hidden Markov model based fault recognition, *NDT&E International*, **38**, 654-664
20. SEKER S., AYAZ E., 2002, A study on condition monitoring for induction motors under the accelerated aging processes, *IEEE Power Engineering*, **22**, 7, 35-37
21. SEN A.K., LITAK G., FINNEY C.E.A., DAWC C.S., WAGNER R.M., 2010, Analysis of heat release dynamics in an internal combustion engine using multifractals and wavelets, *Applied Energy*, **87**, 1736-1743
22. SHAO R., HU W., WANG Y., QI X., 2014, The fault feature extraction and classification of gear using principal component analysis and kernel principal component analysis based on the wavelet packet transform, *Measurement*, **54**, 118-132
23. SHIBATA K., TAKAHASHI A., SHIRAI T., 2000, Fault diagnosis of rotating machinery through visualisation of sound signal, *Mechanical Systems and Signal Processing*, **14**, 229-241
24. TANDON N., PAREY A., 2006, Condition monitoring of rotary machines, [In:] *Condition Monitoring and Control for Intelligent Manufacturing*, Wang L., Gao R.X. (Edit.), Springer-Verlag, London, 109-136
25. WU J.D., LIU C.H., 2008, Investigation of engine fault diagnosis using discrete wavelet transform and neural network, *Expert Systems with Applications*, **35**, 1200-1213
26. XU X., XIAO F., WANG S., 2008, Enhanced chiller sensor fault detection, diagnosis and estimation using wavelet analysis and principal component analysis methods, *Applied Thermal Engineering*, **28**, 226-237
27. YAN R., GAO R.X., CHEN X., 2014, Wavelets for fault diagnosis of rotary machines: A review with applications, *Signal Processing*, **96**, 1-15
28. YANG H., 2004, Automatic fault diagnosis of rolling element bearings using wavelet based pursuit features, Ph.D. thesis, Queensland University of Technology, Australia
29. YAQUB M.F., GONDAL I., KAMRUZZAMAN J., 2011, Resonant frequency band estimation using adaptive wavelet decomposition level selection, *Proceedings of the IEEE International Conference on Mechatronics and Automation ICMA*, Beijing-China, DOI: 10.1109/ICMA.2011.5985687, 376-381

Manuscript received August 13, 2014; accepted for print December 10, 2015

ON GEOMETRICAL INTERPRETATION OF THE FRACTIONAL STRAIN CONCEPT

WOJCIECH SUMELKA

*Poznan University of Technology, Institute of Structural Engineering, Poznań, Poland
e-mail: wojciech.sumelka@put.poznan.pl*

In this paper, for the first time, the geometrical interpretation of fractional strain tensor components is presented. In this sense, previous considerations by this author are shown in a new light. The fractional material and spatial line elements concept play a crucial role in the interpretation.

Keywords: fractional strain, fractional calculus, non-local models

1. Introduction

The fractional strain is a generalisation of the classical strain measure utilising the fractional calculus (the branch of mathematical analysis which deals with differential equations of an arbitrary order (Podlubny, 2002)). Such defined strain is non-local because of the fractional derivative definition.

In the literature, there exist a few concepts of fractional strain. One can mention here those by Klimek (2001), Lazopoulos (2006), equivalent concepts of Atanackovic and Stankovic (2009) and Carpinteri *et al.* (2011) or, finally, that by Drapaca and Sivaloganathan (2012). It is important that except for the concept presented in Drapaca and Sivaloganathan (2012), the previous ones were defined for 1D problems and small strains. Of fundamental meaning is also the fact that these authors consider different physical units of fractional strain tensor components, e.g. in Klimek (2001), Atanackovic and Stankovic (2009), Carpinteri *et al.* (2011) we have $[m^{1-\alpha}]$, in Lazopoulos (2006) $[m^{-\alpha}]$, or in (Drapaca and Sivaloganathan, 2012) $[m^{3-\alpha_1k-\alpha_2k-\alpha_3k}]$ $k = 1, 2, 3$, where m denotes meter, and the parameter α is in general different than 1.

In the paper by Sumelka (2014c) a different concept of fractional strain was presented. In that version, the fractional strain is without physical unit, as in the classical continuum mechanics, and the length scale parameter is given explicitly and simultaneously related to the terminals of the fractional differential operator.

In this paper, we follow the fundamental results given in the above mentioned paper (Sumelka, 2014c), giving finally the geometrical interpretation of fractional strain tensor components.

2. Geometrical interpretation of fractional strain

The description is given in the Euclidean space in Cartesian coordinates. We refer to \mathcal{B} as the reference configuration of the continuum body while \mathcal{S} denotes its current configuration. Points in \mathcal{B} are denoted by \mathbf{X} and in \mathcal{S} by \mathbf{x} .

The regular motion of the material body \mathcal{B} can be written as

$$\mathbf{x} = \phi(\mathbf{X}, t) \tag{2.1}$$

thus $\phi_t : \mathcal{B} \rightarrow \mathcal{S}$ is a C^1 actual configuration of \mathcal{B} in \mathcal{S} , at time t .

Taking the Taylor expansion of motion for $d\mathbf{X}$, we have

$$\phi(\mathbf{X} + d\mathbf{X}, t) = \phi(\mathbf{X}, t) + \frac{\partial\phi(\mathbf{X}, t)}{\partial\mathbf{X}}d\mathbf{X} + |d\mathbf{X}|\mathbf{r}(\mathbf{X}, t, d\mathbf{X}) \quad (2.2)$$

with the property of the residuum that $\lim_{|d\mathbf{X}| \rightarrow 0} |\mathbf{r}(\mathbf{X}, t, d\mathbf{X})| = 0$. Denoting $d\mathbf{x} = \phi(\mathbf{X} + d\mathbf{X}, t) - \phi(\mathbf{X}, t)$ and omitting higher order terms, one gets

$$d\mathbf{x} = \mathbf{F}d\mathbf{X} \quad (2.3)$$

and

$$d\mathbf{X} = \mathbf{F}^{-1}d\mathbf{x} \quad (2.4)$$

where $\mathbf{F}(\mathbf{X}, t) = \partial\phi(\mathbf{X}, t)/\partial\mathbf{X}$ denotes the deformation gradient, and $\mathbf{F}^{-1}(\mathbf{x}, t) = \partial\varphi(\mathbf{x}, t)/\partial\mathbf{x}$.

We introduce non-local effects through multiplication of Eq. (2.3) (left sided) by $\overset{\alpha}{\mathbf{F}}_X$ and Eq. (2.4) (left sided) by $\overset{\alpha}{\mathbf{F}}_x$, thus

$$d\tilde{\mathbf{x}} = \overset{\alpha}{\mathbf{F}}_X d\mathbf{X} \quad (2.5)$$

and

$$d\tilde{\mathbf{X}} = \overset{\alpha}{\mathbf{F}}_x d\mathbf{x} \quad (2.6)$$

where (following the notation in (Sumelka, 2014c)), $d\tilde{\mathbf{x}} = \overset{\alpha}{\mathbf{F}}_X d\mathbf{X}$ is a fractional spatial line element, $d\tilde{\mathbf{X}} = \overset{\alpha}{\mathbf{F}}_x d\mathbf{x}$ is a fractional material line element, while $\overset{\alpha}{\mathbf{F}}_X = \overset{\alpha}{\mathbf{F}}\mathbf{F}$ and $\overset{\alpha}{\mathbf{F}}_x = \overset{\alpha}{\mathbf{F}}\mathbf{F}^{-1}$ are fractional deformation gradients defined as follows

$$\overset{\alpha}{\mathbf{F}}_X(\mathbf{X}, t) = \ell_X^{\alpha-1} D_X^\alpha \phi(\mathbf{X}, t) \quad (2.7)$$

and

$$\overset{\alpha}{\mathbf{F}}_x(\mathbf{x}, t) = \ell_x^{\alpha-1} D_x^\alpha \varphi(\mathbf{x}, t) \quad (2.8)$$

where ℓ_X and ℓ_x are length scales in \mathcal{B} and \mathcal{S} , respectively. In Eqs. (2.7) and (2.8), D^α is the Riesz-Caputo fractional differential operator while α denotes the order of differentiation, cf. Sumelka (2014c). Comparing Eq. (2.3) and Eq. (2.5) (or Eq. (2.4) and Eq. (2.6)), one can also interpret such an assumption (by analogy to (Drapaca and Sivaloganathan, 2012)) as the existence of motion of the order α , which means the motion accounting for non-local effects. The situation is summarised in Fig. 1.

Notice that the length scales ℓ_X , ℓ_x preserve classical physical unit [m], and together with α , they are additional material parameters. As an example, for metallic materials, they can be identified as distances connected with non-homogeneous distribution of dislocations and cell structures (Pecherski, 1983; Sumelka, 2014b).

We have now four ways to define the strain tensor (cf. Fig. 1). Denoting by $\overset{\diamond}{\mathbf{F}}$ deformation gradients \mathbf{F} or $\overset{\alpha}{\mathbf{F}}_X$ or $\overset{\alpha}{\mathbf{F}}_x$ or $\overset{\alpha}{\mathbf{F}}$, one can obtain local/non-local classical/fractional strain tensors through classical rules, namely

$$\mathbf{E} = \frac{1}{2} \left(\overset{\diamond}{\mathbf{F}}^T \overset{\diamond}{\mathbf{F}} - \mathbf{I} \right) \quad \mathbf{e} = \frac{1}{2} \left(\mathbf{i} - \overset{\diamond}{\mathbf{F}}^{-T} \overset{\diamond}{\mathbf{F}}^{-1} \right) \quad (2.9)$$

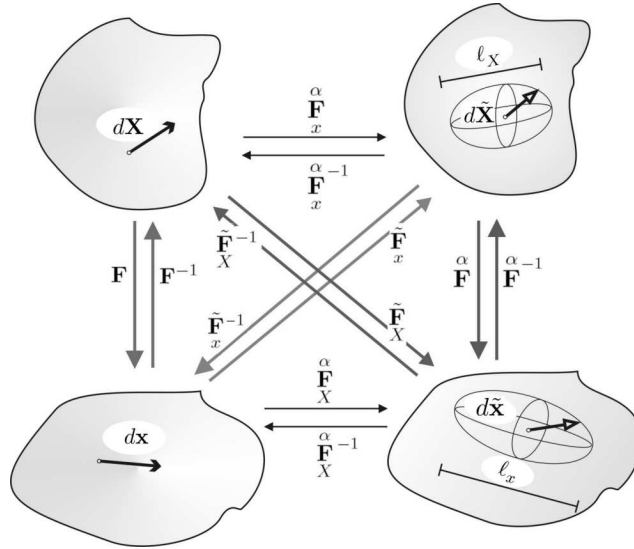


Fig. 1. Relations between the material and spatial line elements with their fractional counterparts

$$(\tilde{\mathbf{F}} = \tilde{\mathbf{F}}_X \mathbf{F}^{-1} \tilde{\mathbf{F}}_x^{-1}, \tilde{\mathbf{F}}_x = \tilde{\mathbf{F}}_X \mathbf{F} \text{ and } \tilde{\mathbf{F}}_X = \tilde{\mathbf{F}}_x \mathbf{F}^{-1})$$

where \mathbf{E} is the classical Green-Lagrange strain tensor or its fractional counterpart, and \mathbf{e} is the classical Euler-Almansi strain tensor or its fractional counterpart.

It should be emphasised that appropriate mapping of terminals from a material to spatial description (or inversely – cf. analogy in Sumelka (2014a)) that fulfil

$$\tilde{\mathbf{F}}_X = \mathbf{F} \tilde{\mathbf{F}}_x^{-1} \mathbf{F}^{-1} \quad \text{or} \quad \tilde{\mathbf{F}}_x = \mathbf{F}^{-1} \tilde{\mathbf{F}}_X^{-1} \mathbf{F} \tag{2.10}$$

assures that $\tilde{\mathbf{F}}_X = \tilde{\mathbf{F}}_x^{-1}$, so then the operating on the pair $d\tilde{\mathbf{X}} \rightarrow dx$ or $d\mathbf{X} \rightarrow d\tilde{x}$ is equivalent.

We can now draw a picture showing the geometrical meaning of fractional strain components – cf. Fig. 2 (\diamond stands for classical or fractional line elements). It is clear that extension (normal strain) of a (fractional) material line element $d\hat{\mathbf{X}} = |d\hat{\mathbf{X}}|e$ is defined as

$$\hat{\varepsilon} = \frac{|d\hat{x}| - |d\hat{\mathbf{X}}|}{|d\hat{\mathbf{X}}|} \quad \text{or} \quad \hat{\varepsilon} = \sqrt{1 + 2\mathbf{e} \cdot \hat{\mathbf{E}}\mathbf{e}} \Leftrightarrow \mathbf{e} \cdot \hat{\mathbf{E}}\mathbf{e} = \hat{\varepsilon} + \frac{\hat{\varepsilon}^2}{2} \tag{2.11}$$

where \mathbf{e} is a unit vector along the fibre direction.

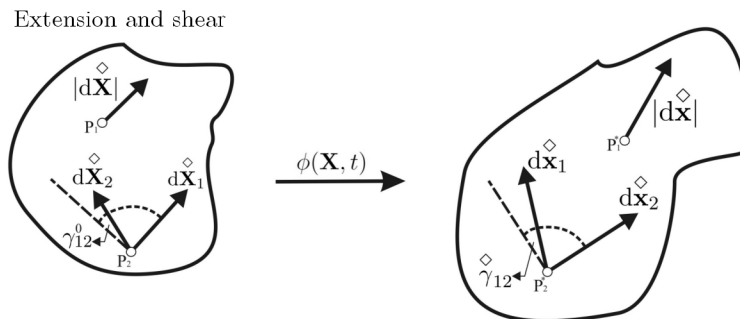


Fig. 2. Geometrical interpretation of the fractional extension and shear

The shear (shear strain) is defined by the deviation from orthogonality of two (fractional) material line elements $d\hat{\mathbf{X}}_1 = |d\hat{\mathbf{X}}_1|e_1$ and $d\hat{\mathbf{X}}_2 = |d\hat{\mathbf{X}}_2|e_2$, namely (cf. Fig. 2)

$$\sin \overset{\diamond}{\gamma}_{12} = \frac{d\overset{\diamond}{\mathbf{x}}_1 \cdot d\overset{\diamond}{\mathbf{x}}_2}{|d\overset{\diamond}{\mathbf{x}}_1||d\overset{\diamond}{\mathbf{x}}_2|} \quad \text{or} \quad \sin \overset{\diamond}{\gamma}_{12} = \frac{2\mathbf{e}_1 \cdot \overset{\diamond}{\mathbf{E}}\mathbf{e}_2 + \mathbf{e}_1 \cdot \mathbf{e}_2}{\sqrt{1 + 2\mathbf{e}_1 \cdot \overset{\diamond}{\mathbf{E}}\mathbf{e}_1} \sqrt{1 + 2\mathbf{e}_2 \cdot \overset{\diamond}{\mathbf{E}}\mathbf{e}_2}} \quad (2.12)$$

where \mathbf{e}_1 and \mathbf{e}_2 are unit vectors along the fibres directions. In the case when initially the material line elements are perpendicular, $\mathbf{e}_1 \cdot \mathbf{e}_2 = 0$.

3. Conclusions

Geometrical interpretation of the fractional strain components is the same as that for classical strain. It is because of its analogical definition which is based on fractional ('scaled') material and spatial line elements. Hence, the extension is the ratio of the difference of squares of current and initial elemental lengths and squared initial elemental length. At the same time, shear defines the deviation from orthogonality of two elemental line elements (in fractional picture they must not be initially perpendicular).

It is important that an analogous geometrical interpretation can also be applied to other competitive formulations known in the literature (cf. Section 1 and paper (Sumelka *et al.*, 2015)), where similarities between formulations are shortly listed) – however one should remember that they operate on different physical units.

References

1. ATANACKOVIC T.M., STANKOVIC B., 2009, Generalized wave equation in nonlocal elasticity, *Acta Mechanica*, **208**, 1/2, 1-10
2. CARPINTERI A., CORNETTI P., SAPORA A., 2011, A fractional calculus approach to nonlocal elasticity, *European Physical Journal Special Topics*, **193**, 193-204
3. DRAPACA C.S., SIVALOGANATHAN S., 2012, A fractional model of continuum mechanics, *Journal of Elasticity*, **107**, 107-123
4. KLIMEK M., 2001, Fractional sequential mechanics – models with symmetric fractional derivative, *Czechoslovak Journal of Physics*, **51**, 12, 1348-1354
5. LAZOPOULOS K.A., 2006, Non-local continuum mechanics and fractional calculus, *Mechanics Research Communications*, **33**, 753-757
6. PECHERSKI R.B., 1983, Relation of microscopic observations to constitutive modelling for advanced deformations and fracture initiation of viscoplastic materials, *Archives of Mechanics*, **35**, 2, 257-277
7. PODLUBNY I., 2002, Geometric and physical interpretation of fractional integration and fractional differentiation, *Fractional Calculus and Applied Analysis*, **5**, 4, 367-386
8. SUMELKA W., 2014a, A note on non-associated Drucker-Prager plastic flow in terms of fractional calculus, *Journal of Theoretical and Applied Mechanics*, **52**, 2, 571-574
9. SUMELKA W., 2014b, Application of fractional continuum mechanics to rate independent plasticity, *Acta Mechanica*, **255**, 11, 3247-3264
10. SUMELKA W., 2014c, Thermoelasticity in the framework of the fractional continuum mechanics, *Journal of Thermal Stresses*, **37**, 6, 678-706
11. SUMELKA W., ZAERA R., FERNÁNDEZ-SÁEZ J., 2015, A theoretical analysis of the free axial vibration of non-local rods with fractional continuum mechanics, *Meccanica*, **50**, 9, 2309-2323

INFORMATION FOR AUTHORS

Journal of Theoretical and Applied Mechanics (JTAM) is devoted to all aspects of solid mechanics, fluid mechanics, thermodynamics and applied problems of structural mechanics, mechatronics, biomechanics and robotics. Both theoretical and experimental papers as well as survey papers can be proposed.

We accept articles in English only. The text of a *JTAM* paper should not exceed **12 pages of standard format A4** (11-point type size, including abstract, figures, tables and references).

- The material for publication should be sent to the Editorial Office via electronic journal system: <http://www.ptmts.org.pl/jtam/index.php/jtam>

Papers are accepted for publication after the review process. Blind review model is applied, which means that the reviewers' names are kept confidential to the authors. The final decision on paper acceptance belongs to the Editorial Board.

- After qualifying your paper for publication we will require the following:
 - L^AT_EX or T_EX or Word document file
 - graphical files in grey scale, 300 dpi, in print quality (e.g.: *.png, *.bmp, *.jpg, *.eps).

Requirements for paper preparation

Contents of the manuscripts should appear in the following order:

- Title of the paper
- Authors' full name, affiliation and e-mail
- Short abstract (maximum 100 words) and 3-5 key words (1 line)
- Article text (equations should be numbered separately in each section; each reference should be cited in the text by the last name(s) of the author(s) and the publication year)
- References in alphabetical order. See the following:
 1. Achen S.C., 1989, A new boundary integral equation formulation, *Journal of Applied Mechanics*, **56**, 2, 297-303
 2. Boley B.A., Weiner J.H., 1960, *Theory of Thermal Stresses*, Wiley, New York
 3. Canon W., 1955, Vibrations of heated beams, Ph.D. Thesis, Columbia University, New York
 4. Deresiewicz H., 1958, Solution of the equations of thermoelasticity, *Proceedings of Third U.S. National Congress of Applied Mechanics*, 287-305
- Titles of references originally published not in English, should be translated into English and formulated as follows:
 5. Huber M.T., 1904, Specific work of strain as a measure of material effort (in Polish), *Czasopismo Techniczne*, **XXII**, 3, 80-81

All the data should be reported in SI units.

New *JTAM* offer for short communication!

Since July 2013, short research communications have been accepted for publication in *JTAM* with all the requirements concerning standard publications, except for their volume that is limited to 4 pages.

Contents

Ferdek U., Łuczko J. — Vibration analysis of a half-car model with semi-active damping	321
Sapiński B., Rosół M., Węgrzynowski M. — Evaluation of an energy harvesting MR damper-based vibration reduction system	333
Zhang Y. — A concentric hydrodynamic journal bearing with the boundary slippage	345
Beneš P., Valášek M. — Optimized re-entry input shapers	353
Ashouri H., Beheshti B., Ebrahimzadeh M.R. — Analysis of fatigue cracks of cylinder heads in diesel engines	369
Kluger K., Łagoda T. — Fatigue life estimation for selected materials in multiaxial stress states with mean stress	385
Beluch W., Długosz A. — Multiobjective and multiscale optimization of composite materials by means of evolutionary computations	397
Lubowiecka I., Szepietowska K., Szymczak C., Tomaszewska A. — A preliminary study on the optimal choice of an implant and its orientation in ventral hernia repair	411
Muc A., Chwał M. — Analytical discrete stacking sequence optimization of rectangular composite plates subjected to buckling and FPF constraints	423
Mallick A., Ranjan R., Sarkar P.K. — Effect of heat transfer on thermal stresses in an annular hyperbolic fin: an approximate analytical solution	437
Kołakowski Z., Teter A. — Some aspects of dynamic coupled response of functionally graded thin-walled columns with square cross-sections under in-plane pulse compression	449
Kakar R., Kakar S. — Modelling of SH-waves in a fiber-reinforced anisotropic layer over a pre-stressed heterogeneous half-space	463
Prakash J., Singh V., Kumar R., Kumari K. — The onset of convection in a rotating multicomponent fluid layer	477
Kozłowska B. — Experimental investigations of elastic-plastic strain states on various stages of material plastifying	489
Dudziak M., Malujda I., Talaśka K., Łodygowski T., Sumelka W. — Analysis of the process of wood plasticization by hot rolling	503
Ghasemi S.E., Hatami M., Salarian A., Domairry G. — Thermal and fluid analysis on effects of a nanofluid outside of a stretching cylinder with magnetic field using the differential quadrature method	517
Sulym H., Pasternak I., Piskozub L., Piskozub Y. — Longitudinal shear of a bi-material with frictional sliding contact in the interfacial crack	529
Molatefi H., Mazraeh A. — On the investigation of wheel flange climb derailment mechanism and methods to control it	541
Fadhil B.M., Ahmed P.S., Kamal A.A. — Improving mechanical properties of epoxy by adding multi-wall carbon nanotube	551
Krawiec P., Marlewski A. — Profile design of noncircular belt pulleys	561
Gupta V., Vashishth A.K. — Effects of piezoelectricity on bulk waves in monoclinic poro-elastic materials	571
Basu S., Mandal S.C. — P-wave interaction with a pair of rigid strips embedded in an orthotropic strip	579
Kaczyński A., Monastyrskyy B. — The thermoelastic problem for a penny-shaped anticrack with heat conductivity in a transversely isotropic space	593
Tounsi M., Beyaoui M., Abboudi K., Feki N., Walha L., Haddar M. — Influence of uncertainty in aerodynamic performance on the dynamic response of a two stage gear system	601
Imani Yengejeh S., Kazemi S.A., Öchsner A. — On the buckling and vibrational response of carbon nanotubes with spiral deformation	613
Wang Y., Li S., Cheng C. — Investigation on a quasi-zero-stiffness vibration isolator under random excitation	621
Ali K., Ahmad S., Ashraf M. — Numerical simulation of flow and heat transfer in hydromagnetic micropolar fluid between two stretchable disks with viscous dissipation effects	633
Filipovic M., Djuric A. — Cable-suspended CPR-D type Parallel Robot	645
Bendjama H., Boucherit M.S. — Wavelets and principal component analysis method for vibration monitoring of rotating machinery	659
<u>Short Research Communication</u>	
Sumelka W. — On geometrical interpretation of the fractional strain concept	671